

Cranfield University

Alessandro Gullia

**Thrust and Flow Prediction in Gas Turbine  
Engine Indoor Sea-Level Test Cell Facilities**

School of Engineering

PhD Thesis

Cranfield University  
School of Engineering  
PhD Thesis

February 2006

Alessandro Gullia

**Thrust and Flow Prediction in Gas Turbine Engine  
Indoor Sea-Level Test Cell Facilities**

Supervisor: Dr. K.W. Ramsden

This thesis is submitted in partial fulfilment of the requirements for the degree of  
Doctor of Philosophy

©Cranfield University 2006. All rights reserved. No part of this publication may be  
reproduced without the written permission of the copyright holder

## **Abstract**

The principal aim of this research was to provide a detailed understanding of the performance of gas turbine engines inside indoor sea-level test beds. In particular the evaluation of both thrust correction factors and the estimation of the mass flow entering the test cell were at the core of the research.

The project has been fully sponsored by Rolls-Royce plc. Initially, their principal objective was to assess the relevance and accuracy of CFD when applied to thrust measurement inside indoor test beds with an intended outcome of minimising the use of expensive experimental measurements.

The different system interfaces and accounting systems for in-flight conditions, available in the open literature have been developed and adapted for indoor environments. This has led to the definition of three different thrust correction equations using alternative definitions of thrust correction factor. Aero-dynamic principles have been applied for the derivation of one-dimensional relationships for the calculation of each thrust correction factor using generic engine-cell performance and dimensions.

A one-dimensional analytical model has been developed to represent the engine-detuner ejector pump. This is able to characterise the engine-cell system performance and is used as the main tool for providing a matching procedure capable of predicting the cell entrainment ratio.

By processing experimental data relevant to different engine-cell configurations through the ejector pump analytical model, a method for achieving the entrainment ratio control inside the cell has been identified.

The CFD work has been concentrated into three main activities:

- A quantitative extrapolation of the thrust correction factors including, the pre-entry force, the external and the total bellmouth force, the throat stream force, the intake momentum drag and the base drag.
- The representation of the engine-detuner ejector performance for a variety of engine-cell configurations.
- The modelling of the generic test cell components including the inlet stack, the cascade elbow, the exhaust stack & the blast basket.

The outcomes of this research have been very successful in enhancing the validity of the thrust correction equations developed.. In particular, the use of a one-dimensional approach in their estimation has been shown to be fully justified. The work has also emphasised the value of CFD in supporting the derivation of the matching procedure for predicting and controlling cell entrainment ratio. Indeed, one of the strongest outcomes of this work has been the conclusion that both the engine-cell characteristic lines computed with the one-dimensional model and those computed with CFD for different cell configurations are almost identical.

In addition, the use of CFD as a tool for the quantitative evaluation of the thrust correction factors has been established. Finally, the CFD results have facilitated an enhanced understanding of the complex flow structure inside indoor test cells

## Acknowledgement

Certainly, without your support, your guidance and your patient understanding my experience in Cranfield would not have been the same. Since the beginning you have been my reference to each kind of difficulty, academic and personal and your help has been each time invaluable.

Dr. KW. Ramsden thank you very much.

I will never forget the hours spent to reading and writing e-mails, those seated together around a table on the middle of English countryside trying to light a candle in the darkness. I will never forget your love for the aero-dynamics and your precious collaboration to this work.

D.D. Williams thank you.

Thanks for the trust which both you put on me and for the opportunity of staying these three years in Cranfield.

Prof. P. Pilidis and Prof. U. Desideri thanks.

Special mention to Rolls-Royce, for funding this project and for supporting it through the supervision of the Performance Engineering UTC in Cranfield University

Thank you very much to the students and the technicians who have collaborated to this project during these three years.

D. Fouflias, R.R. Dejean, G. Lachery, S. Brillat, J. Deen, D. Elysee, A. McLughlin, A. Hagues, R. Kennewell, D. Binks thank you.

Your love, reassurance and support in every single day of these years have been vital for me. Your way of thinking and of looking at things has relieved me each time I was close to fail.

Mamma e Papa', thank you for believing in me.

Together we have managed to overcome these years far from each other.

Together we have learned to enjoy the small things and to appreciate them.

Your confidence has always warmed my cold and lonely nights.

Chiara thank you.

Thank you with all my hart to all my friends.

When I arrived in Cranfield I was introduced to a greek guy who had to work with me in the UTC WP 12. At that time we did not know very much about gas turbine test facilities probably as we do not know so much about it even now. However, we worked together through each step of the project. We stumbled, we fell and we rised together. Now that guy is my friend.

Panos, there are not words to say thanks to you.

I wish you all the best, always.

# Contents

ABSTRACT .....	3
ACKNOWLEDGEMENT .....	4
CONTENTS .....	5
LIST OF FIGURES .....	8
LIST OF TABLES .....	13
NOMENCLATURE .....	14
1. INTRODUCTION .....	20
2. LITERATURE REVIEW .....	25
2.1. GAS TURBINE ENGINE TEST FACILITIES .....	25
2.1.1. Altitude Test Facilities .....	25
2.1.2. Sea-Level Test Facilities .....	27
2.1.3. Chronological Development of Sea-Level Bed for Gas Turbines Engines .....	32
2.1.4. Purposes of Sea-Level Testing .....	35
2.1.5. Outdoor vs. Indoor Sea-Level Test Facilities .....	37
2.1.6. Indoor Test Cell Components .....	39
2.1.7. Engine thrust Frame .....	45
2.1.8. Blast Basket .....	45
2.2. EJECTOR-PUMP EFFECTS IN INDOOR TEST FACILITIES .....	47
2.2.1. Engine-Detuner Ejector-Pump .....	47
2.2.2. Engine Nozzle-Detuner Spacing .....	48
2.2.3. Detuner to Nozzle Diameter Ratio .....	51
2.2.4. Effect of the primary Jet Temperature .....	54
2.2.5. Entrainment Ratio Calculation .....	55
2.3. THRUST CORRECTION FACTORS (TCF) .....	56
2.3.1. Thrust Correction Factors Definition .....	56
2.3.2. Rolls-Royce First Principle Anemometer .....	58
2.3.3. ITP Thrust Correction Methodology .....	60
2.4. FLOW PHENOMENA IN ENCLOSED TEST FACILITIES .....	63
2.4.1. Flow Distortion .....	63
2.4.2. Flow Recirculation .....	66
2.4.3. Flow Separation and Vortex Ingestion .....	70
2.4.4. Pressure Fluctuation .....	74
2.5. CFD SUPPORT TO ENGINE TEST .....	76
2.5.1. Modular Geometry Archive .....	77
2.5.2. Computational Support to Sea-Level Test Facility .....	78
3. RESEARCH OBJECTIVES .....	80
3.1. INTRODUCTION .....	80
3.2. PREVIOUS RESEARCH GAPS - OBJECTIVES & METHODOLOGIES .....	80
3.2.1. Thrust Correction Factors .....	80
3.2.2. Cell Entrainment Ratio Prediction & Control .....	81
3.2.3. CFD as Support to Indoor Sea-Level Test .....	83
3.3. CONTRIBUTION FROM THE CURRENT RESEARCH .....	84
4. THRUST CORRECTION FACTOR .....	86
4.1. INTRODUCTION .....	86
4.2. FUNDAMENTAL CONCEPTS .....	86
4.2.1. Fluid Force Definition .....	86
4.2.2. Ducted and Un-Ducted Bodies .....	87

4.2.3.	<i>Drag Definition</i> .....	90
4.2.4.	<i>Drag Definition for Ducted Body</i> .....	93
4.2.5.	<i>Thrust Definition</i> .....	95
4.2.6.	<i>Momentum Theorem and Stream Force</i> .....	96
4.2.7.	<i>Thrust as a Stream Force</i> .....	98
4.2.8.	<i>Thrust and Drag Accounting System</i> .....	99
4.2.9.	<i>Thrust and Drag Interfaces</i> .....	101
4.3.	<b>THRUST CORRECTION EQUATIONS IN ENCLOSED TEST FACILITY</b> .....	103
4.3.1.	<i>Interface Sections and NPF for Indoor Thrust Measurement</i> .....	103
4.3.2.	<i>Momentum Theorem Application on the Bellmouth</i> .....	105
4.3.3.	<i>Pseudo-infinite Cell</i> .....	107
4.3.4.	<i>Finite Cell</i> .....	110
4.3.5.	<i>Consideration on the Carcase Drag</i> .....	113
4.3.6.	<i>Finite Cell with no Parallel Walls</i> .....	114
4.3.7.	<i>TCF Equation for finite cell using explicitly <math>\Phi_{bell\ ext}</math></i> .....	114
4.3.8.	<i>1 D calculation of <math>\Phi_{Bell\ ext}</math></i> .....	116
4.3.9.	<i>1D Calculation of <math>\Phi_{pre}</math></i> .....	118
4.3.10.	<i>Considerations on the Potential Buoyancy Term</i> .....	119
4.3.11.	<i>Thrust Correction Equation for Finite Cell using <math>FG_{TH}</math></i> .....	125
4.3.12.	<i>1D Calculation of the Term (<math>F_{Gth} + \Phi_{bell}</math>)</i> .....	126
4.3.13.	<i>Cell Size and Entrainment Ratio for Fixed TCF</i> .....	130
4.4.	<b>SPECIAL CASES STUDY</b> .....	131
4.4.1.	<i>Free Air Study</i> .....	131
4.4.2.	<i>Indoor and Free Air Bellmouth Force Comparison</i> .....	135
4.4.3.	<i>Pre-entry Force</i> .....	136
4.5.	<b>THRUST CORRECTION EQUATIONS COMPARISON</b> .....	140
4.5.1.	<i>Rolls Royce Engine "C"</i> .....	141
4.5.2.	<i>Rolls Royce Test Bed "Y"</i> .....	141
4.5.3.	<i>General Assumptions for the Thrust Correction Equations Comparison</i> .....	142
4.5.4.	<i>Comparison</i> .....	145
<b>5.</b>	<b>ANALYTICAL PREDICTION TOOL</b> .....	<b>148</b>
5.1.	<b>INTRODUCTION</b> .....	148
5.2.	<b>ANALYTICAL METHOD</b> .....	148
5.2.1.	<i>Analytical Method Approach</i> .....	148
5.2.2.	<i>Analytical Model Assumptions</i> .....	151
5.2.3.	<i>Preliminary Region</i> .....	151
5.2.4.	<i>Accommodation Region</i> .....	153
5.2.5.	<i>Mixing Region</i> .....	158
5.2.6.	<i>After-Mixing Region</i> .....	162
5.3.	<b>ANALYTICAL EJECTOR MODEL APPLICATIONS</b> .....	165
5.3.1.	<i>Rolls Royce Engine "A"</i> .....	165
5.3.2.	<i>Rolls Royce Engine "B"</i> .....	166
5.3.3.	<i>Rolls-Royce Test Bed "X"</i> .....	166
5.3.4.	<i>Ejector Model Application at the Accommodation Region</i> .....	167
5.3.5.	<i>Ejector Model Application at the Mixing Region</i> .....	170
5.3.6.	<i>Ejector Model Application at the After-Mixing Region</i> .....	174
5.4.	<b>THE MATCHING PROCEDURE FOR PREDICTING THE CELL ENTRAINMENT RATIO</b> .....	177
5.4.1.	<i>Accommodation Region Non Dimensional Analysis</i> .....	177
5.4.2.	<i>Matching Procedure at the Accommodation Region</i> .....	180
5.4.3.	<i>The Uniqueness of the Engine-Detuner Characteristic</i> .....	183
5.5.	<b>THE USEFULNESS OF THE MATCHING PROCEDURE AT THE ACCOMMODATION REGION</b> .....	184
<b>6.</b>	<b>CFD MODELLING FOR ENCLOSED TEST CELL FACILITIES</b> .....	<b>187</b>
6.1.	<b>AUTHOR APPROACH TO THE CFD</b> .....	187
6.2.	<b>CFD MODELLING FOR THE CELL THRUST CORRECTION FACTORS</b> .....	188
6.2.1.	<i>Aim of Calculating the TCF by CFD</i> .....	188
6.2.2.	<i>CFD Modelling Approach and Methodology</i> .....	189

6.2.3.	<i>Model Geometry and Grid</i> .....	192
6.2.4.	<i>Boundary Conditions for Engine C in the Test Cell "Y"</i> .....	197
6.2.5.	<i>Fluent Settings</i> .....	199
6.2.6.	<i>Step-by-Step Approach for the Discretization</i> .....	200
6.2.7.	<i>Convergence Criteria</i> .....	201
6.2.8.	<i>Pre-Entry Force Calculation Methodology by Using CFD</i> .....	202
6.2.9.	<i>Pre-Entry Stream Tube CFD Considerations</i> .....	208
6.2.10.	<i>Bellmouth Force Calculation Methodology by CFD</i> .....	210
6.2.11.	<i>Base Force Calculation Methodology by Using CFD</i> .....	212
6.2.12.	<i>IMD Calculation Methodology by Using CFD</i> .....	213
6.2.13.	<i>Cradle Drag Calculation Methodology by Using CFD</i> .....	214
6.2.14.	<i>Throat Force Calculation Methodology by Using CFD</i> .....	214
6.2.15.	<i>CFD Thrust Correction Factors Results</i> .....	215
6.3.	<b>CFD STUDY OF THE ENGINE-DETUNER EJECTOR PUMP</b> .....	217
6.3.1.	<i>CFD Approach and Methodology to Study the Accommodation Region</i> .....	217
6.3.2.	<i>CFD Models for the Accommodation Region Analysis</i> .....	218
6.3.3.	<i>CFD Setting for the Accommodation Region Analysis</i> .....	220
6.3.4.	<i>CFD Accommodation Region Analysis Results</i> .....	221
6.4.	<b>CFD GENERAL COMPONENTS MODELLING TEST CELL</b> .....	229
6.4.1.	<i>Test Cell Inlet Stack Modelling</i> .....	229
6.4.2.	<i>CFD Test Cell Inlet Stack Results</i> .....	231
6.4.3.	<i>Test Cell Exhaust Stack Modelling</i> .....	233
6.4.4.	<i>Test Cell Exhaust Stack Results</i> .....	235
6.4.5.	<i>Test Cell Entire Model</i> .....	238
7.	<b>DISCUSSION</b> .....	240
7.1.	<b>INTRODUCTION</b> .....	240
7.2.	<b>FIRST LEVEL OF DISCUSSION</b> .....	240
7.2.1.	<i>Thrust Correction</i> .....	240
7.2.2.	<i>Analytical Prediction Tool</i> .....	247
7.2.3.	<i>CFD as Support to Sea-Level Test</i> .....	251
7.3.	<b>SECOND LEVEL</b> .....	261
7.4.	<b>THIRD LEVEL</b> .....	264
8.	<b>CONCLUSION AND FUTURE WORK</b> .....	272
8.1.	<b>CONCLUSION</b> .....	272
8.2.	<b>FUTURE WORK</b> .....	275
	<b>REFERENCE</b> .....	277
	<b>APPENDIX A. ANALYTICAL MODEL</b> .....	284
A1.	<b>PRELIMINARY REGION</b> .....	284
A2.	<b>ACCOMMODATION REGION</b> .....	286
A3.	<b>MIXING REGION</b> .....	289
A4.	<b>AFTER-MIXING REGION</b> .....	290
	<b>APPENDIX B. EXPERIMENTAL WORK IN CRANFIELD UNIVERSITY</b> 292	
B1.	<b>TEST BED FACILITY IN CRANFIELD UNIVERSITY</b> .....	292
B2.	<b>TEST PLAN</b> .....	306
B3.	<b>CFD MODELLING FOR THE CRANFIELD TEST BED FACILITY</b> .....	307
B4.	<b>EXPERIMENTAL AND CFD RESULTS</b> .....	309
B5.	<b>CONCLUSIONS</b> .....	318
	<b>APPENDIX C. ACCOMMODATION REGION ANALYSIS FOR DIFFERENT ENGINE POWER SETTING</b> .....	320
	<b>APPENDIX D. GRID ANALYSIS FOR THE INLET STACK</b> .....	322

# List Of Figures

Figure 2.1: Altitude Test Facility Lay-out (Osborn 1990b) .....26

Figure 2.2: Flight Envelope Used During the UETP (Osborn 1990a).....26

Figure 2.3: Outdoor Test Facility Lay-Out (Walsh and Fletcher 1998) .....28

Figure 2.4: Outdoor Test Acquisition Data Envelope (Parfitt 2001).....28

Figure 2.5: Indoor Test Facility Lay-Out (Rowlands 1984)).....29

Figure 2.6: Indoor Test Facility Components (Rowlands 1984)) .....29

Figure 2.7: General Lay-Out for Indoor Test Facilities (Jaques 1984)) .....30

Figure 2.8: Indoor Test Bed for Bare Engines and Aircraft Trimming Test (Jaques 1984)).....30

Figure 2.9: Test Cell Lay-Out for Turbohaft (Walsh and Fletcher 1998) .....31

Figure 2.10: Turboprop Test Cell Stand (Torella, Liotti, and Bruno 1988) .....31

Figure 2.11: Sir Frank Whittle Test Cell (1937) (Ashwood 1984)).....32

Figure 2.12: Test Bay No 4 at Peystock (1946) (Ashwood 1984).....33

Figure 2.13: Glen test house at Peystock (1958) (Ashwood 1984) .....33

Figure 2.14: Test Cell No. 1 of the Japan Air Lines Located in Narita (Freuler 1993) .....34

Figure 2.15: Modern Test Cell Control Room (Cell Aerospace Test Equipment ) ....35

Figure 2.16: Correlation Indoor-Outdoor.....39

Figure 2.17: Three Different Kind of Inlet Plenum: a) Horizontal, b) Vertical,.....40

Figure 2.18: Effect of the Wind and Cell Inlet Configuration on the Flow Distortion inside the cell.....41

Figure 2.19: Flow Distortion and Cell Depression for Different Cell Inlet Configurations.....41

Figure 2.20: Modern Test Chamber (Wilson 1999).....42

Figure 2.21: Indoor Sea-level Test Bed with Double Air intake (Jaques 1984).....44

Figure 2.22: Blast Basket (Wilson 1999).....46

Figure 2.23: Overall cd Prediction (Adkins and Anas 1996).....47

Figure 2.24: Effect of the Engine-Detuner Distance in the Entrainment Ratio (Large Turbofan) (Karamanlis et al. 1986).....48

Figure 2.25: Effect of the Engine-Detuner Distance in the Entrainment Ratio (Military Engines) (Karamanlis et al. 1986).....49

Figure 2.26: Nozzle Blockage Area Effect in the Cell Entrainment Ratio (Ashwood 1984) .....50

Figure 2.27: Effect of the Engine-Detuner Distance on the Thrust Measured.....51

Figure 2.28: Effect of the Detuner to Nozzle Diameter Ratio on the Entrainment Ratio .....52

Figure 2.29: Effect of the Detuner to Nozzle Diameter Ratio on the Entrainment Ratio (Vyas and Kar 1975) .....53

Figure 2.30: Computational Analysis of the Influence of the (Choi and Soh 1990) ...53

Figure 2.31: Temperature Effect on the Entrainment ratio (Quinn ) .....54

Figure 2.32: Effect of the Primary Flow Temperature on the Mixing Process (Quinn ) .....55

Figure 2.33: Thrust Correction Factors.....57

Figure 2.34: Control Volume for the Application of the Momentum Theorem .....61

Figure 2.35: Control Volume for the Calculation of the Pre-Entry Force .....62

Figure 2.36: ITP Thrust Correction Factor (Rios et al. 1998).....63

Figure 2.37: Completely Paneled Test Cell with Engine and Thrust Frame .....65



Figure 2.38: Axial Velocity Distortion in the Front Cell (Kromer-Oehler and Dietrich 1984) .....	65
Figure 2.39: Scheme of Ducted Mixing Process (Cross 1997) .....	67
Figure 2.40: Overheating Problems in ATF (Prufert and Williamson 2000) .....	67
Figure 2.41: Variation of Nozzle Strut and Cell Temperature with the Cell Pressure.....	68
Figure 2.42: Unsteady CFD Solution (Prufert, McClure, and Power 1994) .....	69
Figure 2.43: Recirculation Reduction Technique (Anderson and Graham 1968) .....	70
Figure 2.44: Axial Variation of the Pressure Coefficient, a) $\mu=0.72$ , b) $\mu=0.86$ , c) $\mu=1.15$ (Kromer-Oehler and Dietrich 1984) .....	71
Figure 2.45: Predicted Wall Separation a) Large Turbofan b) Small Engine (Kromer-Oehler and Dietrich 1984).....	72
Figure 2.46: Experimental Vortex Appearance (Freuler 1982) .....	72
Figure 2.47: Engine Operatin Margin as Function of the Entrainment Ratio (Kromer and Dietrich 1985).....	73
Figure 2.48: Vortex Ingestion Visualization (Brix, Neuwerth, and Jacob 2000) .....	73
Figure 2.49: Inlet Vortex Formation Correlation (Nakayama and Jones 1996) .....	74
Figure 2.50: Example of Pressure Fluctuations in Sea-Level Test Cell Facility .....	75
Figure 2.51: Different Blast Basket End Shape Experimentally Tested.....	75
Figure 2.52: Trend of Relative Computational Cost for Numerical Flow Simulation.....	76
Figure 2.53: Mudular Geometry Archive System (Prufert, McClure, and Power 1994) .....	78
Figure 2.54: 3D Rendering of the Test Facility Model (Prufert, McClure, and Power 1994) .....	78
Figure 2.55: 3D Simulation Results (Prufert, McClure, and Power 1994).....	79
Figure 4.1: Fluid Force Component Over a Solid Surface .....	86
Figure 4.2: $C_p$ Distribution on a Semi-Infinite Body in Potential Flow .....	88
Figure 4.3: $C_p$ Distribution for a Semi-Infinite Body in Real Flow .....	89
Figure 4.4: Semi-Infinite Ducted Body.....	89
Figure 4.5: Flow Around a Sphere: a) In-Viscid Flow b) Real Flow .....	91
Figure 4.6: Enlargement of Figure 4.5 along the Trailing Edge .....	92
Figure 4.7: Drag Components on a Ducted Body.....	95
Figure 4.8: Thrust Components on a Ducted Body .....	96
Figure 4.9: Forces Acting on the Control Volume and on the Body .....	98
Figure 4.10: Representation of the Forces acting on a Duct .....	99
Figure 4.11: Representation of the forces acting on a single stream nacelle .....	100
Figure 4.12: Representation of the Forces Acting on a Centre Body Nacelle .....	102
Figure 4.13: Simplified Test Chamber for Sea-Level Test Bed Facility .....	104
Figure 4.14: Representation of the Forces Acting on the Metric Assembly.....	105
Figure 4.15: Engine Bellmouth (Courtesy of Rolls-Royce) .....	106
Figure 4.16: Sharp Lip Intake .....	106
Figure 4.17: Stagnation Point on the Engine Bellmouth.....	107
Figure 4.18: Momentum Box Used for Moving to Station (1) to Station (0).....	109
Figure 4.19: Control Volume for Calculating the Potential Buoyancy Term.....	109
Figure 4.20: Momentum Box for Calculating the Potential Buoyancy between ( $1_{ext}$ ) and ( $9_{ext}$ ) .....	112
Figure 4.21: Momentum Box for Calculating the Potential Buoyancy between ( $1_{ext}$ ) and ( $9'_{ext}$ ) .....	112
Figure 4.22: Engine After-Body Nomenclature.....	112
Figure 4.23: Cell with not Parallel Walls.....	114

Figure 4.24: Momentum Box for Calculating the Potential Buoyancy Term between (f) and $(9_{ext})$ .....	115
Figure 4.25: Momentum box for calculating the force acting on the external bellmouth .....	116
Figure 4.26 Momentum Box for Calculating the Pre-Entry Force .....	119
Figure 4.27: Different Momentum Boxes for Computing the Potential Buoyancy Term .....	120
Figure 4.28: Effect of the Engine Nozzle Radius in the Potential Buoyancy Effect .....	122
Figure 4.29: Entrainment ratio Effect in the Potential Buoyancy Term .....	123
Figure 4.30: Cell cross Section Area Effect in the Potential Buoyancy Term.....	124
Figure 3.31: Representation of the Forces Acting on the Bellmouth.....	125
Figure 4.32: Representation of the momentum box for calculating the term $(F_{Gth} + \Phi_{bell})$ .....	127
Figure 4.33: Parametric Analysis of the Term $(F_{Gth} + \Phi_{bell})$ Function of $\lambda$ and $\mu$ .....	129
Figure 4.34: Possible Combination of $\lambda$ and $\mu$ for Matching $(F_{Gth} + \Phi_{bell})/L = 1.05$ ..	131
Figure 4.35: Momentum Box for free air Studies .....	132
Figure 4.36: Momentum Box from the Engine Throat to Station (0) in Free Air.....	133
Figure 3.37: Outdoor Momentum Box for Low Free Stream Velocity .....	134
Figure 4.38: Momentum Box for Computing the Pre-Entry Force .....	136
Figure 4.39: $(p-p_0)$ Average as Function of $\mu$ .....	139
Figure 4.40: Pre-Entry Force as Function of $\mu$ .....	139
Figure 4.41: $(p-p_0)$ Average as Function of the Cell Cross Sectional Area .....	140
Figure 4.42: Pre-Entry Force as Function of the Cell Cross Sectional Area .....	140
Figure 4.43: Longitudinal Section of the Rolls Royce Test Bed "X"(Courtesy of Rolls-Royce) .....	142
Figure 4.44: Transversal Section of the Rolls Royce Test Bed "X"(Courtesy of Rolls-Royce) .....	142
Figure 4.45: Turbofan Hanged in a Cradle inside a Test Facility (Courtesy of Rolls-Royce) .....	144
Figure 6.1: Sea-Level Test Cell .....	190
Figure 6.2: CFD Model for Turbojet Engine .....	192
Figure 6.3: Bonduary Condition for a Turbofan Engine.....	192
Figure 6.4: Bellmouth Front View .....	193
Figure 6.5: Bellmouth Rear View .....	193
Figure 6.6: Metric Assembly Side View .....	193
Figure 6.7: Metric Assembly Rear View .....	194
Figure 6.8: Flow Separation and Recirculation in the Rear Part of the Cell.....	195
Figure 6.9: Flow Path around the Engine.....	195
Figure 6.10: Test Chambre Geometry.....	196
Figure 6.11: Enlargement of Figure 6.10 around the Bellmouth .....	196
Figure 6.12: Overview of the Mesh for Engine C in Test Cell "X" .....	197
Figure 6.13: Grid around the Bellmouth for Engine C in Test Cell "X" .....	197
Figure 6.14: Grid around the Bellmouth for Engine C in Test Cell "X" .....	197
Figure 6.15: Boundary Conditions.....	198
Figure 6.16: Pre-Entry Stream Tube .....	202
Figure 6.17: Static Pressure Contour around the Bellmouth .....	203
Figure 6.18: Static Pressure Distribution around the Bellmouth Lip.....	204
Figure 6.19: Flow Path Lines Realesed from the Rake.....	204
Figure 6.20: Enlargement of the Flow Path Lines From the Rake.....	205

Figure 6.21: Cordinate of the Stream Line which Defines the Pre-Entry Stream Tube .....	205
Figure 6.22: Discretization of the Stream Line.....	206
Figure 6. 23: Stagnation Points Used for the Calculation of the Pre-Entry Force.....	206
Figure 5.24: Area Associated at each Discretization Point.....	207
Figure 6.25: Pre-Entry Stream Tube Dimensions .....	208
Figure 6.26: Gauge Static Pressure along the Stagnation Stream Lines .....	208
Figure 6.27: Velocity Plots across the Pre-Entry Stream Tube .....	209
Figure 6.28: Superimpose of Figure 6.25 and Figure 6.28 .....	210
Figure 6.29 Static Pressure Plots across the Pre-Entry Stream Tube.....	210
Figure 6.30: Bellmouth Surfaces .....	211
Figure 6.31: Location of the Static Pressure Probes during the Experimental Tests.	212
Figure 6.32: Static Pressure Contour along the Fan Duct.....	213
Figure 6.33: Velocity Profile 15m Up-Stream the Engine.....	213
Figure 6.34: Model of Test Cell "X" Main chamber .....	218
Figure 6.35: Model of Test Cell "X" Main Chamber .....	219
Figure 6.36: View of the Grid for the Accommodation Region Analysis .....	219
Figure 6.37: Model of Test Cell "X" Main Chamber without the Cradle.....	219
Figure 6.38: Model of Test Cell "X" Main Chamber with a Detuner 45 m Long.....	220
Figure 6.39: Model of Test Cell "X" Main Chamber with a Detuner 95 m Long.....	220
Figure 6.40: Model of Test Cell "X" Main Chamber with a Detuner 145 m Long...	220
Figure 6.41: Visualization of the Accommodation Region in the Computational Model .....	222
Figure 6.42: Static Pressure at the Accommodation Region, Computational Results .....	223
Figure 6.43: Static Pressure at the Accommodation Region, Computational Results (no-Cradle).....	223
Figure 6.44: Static Pressure at the Accommodation Region for Different Detuner Length .....	224
Figure 6.45: Operating Point for Different Detuner Length and the A.R. Ejector Characteristic.....	224
Figure 6.46: Location of the two Lines for the Pressure Study along the Detuner....	225
Figure 6.47: Total Pressure Trend Along the Detuner (45 m) .....	225
Figure 6.48: Total Pressure Trend Along the Detuner (95 m) .....	225
Figure 6.49: Total Pressure Trend Along the Detuner (145 m) .....	226
Figure 6.50: Total Pressure Profile at the Detuner Outlet (45m).....	226
Figure 6.51: Total Pressure Profile at the Detuner Outlet (95m).....	227
Figure 6.52: Total Pressure Profile at the Detuner Outlet (145m).....	227
Figure 6.53: Static Pressure Trend along the Detuner for Primary and Secondary Flow (45m).....	227
Figure 6.54: Static Pressure Trend along the Detuner for Primary and Secondary Flow (95m).....	228
Figure 6.55: Static Pressure Trend along the Detuner for Primary and Secondary Flow (145m).....	228
Figure 6.56: Effect of the Pressure Losses on the Engine-Detuner Characteristic ....	229
Figure 6.57: Geometry of a Turn Wind Deflector .....	230
Figure 6.58: Geometry and Grid of the Inlet Stack.....	231
Figure 6.59: Mass Flow History for the two Simulations with Different Grid.....	231
Figure 6.60: Recirculation without the Cascade Turn Wind.....	232
Figure 6.61: Flow Recirculation and Re-Ingestion .....	232
Figure 6.62: Flow Profiles a) no Turning Wing b) with Turning Wing .....	233

Figure 6.63: Flow Paths With Turning Wind.....	233
Figure 6.64: Exhaust Stack Model.....	235
Figure 6.65: Static Pressure Profiles for Different $C_2$ .....	235
Figure 6.66: Velocity Vector inside the Blast Basket Using P Profiles as Inlet Boundary.....	236
Figure 6.67: Pressure Drop across the Blast Basket.....	237
Figure 6.68: Pressure Trend along the Vertical Stack.....	237
Figure 6.69: Entire Test Cell Model.....	238
Figure 7.1: Parametric Analysis of the Term $(F_{Gth} + \Phi_{bell})$ Function of $\lambda$ and $\mu$ .....	244
Figure 7.2: Non-Dimensional Representation of the Cell Operating and Characteristic Line.....	249
Figure 7.3: Non-Dimensional Representation of the Cell Operating and Characteristic Lines.....	249
Figure 7.4: Matching Procedure Using the Non-Dimensional Primary Mass Flow at P.R.....	250
Figure 7.5: Characteristic at the Accommodation Region for Models with and with the Cradle.....	257
Figure 7.6: Effects of Detuner Lengths on the Operating Point at the Accommodation Region.....	257
Figure 7.7: Comparison between Analytical and CFD Results in the A.R.....	262
Figure 7.8: Comparison between the Engine-Cell Operating Line Worked Out by the Analytical Ejector Pump Model for the Actual Cell Configuration and Two Different Operating Points Representing the Extreme Working Conditions for the Ejector Pump Characteristic Curve.....	265
Figure 7.9: Different System Operating Lines for Different $\Delta P\%$ of the System.....	265
Figure 7.10: Predicted (Red) and Desired (Green) Cell Entrainment Ratio.....	266
Figure 7.11: Operating Point for the Actual Cell Configuration.....	266
Figure 7.12: Prediction and Controlling Matching Procedures.....	267
Figure 7.13: Block Scheme.....	271

## List of Tables

Table 2.1: Degree of Complexity of the Instrumentation Required for Different Test Purposes (Holmes 1984) .....	37
Table 4.1: Summary of the Thrust and Drag Interfaces (MIDAP 1980) .....	103
Table 4.2: R-R Engine “C” Specifications (Rolls-Royce plc. ) .....	141
Table 4.3: Engine and Cell Measurement (Rolls-Royce ) .....	141
Table 4.4: Calculated Thrust Correction Factors .....	145
Table 5.1: R-R Engine “A” Specification (Rolls-Royce plc. ) .....	166
Table 5.2: R-R Engine “B” Specification (Rolls-Royce plc. ) .....	166
Table 6.1: CFD Thrust Correction Factors .....	215
Table 6.2: Static Pressure at the Detuner Outlet and the $\mu$ Obtained as results .....	221
Table 6.3: Static Pressure at the Detuner Outlet and the $\mu$ Obtained as results (no-cradle model) .....	222
Table 6.4: Different Detuner Length, Static Pressure Outlet and $\mu$ Obtained .....	223
Table 6.5: a) B.B. Real Diameter b) B.B. Equivalent Diameter .....	234
Table 6.6: Result Extracted from the Entire Model .....	239
Table 7.1: Thrust Correction Factors .....	243
Table 7.2: Thrust Correction Equation Comparison .....	245
Table 7.3: Static Pressure Comparison for the Base Force Calculation .....	254
Table 7.4: Velocity around the Cradle .....	254
Table 7.5: TCF Computed Using CFD Results .....	255
Table 7.6: Thrust Correction Equation Comparison .....	255
Table 7.7: Thrust Correction Equation Comparison CFD-1-D .....	261
Table 7.8: Thrust Correction Factor Comparison CFD-1-D .....	261
Table 7.9: Parameters for the Thrust Correction Factors Relationship .....	263
Table A. 1: Preliminary Region Starting Parameters .....	284
Table B.1: AMT Olympus Parameters .....	300
Table B.2: Static Probes Position along the Detuner .....	303
Table B.3: summary of the MEaurements .....	306
Table B.4: Different Engine Detuner Tested .....	307
Table B.5: Different Cradle Blockage Areas Tested .....	307

## Nomenclature

### Greek Symbols

$\alpha$	Permeability
$\gamma$	Specific Heat Ratio
$\Delta$	Difference
$\Delta m$	Blast Basket Thickness
$\lambda$	Cell Cross Sectional Area / Engine Throat Area
$\eta$	Efficiency
$\theta$	Angle between the Axial and the Tangential Direction
$\pi$	One radian
$\rho$	Density
$\tau$	Shearing Stress
$\Phi$	Axial Force
$\Phi_v$	Axial Viscous Force
$\psi$	Porosity
$\mu$	Entrainment Ratio: $W_{\text{secondary}}/W_{\text{primary}}$
$\mu^*$	Predicted Entrainment Ratio
$\mu'$	Desired Entrainment Ratio
$\mu_F$	Wall Shear Force Coefficient

### *Symbols*

“A”	Rolls Royce Engine
A	Area
acc	Accommodation Section
atm	Atmospheric Condition
aver	Average

“B”	Rolls Royce Engine
b	Area Cell station (9) over Area Cell at Section (0) ratio
bell	Bellmouth
C	Rolls Royce Engine
c	Area Nozzle over Area Cell at Station (0) ratio
Cp	Pressure Coefficient
cp	Specific Heat at Constant Pressure
Cd	Drag Coefficient
Cd <sub>overall</sub>	Discharge coefficient for the Blast Basket
cell	Test Cell Conditions
comb	combustion
Cx	Measured over Calculated Thrust Ratio
C <sub>2</sub>	Pressure Jump Coefficient
D	Drag
d	Diameter
D <sub>det</sub>	Detuner Diameter
D <sub>noz</sub>	Engine Nozzle Diameter
D <sub>metric</sub>	Drag of the Metric Assembly Until Station (9)
D <sub>metric</sub>	Drag of the Engine Carcase Until Station (9)
dA	Element of Area Normal to the Axial Direction
dS	Element of Area
e	Area Nozzle over Area Cell at Section (0) ratio
eng	Engine
ext	external
F	Absolute Force

$F_m$	Load Measure by the Load Cells
$F_N$	Standard Net Thrust
$F'_N$	Overall Net Thrust
$f$	Area Engine at Station (f) over Area Cell at Section (0) ratio
$G$	Gauge Value
$H$	Total Hentalpy
$H_c$	Distance form th flor to the engine centre line
$i$	Inlet
$int$	Internal
$intr$	Intrinsic
$K_{MT}$	Pressure Losses Coefficient at the After-Mixing Region
$L$	Load Measured by the Load Cells
$M$	Mach number
$max$	Maximum
$metric$	Metric-assembly
$min$	Minimum
$N$	Running Speed
$\bar{n}$	Vector Normal to the Surface
$noz$	Nozzle
$P$	Stagnation Pressure
$p$	Static Pressure
$q$	Dynamic Head
$R$	Universal Gas Constant
$T$	StagnationTemperature
$t$	Static Temperature



v	Velocity
W	Mass Flow
X	Rolls-Royce Test Cell
Y	Rolls-Royce Test Cell
(f)	Test Cell Defined Behind the Bellmouth
(f <sub>ext</sub> )	Test Cell Defined Behind the Bellmouth, Excluding the Engine portion of Area
(f <sub>int</sub> )	Test Cell Defined Behind the Bellmouth, Including the Engine portion of Area
(0)	Test Cell Reference Section Up-Stream to the Engine
(0 <sub>ext</sub> )	Test Cell Reference Section Up-Stream to the Engine, Excluding the Pre-Entry Stream Tube Cross Sectional Area
(0 <sub>int</sub> )	Test Cell Reference Section Up-Stream to the Engine, Including only the Pre-Entry Stream Tube Cross Sectional Area
(1)	Test Cell Section Defined by the Stagnation Point of the Pre-Entry Stream Tube on the Bellmouth
(1 <sub>ext</sub> )	Test Cell Section Defined by the Stagnation Point of the Pre-Entry Stream Tube on the Bellmouth, Excluding the portion of area Internal the Bellmouth
(1 <sub>int</sub> )	Test Cell Section Defined by the Stagnation Point of the Pre-Entry Stream Tube on the Bellmouth, Excluding the portion of area External the Bellmouth
(9)	Test Cell Section Defined at the Engine Nozzle Plain
(9 <sub>ext</sub> )	Test Cell Section Defined at the Engine Nozzle Plain, Excluding the Nozzle Area
(9 <sub>int</sub> )	Test Cell Section Defined at the Engine Nozzle Plain, Including only the Nozzle

## **Sub-Scripts**

Atm	Atmospheric Condition
m	Mixing Region

m'	After-Mixing Region
pc	Primary Cold Nozzle
ph	Primary Hot Nozzle
post	Post-Exit
pot	Potential Flow
pre	Pre-Entry
ref	Reference Section
s	Secondary Flow
st	Stone Guard
th	Throat Section
2	Accommodation Region Section

## **Abbreviations**

AIAA	American Institute Aeronautic and Astronautic
AEDC	Arnold Engineering Development Centre
AGARD	Advisory Group for Aerospace Research and Development
A.M.R.	After-Mixing Region
ARC	Aeronautical Research Council
A.R.	Accommodation Region
ATF	Altitude Test Facility
CFD	Computational Fluid Dynamic
FAR	Fuel Air Ratio
GE	General Electric
IMD	Intake Momentum Drag
ISA	International Standard Atmosphere
LES	Large Eddy Simulation

LHV	Lower Heating Value
MFR	Mass Flow Ratio $A_0/A_1$
MIDAP	Ministry-Industry Drag Analysis Panel
MPH	Miles per Hour
M.R.	Mixing Region
ndmf	Non Dimensional Mass Flow
NGTE	National Gas Turbine Establishment
NPF	Net Propulsive Force
P.R.	Preliminary Region
RANS	Reynolds-Average Navier Stokes
RR	Rolls-Royce
SLTF	Sea-Level Test Facility
TCF	Thrust Correction Factor
UETP	Universal Engine Test Program

# 1. Introduction

Both engine manufacturers and airlines share the requirement to test the engine to determine performance, verify repairs and ensure proper function of each engine component. In general the various types of test activities can be divided in two categories: research and development and production.

Within the research and development category four different types of test can be identified namely, the design test, the proofing test, the capability test and the trouble shooting test. All of them are aimed at supporting the engine manufacturer in the development and the certification of the engine. The production tests include the acceptance tests post-overhaul. Although this need not be done necessarily by the engine manufacturers it must meet the design authority specification.

Each of the above test purposes needs its specific test facility with its own specific instrumentation.

The facilities for gas turbine engine test can be divided into two main categories, namely, altitude and the sea-level test beds.

The former are indoor facilities used to assess the engine performance under the same conditions as those which the engine has to operate during its lifetime.

The latter can be outdoor and indoor facilities and with a corresponding lower degree of complexity, when compared with the altitude facilities.

These are used for the entire above specified test purposes. Indeed, now days, during the design and development of a gas turbine engine, only a few specific and essential tests are made in altitude test facilities to optimise various designs.

The research program described in this thesis deals with the gas turbine engine test in sea-level conditions. In particular within this category the indoor test cells represent the main topic towards which the studies have been addressed.

The main difference between sea-level indoor and outdoor tests is centred on the fulfilment of the fundamental requirements that each kind of test has to meet such as accuracy in performance measurement, reliability and repeatability.

The "free air" outdoor is the "ideal" environment for measuring the thrust delivered by the engine. Indeed, in such conditions the engine draws only the air necessary to satisfy its thermodynamic cycle and therefore, in case of no-wind, the thrust measured is the real gross thrust delivered by the engine. Accordingly, this satisfies the main requirement for the accuracy in performance measurement.

However, the outdoor tests have to face all the issues related to the weather conditions which affect the reliability and the repeatability of the results. Furthermore, they have also to meet all the requirements related with the regulations of noise pollution.

Together, the above described restrictions make of an outdoor test an extremely expensive and time consuming way to assess the performance of a gas turbine engine.

Accordingly it is standard practice to conduct most engine tests in indoor cells and correct the data acquired for the enclosure effects. Indeed, in indoor conditions the engine does not draw only the air necessary for its cycle (primary flow) but an additional amount of air enters the cell (secondary flow) as consequence of the interaction between the engine and the cell exhaust system. Indeed, the engine and the exhaust collector duct (detuner) give rise to an ejector pump effect which allows the secondary mass flow to enter the cell and by-pass the engine. The ratio between the secondary and primary mass flows is usually called the entrainment ratio.

The secondary mass flow is responsible for several aerodynamic forces around the engine which do not allow the measurement of the real thrust delivered by the engine. Therefore, the evaluation of these aerodynamic effects is necessary for determining the real thrust delivered by the engine.

$$\text{Engine Gross Thrust} = \text{Thrust Measured} + \sum \text{aerodynamic forces acting on the engine} \quad (1.1)$$

Equation (1.1) is a thrust correction equation and the elements inside the summation sign are usually called thrust correction factors.

At the same time, the quality of the flow distribution inside the cell represents another issue for indoor tests. It is, for example important to keep this under control in order to avoid flow distortion, separation, recirculation and flow fluctuations. Indeed, these flow phenomena can affect the engine performance and even damage it.

An indoor test environment, however, represents the best solution in terms of reliability and repeatability. Moreover, problems related with the noise pollution can be better controlled indoors.

This research has been fully supported by Rolls-Royce plc.

Their principal objective was to assess the relevance and accuracy of CFD when applied to thrust measurement in indoor sea-level test bed facilities. A parallel ambition was to minimise the use of expensive experimental measurements.

The scope of this research has been defined by the requirements described above and the fact that there are significant gaps in the relevant literature.

Accordingly, the work includes the use of CFD for the estimation of thrust correction factors. In addition the work includes an analytical derivation of the various thrust corrections equations. It has been adjudged also necessary to evaluate the total thrust correction factors using different engine-cell interfaces.

Using a one-dimensional approach initially, a study is carried out to derive useful relationships for quantifying the single thrust correction factors through ordinary cell measurement.

In this research program issues relating to both thrust and mass flow measured in indoor sea-level test are considered

This involves the use of an analytical ejector pump theory to characterise the engine-cell system. This analysis is verified CFD modelling predictions.

The activities listed above converge towards a final outcome for this research which can be synthesised as:

*The development of an analytical tool able to predict and control test cell entrainment ratios in indoor sea-level test cells and which is capable of providing a quantification of the real thrust delivered by an engine.*

This thesis has been divided into a further seven chapters.

**Chapter 2** includes a literature review on indoor sea-level test facilities for gas turbine engines. This starts with a classification of the different types of facility, their

chronological development and their purposes to include a description of the main test cell components.

The second part of the literature review is dedicated to past studies of the effects of engine-detuner ejector pump on the flow inside the cell. In particular, different ejector parameters are taken into account such as the spacing between the engine and the detuner, the nozzle-detuner diameter ratio and the primary jet conditions. Furthermore, an energy balance inside the cell is proposed as a method for computing the cell entrainment ratio.

The third part of the literature review deals with the thrust correction factors. The Rolls-Royce and the ITP experiences are reported for the description of the method actually in use for correcting the thrust measured inside the cell.

The fourth part describes the flow phenomena inside the cell such as distortion, recirculation, separation and fluctuation. Useful guidelines are provided to protect the cell from adverse flows which can compromise the stability of the engine and of the measurement systems.

In the fifth part of the literature review, some CFD approaches for modelling the indoor test cell facilities are reported.

**Chapter 3** underlines the objectives for each area of work of this research programme. In particular, the contributions to knowledge given by this research are highlighted.

**Chapter 4** deals with the definition of different thrust correction equations and with the derivation of useful relationships for computing the majority of the elements of the equations derived.

The first part of this chapter is dedicated to the definition of the aerodynamic first principles which allow the distinction between thrust and drag.

The second part is dedicated to the study of the different system interfaces and accounting systems used in the literature for in-flight conditions and their application in the environment of an indoor sea-level test facility. A pseudo-infinite cell is used as a link between the two conditions.

In the third part of chapter 4 three different thrust correction equations are derived using an hybrid accounting system with different interfaces. For example, using a one-dimensional aerodynamic approach, useful relationships for the calculation of the majority of the thrust correction factors are derived. Graphical trends are presented to visualise the effects of the engine-cell performance and dimensions on the thrust correction factors.

The fourth part of Chapter 4 is dedicated to two special studies. The first is the free air aerodynamics and the second is the pre-entry force. The former underlines the aerodynamic differences between indoor and outdoor cases. The latter characterises the force acting on the engine pre-entry stream tube as a function of the cell dimensions and entrainment ratio.

Finally, the fifth part of Chapter 4 shows a comparison between the different thrust correction equations derived using actual Rolls-Royce data for engine "C" in the Derby test cell "Y".

**Chapter 5** deals with the development of an ejector pump model to characterise the engine-cell system. The model is based on the separation of the detuner into four different regions: the Preliminary Region, the Accommodation Region, the Mixing Region and the After-Mixing Region.

The flow conditions in the above regions are derived using analytical procedures which are described in the first part of the chapter.

The second part of the chapter presents the application of the engine-detuner ejector pump analytical model using Rolls-Royce data for the engines "A" and "B" in Derby test cell "X". The results are shown in graphical format and consist of the representation of the engine-detuner characteristic lines and of the engine-cell operating lines.

The third part of the chapter describes a non-dimensional analysis aimed at the possibility of deriving a graphical representation for defining a unique engine-cell operating line for different engines.

The results of the non-dimensional analysis are used in the fourth part of the chapter as relevant contributions for the definition of a matching procedure which allows the prediction of the cell entrainment ratio. The main characteristic of this prediction tool is that it works by using ordinary engine-cell performance and dimensional parameters.

**Chapter 6** deals with the CFD work carried out in the research program.

It starts with the author's approach to CFD and with his distinction between the CFD user and developer.

The first part of the chapter is dedicated to modelling the Rolls-Royce engine "C" in Derby test cell "Y". Particulars of the software settings and of the modelling are discussed. In this part of the chapter the methodology followed to match the actual cell entrainment ratio with the CFD models is also described. The main use of the model developed in this section is the quantitative estimation of the thrust correction factors. Thereby, the methodology adopted for the calculation of each one of the thrust correction factors is illustrated.

A comparison is made between the different thrust correction equations derived in Chapter 4 using the extrapolated data from the proposed CFD model.

The second part of Chapter 6 is dedicated to the study of the engine-detuner ejector pump effect with the use of the CFD. Different models are used for deriving the engine-cell ejector characteristics and to understand how the operating points of system move along them. Different models include different cradle blockage areas and different detuner lengths.

The third part of the chapter outlines several attempts for modelling different test cell components such as the inlet system, the exhaust system and the blast basket. The CFD settings are discussed as the results obtained.

**Chapter 7** deals with the discussions of the findings of the above previous chapters.

The discussions are structured in three levels.

In the first level the findings of each chapter are discussed separately one by one.

In the second level the findings of different chapters are compared and discussed.

In the third level the findings of this research are gathered together, discussed and presented as a unique tool able to predict and control the cell entrainment ratio and to provide a quantification of the real thrust delivered by the engine.

In this chapter the achievement of the objectives stated in Chapter 3 are discussed.

**Chapter 8** includes the Conclusion and the future work outlined by this research.

The main body of this thesis is followed by four appendixes.

While APPENDIX A, APPENDIX C and APPENDIX D are integrations respectively of Chapter 5 and Chapter 6, APPENDIX B includes the experimental work carried out at Cranfield University as support of this research. The reason this is not included in the main body of the thesis is that it has already been published by the author in an international conference (AIAA 43<sup>rd</sup> Aerospace Meeting and Exhibit 2005 in Reno) In addition, it is also part of the theses of those Master student's contributing to this research.



## 2. Literature Review

### 2.1. Gas Turbine Engine Test Facilities

Engine test facilities are designed to assess engine operation and performance under well controlled conditions. They are divided into two types, the Sea-level Test Facility (SLTF) and the Altitude Test Facility (ATF).

The most common is the sea-level test facility where the engine operates atmospheric conditions.

The Altitude Test Facility is provided with extensive compressor, exhaust, heater and dryer equipment in order to independently control the temperature and the pressure at the engine inlet and exhaust. In such a way the engine operates under a wide range of conditions simulating different altitude and Mach number.

#### 2.1.1. Altitude Test Facilities

In this paragraph only the most important characteristics of an altitude test facility are described. Indeed, the ATF are not the main facilities that this thesis deals with and they are included in this paragraph only for a descriptive purpose.

Most Altitude Test Facilities are designed so that the inlet air flows through the inlet duct directly into the engine. This kind of arrangement is called "connected" and enables the flight conditions to be simply controlled by a relatively simple plant layout.

An essential feature of the altitude test facility is the separation of the inlet of the engine from the exhaust which allows the engine to operate under a wide range of temperatures, pressures (altitudes) and Mach numbers. This can be seen in Figure 2.1 which represents the layout of one of the Altitude Test Facility at the Royal Aerospace Establishment in Peestock, England (Osborn 1990b).

The design of the inlet ducting needs special attention so that it provides the engine under test with a total pressure profile which is closely related to the flow field the engine would experience in the actual installation in flight.

At the same time, the inlet ducting usually incorporates some method of determining the engine mass flow which is a primary measurement requirement.

The following advice for the design of Altitude Test Facility is directly reported from the lecture given by A.R. Osborn in the Agard Lecture Series (Osborn 1990a).

The inlet ducting design should keep the divergence angle below 7°. The instrumentation inside the inlet duct should be kept to the minimum in order to avoid flow distortion inside the ducting.

Usually in the ATF the test conditions are controlled by adjusting three primary variables to achieve true flight conditions: inlet temperature, inlet pressure and ram ratio. Figure 2.2 shows a typical flight envelope (Osborn 1990a) used during the Universal Engine Test Program, one of the most extensive test cells programmes (Propulsion and Energetics Panel Working Group 15 1990).

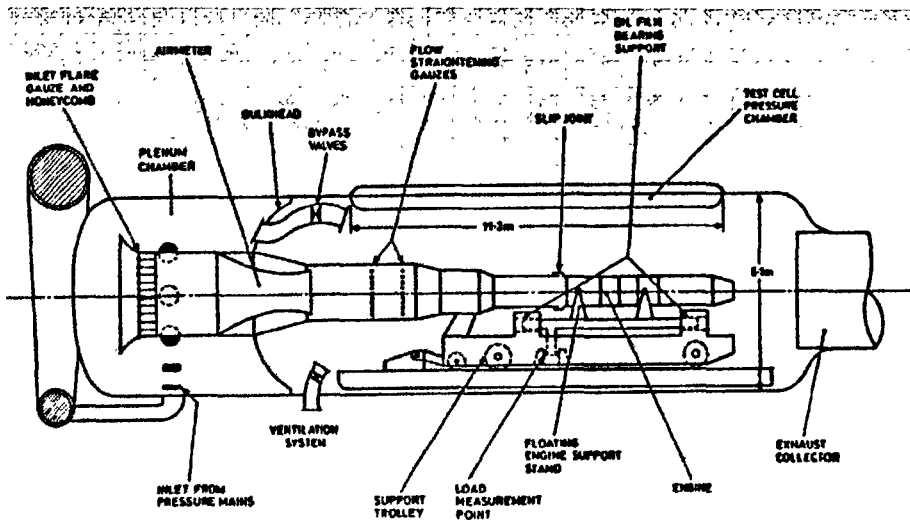


Figure 2.1: Altitude Test Facility Lay-out (Osborn 1990b)

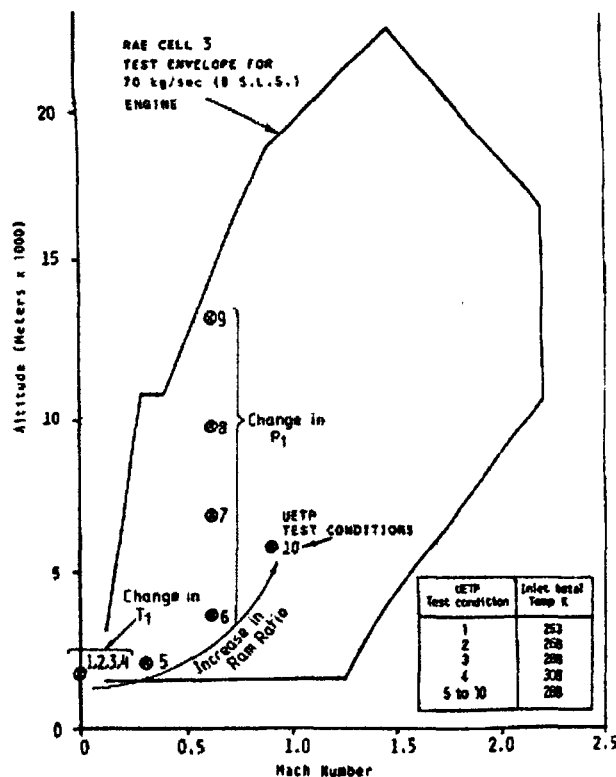


Figure 2.2: Flight Envelope Used During the UETP (Osborn 1990a)

In the flight envelop represented above the changes in  $T_1$  are at constant Mach number. The change in  $P_1$  gives a constant Mach number and changing in altitude and the change in ram ratio leads to both change in Mach number and altitude (Osborn 1990a).

A particular notation regarding the ATF has to be made for the thrust measurement system where a slip joint separates the inlet section from the engine providing a plane at which all the inlet forces can be accounted. Therefore, the load measured by the

load cell does not represent the gross thrust delivered by the engine, but the difference between forces at the slip joint and at the exhaust nozzles. Allowances have to be made for external pressure forces along the engine carcass, skin friction forces resulting from chamber cooling flows, stand forces and other parasitic forces.

A more detailed treatment of this force is given in Chapter 4 when the forces acting on the metric assembly of indoor sea-level test cells are analysed.

Another particular feature of the ATF is the necessity to provide the engine with dry and cold air. An interesting study of the drying and cooling system is presented by P.F. Ashwood of the National Gas Turbine Establishment (NGTE) in 1972 (Ashwood 1972). At that time, for capital cost issues the plant capable of supply continuously dry and cold air was substituted with an intermittent storage system cooled using Freon as refrigerant.

As example for the possible studies carried out in an ATF the cell at the NGTE has also the capability of testing the engine in wet icing condition to allow the anti-icing equipment to be evaluated.

### **2.1.2. Sea-Level Test Facilities**

Sea-Level test facilities are more common than altitude cells primarily due to the complexity as well as the capital and operating cost.

Sea-Level cells for gas turbine engine can be divided in two groups: the outdoor stands and the indoor or enclosed test cell.

The advantages and the disadvantages of both the configurations are taken into account in paragraphs 2.1.5, now the attention is dedicated only to the different configuration of the facilities.

An outdoor cell consists basically of an open air stand supporting the engine and providing the thrust measurements.

The immediate test bed area has to be free of obstructions to assure the validity of the thrust measurements and to avoid flow distortion which can affect the engine performance. Also the thrust stand is located at a suitable elevation off the ground to eliminate inlet flow interferences.

Figure 2.3 shows a general lay-out for outdoor cells.

From this picture it is possible to notice that the airmeter inlet is a bellmouth.

Indeed, in the design of these facilities special attention is dedicated to avoid the influence of ambient disturbances as the wind which could seriously affect the test results.

For this reason the bellmouth can also be supported by a large mesh screen fitted around the engine (Walsh and Fletcher 1998).

Figure 2.4 shows an outdoor acquisition data envelope which limits the data acquisition when the wind conditions exceed some limits (in the vertical axes is represented the wind velocity in MPH) (Parfitt 2001).

A general indoor test cell is a set of building consisting of the test-bay with inlet and outlet channels, the control room, preparation area and the equipment room.

The test bay (or test main chamber) is the section where the engine is located in its thrust measurement stand during the test.

From the control room the engine is fully controlled during the test. Often, this is also the room where all the data acquisition systems and data reduction processors are located.

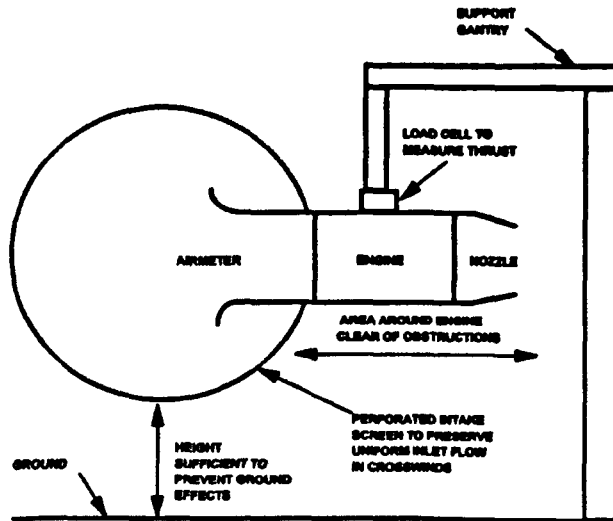


Figure 2.3: Outdoor Test Facility Lay-Out (Walsh and Fletcher 1998)

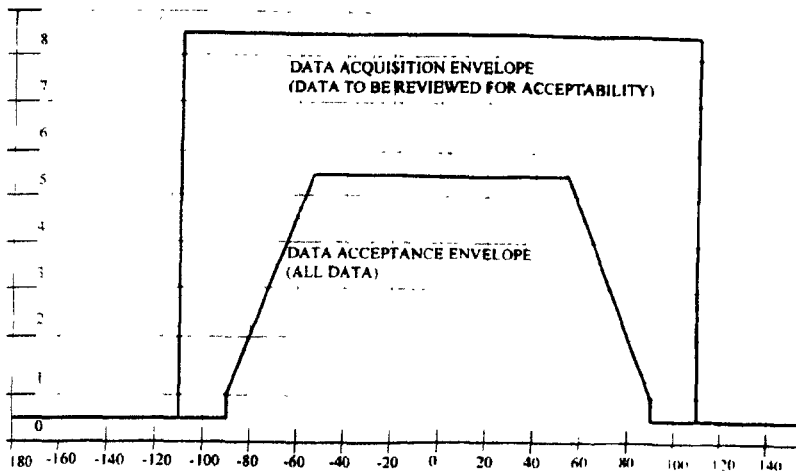


Figure 2.4: Outdoor Test Acquisition Data Envelope (Parfitt 2001)

The preparation room is the area where the engine is set-up prior to the test in order to minimise the non-running time of the engine inside the test room.

The equipment room is dedicated to the storage of the compressed air for the cell and the engine, fuel for the engine and all the components for providing the engine with the needed power electricity.

The components of an indoor test facility are described in paragraph 2.1.6. Figure 2.5 and Figure 2.6 show a general lay-out for indoor test cell with horizontal inlet and vertical outlet stack.

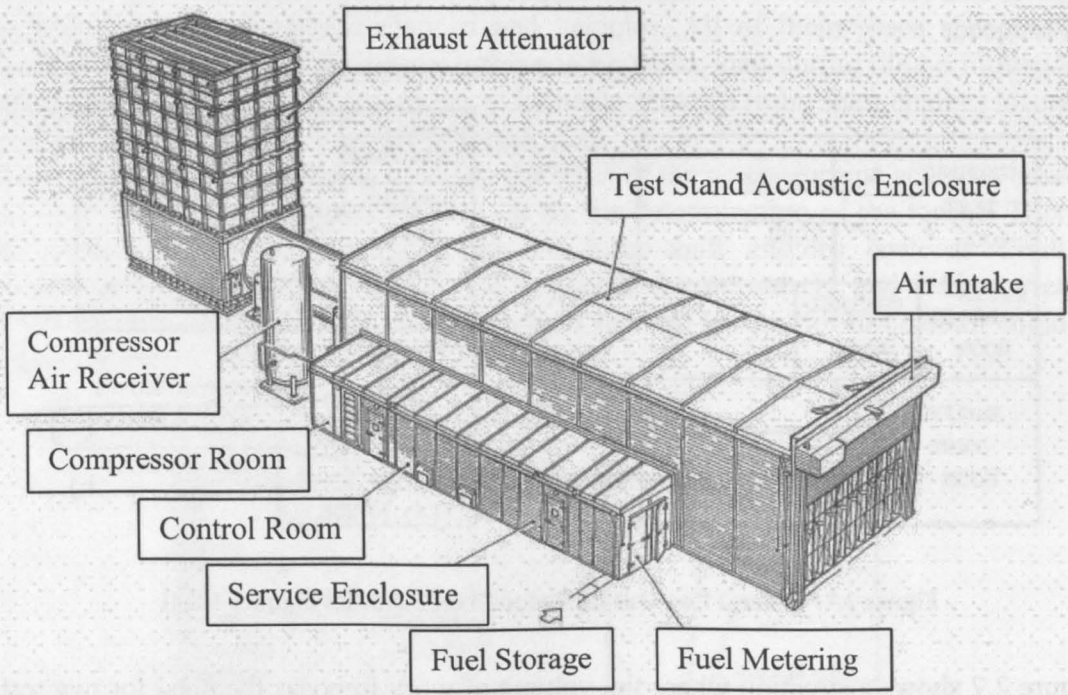


Figure 2.5: Indoor Test Facility Lay-Out (Rowlands 1984)

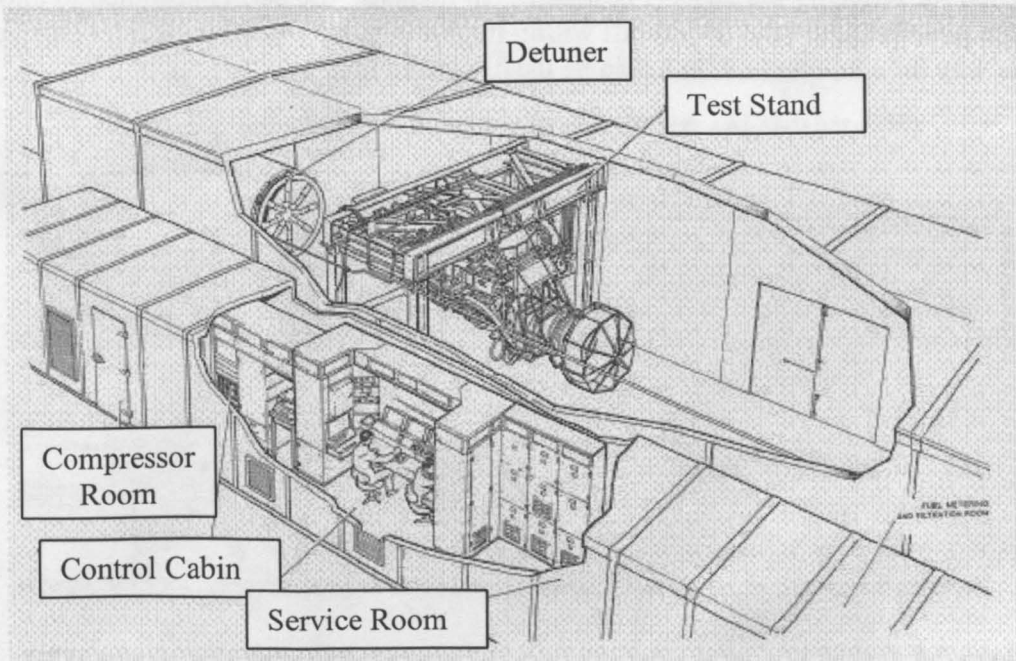


Figure 2.6: Indoor Test Facility Components (Rowlands 1984)

A universal lay-out for a sea-level indoor test facility does not exist. Indeed, it depends on which kinds of tests have to be supported by the facilities. There are several kinds of tests which the facility can deal with and therefore a unique configuration to allow all of them is not possible. The different kinds of tests are listed in paragraph 2.1.4.

Different lay-outs are given by Rene Jacques (Jaques 1984) who underlines the fact that whenever there is the need of building two test cells they have to be parallel in

order to share the control room and the engine preparation room. In this way the costs are reduced.

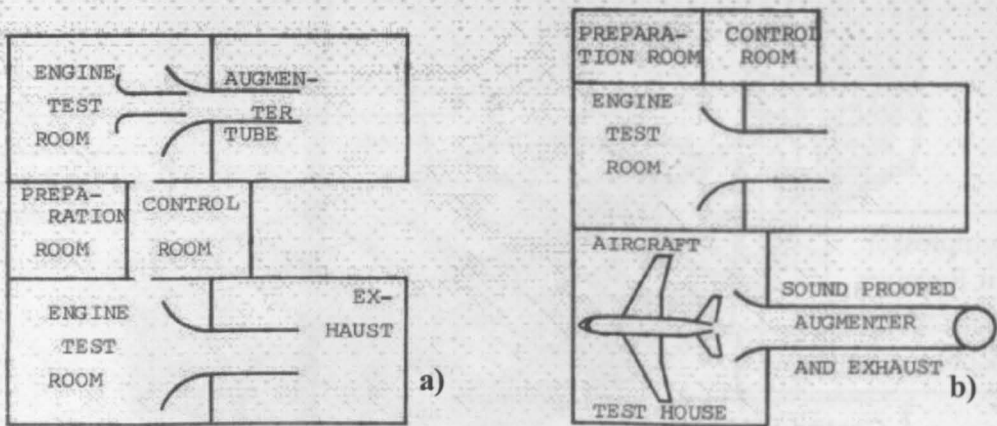


Figure 2.7: General Lay-Out for Indoor Test Facilities (Jaques 1984)

Figure 2.7 shows a situation where the volume of work imposes the need for two test cells. In the right hand side of the picture there is also included a hush house. When the work organization does not impose the need for two cells but still there is the necessity of testing bare engines and on wing engines, another solution is proposed for reducing the costs (Figure 2.8). In this case the cell is designed to allow also the possibility to host an aircraft within its test bay, by a horizontal inlet channel. In this way the same test cell can also be used as a test hush.

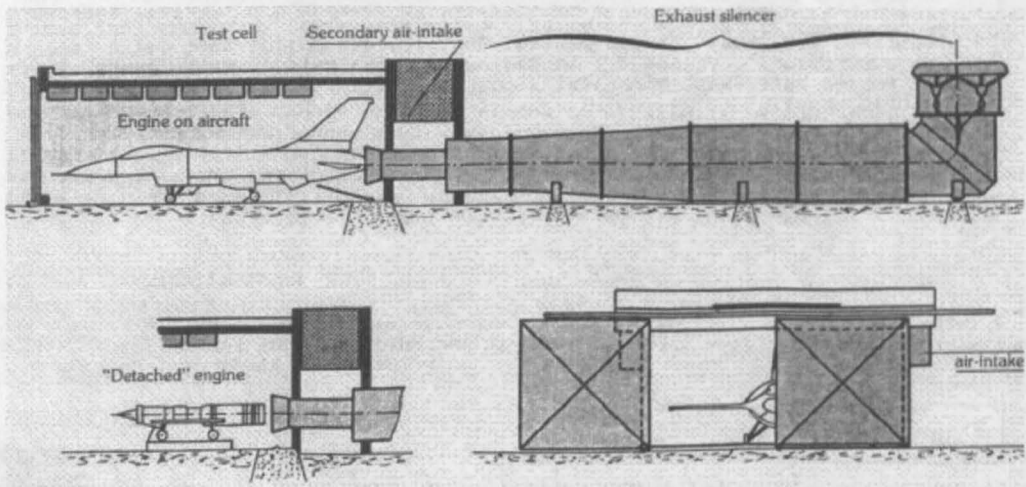


Figure 2.8: Indoor Test Bed for Bare Engines and Aircraft Trimming Test (Jaques 1984)

It is worth to mention that the above illustrated lay-outs are optimised for the construction costs only and therefore they do not represent the best aero-dynamics solutions.

The indoor test cells taken into account until now are specifically designed for gas turbine turbojet or turbofan engines. These facilities represent the core study of this work, but at the same time in this introductory overview for gas turbine test facilities it is also worth to mention the facilities for testing gas turbine turbo shaft engines.

There are different applications for turbo shaft engines as helicopters, turboprop, auxiliary power units, power stations and vehicles. All of them share a common requirement, the need for the power turbine to be under-load during the performance evaluations. However, a difference has to be made between turbo shaft engines loaded by a dynamometer and turboprops by a propeller.

The dynamometer by applying a load to the shaft of the power turbine acts as a brake and by an appropriate instrumentation allows the determination of the torque. There are different kinds of dynamometers for turbo-shaft engines such as Cradle dynamometers, the air compressor, the hydraulic dynamometers and Eddy-current dynamometers (Wunder 1984). An example of test cell lay-out for turbo-shaft engine is given in Figure 2.9.

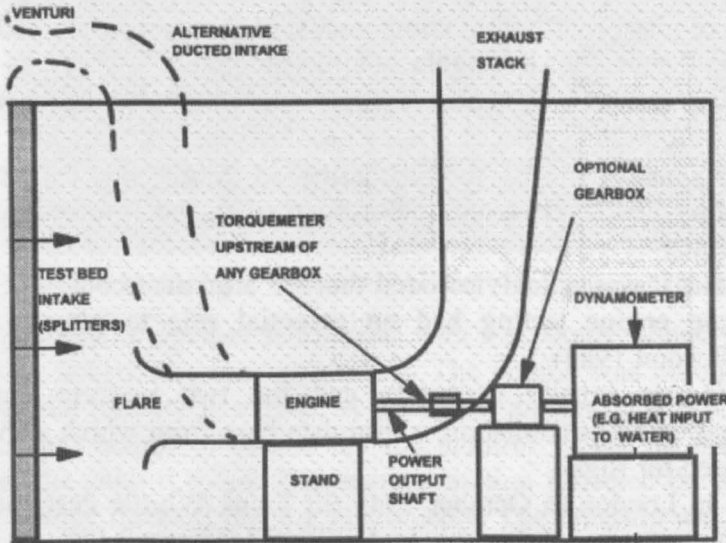


Figure 2.9: Test Cell Lay-Out for Turboshaft (Walsh and Fletcher 1998)

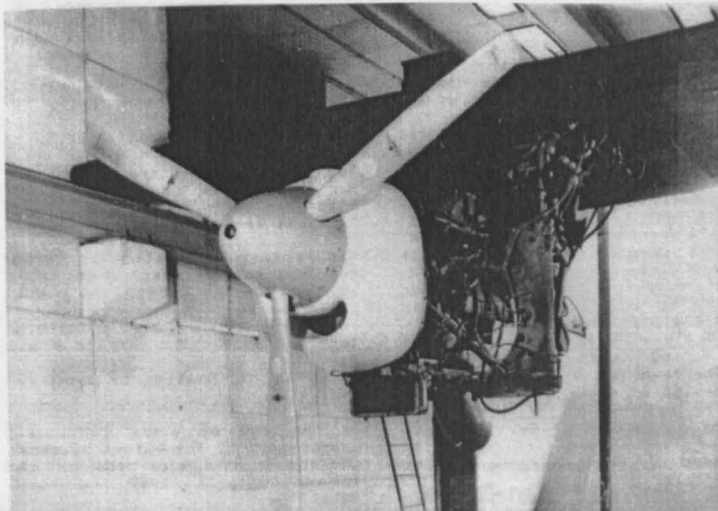


Figure 2.10: Turboprop Test Cell Stand (Torella, Liotti, and Bruno 1988)

Figure 2.10 shows a turboprop set-up for an endurance test.

### 2.1.3. Chronological Development of Sea-Level Bed for Gas Turbines Engines

Before going ahead with the description and the analysis of the sea-level test cells for turbofan and turbojet engines it is believed worth to illustrate their chronological development.

In the early year of engine evolution, relatively simple and low power engines could be tested on what now seem very basic test stands, needing only very elementary methods of measurements and data presentation.

At that time it was also suggested that since the processes of compression, combustion and expansion take place in different components, each could be studied in isolation, therefore avoiding the need for testing the complete engine.

Indeed, it was claimed that component test rigs could be better instrumented than a complete engine.

However, the argument ignored the difficulty of testing the components under transient conditions and overlooked the influence of the interactions that occur between components.

Needless to say that it was quickly realized that the argument could not be sustained and that full-scale engine testing had an essential role to play in aero-engine development (Ashwood 1984).

Component testing is equally necessary and the two perform complementary functions in the process of establishing a firm data base from which a specific design is ultimately cleared for flight.

During a lecture in London in October 1945 Sir Frank Whittle described the set-up used to test his first experimental engine in April 1937 (Figure 2.11).

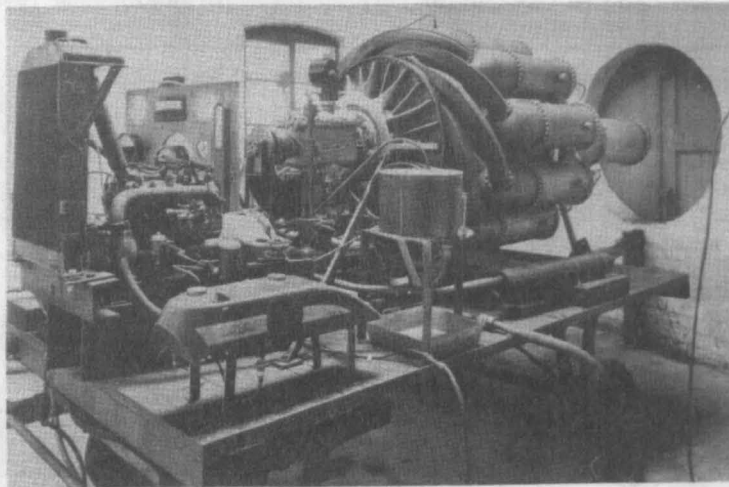


Figure 2.11: Sir Frank Whittle Test Cell (1937) (Ashwood 1984)

The engine was mounted on a four wheeled trailer which carried also the starting motor (top left of the picture), the instruments and the control panel making the whole set self contained except for the fuel and the water supply.

At that time no attempt was made to silence the engine, neither the intake nor the exhaust.

Engine technology has developed over the years and engines have grown in size and complexity resulting in significant gains in specific fuel consumption and power to weight ratio.



In parallel has grown the need for more comprehensive testing and a demand for improved accuracy of measurement, for an increased number of measurements during the test and for more comprehensive displays of processed information.

An example is the Test Bay No 4 at Peystock which was brought into use in 1946 particularly used for the investigation on reheat combustion and engine control systems (Figure 2.12).

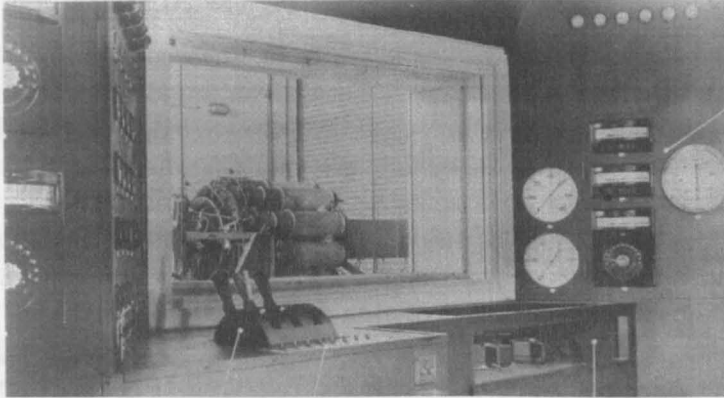


Figure 2.12: Test Bay No 4 at Peystock (1946) (Ashwood 1984)

The cell is essentially an open-ended hangar with a separated sound-proofed control room which also housed the instrumentation. The engine was mounted on a frame suspended from the roof by four rods. A particular design feature was the use of a system of rods and cranks to couple the fuel control valves on the engine to the throttle level in the control room. The instrumentation reflected the standard of that time and used simple directed reading instruments. The pressure was measured with water and mercury manometers and the temperature with thermocouples and resistance thermometers.

The third generation of test is typified by the Glen test house at Peystock which was commissioned in 1958 and is still in regular use (Ashwood 1984)

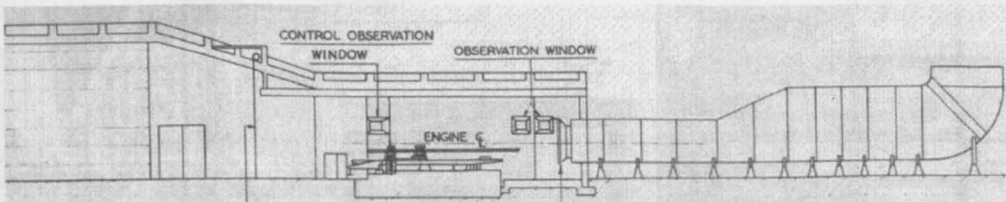


Figure 2.13: Glen test house at Peystock (1958) (Ashwood 1984)

The cell is fully enclosed and includes intake and exhaust silencing. It was designed for hypothetical engine with a mass flow of 115 Kg/s.

The thrust frame is anchored to the floor and this result in the engine centre line being 3 m above the ground level.

A major virtue of this cell is that it is a zero-rate system. This means that there are not pendulum effects due to gravitation such as parts with suspensions using rods or flexure.

The original thrust measuring system used a mechanical linkage to transfer the thrust to two weighted machines located in the control room.

With the advent of gas turbine engine with afterburner and turbofans pumping problems were encountered in the cell design. Indeed, from one side the engines with afterburner needed secondary mass flow entering the cell to cool down the temperature of the exhaust system.

The first cooling systems were achieved by water ingestion inside the detuner or in proximity of the engine.

However, although the water offers superior heat absorbing qualities, spray devices have proved to be insufficient at penetrating the high velocity exhaust core. Also another problem derived by the use of water for cooling down the system is the corrosion of the exhaust parts, with a relative increase of maintenance cost. Furthermore, since most of the water provided is lost by evaporation another issue is to ensure a big water supplier.

Accordingly, in the fifties the test cell research has dedicated part of its work to find alternative solution to cool down the cell.

The most straight forward solution is to use the primary engine jet and the detuner tube (also called for this reason augments tube) for pumping secondary mass flow into the cell in ejector fashion

The research concentrated most of its efforts in achieving the right proportion of secondary flow inside the cell (Sapp and Netzer 1978). Indeed, turbofan engines resulted into too much secondary flow entering the cell causing structural problems.

The problems related with the right amount of secondary flow are examined in more detail in paragraph 2.2. By now in this historical overview it is important to mention that in 1950 in Toronto made its first appearance a colander device with sliding covers which allowed the control of the secondary flow by changing the pressure at the back, the blast basket.

This underlines the fact that the cell design must be suitable for testing not only one kind of engine but a whole range.

The basic design of the Glen test house is still valid today. The only changes found necessary are related with the instrumentation and the thrust measurement system.

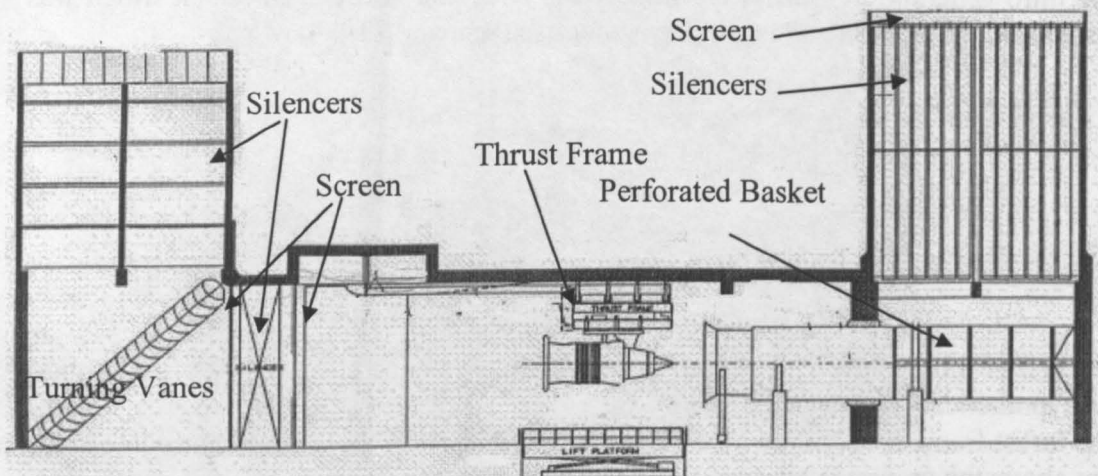


Figure 2.14: Test Cell No. 1 of the Japan Air Lines Located in Narita (Freuler 1993)

All the modern test cells for turbofan and turbojet engine embody the basic features of the Glen test house.

However at now days, the strict environmental regulations regarding noise pollutions have set specific limitations which involve also the design of test beds.

Therefore, particular attention during the design is dedicated to the exhaust and the inlet systems in order to meet the regulations. At the same time the geometry of the

air inlet is also important since it affects the uniformity of the air which goes through the engine.

Another important aspect of the modern design for gas turbine test cell is the data acquisition and processing systems. In this field a lot of progresses have been made in the last two decade in order to improve the accuracy of the measurements (Holmes 1984).

Figure 2.14 shows the cell No. 1 of the Japan Air Lines located in Narita (Freuler 1993).

Figure 2.15 shows the set-up for a modern test cell control room.

In 1981 in context with the symposium on "Turbine Engine Testing" the Advisory Group of Research and Development has conducted a survey among all the NATO countries to register all the air breathing engine test facilities for research and development (paragraph 2.1.4). The survey has been called Air Breathing Engine Test Facilities Register (Krengel 1981).

In this document plenty of information is available about facilities which are still working.

It is interesting to notice how the cell characteristics changed during the years.



Figure 2.15: Modern Test Cell Control Room (Cell Aerospace Test Equipment)

#### **2.1.4. Purposes of Sea-Level Testing**

In generally the various types of propulsion testing can be divided in two different categories, support for the research and development and production test.

The testing as support of the research and development can be divided in four basic categories: design testing; proof testing, capability testing and trouble-shooting (Rudnitski 1984).

Design testing is normally carried out by the engine manufacturer. The results from these tests are used to validate or to correct computed designs and to optimise such elements as cooling passages, boundary layer correction factors, etc. A typical approach is to design the component based on experience and theory and then to check the components or elements in bench tests. Basically the testing in the developing program is divided in three levels: the piece-parts, modules and full engine (Beanland 1984).

Proof testing is done by the manufacturer to show that its product meets the design specification. The specification may call for a large number of tests in addition to a long and complex endurance test that may involve many throttle movements, altitude

testing and running on several fuel types. Only when all the tests have been successfully completed the engine can be properly considered certified.

Capability testing may be undertaken by the manufacturer or carried out in concert with the client if he is a large operator like the military. Such tests concentrate on the errors in adjusting the engine, lapse rate of performance with usage, manoeuvre limitations caused by the flow distortion, limit with the afterburner light with respect to altitude and speed, engine relight limits, surge and stall limitation, low cycle fatigue life and stress rupture life.

Trouble-shooting is a testing function necessary to solve problems that occur in the field after a period of use. In some cases it is necessary to duplicate not only the failure mode, but the elapsed number of cycles or time in the engine life when the failure occurred. Many engine types were originally conceived for an application which may be quite different from the current usage, thus imposing new constraints that were not provided at the original design.

The production testing includes also the post overhaul acceptance testing. Indeed they share the same objective that the engine must meet the minimum performance targets. While production test contains all new parts, overhauled engines may contain some repaired parts with the bulk of the parts being used. The overhaul facility, which may be owned by the user, has a dual role to play; it must satisfy the user who wants engine integrity and performance restored at minimum cost. And at the same time it must cooperate with the design authority and the vendor for new parts. Therefore, the post overhaul acceptance tests are quite important, as the engine will seldom exhibit "as-new" performance, yet it must pass minimum performance guarantees.

The class of facilities required for research and development testing is generally quite complex and expensive, as simulation of both altitude and forward speed, in addition to sea-level conditions, may be required.

Production testing, carried out under sea-level static conditions by the engine assembler, is required to ensure that each engine meets performance guarantees. Due to the tolerance in the production of individual parts and in the build up of assembled components, each engine has a unique performance signature. Using minimal instrumentation the production tests log engine performance and health, adding new information to the manufacturer's data bank.

These tests also demonstrate to the client that each unit meet the specification.

Together with the above test purposes it is also worth for completeness to mention the tests made by the user technicians who have to respond to the pilot complaints about inadequate or erratic engine performance. Sometimes the problems can be rectified on wing without engine removal, but often, especially with older designs, the engine must be installed on a test bed to isolate and repair the fault. Current design techniques do permit a number of components, such as electronic fuel controls, to be changed on wing, provided the fault can be isolated. Fault isolation may be effected by test equipment that does not require engine operation, but if required, the test facility must be capable of monitoring the engine performance while installed in an aircraft (test haush). The objectives of a service technician are somewhat different from the engine over-hauler. The primary function of the user technician is to keep the airplane in the air. Therefore he does not place the same degree of accuracy on performance parameters as fuel flow and thrust as does the engine manufacturer. However with the advent of "on-conditions" maintenance more attention has to be

paid to thrust and fuel flow. Hence the field test facilities now require a better standard instrumentation, data gathering and handling and engine performance assessment.

Each of the above test purposes needs its specific test facility with its own specific instrumentations. An interesting classification of the degree of complexity, based in the instrumentation required, for each test purpose is reported in (Holmes 1984). The complexity increases from the top to the bottom of the Table 2.1.

Type of Test	Objectives
Pass-off	Demonstrate performance guarantees after overhaul
Endurance	Demonstrate capability of mechanical integrity and reliability over an extended period
Fault Diagnosis	Identify reason for performance shortfall or components failure
Ingestion	Demonstrate capability to withstand ingestion of foreign objects
System Development	Evaluate new system and accessories
Engine Development	Evaluate new technology engine components on an established engine
Demonstrator	Asses the overall performance and handling qualities of a completely new engine containing many advanced technology features

**Table 2.1: Degree of Complexity of the Instrumentation Required for Different Test Purposes (Holmes 1984)**

The main topic of this thesis is the enclosed gas turbine test facility, where the whole bare engine is tested.

In such a case several flow phenomena, occur inside an enclosed test facility, which make the engine performance evaluation a not easy task to accomplish.

In particular, this thesis deals with cell airflow and the engine thrust evaluation inside the cell. The first is a very generic field worth to understand every time the engine is operated inside the test cell. The second is more specific and deals with the evaluation of different thrust and drag accounting systems, therefore useful every time the thrust of an engine needs to be evaluated.

From the above brief specification the author would classify this research useful for both research and development and production testing (overhaul tests included). Indeed every time the engine has to run on enclosed cell the first requisite to accomplish is provide the right environment and the cell airflow is one of the most important parameters to keep under control.

### **2.1.5. Outdoor vs. Indoor Sea-Level Test Facilities**

As already said in the above paragraphs this thesis deals with sea-level test. Therefore, it is necessary to go into more details and emphasize the main differences between the two kinds of SLTF.

An important, centre issue to gas turbine engine testing is the conflict between the need for accuracy of performance measurements and the need for a reliable and repeatable test environment.

An outdoor “free air” test (Figure 2.4) environment represents the best possible “ideal” condition in terms of thrust measurement. Indeed, when an engine is tested on an outdoor stand under no-wind conditions draws only the air necessary to satisfy its thermodynamic cycle. This leads to the result that the measured thrust force is a direct reading of the real gross thrust delivered by the engine (SAE international 1999) (Freuler 1993) (Rudnitski 1990). Therefore, such a value is also used as a datum to which all the others results from different techniques can be compared to. This aspect is also examined more in detail in Chapter 4 paragraphs 4.4.1 and 4.4.2.

Therefore, it would seem that the proper approach for all ground-level testing might be to use outdoor “free-air” stands.

However, the ambient conditions which an outdoor test has to deal with do not allow for a reliable and repeatable test environment. Especially the wind conditions are considered the most critical for achieving a successful test result.

Additionally, the use of outdoor facilities can result in objection noise pollution, and therefore as consequence they are located in the more remote and less accessible areas.

All these constraints also make the outdoor test extremely expensive.

Accordingly it is standard practice to conduct the most turbojet and turbofan engine testing indoors in specialized test facilities (Figure 2.6).

However, the enclosed environment does not represent the best solution in terms of accuracy in the measurements. Indeed, in order to determine the actual performance characteristic of an engine operating indoor the interaction between the engine and the cell must be understood and evaluated. To underscore the importance of understanding performance measurements from engine test facilities the Advisory Group for Aerospace Research and Development has undertaken from 1980 to 1987 one of the most extensive experimental and analytical research programs called the Universal Engine Test Program (UETP) (Propulsion and Energetics Panel Working Group 15 1990). Most of the authors of the references used in this literature review have participated to such a program. The main objectives of the UETP are:

- To provide a basis for up-grading the standards of turbine testing within the AGARD countries by comparing test procedures, instrumentation techniques and data reduction methods, thereby increasing confidence in performance data obtained from engine test facilities
- To compare the performance of an engine measured in ground level test facilities (outdoor and indoor) and in altitude test facilities at the same non dimensional conditions and establish the reasons for any difference.

Even though the UETP is a really fascinating piece of work in this thesis can not be illustrated in its integrity. But it is referred to for the most of the topics treated here.

Coming back to the main differences between outdoor and indoor test facilities, it is clear that a compromise needs to be agreed between the above constrains.

Generally, it is a common practice to limit the outdoor tests to a minimum number for defining the datum engine performance characteristics. Once such conditions are acquired, the results from the indoor test are correlated to them by complex procedures in order to work out the actual engine performance also from indoor test results (Propulsion and Energetics Panel Working Group 15 1990).

Figure 2.16 summarizes the interaction and the characteristics of outdoor and indoor test data. Once the correlation has been established for a defined engine in a defined cell all the same kind of engine can use it to work out the real performance characteristic.

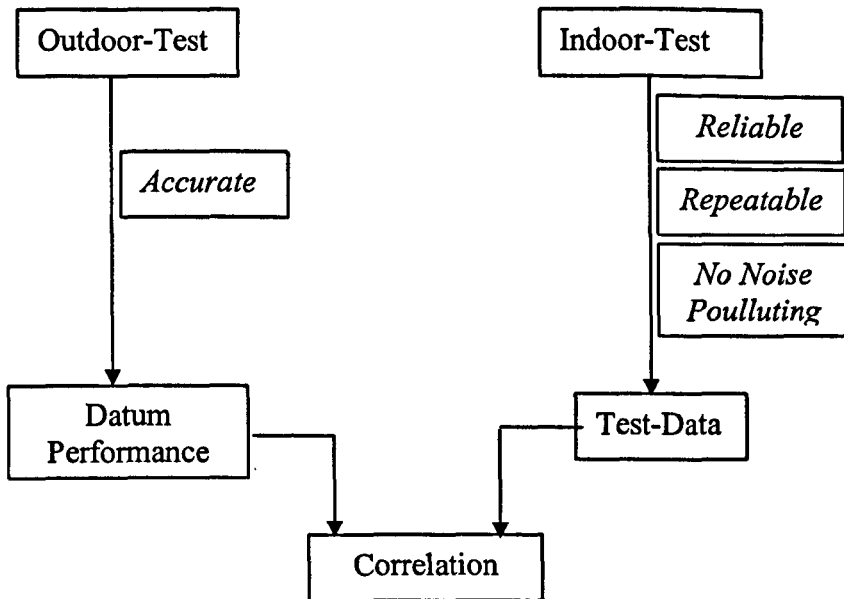


Figure 2.16: Correlation Indoor-Outdoor

### 2.1.6. Indoor Test Cell Components

Three primary components can be identified inside an enclosed ground level test bed facility: the inlet plenum, the test chamber, and the exhaust system.

Each one must be designed not only to acquitting its individual function but also looking at the compatibility with the other components with respect to aero-thermodynamics and acoustic performance.

#### *The inlet plenum*

The inlet plenum includes the inlet stack (assuming that the cell has a vertical inlet), the acoustic treatment, the cascade turn wind, honeycomb, baffles and flow screens.

The primary function of the inlet plenum is to deliver clean and adequate air flow to the test chamber. It should be designed to provide stable inlet flow up-stream the engine inlet and to eliminate problems caused by physical and environmental conditions. The first thing to achieve is a clean airflow, indeed, the inlet system must allow for cell operation independent from outside wind direction and magnitude so that testing can be conducted under all weather conditions. At the same time it should isolate the no-uniform characteristic present in a free flow, in events of windy conditions, in order to reduce the flow distortion inside the cell. Such a distortion indeed could affect the engine performance and at last also damage the engine components (SAE international 1999).

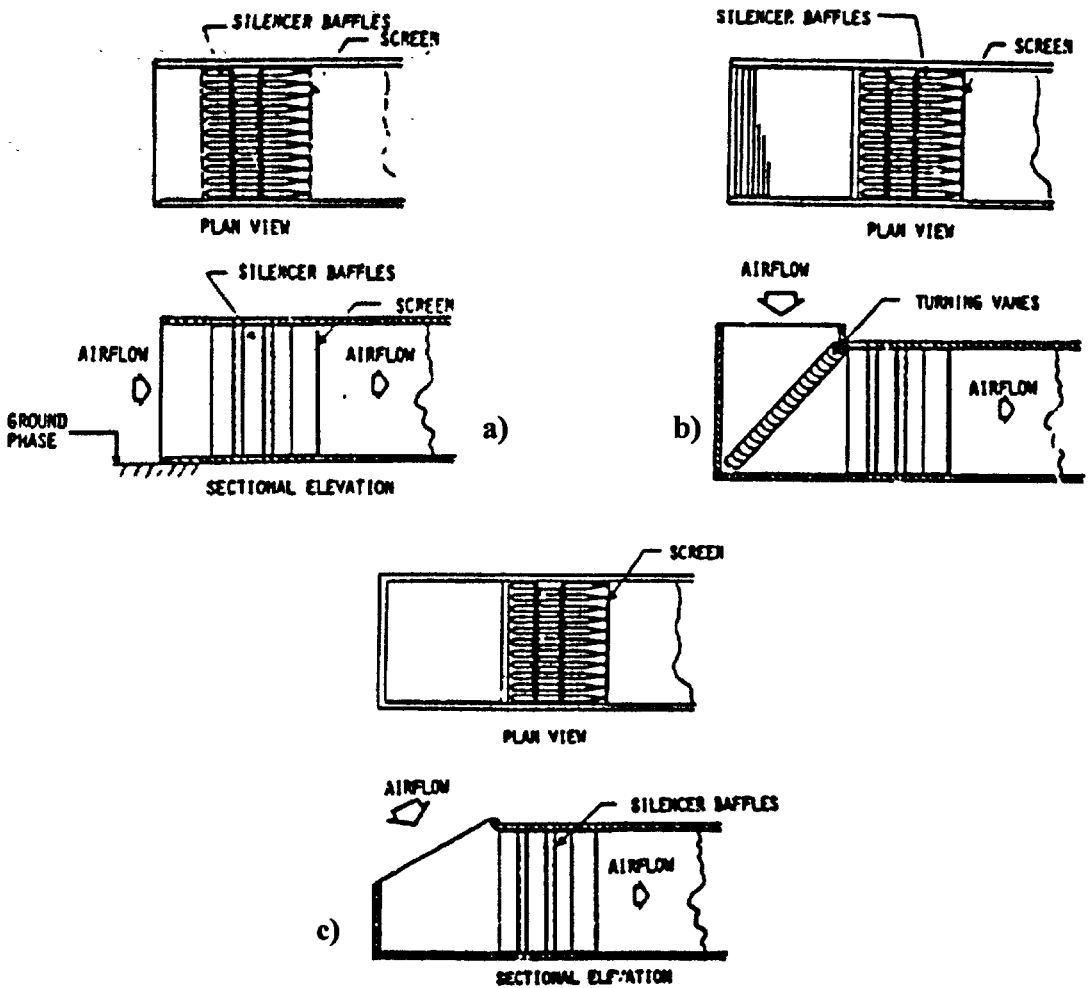


Figure 2.17: Three Different Kind of Inlet Plenum: a) Horizontal, b) Vertical, c) Vertical Truncated (Freuler 1982)

As it is possible to see from Figure 2.13 and Figure 2.14 two different kind of inlet plenum are available, the horizontal and the vertical. In terms of cell aero-dynamics in a horizontal inlet system without bends the flow is less disturbed and under ideal external conditions (i.e. no-wind) the distortion level is very low.

At the same time with vertical inlet systems the air is sucked inside the cell with less danger of foreign objects and therefore erosion of the acoustic treatment. There is not a direct wonder about foreign objects regarding the engine, the flow screen and the debris guards located in the cell avoid the ingestion of such objects in the engine. Also with vertical inlets the noise radiation at the ground level is lower.

An interesting study, for scale model test cell, of different inlet configurations under crosswind conditions is presented in (Freuler 1982). Three different inlet plenums were studied, horizontal straight, vertical 90° with turning wind and a truncated courtyard version (Figure 2.17).

The results in terms of inlet distortion clearly show that most sensitive configuration at the external wind direction is the truncated courtyard (Figure 2.18).

The flow distortion is accounted as it is shown in equation (2. 1)

$$distortion = \frac{v_{max} - v_{min}}{v_{aver}} \quad (2. 1)$$



Another important parameter of the inlet plenum is the pressure loss which the flow experiences passing through it. Loss in total pressure along the inlet system can be reflected in cell depression inside the cell. An excessive cell depression can be a cause of structural problem first and second could affect the stability of the flow around the engine and the accuracy of the measurements. It is generally recommended to limit the cell depression to 150 mm H<sub>2</sub>O (Jaques 1984). Such a limit is not particularly for the structural load but primarily for allowing the engine to work in conditions close to the free air and secondly for the corrections necessary during the correlation.

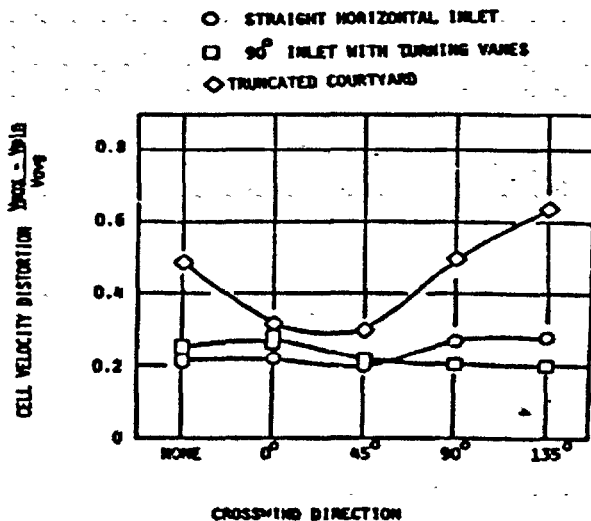


Figure 2.18: Effect of the Wind and Cell Inlet Configuration on the Flow Distortion inside the cell

In the above mentioned paper (Freuler 1982) the effects of different flow screen porosity and position on the cell depression and inlet velocity distortion are also investigated. The study involves two different inlet configurations, a vertical with 90° curvature including turning wind and a horizontal. The lowest cell depression was obtained with a horizontal inlet, without a flow screen and baffles (Figure 2.19).

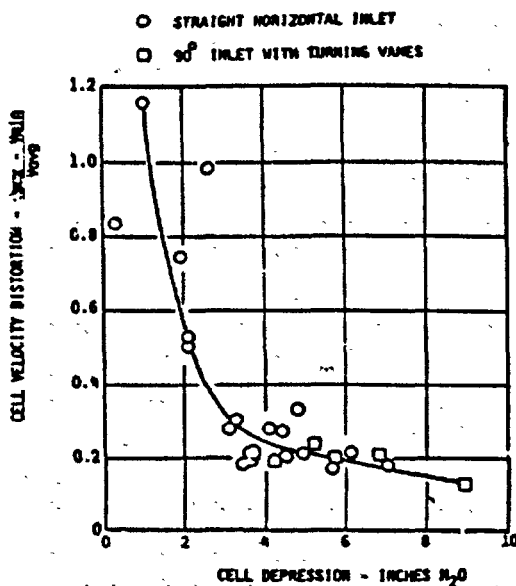


Figure 2.19: Flow Distortion and Cell Depression for Different Cell Inlet Configurations (Freuler 1982)

However, such a configuration corresponds to the highest flow distortion. Figure 2.19 suggest also that inlet flow distortion of 0.2 or less results when flow screen porosity or baffles are chosen to produce a cell depression of at least three inches of water. Furthermore it implies that higher loss flow screens result in more uniform flow, but at the same time they correspond also at higher cell depression. Therefore a compromise between flow distortion and cell depression needs to be achieved.

### *Test chamber*

The test chamber is the room where the engine is located during the test.

It includes the engine test frame and the cell supporting equipment, such as lift platforms, ladder, the inlet of the augments pipe, the engine monorails and so on (Figure 2.20).



**Figure 2.20: Modern Test Chamber (Wilson 1999)**

Attention must be paid to the design of the test chamber to minimize or eliminate projections which affect portion of the flow entering the engine. Such projection can cause wakes and distortion in the bellmouth and produce unacceptable variations in the engine performance and mass flow measurements. In addition consideration should be given to those aspects of the test chamber design which affect the airflow in the vicinity of the engine to ensure that there is not air recirculation and that the engine does not re-ingests hot gasses.

The recirculation (paragraph 2.4.2) can affect the flow measurements inside the cell and the re-ingestion can alter the engine performance. Hot gas recirculation can be dangerous even without re-ingestion. Indeed, it can generate temperature gradients in the flow up-stream to the engine which is seriously adverse affected by temperature distortion (similar to velocity distortion) (Rudnitski 1990).

Furthermore, the flow recirculation can also affect the pressure distribution along the engine and therefore its thrust determination.

Therefore, inside the test chamber the temperature is usually well monitored.

Recirculation and re-ingestion are not the only risky flow phenomena inside the test chamber but also due to the boundary layer separation from the cell walls also vortices can appear.

The above flow phenomena will be better taken into account later on, when the cell aero-dynamic will be better illustrated. At the moment they are listed only to underline importance of a well designed test chamber. Indeed, a lot of risks can be avoided designing a test room with the appropriate dimensions.

Even though, one of the most important flow parameter i.e. the entrainment ratio ( $\mu$ ) it has not been introduced yet (equation (2.4)). It is useful to provide one important rule which link together the engine and the test room dimensions in order to achieve flow velocities inside the cell which are not higher than 10 m/s (Rudnitski 1990).

$$W_{eng} = \frac{12A_{cell}}{(\mu + 1)} \quad (2.2)$$

Such a velocity maximum value is advised in order to limit the flow distortion inside the cell.

Another ratio often used in the tailoring of the test chamber is given by the engine diameter over the cross sectional area of the cell.

In the above equation (2.2) it is shown one of the most important out-comes of every test cell study i.e. how the engine dimensions, the cell dimensions and the cell flow are strictly correlated together to achieve high-quality aero-dynamic inside the cell.

### *Exhaust System*

Probably the greatest impact on the engine performance and on the cell performance is the design of the exhaust system.

The exhaust system not only controls the total amount of mass flow entering the test cell but it also controls the back pressure on the engine, the sound absorption and also the production of exhaust pollution.

In the exhaust system are included the detuner pipe, the blast basket (perforated cylinder Figure 2.14) or a cascade turn wind, silencers and flow screens.

In order to describe the exhaust system it is necessary to mention that the engines jet exhaust (or jets for a turbofan engine) momentum in combination with the detuner pipe act to form an ejector pump, which entrains cool secondary flow air from the cell inlet. The amount of secondary flow is strictly dependent on the exhaust system configuration by several relations which involve several parameters. These issues are further discussed in paragraph 2.2.

In the past, the design of the augmentser pipe was considered an art and test facility designers and operators had only quantified some of the parameters concerning ejector performance (Sapp and Netzer 1978).

The amount of secondary flow is probably responsible for most of the flow phenomena inside the cell but at the same time it is used for cooling-down the engine (exhausts nozzle and the exterior of the turbine), as well as the exhaust silencers and the augmentser it self. Therefore it is preferable to use a detuner pipe that has a collector which can be moved relative to engine exhaust plane and a variety of insert size to modify the flow area.

As it will be better shown later on (paragraphs 2.2.2 and 2.2.3) the engine-detuner distance and the area ratio of the detuner and of the engine nozzle are two crucial parameters in the ejector theory. By them indeed, and by knowing the characteristic of the engine exhaust it is possible to control the total mass flow entering the cell, the pressure and the temperature around the engine and in the exhaust stack.

An important limit of the exhaust stack is the flow temperature which should not overtake the 400 °C in order to preserve the silencers.

At the same time for example a military jet engine in full- afterburner reach 1800°C. Therefore the exhaust gasses must be cooled.

Cooling down the hot exhaust gasses only by dry air (by pumping air inside the cell with the ejector pump), in the case of engine with afterburning, would require a large amount of secondary flow. Probably such an amount would not suit at the best the flow quality request inside the cell (in terms of flow velocity, distortion and accuracy in the measurements). Therefore different cooling systems have to be used.

Quite common is the water injection in the augments tube as described during paragraph 2.1.3.

Another approach is that of using two ejectors in series as illustrated in Figure 2.21.

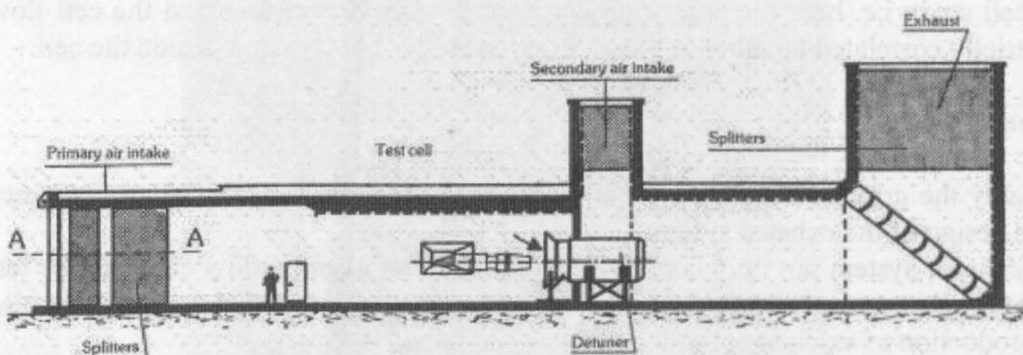


Figure 2.21: Indoor Sea-level Test Bed with Double Air intake ((Jaques 1984))

The first ejector will drive only the required amount of air necessary to guarantee the good cell aero-dynamic in the test room. The second will drive the right amount of air for cooling down the exhaust stack.

In addition the velocity along the exhaust stacks is an important parameter. Indeed, in order to improve the efficiency of the anti-noise treatments the velocity has to be limited at 30- 40 m/s along the exhaust stack. Accordingly, this would determine the cross sectional area of the stack (Jaques 1984).

Another important aspect of the exhaust system is the cost. Indeed, a round detuner pipe is the most expensive component of the cell with a primary building cost of the \$ 1500000. About half of this cost is the labour required to cut, align and weld the round sections. In addition to this primary costs also \$ 400000 have to be added as maintenance during a 20 years life span.

It has been estimated that the incorporation of a rectangular detuner pipe could save \$540000 on the construction costs and \$260000 in the maintenance costs.

However, the performances of the two duct typologies have to be assessed before switching from one to another.

Kodres and Murphy (Kodres and Murphy 1998) have presented a computational analysis (using the PHOENICS CFD code), that dealt with three different detuner cross sectional configurations: round, square and rectangular.

The square detuner shows the best aero-thermo-dynamics performance avoiding recirculation at the inlet and reaching lower surface temperature with an entrainment ratio a bit smaller than that found for a round detuner.

However has to be said that the cross sectional area of the square detuner was about 27% greater than that of the round detuner (with its diameter equal to the side of the square shape).

Even though this analysis did not include structural and noise considerations it concludes that construction and maintenance costs can be reduced by switching from a round to a rectangular (or square) detuner without any decrease in aero-thermal performance.

### **2.1.7. Engine thrust Frame**

The accurate measurement of the thrust is not only one of the most important but also one of the most difficult parameter to achieve in the entire range of test bed parameters.

The system most commonly used to measure the thrust of a turbojet/turbofan utilizes strain gauge beams or diaphragms which give an electrical output proportional to the applied load. Electrical circuits provide excitation voltages to the strain gauge from 10-15 volts and the strain gauges used are typically 350 ohms resistance (Holmes 1984).

They may be mounted near the front or at the rear of the thrust stand and work either in compression or in tension. The forward location is preferred to reduce the possibility of error due to thermal radiation from the engine exhaust. The thrust measuring system should be designed to minimise false loading of the load cell due to temperature gradients in the structure and/or calibration in a different horizontal plane than the thrust loading.

The three basic flexure designs most commonly used with thrust stands are compression, tension and compound. Flat plate flexures should only be used in tension, whereas compound flexures have been satisfactory employed in both tension and compression.

A centre-pull calibration with the engine in position is mandatory, as the pitching moments induced in the stand can cause the flexures to change loading from tension to compression. Should this happen, the calibration will likely be non-linear.

Stand stiffness, spring rate and hysteresis have to be accounted for as measurable deflections of the thrust bed relative to the ground reference.

A regular centreline thrust calibration, as close as possible to the working conditions, is the procedure needed to compensate for any moments effects.

### **2.1.8. Blast Basket**

A complete reassessment of the test house design has been required with the advent of the new generation large by-pass engines.

The mixing between the cold jet (coming from the fan nozzle) and the hot (coming from the engine core) makes the global exhaust temperature lower than that experienced with turbojet engines. This is especially true if the turbofan has mixed exhaust.

The immediate consequence of having exhaust jets at lower temperatures is that less secondary flow is needed for cooling-down the exhaust system and preserve the acoustic treatment.

However, if less secondary flow is needed, the global velocity along the detuner and the exhaust stack is higher. Indeed, one of the main consequences of the mixing process between primary and secondary flow is to slow down the primary flow.

Therefore the new smaller pumping task (described in paragraph 2.2) leaves a surplus of kinetic energy in the exhaust stream.

Such a surplus is advantageous from the point of view of the interaction between the cell flow and the outside weather conditions but has unfavourable impact in the acoustic treatment. Indeed, the maximum efficiency from the acoustic treatment is obtained if the flow velocity is kept below 40 m/s.



Figure 2.22: Blast Basket (Wilson 1999)

Therefore a new cell component is needed in order to help the flow mixing and accordingly reduce the exhaust velocity. This component is the blast basket and takes the form of a cylindrical colander closed at the end and it is located at the end of detuner pipe.

Figure 2.22 shows a blast basket picture taken from the inside. It is interesting to note that some of the holes are covered by plates. This technique is used for controlling the pressure losses of the exhaust system and therefore the cell entrainment ratio.

The kinetic energy dissipation is achieved by the turbulent mixing between primary and secondary flow and also by the flow crossing the holes.

Although blast baskets are mechanically simple and therefore attractive components for inclusion in the test cell there is a shortage of aero-dynamics data on their performance (Adkins and Anas 1996).

This has aimed Adkins and Anas (Adkins and Anas 1996) in their experimental and numerical research for determining an overall discharging coefficient for the blast basket as a whole.

$$cd_{overall} = \frac{W}{\pi d L \Psi \sqrt{2\rho(P - p_e)}} \quad (2.3)$$

Equation (2.3) is the formulation of the overall discharge coefficient defined where  $d$ ,  $L$  and  $\Psi$  are respectively diameter, length and porosity factor (free area over the total area) of the cylinder,  $P$  the total pressure inside and  $p$  the static pressure outside.

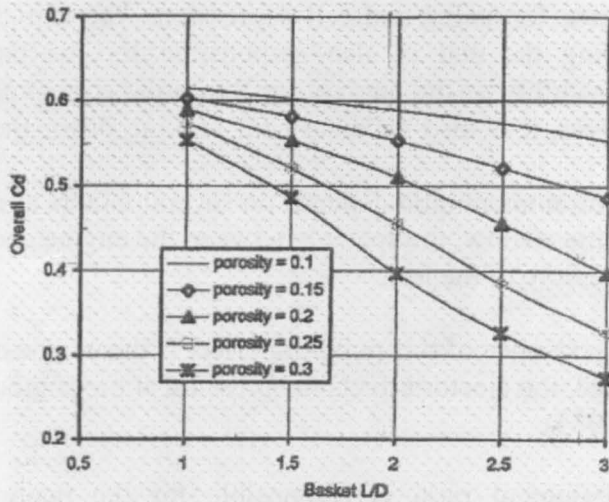


Figure 2.23: Overall cd Prediction (Adkins and Anas 1996)

Figure 2.23 shows the numerical results of the discharge coefficient for the overall blast basket, for different porosity factors, found by Adkins and Anas (Adkins and Anas 1996).

These results have been found to agree very well with the experimental results point (Adkins and Anas 1996).

## 2.2. Ejector-Pump Effects in Indoor Test Facilities

### 2.2.1. Engine-Detuner Ejector-Pump

The interaction between the high momentum engine exhaust jets and the detuner give arise to an ejector pump effect inside the test cell. Such an effect is responsible for the fact that the cell mass flow is not only the mass flow needed by the engine to satisfy its thermodynamic cycle. Indeed, in an indoor test facility the total mass flow entering the cell can be split in two parts: the primary flow which is breathed by the engine and the secondary which flows around the engine.

When the engine runs, the high energy primary flow drags, through viscous shearing, the secondary flow which surrounds it.

Accordingly, the secondary flow starts to accelerate and enters the detuner pipe. Such acceleration, within the enclosed environment of the test cell, generates a low pressure region at the detuner inlet which at the same time drives other flow inside the test cell.

The ratio between the secondary and the primary flow is called entrainment ratio (equation (2.4)).

$$\mu = \frac{W_{secondary}}{W_{primary}} \quad (2.4)$$

The entrainment ratio is a very important parameter in the study of the cell aerodynamic. Indeed, it influences most of the flow parameters and consequently the majority of the flow phenomena which take place inside the cell i.e. flow distortion,

flow recirculation, vortex formation and cell depression. Accordingly the amount of secondary flow entering the cell is also responsible for the uncertainty in the measurement, for the stability of the engine, for the thrust correction factors, for the noise emission. However, it is also necessary for cooling down the engine and the exhaust system.

At the same time the entrainment ratio depends on several factors as nozzle to detuner diameter ratio, the engine airflow, the spacing between the engine and the detuner and the temperature and pressure of the jets.

Another important consequence of this pumping effect is the engine oscillation in fuel flow and airflow. Indeed, the ejector affects the pressure at the engine inlet altering its performance (Jaques 1984).

Summarising the entrainment ratio is responsible for the majority of the flow phenomena occurring inside the cell and at the same it is dependent on several factors. Including also the fact that one cell has to be used for testing not only one kind of engine but for a large variety, the cell design and in particular the exhaust system design is very complicated.

### 2.2.2. Engine Nozzle-Detuner Spacing

In the past, several attempts have been made to study the effects of the engine-detuner gap.

Due to the complexity of the operations and the costs associated moving the engine with respect to the inlet detuner lip in full scale test facilities, most of the studies have been done in model test facilities.

In his experimental research for adapting an existing GE air-cooled test facility to large turbofan engines Karamanlis et al.(Karamanlis et al. 1986) found that the secondary mass flow decreases moving the engine closer to the detuner.

The results for a civil turbofan engine simulator are shown in Figure 2.24.

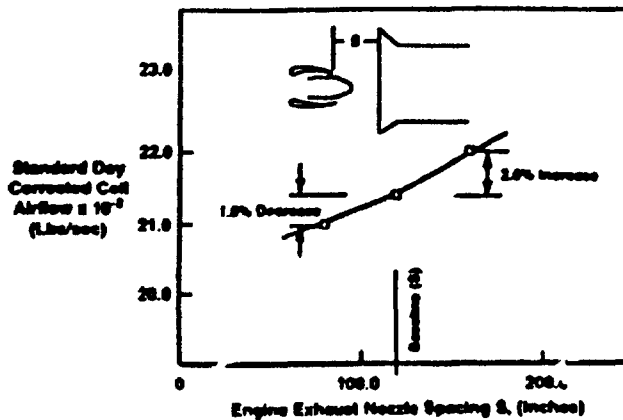


Figure 2.24: Effect of the Engine-Detuner Distance in the Entrainment Ratio (Large Turbofan) (Karamanlis et al. 1986)

Moving the engine 40 inches closer to the exhaust collector (with respect to the baseline configuration), the cell airflow reduced by 1.8 %. By moving the engine 40 inches away from the exhaust collector the cell airflow is increased by 2.6%.



Similar results were obtained also for a military engine simulator (with afterburner) and are shown in Figure 2.25.

By moving the engine nozzle inside the exhaust collector the pumping effect can be reduced up to 12%.

This may be necessary to avoid some noise problem.

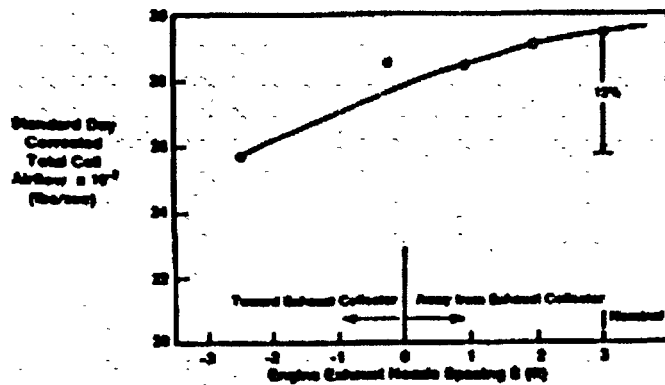


Figure 2.25: Effect of the Engine-Detuner Distance in the Entrainment Ratio (Military Engines) (Karamanlis et al. 1986)

Karamanlis et al. also obtained similar results to those just shown above for turbo-shaft engines test cells (Karamanlis, Holmer, and Bellomy 1985).

This confirms that by moving the engine closer to the detuner the entrainment ratio decreases.

Such a trend of results is confirmed also by Sapp and Netzer (Sapp and Netzer 1978) with the limitation that his engine simulator could not supply enough mass flow to underline the engine-detuner gap effect. Therefore, it was found that there was only slightly increasing with the engine detuner gap.

Franco in 2000 (Franco 2000) carried out in Cranfield University a series of two dimensional CFD simulations, in real scale, for different engine power settings (idle, max-dry and reheat) and for different engine-detuner distances. The results show that for the idle and the reheat engine conditions the entrainment ratio is almost constant. Instead, when the engine operates in max-dry conditions the entrainment ratio at the beginning starts to decrease by increasing the engine detuner distance and afterward increases.

Another CFD work was carried out in Cranfield by (Dejean 2003) in 2003. This time some three dimensional simulations were conducted and the results show a decreasing trend of the entrainment ratio with the engine detuner distance. However, the engine-detuner distances taken into account by Dejean (Dejean 2003) were only two and therefore not enough for defining a real trend.

The fact that cell entrainment ratio increases with the engine-detuner gap is underlined also in Gullia's work (Gullia et al. 2005) by experimental and computational analysis. The results (presented to the AIAA 43<sup>rd</sup> Aerospace Meeting and Exhibit 2005 in Reno) are illustrated in Appendix B4 of this thesis and shown that the cell secondary mass flow increases when the engine is moved further from the detuner lip. However, it is also possible to notice that once the distance has reached four engine nozzle diameters the secondary mass flow tends to remain constant.

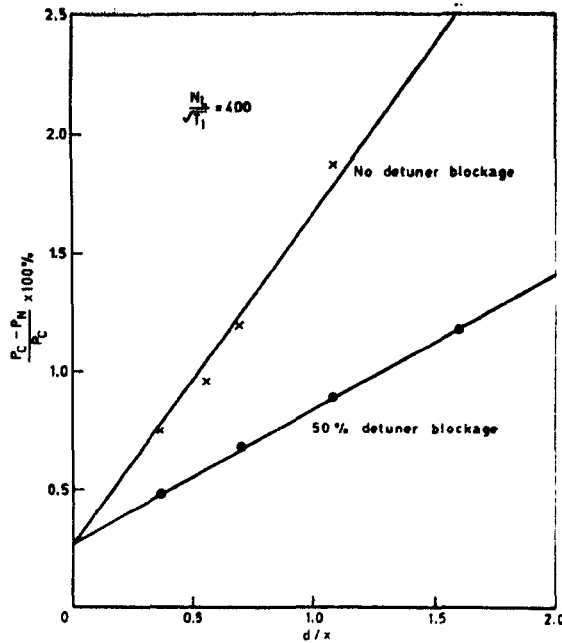


Figure 2.26: Nozzle Blockage Area Effect in the Cell Entrainment Ratio ((Ashwood 1984))

Another interesting ejector-pump performance study was carried out by Vyas et al. (Vyas and Kar 1975). This time, the study is not related with gas turbine engine performance in test bed but involves 2 mm, 3mm, 4 mm and 5 mm nozzle diameters and a mixing pipe of 38 mm diameter. The results of this experimental study show that the entrainment ratio decreases with the nozzle-mixing pipe distance.

Apparently the trend of the results found by Vias does not agree with the above illustrated trends (Figure 2.24 and Figure 2.25). A simple possible explanation for this can be related to the fact that Vias has used very small nozzle diameters compared to that of the mixing pipe. Therefore, this results in a very small blockage area, at the inlet of the mixing pipe, which does not affect the ejector performance.

On the contrary, the blockage area of the engine nozzle has a really big impact in the ejector performance (Sapp and Netzer 1978) and (Ashwood 1984)

The influence of the blockage area at the entrance of the detuner is shown in Figure 2.26. In the horizontal axis is plotted the ratio between the nozzle diameter and the engine-detuner distance while in the vertical the percentage of the pressure variation along the engine. Such a percentage represents the depression around the engine which is strongly related to the secondary mass flow entering the cell. The graph shows that without any blockage area at the detuner entry the depression along the engine is much higher compared with a 50% of the detuner area blocked.

The engine-detuner spacing does not affect only the amount of secondary flow entering the cell. Indeed, also the pressure distribution along the engine is dependent on the distance between the engine nozzle and the detuner entrance.

As already said, as the secondary flow enters the detuner it starts to accelerate and generate a low pressure region around the engine after-body. Therefore, the closer the engine is to the detuner higher is the depression felt around its after-body.

This is one of the causes, which are better illustrated later (paragraph 2.3), of the fact that the load measured during the test is not the real gross thrust delivered by the engine.

An example of how the engine detuner gap affects the measured thrust is given in (Ashwood 1984) where a full scale parametric experimental analysis is illustrated (Figure 2.27).

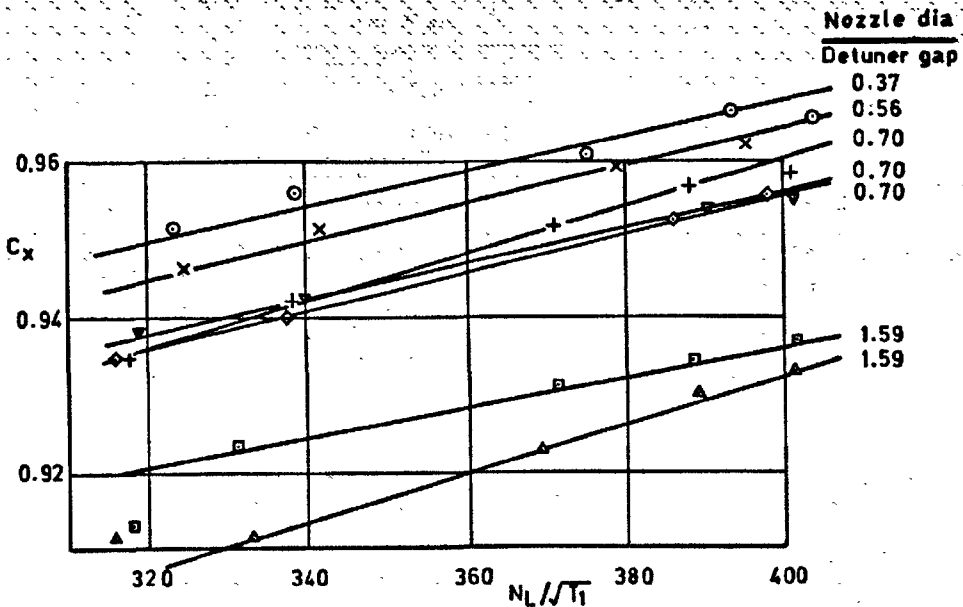


Figure 2.27: Effect of the Engine-Detuner Distance on the Thrust Measured (Ashwood 1984)

The analysis has been conducted with only one nozzle diameter and therefore the different lines correspond to different engine positions. The parameters on the vertical and horizontal axis are respectively the ratio of the measured over the calculated thrust and the non dimensional rotational speed of the engine.

It is clear that as the engine-detuner gap increases the difference between the measured and the calculated thrust reduces and the  $C_x$  get closer to one.

Apparently this does not agree with the fact that the depression around the engine increase with entrainment ratio (which is worth to remember that increases with the engine-detuner gap). However, it is important to underline the fact that the lowest pressure region, due to the ejector effect, is not located around the engine but at the entrance of the detuner (Accommodation Region paragraph 5.2.4). Therefore, even though in absolute terms the depression inside the cell is higher when the engine is not very close to the detuner the thrust correction increases when the engine is closer to it (this is confirmed by the findings presentes in the APPENDIX B.

### 2.2.3. Detuner to Nozzle Diameter Ratio

The detuner to nozzle diameter ratio is another very important parameter for the ejector-pump design.

Primarily it affects the area available for the secondary flow along the detuner.

Indeed, as the diameter ratio increases, the entrance loss becomes less important because the secondary flow enters the detuner in a more axial direction.

An example of the effect of collector to nozzle size is shown in Figure 2.28 which is extracted from an experimental study carried out by Hastings (Hastings 1983) with a scale test cell facility (1/12 scale). The tests were made keeping constant the nozzle

pressure ratio, the engine-detuner gap and the nozzle diameter and by varying the exhaust collector diameter.

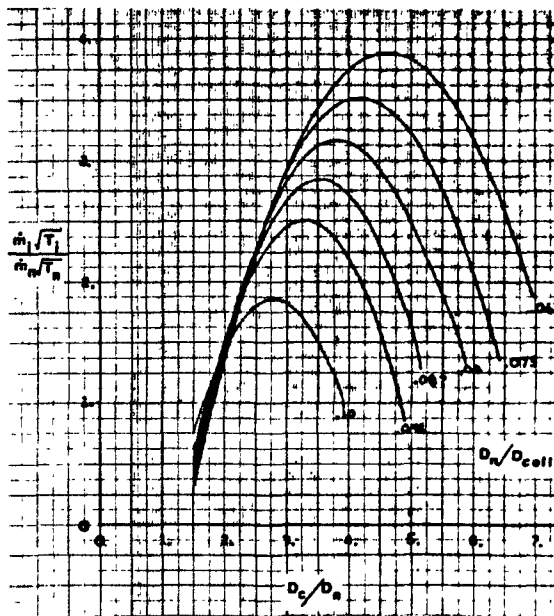


**Figure 2.28: Effect of the Detuner to Nozzle Diameter Ratio on the Entrainment Ratio (Hastings 1983)**

It is possible to see that, the entrainment ratio (vertical axis) varies almost linearly with the diameter ratio (horizontal axis) until a maximum value and then drops off. From Figure 2.28 it is also possible to understand that, as the cell increases the collector diameter has to increase in order to maximise the amount of secondary flow entering the cell.

Vyas et al. (Vyas and Kar 1975) in his air to air experimental ejector analysis has found a linear dependence between the entrainment ratio and the diameter ratio, as it is shown in Figure 2.29.

In Figure 2.29 it is also plotted the Week’s rule, which is an empirical rule (equation (2.5)) derived by the application of the momentum theorem without taking into account any loss. Such a rule has been found to give satisfactory results when driving nozzles are surrounded by a suction nozzle.

$$\mu = 0.22 \frac{D_{det}}{d_{noz}} + 10.7 \quad (2.5)$$

The comparison between the Week’s rule and the experimental analysis shows that the measured entrainment ratio is high for small diameter ratios and low at higher diameter ratios. The difference at small diameter ratios is probably due to the absence of a suction chamber during the experimental sessions. Instead, at high diameter ratio such a difference is probably due to the flow recirculation at the inlet of the detuner which reduces the amount of secondary flow

Similar linear trends, to those shown above, were also obtained by Karamanlis et al. (Karamanlis et al. 1986) in is model test cell experimental analysis. In his analysis it was found that increasing the exhaust collector diameter from 10 inches to 13.25 inches the cell airflow increases of by 7.5%.

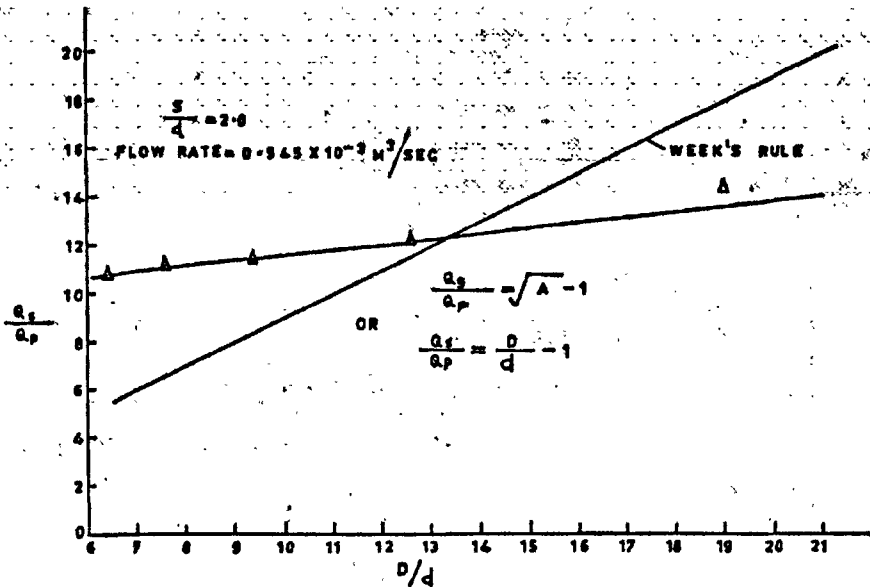


Figure 2.29: Effect of the Detuner to Nozzle Diameter Ratio on the Entrainment Ratio (Vyas and Kar 1975)

An interesting computational study, regarding the influence of the diameter ratio and nozzle pressure ratio on the ejector pump performance, has been presented by Choy and Soh (Choi and Soh 1990). The aim of the study was to develop a computational approach for improving the understanding of the complex flow phenomena occurring along a mixing pipe of an ejector pump. The computational approach used is a time iterative full Navier-Stokes equation solver (PARC code).

Four different area ratios (collector to nozzle) have been studied: 6, 2.5, 1.5 and 1. For a nozzle pressure ratio of 3.5 the results of the calculations show that an area ratio of 6 is too high and the secondary flow passes through the collector pipe without mixing.

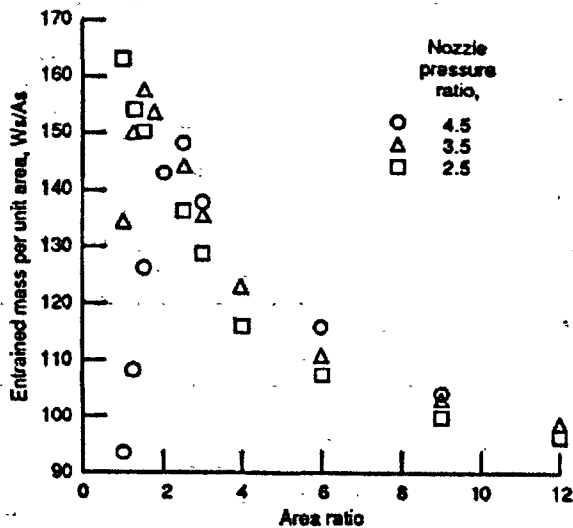


Figure 2.30: Computational Analysis of the Influence of the (Choi and Soh 1990)

The situation improves for 2.5 area ratio where some secondary flow acceleration can be seen at the inlet of the mixing pipe. For 1.5 area ratio the Mach number changes

continuously along the detuner with much faster incoming flow at the mixing duct inlet. When the area ratio is brought to 1 the primary flow impinges into the boundary of the mixing duct and does not any allow the secondary to enter it. Therefore, the pumping performance decays.

From the above summary arises the fact that for a nozzle pressure ratio of 3.5 the best area ratio is 1.5. The same analysis has been repeated for different nozzle pressure ratios and the results are shown in Figure 2.30

### 2.2.4. Effect of the primary Jet Temperature

Due to the fact that an engine test cell has to be designed for testing different kind of engines, the influence of the primary jet temperature on the ejector performance is an important point, worth to be investigated.

The results of the Quinn experimental analysis (Quinn) are shown in Figure 2.31.

In that picture  $\pi$  represent the stagnation pressure ratio of the primary to secondary flow, L and D are respectively the length and the diameter of the mixing pipe,  $\psi$  is the entrainment ratio and  $\theta$  the temperature ratio (primary over secondary). In Figure 2.31 are also plotted the results of analytical ejector model (illustrated in (Quinn) for  $L/D = 12.36$  and  $L/D = 4.36$  (dotted and solid lines)).

The figure shows that for the longer detuner an increase in the primary flow temperature has a negative effect in the performance of the ejector. Indeed, the entrainment ratio decreases by increasing the temperature of the primary jet.

This is probably related to the fact that, for a long detuner the fully mixed conditions are reached inside the detuner also. Therefore, an increase in temperature has the negative effect of increasing also the mixed flow velocity and accordingly the pressure losses of the system.

As the ejector becomes shorter the above described trend is not longer respected.

Indeed for  $L/D = 8.73$  and  $6.55$  at pressure ratios of 5.2 and 6.6 the ejector performance at  $\theta = 1$  and  $\theta = 2$  are almost identical. And for  $L/D = 5.82$  the cell entrainment ratio is higher for  $\theta = 2$  than for  $\theta = 1$ .

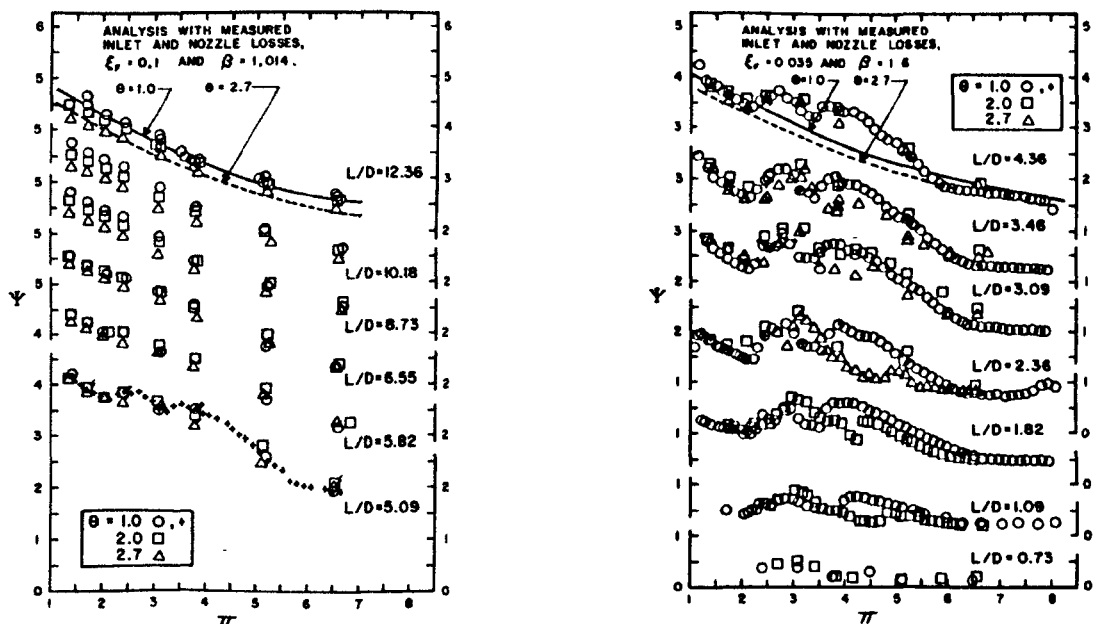


Figure 2.31: Temperature Effect on the Entrainment ratio (Quinn)

This tendency continues with further reductions in length, although obscured to some extent by another phenomenon. For  $L/D=5.09$  and lower, the entrainment ratio trend start to depart from the monotonic shape found for the longer detuner. Indeed, it starts to show two relative maxima. As the detuner length drops below four nozzles diameters the temperature effect slightly increases the pressure ratio at which the maxima were observed. It is worth to notice the substantial increase in performance found in the two relative maxima compared to the analytical solutions.

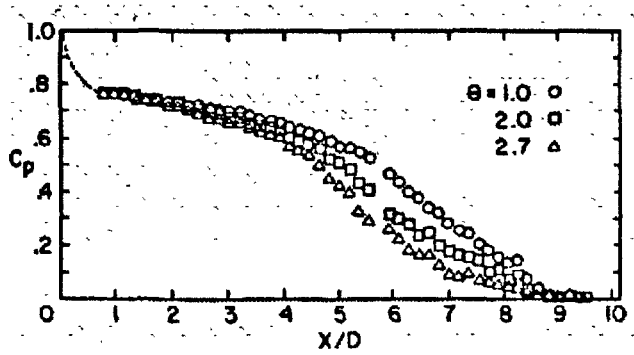


Figure 2.32: Effect of the Primary Flow Temperature on the Mixing Process (Quinn)

During the experiments abrupt changes in noise radiation were observed for the pressure ratio and the detuner length related with the two maxima. These effects have addressed the investigations towards a possible aeroacoustic interaction that promote very rapid mixing for some defined pressure ratio. Also the velocity profiles at the exit of the detuner and the static pressure along it show that for the pressure ratio of 3.8 the mixing process is accelerated (Quinn).

Another important effect of the primary flow temperature in the ejector performance is that high temperatures accelerate the mixing process. This is shown in Figure 2.32 where the increase of static pressure (or the decrease of  $C_p$ ) along the detuner wall is plotted.

For higher  $\theta$  the flow reach earlier the asymptotic value of zero, which means that the flow is completed mixed.

Summarising the above analysis and taking into account that for gas turbine test cell the detuner length is never enough to achieve the fully mixed conditions, an increase in primary flow temperature increases the amount of secondaryflow entering the cell.

This is also stated during the lecture given by Rudnitski for the Agard lectures Series (Rudnitski 1990).

### 2.2.5. Entrainment Ratio Calculation

In this paragraph it is illustrated an example of calculation of the entrainment ratio for sea-level indoor test bed facilities.

Such a calculation is accomplished by an energy balance between the entry and the exit section of the test cell (Jaques 1984) (Figure 2.14).

The cell mass flow enters the test facility at the entry section of the inlet stack (which in this calculation section is called (i)) and at that section its composition is made by 100% air. From that section the cell mass flow passes through the cell inlet, the main chamber, the exhaust system and exits the cell at the exit section of the exhaust stack (which in this calculation section is called (e)). At this section the cell mass flow

contains also the combustion products coming out from the engine cycle which increases the energy level inside the cell.

By the energy conservation principle it is possible to write equation (2.8)

$$W_{air}H_i + W_{fuel}(LHV * \eta_{comb} + H_{fuel}) = W_{air}H_e + W_{fuel}H_e \quad (2.6)$$

From the above equation it is possible to derive the total mass flow entering the cell as it is shown in equation (2.7)

$$W_{air} = \frac{W_{fuel}(LHV * \eta_{comb} + H_{fuel} - H_e)}{(H_e - H_i)} \quad (2.7)$$

Once the total mass flow entering the cell has been derived it is possible, by knowing the engine mass flow (usually directly measured by flow airmeter), to calculate the cell entrainment ratio by equation (2.4).

It is worth to underline the fact that in order to solve equation (2.6) it is necessary to know the temperature at the exit of the exhaust stack. Indeed, such a temperature it is necessary for computing the  $H_e$  ( $H=cp T$  and also  $cp=f(T)$  see appendix A1). Accordingly, some problems could arise if the flow at the exit of the exhaust stack is not fully mixed and still shows a profile. In such a situation the above calculation is not able to calculate the right cell entrainment ratio. Therefore an important assumption for the validity of the equation (2.7) is that the flow at exit of the cell is fully mixed.

## 2.3. Thrust Correction Factors (TCF)

### 2.3.1. Thrust Correction Factors Definition

In the previous discussion about test cell types, the outdoor stand was held out as the standard to which indoor cells were compared. The act of enclosing the engine and directing the airflow through the cell brings with it a number of problems primarily related to the determination of the gross thrust delivered by the engine.

In this paragraph a small introduction to the thrust correction factors is given. Indeed, in Chapter 4 of this thesis this topic will be further discussed using a more deep approach.

As it is better shown in the paragraphs 4.2.8 and 4.2.9 there is not a unique accounting system to estimate the forces acting on the engine inside a test bed facility. Therefore, also the forces can change depending on the interfaces chosen.

As already mentioned in the above paragraph 2.2, the ejector pump effect induces inside the cell a secondary flow which by-passes the engine and enters the exhaust system.

Such a secondary flow affects the pressure distribution around the engine the thrust stand. Altering the pressure fields, the secondary flow gives rise to forces which affect the load measured by the load cells. Therefore, the identification of these forces is a



primary requirement in order to estimate the actual gross thrust delivered by the engine.

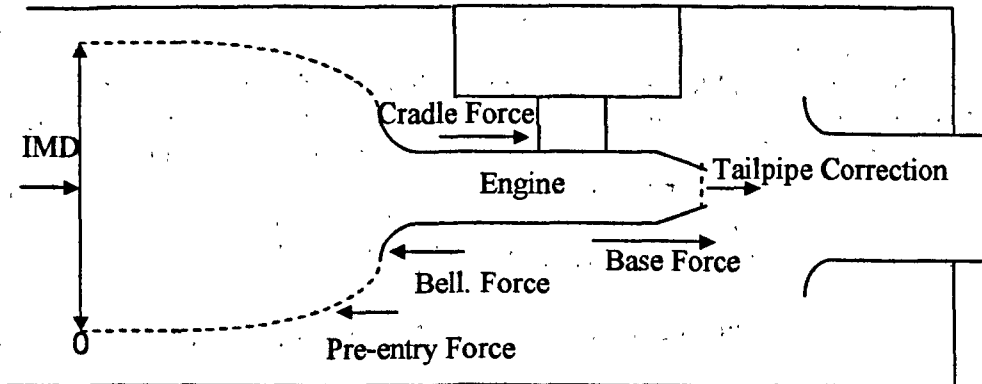


Figure 2.33: Thrust Correction Factors

However, independently on the accounting system the final resultant of the actions on the engine and on the metric-assembly has to be always the same.

The following paragraphs include the definition of the most common thrust correction factors found in the open literature. In order to facilitate their understanding Figure 2.33 shows the forces acting on the metric assembly.

The *Inlet Momentum Drag* (analogous to an inlet momentum effect in flight conditions) represents the momentum effect acting on the entry section of the pre-entry stream tube. For usual cell dimensions and condition the inlet momentum drag represents the most of the total thrust correction, around the 85-95 % of it (Parfitt 2002a).

The *External Bellmouth Force* is the force acting on the external part of the bellmouth and exerted by the secondary flow which by-passes the engine. Usually the bellmouth is directly attached to the engine and therefore the force acting on it is credited in the load measured by the load cells.

The *Skin Friction Drag* is the drag acting along the engine body and originated by the viscosity effects of the secondary airflow.

The *Cradle Force* is the force acting on the movable part of the cradle by the secondary flow which impinges on it. For usual cell conditions it represents the 1% of the load measured.

The *Base Drag*. Around the detuner entrance the secondary flow starts to accelerate as consequence of the ejector effect. Such an acceleration gives rise to a low pressure region around the engine after-body which sucks the engine backward. This effect is usually called *base Force* and represents another thrust correction factor which must be accounted in force accounting system.

**The pre-entry force. If station (0) (Error! Reference source not found.) is used for the thrust and drag accounting system also the pressure force acting on the pre-entry stream tube, usually called *pre-entry force*, has to be taken into account.**

**In the literature the sum of the pre-entry force plus the force acting on the external part of the bellmouth has been estimated to be 10% of the inlet momentum drag (Rios et al. 1998)**

**Finally in the open literature it is also underlined the fact that due to the low pressure region which takes place at the engine after-body the engine nozzles discharge in lower pressure conditions. Therefore, the engine produces more thrust than, for example, in outdoor condition when it runs at the same RPM or with the same fuel flow. This effect it is usually called *Tailpipe Pressure Correction*. Such an effect is accounted through the following equation (2.1) (Rudnitski 1984).**

$$\text{Tailpipe Correction} = A_{\text{nozzle}}(P_{\text{nozzle}} - P_{\text{reference}}) \quad (2.1)$$

**For usual cell condition and dimensions the total sum of the above terms (thrust correction factors) represents 1-5% of the engine gross thrust.**

**In this introduction to the trust correction factors two different methods are taken into account. The first is the Rolls-Royce experience referred to as First Principle Anemometer Method (Parfitt 2001; Parfitt 2002b; Parfitt 2002a) and the second is that of the Industria de Turbo Propulsores (Rios et al. 1998).**

INTENTIONALLY BLANK

### **2.3.3 ITP Thrust Correction Methodology**

It is of relevant interest to report the ITP experience regarding the thrust correction factors (Rios et al. 1998) in this overviewing chapter dealing with cell aero-dynamics. Indeed, such an experience offers the opportunity of understanding the derivation of the thrust correction equations and also provides a quantification of each single thrust correction factor in indoor test facilities.

The dashed line in Figure 2.34 defines the control volume used for deriving the thrust correction equation by mean of the momentum equation (2.13).

The sub-scrits “st” refers to the stone guard and “v” to the viscous forces and  $\Phi$  represents the axial force.

The measured thrust is the net force resulting from all the pressure and viscous stresses on the surfaces wetted by the fluid either passing through the engine or flowing along the outside metric assembly.

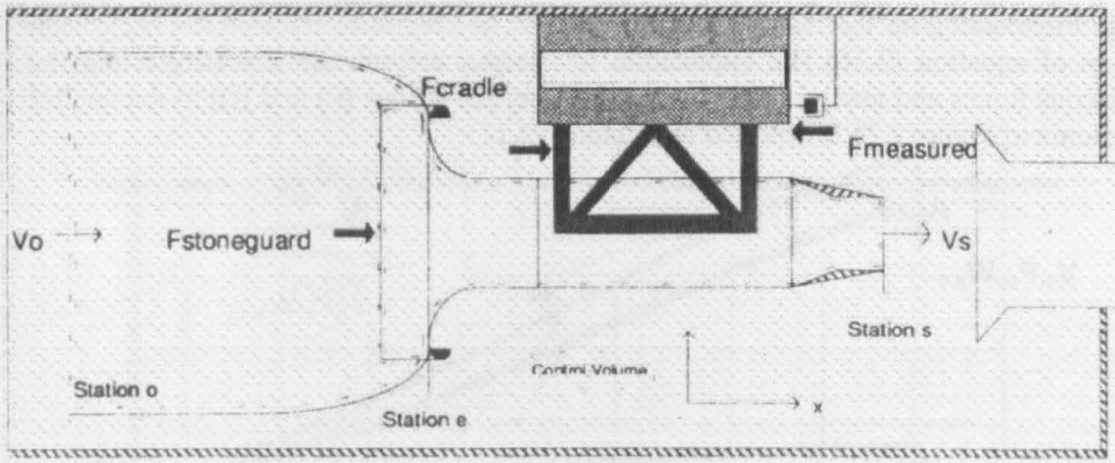


Figure 2.34: Control Volume for the Application of the Momentum Theorem  
(Rios et al. 1998)

$$-\phi_{ve-s(int)} + (p - p_{ref})A_s - \int_0^e (p - p_{ref})dA - \int_{e(int)}^s (p - p_{ref})dA - \phi_{st} = \quad (2.13)$$

$$= W_{eng}v_s - W_{eng}v_0$$

Therefore, the load measured by the load cells can be defined as in equation (2.14).

$$-F_m = \int_{e(int)}^s (p - p_{ref})dA - \int_{e(ext)}^s (p - p_{ref})dA + \phi_{cradle} + \phi_{st} + \phi_{ve-s(int)} + \phi_{ve-s(ext)} \quad (2.14)$$

It has been agreed that the real gross thrust delivered by the engine is equal to the thrust measured in outdoor test facility in ideal condition of no wind. Therefore, substituting  $p_0 = p_{ref}$  and assuming no-flow around the engine, equations (2.13) and (2.14) together can be written as equation (2.15).

$$F_m = F_G = W_{eng}v_s + (p - p_0)A_s \quad (2.15)$$

From equation (2.15) and by using equations (2.13) and (2.14) it is possible to define a thrust correction equation (equation (2.16)).

$$F_G = W_{eng}v_s + (p - p_{ref})A_s =$$

$$= F_m + W_{eng}v_0 - \int_0^e (p - p_0)dA - \int_{e(ext)}^s (p - p_0)dA + \phi_{cradle} + \phi_{ve-s(ext)} \quad (2.16)$$

The terms of equation (2.16) have already been described in paragraph 2.3.1. The third term on the right hand side of equation (2.16) represents the force acting on the pre-entry stream tube (pre-entry force). In order to quantify such a term it is possible to apply the momentum theorem to an external momentum box as that shown

in Figure 2.35. This momentum box ends at section (f) and therefore it includes also the force acting on the bellmouth which is part of the fourth term on the right hand side of equation (2.16). The application of the momentum theorem (neglecting the viscous forces and assuming uniform conditions at sections (0) and (f)) to the control volume of Figure 2.35 is reported in equation (2.17).

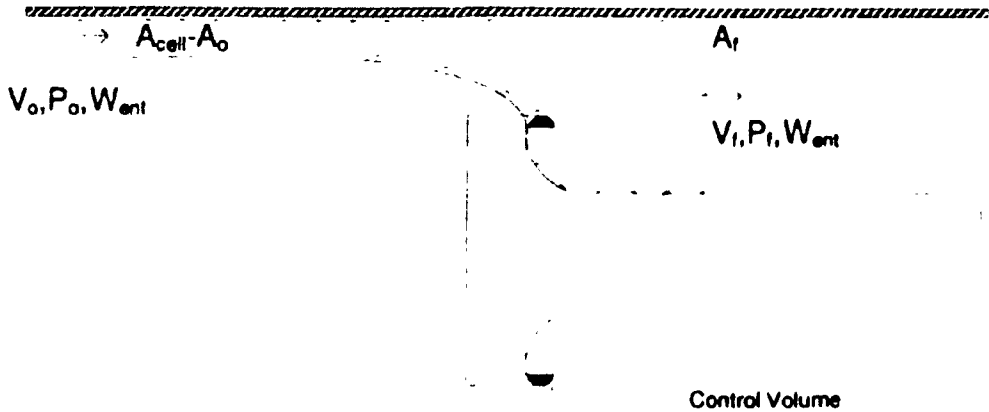


Figure 2.35: Control Volume for the Calculation of the Pre-Entry Force (Rios et al. 1998)

$$(p_f - p_0)A_f + \int_0^e (p - p_0)dA + \int_{e(ext)}^f (p - p_0)dA = -W_{sec}v_0 + -W_{sec}v_f \quad (2.17)$$

Equation (2.17) can also be written as equation (2.18).

$$\phi_{pre} + \phi_{bellmouth} = -(p_f - p_0)A_f - W_{sec}v_0 + -W_{sec}v_f \quad (2.18)$$

Using the continuity equation and assuming that there are not pressure losses between section (0) and (f) it is possible to write ((Rios et al. 1998)) equation (2.19)

$$\frac{\phi_{pre} + \phi_{bellmouth}}{W_{eng}v_0} = \frac{W_{sec}}{W_{eng}v_0} \left( 1 - \frac{1}{2} \left( \frac{v_f}{v_0} + \frac{v_0}{v_f} \right) \right) \quad (2.19)$$

For the ITP test bed when an engine with afterburner is tested the above terms can be quantified as shown below

$$v_f / v_0 = 0.8$$

$$W_{sec} / W_{eng} = 3.8$$

$$(\Phi_{pre} + \Phi_{bellmouth}) / W_{eng}v_0 = -0.095$$

This means that the thrust correction due to the pre-entry force and to the bellmouth force is less than the 10% of the inlet momentum drag.

The important output suggested by the ITP experience is that before neglecting any force, in the thrust correction equation, it is worth to check its magnitude and equation (2.19) is a very useful tool for this purpose.

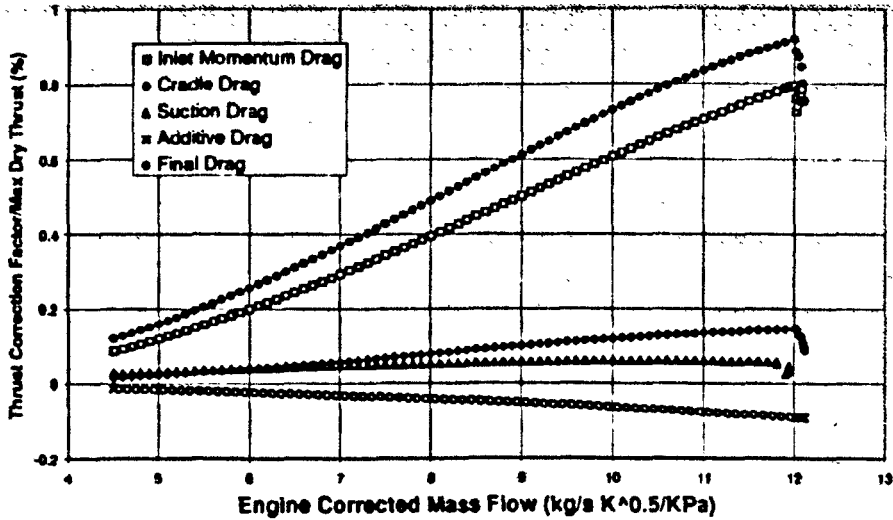


Figure 2.36: ITP Thrust Correction Factor (Rios et al. 1998)

Figure 2.36 shows the result coming out from testing a gas turbine engine with afterburner in the ITP facilities.

In this figure are illustrated the trends of the measured thrust correction factors inside the cell.

It is interesting to note that for the higher engine mass flow the Inlet Momentum Drag, the Suction Drag (Base force) and the Additive Drag (pre-entry force) decrease. This is due to the fact that for such engine mass flows, the engine (with the afterburner on) is working with a bigger nozzle throat which represents a higher blockage to the detuner area. For this reason the performance of the engine-detuner ejector reduce and less mass flow is pumped into the cell.

Accordingly the above thrust correction factors reduce.

## 2.4. Flow Phenomena in Enclosed Test Facilities

### 2.4.1. Flow Distortion

Important performance assessment criteria include front cell flow field distortion and engine face distortion. The front cell, and consequently the engine bellmouth flow field, should be uniform to avoid excessive engine speed fluctuations and thrust measurement uncertainty.

The front cell flow is strongly influenced by the test cell inlet design.

As already seen in paragraph 2.1.6 there are two possible types of inlet system, horizontal and vertical. Obviously the later requires the flow to turn 90° and is the most challenging for the flow quality. However the vertical inlet has also its advantages in terms of noise reduction and weather conditions dependency. Not only the inlet type affects the flow quality inside the cell but also all the equipment installed inside it i.e the flow screens, silencers, turning wind, baffles.

At the same time, however, also the cell equipment installed inside in the test bay as lighting, engine monorails and personnel access stairways affect the flow quality. Moreover, any other projections into the flow can distort the airflow in the front cell and thereby cause a distortion in the engine fan face flow field (SAE aerospace 2002). Also the flow-length between the down-stream edges of the panel or air-straighteners, inside the cell inlet stack, and the engine inlet has been found to influence the quality of the flow (Jaques 1984).

Though the inlet cell design is very important also the flow velocity both ahead of the engine and around it is very important. Indeed, flow perturbations are unavoidable and their resultant distortion augments with the flow velocity. Therefore, the rule is to set an upper limit for the flow velocity up-stream the engine of 15 m/s ((Jaques 1984)). The fact of limiting the cell flow velocity has also an important effect on the design of the cell dimensions and therefore also in the building costs.

About the flow distortion there are several indices defined in the stall theory but none of them can be used for test cell flows. Therefore there are not methods available for predicting the flow distortion down-stream the cell inlet and only a simple rule is given by General Electric ((Jaques 1984)). The rule says that total distortion greater than 50 mm H<sub>2</sub>O above or below the average is unacceptable and it is recommended to keep this difference below 25 mm H<sub>2</sub>O.

Since is not possible to really predict the flow distortion inside the cell in the literature it is strongly advised to use scale test cells to asses the quality of the flow.

An example of such a kind of study was made Freuler (Freuler 1993) where some structural modification are proposed in order to improve the quality of the flow inside the cell. An interesting outcome from this analysis is that flow instability around the engine bellmouth was found dependent on the engine monorail shape which protruded down from the ceiling in the front cell region. In the proximity of the monorail it was also found that flow separates from it and gives arise to some recirculation. Accordingly, aero-dynamics fairings were proposed as solution to this problem.

Furthermore, temperature distortion can also be present in the test bay. This is principally associated with flow recirculation problem as it is shown in paragraph 2.4.2. Temperature distortions at the compressor entry face can seriously alter the engine performance and make really difficult each kind of correlations between different facilities. Therefore it should be avoided.

Computational approaches have been found in literature to asses the quality of the flow inside the cell.

An interesting example is that proposed by Kromer and Dietrich (Kromer-Oehler and Dietrich 1984) by using the combination technique. Such a technique uses the panel methods for deriving the incompressible potential solution to the problem and afterward it applies to that the compressibility corrections. This approach it has been used because of the complexity of the test cell geometry.

In this combination technique the pressure loss are not taken into account and therefore the front cell flow distortion is a static distortion rather than a total. Furthermore, the flow distortion has been introduced by a no-axial velocity component at the inlet of the model.

In order to quantify the flow distortion the same term expressed in equation (2. 1) has been used.



Figure 2.38 shows a typical variation of axial velocity calculated analytically as a function of the height above and below the engine centreline. This profile is located at 27.5% of total test cell axial length up-stream of the bellmouth highlighted section. Though above have been listed all the negative consequence related with the flow distortion inside a test bed facility and possible solutions in some cases, specific tools are included in the cell inlet to simulate the flow distortion.

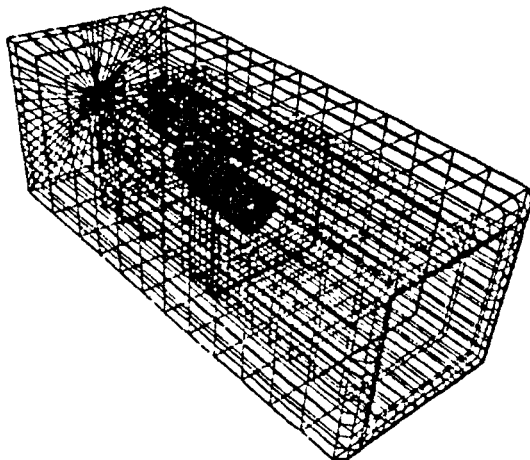


**Figure 2.37: Completely Paneled Test Cell with Engine and Thrust Frame (Kromer and Dietrich 1985)**

This happens because the development of high-performance aircraft, demands the successful integration of airframe, engine, and control system. Beale’s experience (Beale 2002) deals with the distortion generators capabilities including also those simulating transient distortions. These (as variable-position plug, variable position ramps, rotor and stator, planar pulse generator) would allow the simulation in ATF of flight profiles in real time.

A complete treatment of this subject is outside the aim of this thesis, but it represents a valid topic of research at nowadays.

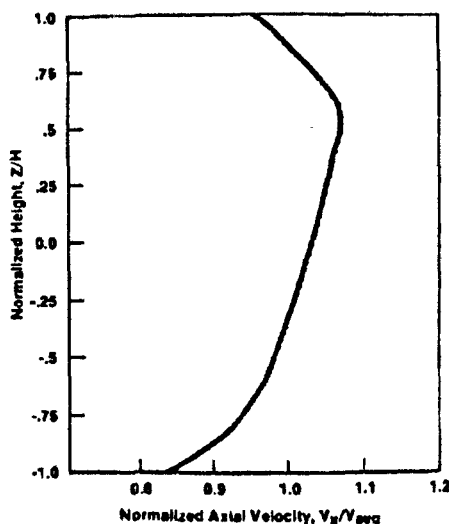


**Figure 2.38: Axial Velocity Distortion in the Front Cell (Kromer-Oehler and Dietrich 1984)**

### **2.4.2. Flow Recirculation**

Two different kinds of recirculation can rise inside a test bed facility, one internally the bed and the other externally.

The internal recirculation is due to an excess of back pressure either along the detuner or along the exhaust stack which allows the hot gasses to return forward from the detuner to the test bay. The re-ingestion of these hot gasses into the engine can cause many problems (as thrust definition and correlation) and serious damages to the engine components.

The recirculation of the hot gasses inside the cell leads also to overheating the cell components and instrumentation affecting their functionality.

The cell maximum temperature limits are typically set to 90 °.

For example the engine thrust stand must be held within a specific temperature range in order to avoid thermally induced loads, which would increase the measurement uncertainty. The instrumentations temperature must be maintained to avoid calibration shifts. Cables and wiring are subject to degradation or failure if heated excessively. Furthermore, the engine has to be maintained within a specific maximum temperature to protect the engine electronic controls and other components particularly in the region of the tailpipe and nozzle.

It is also interesting to say that it is worth to divide the heating problems into two, those related with the cell and those related with the engine. This is basically because, with recent military engines, overheating problems have been found for the engine even when the cell temperature is well below the limits (Prufert and Williamson 2000).

With a high entrainment ratio there is a little likelihood of air recirculation in the test bay. The excess of back pressure can appear when the pressure losses due to the water injection rings, rods or bars, diffuser or blast basket, acoustic panels are too high.

Therefore, in the case of recirculation the back pressure can be reduced by re-shaping the obstructions, increasing the flow area through the exhaust stack and installing a recovery diffuser at the exit of the exhaust stack (Jaques 1984).

An interesting computational and experimental analysis of the flow recirculation inside the test cell is proposed by Cross (Cross 1997). This analysis involves a turbofan engine with afterburning in an altitude test facility. Though this can seem a bit outside the aim of this thesis it represents a valid study useful for improving the understanding of the flow phenomena inside the cell, also sea-level test cell.

The study is concentrated in the flow recirculation inside the exhaust collector as a consequence of the mixing process between the primary and the secondary flow.

Figure 2.39 shows the scheme of the mixing process taken into account by Cross in his analysis (the engine exhausts with the afterburner have Mach number greater than one). If the initial velocity is gradually reduced the flow in the duct is forced to include both a positive and a negative velocity zone.

Note that the mean streamlines represented in the figure take the form of a closed loop with two stagnation points one in the front and one at the rear.

In altitude test facilities the hot gasses blowback phenomena often occur in that part of the flight envelop which represents near sea-level static conditions.

Figure 2.40 shows the different overheating problems in the flight envelope of ATF.

The experimental results were obtained from full-scale testing. The cells were fully instrumented including a thermo-vision infrared camera useful for monitoring the high temperature gas paths.

The computational model was based on a solution of the Navier-Stokes equation in a two dimensional axisymmetric form (PARC2D). The experimental program was conducted to identify the relation between cell pressure and cell and nozzle strut temperature (as index of cell recirculation) at constant nozzle operating conditions.

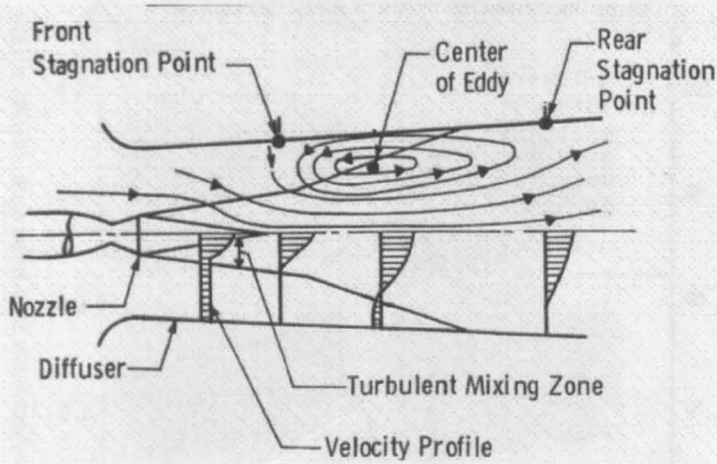


Figure 2.39: Scheme of Ducted Mixing Process (Cross 1997)

(The results show that the hot gas recirculation into the test cell initiates when the primary flow passes from under-expanded to over-expanded condition) This is shown in Figure 2.41 which represents the trend of the nozzle strut and exhaust collector shield temperature as function of the cell static pressure. However, the infra red camera shows that a recirculation is always present inside the detuner even when the cell temperature does not increase and underlining the unsteady nature of the phenomenon.

With the nozzle flow under-expanded, additional expansion of the jet within the diffuser appears to play a role in blocking the recirculation.

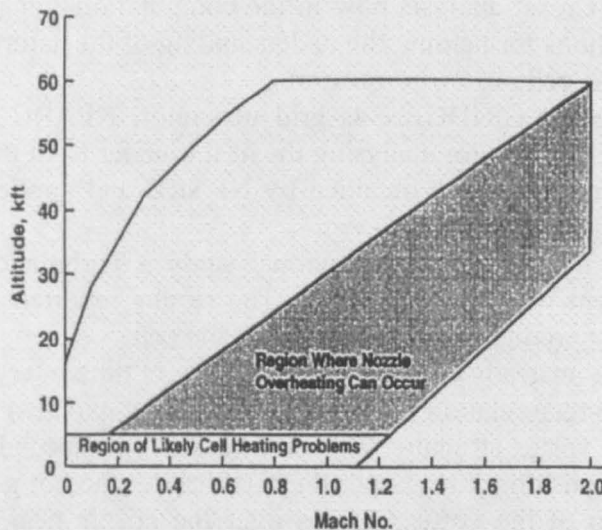


Figure 2.40: Overheating Problems in ATF (Prufert and Williamson 2000)

When the nozzle is operating over-expanded the jet flow angle turns toward the diffuser centreline allowing more area for the secondary flow and effectively reducing the ability of the jet in blocking the recirculation.

The computational results show that the boundary conditions and the model geometry play an important role in the details of the flow field. For example, the diffuser wall temperature boundary condition changes significantly the diffuser wall pressure profile.

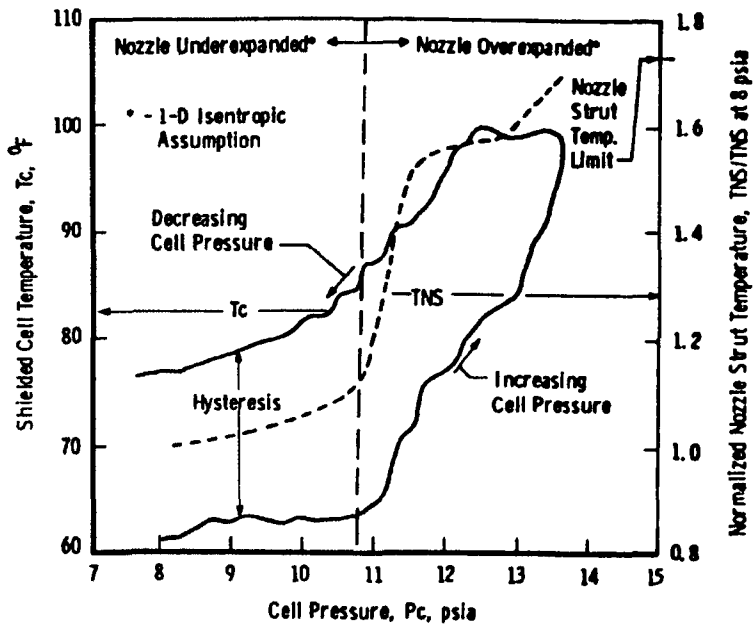


Figure 2.41: Variation of Nozzle Strut and Cell Temperature with the Cell Pressure  
(Cross 1997)

Basically increase in test cell temperature was not indicated by the code even when recirculation into the cell was predicted.

Following the above described Cross's experience the research at Arnold Engineering Development Center was carried on by Prufert and Williamson (Prufert and Williamson 2000).

The object of the study is always the hot recirculation in altitude test facilities.

Differently from the Cross' analysis now in the computational analysis are involved also unsteady simulations for helping the understanding of the nature of the hot gasses recirculation inside the cell.

The software used were: GRIDGEN as grid generator, NPARC as aero-dynamics solver and the BLAYER code for analysing the heat transfer from the boundary layers (this code uses the result directly obtained by NPARC and applies to the them the laws of the heat transfer).

It is also interesting that in this computational study a Turbulence Model analysis between three different was also conducted. The results reported in the publication show that the K-ε best predicts the pressure inside the cell.

Figure 2.42 shows the unsteady CFD solution at different time intervals.

The hot gasses in the recirculation region are periodically expelled from the diffuser, resulting in an annular vortex structure. The cooling flow (the secondary flow) entrains the vortex of hot gas pushing it back into the diffuser. As the hot gasses go back into the diffuser a portion of the vortex sweeps over the nozzle near the trailing edge, potentially heating the nozzle. This indicates that the NPARC code is able to qualitatively predict the presence of diffusing puffing phenomenon.

In the Prufert and Williamson study (Prufert, Mclure, and Power 1994) three different types of cooling flow injection into the cell were investigated. In the first case the cold flow was injected at sonic conditions in a narrow zone upstream to the engine. In the

second the cooling flow was injected from a uniform zone upstream to the engine and in subsonic conditions. Finally in the third the cooling flow was injected around the engine after-body and the cell upstream that position was not included in the simulation. The results of the simulations show that the third configuration (the localized cooling) is the most efficient in terms of engine cooling rate. However, the final outcomes of this study underline the fact that although the current cell configurations are adequate to maintain the test cell air and cell outer wall temperature, the engine cooling rates are not highly effective.

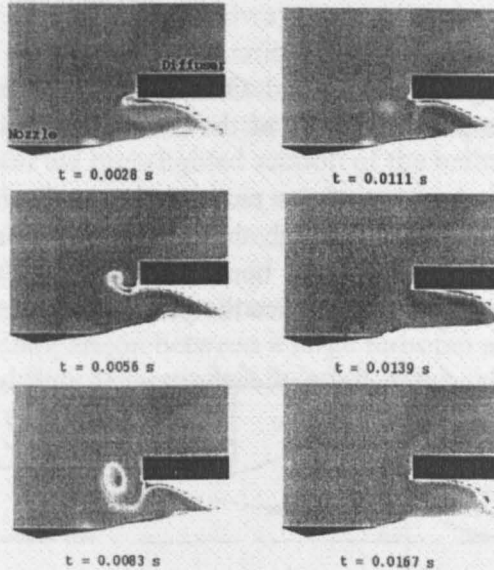


Figure 2.42: Unsteady CFD Solution (Prufert, Mclure, and Power 1994)

This is basically due to the large test cell volumes and the random-directional patterns of the flow within the cell which result in extremely low airflow velocity. For this reason the localized cooling option is the more efficient. Indeed for this configuration the cooling flow is accelerated just above the hottest part of the engine, the nozzle.

Another study related to the flow recirculation for altitude test facility which also addresses some issues related to the computational problems, is that one carried out by Huddleston et al. (Huddleston, Cooper, and Phares 1986).

In this study three different Navier-Stokes solvers were evaluated. They were respectively developed by Thomas, Pulliam and Kneile and McCormack (the above cited reference refers to other works more specifically dealing with the three solvers). The code developed by Pulliam using a Beam-Warming algorithm gives the correct results with the problem encountered in such an analysis. Primarily this is due to its speed, robustness and versatility.

Two different models were simulated, both dealing with turbofan engines in ATF.

The first is a subscale model and only the fan and the secondary flow were simulated (the core flow was substituted by a long sting all along the exhaust collector). The computational results have been found to agree reasonably well with experimental. As outcome also it has been found that the flow recirculation around the engine after-body slow down the convergence of the simulation. This problem it has been addressed with an inadequacy of the algebraic turbulence model used for the recirculation.

The second model is a full scale test facility and this time the core flow was also simulated (both the primary jets were choked). From the experimental data available,

relevant three dimensional effects were found but such effects were neglected in the simulation (axisymmetric simulation). Despite the above assumption the computational results have been found to agree reasonably well with the experimental. All the discrepancies were addressed to the computational grid which it has been found to play an important role in the simulations.

The final outcome of this study is that, cell design problems as nozzle and test cell heating, variable area ejector performance and engine exhaust collector designs can be addressed by computational analysis. Such an analysis for test cell issues, however, requires powerful computational capability and they represent an essential requisite for the success.

In order to reduce the cell internal recirculation a simple back-flow reduction technique was proposed by Anderson and Graham (Anderson and Graham 1968). This consists of an orifice plate installed at the inlet of a straight exhaust collector duct.

Figure 2.43 shows the mechanism of the recirculation reduction. The orifice plate allows the secondary flow to pass through the detuner but obstruct any back flow. Different detuner and orifice sizes have been tested and the results show that the nozzle pressure ratios with orifice were twice the pressure ratios without orifices.

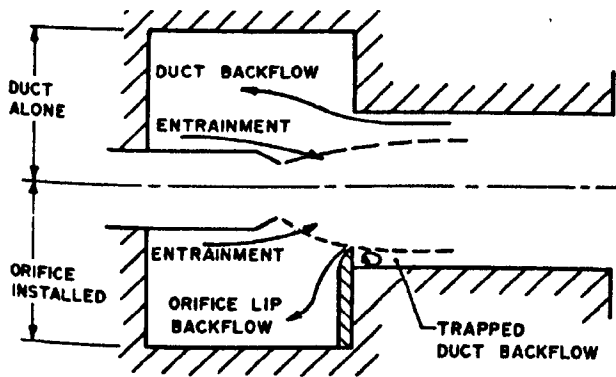


Figure 2.43: Recirculation Reduction Technique (Anderson and Graham 1968)

The external recirculation consists of the reingestion of the hot gasses ejected through the exhaust stack. This kind of recirculation can be minimized by proper cell designs which take into account the prevailing wind direction and the separation of the upper parts of the exhaust and inlet stacks

### 2.4.3. Flow Separation and Vortex Ingestion

The analysis of the flow along the cell walls can be an important indicator of the overall test cell flow quality.

Indeed, the separation of the flow from the walls has a negative impact in both engine performance and quality of the flow inside the cell.

Figure 2.44 shows the axial variation of the static pressure along the cell wall derived from the Kromer and Dietrich analysis (Kromer and Dietrich 1985) described above. In the vertical axis is reported the pressure coefficient and in the horizontal axis the normalized axial station. The solid line normal to the horizontal axis represents the position of the high-lighted section of the bellmouth, and the dashed one the predicted flow separation position. The round symbols in the plot are the experimental results.

Far up-stream the high-lighted section of the bellmouth the pressure coefficient is negative because the contraction of the test cell walls at the front of the test cell.

Up-stream of the bellmouth it is shown that the flow experiences a severe diffusion due to the shape of the pre-entry stream tube, which for the conditions Figure 2.44 is referred to, works in suction mode.

Therefore, if the flow in the test cell is unable to diffuse flow separation along the walls can occur.

Using the Integral Boundary Layer Method the flow along the cell wall has been analysed and it has been found that for every cell entrainment ratio, therefore for every secondary flow velocity, the flow always separates along the walls.

As may be seen in Figure 2.44, the location of the separation moves down-stream as the cell entrainment ratio increases. For the largest entrainment ratio the separation point moves down-stream the high-lighted section of the bellmouth.

When the location of the flow separation is up-stream the bellmouth, it can give rise to vortex formation and ingestion into engine, with a severe negative effect in the engine performance and health.

The above described results have been obtained by modelling a large turbofan engine. Figure 2.45 shows the comparison between a large turbofan and a small engine on the location of the predicted flow separation as function of the cell entrainment ratio. This is also reported in (Rudnitski 1990).

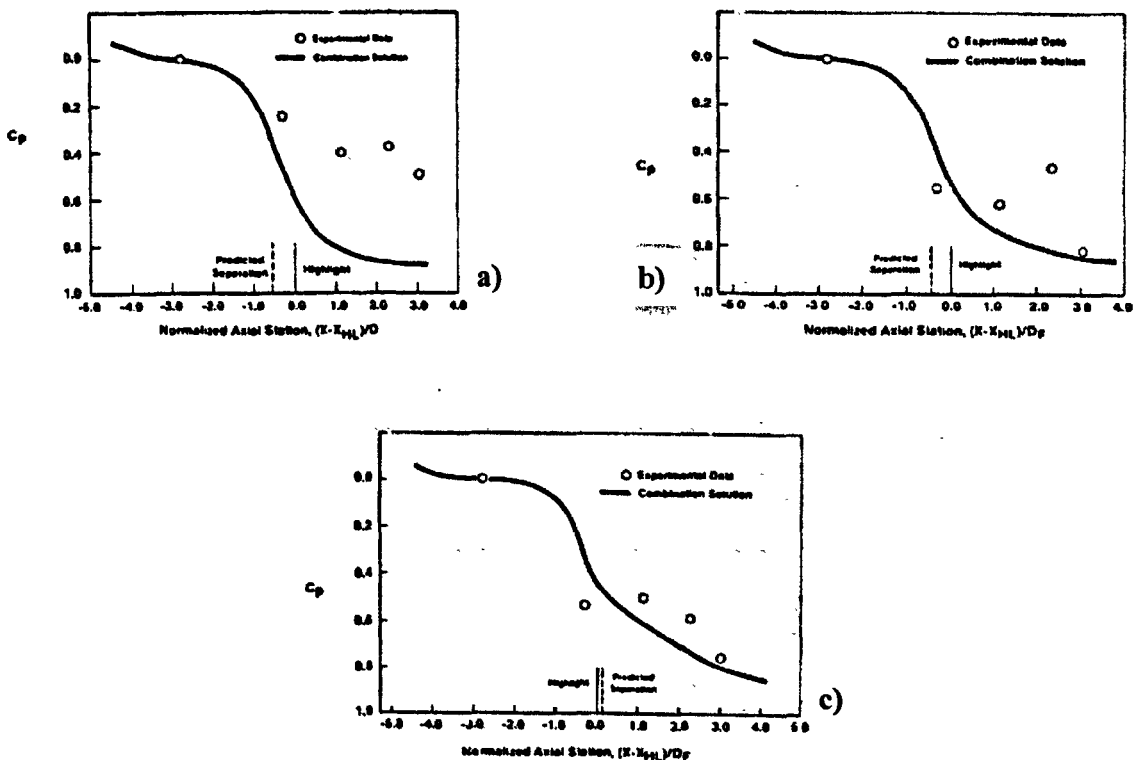


Figure 2.44: Axial Variation of the Pressure Coefficient, a)  $\mu=0.72$ , b)  $\mu=0.86$ , c)  $\mu=1.15$   
(Kromer-Oehler and Dietrich 1984)

The figure shows that the flow separates for both engines up-stream to the high-lighted section of the bellmouth. This separation occurs for  $\mu < 1.1$  for the large engine and for  $\mu < 2.6$  for the small engine. Therefore, for entrainment ratios smaller than

those just mentioned, there is a high likelihood of having vortex formation and ingestion.

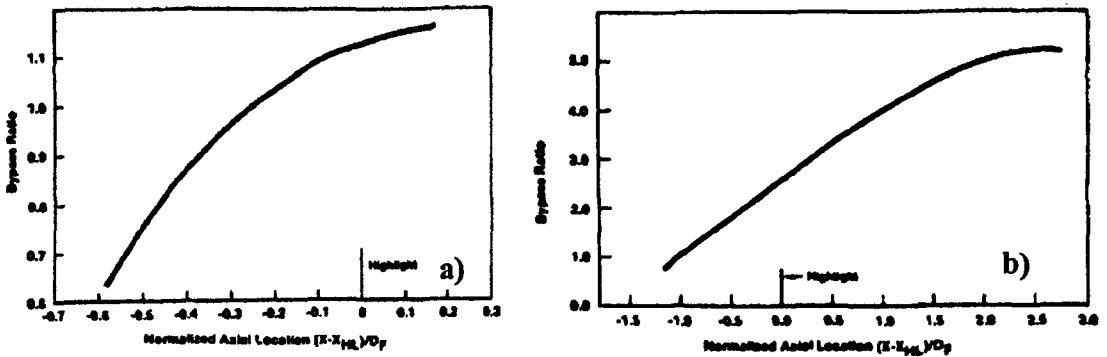


Figure 2.45: Predicted Wall Separation a) Large Turbofan b) Small Engine  
(Kromer-Oehler and Dietrich 1984)

By an experimental analysis involving scale models of large turbofan Freuler (Freuler 1982) derived the map represented in Figure 2.46. This represents the velocity ratio of the flow velocity around the bellmouth highlighted section over the front cell velocity (vertical axis) as function of the cell entrainment ratio (horizontal axis).

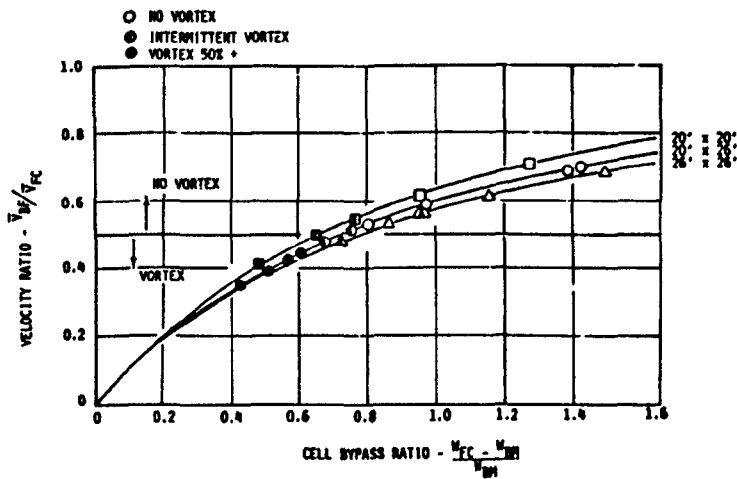


Figure 2.46: Experimental Vortex Appearance (Freuler 1982)

From the above figure it is clear that vortices were observed to appear and be ingested into the simulated engine bellmouth at velocity ratios below 0.5.

It is also worth to note that the vortices appear at or below entrainment ratios of approximately 0.75.

Following the Freuler's experience, and by the use of the combination technique Kromer and Dietrich (Kromer and Dietrich 1985) derived a map similar to that represented in Figure 2.46. The results are shown in Figure 2.47.

The parameters represented in Figure 2.47 are the same than those used in Figure 2.46. The only difference is that in the former the characteristic of two engines are represented. The solid line represents a large engine and the dashed line represents a small engine.

Usually large turbofan engines in sea-level test cells operate with an entrainment ratio between 1 and 2, when small engines operate with entrainment ratios which can be greater than 5.



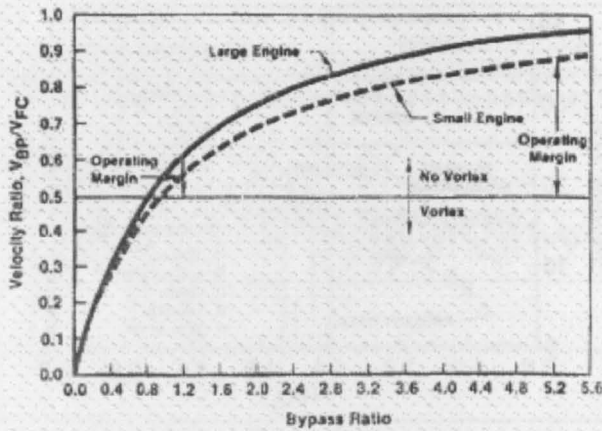


Figure 2.47: Engine Operatin Margin as Function of the Entrainment Ratio  
(Kromer and Dietrich 1985)

From the above consideration Figure 2.47 shows that the operating margin to prevent vortex formation and ingestion for small engines is higher than for large turbofan engines.

Therefore, when a large turbofan is tested attention has to be payed in order to prevent the appearance of the vortices inside the cell and their ingestion into the the engine.

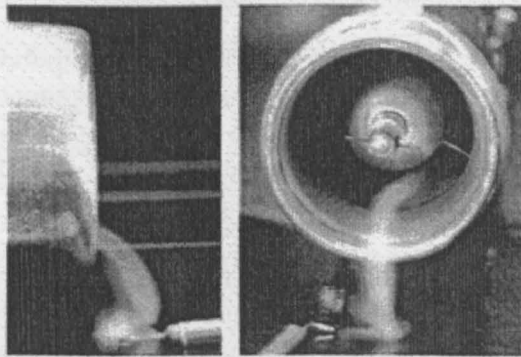


Figure 2.48: Vortex Ingestion Visualization (Brix, Neuwerth, and Jacob 2000)

Up to now the review about the vortex formation has been taken into account only as a consequence of the flow separation. There are several theories behind the vortex formation in inlet flows near the walls (i.e existence of the inlet vorticity in the ambient, presence of the stagnation point in the wall, updraft from the stagnation point to the inlet (Kline 1957) but their analysis is beyond the scope of this work. However, it is important to provide a criterion which links the engine position inside the cell and the flow conditions with the vortex formation.

Such a criterion is extracted from the analysis carried out from Nakayama (Nakayama and Jones 1996) which demonstrates that the theory of the stagnation point as essential condition for the vortex appearance predicts the right trends but underestimates the vortex formation. In its analysis Nakayama put also together the experimental results obtained from pioneers in the ground vortex as Glenny (Glenny 1968) Motika (Motycka 1975) Shin et al. (Shin et al. 1986) and completed them by adding the cases of large engine diameters.

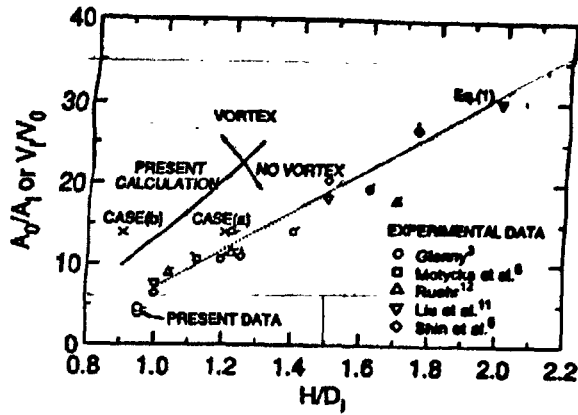


Figure 2.49: Inlet Vortex Formation Correlation (Nakayama and Jones 1996)

Figure 2.49 shows the results relative to inlet vortex formation obtained from different studies. In the horizontal axis is represented the ratio between the distance of the engine centre line to the wall ( $H_c$ ) and the inlet diameter ( $D_i$ ) when in the vertical axis the ratio between the flow condition at the engine inlet section (1) and those upstream the engine (0).

The dashed line represents the experimental border line between the vortex and no-vortex region. Above the line, there is the vortex appearance when below the line there is not.

The solid line represents the border line derived from computational analysis where the vortex appearance was related to the formation of a stagnation stream line. It is possible to see that this line underestimates the vortex formation. A possible reason is that enough air vorticity for the vortex appearance can be gathered together also without the formation of a stagnation stream line.

Equation (2.20) (Nakayama and Jones 1996) represents the correlation between the experimental data reported in the dashed line and it is a useful relation to use in order to prevent the inlet vortex formation and ingestion in indoor sea-level test bed facilities.

$$\frac{A_0}{A_1} = 24 \frac{H_c}{D_i} - 17 \quad (2.20)$$

#### 2.4.4. Pressure Fluctuation

Inside test cell facilities it is possible to experience extreme pressure fluctuations which can also lead to unacceptable pressure values, greater than the barometric atmospheric pressure.

These pressure excursions contribute to a history of cell structural problems owing to the reversal of pressure loads on walls and panels and particularly door systems.

The probability of un-steady flows increases with the fact that one test cell is used for several types of engines differing in configuration, thrust level, inlet flow requirement and exhaust temperature.

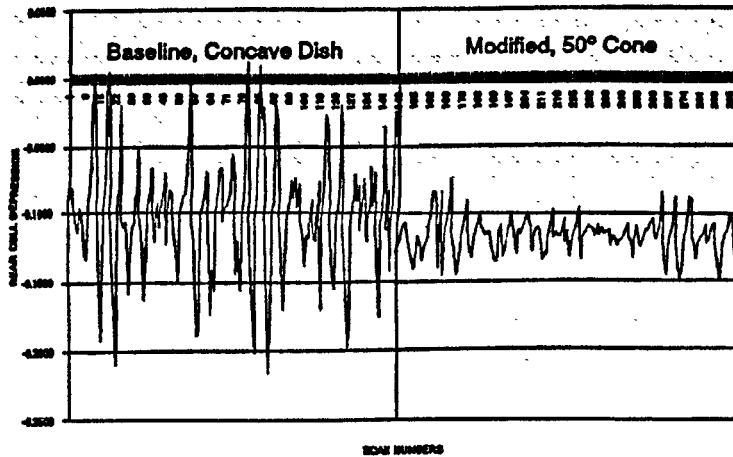


Figure 2.50: Example of Pressure Fluctuations in Sea-Level Test Cell Facility  
(Freuler and Montgomery 1995)

A critical pressure fluctuation example is reported in the Freuler and Montgomery (Freuler and Montgomery 1995) study of a General Electric test cell in Cincinnati. Figure 2.50 shows the pressure fluctuation measured in the above mentioned test cell. Such fluctuations are responsible for noticeable door movements inside the cell and one of them in the upper part of the inlet stack went also out of track. In the left side of Figure 2.50 are reported the pressure fluctuation in the cell baseline configuration and in the right side in modified configuration.

The study conducted by Freuler and Montgomery about the attenuation of these pressure excursions was concentrated on the analysis of the exhaust system design (including the detuner, the stack and the blast basket) and in the cell overall flow path length. Prior to any modification in the full scale test cell a study was conducted in a fully instrumented scale model (1:12) representing as much as possible the full scale cell. The attention was concentrated on different blast basket end shapes. Figure 2.51 shows the results obtained with the different blast basket test. In the last column of the picture is reported the amplitude of the fluctuation reduction measured for the different cases.

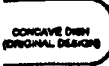


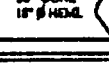
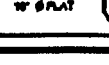
Basket End Design Type	Configuration Description	Exh Stack SPL dB	Peak-to-peak psi (kPa)	Peak in H <sub>2</sub> O (mm H <sub>2</sub> O)	R <sup>2</sup> %
	Concave Dish (Baseline)	128.3	0.0214 (0.1475)	±0.30 (±7.53)	-
	Flat Plate End	120.6	0.0088 (0.0606)	±0.12 (±3.09)	59
	Convex Dome	120.6	0.0088 (0.0606)	±0.12 (±3.09)	59
	50° Semi-Vertex Cone (with hemispherical nose)	118.4	0.0068 (0.0469)	±0.09 (±2.39)	68
	55° Semi-Vertex Cone (with truncated nose)	116.6 <sup>a</sup>	0.0056 (0.0386)	±0.08 (±1.97)	74

Figure 2.51: Different Blast Basket End Shape Experimentally Tested  
(Freuler and Montgomery 1995)

From the results shown above it was chosen to reproduce in the full scale test cell a blast basket with a 50° semi-vertex cone. The full scale results are shown in Figure 2.50 and they show that the modification has achieved the scope of drastically reducing the pressure fluctuations.

## 2.5. CFD Support to Engine Test

The modern Computational Fluid Dynamic techniques arise from the convergence of three main fields: the aero-dynamics theory, computer performance, applied mathematical methods (in the Graves's analysis (Graves 1982). The chronological steps of the above mentioned fields are listed and commented).

The develop of CFD techniques now days can be related to three main compelling motivations in the past few years.

The first motivation is to provide new technological capabilities that can not be provided by experimental facilities. Indeed, the experimental aero-dynamics facilities have notorious limits in the flow representation as high Reynolds number, propulsive and external flow interaction during flight conditions, planetary atmosphere conditions etc. Numerical simulations do not have any of these limitations but however they are limited by other parameters such as the speed and the memory of the computer.

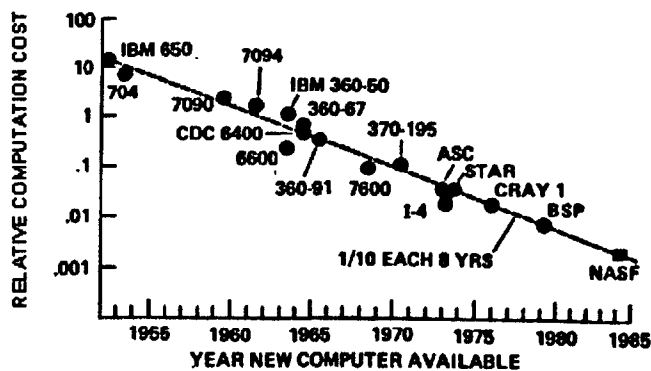


Figure 2.52: Trend of Relative Computational Cost for Numerical Flow Simulation  
(Graves 1982)

The second motivation concerns with the energy conservation. Indeed, the large development wind tunnels require a large amount of energy whereas computers require comparatively negligible amounts.

The third motivation for developing CFD is related to the economics in the sense that computer speed and memory has increased with time at a much greater rate than computer costs. In addition, the rate of improvement in the computational efficiency of numerical algorithms for a given computer has been remarkable

Practically this means that the net cost of conducting a given numerical simulation with a fixed algorithm has decreased rapidly with time (Chapman 1979).

Figure 2.52 shows the trend of the computational costs of numerical simulation for a given flow and algorithm.

At the same time with the above described escalation of computational and numerical resources also the propulsion systems have become increasingly complex. A result the

limits of present technologies are pushed for reaching improvement in performance or other mission criteria. Accordingly, in engine test environment a more detailed understanding of component performance and test/cell article interactions are required.

Thus, CFD is growing into a role which complements and enhances all phases of system design including test and evaluation. In fact, CFD is becoming an integral part of the hardware testing process by providing information for pre-test facility design and instrumentation and post-test analysis.

Several interesting practical examples of CFD application in aeropropulsion test environment are reported in the Power's experience (Power and Heikkenen 1993) as:

- understanding flow phenomena (as flow separation)
- propose and evaluate modification (detuner lip)
- evaluate component interaction (engine/fuselage)
- improve experimental measurements (sub-scale supersonic nozzle)
- chemistry process (combustion of the hydrogen deposition)

Summarizing, it can be said that CFD is being incorporated in the design process by engine and aircraft manufacturers and test facility operator with three main objectives:

- to minimize parametric and scale test
- to reduce the risk by permitting more configuration to be evaluated numerically
- to remove the constraint of limitations in the existing data base

The goal is to eliminate as much test as possible (Barton 1984).

### ***2.5.1. Modular Geometry Archive***

The Modular Geometry Archive arises from the experience of AEDC Group (Sverdrup Technology, Inc.) which has over ten major turbine engine altitude test cells and sea-level test stands. Test cell configurations are flexible to meet a wide variety of test requirements. Therefore, although the general cells components are present in each facility their characteristics such as shape and dimension can be different for each one of them.

The Modular Geometry concept addresses hardware reconfigurations by maintaining a computational model of each component, allowing construction of a new configuration without starting from scratch.

In the past, modelled test cell hardware required weeks to months to generate computationally and there was no mechanism to store critical geometry information. Therefore each calculation of different but related configurations was a restart from a ground zero.

Capitalizing on emerging grid generation technologies, engine and test cell hardware component models are stored in a manner which enables quick turnaround model generation for specific test cell and engine computational models.

Figure 2.53 shows the Modular Archive system hierarchy with the branched partially expanded for the altitude test facilities and test article geometry (Prufert, McClure, and Power 1994).

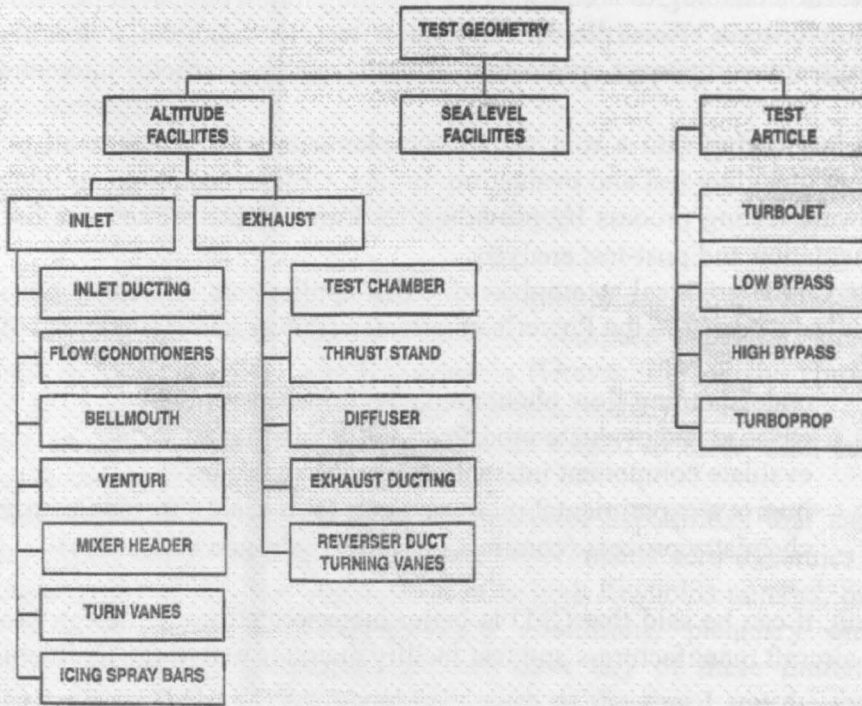


Figure 2.53: Modular Geometry Archive System (Prufert, McClure, and Power 1994)

Utilization of this data-base relies on the capabilities of work-station to construct files with textual and image links to those databases.

This process speeds-up the initial development of complex models by eliminating the confusion over how to get the necessary model geometry information

### 2.5.2. Computational Support to Sea-Level Test Facility

In this paragraph a computational exercise done within the AEDC Group for evaluating the amount of secondary flow for a sea-level test cell is reported ((Prufert, McClure, and Power 1994)).

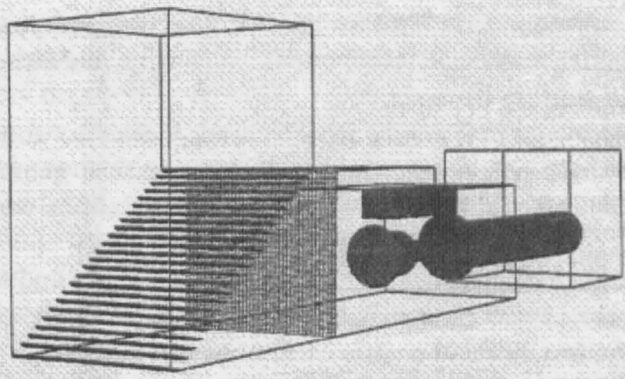


Figure 2.54: 3D Rendering of the Test Facility Model (Prufert, McClure, and Power 1994)

Figure 2.54 shows a three dimensional rendering of the model of the sea-level test cell.

Only half of the model was computed by specifying symmetry along the horizontal centreline of the cell.

Neither baffles nor struts were modelled in either the inlet or exhaust stack because the velocities at those sections of the cell are sufficiently low to have a little effect on the overall flow.

Turning vanes were modelled but the viscosity effects in the vicinity of the vanes were assumed to be small.

The inlet flow screen was modelled by using an empirical porous media model in which the pressure losses are a function of the porosity of the screen and of the local velocity.

The thrust frame was modelled as complete blockage to the flow.

The model engine geometry simulated the overall engine dimensions in order to maintain the inlet area, the fan discharge area and the core nozzle area. This was done for simulating the correct flow rate and velocities into and out the engine.

The detuner pipe was modelled without any assumptions and the blast basket was modelled with an empirical porous media.

Figure 2.55 shows the results of the three dimensional simulation. And it is possible to note a recirculation inside the cell with some path lines ingested by the engine coming from the rear of the cell.

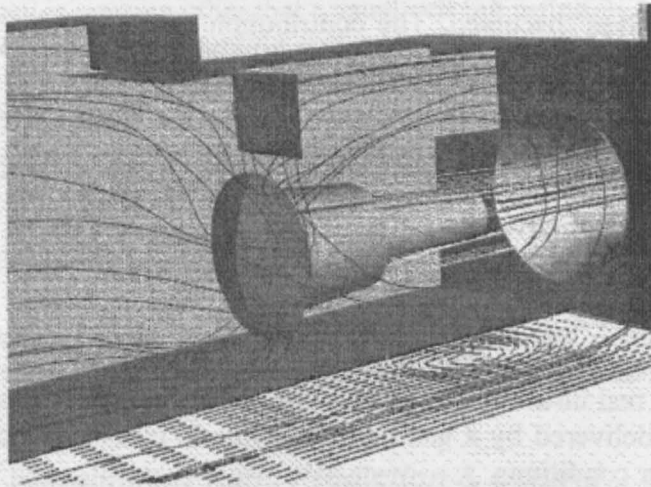


**Figure 2.55: 3D Simulation Results (Prufert, McClure, and Power 1994)**

## **3. Research Objectives**

### **3.1. Introduction**

The work described in this thesis has been fully supported by Rolls-Royce plc. Their principle objective was to assess the relevance and accuracy of CFD when applied to thrust measurement in indoor sea-level test bed facilities with the outcome to minimise the use of expensive experimental measurements.

In response, one of the outcomes of this research provides a clear and detailed definition of all the forces acting on the metric-assembly inside a typical test cell. This information was needed to support the First Principle Anemometer method then in current use within the company.

Accordingly, once the force accounting system has been defined and the forces detected, a CFD methodology is developed to allow computational calculation of thrust correction factors needed to predict outdoor thrust.

In this chapter the research objectives will be outlined and the research method to achieve those objectives discussed. The contribution to the science and the benefit resulting from undertaking this investigation are anticipated.

### **3.2. Previous Research Gaps - Objectives & Methodologies**

#### **3.2.1. Thrust Correction Factors**

It is well known in the literature that the force measured by the load cell during sea-level tests is not the real thrust delivered by a gas turbine engine. It is also well known that the real thrust delivered by a gas turbine engine is measurable only by outdoor tests in ideal weather conditions.

However, neither of the topics described above have, hitherto, been adequately addressed in the literature. The correction terms for calculating the real thrust delivered by an engine from indoor test results are defined and described (paragraph 2.3) but only from a simplified point of view. Indeed, only the ITP paper ((Rios et al. 1998)) defines proper system interfaces and analyses all the components acting on the metric assembly.

Furthermore, there is no attempt, in the literature, to quantify such correction terms as functions of the engine-cell configuration and of the flow inside the cell.

#### *Objectives -Thrust Correction Factors*

The objectives of the work dealing with the thrust correction factors are as follow:

- To use different system interfaces in order to account for all the forces acting on the metric-assembly and understand the meaning of each thrust correction factor.



- To evaluate the most useful system interface in order to achieve a repeatable, reliable and accurate evaluation of the thrust correction factor by means of flow measurement during the test.
- To express each single thrust correction factor as function of the cell and engine dimensions and of the flow inside the cell. This is in order to make a thrust correction derivation possible from common flow measurements during the engine test and to understand how such correction factors change with the flow structure inside the cell.
- To analyse the differences between the flow structure for indoor and outdoor environment and evaluate the difference in the metric-assembly forces

### *Methodology - Thrust Correction Factors*

The research done in the past for the estimation of the thrust and drag of propulsion systems in-flight conditions is used in Chapter 3 for defining different system interfaces for the engine inside a test cell facility.

One approach is to move from the in flight conditions (infinite in terms of external environment) to the enclosed conditions inside the cell using a pseudo-infinite cell concept. Such a cell is nothing other than a usual cell but infinitely large.

At the same time, different accounting systems are being taken into account in order to propose thrust correction equations which involve either drag or force terms or drag and force together (hybrid).

One dimensional gas dynamic relationships (based on the Newton's second and third laws, continuity, isentropic compressible flow and energy conservation) are used to derive functions which link each thrust correction factor with the cell and the engine dimensions and the flow inside the cell.

As validation for the different thrust correction equations derived, a comparison among them is proposed using genuine test data provided by Rolls-Royce.

### **3.2.2. Cell Entrainment Ratio Prediction & Control**

As has been outlined in the literature review, the cell entrainment ratio is the main engine-cell performance parameter.

Indeed, most of the flow phenomena which take place inside the test cell (like distortion, recirculation, separation, fluctuation) depend on the amount of mass flow entering the cell. As a result of this the engine performance inside the cell and the cell structural integrity, are also dependent on the cell entrainment ratio (paragraphs 2.2, 2.3, 2.4).

Experimentally, entrainment ratio thresholds have been defined in order to protect the cell environment from these various flow phenomena. However, the thresholds need conflicting entrainment ratio requirements for each flow phenomena taken into account. For example, in order to reduce the flow distortion it is advisable to keep the entrainment ratio as low as possible. At the same time, however, for the recirculation, it would be better to have high entrainment ratio. The same phenomenon occurs between the temperature limits inside the cell and flow separation.

Although, the cell entrainment ratio and its effects on the cell environment have been broadly studied, there is no particular published reference which studies how to predict and control cell entrainment ratio before testing the engine in the cell.

The advantages of knowing the cell entrainment ratio before running the engine can be enormous.

First, for example, this would help to preserve the cell environment from the adverse flow phenomena which could alter the test results or even damage the engine.

Second, a preliminary thrust correction factor calculation can be done before running the engine. Indeed, if the objective (defined in the previous paragraph) of expressing the thrust correction factor as a function of the cell and engine dimensions and of the entrainment ratio is achieved, a preliminary calculation of the real thrust delivered by the engine could be undertaken.

Furthermore, if the control of the cell entrainment ratio is also achieved, cell readjustments can be made in order to best suit the engine within its environment.

Another advantage of knowing the cell entrainment ratio is the possibility of supporting CFD studies. Indeed, by knowing the total mass flow entering the cell, it would be possible to extrapolate flow parameters which can be useful in the modelling and validation of CFD predictions.

### *Objectives – Entrainment Ratio Prediction & Control*

With the above considerations in mind, the objectives of this part of the thesis dealing with entrainment ratio prediction and control are the following:

- To develop a method for predicting the cell entrainment ratio based in engine and cell parameter measurable during tests
- To develop a method for controlling the cell entrainment ratio
- To provide a tool which can support CFD fluid dynamic study in the definition and of the boundary condition and in their validation

### *Methodology - Entrainment Ratio Prediction & Control*

As described in Chapter 2 the secondary mass flow enters the test cell as a consequence of the ejector pump defined by the engine and the exhaust collector pipe (detuner).

Therefore, the methodology for developing an analytical tool able to predict the cell entrainment ratio has been found in an ejector pump theory.

In particular, a steady and one dimensional ejector pump analysis is used as a starting point, firstly to understand and secondly to characterise the interaction between the engine and the detuner.

However, due to the fact that the primary and secondary flows are not completely mixed at the exit of the detuner, another section is needed within the detuner to characterise its performance.

In order to control the entrainment ratio, a characterisation of the entire cell is based on the ejector theory and on the measurements taken inside the cell.

The results obtained from the analytical tool are then compared with those obtained by CFD simulations. The main purposes of this are: understand, prove and validate the findings.

### **3.2.3. CFD as Support to Indoor Sea-Level Test**

In the open literature, CFD applied to sea-level test cells is for the most part concentrated on the analysis of the flow quality inside the cell. (paragraphs 2.4.1, 2.4.2, 2.4.3, 2.4.4 and 2.5.2). At the same time, however, qualitative results have been extrapolated by the calculations and also very useful relationships have been found in order to protect the cell environment from adverse flow phenomena.

The CFD step by step is taking the role which, before its development, was of the small scale test cell facilities. Therefore, CFD it is used for improving test cell performance, supporting cell modification and for visualise the flow within the cell.

In this work the CFD is used firstly to clarify the understanding of the flow structure which was not well defined in the literature review (probably because of the impossibility of measuring some flow regions inside the cell, as for example the pre-entry stream tube). Secondly, it is used to help the validation of the objectives previously proposed in paragraphs 3.2.1 and 3.2.2 by quantitative extrapolations.

#### *Objectives – CFD as a Support to Indoor Sea-Level Test*

- To asses the suitability of a commercial CFD package (with defined settings) for modelling engine-cell performance in terms of: flow structure, entrainment ratio prediction and test cell characterization.
- To provide guidelines and recommendations about the software settings and about the test cell components representations
- To use the ejector-pump analytical experience to improve the CFD modelling and at the same time validate the models
- To use the CFD experience to improve the ejector pump analytical experience
- To evaluate quantitatively the thrust correction factors for a sea-level indoor test facility.
- To compare the CFD calculated thrust correction factors with those analytically derived (paragraph 3.2.1)

#### *Methodology - CFD as Support to Indoor Sea-Level Test*

The CFD package used for the computational analysis is that provided by the Fluent .inc.

The objective is to evaluate several models. Each model includes the main features of a sea-level test bed facility but depending on the scope of the simulation the model geometry can also vary. For example, single test cell components such as the inlet

stack, the test bay and the exhaust system are first studied separately and then added together to form the entire test cell. Due to the dimensions of each single component, the total test cell represents a very large model which has, therefore, to face the compromise of result accuracy, time and computational resource.

This compromise practically does not allow the modelling of the entire cell with enough accuracy for a quantitative data extrapolation. Therefore, a methodology has to be provided to recreate flow conditions close enough to the actual case without simulating the entire test cell.

This approach particularly interests those simulations aimed by quantitative data extrapolations as for example those used for the calculation of the thrust correction factors. In such a case a methodology is proposed for allowing the data extrapolation from a model which takes into account only the test bay.

Flow contours, path line plotting and computational integration and plotting are used to improve the understanding of the flow structure inside the cell and to assess the suitability of the commercial CFD package for test cell studies.

Several CFD models are also generated to represent the ejector pump effect taking place between the engine and the exhaust system. In addition, the entire model of the test bay plus the exhaust system would be too large to allow quantitative data extrapolations. Therefore, a methodology must also be determined to reach the characterization of this ejector effect.

The cell characterization results obtained by the analytical engine-detuner ejector model are compared with those obtained by CFD in order to achieve an auto-validation for both.

Based on the results some useful CFD guidelines for the modelling of indoor sea-level test cell are given.

### **3.3. Contribution from the Current Research**

From the combination of the above objectives for the three main areas involved in this project it is now possible to derive the following contributions

#### *Thrust Correction Factors*

Derivation of different thrust correction equations for the calculation of the real gross thrust delivered by a gas turbine engine in indoor sea-level test facilities.

The modelling of thrust correction factors as a function of ordinary engine-cell dimensions and performance parameters.

#### *Analytical Cell Entrainment Ratio Analysis*

Develop a tool capable of predicting and controlling the cell entrainment ratio for gas turbine engine test cell facilities knowing only usual engine performance parameters and cell dimensions.

*CFD as support to Indoor sea-level test*

A quantitative estimation of the thrust correction factors for gas turbine indoor sea-level test.

The provision of methodologies for helping the CFD modelling and the test cell characterization

By the combination of the three main field of this research outlined above a final outcome and contribution can be summarized as follows:

*Development of an analytical tool able to predict and control the cell entrainment ratio in indoor sea-level test cells and capable of providing a quantification of the real thrust delivered by the engine.*

## 4. Thrust Correction Factor

### 4.1. Introduction

Since the early stages of the jet engine develop there has been the necessity of measuring the thrust delivered by a gas turbine engine in in-flight conditions.

This necessity has emphasized the needing for a precise definition of the jet engine thrust, and for the drag of the body housing the engine.

These definitions will be of interest to thermo-dynamicist and aero-dynamicsists and though each one of them considers certain forces to be important, unambiguous and mutually-agreed definitions must be accepted.

At the same time, once thrust and drag have been defined, their formulation will be used for all purposes and not for only in-flight thrust determination.

The estimation of the real thrust delivered by the engine within an indoor test bed involves knowing both the magnitude and the direction of the all the forces on the engine and on what it is called the “metric assembly”.

Therefore, the agreed definition of thrust and drag will be used even for assessing the performance of the gas turbine engine within an enclosed facility.

### 4.2. Fundamental Concepts

#### 4.2.1. Fluid Force Definition

The force locally exerted on a surface by a real fluid consists of two components, the pressure force and the friction force. The pressure force, which acts normally to the surface, represents the product of the local static pressure,  $p$ , and the corresponding element of area  $dS$ . The friction force which acts tangentially to the surface, represents the product of the shearing stress,  $\tau$ , and of the element of area  $dS$  (Figure 4.1).

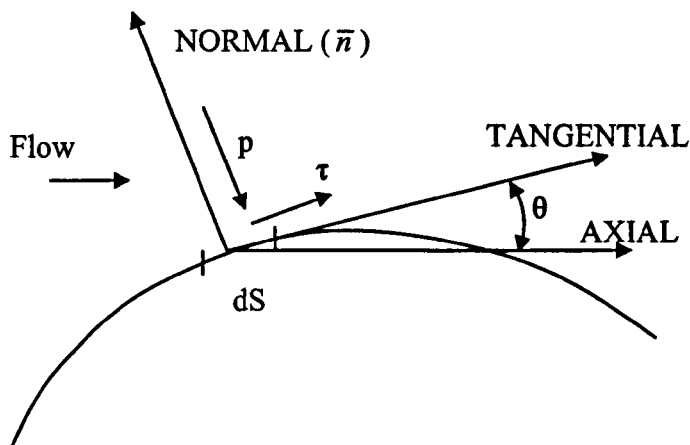


Figure 4.1: Fluid Force Component Over a Solid Surface

Using the above vector notation, the absolute total force acting on the surface is:

$$\bar{F} = \int_{SURFACE} (-p \cdot \bar{n} + \bar{\tau}) dS \quad (4.1)$$

Solving the element of force,  $d\Phi$ , in the axial direction as

$$d\phi = (p \sin \theta + \tau \cos \theta) dS \quad (4.2)$$

$$d\phi = (p + \tau \cot \theta) dA \quad (4.3)$$

Where  $dA = \sin \theta dS$ .

It is possible to get the absolute total axial force acting on the surface as

$$\phi = \int_A (p + \tau \cot \theta) dA \quad (4.4)$$

Now allowing for the hydrostatic buoyancy of the body through the introducing of the gauge pressure,  $(p-p_a)$ , it is possible to write the elemental gauge axial force as

$$d\phi_G = [(p - p_a) + \tau \cot \theta] dA \quad (4.5)$$

And consequently the total axial gauge force acting on the whole surface as

$$\phi_G = \int_A [(p - p_a) + \tau \cot \theta] dA \quad (4.6)$$

In this chapter, the special case of a non viscous, potential, flow will be considered. In such a case only the pressure force will contribute to the general definition of the overall force and so

$$d\phi_{Gpot} = (p - p_a) dA \quad (4.7)$$

And

$$\phi_{Gpot} = \int_A (p - p_a) dA \quad (4.8)$$

#### 4.2.2. Ducted and Un-Ducted Bodies

A clear distinction must be made in this chapter between “force” and “drag” and whether they act on the whole body or only part of it. Indeed, these two words are too often used to describe the same thing.

In order to make this distinction two statements can help. The first is the D’Alembert paradox that: “The net force on a closed non-lifting body in isolation in infinite subsonic, potential flow is zero”. The second is the Prandtl’s extension to the

D'Alembert's paradox, namely that: "Bodies of infinite or semi-infinite extension in the stream wise direction have a net force equal to zero in a subsonic, potential flow. Before going ahead with the drag definition and derivation it is worth spending few words on saying what an infinite or semi-infinite body is. Indeed, a gas turbine engine might be referred to a ducted body.

In potential flow a body is said to be semi-infinite when the static pressure at the centre or at the mid chord of it is equal to the ambient ("infinity" upstream or downstream) static pressure and the velocity at that section is equal to free stream velocity. In terms of the  $C_p$  (pressure coefficient expressed in equation (4.9)) this means that the static pressure coefficient is zero on the middle section of the body shown as Figure 4.2 below.

$$C_p = \frac{p - p_a}{\frac{1}{2} \rho v^2} \quad (4.9)$$

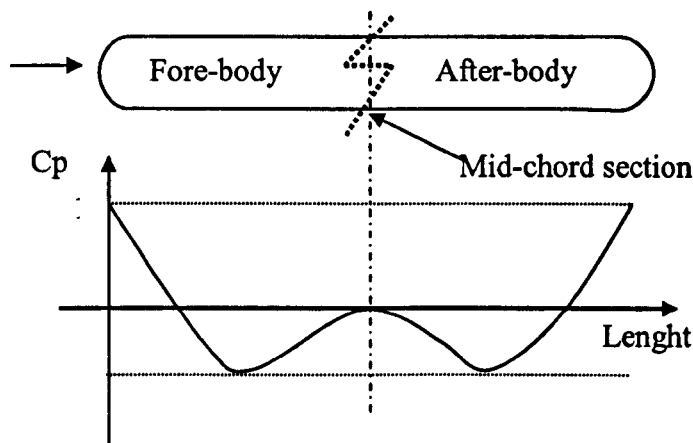


Figure 4.2:  $C_p$  Distribution on a Semi-Infinite Body in Potential Flow

Under these conditions the body can be divided into two parts: the fore-body and the after-body and in virtue of the "ambient" mid section they are aero-dynamically separated. This de-coupling allows the two parts of the body to be treated separately there being no interaction between them.

The general D'Alembert paradox may be directly applied to a semi-infinite non-lifting body in isolation and leading in potential flow to equation (4.10).

$$\phi_{G_{pot}} = \int_A (p - p_a) dA = 0 \quad (4.10)$$

This means that the rearward pressure force acting on the fore-body is balanced by a forwarding pressure force acting on the after-body.

However, a key additional feature of the semi-infinite bodies, in potential flow, is that the forces acting in the stream wise direction on the fore-body and on the after-body are both zero (equation (4.11)).

$$\phi_{G_{pot \text{ fore-body}}} = \phi_{G_{pot \text{ after-body}}} = 0 \quad (4.11)$$



In real flow the static pressure distribution on the fore-body of a semi-infinite body is closely similar to that in in-viscid flow. But crucial changes occur for the after-body where the boundary layer can not negotiate the positive (adverse) gradient of pressure imposed on the flow by the shape of the body (Figure 4.2). Consequently the flow separates along the after-body and the pressure forces acting on it are not longer able to balance the rear warding force acting on the fore-body (paragraph 4.2.3). This leads to the equation (4.12)

$$\phi_{Greal} = \int_A (p - p_a) dA \neq 0 \quad (4.12)$$

And

$$\phi_{Greal \text{ forebody}} \neq \phi_{Greal \text{ afterbody}} \neq 0 \quad (4.13)$$

Figure 4.3 shows the  $C_p$  distribution along the same semi-infinite body of Figure 4.2 but this time in real flow.

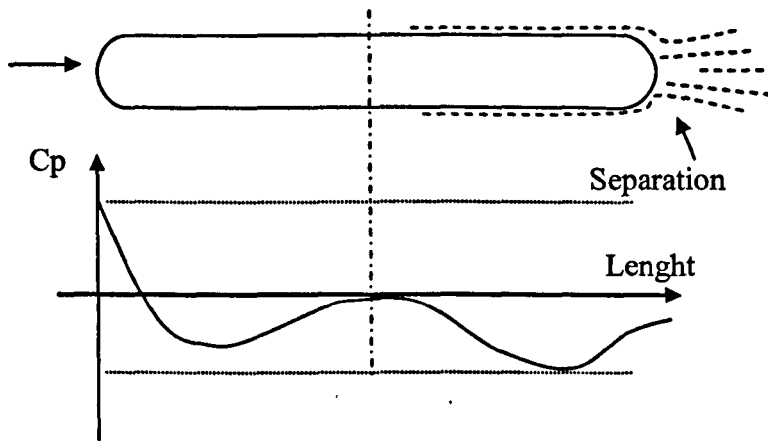


Figure 4.3:  $C_p$  Distribution for a Semi-Infinite Body in Real Flow

The above analysis is referred to semi-infinite un-ducted body and so only the flow surrounding the body has been taken into account.

Instead, Figure 4.4 shows the flow field for a semi-infinite ducted body in potential flow and its notional division in the internal and external flow regimes.

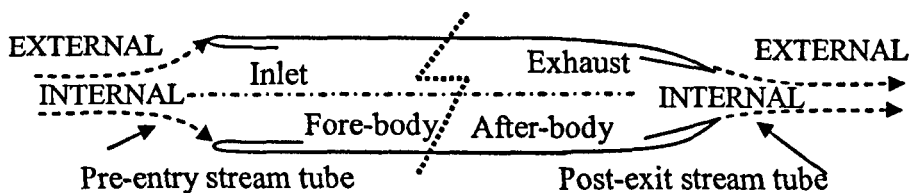


Figure 4.4: Semi-Infinite Ducted Body

Both the internal and the external flows are supposed to include even the pre-entry and post-exit stream tubes, both of infinite extent. The former starts from infinity up-

stream until the stagnation region on the nose of the intake and the second originating from the nozzle and extending until infinity down-stream. Therefore the name “internal flow” not only includes the flow instantaneously within the body but also includes the flow which will pass (pre-entry stream tube) or has already passed (post-exit stream tube) through the body from infinity upstream to infinity downstream.

Applying now the Prandtl paradox with reference to the external flow:

$$\phi_{Gpot} = \int_{+\infty}^{-\infty} (p - pa) dA = 0 \quad (4.14)$$

The axial component of the force acting on the infinite extended body is zero in potential flow.

And for the semi-infinite body properties:

$$\phi_{Gpot \text{ fore-body}} + \phi_{Gpot \text{ pre-entry}} = 0 \quad (4.15)$$

$$\phi_{Gpot \text{ after-body}} + \phi_{Gpot \text{ post-exit}} = 0 \quad (4.16)$$

Semi-infinite ducted bodies lead to the same results as un-ducted bodies when at the fore-body and at the after-body are added the respective stream tube.

### 4.2.3. Drag Definition

However having said that, whether only a part of an infinite or semi-infinite closed and non-lifting body is considered in potential flow the pressure force acting on it will in general be non zero. It is important to recall that for the validity of the paradoxes above mentioned it is strictly necessary to take into account the “whole” body (finite or infinite) as it is.

It is also important to say that within the validity of D’Alembert and Prandtl statement *the force acting on a part of the body may be not defined as a drag* because it will be balanced by one acting on another part of the body of equal and opposite magnitude.

Therefore in potential infinite subsonic flow, for closed no lifting, semi-infinite and infinite body, no drag is experienced.

Instead, of course, in real flow all bodies exhibit a drag.

In a subsonic flow regime two different types of drag will arise: the “skin friction” and the “normal pressure drag”. In supersonic flow regime there is also the drag associated with the shock wave together with the other two. ((Houghton and Carpenter 1993) & (Douglas, Gasiorek, and Swaffield 1995))

The skin friction drag rises from the resolved components of the shear stresses on the surface of the body. All the points of a surface where a viscous flow is acting are subject to tension in the flow direction. This tension is directly due to viscosity, as

consequence of the no slip condition at the surface. The resultant of the traction force will act on the flow direction (or in the opposite direction of the reciprocal motion). The normal pressure drag may itself be considered as the sum of several distinct items: boundary layer normal pressure drag (form drag), trailing vortex drag and wave drag (Aeronautical Research Council 1958).

For the purpose of this thesis only the boundary layer normal pressure drag is taken into account and an explanation for describing it is attempted below. This as consequence of the fact that the trailing vortex drag depends on the body lift and the wave drag is associated with the formation of shock waves in supersonic flow. And both are especially related to the flow around airfoils. (Houghton and Carpenter 1993). Therefore these two drag components are not of relevance or important for the scope of this thesis.

The form drag is even itself a direct consequence of the viscous effects on the boundary layer and its displacement thickness (Shapiro 1953) which will change the actual shape of the body. Figure 4.5 shows the same object, a sphere, in (a) surrounded by in-viscid flow and in (b) by viscous flow.

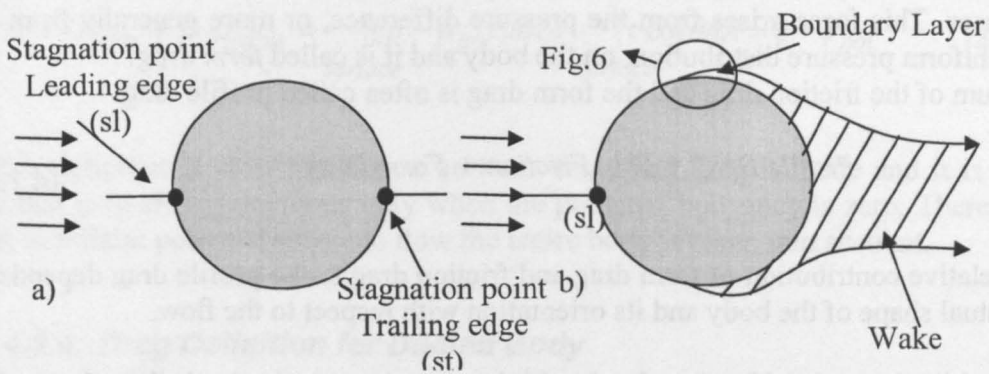


Figure 4.5: Flow Around a Sphere: a) In-Viscid Flow b) Real Flow

The main difference between the two flows is at the trailing edge.

In the case of the in-viscid flow there is a complete pressure recovery along the trailing edge and a second stagnation point appears on the rear part of the body (st). Instead in the viscous case the combination of the actual shape of the trailing edge and the viscosity effects lead to a flow separation.

Figure 4.6 shows an enlargement of the boundary layer phenomenon of Figure 4.5. It is possible to see that the flow deceleration bring to  $\delta p/\delta x > 0$  (adverse pressure gradient) along the trailing edge. By itself the flow adjacent to the surface has already a very low velocity, due to the viscous effects, and a further decreasing may generate a layer of reverse flow and therefore to separate.

The flow path when it is separated does not follow the shape of the surface and detaches from it giving rise to a new flow region: the wake.

Within the wake the flow is highly turbulent and consists of large-scale eddies. Consequently a high rate of energy dissipation takes place and a pressure reduction occurs. Therefore, in real flow, the separation alters the pressure field at the rear of the body and consequently the resultant of the pressure force is no longer zero as was the case for potential flow (paragraph 4.2.2).

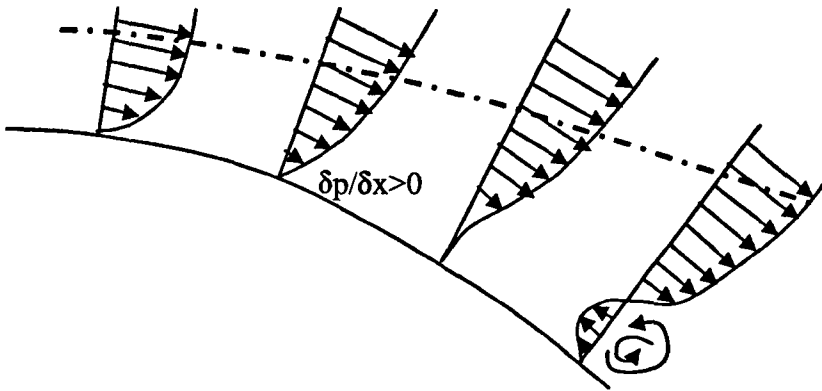


Figure 4.6: Enlargement of Figure 4.5 along the Trailing Edge

$$\phi_{Greal} = \int_A (p - p_a) dA \neq 0 \quad (4.17)$$

Equation (4.17) is the consequence of the pressure unbalance in real flow. The pressure acting on the front of the body is higher than that acting on the rear part. Therefore, the force acting on the body in the direction of the relative fluid motion increases. This force arises from the pressure difference, or more generally from the non-uniform pressure distribution, on the body and it is called *form drag*. The sum of the friction drag and the form drag is often called profile drag:

$$Profile\ Drag = Skin\ Friction + Form\ Drag \quad (4.18)$$

The relative contribution of form drag and friction drag to the profile drag depends on the actual shape of the body and its orientation with respect to the flow.

After this drag classification it should be anyway emphasized that these drag components are not independent one from each other. For example the change of pressure distribution caused by the boundary layer leads to a change in the shock wave system so that a part of the form drag may appear as a contribution to the wave drag. Again the energy dissipation associated with the region of interaction between the shock wave and boundary layers can not be separated into wave drag and boundary layer drag.

Another approach for defining the drag is the energy dissipation.

Such energy dissipation occurs in the flow surrounding the body (for a non-lifting body) and it is mainly due to the viscous effects (skin friction), flow separation and shock waves (Houghton and Carpenter 1993).

Indeed, the profile drag appears as a loss in momentum between two sections one upstream of the body (in free stream conditions) and one far downstream (where the static pressure has recovered the ambient static value) and an increase of energy in the wake. The loss in momentum appears as a reduction of the average flow velocity whilst the increase of energy is seen as a non-steadying eddying on the wake.

Following this consideration the intensity and the size of the wake gives an indication of the profile drag of the body.

It is now worth recalling that in real flow behind any body there is a wake (as the wake behind a ship). This is a further proof that any body in real flow experiences a drag.

As the drag for a closed non-lifting body in infinite subsonic potential flow is zero, the form drag in real flow can be expressed as the difference between the integrated pressure force in real flow and the integrated pressure force in potential flow, considering the same body shape in both cases (MIDAP Study Group 1979).

This concept is particular useful when considering sections of bodies, indeed as stated above, the integrated pressure force on part of a body is not zero also in potential flow. Furthermore, this concept is also useful when the bodies taken into account are not in infinite flows and therefore their pressure distribution is affected by the surrounding environment.

Thus the drag of part of a body is not the sum of the integrated shear stresses (skin friction) and the integrated pressure force. Indeed, the form drag is the difference between the integrated pressure force in real flow and the non-zero integrated pressure force in potential flow.

The integrated pressure force in potential flow is termed “potential flow buoyancy” and its magnitude generally varies dependently on which portion of the body is being considered. In addition such a term tends to zero as the portion is extended to include the whole body (for infinite flows).

$$D = D_{form} + D_{friction} = \int_{surface} (p - p_{pot}) dA + \int_{surface} \tau \cot \theta dA = \phi - \phi_{pot} \quad (4.19)$$

By this definition a clear distinction between force and drag is made and it is now clear that they are synonymous only when the potential buoyancy is zero. Therefore, when in infinite potential subsonic flow the entire body is taken into account.

#### 4.2.4. Drag Definition for Ducted Body

The notional difference between internal and external flow is of importance in order to define the drag for the ducted bodies. Indeed it allows the possibility of working with infinite and semi infinite body and consequently the validity of the Prandtl paradox.

The surfaces bounding the internal and the external flows will be called the internal and the external surfaces and the drags associated with the internal and external flows internal and external drags.

It is desirable, however, to divide the two contributions into internal thrust and external drag being the general case under consideration, in this thesis, as one in which the internal flow contributes as thrust rather than as drag.

This in view of the fact that the ducted bodies considered in this work are gas turbine engine. However this will better illustrated later on this chapter (paragraph 4.2.5), when even a thrust definition will be attempted.

In order to analyze the external drag, it is necessary to assume that no mixing take place between internal and external flow, both ahead of and behind the body. Thus ahead of the body the flows are considered to be separated by the surface of the pre-entry stream tube. Behind the body, instead, where usually the turbulent mixing between internal and external flow takes place it is convenient to postulate the existence of a post-exit stream tube.

It is also assumed that not shearing stresses occur along the stream tubes.

Following the definitions given in the paragraph 4.2.3 the profile drag, associated with the external flow for a ducted body, is given by the rate of decreasing of momentum of the external flow in a direction parallel to the undisturbed flow.

The momentum difference is calculated between two sections, one at infinity upstream and one at infinity down-stream both having recovered the ambient static pressure.

From this definition of profile drag it follows that for ducted bodies the form and friction drags are not arising only from the effective external surface of the duct but, also from the pre-entry and post-exit stream tube. However, by the above assumption of no shearing stress along the stream tubes, no friction drag will be accounted for the pre-entry and post-exit stream tube.

The drags from the pre-entry and post-exit stream tubes are not associated with any dissipative process or increase in entropy but they arise solely from the division of the forces on the ducted body into components due to the internal and external flows. At the same time, however, it is worth to say that the pressure forces acting by the external flow on the stream tube are equal and opposite of the pressure forces exerted on it by the internal flow.

This concept will lead during this chapter to the definition of the thrust and drag accounting systems.

Anticipating what it is better discussed later on regarding the thrust and drag interfaces it may be useful to have a name for the drag associated with the pressure distribution actually observed or estimated on the body's external surface. This drag component it is called "Intrinsic Form Drag". Additionally, if the friction drags, it is also accounted on the actual surface of the ducted body the whole drag it may be called "Intrinsic Drag".

Following the above theory if equation (4.19) is applied to the ducted body comprising its pre-entry and the post-exit stream tubes it can be obtained

$$\begin{aligned}
 D &= [\phi - \phi_{pot}]_{-\infty}^{+\infty} = \\
 &= (\phi_{pre} + \phi_{body\ ext} + \phi_{post}) - (\phi_{pre\ pot} + \phi_{body\ pot\ ext} + \phi_{post\ pot}) = \\
 &= (\phi_{pre} + \phi_{body\ ext} + \phi_{post}) - (\phi_{pre} + \phi_{body\ pot} + \phi_{post})
 \end{aligned} \tag{4.20}$$

It can be shown now that equation (4.20) by the Prandtl paradox becomes:

$$D = (\phi_{pre} + \phi_{body\ ext} + \phi_{post}) \tag{4.21}$$

From the above results it appears that for a ducted body the drag is equal to the external forces acting on it from the infinity upstream to the infinity downstream. This is the definition derived by ARC panel (Aeronautical Research Council 1958) for the drag of ducted body and is valid when the drag of the entire body it needs to be estimated and under the assumption of the validity of the D'Alembert and Prandtl paradoxes. Instead, when the drag of only a portion of the ducted body needs to be calculated has not to be forgotten of taking into account even the potential components as illustrate on equation (4.20). Figure 4.7 summaries the drag components on a ducted body.

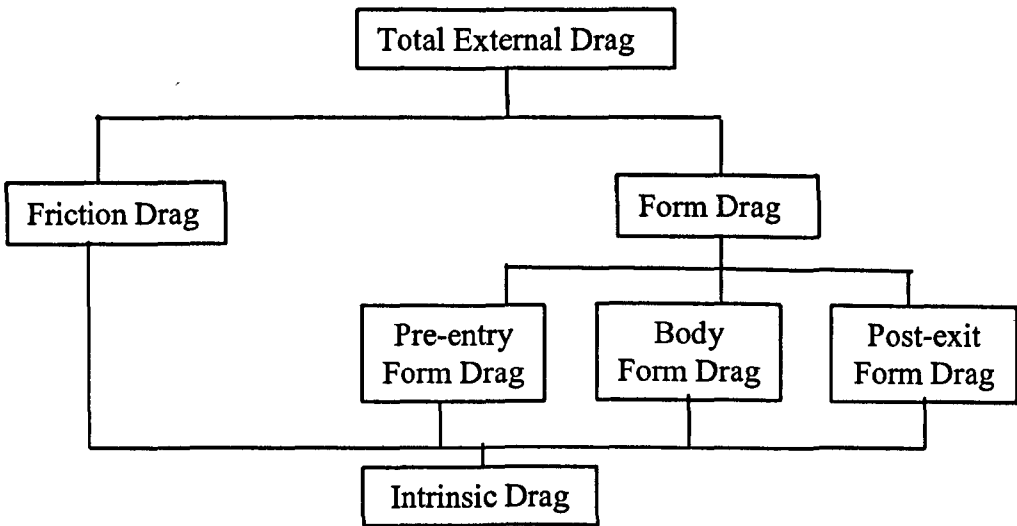


Figure 4.7: Drag Components on a Ducted Body

#### 4.2.5. Thrust Definition

Differently from the drag, the determination of the thrust requires the consideration of a propulsion system which generates a force at least equal to the drag in order to allow the body to move in the forward direction.

The propulsion system studied in this work is, of course, the gas turbine engine.

In this chapter attention is paid to the different propulsion interface systems which represent the different ways to account the thrust delivered by an engine and the drag acting on it.

However, at this stage of the chapter it is worth making the point that even though the engine within the test cell is tested without the nacelle, it represents anyway a ducted body. Where the air is sucked from the engine face (from the first stage of the compressor or at the fan face) and is expelled from the nozzle (two nozzles if the engine is a turbofan with a short cowl). At the same time, around the engine in an enclosed test facility there is a secondary flow flows which makes the analogy with the ducted body even more realistic. For this reason special attention in the previously sections of this chapter has been made to the ducted bodies.

As it has been said above in order to analyse the thrust and the drag for a ducted body, it is of importance to draw a distinction between internal and external flow. When the ducted body is referred to a jet engine the difference in momentum between the exhaust flow at a station infinitely downstream and the internal flow at a station infinitely upstream is called thrust.

Consequently from the above definition the thrust for a jet engine is equivalent to the sum of all the forces acting inside the ducted body plus those acting on the pre-entry and post-exit stream tube.

$$F'_N = \phi_{pre} + \phi_{body\,int} + \phi_{post} \quad (4.22)$$

The representation of a gas turbine engine as a ducted body allows the possibility of looking at the thrust above defined as a negative drag. Indeed, equation (4.22) can be written as equation (4.23).

$$F'_N = (\phi_{pre} + \phi_{bodyint} + \phi_{post}) + \quad (4.23)$$

$$-(\phi_{pre} + \phi_{bodyint\ pot} + \phi_{post})$$

Indeed the second term on the right hand side of equation (4.23) is equal to zero under the assumption of the Prandtl paradox. Further more the drag is defined positive when directed downstream instead the thrust is positive when directed upstream. This fact makes the definitions of drag and thrust consistent with each other.

Figure 4.8 summarizes the thrust component on a ducted body.

Even though the above thrust definition is theoretically correct it requires the direct integration of the pressure and friction components all over the internal surfaces of the ducted body and stream tubes. In practice, the usual complexity of the duct shape including the internal components of the engine makes this an impossible task.

Thus it is necessary to adopt an alternative approach.

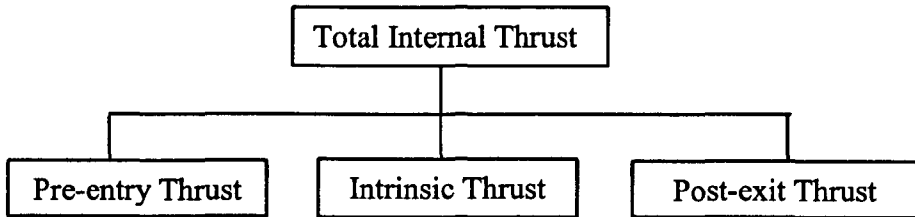


Figure 4.8: Thrust Components on a Ducted Body

#### 4.2.6. Momentum Theorem and Stream Force

During the previous paragraphs it has been recognized the impracticability of calculating by direct integration the forces acting on the internal surfaces of a jet engine. At the same time there have been some references to the momentum theorem in order to calculate the pressure and the friction forces acting on a body.

In this paragraph the momentum theorem and its application will be shown more in details.

The momentum theorem is a statement of the Newton's second law adapted to a continuum fluid.

It may be stated as: *"the sum of all forces acting on the fluid within the control volume is equal to the rate of change of linear momentum within the volume and the net outflow of linear momentum"* (SAE Committee E-33 1985) (equation (4.24)).

$$\sum \bar{F} = \frac{d}{dt} \int_{\text{control volume}} \rho \bar{v} dV + \oint_{\text{control surface}} \rho \bar{v} (\bar{v} \cdot \bar{n}) dS \quad (4.24)$$

Where  $\sum \bar{F}$  is the vector sum of all the forces acting on the fluid within the control volume and it is conventionally considered positive when it acts in the downstream direction. The forces included in the sum are body forces such as gravitational, magnetic and electromagnetic and the surface forces resulting from normal and shearing stresses.



The first term on the right hand side of equation (4.24) represents the time rate of the change of fluid momentum within the control volume.

The second term represents the net outflow of linear momentum through the closed control surface.

In order to avoid misunderstanding it is worth recognize that if a surface force it has been assumed to be positive acting in the downstream direction that force will be accounted as a negative term in the momentum theorem forces summation.

For a two dimensional or axis-symmetric, steady flow with body and hydrostatic forces neglected, the axial component of the net force acting on the flow is given by:

$$\sum \bar{F}_{net} = \int_{\substack{\text{control} \\ \text{surface}}} \rho v_x v_n dS \quad (4.25)$$

By the application of the above definition of the momentum theorem it is possible to work out the resultant of the force acting on the fluid by the solid or stream surface present within the control volume.

Therefore the application of the Newton's third law it allows to compute their reaction and thus the force acting directly on the surface.

The following application of the momentum theorem should help to clarify doubts, and introduces the definition of stream force.

The net gauge force exerted by the flow on the body is:

$$\phi_{Gbody} = \int_A [(p - p_0) + \tau \cot \theta] dA \quad (4.26)$$

The net force exerted by the stream surface to the fluid is:

$$\phi_{G stream tube} = \int_{streamtube} (p - p_0) dA \quad (4.27)$$

The momentum equation is:

$$(p_1 - p_0)A_1 + \phi_{G stream tube} - \phi_{Gbody} - (p_2 - p_0)A_2 = W(v_2 - v_1) \quad (4.28)$$

Where, the condition at station (1) and (2) are considered as averaged value from the real condition at those two sections.

The same equation can be written in a different way as

$$\phi_{G stream tube} - \phi_{Gbody} = W(v_2 - v_1) + (p_2 - p_0)A_2 - (p_1 - p_0)A_1 \quad (4.29)$$

$$\phi_{G stream tube} - \phi_{Gbody} = Wv_2 + (p_2 - p_0)A_2 - Wv_1 - (p_1 - p_0)A_1 \quad (4.30)$$

$$\phi_{G stream tube} - \phi_{Gbody} = F_{G2} - F_{G1} \quad (4.31)$$

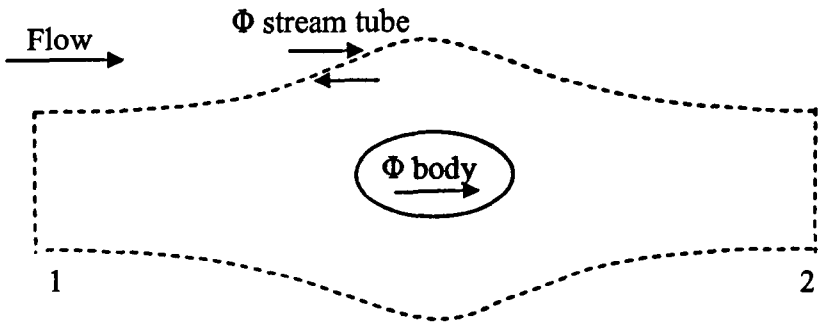


Figure 4.9: Forces Acting on the Control Volume and on the Body

Where  $F_G = Wv + (p-p_0) A$  it is called gauge stream force.

From the above application of the momentum theorem it is possible to make a couple of interesting considerations.

If section (1) and (2) are sufficiently far upstream and downstream so that a complete pressure recovery is allowed it is possible to say that  $p_1 = p_2 = p_0$  and so

$$\phi_{G \text{ stream tube}} - \phi_{G \text{ body}} = Wv_2 - Wv_1 \quad (4.32)$$

If now the surfaces of the stream tube are sufficiently far from the body the static pressure along the stream tube will constant and equal at  $p_0$ , such that

$$\phi_{G \text{ body}} = Wv_2 - Wv_1 \quad (4.33)$$

If now a potential flow is taken into account any wake can be generated by a flow around a body,  $v_2 = v_1$  and

$$\phi_{\text{body}} = 0 \quad (4.34)$$

This is the proof of the D'Alembert paradox.

#### 4.2.7. Thrust as a Stream Force

In the paragraph 4.2.5 has been underlined the difficulty of determining the thrust delivered by a gas turbine engine directly by integration of the pressure and friction components all along the internal engine surface.

In the previous paragraph 4.2.6 the gauge stream force has been introduced and in this paragraph its application for estimating the thrust of an engine is shown.

Applying the momentum theorem to the duct of Figure 4.10

$$p_1 A_1 - p_2 A_2 + \int_{\text{tube}} p dA = W(v_2 - v_1) \quad (4.35)$$

$$\int_{tube} p dA = W(v_2 - v_1) - p_1 A_1 + p_2 A_2 \quad (4.36)$$

$$\int_{tube} p dA = Wv_2 + p_2 A - Wv_1 - p_1 A_1 = F_2 - F_1 \quad (4.37)$$

In terms of gauge force:

$$\int_{tube} (p - p_0) dA = F_{G2} - F_{G1} \quad (4.38)$$

From the definition of the momentum theorem, equation (4.38) represents the force acting on the fluid by the duct. Now Newton's third law gives the force by the flow on the bounding surfaces that is the thrust.

Thus:

$$\text{Net Gauge Thrust} = F_{G2} - F_{G1} \quad (4.39)$$

This is conventionally positive when acting in forwarding direction.

It appears from the above definition that the thrust for a gas turbine propulsion system (by the analogy previously stated with the ducted body) may be defined as the change of stream force between the entry and the exit stations.

This concept of thrust as a change in stream force is generally far more convenient than the alternative concept of the integral of pressure and viscous forces. However, the two concepts are essentially equivalent.

Using this concept it is now possible to define the thrust of a propulsion system as the change in stream force between two reference sections. However by the definition of thrust given in the paragraph 4.2.5 if the two reference sections are not taken at infinities upstream and downstream even the potential buoyancy effect must be taken into account.

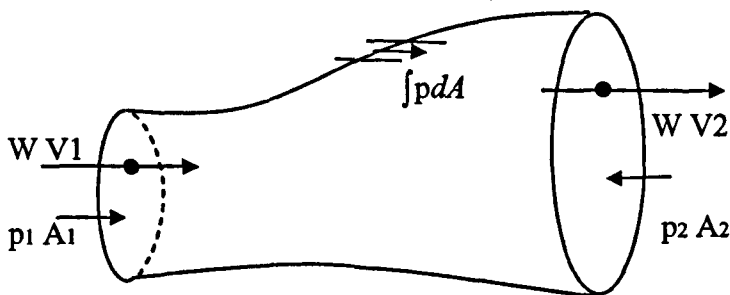


Figure 4.10: Representation of the Forces acting on a Duct

#### 4.2.8. Thrust and Drag Accounting System

In Figure 4.11 are represented all the forces acting on a ducted body associated to a single stream nacelle from infinity up-stream (0) to infinity down-stream (∞). For simplicity, all the equations and diagram on this chapter will assume an axis-

symmetric flow where velocity vector and pressure forces act parallel to the engine axis.

In order to visualize the stream tubes one could imagine them as an impervious membrane where the flow can not pass through it and incapable of facing any pressure gradient across it.

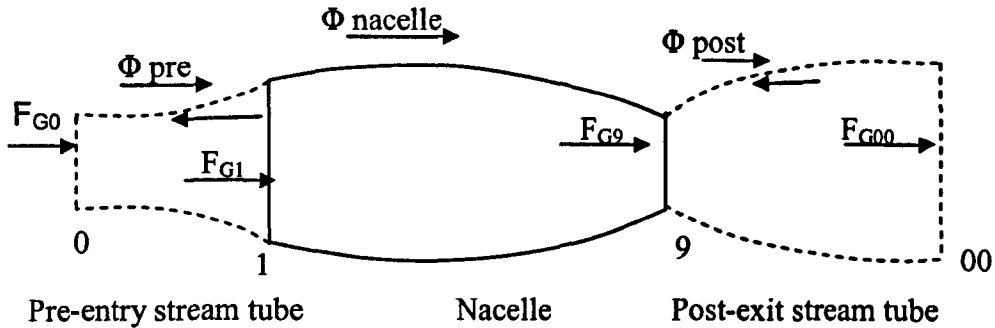


Figure 4.11: Representation of the forces acting on a single stream nacelle

Therefore, whatever is the force exerted by the external flow on the stream tube then another force exists equal and opposite exerted by the internal flow.

Now from the above defined concepts of thrust and drag it is possible to define what it is called the “Net Propulsive Force” as: (MIDAP Study Group 1979)

$$NPF = (F_{G9} - F_{G1}) - \phi_{Gnacelle} \quad (4.40)$$

Where  $\phi_{Gnacelle}$  is the gauge force exerted by the external flow onto the nacelle, taken to be positive when directed down-stream. The term  $(F_{G9} - F_{G1})$  is the summation of the forces exerted by the flow on the internal surface of the nacelle and it is taken to be positive when directed up-stream.

Now remembering that the nacelle drag may be evaluated as:

$$D_{nacelle} = \phi_{nacelle} - \phi_{nacelle\ pot} = \int_{surface} (p - p_{pot}) dA + \int_{surface} \tau \cot \theta dA \quad (4.41)$$

Moreover, the resultant of the forces acting on a ducted body in potential flow, including the pre-entry and the post-exit stream tube, is zero (equation (4.42))

$$\phi_{pre} + \phi_{nacelle\ pot} + \phi_{post} = 0 \quad (4.42)$$

Therefore

$$D_{nacelle} = (\phi_{pre} + \phi_{nacelle} + \phi_{post}) \quad (4.43)$$

Following the above steps:

$$\begin{aligned} NPF &= (F_{G9} - F_{G1}) - D_{nacelle} - \phi_{nacelle-pot} = \\ &= (F_{G9} - F_{G1}) - D_{nacelle} + \phi_{pre-entry} + \phi_{post-exit} \end{aligned} \quad (4.44)$$

Equations (4.40) and (4.44) represent two different approaches to evaluate the Net Propulsive Force. In the first, (equation (4.40)) the force exerted on the external nacelle body are evaluated directly and it is called “force accounting system”. In the second approach (equation (4.44)) the nacelle contribution to the net propulsive force is made by its drag and it is called “drag accounting system”.

Essentially the two systems must give the same result, indeed they are equivalent.

#### 4.2.9. Thrust and Drag Interfaces

In paragraph 4.2.7 it has been shown that the thrust of a gas turbine engine may be defined as the change of stream force between the entry and the exit stations. In order to use this definition of thrust it is anyway necessary to specify what the entry and exit sections are for a gas turbine engine.

Indeed there are different interesting and adoptable choices which will lead to different thrust equations but always to the same result, if correctly used.

At the first sight the more appropriate choice could seem to locate the interfaces at the physical engine entrance and exit, so at station (1) and (9) (Figure 4.11). Using these two sections the thrust evaluated is called “Intrinsic Net Thrust” (equation (4.45)) as earlier stated for the drag evaluation.

$$F_{N_{intr}} = F_{G9} - F_{G1} \quad (4.45)$$

Though this could seem the more straight forward definition, due to the physical assonance and to the fact that effectively it represents the internal forces exerted on the breathing body, it could lead to some problems.

Indeed, the intrinsic thrust uses station (1) as entry station which is strictly dependent on the nacelle configuration and consequently on any change in entry area. Thus if the thrust is defined using these two sections the engine manufacturers would not be able to express the engine performance by a compact series of curves applicable to all the installations.

Moreover, for measuring the flow characteristics at station (9) and (1) it would be necessary to traverse the flow with instrumentation which can affect the engine performance. Station (1) also presents the intrinsic difficulty related with its effective position dependent on the location of the pre-entry stagnation point.

Another section useful as entry section in the thrust determination could be defined upstream section (1) where the flow conditions are those at free stream, station (0). For in flight thrust measurements the flow conditions at station (0) are:

$$P_0 = P_{atm} \quad (4.46)$$

$$v_0 = v_{aircraft} \quad (4.47)$$

In case of indoor test facility the flow conditions at station (0) are:

$$P_0 = P_{cell0} \quad (4.48)$$

$$v_0 = v_{cell0} \quad (4.49)$$

So the gauge stream force at station (0) is:

$$F_{G0} = W_{eng0}v_0 \quad (4.50)$$

This definition is true for both cases, either when as reference pressure it is used the cell inlet static pressure (for indoor measurements) or when it is used the atmospheric pressure (for outdoor measurements).

Following the choice of station (0) as entry station a possible exit station could be (00) at infinity down-stream where a complete pressure recovery has already occurred. Consequently, the pressure at station (00) is the free stream atmospheric (the same that a station (0)), the engine mass flow is  $W_{eng9}$  and the flow velocity is  $v_{00}$ . The stream force at station (00) is

$$F_{G00} = W_{eng9}v_{00} \quad (4.51)$$

This is called Overall Thrust.

The "Overall Net Thrust" is defined as in equation (4.52)

$$F'_N = W_{eng0}v_0 - W_{eng9}v_{00} \quad (4.52)$$

From the momentum theorem above illustrated, a natural consequence of the definition of the Overall Net Thrust is the automatic inclusion of all forces exerted by the internal flow on all the surfaces wetted by it between station (0) and (00). This means that for a simple nacelle even the pre-entry and the post-exit stream tube have to be included. Additionally, the forces acting on the fore-body and the plug have to be accounted for a centre-body nacelle.

Figure 4.12 shows the forces acting on a centre-body nacelle (SAE Committee E-33 1985).

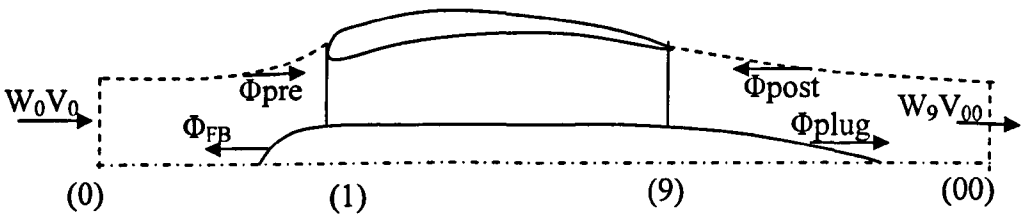


Figure 4.12: Representation of the Forces Acting on a Centre Body Nacelle

So the Overall Net Thrust is:

$$\begin{aligned} F'_N &= W_{eng0}V_0 - W_{eng9}V_{00} = \phi_{Gpre} - \phi_{GFB} + \phi_{Gplug} - \phi_{Gpost} + F_{Nintr} = \\ &= W_{eng9}V_9 + A_9(p_{s9} - p_{s0}) + \phi_{Gplug} - \phi_{Gpost} - W_{eng0}V_0 \end{aligned} \quad (4.53)$$

As a practical interface station (00) suffers because the wake make of  $F_{G00}$  a difficult value to be evaluated. Indeed the flow downstream the exit station is complicated by the transfer of momentum and energy between the internal and the external flow

As a practical interface station (00) suffers because the wake make of  $F_{G00}$  a difficult value to be evaluated. Indeed the flow downstream the exit station is complicated by the transfer of momentum and energy between the internal and the external flow which takes place in the wake of the body. Furthermore if the pressure of the internal flow differs from that in the adjacent external flow (around the nozzles) also shock waves may be present in the internal and external flow.

For indoor thrust measurement station (00) practically does not exist so this interface system can not be used.

A useful and convenient form for the thrust can be derived deleting from the above equation the terms  $\Phi_{plug}$  and  $\Phi_{post}$ .

$$F_N = W_{eng9}V_9 + A_9(p_{s9} - p_{s0}) - W_{eng0}V_0 \quad (4.54)$$

$F_N$  is usually called Standard Net Thrust.

The use of the Standard Gross Thrust has been proved to be very useful. Indeed, for single stream nozzle the flow conditions at station (9) are often independent from the external flow effect and under the control of the engine manufacturer.

Following the above illustrated system interfaces Table 4.1 summarizes the various Net Propulsive Forces defined.

Entry and Exit Stations	Net Thrust Definition	Accounting System	Net Propulsive Forces
(1-9)	Intrinsic Thrust $F_{N-intr} = F_{G9} - F_{G1}$	Force	$F_{N-intr} - \Phi_{nacelle}$
		Drag	$F_{N-intr} + \Phi_{pre} + \Phi_{post} - D_{nacelle}$
(0-9)	Standard Net Thrust $F_N = F_{G9} - F_{G0}$	Force	$F_N - \Phi_{pre} - \Phi_{nacelle}$
		Drag	$F_N + \Phi_{post} - D_{nacelle}$
(0-00)	Overall Net Thrust $F'_N = F_{G00} - F_{G0}$	Force	$F'_N - \Phi_{pre} - \Phi_{pos} - \Phi_{nacelle}$
		Drag	$F'_N - D_{nacelle}$

Table 4.1: Summary of the Thrust and Drag Interfaces (MIDAP 1980)

### 4.3. Thrust Correction Equations in Enclosed Test Facility

#### 4.3.1. Interface Sections and NPF for Indoor Thrust Measurement

As it has been described in Chapter 2 (paragraph 2.1.5), the thrust measured within enclosed test bed facility is not the real thrust delivered by the engine. Therefore the thrust measured by the load cells needs to be corrected by the so called thrust correction factors.

Each one of the thrust correction factors it is related to a force acting on the accounting system which has been chosen to evaluate the thrust delivered by the

engine. Therefore, a thrust correction factor can act either directly on the engine metric assembly or on one of the stream surfaces belonging to that system.

It may be worth to say that as accounting system for the engine is now meant the set of surfaces derived as consequence of the interface sections chosen (entry and exit section as in the paragraph 4.2.9). Therefore, it represents the set of surfaces where the forces are applied.

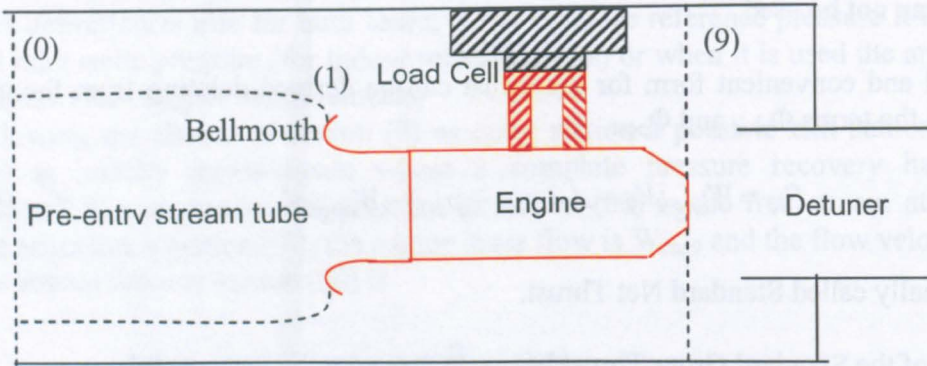


Figure 4.13: Simplified Test Chamber for Sea-Level Test Bed Facility

Having said that, it is clear that also within enclosed test cells the gas turbine engine behaves as a ducted body and so it is necessary to choose the right interfaces in order to calculate the force resultant acting on the engine.

Or by analogy, as it will be shown better later, on the load cells.

Figure 4.13 shows a sketch which represents a simplified test chamber for a classic indoor sea-level test bed facility, with the metric-assembly (in red) and the non-metric components (in black). In this figure are also represented the possible inlet and exit interfaces, (0), (1) and (9).

It is easy to see that station (00) does not appear within the cell. This happens because within the cell the primary jet is forced to mix with the secondary flow along the detuner. Therefore the definition of a post-exit stream tube, which was difficult even in free air conditions (Aeronautical Research Council 1955), is now not suitable.

In free air conditions it has been defined the Net Propulsive Force as the resultant of the force acting on the accounting system.

The load cells inside the test cell, which link the movable part of the cradle to the stationary one, measure directly the resultant of the forces applied to the accounting system taken into account. Indeed, whatever are the entry and exit sections of the ducted body the load cells measure the load transferred to them by the metric assembly. Such a load, by the Newton third law, includes all the forces which are not exerted directly on the metric assembly but on the different surfaces belonging to the accounting system in use.

Though Figure 4.14 might be a bit misleading showing all the forces acting on the system at the same time, it can still make the point that the load measured is the reaction of all the forces acting on the system (equation (4.55)).

$$L = \sum_{i=1}^n \sum_{j=1}^m (\phi_{Gi} + F_{Gj})_{\text{accounting-system}} \quad (4.55)$$



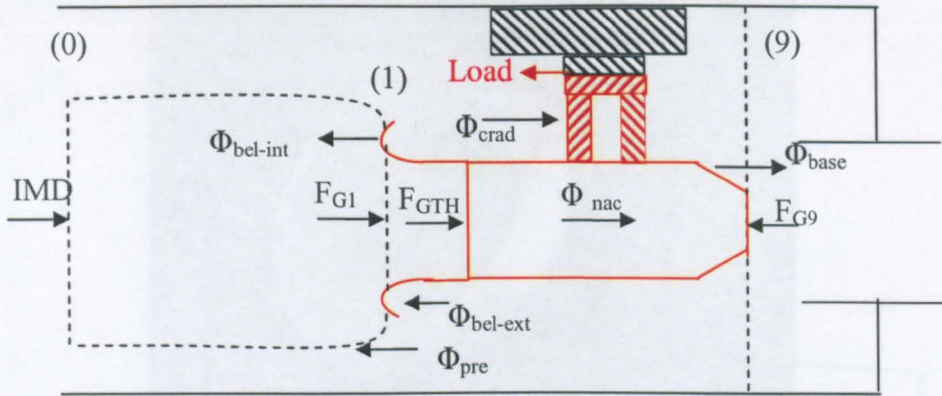


Figure 4.14: Representation of the Forces Acting on the Metric Assembly

It will be the main aim of this chapter to clarify Figure 4.14 and the right use of the forces there represented.

Referring to the in flight condition is now possible make an analogy between the load measured by the load cells and the Net Propulsive Force.

$$NPF = L = \sum_{i=1}^n \sum_{j=1}^m (\phi_{Gi} + F_{Gj})_{accounting-system} \quad (4.56)$$

Therefore for indoor thrust measurement the load measured by the load cells can be seen as the Net Propulsive Force for in flight thrust measurement. Accordingly even the use of the interface sections can be the same.

#### 4.3.2. Momentum Theorem Application on the Bellmouth

Usually for indoor and outdoor sea-level test the engine is mounted on the thrust stand without the nacelle and a bellmouth is generally attached to the stand as intake. For indoor test the main task of the bellmouth is to smooth the inlet flow, avoiding flow distortion and separation.

Figure 4.15 shows an engine mounted on an indoor stand with the bellmouth.

All the previous analysis regarding the interface choice for the determination of the NPF has been undertaken using a sharp lip intake (Figure 4.16), as is done in the most of the literature, and using the highlighted section as possible stagnation region. In such a situation section (1) is almost straight forwardly identified and it could be used as section for the momentum theorem without further complication (equation (4.57)).

$$F_{G1} = (p - p_{ref})A_1 + W_{eng}V_1 \quad (4.57)$$

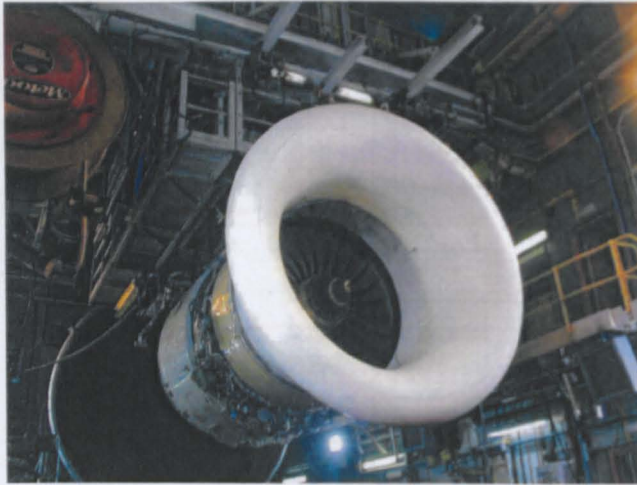


Figure 4.15: Engine Bellmouth (Courtesy of Rolls-Royce)

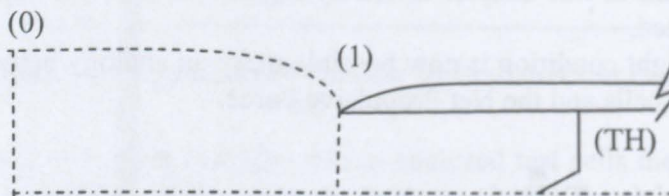


Figure 4.16: Sharp Lip Intake

The application of the momentum theorem on a pre-entry stream tube which ends into a bellmouth is more complicated. Especially when the stagnation region is not on the highlighted section

Figure 4.17 shows a general arrangement for the pre-entry stream tube in suction condition and its stagnation point on the bellmouth. It is clear that in such conditions section (1) includes a part of the bellmouth surface (shd) and not only the free surface (cd).

Applying now the momentum theorem in the pseudo momentum box abcdhs, neglecting the friction forces and taking into account only axial forces it is possible to obtain the following equation:

$$\int_{A_1^*} (p - p_{ref}) dA - \int_{A_{cd}} (p - p_{ref}) dA - \int_{A_{shd}} (p - p_{ref}) dA = W(v_{cd} - v_{ab}) \quad (4.58)$$

Which it may be written as (Williams and Gullia c):

$$F_{G1}^* = F_{Gdc} + \int_{A_{shd}} (p - p_{ref}) dA = F_{G1} \quad (4.59)$$

The above relationship gives the equivalence of  $F_{G1}$  at station (1)\*. This relation could be very useful in terms of one dimensional calculation. Indeed, it is possible to calculate  $F_{G1}^*$  by knowing for example the non-dimensional mass flow going through the engine, P, T and of course the dimension of  $A1^*$ . The last requirement is the most restrictive because in order to know the value of  $A1^*$  it is necessary to know the position of the stagnation point on the bellmouth.

However, this happens any time it is wished to operate with  $F_{G1}$  and it is one of the bigger limitations of using section (1) as interface for the accounting system.

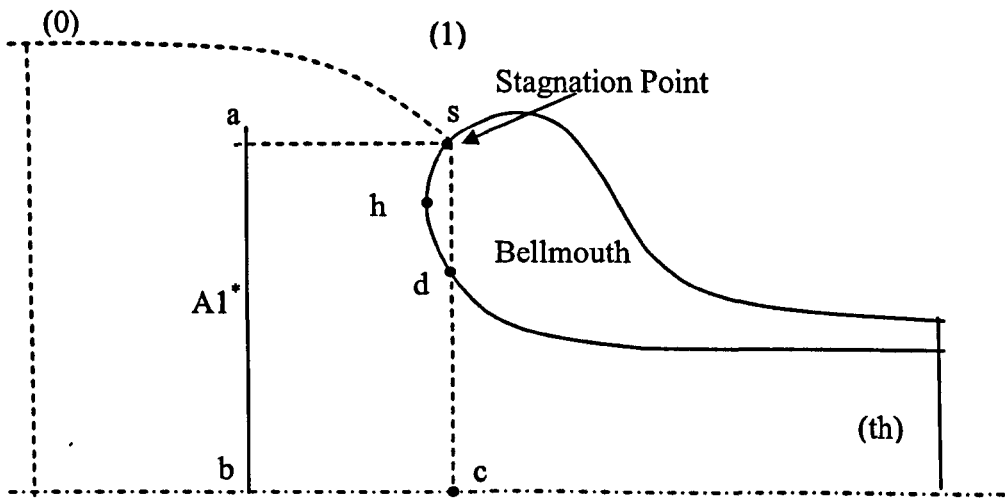


Figure 4.17: Stagnation Point on the Engine Bellmouth

However, the relationship above derived, even though its implicit difficulties, clearly shows the flow structure around the stagnation point on the bellmouth. In addition, equation (4.58) defines  $F_{G1}$  which will be used later on as a starting point for the derivation of the thrust correction equations.

### 4.3.3. Pseudo-infinite Cell

In Chapter 4 of this work it is intended to move towards the definition of the thrust correction equations using a step by step approach. In this way it is believed by the author that a better understanding of all the issues related with the flow inside the cell will be achieved.

For this reason it is thought that using the pseudo-infinite cell as a starting point it will be helpful.

A pseudo-infinite cell is defined as one in which the cross sectional area is infinitely large (Williams and Gullia a ). It is clear that such a cell does not exist in reality but the same effect can artificially be obtained by testing the engine in an outdoor facility in the presence of a head wind

The static pressure will be everywhere constant around the metric assembly and equal to the reference pressure. This is the main difference with an indoor test cell where the static pressure changes along the metric-assembly because of the enclosure effects.

The flow within a cell infinitely large looks like that in Figure 4.13. Indeed, differently from the free stream condition with no wind there is the pre-entry stream tube and consequently a stagnation point either on the bellmouth or in the metric assembly (it depends on the free stream velocity (Seddon and Goldsmith 1985)).

Both the stream tube and the bellmouth aero-dynamics effects in free air will be better taken into account later during this chapter (paragraph 4.4.1). By now it is important just notice that differently from the in-flight condition the engine during sea-level test is mounted without the nacelle and the intake is replaced by the bellmouth.

The fundamental equation which will be used as starting point for the derivation of all the thrust correction equations is equation (4.60):

$$L = F_{G9} - F_{G1} - \phi_{Gmetric} \quad (4.60)$$

Where

$$\phi_{Gmetric} = \phi_{Gcarcase} + \phi_{Gcradle\ metric} + \phi_{Gbell\ ext} \quad (4.61)$$

Equation (4.60) is the correspondent for indoor test facility of equation (4.40).

It is of interest to underline the fact that if the accounting system including station (9) and (1) is used, the metric force is the sum of all the forces acting on the external metric surfaces from (1) to (9). This statement is useful because later on, using different accounting system, it is shown how the metric force could hold even forces acting on surfaces wetted by the internal fluid.

As discussed in the paragraph 4.3.2  $F_{G1}$  can not be readily determined so it is preferred to use station (0) as inlet interface.

In order to move to station (0) it is necessary to apply the momentum theorem in the control box defined by the pre-entry stream tube from section (0) to section (1). Figure 4.18 shows the momentum box (dashed line) and the force acting on it.

Applying the momentum theorem and from what it has been discussed in paragraph 4.3.2 it is possible to obtain the relationship represented in equation (4.62)

$$-\phi_{Gpre} = F_{G1} - F_{G0} \quad (4.62)$$

It is worth noticing that in the above application of the momentum theorem no viscous forces (from (s) to (d)) have been taken into account, so the flow is assumed to be inviscid.

Substituting equation (4.62) in equation (4.60) it is possible to obtain (4.63)

$$L = F_{G9} - F_{G0} + \phi_{Gpre} - \phi_{Gmetric} \quad (4.63)$$

Assuming one dimensional calculation, the inlet momentum drag can be written as

$$F_{G0} = W_{eng} v_0 \quad (4.64)$$

In equation (4.64)  $v_0$  is assumed to be a bulk flow property at station (0). Following equation (4.64), equation (4.63) becomes

$$L = F_N + \phi_{Gpre} - \phi_{Gmetric} \quad (4.65)$$

To fully understand the meaning of a pseudo-infinite cell it is now worth to go from the force accounting system (equation (4.65)) to a drag accounting system.

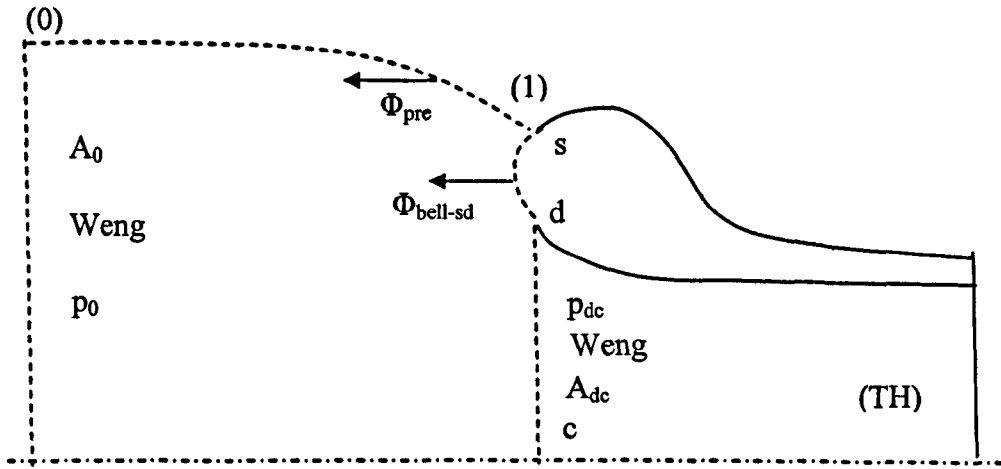


Figure 4.18: Momentum Box Used for Moving to Station (1) to Station (0)

Thus

$$D_{metric} = \phi_{metric} - \phi_{metric\ pot} \quad (4.66)$$

Substituting equation (4.66) into equation (4.65)

$$L = F_N + \phi_{pre} - D_{metric} - \phi_{metric\ pot} \quad (4.67)$$

The potential buoyancy term of the metric assembly (last term in equation (4.67)) can be defined using the momentum theorem in potential flow for the secondary mass flow. The control box used must contain the metric assembly and therefore it has been chosen that represented in Figure 4.19 which encloses the secondary flow from station  $(0_{ext})$  to station  $(9_{ext})$ .

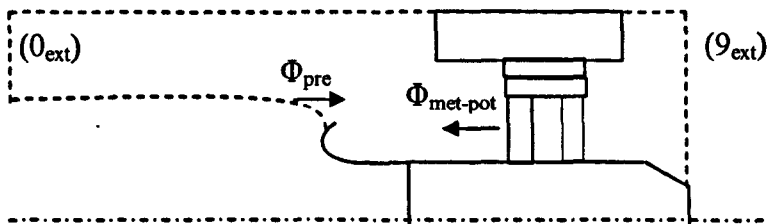


Figure 4.19: Control Volume for Calculating the Potential Buoyancy Term

Applying the momentum theorem to this momentum box (neglecting the wall friction forces):

$$(F_{G9} - F_{G0})_{ext\ pot} = \phi_{Gpre} - \phi_{Gmetric\ pot} \quad (4.68)$$

Substituting equation (4.68) into equation (4.67)

$$L = F_N - D_{metric} + (F_{G9} - F_{G0})_{ex-tpot} \quad (4.69)$$

Now, by the the pseudo-infinite cell assumption it is possible to write:

$$(F_{G9} - F_{G0})_{ext-pot} = 0 \quad (4.70)$$

Indeed, in an infinite large cell the static pressure is the same in both stations (9) and (0). In potential flow this means that also the secondary flow velocity is the same at those two sections (equation (4.71) and equation (4.72)).

$$p_{9ext} = p_{0ext} \quad (4.71)$$

$$v_{9ext} = v_{0ext} \quad (4.72)$$

Following the above considerations the thrust correction equation for pseudo-infinite cell becomes as equation (4.73)

$$L = F_N - D_{metric} \quad (4.73)$$

A consideration may rise by comparing equation (4.65) and equation (4.73).

The former represents the thrust correction equation as a result of a force accounting system instead the later as a result of a drag accounting system.

The two equations appear different but this only because in equation (4.65) it has not been applied the assumption of the pseudo-infinite cell yet. Indeed, by that assumption it can obtained that the force acting on the metric is equal to the drag (equation (4.74))

$$\phi_{met} = D_{metric} \quad (4.74)$$

And

$$\phi_{pre} - \phi_{metric\ pot} = 0 \quad (4.75)$$

It is easy now to show that applying the above two assumptions to the equation (4.65) it is possible to obtain equation (4.73).

#### 4.3.4. Finite Cell

The validity of the pseudo-infinite cell assumption is strictly dependent on the engine and cell size and so can not be generalised with enough accuracy. However, in the previously paragraph all the consequences of that assumption have been listed and so it can be used as starting point to approach a one dimensional calculation for a finite cell.

Indeed, up to the equations (4.65) and (4.69) the analysis for the pseudo-infinite is still valid for the finite cell with the only difference that now in the  $\Phi_{metric}$  also the base force needs to be added to. This happens as consequence to the fact that the static

pressure does not remain constant anymore along the metric assembly. Therefore the depression generated by the engine-detuner ejector pump results in a force applied on the engine.

Formally the base force is directly included in the carcass force. Indeed the pressure integral along the carcass, covering the whole carcass surface, includes also the pressure effects along the engine after-body.

Therefore, formally the equation representing the forces acting on the metric assembly could still remain equation (4.61) also in the finite cell analysis. However, it is worth to remember one more time that implicitly now the  $\Phi_{metric}$  term it includes also another force, the so called base force, now directly incorporated in the carcass force term.

The thrust correction equation for a finite cell is

$$L = F_N + \phi_{Gpre} - \phi_{Gmetric} \quad (4.76)$$

Which it can be written even in terms of drag as (equation (4.77))

$$L = F_N - D_{metric} + (F_{G9} - F_{G0})_{ext-pot} \quad (4.77)$$

Now the potential buoyancy terms can not be cancelled out because it is not zero as was in the case of the pseudo-infinite cell.

It is at the moment believed worthwhile making the following observation before going ahead with the analysis.

In order to account for the potential buoyancy of the metric assembly in the previous paragraph stations ( $0_{ext}$ ) and station ( $9_{ext}$ ) have been chosen, (Figure 4.19). At the same time, it would have been even possible to work with stations ( $1_{ext}$ ) and ( $9_{ext}$ ) (Figure 4.19).

Indeed those two sections include, by themselves, the whole metric assembly which is intended to calculate the potential buoyancy term for.

The effect of extending the control volume up to station (0) is the immediate inclusion in the potential metric buoyancy of the pre-entry force which results to be the same in potential and real flow. This can be seen also from the equation (4.68).

In general, if station ( $0_{ext}$ ) and station ( $9_{ext}$ ) are used in order to compute the potential metric buoyancy term the pre-entry force will not explicitly appear in the thrust correction equation. But implicitly it is still there, enclosed on the term  $(F_{G9} - F_{G0})_{ext-pot}$ .

This concept could be used in practical calculation of the thrust correction factors in order to avoid an explicit calculation of  $\Phi_{pre}$  and allowing for a more straightforward calculation of the buoyancy term in potential flow.

Some misunderstanding could arise looking at  $\Phi_{base}$  as part of the carcass force. Indeed this force is induced by the ejector pump effect onto the engine and it is more opportune to account for it in the thrust correction equation directly by a force instead that as drag.

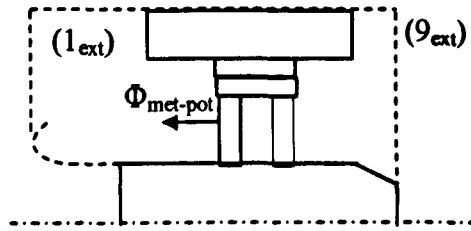


Figure 4.20: Momentum Box for Calculating the Potential Buoyancy between  $(1_{ext})$  and  $(9_{ext})$

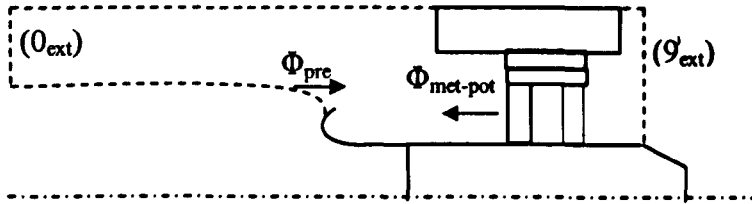


Figure 4.21: Momentum Box for Calculating the Potential Buoyancy between  $(1_{ext})$  and  $(9_{ext})$

So for example, it could be more opportune to consider station  $(9_{ext})$  as exit station for the momentum box, Figure 4.21. In this case the potential buoyancy force related with the engine after-body is not included on the whole potential metric buoyancy. Therefore in the general thrust correction equation  $\Phi_{base}$  appears as a force. Like a force  $\Phi_{base}$  has to be accounted as described in equation (4.78)

$$\phi_{Gbase} = \int_{A_{ext-noz}}^{A_{th-noz}} (p_{base} - p_{ref}) dA + \int_{A_{ext-noz}}^{A_{th-noz}} r \cot \theta dA \quad (4.78)$$

The terms of equation (4.78) are shown in Figure 4.22.

At the same time, however, the drag of the engine carcass has not to include the engine after-body. Otherwise the same effect will be accounted two times.

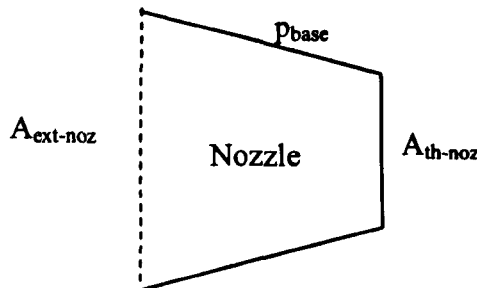


Figure 4.22: Engine After-Body Nomenclature

Following this consideration the thrust correction equation (4.77) would become

$$L = F_N - D'_{metric} + (F_{G9'} - F_{G0})_{ext\ pot} - \phi_{Gbase} \quad (4.79)$$

This time the metric drag is



$$D'_{metric} = D_{cradle\ metric} + D_{bellext} + D'_{carcase} \quad (4.80)$$

And  $D'_{carcase}$  includes the carcase up to station ( $9'_{ext}$ ).

#### 4.3.5. Consideration on the Carcase Drag

The advantage of working directly with the drag instead that with force is represented by the possibility of determining the drag by means of the drag coefficient  $Cd$  (Anderson 2001).

$$Cd = \frac{Drag}{\frac{1}{2} \rho v_0^2 A_{ref}} \quad (4.81)$$

So the drag coefficient allows for avoiding the integration of the static pressure along the body surface necessary for computing the force acting on it.

However the drag coefficient has to be experimentally defined by real or scale model which have to represent the actual situation. In order to represent the actual situation by means of wind tunnels or water tanks some flow similarities have to be established. In Gas dynamic the most common parameters to compare two different situations are the Reynolds number ( $Re$ ), the Mach number ( $Ma$ ) and the altitude (for rarefied gasses). The body shape is very important as well (Hoerner 1958).

A complete treatment of all the drag properties is beyond the aim of this work. However, it is believed opportune by the author to make some considerations on the use of  $D_{carcase}$  and  $D'_{carcase}$ .

Indeed, two different approaches have been illustrated in the above paragraphs.

The first sees the inclusion of the base force directly within the  $D_{carcase}$  (equation (4.77)) and the second treats the base force as a separate force (equation (4.79)).

Now has to be underlined the fact that when the first approach wants to be used a specific drag coefficient for the carcase needs to be defined. This drag coefficient has to be worked out by experimental test in which the ejector pump effect has to be either reproduced of the same magnitude as the actual one or properly derived by scale coefficients. So the complete use of equation (4.77) requires the proper determination of the drag coefficient for the engine carcase.

When the second approach needs to be used the drag coefficient for the engine carcase at this time, has not to include the engine after-body. Therefore, specific experimental test have to be worked out to derive the right  $Cd$ .

An assumption whose validity it depends on the effective engine shape could be suggested in the application of the second approach. Being the ejector effect concentrated on the engine after-body (due to its vicinity to the detuner and to its shape which has on the engine after-body the most of the projected area ( $dA$ )) the experimental determination of the  $Cd$  may not include the ejector pump effect. This assumption can be better understood looking at Figure 4.21 where the carcase, after-body apart, is not subjected to any pressure drag due to its shape (un-realistic). Accordingly, the drag includes only friction which is well represented once the cell flow velocity is matched.

### 4.3.6. Finite Cell with no Parallel Walls

Up to now both the pseudo-infinite cell and the finite cell illustrated are with parallel walls between sections (0) and (9). It could happen that the cell has not parallel walls as show in Figure 4.23. In such a situation the general thrust correction equation for the finite cell would change and it will account also for the force exerted on the walls (Williams and Gullia a).

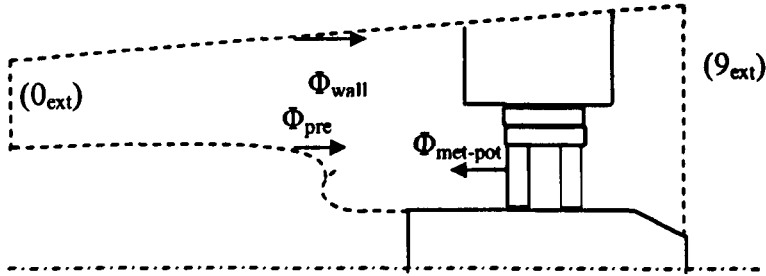


Figure 4.23: Cell with not Parallel Walls

The change will occur only for the finite cell, because for the pseudo-infinite cell the static will still remain constant along the wall and the metric assembly. With no parallel walls the momentum equation for the potential secondary flow (equation) becomes:

$$(F_{G9} - F_{G0})_{ext\ pot} = \phi_{pre} - \phi_{metric\ pot} + \phi_{wall\ pot} \quad (4.82)$$

And consequently the thrust correction equation can be written in the same way as equation (4.83) (Williams and Gullia a).

$$L = F_N - D_{metric} + (F_{G9} - F_{G0})_{ext\ pot} - \phi_{wall\ pot} \quad (4.83)$$

### 4.3.7. TCF Equation for finite cell using explicitly $\Phi_{bell\ ext}$

Different forms of the thrust correction equations can be worked out always using as engine interfaces stations (0) and (9). However it is worth to keep in mind that station (0) in the previously analysis (paragraph 4.3.3 and consequently on paragraph 4.3.4) has been introduced by moving the accounting system from station (1).

Equation (4.60) will be referred as the reference unquestionable equation.

Using stations (0) and (9) another useful thrust correction equations can be derived by taking out the  $D_{bell\ ext}$  from the  $D_{metric}$ . Indeed, rather than estimating the external bellmouth contribute by mean of its drag it could be more opportune accounting for it by the force acting on it.

This because that force can be directly measured by static pressure measurements along the bellmouth or even worked out by a CFD analysis. The main difficulty of such measurements is represented by the needing of finding out the real position of the stagnation point on the bellmouth. Indeed, what it has been defined external bellmouth includes the portion of the bellmouth starting from the stagnation point up

to the engine carcass. To complicate such a determination there are the three dimensional effects which characterize the whole flow within the cell and whose effects are not going to provide a uniform stagnation point along the bellmouth. These integration difficulties are the same which can be found on the calculation of the pre-entry force which can not be directly measured experimentally.

Therefore computational resources as CFD are needed to accomplish these integrations in circumferential and axial direction. .

In order to carry out the bellmouth drag from the metric drag in equation it is necessary to define a new reference section (f) as it has been introduced on reference (Rios et al. 1998).

Section (f) is shown in Figure 4.24.

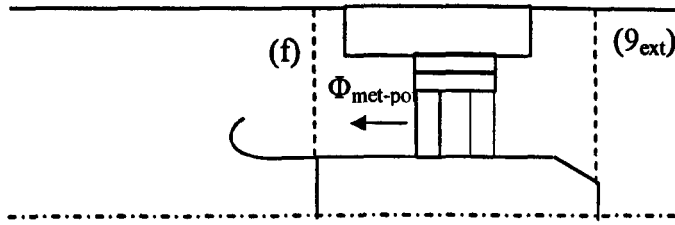


Figure 4.24: Momentum Box for Calculating the Potential Buoyancy Term between (f) and (9<sub>ext</sub>)

The metric force will be defined as usual (equation (4.61)) what it is going to change is the metric drag definition. Therefore all the difference will be on the thrust correction equation written using the drag accounting system.

In order to avoid nomenclature confusion it is opportune to introduce another name for the metric drag from station (f) to station (9),  $D_{metric\ f-9}$ .

$$D_{metric\ f-9} = D_{carcase} + D_{cradle} = (\phi_{carcase} + \phi_{cradle}) + \quad (4.84)$$

$$- (\phi_{carcase} + \phi_{cradle})_{pot}$$

Applying the momentum theorem for the secondary flow from station (f) to station (9), as shown in Figure 4.24, it is possible to obtain (supposing a cell with parallel wall and neglecting the wall friction)

$$- (\phi_{Gcarcase} + \phi_{Gcradle})_{pot} = (F_{G9} - F_{Gf})_{ext\ pot} \quad (4.85)$$

Hence the force acting on the metric assembly

$$\phi_{Gmetric} = \phi_{Gbell\ ext} + D_{carcase} + D_{cradle} - (F_{G9} - F_{Gf})_{ext\ pot} \quad (4.86)$$

Now substituting equation (4.86) into equation (4.76) it is possible to derive a hybrid (force and drag) form of the thrust correction equation

$$L = F_N + \phi_{Gpre} - \phi_{Gbell\ ext} - D_{carcase} - D_{cradle} + (F_{G9} - F_{Gf})_{ext\ pot} \quad (4.87)$$

Whenever the cell wall friction forces do not want to be neglected another term would appear in equation (4.87)  $\Phi_{wall}$  which being the wall parallel would include only the friction term.

#### 4.3.8. 1 D calculation of $\Phi_{Bell_{ext}}$

In the previously paragraph the force acting on the external bellmouth it has been introduced directly on the thrust correction equation.

Now its calculation will be attempted using the fundamentals of the one dimensional gas-dynamic for incompressible flow and the momentum theorem.

The momentum box chosen is that one of Figure 4.25 between sections (1<sub>ext</sub>) and (f) and following the momentum theorem application (in this application the cell wall friction forces are neglected) it is possible to derive equation (4.88).

$$-\phi_{G_{bell_{ext}}} = F_{Gf} - F_{G1_{ext}} \quad (4.88)$$

$$\frac{F_{Gf}}{q_0 A_{cell}} = \frac{W_s v_f + (p_f - p_0) A_f}{\frac{1}{2} \rho v_0^2 A_{cell}} \quad (4.89)$$

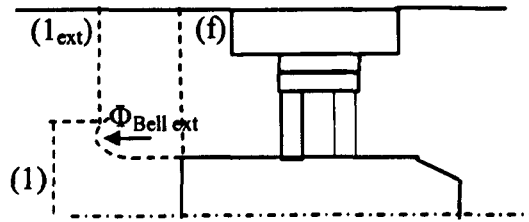


Figure 4.25: Momentum box for calculating the force acting on the external bellmouth

Dividing the stream gauge force at section (f) by the dynamic head at station (0) it is possible to obtain equation (4.89)

Calling  $\lambda = \frac{A_{cell}}{A_{th}}$  and using

$$W_s = (A_{cell} - A_{th}) v_f \rho_f \quad (4.90)$$

Introducing now the assumption of potential incompressible flow it is possible to obtain equation (4.91)

$$\frac{F_{Gf}}{q_0 A_{cell}} = \left(1 - \frac{1}{\lambda}\right) \left(\frac{v_f^2}{v_0^2} + 1\right) \quad (4.91)$$

Then using

$$W_{cell} = A_{cell} v_0 \rho \quad (4.92)$$

It can be obtained

$$\frac{v_f}{v_0} = \frac{W_s A_{cell}}{(W_s + W_p)(A_{cell} - A_{th})} = \left( \frac{\mu}{\mu + 1} \right) \left( \frac{\lambda}{\lambda - 1} \right) \quad (4.93)$$

Therefore equation (4.89) can be written as equation (4.94)

$$\frac{F_{Gf}}{q_0 A_{cell}} = \left( 1 - \frac{1}{\lambda} \right) \left\{ \left[ \left( \frac{\mu}{\mu + 1} \right) \left( \frac{\lambda}{\lambda - 1} \right) \right]^2 + 1 \right\} \quad (4.94)$$

At the same time the ratio of the stream gauge force at section (1<sub>ext</sub>) and the dynamic head at station (0) can be written as equation (4.95)

$$\frac{F_{G1ext}}{q_0 A_{cell}} = \frac{W_s v_{1ext} + (p_{1ext} - p_0) A_{1ext}}{\frac{1}{2} \rho v_0^2 A_{cell}} \quad (4.95)$$

Using the secondary mass flow at section (1<sub>ext</sub>) as represented in equation (4.96)

$$W_s = (A_{cell} - A_1) v_{1ext} \rho \quad (4.96)$$

It is possible to obtain

$$\frac{F_{G1ext}}{q_0 A_{cell}} = \left( \frac{v_{1ext}^2}{v_0^2} + 1 \right) \left[ \frac{(\lambda - 1) - \frac{(A_1 - A_{th})}{A_{th}}}{\lambda} \right] \quad (4.97)$$

Using equations (4.92) and (4.96) it is possible to write the ratio  $v_{1ext} / v_0$  as represented in equation (4.98)

$$\frac{v_{1ext}^2}{v_0^2} = \left[ \frac{\mu}{(1 + \mu)} \right] \left\{ \frac{\lambda}{\left[ \left( \lambda - 1 - \frac{(A_1 - A_{th})}{A_{th}} \right) \right]} \right\} \quad (4.98)$$

Consequently

$$\frac{F_{G1ext}}{q_0 A_{cell}} = \left\{ \left[ \frac{\mu}{(1 + \mu)} \right] \left\{ \frac{\lambda}{\left[ \left( \lambda - 1 - \frac{(A_1 - A_{th})}{A_{th}} \right) \right]} \right\} + 1 \right\} \left[ \frac{(\lambda - 1) - \frac{(A_1 - A_{th})}{A_{th}}}{\lambda} \right] \quad (4.99)$$

After derived the above formulas (equation (4.99) and equation (4.94)) it is possible to substitute them into equation (4.88) and find out the force acting on the external part of the bellmouth (equation (4.100)) (Williams and Gullia d ).

$$\frac{\phi_{bell\ ext}}{q_0 A_{cell}} = \left\{ \left[ \frac{\mu}{(1+\mu)} \right] \left\{ \frac{\lambda}{\left[ \left( \lambda - 1 - \frac{(A_1 - A_{th})}{A_{th}} \right) \right]} \right\} + 1 \right\} \left[ \frac{(\lambda - 1) - \frac{(A_1 - A_{th})}{A_{th}}}{\lambda} \right] + \left( 1 - \frac{1}{\lambda} \right) \left\{ \left[ \left( \frac{\mu}{\mu + 1} \right) \left( \frac{\lambda}{\lambda - 1} \right) \right]^2 + 1 \right\} \quad (4.100)$$

This calculation requires the knowledge of the flow conditions up-stream the engine in order to calculate  $q_0$ . Anyway the velocity (which is the main parameter needed) at station (0) upstream it is also necessary to compute the intake momentum drag which is another fundamental component of equation (4.87).

Therefore, the knowledge of such a velocity should not be a problem if equation (4.87) it has been chosen for correcting the measured engine thrust within the test cell. The only problem for the application of equation (4.100) could be the knowledge of  $A_1$ . Indeed, to calculate the force acting on the external bellmouth it is necessary to know where the external bellmouth starts or where the pre-entry stream tube ends. Experimentally it is very difficult and time consuming (consequently it is even expensive) to find out the exact position of such a region and so it is not a common practice to work in this direction.

However, have the possibility of calculating  $\Phi_{bell\ ext}$ , once the stagnation point is known, could be very useful. Indeed by a CFD analysis  $A_1$  could be defined. Therefore, the one-dimensional analysis can be carried ahead and then its thrust correction factors can be compared with the more complex three dimensional CFD results. At the same time if all the terms of the different thrust correction equations can be calculated a comparison between them and their validation can be achieved.

It is now believed useful by the author make the point that the above analysis is done for incompressible flow. However, due to the low velocity of the secondary flow, around the engine, generally experienced in regular cell, this assumption is acceptable. But it must be kept in mind that when the secondary flow velocity exceeds some value even the flow compressibility effects have to be kept into account.

#### 4.3.9. 1D Calculation of $\Phi_{pre}$

In the paragraph 4.3.3 the force acting on the pre-entry stream tube it has been defined by the difference between the stream force at the engine section (1) and the intake momentum drag (the engine stream force at section (0)). Due to the high Mach number at section (1) an incompressible estimation of the pre-entry force (using as momentum box the internal flow volume between the two above mentioned sections) is not valid. For this reason in order to estimate the pre-entry force it will be taken into account the external momentum box between (0<sub>ext</sub>) and (1<sub>ext</sub>) as it shown in Figure 4.26. At those sections the flow velocity, for common cell dimensions, it allows an incompressible flow analysis.

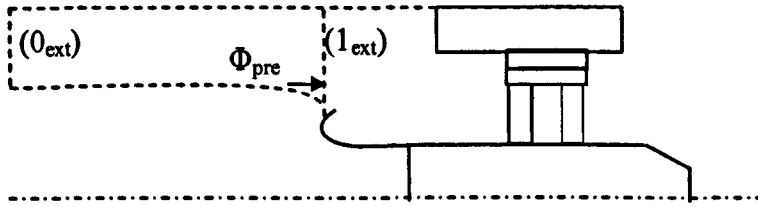


Figure 4.26 Momentum Box for Calculating the Pre-Entry Force

Consequently, applying the momentum theorem between  $(0_{ext})$  and  $(1_{ext})$  (neglecting the cell wall friction force) it is possible to derive equation (4.101)

$$\phi_{pre} = F_{G1ext} - F_{G0ext} \quad (4.101)$$

Using the same form already used in paragraph 4.3.8 it can be obtained equation (4.102) under the assumption of potential and incompressible flow

$$\frac{F_{G0ext}}{q_0 A_{cell}} = 2 \frac{\mu}{\mu + 1} \quad (4.102)$$

Substituting equations (4.99) and (4.102) into equation (4.101) it is possible to obtain equation (4.103) (Williams and Gullia d)

$$\begin{aligned} \frac{\phi_{pre}}{q_0 A_{cell}} = & \left\{ \left[ \frac{\mu}{(1 + \mu)} \right] \left\{ \frac{\lambda}{\left[ \left( \lambda - 1 - \frac{(A_I - A_{th})}{A_{th}} \right) \right]} + 1 \right\} + \right. \\ & \left. \times \frac{\left[ (\lambda - 1) - \frac{(A_I - A_{th})}{A_{th}} \right]}{\lambda} - 2 \frac{\mu}{\mu + 1} \right\} \end{aligned} \quad (4.103)$$

All the considerations expressed in paragraph 4.3.8, regarding the application of equation (4.100) and the knowledge of the location of the stagnation point are still valid for equation (4.103). However, equation (4.103) still remains very useful especially for comparison and validation between the one dimensional analysis and the CFD results.

#### 4.3.10. Considerations on the Potential Buoyancy Term

Before going ahead with a further develop of useful thrust correction equations it is believed worth to make some comments on the effect that the buoyancy term has on the global equations.

First of all it is interesting to make some geometric considerations

Following Figure 4.27, it is easy to understand all the terms enclosed on  $(F_{G9}-F_{G0})_{ext\ pot}$ . Indeed the global momentum box between sections  $(0)_{ext}$  and  $(9)_{ext}$  can be separated in four different momentum boxes.

The first box is that one between  $(0)_{ext}$  and  $(1)_{ext}$ , the second one is between  $(1)_{ext}$  and  $(f)$ , the third one is between  $(f)$  and  $(9')_{ext}$  and the fourth between  $(9')_{ext}$  and  $(9)_{ext}$ .

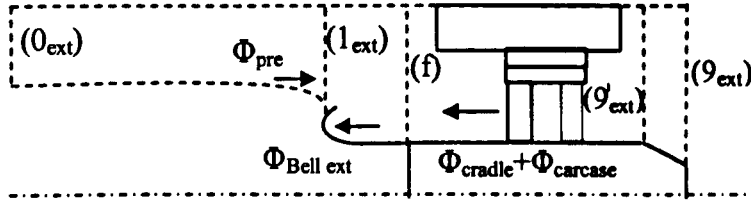


Figure 4.27: Different Momentum Boxes for Computing the Potential Buoyancy Term

Now, if the base force is directly incorporated within the thrust correction equation as a force (equation (4.79)) there is not any needing of including station  $(9)_{ext}$ . This because the potential buoyancy effect of the engine after-body is not required if its drag it is not included in the equation.

At the same time station  $(9')_{ext}$  is not needed if the whole engine carcase (including the after-body) drag is accounted in the thrust correction equation (equation (4.77)) (in such a case it will be used station  $(9)_{ext}$  as already discussed above).

However a useful consideration which could help in future analysis can be made looking at the drawing in Figure 4.27. Indeed in that drawing the area of station  $(f)$  is equal to the area of station  $(9')_{ext}$  and this means that in potential flow the respective stream gauge forces are equal (equation (4.104))

$$(F_{G9'} - F_{Gf})_{ext\ pot} = 0 \quad (4.104)$$

Consequently by the momentum theorem equation (4.104) bring to equation (4.105)

$$-(\phi_{carcase\ f-9'} + \phi_{cradle})_{pot} = 0 \quad (4.105)$$

The above consideration is valid for engine and cell configurations like that in Figure 4.27 and its use for different configurations must be evaluated each time, as an assumption.

Now a one dimensional analysis for the buoyancy term is attempted in incompressible potential flow. Although its limitation this analysis it is believed useful in order to understand the aero-dynamics of the secondary flow within the cell.

So an equation representing the buoyancy effect between station  $(0)_{ext}$  and  $(9)_{ext}$  will be derived and used for a parametric analysis.

The assumption of incompressible flow it is quite reasonable for the usual secondary flow velocity within the cells.

Equation (4.106) defines the nomenclature for this analysis

$$\frac{\Delta F_{09\ ext\ pot}}{q_0 A_{9\ ext}} = \frac{(F_{G0} - F_{G9})_{ext\ pot}}{q_0 A_{9\ ext}} = \frac{W_s(v_0 - v_{9\ ext}) - (p_9 - p_0)A_{9\ ext}}{q_0 A_{9\ ext}} \quad (4.106)$$



Applying Bernoulli theorem between (0<sub>ext</sub>) and (9<sub>ext</sub>) it is possible to derive equation (4.107)

$$\frac{\Delta F_{09ext\ pot}}{q_0 A_{9ext}} = - \left( 1 - \frac{v_{9ext}}{v_0} \right)^2 \quad (4.107)$$

The total cell mass flow can be written as equation (4.108)

$$W_{tot} = \rho v_0 A_{cell0} \quad (4.108)$$

And the secondary mass flow as equation (4.109).

$$W_s = \rho v_{9ext} A_{9ext} \quad (4.109)$$

In order to avoid nomenclature complication it is believed better introducing the terms b and c defined in equations (4.110) and (4.111)

$$b = \frac{A_{cell9}}{A_{cell0}} \quad (4.110)$$

$$c = \frac{A_{nozzle}}{A_{cell0}} \quad (4.111)$$

It is possible now to obtain

$$\frac{v_{9ext}}{v_0} = \frac{\mu}{\mu + 1} \frac{1}{b - c} \quad (4.112)$$

And

$$q_0 A_{9ext} = \frac{1}{2} \frac{W_p^2 (\mu + 1)^2}{\rho A_{cell0}} (b - c) \quad (4.113)$$

Then substituting equations (4.112) and (4.113) into equation (4.106) the stream gauge force difference between stations (0<sub>ext</sub>) and (9<sub>ext</sub>) can be represented as equation (4.114)

$$\begin{aligned} \Delta F_{09ext\ pot} = & - \{ \mu^2 [(b - c)^2 + 1 - 2b - 2c] + 2\mu [(b - c)^2 - b + c] + \\ & + (b - c)^2 \} \times \frac{W_p}{2 \rho A_{cell0}} \end{aligned} \quad (4.114)$$

The advantage of including the term  $b$  into the equation is represented by the fact that in this way even the potential buoyancy for a cell with not parallel wall can be calculated using equation (4.114).

Furthermore including the term  $c$  also the effect of different engine nozzle dimensions can be represented with that formula.

Different engine nozzles can also represent different kind of engine tested in the same indoor test cell.

The buoyancy effect appearing on the thrust correction equations is

$$\Delta F_{09ext\ pot} = -(F_{G9} - F_{G0})_{ext\ pot} \quad (4.115)$$

Assuming that  $A_{cell\ 0} = A_{cell\ 9ext}$  and so neglecting the area of the engine nozzle equation (4.114) can also assume the easy form of

$$\Delta F_{09ext\ pot} = -\frac{l}{[2(1 + \mu)]} \quad (4.116)$$

However, the validity of this assumption is strictly dependent on the engine dimensions compared to those one of the cell.

The engine nozzle radius is taken into account as first parameter for the potential buoyancy parametric study.

The cell dimensions (assumed to be 100 m<sup>2</sup>) will be kept constant as the cell entrainment ratio (1.074), the engine mass flow (1190 Kg/s) and the cell is assumed having parallel walls.

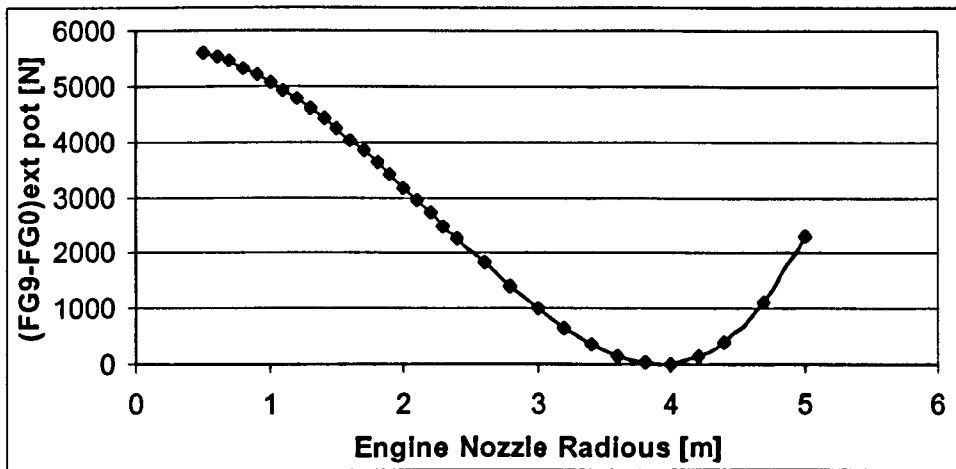


Figure 4.28: Effect of the Engine Nozzle Radius in the Potential Buoyancy Effect

Figure 4.28 shows that increasing the engine nozzle radius the potential buoyancy effect decreases until a given point. That is practically due to the fact that  $A_{9ext}$  reduces and it is getting closer to  $A_{0ext}$ . Indeed, with the entrainment ratio chosen for this parametric analysis the pre-entry stream tube works in suction condition (as for all the cell sketches drawn up to now) which means that  $A_{0ext}$  is smaller than the  $A_{9ext}$ . However if the cell dimensions and the cell entrainment ratio are kept the same and only the area of the engine nozzle is increased it will be possible to arrive at a point when  $A_{0ext} = A_{9ext}$ . Consequently the potential buoyancy effect will be zero. Afterward

if the nozzle area is increased further more the potential buoyancy increases again due to an unbalance in area between  $A_{0ext}$  and  $A_{9ext}$ . The slope of this part of the curve is even steeper than the former part due to higher velocities at station  $A_{9ext}$  which are accounted with square value in the formula (4.114).

Now, keeping constant the cell dimensions ( $100 \text{ m}^2$ ), fixing the engine nozzle area ( $6.15 \text{ m}^2$ ) and the engine mass flow ( $1193 \text{ Kg/s}$ ) in equation (4.114), it is possible to understand the entrainment ratio effect on the potential buoyancy.

Figure 4.29 shows that increasing the entrainment ratio the potential buoyancy force decreases. This because increasing the amount of secondary flow into the cell, though the engine mass flow is the same, leads to an increasing of velocity at section (0). And if the flow velocity at station (0) increases the same engine mass flow needs a smaller pre-entry stream tube for entering the engine. Consequently  $A_{0ext}$  increases getting closer to  $A_{9ext}$  and therefore the potential buoyancy term decreases.

The shape of the stream tube depends on the velocity at station (0). Indeed, with increasing this velocity the pre-entry stream tube changes shape from suction to spillage condition. And for a given entrainment ratio the pre-entry stream tube will also work in datum condition (parallel stream tube).

Due to the shape of the bellmouth whose crown radius it is in general bigger than the engine nozzle radius a potential buoyancy force equal to zero correspond to a stream tube working in spillage conditions (the pre-entry stream tube area has to be the same than the engine nozzle area).

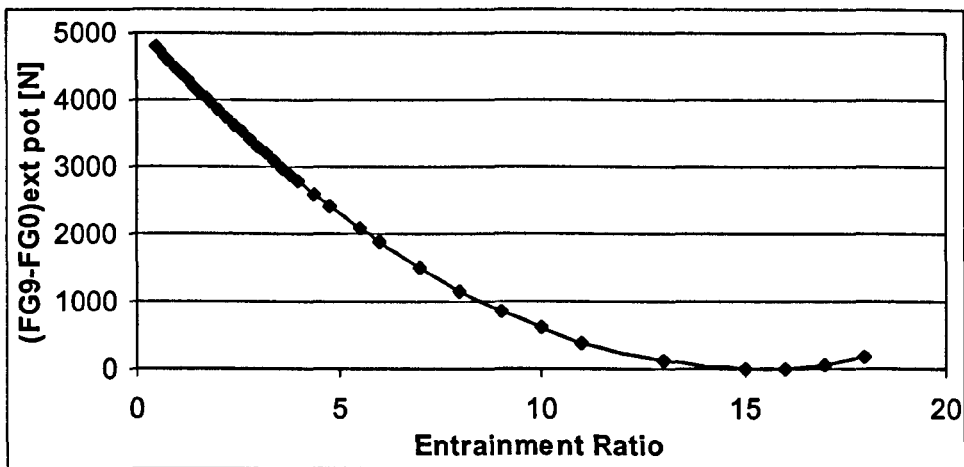


Figure 4.29: Entrainment ratio Effect in the Potential Buoyancy Term

Carrying on with the parametric analysis, if the engine mass flow, the entrainment ratio and the engine nozzle area are kept constant ( $1193 \text{ Kg/s}$ ,  $1.074$ ,  $6.15 \text{ m}^2$ ) the cell cross sectional area can be used as variable parameter in equation (4.114).

Figure 4.30 shows the results obtained changing the cell cross sectional area.

The first comment which automatically rises up is that increasing the cell dimensions the potential buoyancy term decreases and it tends asymptotically to zero.

Indeed, increasing the cell cross sectional area the flow aero-dynamics within the cell becomes more like to that in free stream conditions (outdoor test bed cell), or in a pseudo-infinite cell as shown earlier in this chapter.

It is interesting to look at what happens at the thrust correction equations (equation (4.77)) once the cell is big enough to neglect the potential buoyancy term. Neglecting the buoyancy term equation (4.77) becomes

$$L = F_N - D_{metric} \tag{4.117}$$

But at the same time if the cell is big enough even the flow velocity at section (0) and the secondary flow velocity around the engine become low. Accordingly the intake momentum drag and the metric drag become enough small to be neglected. This leads to the fact that for infinitely large cell the thrust correction factor equation becomes

$$L = F_{G9} \tag{4.118}$$

This effect is the similar to that experienced for free air test, where the static pressure is constant all along the engine (this will be better treated in paragraph 4.4.1). The assumption of incompressible flow, as it has been said before starting the above parametric analysis, is reasonable for usual secondary flow velocity within the cell.

However the above analysis uses quite unrealistic values for the variables in order to point out the characteristic flow behaviours and trends for an indoor test cell. For example it is not common practice to have an entrainment ratio equal to 15 in usual cells. But here it has been used to understand and mark the effect of increasing the flow velocity within the cell. At the same time however, it is worth to remember that special attention has to be made in order of not overtaking velocity values to make unrealistic the assumption of incompressibility for the secondary flow.

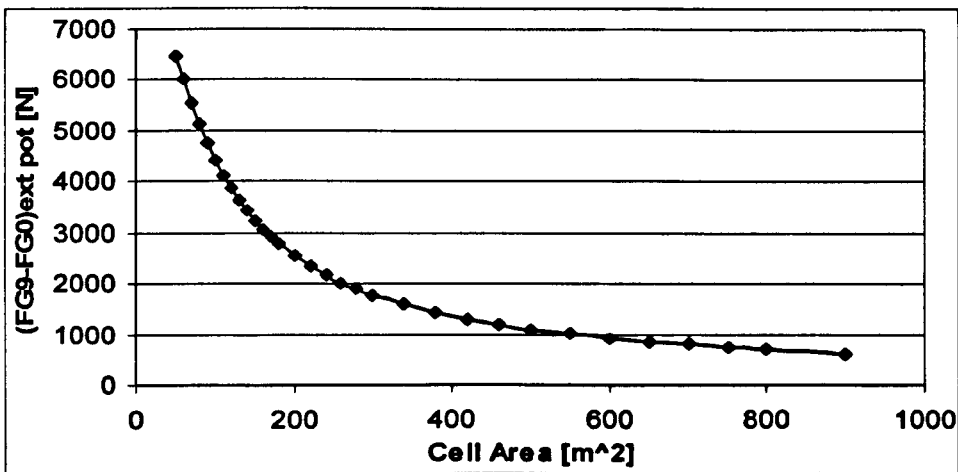


Figure 4.30: Cell cross Section Area Effect in the Potential Buoyancy Term

Even with its limitations the above analysis can be useful in order to understand the cell aero-dynamics and it could be used as starting points for preliminary test bed cells design.

An analogous formula as equation (4.114) can be obtained for the potential buoyancy between section (f) and (9<sub>ext</sub>) (equation (4.119)). At this time the pre-entry stream

tube and the bellmouth will not be included in the momentum box. The main consequence of such an approach is that all the different stream tube shape effects are not taken into account allowing for a more realistic analysis by using a fix value for the engine area at station (f).

$$\Delta F_{f9ext pot} = \left[ \frac{(1-f)}{(1-d)} + (1-f)^2 \left( \frac{(1-f)}{(1-d)} - 1 \right) - \frac{(1-f)^2}{(1-d)^2} \right] \frac{\mu^2 W_p^2 (1-d)}{\rho (1-f)^2 A_{cell0}} \quad (4.119)$$

Where the parameters e and f are defined in equations (4.120) and (4.121)

$$e = \frac{A_{nozzle}}{A_{cell0}} \quad (4.120)$$

$$f = \frac{A_{engf}}{A_{cell0}} \quad (4.121)$$

#### 4.3.11. Thrust Correction Equation for Finite Cell using $FG_{TH}$

In the above derived thrust correction equations as engine inlet interfaces two different sections have been taken into account. The first it has been section (1) for deriving the thrust correction equation represented in equation (4.60). The second it has been station (0) and the thrust correction equations derived with it, are equations (4.76), equation (4.77) and equation (4.87).

An important feature of the above mentioned equations is that implicitly or explicitly all of them are dealing with the force acting on the external bellmouth. But none of them is dealing with the force acting on the whole bellmouth including also its internal surface. Indeed, from the statement of equation (4.59) only equation (4.60) it includes  $\Phi_{bell int 1}$ ; (see Figure 3.31) which is only a portion of the  $\Phi_{bell int}$ .

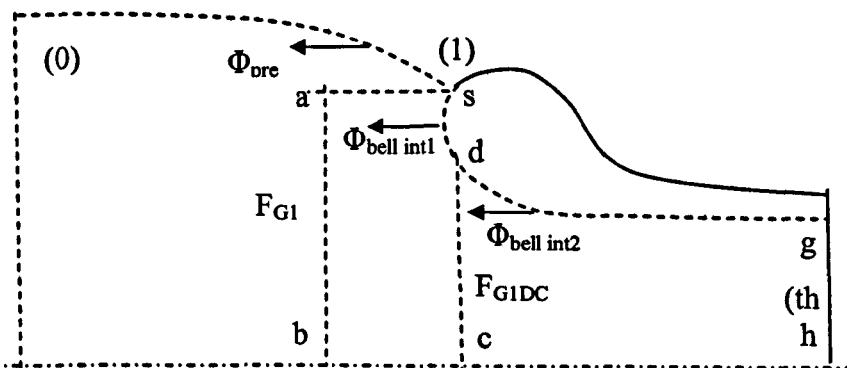


Figure 3.31: Representation of the Forces Acting on the Bellmouth

Applying the momentum theorem in the two momentum boxes abcds and cdgh it is possible to derive respectively equations (4.122) and (4.123)

$$-\phi_{bell int 1} = F_{G1dc} - F_{G1} \quad (4.122)$$

$$-\phi_{bell\ int2} = F_{Gth} - F_{G1dc} \quad (4.123)$$

If added together equations (4.122) and (4.123) lead to the total force acting on the internal surface of the bellmouth (equation (4.124))

$$-\phi_{bell\ int} = F_{Gth} - F_{G1} \quad (4.124)$$

Extending now the momentum box from station (1) to station (0) by equation (4.62) it can be obtained equation (4.125)

$$-\phi_{bell\ int} - \phi_{pre} = F_{Gth} - F_{G0} \quad (4.125)$$

Equation (4.125) can be easily incorporated in the thrust correction equation (4.87) and obtain the following equation (4.126) (Williams and Gullia d)

$$L = F_{G9} - F_{Gth} - \phi_{bell} - D_{carcase} - D_{cradle} + (F_{G9} - F_{Gf})_{ext\ pot} \quad (4.126)$$

Where,  $\Phi_{Bell}$  represents the entire force acting on the bellmouth. The use of equation (4.126) as thrust correction equation it offers the main advantage of avoiding the involvement of the pre-entry force which by it self is a term difficult to calculate and not possible to measure experimentally. Further more that equation avoids also the necessity of dealing with partial bellmouth forces which require the localization of the stagnation point. At the same time now the force acting on the entire bellmouth it needs to be established.

#### 4.3.12. 1D Calculation of the Term ( $F_{Gth} + \Phi_{bell}$ )

Equation (4.126) represents the sum of the axial forces acting on the “flange to flange” engine and it may be written as equation (4.127) (keeping in mind that the cell wall friction forces are neglected)

$$L = F_{G9} - (F_{Gth} + \phi_{bell}) - D_{carcase} - D_{cradle} + (F_{G9} - F_{Gf})_{ext\ pot} \quad (4.127)$$

As it will be better shown later on during this chapter the main term of equation (4.127) is ( $F_{Gth} + \Phi_{bell}$ ) and for this reason a relation able to quantify it is derived using one dimensional incompressible flow theory.

As main tool it will be used as usual the momentum theorem and the momentum box used is shown in Figure 4.32.

Applying the momentum theorem between sections (0), (f) and (th) it is possible to obtain equation (4.128)

$$F_{Gf} - F_{G0cell} = -(\phi_{bell} + F_{Gth}) \quad (4.128)$$

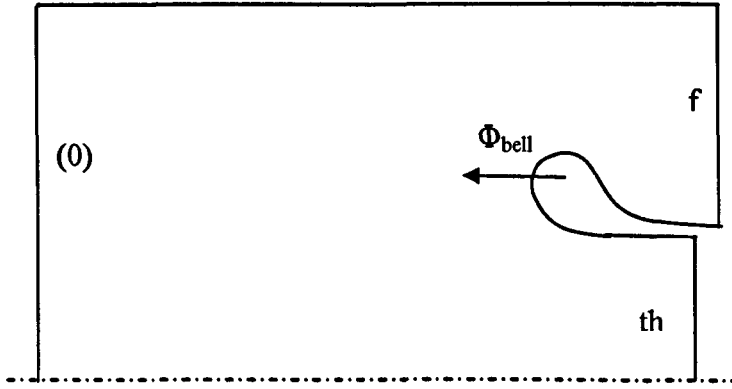


Figure 4.32: Representation of the momentum box for calculating the term  $(F_{Gth} + \Phi_{bell})$

The force on the whole bellmouth by the fluid it has been assumed to act in the downstream direction.

Substituting equation (4.128) into equation (4.127) another thrust correction equation is obtained (equation (4.129)).

$$L = F_{G9} - (F_{G0cell} - F_{Gf}) - D_{carcase} - D_{cradle} + (F_{G9} - F_{Gf})_{ext\ pot} \quad (4.129)$$

Therefore the term  $(F_{Gth} + \Phi_{bell})$  is substituted with the term  $(F_{G0cell} - F_{Gf})$  which by the potential incompressible flow assumption may be calculated as it follows.

However, before going ahead with the calculation it is worth underline that due to the low Mach number at section (0) and (f) (usually experienced in common cells) the assumption of incompressible flow leads to results which are not extremely far from the reality.

Dividing the stream gauge force at station (0) (representing the total cross sectional area of the cell) by the dynamic head still at station (0)

$$\frac{F_{G0cell}}{q_{0cell} A_{cell}} = \frac{(W_{eng} + W_s) v_0}{\frac{1}{2} \rho v_0^2 A_{cell}} = \frac{\rho v_0^2 A_{cell}}{\frac{1}{2} \rho v_0^2 A_{cell}} = 2 \quad (4.130)$$

Substituting equation (4.94) equation (4.130) it is possible to obtain equation (4.131)

$$\frac{F_{G0cell} - F_{Gf}}{q_0 A_{cell}} = 2 - \left(1 - \frac{1}{\lambda}\right) \left\{ \left[ \left( \frac{\mu}{\mu + 1} \right) \left( \frac{\lambda}{\lambda - 1} \right) \right]^2 + 1 \right\} \quad (4.131)$$

And accordingly equation (4.132) (Williams and Gullia d)

$$\frac{\phi_{bell} + F_{Gth}}{q_0 A_{cell}} = 2 - \left(1 - \frac{1}{\lambda}\right) \left\{ \left[ \left( \frac{\mu}{\mu+1} \right) \left( \frac{\lambda}{\lambda-1} \right) \right]^2 + 1 \right\} \quad (4.132)$$

The most important thing to underline in equation (4.131) is the fact that despite the high flow velocity along the internal bellmouth and at engine throat the term ( $F_{Gth} + \Phi_{bell}$ ) can be calculated under the incompressible flow assumption.

This is a consequence of the momentum conservation shown in Figure 4.32.

An important form of equation (4.132) is that one in which the left hand side involves only bellmouth and throat terms. This categorically can not utilise an incompressible flow assumption because the high Mach number at the engine throat which will act to reducing the density.

Equation (4.133) shows the compressibility effects

$$\frac{\rho_{th}}{\rho_0} < 1 \quad (4.133)$$

At the same time the velocity ratio between the stations (0) and (th) can be written as in equation (4.134)

$$\frac{v_0}{v_{th}} = \frac{(W_s + W_p)}{\rho_0 A_{cell}} \frac{\rho_{th} A_{th}}{W_p} = \frac{1 + \mu}{\lambda} \frac{\rho_{th}}{\rho_0} \quad (4.134)$$

and accordingly it is possible to write the dynamic head ratio as in equation (4.135)

$$\frac{q_0}{q_{th}} = \frac{\rho_{th}}{\rho_0} \left( \frac{1 + \mu}{\lambda} \right)^2 \quad (4.135)$$

Using only throat terms, equation (4.132) would become (Williams and Gullia d)

$$\frac{\phi_{bell} + F_{Gth}}{q_{th} A_{th}} = \left\{ 2 - \left(1 - \frac{1}{\lambda}\right) \left\{ \left[ \left( \frac{\mu}{\mu+1} \right) \left( \frac{\lambda}{\lambda-1} \right) \right]^2 + 1 \right\} \right\} \frac{q_0}{q_{th}} \frac{A_{cell}}{A_{th}} \quad (4.136)$$

Substituting equation (4.135) into equation (4.136)

$$\frac{\phi_{bell} + F_{Gth}}{q_{th} A_{th}} = \left\{ 2 - \left(1 - \frac{1}{\lambda}\right) \left\{ \left[ \left( \frac{\mu}{\mu+1} \right) \left( \frac{\lambda}{\lambda-1} \right) \right]^2 + 1 \right\} \right\} \frac{\rho_{th}}{\rho_0} \frac{(1 + \mu)^2}{\lambda} \quad (4.137)$$

Adjusting equation (4.137), equation (4.138) can be derived

$$\frac{\phi_{bell} + F_{Gth}}{q_{th} A_{th}} = \left[ \left( \frac{1 + \mu}{\lambda} \right)^2 (\lambda - 1) - \left( \frac{\mu^2}{\lambda - 1} \right) \right] \frac{\rho_{th}}{\rho_0} \quad (4.138)$$



It is worth to underline the fact that the ratio  $\rho_{th}/\rho_0$  can be incorporated in the left hand side of the equation (4.138) together with the throat dynamic head (equation (4.139)). Therefore the left hand side of such an equation involves only throat terms, apart the force acting on the bellmouth, which can be regarded as invariant between indoor and free air. This is very useful to calculate and establish a comparison of the force acting on the bellmouth between free air and indoor conditions, as it will be shown later on during this chapter (paragraph 4.4.2).

$$\frac{\phi_{bell} + F_{Gth}}{q_{th} A_{th} \frac{\rho_{th}}{\rho_0}} = \left[ \left( \frac{1 + \mu}{\lambda} \right)^2 (\lambda - 1) - \left( \frac{\mu^2}{\lambda - 1} \right) \right] \quad (4.139)$$

Now the left hand side of the equation (4.139) is a function of the engine and cell dimensions and of the entrainment ratio. Furthermore its numerator is the main term of the thrust correction equation represented in equation (4.127). Therefore, a graphic representation of equation (4.139) is useful to understand how the thrust correction factors change with  $\mu$  and  $\lambda$ .

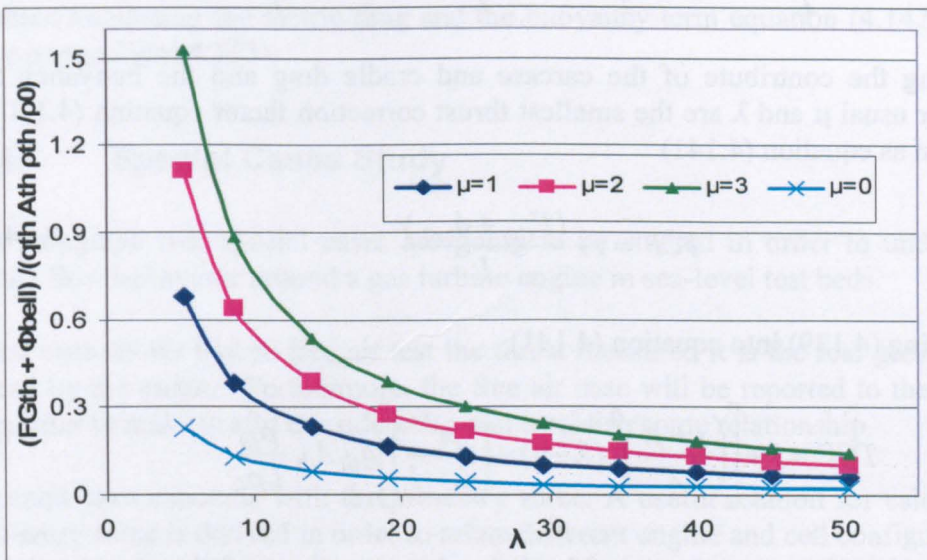


Figure 4.33: Parametric Analysis of the Term  $(F_{Gth} + \Phi_{bell}) / (q_{th} A_{th} \rho_{th} / \rho_0)$  Function of  $\lambda$  and  $\mu$

A similar analysis was worked out by Ashwood (Ashwood 1984), with the intent of calculating the force acting on the bellmouth and the results are reported in ((Ashwood 1984)). However, it has to be said that the Ashwood's final result is expressed in a different form, probably less useful for parametric analysis.

Figure 4.33 shows that for a given engine mass flow ( $W_{eng} = \text{constant}$ ) and dimension ( $A_{th} = \text{constant}$ ) the term  $(F_{Gth} + \Phi_{bell}) / (q_{th} A_{th} \rho_{th} / \rho_0)$  increases in a very non linear fashion as the cell cross sectional area reduces and the entrainment ratio increases. A possible explanation to confirming this trend can be obtained comparing the two thrust correction equations represented in the equations (4.87) and (4.127).

Comparing the two equations it is possible to see that the term  $(F_{Gth} + \Phi_{bell})$  includes in itself the intake momentum drag, which is well known to be the biggest thrust correction factor in equation (4.87) (Rios et al. 1998). Therefore, being equations (4.127) and (4.87) equivalent a change in one of them must be reflected even in the other in a mutual way

Therefore, a reduction in cell cross sectional area or even an increase in entrainment ratio bring to an increase in cell velocity by keeping the same engine mass flow. Such an increase in cell velocity leads to an increase in inlet momentum drag (equation (4.64)) which even if does not appear in  $(F_{Gth} + \Phi_{bell})$  is implicitly incorporated.

Another important consideration which can be made looking at Figure 4.33 is that increasing the cell cross sectional area the thrust correction factor reduces and it tends asymptotically to zero when the cell is infinitely large as in free air conditions. This will be better shown later on when a comparison between indoor and outdoor thrust corrections factors will be made (paragraph 4.4.2).

#### 4.3.13. Cell Size and Entrainment Ratio for Fixed TCF

Equation (4.127) might also be written in terms of total thrust correction factor (TCF)

$$\frac{F_{G9}}{L} = 1 + \frac{(F_{Gth} + \phi_{bell})}{L} + \frac{D_{carcase}}{L} + \frac{D_{cradle}}{L} - \frac{(F_{G9} - F_{Gf})_{ext\ pot}}{L} = TCF \quad (4.140)$$

Neglecting the contribute of the carcase and cradle drag and the buoyancy term, which for usual  $\mu$  and  $\lambda$  are the smallest thrust correction factor equation (4.140) can be written as equation (4.141)

$$TCF = 1 + \frac{(F_{Gth} + \phi_{bell})}{L} \quad (4.141)$$

Substituting (4.139) into equation (4.141)

$$TCF = 1 + \left[ \left( \frac{1 + \mu}{\lambda} \right)^2 (\lambda - 1) - \left( \frac{\mu^2}{\lambda - 1} \right) \right] q_{th} A_{th} \frac{\rho_{th}}{L \rho_0} \quad (4.142)$$

Equation (4.142) represents a useful relation between the total thrust correction, the cell and engine dimensions and cell and engine mass flow.

For example fixing the TCF by equation (4.142) it would be possible to find out the possible combinations of  $\mu$  and  $\lambda$  which match the fixed TCF.

Figure 4.34 shows the possible combination of  $\mu$  and  $\lambda$  in order to get TCF equal to 1.05. All the possible combinations above the line (represented in figure) give TCF bigger than 1.05 and all the combinations below it give TCF smaller than 1.05 (Williams and Gullia d).

This can also be seen in Figure 4.33 where by increasing the entrainment ratio or reducing the cell cross sectional area the thrust correction factors increase

Equation (4.142) can be improved without neglecting the carcase and cradle drag and the buoyancy factor. Indeed, these three terms are all function of the velocity square of the secondary flow (equation (4.81) and equation (4.119)).

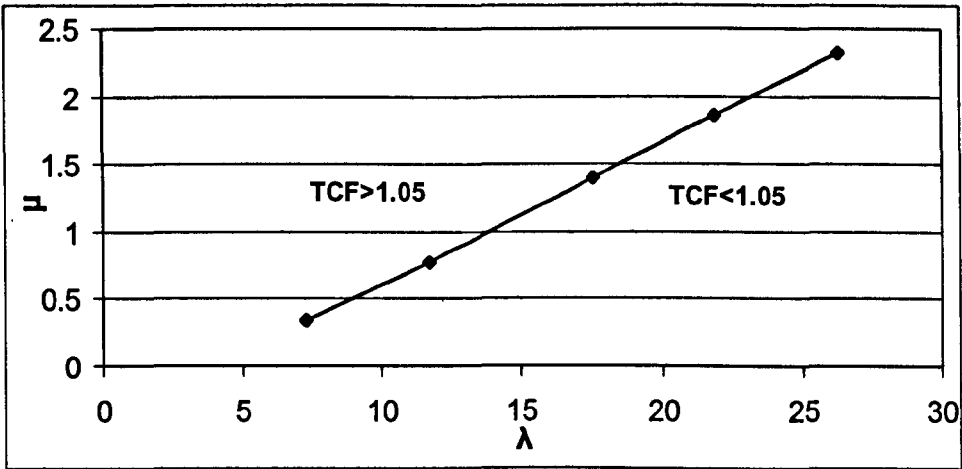


Figure 4.34: Possible Combination of  $\lambda$  and  $\mu$  for Matching  $(F_{Gth} + \Phi_{bell})/L = 1.05$

$$TCF = 1 + \left[ \left( \frac{1+\mu}{\lambda} \right)^2 (\lambda - 1) - \left( \frac{\mu^2}{\lambda - 1} \right) \right] q_{th} A_{th} \frac{\rho_{th}}{L\rho_0} + C\mu^2 \quad (4.143)$$

So without neglecting the metric drag and the buoyancy term equation (4.142) could become as equation (4.143).

#### 4.4. Special Cases Study

In this paragraph two special cases are going to be studied in order to understand better the flow behaviour around a gas turbine engine in sea-level test beds.

The first case shows that in free air test the thrust measured it is the real gross thrust delivered by the engine. Furthermore, the free air case will be reported to the indoor case in order to make useful consideration and establish some relationship.

The second case concerns with the pre-entry force. A useful relation for calculating the pre-entry force is derived in order to relate different engine and cell configurations

##### 4.4.1. Free Air Study

As it has been assumed in the literature review (paragraph 2.1.5) in free air test the thrust measured is equal to the real gross thrust delivered by the gas turbine engine. However, this statement (under the assumption of no-wind) is only true for jet engines. Indeed, it needs to be adjusted for turbofan engine where the force exerted on the hot nozzle and on the plug may affect the thrust measured as well (SAE Committee E-33 1985).

In this paragraph it will be taken into account a simple jet engine whose configuration is the same sketched up to now in the previously paragraphs. Although this is a

restriction it is believed to be a general starting point from where more considerations can be made and referred to even in the case of turbofan.

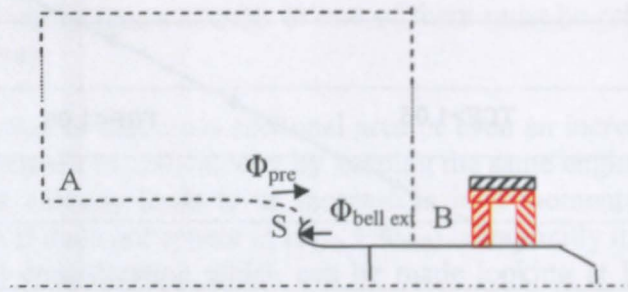


Figure 4.35: Momentum Box for free air Studies

Assuming of working with a free air velocity  $V_0 \gg 0$  which allows the stagnation point of the pre-entry stream tube to be on the bellmouth (Figure 4.35). Under the assumption of potential subsonic flow it is possible to show that the force acting on the pre-entry stream tube is equal and opposite of the force acting on the engine fore-body.

The starting point for showing the above statement is to account for an infinitely large control box enclosing the pre-entry stream tube and the engine fore-body. Being in free air this is reasonably possibly and it is shown in Figure 4.35 by the dotted and dashed lines.

Then, on the horizontal momentum box's surfaces the flow stream lines are not affected by engine and test equipment blockage area. Therefore, they are unchanged from the free stream streamlines conditions, strictly this can occur only at a distance infinitely far from the body.

This concept might help the physical understanding of such a momentum box which ends when the flow streamlines have reached the free stream configuration.

The main characteristic of this kind of control volume is the fact that the top of it has not any projected area in the flow direction and so no pressure force can be applied on it.

Further more the two cross sections passing for A and for B are infinitely large and the bulk static pressure under the on working assumption may be assumed to be the same. In particular being the flow in-viscid and so not allowing for any total pressure loss even the velocity at the cross section B will be the same than that one at A.

This defines the "semi infinite" body.

Applying now the momentum theorem

$$\int_{ASB} (p - p_0) dA = 0 \quad (4.144)$$

Equation (4.144) can also be splitted in two parts (equation (4.145))

$$\int_{AS} (p - p_0) dA + \int_{SB} (p - p_0) dA = 0 \quad (4.145)$$

This means that the force acting on the pre-entry stream tube is equal and opposite of the force acting on the external bellmouth. However, if the same sign convection used in the previously paragraphs is also used here from equation (4.88) it is possible to derive equation (4.146).

$$\phi_{pre} = \phi_{bell\ ext\ freeair} \quad (4.146)$$

It is worth to say that in this derivation the engine fore-body is assumed to have not any projected area  $dA$  and consequently no pressure force will act on it. Otherwise the second integral on the left hand side of equation (4.145) would also include the force acting on the engine fore-body.

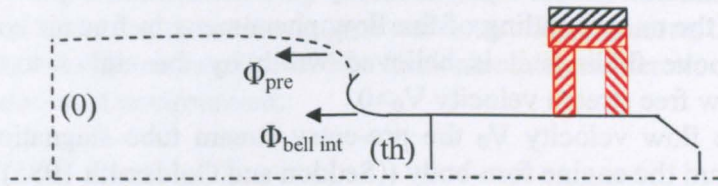


Figure 4.36: Momentum Box from the Engine Throat to Station (0) in Free Air

Now applying the momentum theorem from station (0) to station (th) (Figure 4.36) in the internal flow it is still possible to derive equation (4.125) previously defined for the indoor flow conditions.

Substituting equation (4.146) into equation (4.125)

$$-\phi_{bell\ ext\ freeair} - \phi_{bell\ int\ freeair} = F_{Gth} - F_{G0} \quad (4.147)$$

And consequently

$$-\phi_{bell\ freeair} = F_{Gth} - F_{G0} \quad (4.148)$$

Equation (4.148) is an important out-coming from this free air analysis especially when equation (4.148) is reported to zero free stream velocity which, by the way, is the usual condition for outdoor tests.

Indeed, if the free stream flows velocity is zero the inlet momentum drag becomes zero and accordingly it is possible to write equation (4.149) (Williams and Gullia d)

$$-\phi_{bell\ freeair} = F_{Gth} \quad (4.149)$$

Equation (4.149) clearly states that under the above assumptions in free air conditions with free stream velocity equal to zero the force acting on the bellmouth is equal and opposite to the stream force acting on the engine throat.

If now the equation (4.149) is substituted in the thrust correction equation (4.127) and considering that in this “ideal” condition even the drag and the buoyancy terms will be zero (no flow will flow around the engine) it is possible to obtain

$$L = F_{G0} \quad (4.150)$$

Equation (4.150) clearly states that in free air condition with  $V_0$  equal to zero the load cells measure the real gross thrust delivered by the engine.

Therefore, in such flow conditions and for the gas turbine engine model taken into consideration (represented in the sketches) the presence of the bellmouth allows the compensation for the throat stream force and consequently make possible equation (4.150).

Also the engine fore-body (until the section with the completely pressure recovery (B)) would contribute to such force compensation if it had a projected area in the flow direction. And its contribution would be included in the second integral of equation (4.145) (which at the moment represents only the bellmouth force).

For improving the understanding of the flow phenomena in free air conditions and to validate the above findings it is believed worth by the author to show the flow structure for low free stream velocity  $V_0 > 0$ .

Decreasing the flow velocity  $V_0$  the pre-entry stream tube stagnation point moves back ward toward the engine fore-body ((Seddon and Goldsmith 1985)).

Accordingly, the flow structure is represented by Figure 3.37.

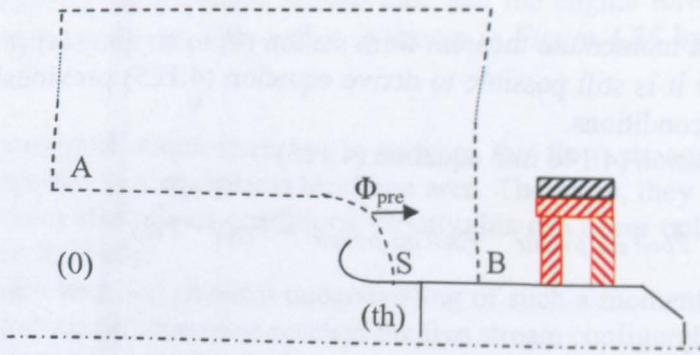


Figure 3.37: Outdoor Momentum Box for Low Free Stream Velocity

Still in this case the infinitely large momentum box can be drawn but now the final result is slightly different from that obtained before. Indeed, though the global integral along the surface ASB is still equal to zero, equation (4.144) now includes only the pre-entry force. This because the flat shape of the engine fore-body which has  $dA=0$ .

$$\int_{ASB} (p - p_0) dA = \int_{AS} (p - p_0) dA = \phi_{pre} = 0 \quad (4.151)$$

Equation (4.151) states that under the assumption of potential flow when the free stream velocity is low but not zero the flow readjusts itself in order to allow the pre-entry force to be zero. Practically if the stagnation point is not on the bellmouth there is not any possibility to compensate the pre-entry force.

Under such circumstances equation (4.125) becomes

$$-\phi_{bell \text{ int } freeair} = F_{Gth} - F_{G0} \quad (4.152)$$

But now the term  $\Phi_{bell\ int}$  includes also that part of the bellmouth which before was called external. Indeed the whole bellmouth is now inside the pre-entry stream tube (Figure 3.37).

So in this case equation (4.152) can be reduced to equation (4.148) and to equation (4.149) when the free stream velocity is zero.

Another case which could be mentioned is when the pre-entry stream tube is in datum condition. In such a case for both  $V_0 \gg 0$  and  $V_0 > 0$  the pre-entry force is equal to zero. It is straight forward now by applying equation (4.144) to show that even the force acting on the bellmouth in the former case and in the engine fore-body in the latter case are equal to zero.

The free air cases shown above are very useful in order to help the understanding of the general flow phenomena around an engine under test. Furthermore, their use is not only limited with the free air conditions but fundamental considerations can also be applied to the indoor test environment.

#### 4.4.2. Indoor and Free Air Bellmouth Force Comparison

In the previous paragraph it has been shown that in free air conditions when the free stream velocity is equal to zero the force acting on the bellmouth counteracts the whole throat stream force.

Such compensation allows the force measured by the load cell to be the real gross thrust delivered by the engine. Therefore in such conditions none of the thrust correction factors is needed.

At the same time it is clear from Figure 4.33 that in indoor beds the suction force acting on the bellmouth does not compensate for the throat stream force. Further more this unbalance becomes even bigger by increasing either  $\mu$  or decreasing  $\lambda$ .

Substituting equation (4.149) into equation (4.127)

$$L = F_{G9} - (-\phi_{bell\ freeair} + \phi_{bell}) - D_{carcase} - D_{cradle} + (F_{G9} - F_{Gf})_{ext\ pot} \quad (4.153)$$

It is interesting now analyse only the second term on the right hand side of equation (4.153) which is responsible for most of the total thrust correction factors. This term can be substituted in equation (4.139) obtaining

$$\frac{\phi_{bell} + F_{Gth}}{q_{th} A_{th} \frac{\rho_{th}}{\rho_0}} = \frac{-\phi_{bell\ freeair} + \phi_{bell}}{q_{th} A_{th} \frac{\rho_{th}}{\rho_0}} = \left[ \left( \frac{1 + \mu}{\lambda} \right)^2 (\lambda - 1) - \left( \frac{\mu^2}{\lambda - 1} \right) \right] > 0 \quad (4.154)$$

In the derivation of equation (4.139) the force on the fluid by the bellmouth has been taken acting in the thrust direction (forward direction). This means that the force from the fluid to the bellmouth it has been assumed acting on the drag direction. However from the thrust correction factor calculation  $\Phi_{bell}$  comes up to be negative (paragraph 4.5.4). Therefore the force on the bellmouth surface exerted by the surrounding fluid it acts in the thrust direction as it also well know for mass flow ratio greater than one (suction mode as is represented in the figures).

Now the denominator in equation (4.154) is always a positive number therefore also the numerator has to be positive in order to satisfy the whole equation (4.154).

So it is possible to write equation (4.155)

$$-\phi_{bell\ freeair} + \phi_{bell} > 0 \quad (4.155)$$

As has said above the two forces in equation (4.155) result to be negative and can be written as

$$\phi_{bell} = -L_{bell} \quad (4.156)$$

Where  $L_{bell}$  is the load on the bellmouth and it is always positive

Following equation (4.156) equations (3.155) and (4.156) becomes equation (4.157) (Williams and Gullia d)

$$L_{bell\ freeair} - L_{bell} > 0 \quad (4.157)$$

Equation (4.157) proves that in free air test the load exerted by the flow on the bellmouth is greater than the load exerted in indoor facility.

This means that for the same throat conditions the force exerted on the bellmouth in free air condition is bigger than the force exerted in indoor conditions.

Therefore in indoor conditions  $\Phi_{bel}$  does not compensate the whole throat stream force, making necessary the presence of the thrust correction factor represented in Figure 4.33.

In indoor conditions there is a progressive increase in the failure of the bellmouth thrust force to compensate for the rearwards throat stream gauge force as the entrainment ratio increases and the cell size reduces.

#### 4.4.3. Pre-entry Force

All along this chapter there have been plenty of references to the pre-entry stream tube and to its shape. For example during the consideration made for the buoyancy term the passage from the suction to the spillage conditions it has been mentioned in order to explain the increase of  $A_{0ext}$  as the entrainment ratio was increased.

Now in this paragraph an attempt to derive a useful relation for the pre-entry force is made.

The main aim of this attempt would be to separate the pressure term from the area term along the definition of the pre-entry force. In such a way both the effects will be monitored. Indeed when the stream tube changes configuration both the pressure component and the projected area change (from a diffusion process in suction condition to a compression process in spillage condition).

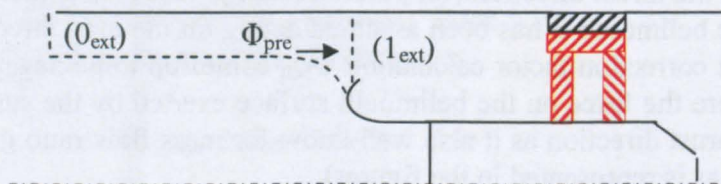


Figure 4.38: Momentum Box for Computing the Pre-Entry Force



Equation (4.158) represents the application of the momentum theorem to the air box drawn by dashed lines in Figure 4.38 (between (0<sub>ext</sub>) and (1<sub>ext</sub>)) assuming the flow to be potential and incompressible.

$$\phi_{pre} = F_{G1ext} - F_{G0ext} = 2q_{1ext}A_{1ext} + (p_{1ext} - p_0)A_{1ext} - 2q_{0ext}A_{0ext} \quad (4.158)$$

In the above momentum balance have been neglected the cell friction forces (assumed the flow potential).

By Bernoulli theorem between (0<sub>ext</sub>) and (1<sub>ext</sub>)

$$\phi_{pre} = (q_{0ext} + q_{1ext})A_{1ext} - 2q_{0ext}A_{0ext} \quad (4.159)$$

Dividing both the left hand side and the right and side of equation (4.159) by  $q_0A_{0ext}$  it is possible to obtain equation (4.160)

$$\frac{\phi_{pre}}{q_{0ext}A_{0ext}} = \left(1 + \frac{q_{1ext}}{q_{0ext}}\right) \frac{A_{1ext}}{A_{0ext}} - 2 = \left(1 + \frac{A_{0ext}^2}{A_{1ext}^2}\right) \frac{A_{1ext}}{A_{0ext}} - 2 = \left(\frac{A_{1ext}}{A_{0ext}} + \frac{A_{0ext}}{A_{1ext}}\right) - 2 \quad (4.160)$$

Equation (4.160) can also be written as

$$\phi_{pre} = \left[ \left( \frac{A_{1ext}}{A_{0ext}} + \frac{A_{0ext}}{A_{1ext}} \right) - 2 \right] q_{0ext}A_{0ext} \quad (4.161)$$

Dividing both side of equation (4.161) by  $(p_{1e}-p_0) A_0$

$$\frac{\phi_{pre}}{(p_{1ext} - p_0)A_{0ext}} = \left[ \left( \frac{A_{1ext}}{A_{0ext}} + \frac{A_{0ext}}{A_{1ext}} \right) - 2 \right] \frac{q_{0ext}A_{0ext}}{(p_{1ext} - p_0)A_{0ext}} \quad (4.162)$$

Now the pre-entry force can be seen also as the integral of the gauge pressure along the pre-entry stream tube

$$\phi_{pre} = \int_{pre} (p - p_0) dA \quad (4.163)$$

By the first mean value theorem the integral of equation can be solved as

$$\phi_{pre} = (\overline{p - p_0})(A_0 - A_1) \quad (4.164)$$

Where  $(\overline{p - p_0})$  is the mean pressure value along the pre-entry stream tube.

Dividing equation (4.162) by equation (4.164) it is possible to obtain equation (4.165)

$$\frac{\overline{(p-p_0)} (A_0 - A_1)}{(p_{1ext} - p_0) A_{0ext}} = \frac{\left[ \left( \frac{A_{1ext}}{A_{0ext}} + \frac{A_{0ext}}{A_{1ext}} \right) - 2 \right]}{\left( 1 - \frac{A_{0ext}^2}{A_{1ext}^2} \right)} \quad (4.165)$$

Keeping in mind that the mass flow ratio (MFR) is equal to  $A_0/A_1$

$$\frac{(A_0 - A_1)}{A_{0ext}} = \frac{A_1(MFR - 1)}{A_{0ext}} \quad (4.166)$$

Substituting equation (4.166) into equation (4.165)

$$\frac{\overline{(p-p_0)}}{(p_{1ext} - p_0)} = \frac{\left[ \left( \frac{A_{1ext}}{A_{0ext}} + \frac{A_{0ext}}{A_{1ext}} \right) - 2 \right]}{\left( 1 - \frac{A_{0ext}^2}{A_{1ext}^2} \right) \frac{A_1(MFR - 1)}{A_{0ext}}} \quad (3.167)$$

Equation (3.167) can also written as (4.168) by including even the cell cross sectional area (Williams and Gullia b )

$$\frac{\overline{(p-p_0)}}{(p_{1ext} - p_0)} = \frac{\left[ \left( \frac{A_{1ext}}{A_{0ext}} + \frac{A_{0ext}}{A_{1ext}} \right) - 2 \right]}{\left( 1 - \frac{A_{0ext}^2}{A_{1ext}^2} \right) (MFR - 1) \frac{A_{cell} - A_{1ext}}{A_{0ext}}} \quad (4.168)$$

Using  $\overline{(p-p_0)}$ , MFR or even directly  $\Phi_{pre}$  as dependent parameter, equation (4.168) can be used for parametric analysis.

Figure 4.39 shows how  $\overline{(p-p_0)}$  changes with the entrainment ratio for a cell of 115  $m^2$  and an engine mass flow of 1200 Kg/s.

For low  $\mu$  Figure 4.39 shows a growing tendency of  $\overline{(p-p_0)}$  as the entrainment ratio increases. The reason why this happens is because for small secondary mass flow the velocity at station (1<sub>ext</sub>) increases less than the velocity at station (0<sub>ext</sub>). This allows the term  $(p_{1ext} - p_0)$  to increase and consequently  $\overline{(p-p_0)}$  to have a growing tendency despite the total mass flow in the cell increases and the right hand side of equation (4.168) decreases.

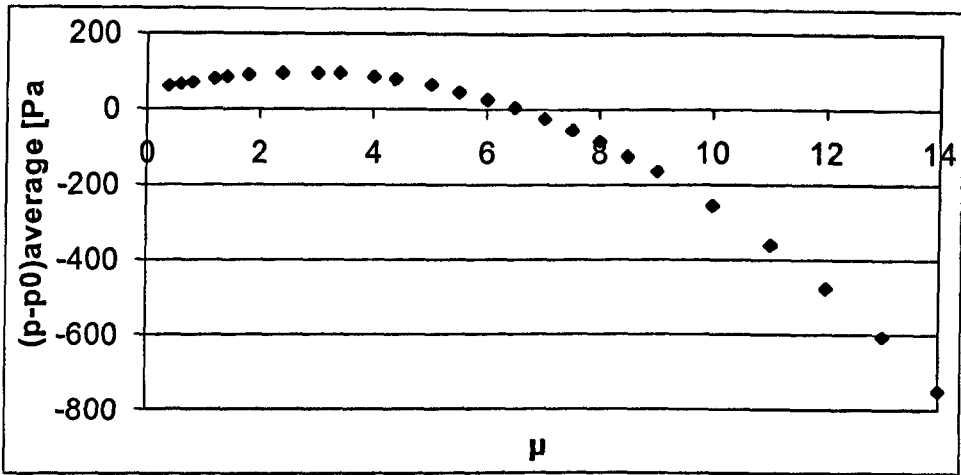


Figure 4.39:  $(p-p_0)$  Average as Function of  $\mu$

When the velocity at station  $(1_{\text{ext}})$  starts to increase more than the velocity at  $(0_{\text{ext}})$  the trend of the curve of Figure 4.39 decreases and for a defined  $\mu$  the term  $\overline{(p-p_0)}$  becomes negative meaning that the pre-entry force has changed sign. This means also that from suction condition the pre-entry stream tube has moved to spillage conditions because. This also means that the velocity at section (0) it is high enough to allow the stream tube cross section area to be smaller than  $A_1$ .

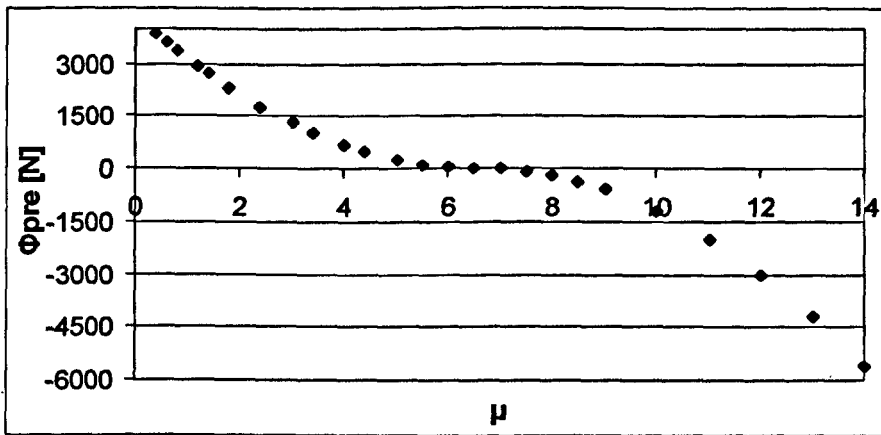


Figure 4.40: Pre-Entry Force as Function of  $\mu$

Figure 4.40 shows the trend for the pre-entry force as function of the cell entrainment ratio. It is clear that for a certain entrainment ratio the pre-entry force changes sign. This corresponds to the change in the way of such force acts. Indeed has to kept in mind that the whole derivation of equation (4.168) starts from the application of the momentum theorem which uses a well defined signs convention. It is important to say that in the above analysis the pre-entry stream tube stagnation point is kept always in the same position on the bellmouth, not allowing for it any movement as function of the upstream velocity  $V_0$ .

Under the same assumption Figure 4.41 shows how the  $\overline{(p-p_0)}$  changes as function of the cell cross sectional area. Increasing that area the flow velocity inside the cell

reduces. If from one side this allows a reduction in the pressure difference from the other side this increases the projected area of the stream tube. From the pre-entry force point of view these two effects act in opposite way. Indeed a reduction in  $(\overline{p-p_0})$  bring to a reduction in  $\Phi_{pre}$  and an increase in projected area bring to an increase in  $\Phi_{pre}$ . However must be remembered that if the stagnation point was allowed to move along the bellmouth the stream tube projected area would change as well.

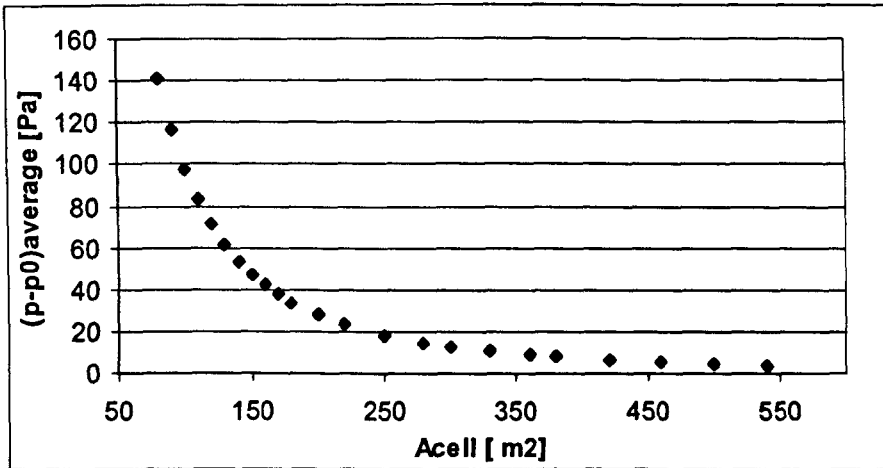


Figure 4.41: (p-p<sub>0</sub>) Average as Function of the Cell Cross Sectional Area

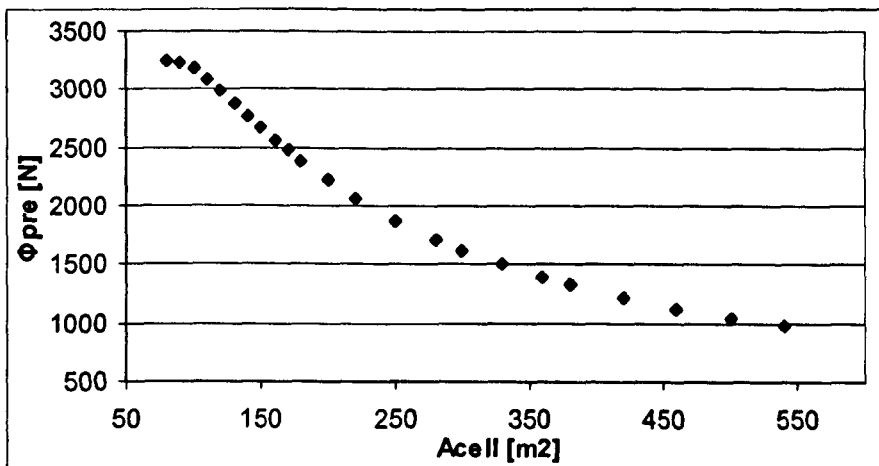


Figure 4.42: Pre-Entry Force as Function of the Cell Cross Sectional Area

The sum of the two effects above mentioned is shown in Figure 4.42 where the pre-entry force is plotted against the cross sectional area.

It is clear that the pressure reduction has a bigger contribute than the area increasing and therefore the pre-entry force decrease as the cross sectional area increases and it tends asymptotically to zero.

#### 4.5. Thrust Correction Equations Comparison

In this paragraph the three thrust correction equations above derived ((4.77)(4.79) , (4.87) and (4.126)) will be compared using the data worked out during preliminary

test of the Roll-Royce Engine “C” in Test Bed “Y” sited in Derby. The data used are engine performance measurement and the flow fields measurements inside the cell necessary for the application of the First Principle Anemometer (paragraph 2.3.2).

However, before applying the thrust correction equations it is necessary to make some assumptions which are described below (paragraph 4.5.3).

However, before it is preferred to give a small description in terms of dimensions and performance of the Engine “C” and of the Test Bed “Y”.

#### 4.5.1. Rolls Royce Engine “C”

For confidential reasons the Rolls-Royce engine used for the comparison between the different thrust corrections equation, above derived, is called engine “C”.

In Table 4.2 some engine specification are provided.

In the next Table 4.3 are summarized some useful data extrapolated from the engine test carried out on the 4<sup>th</sup> of April 2005 relative to the cell scanning 1495 which correspond to an engine power setting measured of 90% ((Rolls-Royce)).

Thrust	315000-340000N
Bypass Ratio	8.7-8.5
Inlet Mass Flow	1204-1245 Kg/s
Fan Diameter	
Length	
Weight	

Table 4.2: R-R Engine “C” Specifications (Rolls-Royce plc.)

Day Temperature	285 K
Day Pressure	101997 Pa
Inlet Mass Flow	1283 Kg/s
Non Dimensional Mass Flow	3275
Load Measured	385161 N
Test inlet Temperature	284.83 K
Test Inlet Total Pressure	100899 Pa
Test Cell Static Pressure	100828Pa

Table 4.3: Engine and Cell Measurement (Rolls-Royce)

#### 4.5.2. Rolls Royce Test Bed “Y”

Rolls-Royce test cell “Y” (for confidential reasons the real name of the cell can not be mentioned) is a large test bed whose dimensions allow testing for high by-pass ratio turbofan. All along the bed it runs a cavity in order to reduce the noise pollution. Figure 4.43 and Figure 4.44 show the layout of the cell and some general dimensions. From these pictures which are not to be scaled for confidentiality reason it is not clear the presence of a screen just down-stream the turn wind. Such screen is used to

preserve the flow from distortion and to smooth it as much as possible in order to do not affect the engine performance (paragraph 2.4.1).

Along the inlet and outlet stacks there are splitters covered by special material in order to preserve the environment from noise pollution.

The "Y" cell is a parallel wall cell and its testing cross sectional area is  $203 \text{ m}^2$ .

For the test scanning number 1495 of the 4<sup>th</sup> of April, whose engine and cell measurement are above reported, the cell entrainment ratio was 1.6963, which means that the total mass flow entering the cell was 3459 Kg/s

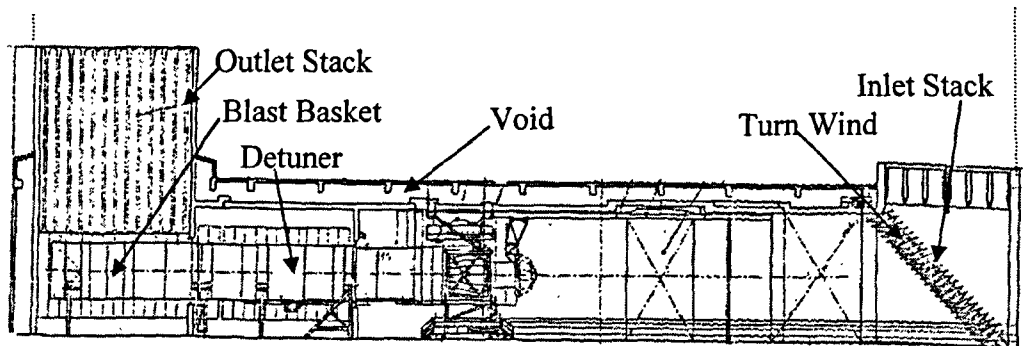


Figure 4.43: Longitudinal Section of the Rolls Royce Test Bed "Y"(Courtesy of Rolls-Royce)

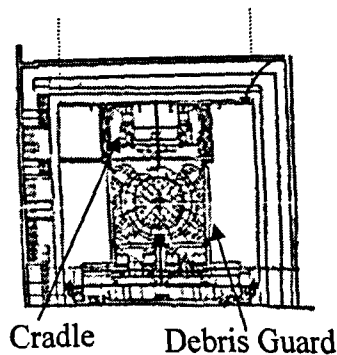


Figure 4.44: Transversal Section of the Rolls Royce Test Bed "Y"(Courtesy of Rolls-Royce)

### 4.5.3. General Assumptions for the Thrust Correction Equations Comparison

In this paragraph are discussed the general assumption valid for each one of the thrust correction equations. Following, if a specific equation needs a specific assumption for its application this is made when the equation is applied.

The first assumption which it has been made is that the drag of the engine carcass is neglected. It would not be easy to work out the drag coefficient of the engine carcass within a test bed either by experimental or by specific manual book. Indeed the flow interactions between the carcass, the pre-entry stream tube, the bellmouth, and the detuner (ejector pump) make of the engine carcass in the test bed a very specific case.

However, this term appears in all the thrust correction equations above derived, consequently it affects each equation in the same way.

Therefore, the purpose of comparison between different equations can justify such an assumption.

Another assumption is related with the potential buoyancy term. Indeed, in the Rolls-Royce first principle anemometer the static pressure around the engine after-body is directly measured allowing for the base gauge force to be directly worked out. Therefore there is not any needing for the potential buoyancy to be calculated along the engine after-body (this means up to station ( $9_{ext}$ )).

However the shape of engine C is not as simple as the engine shapes above represented in the sketches where the axial engine projected area is concentrate only in the engine after-body. Accordingly, in the following equations comparison the base force it has been calculated using the pressure experimentally measured on the engine after-body and the axial projected area from station (f) to station (9). At the same time to cope the difficulties on determining the potential buoyancy effect, two different approaches have been used for each equation. In the first approach the buoyancy it has been calculated up to station ( $9_{ext}$ ) (starting from either from station ( $0_{ext}$ ), or station (f) depending on thrust equation used) and in the second up to station ( $9_{ext}$ ) using the equaliance  $A_{9_{ext}} = A_f$ .

The main implication of the first approach is that the engine after-body is accounted for both base force and potential buoyancy effect. For the second approach the main implication is due to the potential buoyancy related with movable part of the cradle. Indeed by the assumption of  $A_{9_{ext}}$  equal to  $A_f$  there is not any difference between the cell cross sectional area upstream the movable cradle and that one downstream. This does not give arise to any cradle buoyancy effect.

Furtehmore, however, by the two different approaches it will be also possible to quantify the effective impact of using different buoyancy term in the thrust correction equations.

Another important assumption made is that the friction force component is neglected for the metric assembly (equation (4.61)).

Regarding the metric assembly the one dimensional thrust correction equations derive in this chapter are not able to calculate the neither the base nor the cradle drag. Therefore, both of them are derived by the Rolls-Royce First Principle measurements. Since this two terms influence all the thrust correction equations in the same way the final comparison is not affected by this assumption. Furthermore, an important consideration has to be made concerning the drag of the external part of the bellmouth which appears into the thrust correction equation (4.79). The determination of the drag coefficient to estimate such a drag would require a long and expensive experimental work in an environment as much as close to that found in the test cell. Such a work is not included in the specifications of this project and therefore for the moment the bellmouth external drag is not taken into account. The consequence of this are discussed during the chapter of this thesis dedicated to the discussion (paragraph 7.2.1)

The last but not less important assumption is related with the effective shape of the engine after-body. As it has been said above engine A is a large turbofan which implies the presence of two jets one coming from the hot nozzle and the other form the cold nozzle. Further more also the presence of the engine plug and the pylon

should not be neglected in the interaction between the flow and the engine components. Indeed, these components are present during the engine test.

Figure 4.45 shows a Rolls-Royce turbofan engine in the test bed and it is possible to see the presence of all the components above mentioned.

Due to their high velocity characteristic both the jet's path affect the pressure distribution along the engine components which are in contact with them. Altering the static pressure along the engine the two jets are also a source of additional forces on the engine which will affect the load measured during the test.

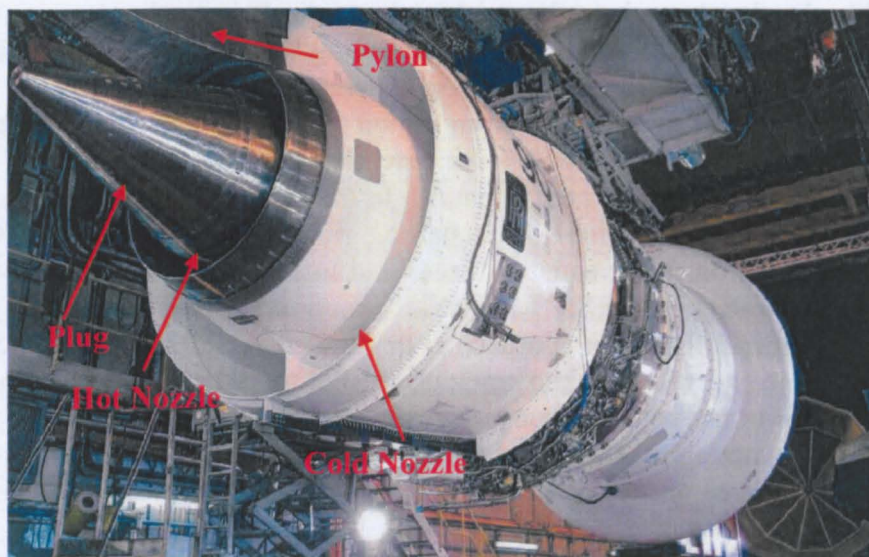


Figure 4.45: Turbofan Hanged in a Cradle inside a Test Facility (Courtesy of Rolls-Royce)

For example the hot jet coming out along the plug affects the static pressure on it giving rise to a force (due to friction and pressure) acting on the plug which should be accounted on the force bookkeeping of the engine within a test bed. The same it happens for the cold jet which hits the hot nozzle and the pylon. The estimation of such forces is also made more difficult by the fact that the two nozzles are not discharging to the cell pressure. In reality the pressure around the engine after-body is affected by the ejector pump effect taking place between the engine and the detuner. So, the calculation of the forces acting on the engine pylon, plug and hot nozzle should account also for such effect (SAE Committee E-33 1985).

This aspect it has not been taken into account in this thesis and it represents a really valid topic for further researchers who want to deal with the engine performance in enclosed test bed.

However for the purpose of comparison of different thrust correction equations using a chosen engine power setting and cell conditions the forces acting on the plug, pylon and hot nozzle are the same for each equation. This means that each equation will be affected in equal terms. Therefore, this can justify the assumption, but still it remains the fact the equations above derived are not complete and the terms missing should be included in the future work as important issue to be solved.



#### 4.5.4. Comparison

In order to make the comparison it is necessary first to derive all the values for completing the thrust correction equations.

TERM	FROM	VALUE
Load Measured	RR First Principle Measurements	385161 N
IMD ( $F_{G0}$ )	Equation (4.64)	17263 N
( $F_{GTHROAT} + \Phi_{Bellmouth}$ )	Equation (4.138)	14462 N
$\Phi_{BASE}$	RR First Principle Measurements	969 N
$\Phi_{pre}$	Equation (4.103)	2307 N
$\Phi_{Bellmouth\ ext}$	Equation (4.99)	-504 N
$D_{Cradle}$	RR First Principle Measurements	723N
( $F_{G9'} - F_{G0}$ ) <sub>ext pot</sub> [ $A_{9'ext} = A_{9ext}$ ]	Equation (4.114)	2699 N
( $F_{G9'} - F_{G0}$ ) <sub>ext pot</sub> [ $A_{9'ext} = A_f$ ]	Equation (4.114)	2388 N
( $F_{G9'} - F_{Gf}$ ) <sub>ext pot</sub> [ $A_{9'ext} = A_{9ext}$ ]	Equation (4.119)	-18 N
( $F_{G9'} - F_{Gf}$ ) <sub>ext pot</sub> [ $A_{9'ext} = A_f$ ]	Equation (4.119)	0 N

Table 4.4: Calculated Thrust Correction Factors Engine C Test Cell Y

In the above Table 4.4 it is possible to find out all the thrust correction terms and the equations used for computing them.

The first equation to be completed is equation (4.79). Following the above assumptions the term  $D_{metric}$  will only include the Cradle Drag.

From equation (4.79) the term  $F_{G9}$ , which is the real unknown of any thrust correction equation, can be written in a explicitly form as in equation (4.169)

$$F_{G9} = L + F_{G0} + D_{metric} - (F_{G9'} - F_{G0})_{ext\ pot} + \phi_{Gbase} \quad (4.169)$$

It is preferred by the author to make the comparison between the thrust corrections equations in terms of percentage of the load measured, so the above equation can also be written as

$$\frac{F_{G9}}{L} = 1 + \frac{F_{G0}}{L} + \frac{D_{metric}}{L} - \frac{(F_{G9'} - F_{G0})_{ext\ pot}}{L} + \frac{\phi_{Gbase}}{L} \quad (4.170)$$

It is easy now to substitute the in equation (4.170) the value of Table 4.4.

Using for the potential buoyancy factor  $A_{9'ext} = A_{9ext}$  it can be obtained

$$\frac{F_{G9}}{L} = 1.042204 \quad (4.171)$$

At the same time using for the potential buoyancy factor  $A_{9'ext} = A_f$  it can be obtained

$$\frac{F_{G9}}{L} = 1.043014 \quad (4.172)$$

The next equation to be completed is going to be equation (4.87) which can be expressed by using the base force and neglecting the carcase drag as

$$L = F_N + \phi_{pre} - \phi_{bell\ ext} - \phi_{base} - D_{cradle} + (F_{G9'} - F_{Gf})_{ext\ pot} \quad (4.173)$$

Expressing equation (4.173) in the same form of equation (4.170) it is possible to obtain

$$\frac{F_{G9}}{L} = 1 - \frac{\phi_{pre}}{L} + \frac{\phi_{bell\ ext}}{L} + \frac{D_{cradle}}{L} + \frac{\phi_{base}}{L} - \frac{(F_{G9'} - F_{Gf})_{ext\ pot}}{L} \quad (4.174)$$

It has not been said yet that in order to compile equation (4.87) it is strictly necessary to know the position of the pre-entry stream tube stagnation point. This is something that should be experimentally measured. But because in the static pressure along the bellmouth data provided by Rolls Royce (worked out during the preliminary Engine "C" test) contain a lot of scattering it has been decided to use the value provided by the CFD analysis, which will be better described in paragraph 6.2.8.

The flow around the bellmouth and the pre-entry stream tube is clearly affected by three dimensional flow phenomena, as the CFD analysis shows, and therefore the stagnation point has not a constant radius all around the bellmouth. By averaging the entire radius found it is assumed that the stagnation point radius is 2.18 m. The value in Table 4.4 for the external bellmouth force it has been worked out by using the above mentioned stagnation point radius.

Completing equation (4.174) with the values of Table 4.4 and using the potential buoyancy from station (f) to station ( $9'_{ext}$ ) with  $A_{9'_{ext}} = A_{9_{ext}}$  it has been obtained

$$\frac{F_{G9}}{L} = 1.041866 \quad (4.175)$$

At the same time using for the potential buoyancy factor  $A_{9'_{ext}} = A_f$  it can be obtained

$$\frac{F_{G9}}{L} = 1.041913 \quad (4.176)$$

The next equation to be completed is equation (4.126). This equation similarly to equation (4.87) can be written by using the base force and neglecting the carcase drag as equation (4.177).

$$L = F_{G9} - F_{Gth} - \phi_{bell} - \phi_{base} - D_{cradle} + (F_{G9'} - F_{Gf})_{ext\ pot} \quad (4.177)$$

Expressing equation (4.177) as equations (4.170) and (4.174) it can be obtained

$$L \frac{F_{G9}}{L} = 1 + \frac{F_{Gth}}{L} + \frac{\phi_{bell}}{L} + \frac{\phi_{base}}{L} + \frac{D_{cradle}}{L} - \frac{(F_{G9'} - F_{Gf})_{ext\ pot}}{L} \quad (4.178)$$

Completing equation (4.178) with the values of Table 4.4 and using the potential buoyancy from station (f) to station ( $9'_{ext}$ ) with  $A_{9'_{ext}} = A_{9_{ext}}$  it has been obtained

$$\frac{F_{G9}}{L} = 1.041895 \quad (4.179)$$

At the same time using for the potential buoyancy factor  $A_{9'ext} = A_f$  it can be obtained

$$\frac{F_{G9}}{L} = 1.041943 \quad (4.180)$$

## **5. Analytical Prediction Tool**

### **5.1. Introduction**

The magnitude of the thrust correction factors depends on the amount of the flow entering the cell. Indeed, the velocity and the pressure fields around the on testing engine are strictly correlated with the total mass flow entering the cell.

Therefore the possibility of having a tool able to predict the cell entrainment ratio is believed as a quite attractive opportunity, worth to be investigated.

The secondary flow inside the cell and consequently the cell entrainment ratio are driven by the ejector pump taking place between the engine and the detuner. By this effect the low pressure secondary flow surrounding the engine and the metric assembly get energised by the primary flow and starts to move in the detuner.

Following the above consideration, the ejector pump theory is applied in the indoor test bed facilities in order to develop a tool able to predict the cell entrainment ratio.

Once the cell secondary mass flow is known also its control could be an important point to arise. Indeed, in order to limit all the uncertainties shown in Chapter 2 is better to keep the entrainment ratio within reasonable values. So, the opportunity of controlling the amount of entrained flow could be a very important feature for the test cell.

In this chapter an analytical approach based on the ejector theory is proposed for the describing the flow characteristic along the test cell exhaust system.

Furthermore, a matching procedure based on the use of the analytical ejector pump approach is proposed for predicting the cell entrainment ratio.

### **5.2. Analytical Method**

#### ***5.2.1. Analytical Method Approach***

The approach used in this thesis to configure an analytical method for predicting the cell entrainment ratio is based on the approach used by Hickman et al. (Hickman, Gilbert, and Carey 1970) in their ejector pump analytical model.

The reason why it has been decided to follow such an approach is primarily because of its simplicity and its flexibility to be integrated with different formulations.

The literature research done about the sea-level test cell appears not to offer any ejector analytical model application on such facilities. Therefore, as a starting point to see the effective capabilities of such modelling it has been thought more opportune to use a simpler but at the same time complete model.

Another point of the Hickman et al. (Hickman, Gilbert, and Carey 1970) model which plays an important role in the overall prediction tool described in this thesis is the sub division of the mixing tube in different regions, as is shown later in this paragraph. This leads to the possibility of studying the flow phenomena along the detuner in separate phases.

Indeed, the usual detuner lengths found in indoor facilities do not allow for a complete mixing between primary and secondary flow. It is, therefore, of

fundamental importance to have at least another reference section before the mixing is completed. In the Hickman et al. model this is called the Accommodation Region. This is described later (paragraph 5.2.4).

At the same time the assumed model does not finish at the Accommodation Region but goes further to include a Mixing Region and an After-Mixing Region where the mixing effects can be accounted. This allows the model to be a completed ejector model and gives the possibility of making some useful considerations to relate to indoor test facilities. However, as has already been said, complete mixing is not achieved for the standard test bed detuner length.

Originally the model was applied to air-to-air jet pumps but its application to gas turbine engines has involved the requirement of adjustments to include the effects of combustion products of kerosene. This means that all the parameters for the primary jet, such as specific heats and the universal gas constant were all expressed as functions of the fuel area ratio (FAR).

As far as the primary jet is concerned, it has to be underlined that turbofan engines do not discharge only a single jet into the detuner. Indeed they have two concentric jets, the cold jet coming from the fan and the hot jet coming from the engine core.

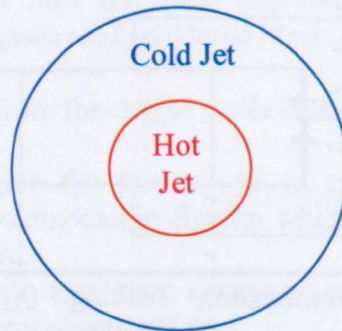


**Figure 5.1: Exhaust Jets for Turbofan Engines**

The former surrounds the later by an annulus shape as shown in Figure 5.1.

This represents the main difference between the Hickman et al. ejector model and its adaptation to gas turbine engines in enclosed test bed facilities proposed in this work. As will be shown better later on during this chapter (paragraph 5.2.3) the two jets have been averaged by a mass flow weighted criterion with the purpose of getting a single effective working jet and thus to be similar to the Hickman et al. model.

Following the above considerations, the Hickman et al. model has been integrated with a Preliminary Region where the two jets are adjusted into one accounting also for the different gas composition.

The fundamental purpose of the above modifications to the Hickman et al. is to develop the performance characteristic of the ejector pump taking place between the engine and the detuner within an indoor test bed. These performance characteristics can be represented by plots of jet pump pressure rise as a function of the cell entrainment ratio at different working sections into which the model is subdivided.

In order to derive the ejector pump characteristic, the equations involved in the procedure use the entrainment ratio as independent parameter.

The assumption of the entrainment ratio together with the primary and secondary flow conditions and the geometrical dimensions allow the calculation of all the flow parameters at the different working sections.

Another important characteristic of this analytical model is the fact that it does not take into account pressure loss effects for most of its sections. Indeed, until the flow is completely mixed, no pressure losses are included in the model. After the mixing is achieved it is possible to add pressure loss effects in the After-Mixing region. In this way only a global effect of pressure losses on the overall ejector performances can be studied.

Once it has been seen that the ejector theory can be used in an enclosed test bed facility, inclusion of pressure losses throughout the entire model would represent a big step forward. This is proposed as a subject for future study.

The fact that the detuner is divided in different working sections has been mentioned many times already. However, their specific location has yet to be established. Accordingly, this is dealt with at the end of this paragraph.

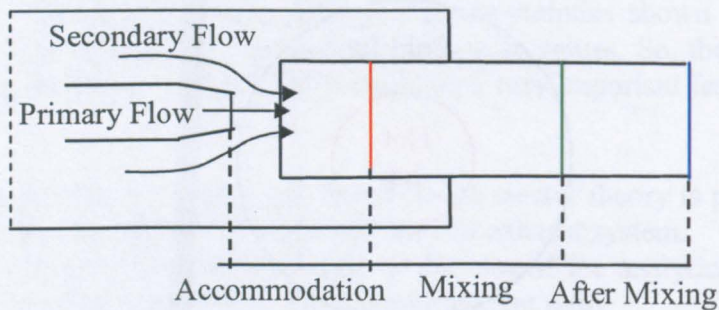


Figure 5.2: Analytical Division of the Hickman et al.'s Ejector Model

Figure 5.2 shows a sketch of the original model proposed by Hickman et al. showing the three main sections into which the model is divided.

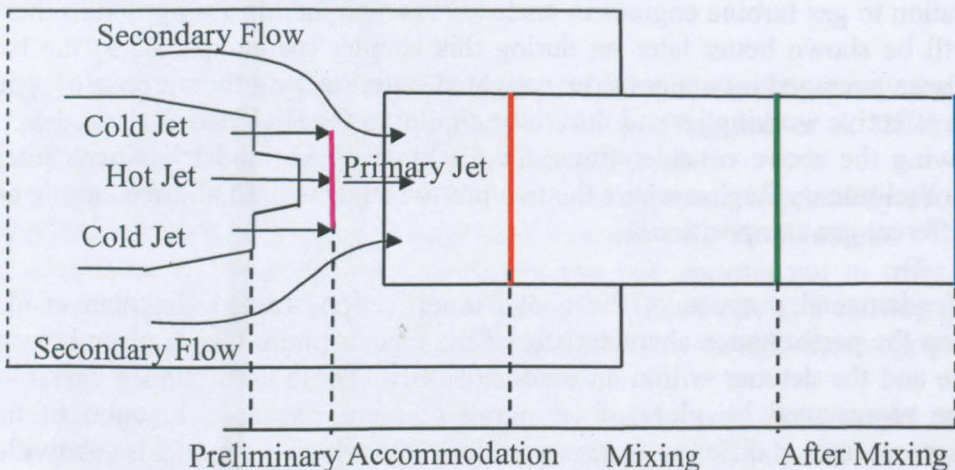


Figure 5.3: Analytical Division of the Adapted Hickman et al.'s Ejector Model

The first is called the Accommodation Region, the second the Mixing Region and the third the After-Mixing Region.

The characteristics of each section will be described later in this chapter.

Figure 5.3 shows, the adaptations of the original ejector model to represent gas turbine turbofan engines

### **5.2.2. Analytical Model Assumptions**

The first assumption for the analytical model is that the wall shear forces are negligible upstream of the After-Mixing Region.

Accordingly, pressure losses are accounted for only in the After-Mixing Region. Therefore, in the momentum theorem applications only the pressure forces and the momentum forces of the primary and secondary flow are taken into account.

A weighted mass flow average has been used to reduce the two engine jets into only one. The mass weighted average is used to compute global primary values of specific heat, gas universal constant, total pressure and total temperature.

This is to simplify the analysis of the three flows.

The specific heat for each flow has been expressed as a function of the static temperature; otherwise the gases are considered ideal.

No heat transfer is allowed from the engine walls or the detuner walls.

From the Preliminary Region the primary jet is assumed to expand or contract isentropically until the Accommodation Region where primary and secondary flows reach the same static pressure.

The corresponding changes in area have always to meet the fact that the detuner is supposed to be of constant cross-sectional area.

For the application of the following analytical model to the Rolls-Royce indoor test bed facility it has also been assumed that the total pressure and temperature of the secondary flow around the engine after-body are the same as those at the inlet of the test chamber (experimentally measured).

### **5.2.3. Preliminary Region**

It is useful before going ahead with description of the Preliminary Region to define the nomenclature which will be used throughout this chapter in the description of the proposed analytical tool. See Figure 5.4.

The role of the Preliminary Region in this ejector model is strictly related to the fact that the gas turbine engines used are turbofans. This means that there are two primary jets coming out from the engine at different conditions and with different gas compositions.

Obviously, the cold jet does not go through the engine core and so does not contain combustion products as does the hot jet.

At the same time the Hickman et al. ejector model deals only with a primary jet.

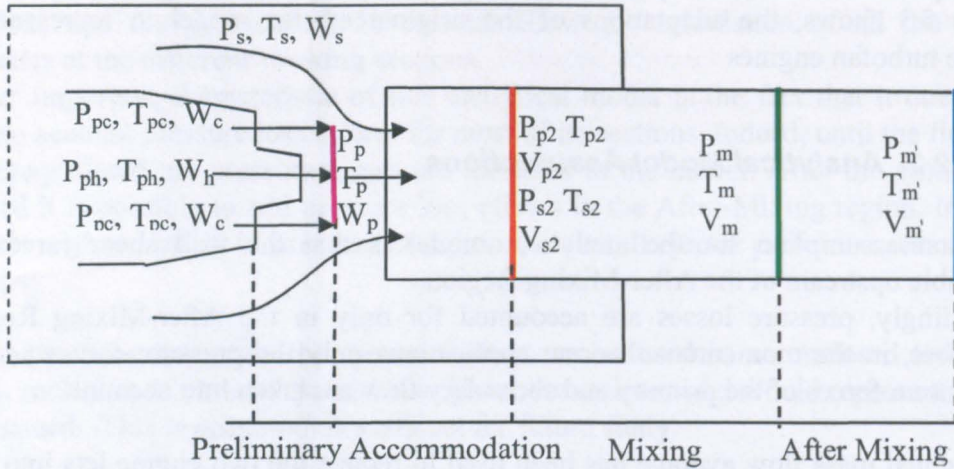


Figure 5.4: Nomenclature for the Analytical Model

The main purpose of the Preliminary Region, therefore, is to reduce the two engine jets to only one from the stand points of both gas composition and flow conditions. In order to achieve this mass flow weighted average technique has been used (equation (5.1)).

$$T_{average} = \frac{\sum_{i=1}^n T_i \times W_i}{\sum_{i=1}^n W_i} \quad (5.1)$$

Once the flow conditions are calculated from the experimental data (provided by Rolls-Royce 2002) at the engine nozzles it is possible to use equation (5.1) to average the two jet flows.

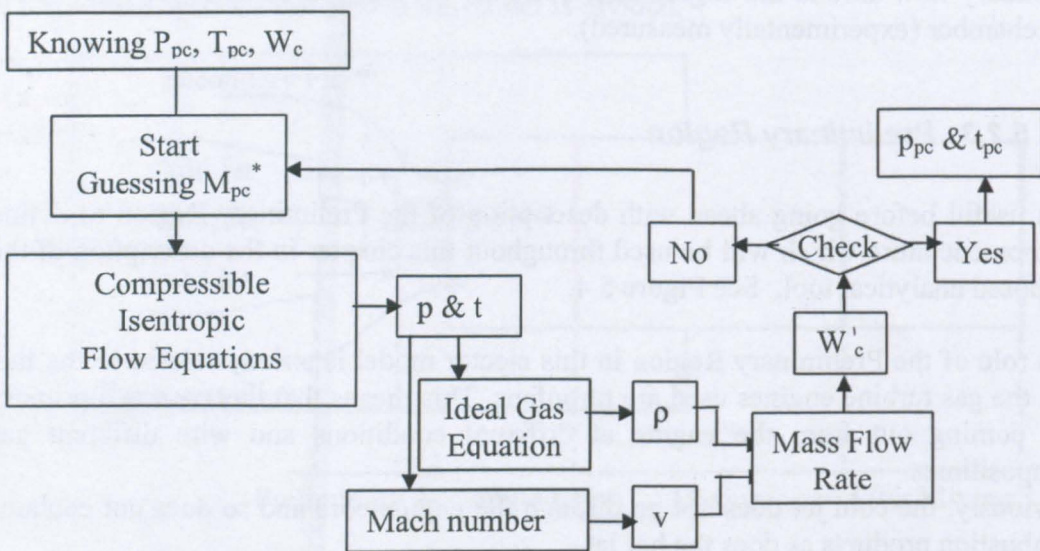


Figure 5.5: Iterative Procedure at the Preliminary Region



Indeed, the engine performance parameters provided are mostly for total rather than static conditions. This is required by the formulae used for computing the thermodynamic parameters which need to be averaged. Therefore, by the theory of isentropic compressible flow, an iterative procedure has been established to work out the static temperature and pressure by matching the mass flow rate of the nozzle. The Mach number is then used as a handle for this procedure

Figure 5.5 shows such an iterative procedure used in the Preliminary Region for the cold jet.

A similar procedure can also be used for the core jet.

In particular, the parameters which have to be averaged are the specific heats, the universal gas constant, the total temperatures and the total pressures.

The specific heats and gas constant are calculated by the standard formulas of order eighth presented in Walsh and Fletcher book (Walsh and Fletcher 1998) as a function of only the static temperature for the cold jet and as a function of the static temperature and the FAR for the hot jet (appendix A1).

However, to compile the above iterative procedure, it is necessary to know the specific heat for both the jets before running the model. In order to overcome this problem, the initial values for the specific heats and for the gas constant are taken from Savaranamooto's book (Saravanamuttoo, Rogers, and Cohen 1996).

Once the static conditions are known, the new mass flow weighted averaged thermodynamic parameters can be calculated and used in the next ejector model region.

Appendix A1 shows the formula used for these calculations.

#### 5.2.4. Accommodation Region

The Accommodation Region can be regarded as the first region of the ejector model since the Preliminary Region deals only with the primary flow.

After the first energy exchange between the two flows, (primary and secondary) which takes place upstream the detuner, the secondary flow accelerates and starts to move toward the exhaust collector. As soon as the two flows enter the detuner which has a limited cross sectional area they start to expand and contract until their static pressures match.

Initially, the primary flow static pressure drops whilst the secondary increases.

When the two static pressures reach the same value the accommodation process is assumed to be completed and the flows are parallel.

Therefore, the Accommodation Region is defined as the section where the primary and secondary flows achieve the same static pressure.

$$\frac{P_{p2}}{\left(1 + \frac{\gamma-1}{2} M_{p2}^2\right)^{\frac{\gamma}{\gamma-1}}} = \frac{P_{s2}}{\left(1 + \frac{\gamma-1}{2} M_{s2}^2\right)^{\frac{\gamma}{\gamma-1}}} \quad (5.2)$$

Equation (5.2) above represents the relationship which has to be satisfied at the Accommodation Region.

During this accommodation process the pressure losses are neglected for both flows in the analytical model. However, this assumption is partially justified by “Hickman et al.” who has found good agreement between his ejector model results in the Accommodation Region and experimental data (Hickman, Gilbert, and Carey 1970). The fact that the pressure losses are not deeply affecting the ejector performance at the Accommodation Region has represented another important aspect which has influenced the author’s opinion to the use of the Hickman et al. model. Indeed the Accommodation Region will turn up to be an important region for the overall analytical prediction tool proposed in this thesis. Essentially, because the level of mixing achieved along the detuner in a test cell is not really known. This is because the detuner length is usually insufficient for complete mixing. Therefore, it would not be possible to refer to fully mixed conditions in the detuner.

The analysis of the Accommodation Region starts by guessing a value for the entrainment ratio. As has already been said above, in the overall approach used for the model the entrainment ratio of the system is used in the equations as an independent parameter. Fixing the entrainment ratio basically means fixing the secondary mass flow because the primary is a *known parameter*. *This allows the equations of the system to be solved and the flow characteristics to be plotted. There is a limit for the entrainment ratio guessed initially due to the limitations imposed by the sonic conditions for the secondary flow at the Accommodation Region. When the flow becomes choked along the detuner a further increase in entrainment ratio will not result in any solution from the equation system shown below.*

From the Preliminary Section all the “pseudo” primary flow thermodynamic parameters are known, for example, the specific heat  $cp_p$ , the gas constant  $R_p$ , total pressure  $P_p$ , total temperature  $T_p$  and the mass flow  $W_p$ .

The thermodynamic parameters of the secondary flow are known from the cell conditions, e.g. the secondary specific heat  $cp_s$ , the gas constant  $R_s$ , the total temperature  $T_s$ , the total pressure  $P_s$ .

From the guessed value of entrainment ratio, the secondary mass flow is guessed.

Now if the secondary flow is treated as isentropic its mass flow per unit area can be expressed as in equation (5.3) (appendix A2)

$$\frac{W_{s2}}{A_{s2}} = \frac{P_{s2}}{\sqrt{T_{s2}}} \sqrt{\frac{\gamma_{s2}}{R_s}} \left[ \frac{M_{s2}}{\left(1 + \frac{\gamma-1}{2} M_{s2}^2\right)^{\frac{\gamma_{s2}+1}{2(\gamma_{s2}-1)}}} \right] \quad (5.3)$$

Introducing  $A_m$  to identify the area of the detuner (or mixing tube) equation (5.3) can also be expressed as equation (5.4).

Where the  $A_p$  is the area of the pseudo-primary jet at the Preliminary Region.

All the parameters on the right hand side of equation (5.4) are known (remember the assumption of compressible isentropic flow). Therefore, an iterative procedure can be established in the left hand side to match both side of the equation.

Mach number is used as the handle parameter for the matching procedure of the secondary flow at the Accommodation Region.

$$\frac{W_{s2}}{(A_m - A_p)} \frac{\sqrt{T_{s2}}}{P_{s2}} \sqrt{\frac{R_s}{\gamma_{s2}}} = \left[ \frac{M_{s2}}{\left(1 + \frac{\gamma_{s2} - 1}{2} M_{s2}^2\right)^{\frac{\gamma_{s2} + 1}{2(\gamma_{s2} - 1)}}} \right] \quad (5.4)$$

So practically by changing the Mach number of the secondary flow at the Accommodation Region in the left hand side of equation (5.4) a trial process can be started in order to match the value of the right hand side of the same equation.

Once the right Mach number has been found by equations (5.5) to (5.7) below all the thermodynamic parameters of both secondary and primary flows at the Accommodation Region can be found.

$$P_{s2} = \frac{P_{s2}}{\left(1 + \frac{\gamma_{s2} - 1}{2} M_{s2}^2\right)^{\frac{\gamma_{s2}}{\gamma_{s2} - 1}}} \quad (5.5)$$

$$t_{s2} = \frac{T_{s2}}{\left(1 + \frac{\gamma_{s2} - 1}{2} M_{s2}^2\right)} \quad (5.6)$$

$$v_{s2} = M_{s2} \sqrt{\gamma_{s2} R_s t_{s2}} \quad (5.7)$$

Applying now the Accommodation Region assumption (equation (5.2)) it is possible to find out also the thermodynamic conditions of the pseudo-primary flow.

Indeed the Mach number of the primary flow can be found by using equation (5.5) but this time referred to primary where the only unknown now is the primary Mach number (equation (5.8))

$$M_{p2} = \sqrt{\left[ \frac{\left(\frac{P_{p2}}{P_{p2}}\right)^{\frac{\gamma_{p2} - 1}{\gamma_{p2}}}}{\left(\frac{P_{p2}}{P_{p2}}\right)} - 1 \right] \frac{2}{\gamma_{p2} - 1}} \quad (5.8)$$

When the primary Mach number is known it is also possible find out the static temperature and the primary flow velocity at the Accommodation Region by equations (5.6) and (5.10) this time referred to the primary flow (equations (5.9) and (5.10)).

$$t_{p2} = \frac{T_{p2}}{\left(1 + \frac{\gamma_{p2} - 1}{2} M_{p2}^2\right)} \quad (5.9)$$

$$v_{p2} = M_{p2} \sqrt{\gamma_{p2} R_s t_{p2}} \quad (5.10)$$

Further more when the two static temperatures are known it is also possible to recalculate the specific heats of the two flows, following always the equation shown in the appendix A2.

The specific heat ratio ( $\gamma_s$ ) in equation (5.4) has been used also in the Accommodation Region when would have been be more correct to use the value of  $\gamma_{s2}$ . However, until the static temperature in the Accommodation Region is worked out is not possible to calculate the new value of  $\gamma_{s2}$  at the Accommodation Region (equation (5.12)).

$$\gamma_{s2} = \frac{cp_{s2}}{cp_{s2} - R_s} \quad (5.11)$$

Therefore, the use of  $\gamma_s$  instead of  $\gamma_{s2}$  in the above iterative procedure is another assumption.

However, once the static conditions are known,  $\gamma_{s2}$  can be calculated and a comparison between them shows that they are identical at least as far as the sixth decimal place.

Up to now the above procedure neglects the effects of primary stream expansion or contraction along the Accommodation Region. This is because the primary flow area used in equation (5.4) is that calculated for the Preliminary Region.

Therefore another condition has to be imposed in the procedure described above. That is that the area of the primary flow plus the area of the secondary flow must be equal the detuner area (equation (5.12)).

$$A_{p2} + A_{s2} = A_{\text{detuner}} \quad (5.12)$$

Equation (5.12) can also be written (as shown in the Appendix A2) using the thermodynamic flow property as equation (5.13)

$$A_{\text{detuner}} = \frac{W_p \sqrt{R_p} \sqrt{T_{p2}} \left(1 + \frac{\gamma_p - 1}{2} M_{p2}^2\right)^{\frac{\gamma_p + 1}{2(\gamma_p - 1)}}}{\sqrt{\gamma_p P_{p2} M_{p2}}} + \frac{\mu W_p \sqrt{R_s} \sqrt{T_{s2}} \left(1 + \frac{\gamma_s - 1}{2} M_{s2}^2\right)^{\frac{\gamma_s + 1}{2(\gamma_s - 1)}}}{\sqrt{\gamma_s P_{s2} M_{s2}}} \quad (5.13)$$

Equation (5.13) can be used to correct the secondary flow Mach number previously calculated by the iterative procedure established to match both sides of equation (5.13).

Indeed, the detuner area is a known fixed geometric condition which must be matched by the stream flow areas of the two flows.

When the secondary and primary flow Mach numbers also satisfy equation (5.13) the Accommodation Region is solved.

With the final primary and secondary Mach numbers is now possible to compute all the thermodynamic flow properties at the Accommodation Region by the equations (5.5), (5.6), (5.7), (5.9) and (5.10) (including also the specific heats).

A simplified scheme representative of the iterative procedure above established at the Accommodation Region is represented in Figure 5.6. In this diagram, boxes also include the reference to the equations used in the different steps.

The numerical criterion for acceptable convergence in the areas balance is agreed to be within 0.0005. This gives an error within 0.005 Kg/s for the secondary mass flow.

For clarity, the complete procedure for computing the flow parameters in the Accommodation Region is summarized below.

The starting point is the guess of a value for the entrainment ratio.

This will automatically define the secondary mass flow since the primary one is known.

Knowing the total mass in the detuner, the iterative procedure used in the Accommodation Region is the tool which enables the calculation of the primary and secondary flow parameters when the two flows reach the same static pressure (parallel streams).

Such a calculation uses the secondary Mach number as a handle. There are, however, two additional checks. The first is the secondary mass flow matching and the second is the areas balance with the real detuner area. Once the secondary Mach number satisfies these two conditions it is assumed to be the right one.

From this value, it is now possible to calculate the rest of the parameters for primary and secondary flow using the isentropic compressible flow equations.

The same process can then be used for a different entrainment ratio. However, the same primary flow is used again. The result is a set of different flow conditions in the Accommodation Region.

With this procedure repeated for a range of entrainment ratios allows the characteristic curve for the ejector pump to be established.

The outcome is illustrated in paragraph 5.3.4.

However, it must be noted that the characteristic curve itself is not sufficient to define the actual operating point of the system.

However, it does show where the operating point of the Accommodation Region can move.

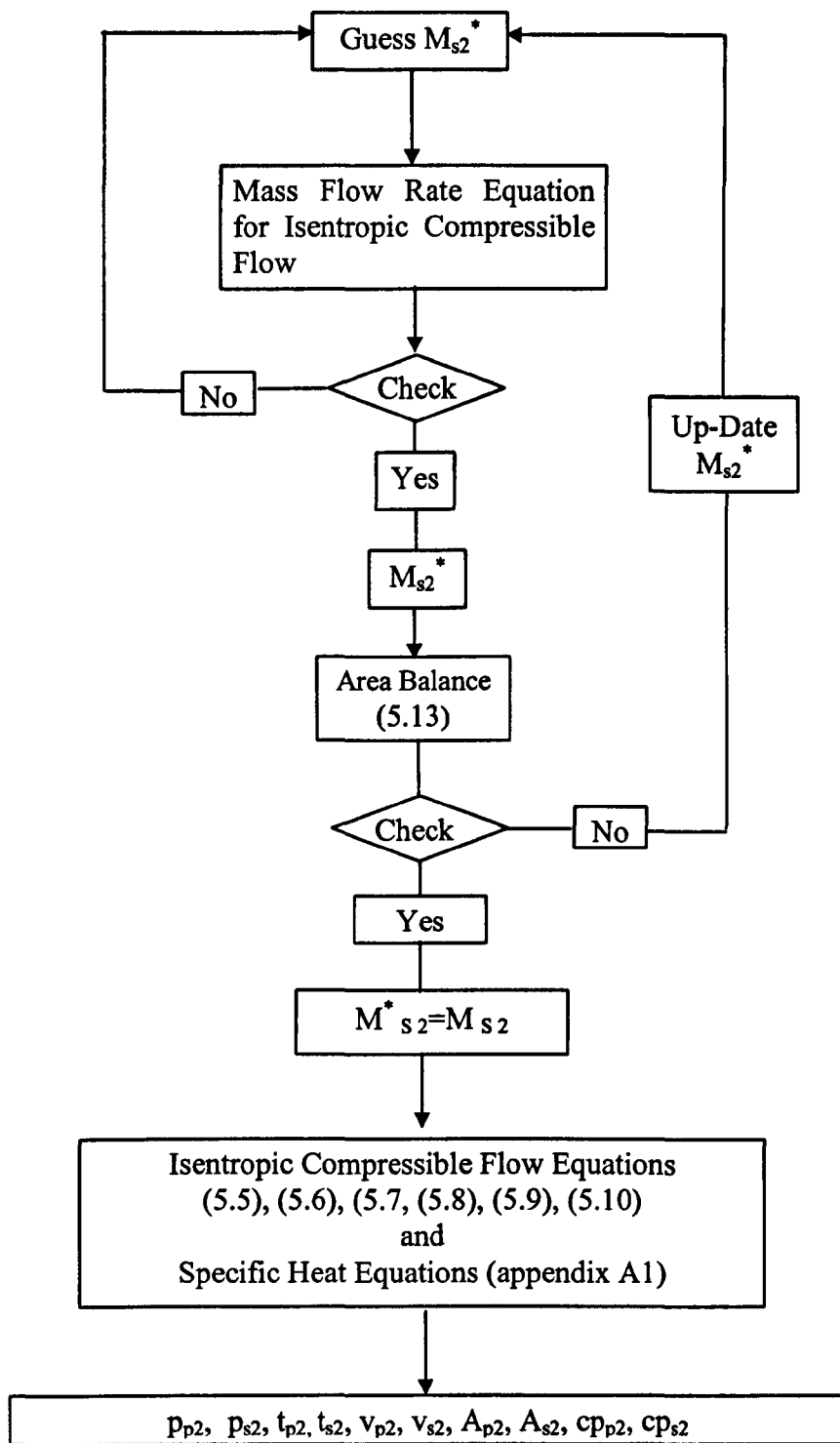


Figure 5.6: Scheme of the Accommodation Region Calculation Procedure

### 5.2.5. Mixing Region

The location of the Mixing Region is shown on Figure 5.4.

As the flows enter this region the mixing process has not yet started so individual streams can still be identified. In the case of a turbofan engine in an enclosed test bed

facilities at the entrance to the Mixing Region there are still three individual flows, the entrained, the cold jet and the hot jet.

However, in the representation of the ejector pump effect used in this work the three flows are converted into two by the process described above in the Preliminary Region.

The two flows at the entrance of the Mixing Region have the same static pressure, are parallel streams and have already passed through the accommodation process.

The aim of the Mixing Region is that of letting the flows to mix together into one uniform flow until common properties are achieved. As for the Accommodation Region, the model presented here is not able to monitor the flow properties all along the channel at different detuner lengths. It will, however, provide the flow conditions at the exit when completely mixing is achieved. The total pressure and temperature of the flows are kept constant along the Mixing Region since pressure losses are not yet considered. Accordingly, at the exit plane of the Mixing Region the flow will have its own total pressure and temperature value which is different from those of the primary and secondary flows.

The equations used to solve the flow at the exit of the Mixing Region are the continuity equation (5.14), the equation for ideal gas (5.15), the mass flow rate (5.16), the specific heat equation (5.17)(appendix A1), the momentum equation (5.19) (Figure 5.7) and the energy equation (5.20) and (5.21).

$$W_m = (1 + \mu)W_p \quad (5.14)$$

$$\frac{p_m}{\rho_m} = R_m t_m \quad (5.15)$$

$$W_m = \rho_m v_m A_m \quad (5.16)$$

$$cp = f(t, FAR) \quad (5.17)$$

$$\gamma = \frac{cp * 1000}{cp * 1000 - R} \quad (5.18)$$

$$A_{s2} P_{s2} + A_{p2} P_{p2} - A_m P_m = W_m v_m - W_p v_{p2} - W_s v_{s2} \quad (5.19)$$

$$W_{s2} H_{s2} + W_{p2} H_{p2} = W_m H_m \quad (5.20)$$

$$H = cp \left( t + \frac{v^2}{2cp} \right) \quad (5.21)$$

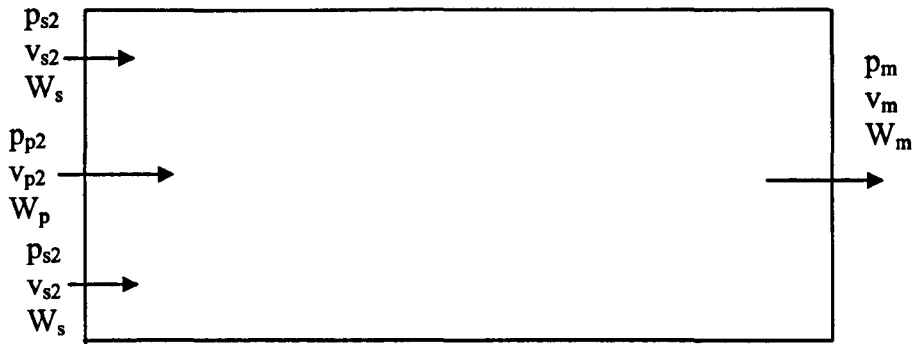


Figure 5.7: Mixing Region Momentum Balance

Using the above equations it is possible to establish an iterative procedure for working out the flow conditions at the exit of the Mixing Region. The solution is obtained by an iteration technique in which the value of one variable is assumed and the equations solved to obtain a calculate value of that parameter. Appendix A3 lists all the equations with their explicit variables.

The procedure is now explained to show how to use these equations.

The parameter for the iterations used as a handle is the static pressure at the exit of the Mixing Region.

The first equation to be compiled with the guessed  $p_m$  is the momentum balance (5.19). Thus, we now consider how to calculate the flow velocity at section (m)  $v_m$ . The total mass flow in the cell is a known parameter because the calculation of section (m) follows the calculation of the Accommodation Region (section 2) where the entrainment ratio was used as independent parameter.

Substituting the density as a function of  $t_m$  and  $p_m$  (equation (5.15)) into equation (5.16) it is possible to calculate the static temperature at section (m). It is now possible to calculate the specific heat  $cp_m$ . This parameter is calculated as a mass flow average of the two different flows which are not the primary and the secondary. Indeed the specific heat is dependent on the flow composition and so the flows are divided into core flow and clean air flow, where the clean air flow includes the cold jet and the secondary flow.

The equations used to calculate the specific heat are shown in Appendix A3.

It should be remembered that for combustion products,  $cp$  is function of the fuel air ratio.

Once the  $cp_m$  is know by the energy equation (5.20) the new value of the static pressure at section (m) can be calculated and compared to the guessed one. If the difference is less than 0.1% the trial value is assumed to be correct. Otherwise a new value of  $p_m$  is guessed and the whole procedure is repeated.

When this iterative procedure is assumed to have converged the flow parameters  $v_m$ ,  $t_m$ ,  $cp_m$ ,  $p_m$ , are known.

From these it is possible to calculate all the stagnation values like  $P_m$  and  $T_m$  using isentropic compressible flow equations.

At section (m) there is no distinction between primary and secondary flow.

The flow is assumed to fully mixed.

It is important to say that in the momentum balance represented in equation (5.19) the flow is assumed frictionless. Tangential forces are, therefore, not included in the balance equation. A simplified scheme representative of the iterative procedure established at the Mixing Region is shown in Figure 5.8.



Summarizing, the mixing procedure here represented it can be said that two different flows enter the Mixing Region coming from the Accommodation Region and only one flow with uniform properties it is obtained at the its exit.

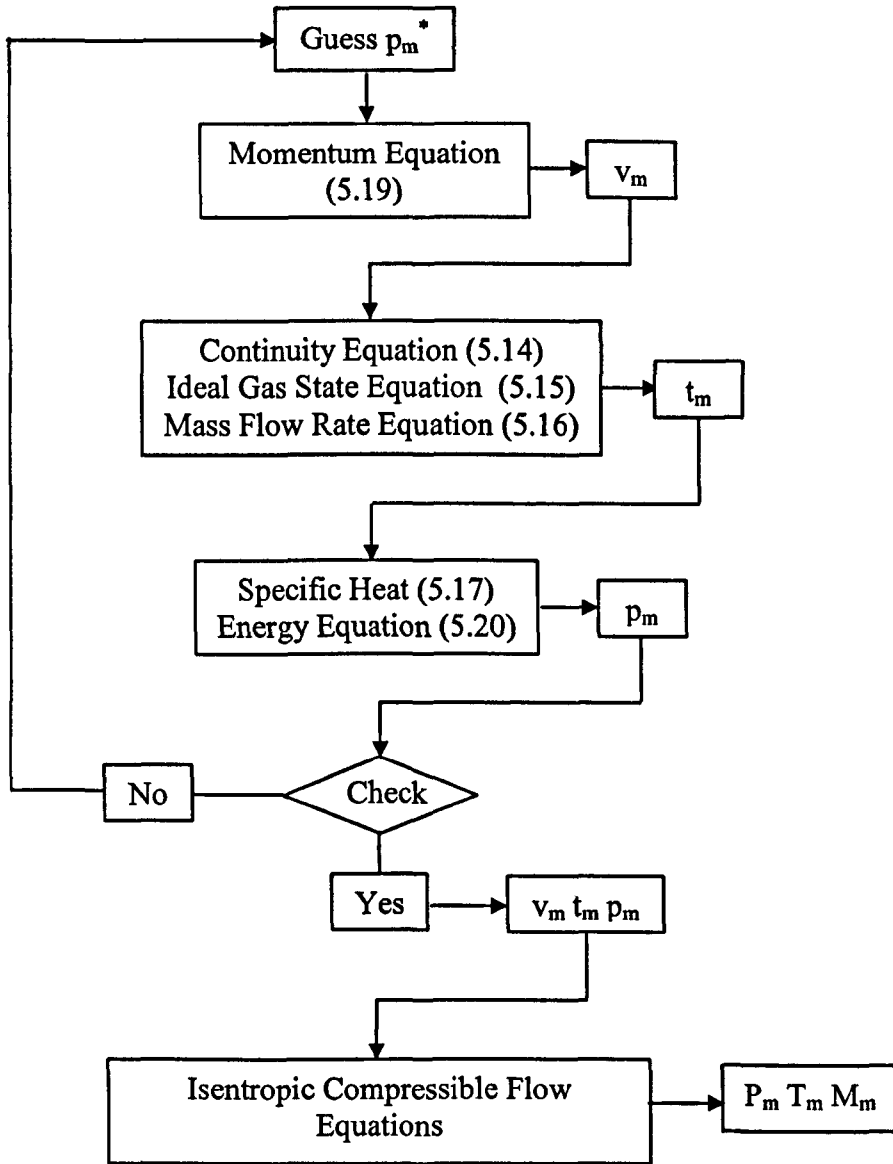


Figure 5.8: Scheme of the Mixing Region Calculation Procedure

The flow along the Mixing Region is not taken into account. Indeed only the entrance and exit sections are studied. Static pressure is used as the handle at section (m) and the final check comparison is directly made on its value. Differently from the Accommodation Region where the presence of two different flows imposes also the check for the flow expansions or contractions.

Once the procedure has converged for one value of the entrainment ratio previously selected at the Accommodation Region another value can be chosen and the procedure repeated. This will enable the user to produce ejector characteristics at the Mixing Region. These characteristics are particularly useful first to establish the performance of the ejector pump but also to better understand how the engine within an enclosed test bed behaves.

### 5.2.6. After-Mixing Region

The ejector pump analysis shown above does not include any pressure loss due to the detuner wall friction neither in the Accommodation Region nor in the Mixing Region. In reality the friction loss takes place all along the Accommodation and Mixing Regions.

However it is not easy to predict the pressure losses for flows which are not completely mixed due to the complexity of the mixing process in the pipe and the high degree of turbulence carried by the flow.

For these reasons in the ejector pump proposed by Hickman et al. the friction losses are accounted for in a specific region afterward the different flows are fully mixed. Such a region it is called the After-Mixing Region. Therefore, rather than adjust the Mixing and the Accommodation region analysis to include the wall friction effects, it is preferred to treat the mixing and the wall friction processes as independent effects. To achieve this, the mixing tube will be imaginarily extended beyond the point where completely mixing has been achieved. The friction losses are then assumed to be concentrated here.

Usually the wall shear forces in a duct are represented by a coefficient  $\mu_f$  represented in equation (5.22).

$$\mu_f = \frac{\tau_w}{\rho \frac{v^2}{2}} \quad (5.22)$$

Once the friction coefficient is know it is possible to relate it to the total pressure loss by the Darcy-Weisbach equation, namely

$$\Delta P = 4\mu_f \frac{L}{D} \frac{\rho v^2}{2} \quad (5.23)$$

Where L is the duct length and D is the diameter.

For most of the application the value of the friction coefficient is taken from experimental results which are used to classify  $\mu_f$  by the roughness of the walls and the Reynolds number (equation (5.24)).

$$\text{Re} = \frac{\rho v D}{\nu} \quad (5.24)$$

However in the detuner the streams flow in a very non-uniform way with a high level of turbulence. This does not allow the use of pipe flow data experimentally derived for uniform flow.

It is therefore convenient to represent the pressure loss directly as a head loss by the use of loss coefficient ( $K_{MT}$ ) (equation (5.25))

$$\Delta P_m' = K_{MT} \frac{\rho_m v_m^2}{2} \quad (5.25)$$

The friction as a fraction of the dynamic head will be the approach followed in this work in order to account for the shear forces on the detuner walls.

The flow enters the pseudo region called After-Mixing Region with all the properties found at the exit of the Mixing Region and will exit such region with a percentage of its dynamic head lost along this path.

Therefore the first equation which can arise in the analysis of the After-Mixing Region is equation (5.26) which represents the total pressure loss across this region.

$$p_m \left(1 + \frac{\gamma - 1}{2} M_m^2\right)^{\frac{\gamma}{\gamma - 1}} - p_{m'} \left(1 + \frac{\gamma_{m'} - 1}{2} M_{m'}^2\right)^{\frac{\gamma_{m'}}{\gamma_{m'} - 1}} = K_{MT} \frac{\rho_m v_m^2}{2} \quad (5.26)$$

The energy balance between section (m) and (m') is written in equation (5.27)

$$c p_m t_m + \frac{v_m^2}{2} = c p_{m'} t_{m'} + \frac{v_{m'}^2}{2} \quad (5.27)$$

The ideal gas equation at section (m') (equation (5.28))

$$\frac{p_{m'}}{\rho_{m'}} = R_{m'} t_{m'} \quad (5.28)$$

The Mach number equation at section (m') as equation (5.29)

$$M_{m'} = \frac{v_{m'}}{\sqrt{\gamma_{m'} R_{m'} t_{m'}}} \quad (5.29)$$

The continuity equation for the After-Mixing Region can be expressed as equation (5.30).

$$v_m \rho_m = v_{m'} \rho_{m'} \quad (5.30)$$

The specific heat at section (m) can be calculated using equation (5.17) this time referred to section (m'). The exact calculation of cp is shown in Appendix A4.

Using the above equations it is possible to establish an iterative procedure for the After-Mixing Region which will allow all the flow parameters at section (m') to be evaluated.

In Appendix A4 are listed all the relevant equations with their explicit variables.

This paragraph explains the use of those equations and the values which can be worked out from each one of them in an iterative manner.

Before starting the procedure it necessary to fix a value for the coefficient  $K_{MT}$  which represents the percentage of the dynamic head lost along the After-Mixing Region.

In this case the handle is  $t_{m'}$ .

The first step is to calculate the specific heat at section ( $m'$ ) using equation (5.17). As has been already said for the Mixing Region the specific heat  $cp$  is calculated by a mass flow weighted average accounting for the flow composition using the fuel to air ratio (FAR) (appendix A1).

Once the  $cp$  is known it is possible to calculate  $\gamma_{m'}$  by a similar formula to equation (5.11).

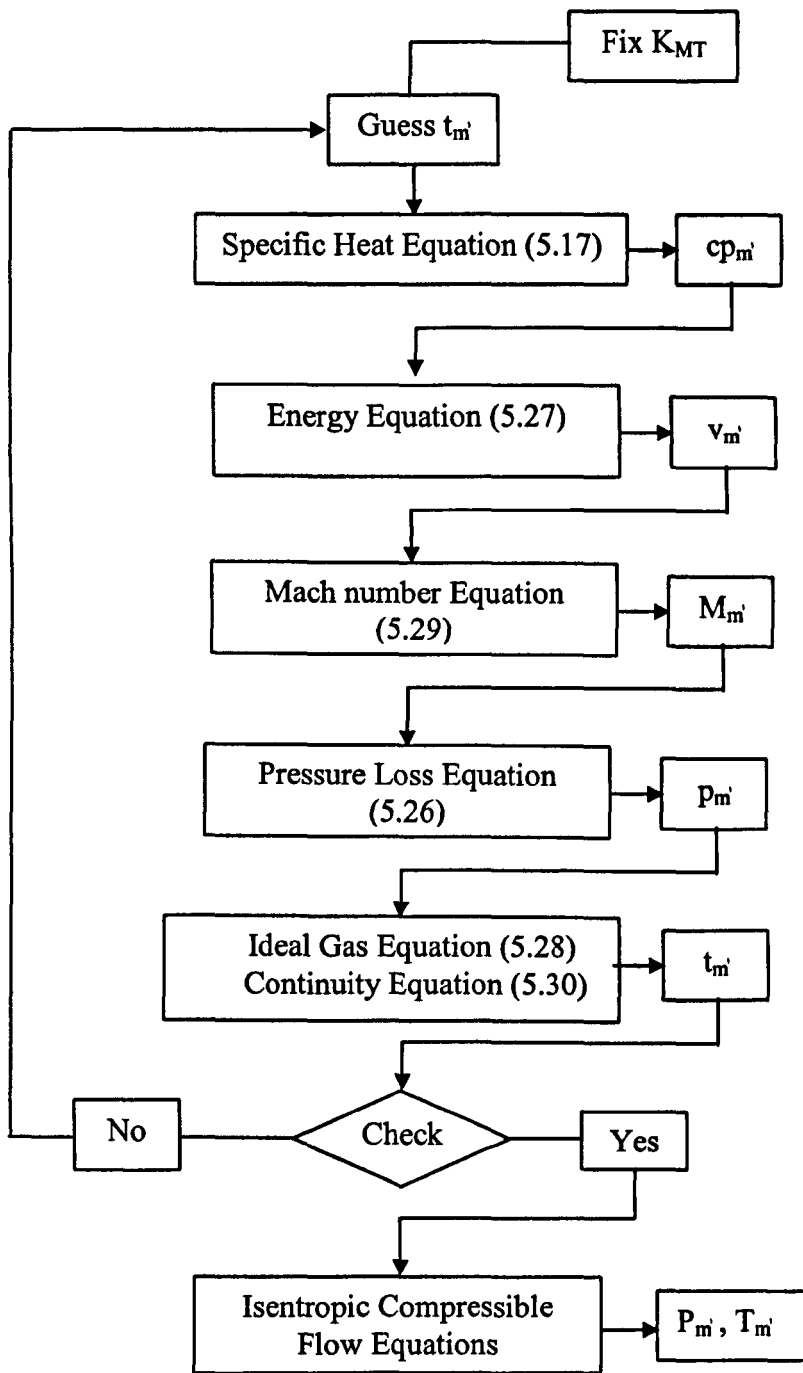


Figure 5.9: Scheme of the After-Mixing Region Calculation Procedure

Using the equation for ideal gases (4.28) and the continuity equation (5.30) with the new  $\gamma_{m'}$  it is possible to work out the flow velocity  $v_{m'}$  which will allow the calculation of the Mach number  $M_{m'}$  by the equation (5.29).

Up to now the  $K_{MT}$  has not been used but once the flow  $M_{m'}$  is known it is possible to compile equation (5.26) and find out the static pressure at section ( $m'$ ).

Now, an updating of  $t_m$  is made using the energy equation.

When the difference between the calculated value  $t_m$  and that one guessed is within the 0.001% the procedure is assumed to have converged. If not a new value of  $t_m$  has to be guessed and the whole procedure rerun until convergence is achieved.

All other flow parameters can then be calculated by the equations used in a similar manner to that described above.

A simplified scheme of the iterative procedure established for the After-Mixing Region is represented in Figure 5.9.

Summarizing, the After-Mixing Region represents the part of the ejector model analyzed in this thesis where dynamic head loss is taken into account. Indeed the first step of the procedure is to assume a dynamic head loss coefficient.

The procedure above uses the static temperature at section (m) as the handle parameter.

The thermodynamic up-dating of the cp is different from the Hickman et al. model where the specific heats are considered always constant.

Once the procedure has converged, the flow parameters can be extracted and used for drawing the characteristic curves of the system.

This is illustrated in paragraph 5.3.6.

By changing the entrainment ratio at the Accommodation Region it is possible to find new values for the After-Mixing Region always keeping the same jets conditions and the same dynamic head loss. These values will define the curve where the ejector will operate under such conditions.

Using also the same engine conditions and the same set of entrainment ratios previously defined and at this time changing the value of  $K_{MT}$  it is possible to draw new ejector characteristics.

These characteristics will be particularly useful for understanding how pressure loss can affect the ejector engine pump performance within the test bed. More specifically this could be useful to understand how the amount of secondary flow changes as a function of the pressure loss.

### 5.3. Analytical Ejector Model Applications

The above analytical ejector model has been applied to two different Rolls-Royce engines tested in the same cell. For confidential reasons the engines are called in this work engine "A" and engine "B" and the test facility is here named test cell "X".

Before describing the results derived from the application of the ejector model, a small description of the engines is given below.

#### 5.3.1. Rolls Royce Engine "A"

Table 5.1 provides some useful specification of the Rolls Royce engine "A".

Thrust	333000-422000 N
By-pass Ratio	6.2 5.7
Inlet Mass Flow	1078 – 1200 Kg/s
Fan Diameter	2.2m

Length	4368 m
Area Cold Nozzle	272 m <sup>2</sup>
Area Hot Nozzle	0.96 m <sup>2</sup>

Table 5.1: R-R Engine "A" Specification ((Rolls-Royce plc. ))

### 5.3.2. Rolls Royce Engine "B"

Table 5.2 provides some useful specification of the Rolls Royce engine "B".

Thrust	235744 -249100 N
By-pass Ratio	7.6 – 7.5
Inlet Mass Flow	860 – 880 Kg/s
Fan Diameter	7.47 m
Length	3.95 m
Area Cold Nozzle	2.03 m <sup>2</sup>
Area Hot Nozzle	0.65 m <sup>2</sup>

Table 5.2: R-R Engine "B" Specification ((Rolls-Royce plc. ))

### 5.3.3. Rolls-Royce Test Bed "X"

Test Bed "X" is located in Derby in the main Rolls-Royce site. Its dimensions are smaller than those of Test Cell "X" above described. This is mainly because when Test Bed "X" was built, engine sizes were much smaller than they are today. Accordingly, the flow fields could be preserved from possible distortion generated by the interactions in the engine-cell. However, test bed "X" is still in service and actual high by-pass ratio engines are still tested in it with good results.

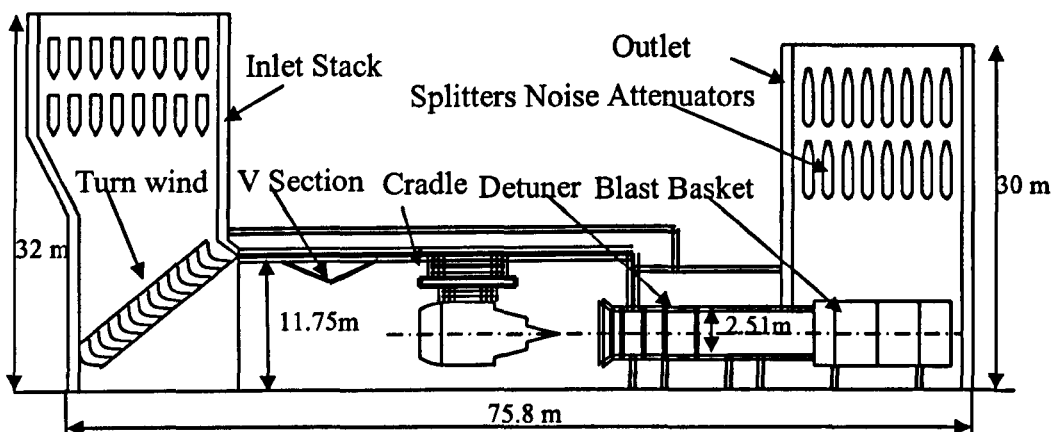


Figure 5.10: R-R Test Bed "X"

The main peculiarity of this cell is the presence of a "V-shape" structural feature in the roof which restricts the cell cross section area just upstream of the engine. The main purpose of this feature is to accelerate the flow and allow more uniform flow measurements. Indeed, in that section the cell velocity measurements are taken with

the intention of calculating the thrust correction factors (in particular the intake momentum drag) as described in the First Principle Anemometer (paragraph 2.3.2). Due to the sensitivity of some cell dimensions a detailed picture of Test Bed "X" can not be included in this document. An approximate sketch is, however, shown below (Figure 5.10) with the information needed for the application of the ejector model above described.

The effective cross sectional area of Test Cell "X" is 114.5 m<sup>2</sup>.

### 5.3.4. Ejector Model Application at the Accommodation Region

As described in the previous paragraphs 5.2.4, after the Preliminary Region treatment only two flows approach the Accommodation Region, the primary and the secondary. Indeed the two engine jets are reduced to one by applying a mass flow weighted averaging technique in the Preliminary Region.

An engine power setting with its set of data (describing the engine's jets and the secondary flow conditions) has to be chosen to start the iterative procedure described for both the Preliminary and Accommodation Region. An entrainment value must be chosen as well and it is worth remembering that this is the independent parameter for the whole procedure.

Running both the Preliminary and the Accommodation Regions it is possible to work out the static pressure at the Accommodation Region for the chosen settings.

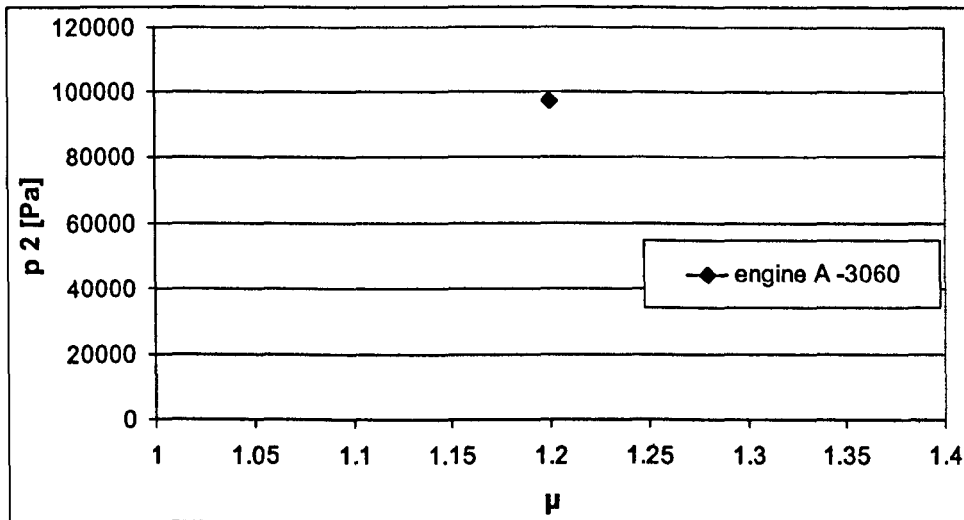


Figure 5.11: Single Point of An Ejector Characteristic at the Accommodation Region

Figure 5.11 shows the result for the engine A for a non-dimensional mass flow at the engine inlet of 3060 and with an imposed entrainment ratio of 1.2. The same procedure can now be repeated for different entrainment ratios but keeping the same engine power setting. It is worth underlining again that with the engine power setting also the secondary flow conditions at the entrance of the main chamber of the test cell are kept the same.

Figure 5.12 shows the characteristic line for the engine A derived using a range of entrainment ratio from 0.2 and 2.

From Figure 5.12 it is possible to understand the trend of the static pressure at the Accommodation Region as a function of the entrainment ratio. Resulting from the assumptions in the iterative procedure, the total pressures of the primary and secondary flows are still the same as those up-stream before entering the detuner. The static pressure drops at the Accommodation Region as the total flow entering the detuner increases, so to allow the entrainment ratio increases.

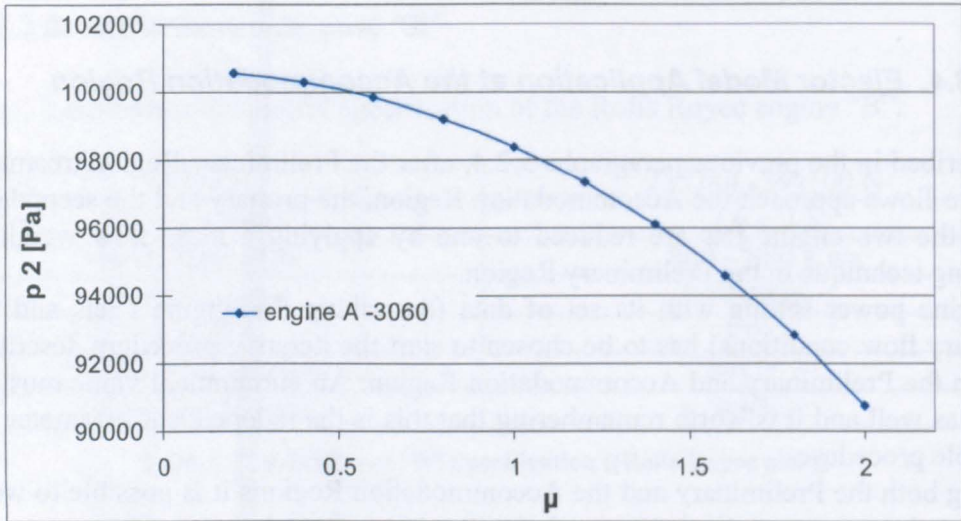


Figure 5.12: Ejector Characteristic at the Accommodation Region

Repeating the same procedure for different engine's non dimensional mass flow (engine power setting) different curves can be derived as represented in Figure 5.13 for non dimensional engine mass flows of 3060, 1753, 2451.

It is clear that decreasing the engine non dimensional mass flow the static pressure increases keeping the same entrainment ratio.

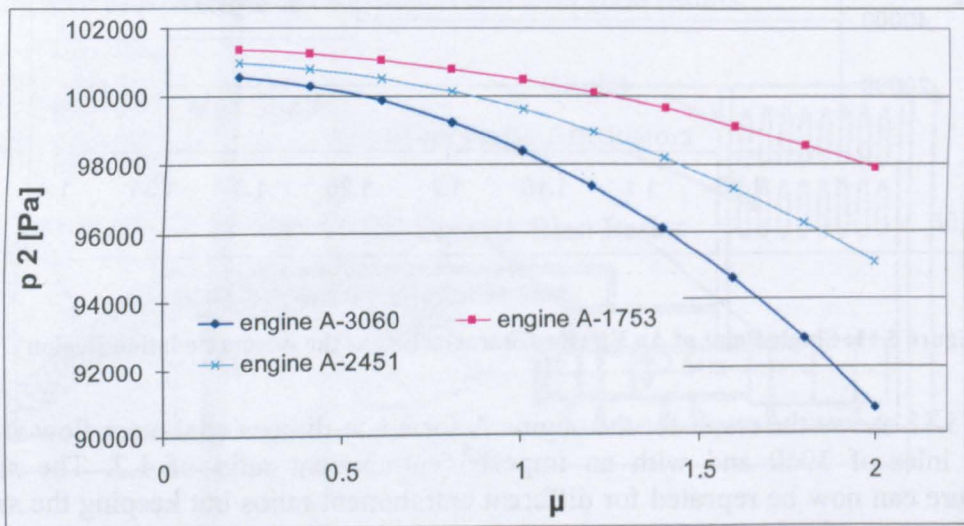


Figure 5.13: Ejector Characteristic at the Accommodation Region for Different Engine ndmf

The curves represented in the above figures are not able to specify the real operating point of the system, at this stage, but they define where it could lay for different cell configurations.



With different cell configurations there are different system pressure losses. For example a different cradle configuration or a different cell structure could lead to a different pressure loss which will affect the operation of the ejector pump. The system will, however, operate at one point only along the curve. However, the uniqueness of the characteristic curve at the Accommodation Region is better discussed in the next chapter (paragraph 6.3.4) by the use of the CFD. Indeed, it will be shown that the operating point will change for different system configurations but will move only along one characteristic curve. At this stage, in Chapter 5, the uniqueness of the curves represented in Figure 5.13 can only be assumed.

For each engine's non dimensional mass flow, the cell entrainment ratio is also experimentally measured by an energy balance (paragraph 2.2.5). This is a quite interesting prospective because it means that the real operating points for the different engine power setting can also be plotted on Figure 5.13.

Therefore the same procedure used to derive the characteristic curves at the Accommodation Region will also be used to work out the effective  $p_2$  for all the different engine non dimensional mass flows. To do this rather than assume a value for the entrainment ratio it will be used that experimentally measured.

Figure 5.14 shows the estimated operating line for engine A.

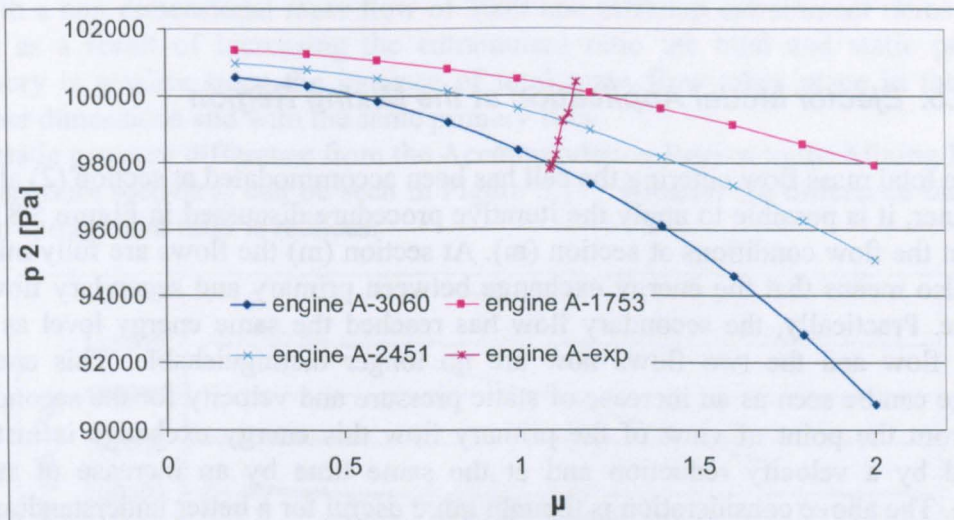


Figure 5.14: Operating Line for the Engine A

The name operating line arises because such line describes how the real working points of engine A in test cell X move in engine-detuner characteristic in the Accommodation Region. It is clear that the operating line cuts each ejector characteristic curve of Figure 5.13 at only one point.

The operating line for engine B can also be derived using the same procedure and plotted in the same map as that used to represent engine A, Figure 5.15.

The first comment which may arise is that the two operating curves do not lie on the same curve.

This is essentially because the representations used do not allow the two curves to do that. Indeed the engine parameters are different, starting from the nozzle area and also because the testing conditions were not the same for the two engines. However a better representation to make the two operating lines lie together will be studied and proposed later on (paragraph 5.4.1) during this chapter.

At the moment the main conclusion is that iterative procedure established for the Accommodation Region is able to represent the characteristic lines for the ejector pump generated by the engine and the detuner.

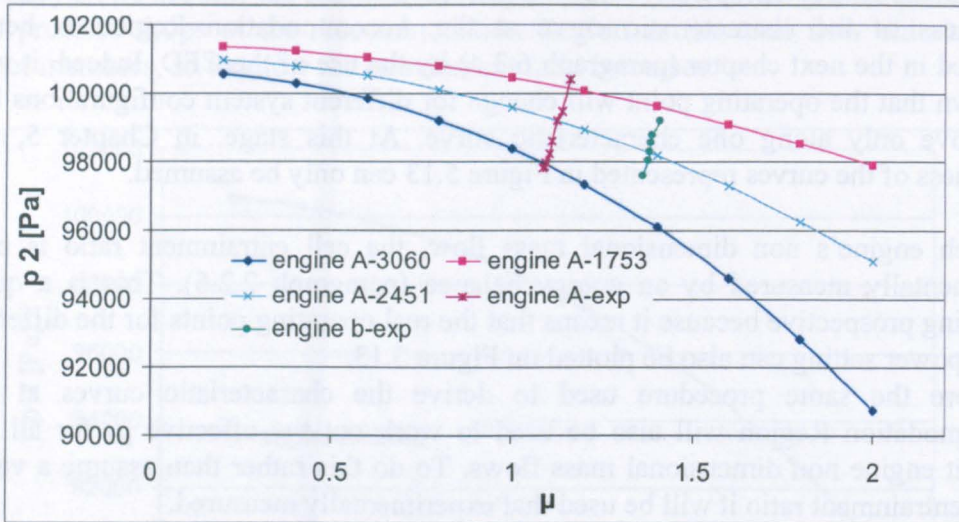


Figure 5.15: Operating Lines for the engines A and B

### 5.3.5. Ejector Model Application at the Mixing Region

Once the total mass flow entering the cell has been accommodated at section (2) along the detuner, it is possible to apply the iterative procedure discussed in Figure 5.8 and work out the flow conditions at section (m). At section (m) the flows are fully mixed which also means that the energy exchange between primary and secondary flow is complete. Practically, the secondary flow has reached the same energy level as the primary flow and the two flows now are no longer distinguishable. This energy exchange can be seen as an increase of static pressure and velocity for the secondary flow. From the point of view of the primary flow this energy exchange is instead followed by a velocity reduction and at the same time by an increase of static pressure. The above consideration is thought quite useful for a better understanding of the flow behaviour along the detuner. Indeed the static pressure for both primary and secondary flows starts to increase in the same way after the Accommodation Region giving rise to what it is called pressure recovery.

At every section, therefore, downstream of the Accommodation Region the static pressure will always be uniform across every section. At the same time the velocity of the primary flow decreases allowing the secondary flow velocity to increase. Globally these two effects allow the total pressure of the primary flow to decrease and that of the secondary to increase. These trends will be explained later in this paragraph and in the next Chapter 6 where the use of CFD techniques will help the understanding.

Choosing an engine power setting it is now possible to apply the Mixing Region procedure and find out the values at section (m).

The procedure starts by guessing a value of  $p_m$ .

Repeating the same procedure for the same engine power setting and for the same range of entrainment ratios used for the Accommodation Region (from 0.2 to 2) it is possible to derive the plot of Figure 5.16.

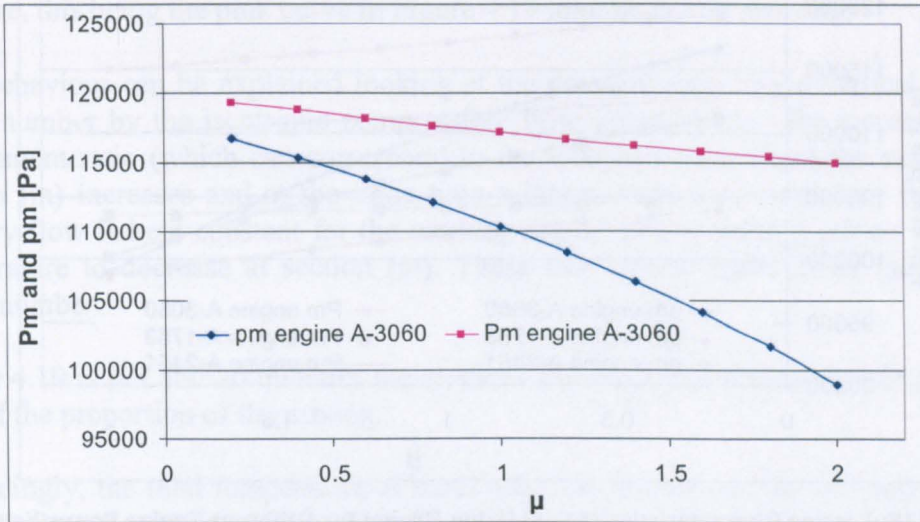


Figure 5.16: Ejector Characteristic at the Mixing Region

Figure 5.16 shows the trends of the static and total pressure at section (m) for engine A with a non dimensional mass flow of 3060 and different entrainment ratios. As is seen, as a result of increasing the entrainment ratio the total and static pressure recovery is smaller since the increase of total mass flow takes place in the same detuner dimensions and with the same primary flow.

The static pressure difference from the Accommodation Region to the Mixing Region (the pressure recovery) can be seen in Figure 5.17. Clearly, the difference increases as the entrainment ratio is reduces.

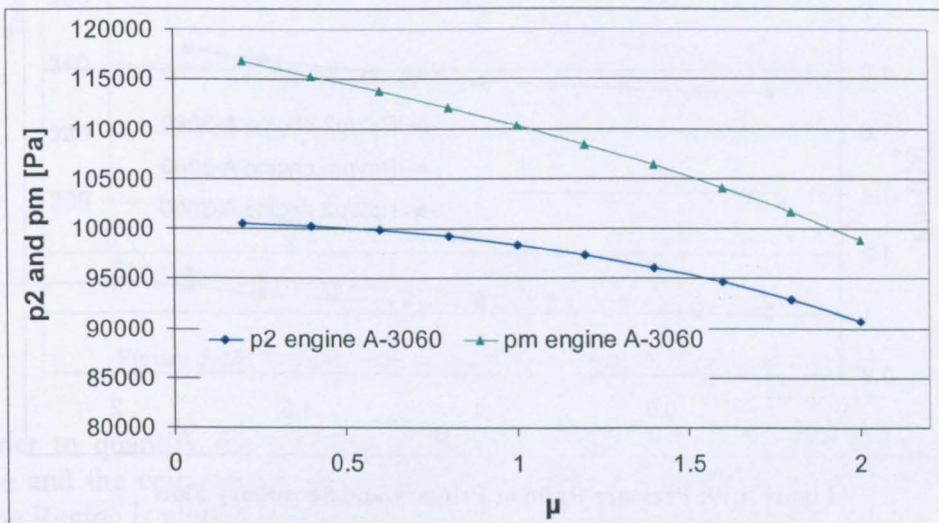


Figure 5.17: Static Pressure Difference between Accommodation and Mixing Region

The same iterative procedure can also be repeated for different engine power settings as it has been done for the Accommodation Region.

Figure 5.18 shows the situation at the Mixing Region for engine A with three different non dimensional mass flows.

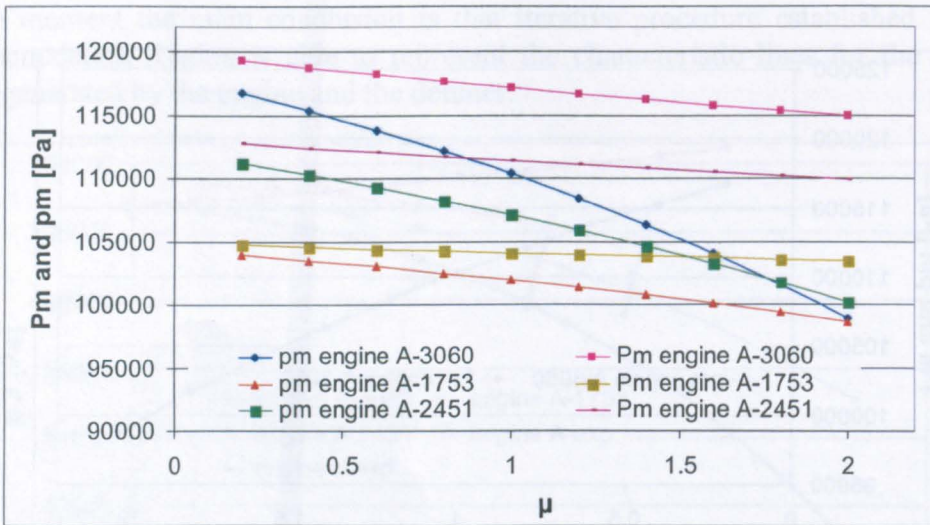


Figure 5.18: Ejector Characteristics at the Mixing Region for Different Engine Power Setting

Increasing the primary mass flow causes the total pressure at section (m) to increase due to the higher energy reservoir kept in the engine jets and exchangeable with the secondary flow. The same does not happen for the static pressure which has to compromise its trend with the detuner geometric conditions and with the fact that increasing engine mass flow also the total mass flow increases.

In order to show the mixing effect the total to static pressure ratio for the primary and secondary flow at the Accommodation Region and for the uniform flow at the Mixing Region are plotted in Figure 4.19.

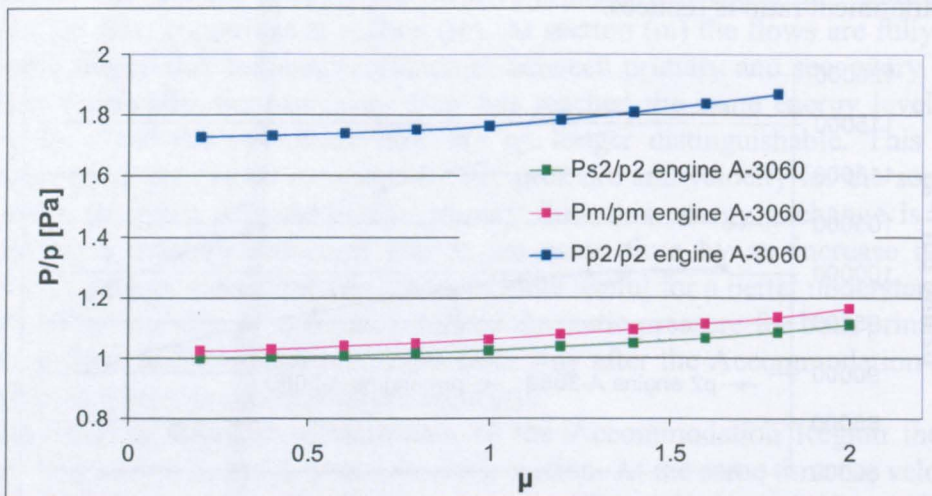


Figure 4.19: Pressure Ratio of Primary and Secondary Flow

This may help the understanding keeping also in mind that for a defined engine power setting the engine and the secondary flow starting parameters are kept always the same for the entire different entrainment ratio analyzed. So within the assumption of the procedure illustrated above, Figure 4.19 can give an idea of the energy transfer from the primary to the secondary flow.

Figure 4.19 can be misleading because both the total and the static pressures vary at section (m) when entrainment ratio is changed. Indeed as is shown in Figure 5.16 the two pressures at section (m) decrease by increasing the entrainment ratio.

It is obvious, however, that the drop in static pressure is larger than the drop in total pressure, this being the pink curve in Figure 4.19 monotonically growing.

This behaviour can be explained looking at the pressure ratio in the vertical axis as Mach number by the isentropic compressible flow formulations. By increasing the entrainment ratio (which can correspond to the total cell mass flow) the velocity at section (m) increases and at the same time a larger amount of secondary flow (the primary flow is kept constant for the working engine power setting) allows the total temperature to decrease at section (m). These two effects result in an increase of Mach number.

Figure 4.19 is not able to quantify the result of the mixing process but only gives an idea of the proportion of the mixing.

Accordingly, the total temperature at section (m) as function of the cell entrainment ratio is plotted on Figure 5.20. The total temperature is able to quantify the global level of energy owned by the flow (for unit of mass flow) at section (m). From the trend represented in the graph it is clear that such a level decreases with an increase of entrainment ratio.

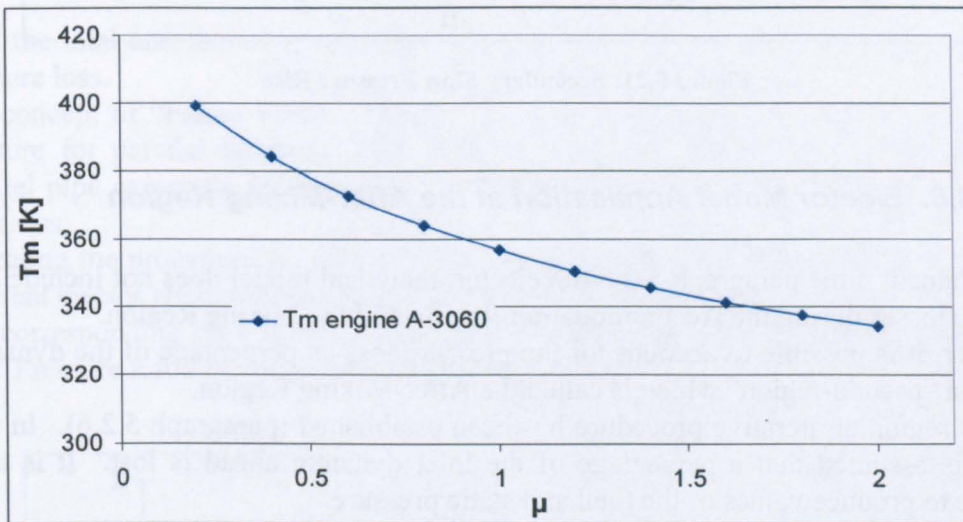


Figure 5.20: Temperature at the Mixing Region as Function of  $\mu$

In order to quantify the performance of the ejector pump generated between the engine and the cell detuner the total pressure rise of the secondary flow up to the Mixing Region is plotted in Figure 5.21.

It is clear that increasing the energy available with the primary jet causes the secondary total pressure to increase.

However it has to be remembered that the analysis up to now does not include any pressure loss. Secondly, the fully mixed condition is also reached for each one of the cases above illustrated.

In reality due to the detuner length complete mixing is not achieved. This means that the above maps may not be fully realistic. However, they do help the understanding of the flow phenomena in an enclosed test bed facility.

Indeed the flow behaviour along the detuner is responsible for the total mass flow entering the cell.

Summarizing, the analytical procedure established for the Mixing Region is able to represent the flow characteristics when fully mixed conditions are achieved (see Figure 5.16). Furthermore it helps the understanding of the flow mechanism along the detuner which can be applied for controlling the total flow entering the cell

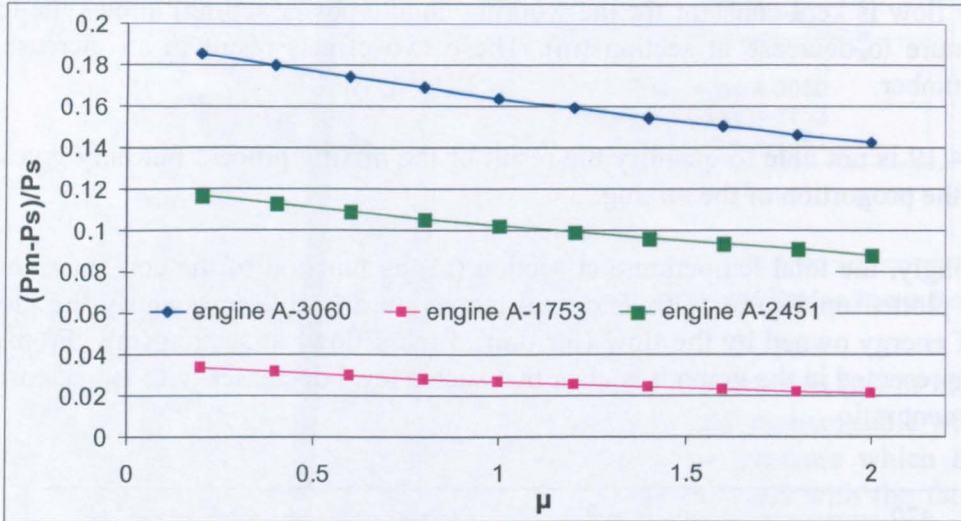


Figure 5.21: Secondary Flow Pressure Rise

### 5.3.6. Ejector Model Application at the After-Mixing Region

As explained in the paragraph 5.2.6 the ejector analytical model does not include any pressure losses during the Accommodation Region and the Mixing Region.

However, it is possible to account for the pressure loss as percentage of the dynamic head in a “pseudo-region” which is called the After-Mixing Region.

For this region an iterative procedure has been established (paragraph 5.2.6). In this case it is assumed that a percentage of the inlet dynamic ahead is lost. It is then possible to produce values of the total and static pressure.

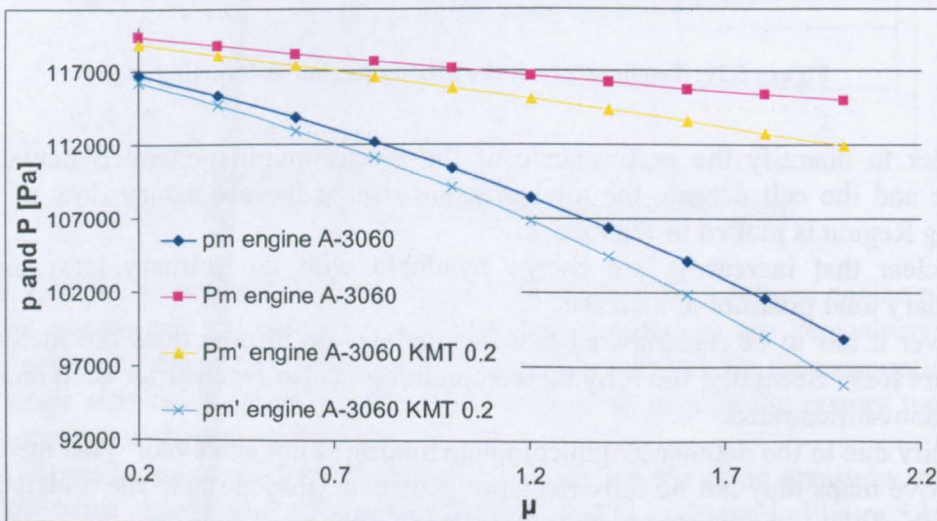


Figure 5.22: Comparison of the Ejector Characteristics with and without Pressure Losses

Figure 5.22 shows the ejector characteristic for engine A with a non dimensional mass flow of 3060. Both cases with ( $K_{MT}$  equal to 0.2) and without pressure loss are illustrated.

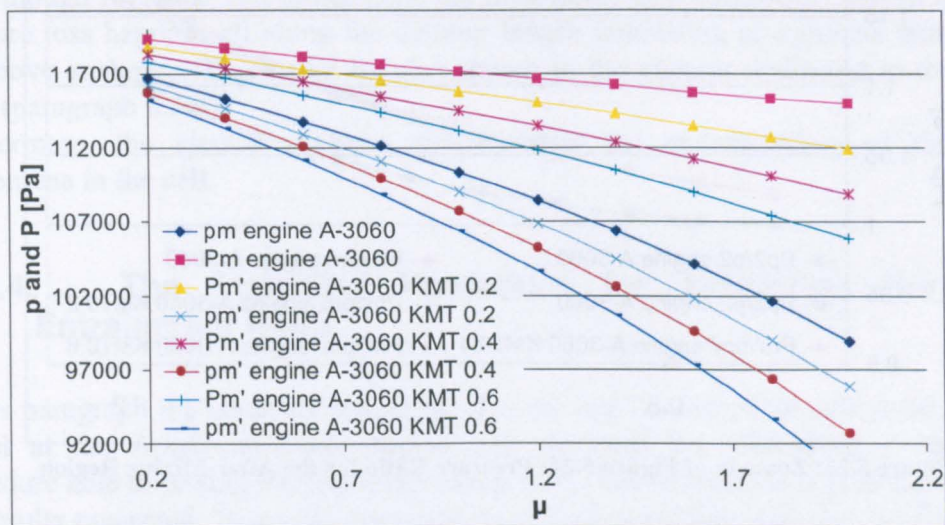


Figure 5.23: Ejector Characteristic with Different Pressure Loss Factors

Both the total and the static pressure drop are compared for cases with and without pressure loss.

The concept of “Fanno Flow” (Shapiro 1953) is used to quantify the drop in static pressure for parallel adiabatic flow with friction. In subsonic flow, friction in a parallel pipe causes an increase in Mach number. Simultaneously, the total pressure decreases.

Repeating the procedure for different loss coefficients  $K_{MT}$  it is possible to work out different ejector characteristics (see Figure 5.23).

The corresponding ratio between the total and the static pressure is shown on Figure 5.24: Pressure Ratio for the After-Mixing Region

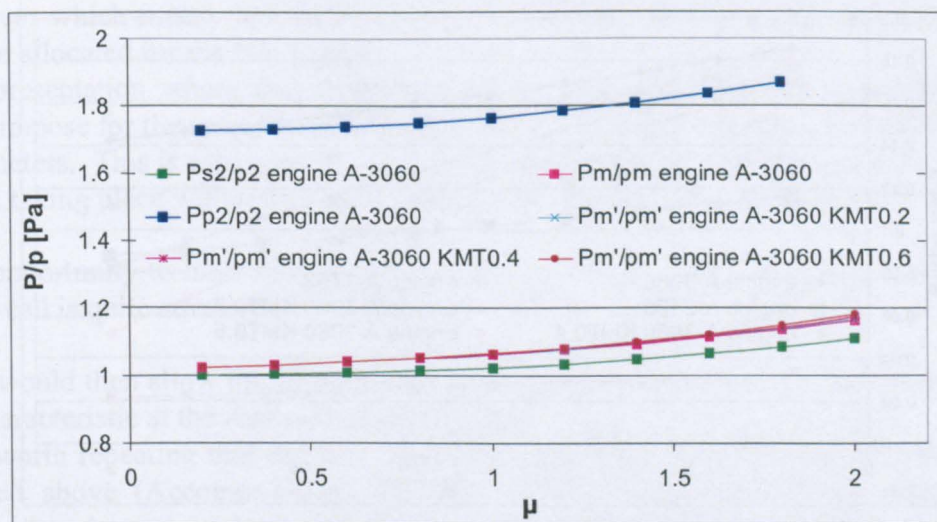


Figure 5.24: Pressure Ratio for the After-Mixing Region

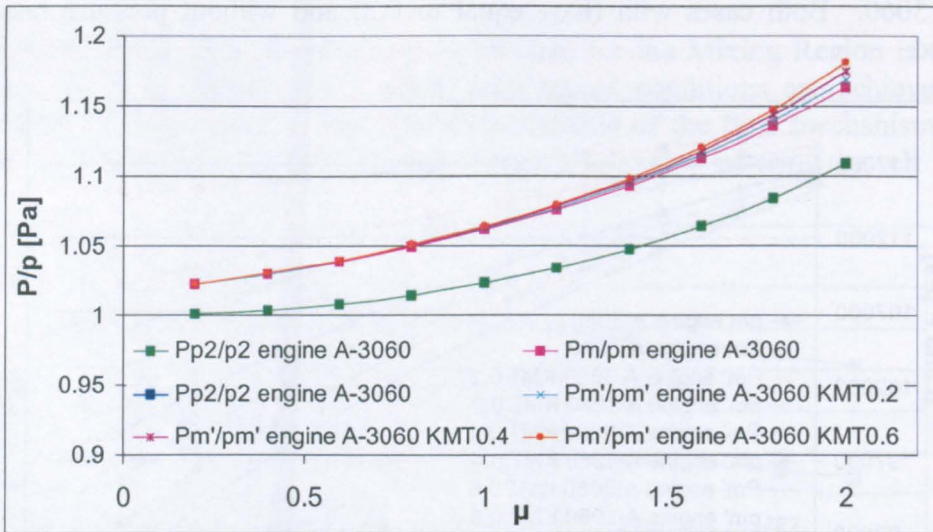


Figure 5.25: Zoom in of Figure 5.24: Pressure Ratio for the After-Mixing Region

Such a figure shows the same map as Figure 4.19 but includes the results of the After-Mixing Region with different levels of pressure loss.

Zooming in closer to the results of the After-Mixing Region (Figure 5.25) it is possible to see how increasing the pressure loss coefficient the total to static pressure ratio increases especially for the higher entrainment ratios.

For low values of entrainment ratio the Mach number is less than 0.2 so the effects of compressibility are very small.

In order to understand how the ejector performances are affected by the pressure loss it is interesting to plot the secondary flow total pressure rise (Figure 5.26).

The result of increasing the total pressure loss is that the total pressure of the secondary flow drops. This means that the pressure loss counteracts the energy transfer from the primary to the secondary flow, reducing the energy gain of the secondary flow.

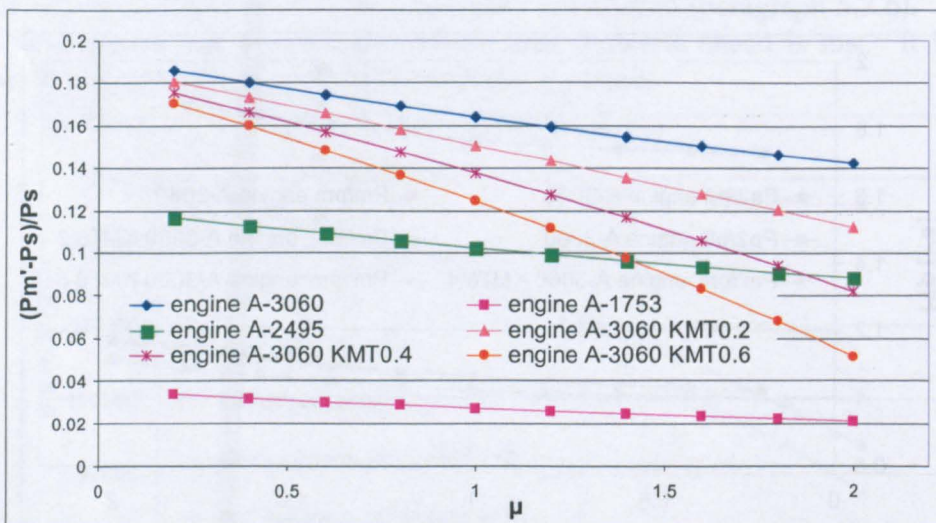


Figure 5.26: Engine-Detuner Ejector Performance at the After-Mixing Region



Summarizing, the After-Mixing Region procedure, it is possible to reproduce the effects of a loss in dynamic head and how that affects the flow field and the ejector performance.

Even though for usual cell dimensions the flow never gets completely mixed and the pressure loss happens all along the detuner length interesting phenomena arise from the above analysis. These will be also shown in the chapter dedicated to the CFD work (paragraph 6.3.4).

Furthermore, the ejector analysis really assists the understanding of the flow phenomena in the cell.

## **5.4. The Matching Procedure for Predicting the Cell Entrainment Ratio**

In this paragraph the results obtained through the application of the analytical ejector model at the Accommodation Region will be used for attempting a matching procedure able to predict the cell entrainment ratio. The methodology is discussed and the results presented. However the whole matching procedure will also be discussed in the next chapter with the findings of the CFD analysis (paragraph 6.3.4).

### ***5.4.1. Accommodation Region Non Dimensional Analysis***

In the paragraph dedicated to the application of the analytical model at the Accommodation Region (paragraph 5.3.4) the operating lines of two different engines in the same test bed cell, Figure 5.15 have been presented. These two lines have been derived by using experimental measurements of the entrainment ratio together with the engine conditions needed for the procedure.

As it turns out, a direct application of the iterative procedure does not result in the two operating lines superimposing in the map. This is because the static pressure at the Accommodation Region is not the right parameter to represent the two engine-detuner ejector performances in only one curve. This is mainly because the jet dimensions are different which means that different accommodation areas (primary and secondary) can be allocated for the two engines.

A representation where the operating lines of two engine-detuner ejectors do not superimpose for the same test cell is not a very useful way of plotting the performance parameters. This is especially the case if the primary aim is to characterize the ejector effect taking place within the cell from the point of view of the facility itself.

The opportunity to have only one cell operating line for every engine running in the same cell is quite attractive.

This would then allow the study of how the ejector operating point would move along its characteristic at the Accommodation Region.

It is worth repeating that the Accommodation Region is the only region of the three studied above (Accommodation, Mixing, After-Mixing) which really takes place along the detuner without making any further assumption. For the usual cell dimensions, the flow does not achieve fully mixed conditions along the detuner itself. In fact this needs a special tool like the blast basket to reach uniform conditions (paragraph 2.1.8).

Accordingly, the Mixing and the After-Mixing Regions are not able to identify real operating conditions inside the cell. However their contribution to the understanding of the cell flow behaviour is relevant and can still be used for different purposes.

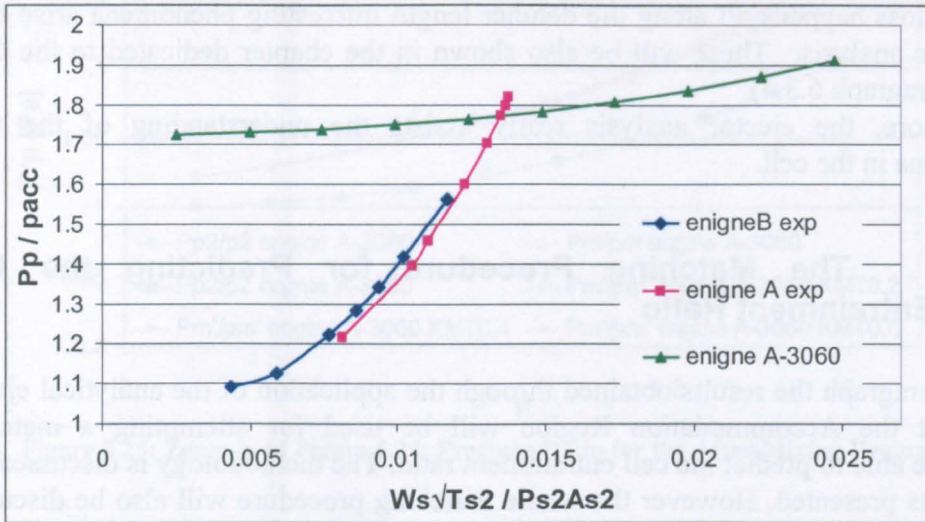


Figure 5.27: Non dimensional Representation of the Cell Operating and Characteristic Lines

Several attempts have been made to superimpose the operating lines of engine A and B on the Accommodation Region characteristic map.

The main tool used is to non-dimensionalise the key parameters.

A number of different strategies have been used to achieve the desired form. For obvious reasons, however, only the most relevant are presented in this thesis.

The earlier attempts made looked at the possibility of representing the single operating line and the ejector characteristic in the same map.

Figure 5.27 shows the results of plotting the non dimensional secondary mass flow at the Accommodation Region versus the ratio of total to static pressure of the primary flow at the Accommodation Region. As can be seen, the two engine operating lines in this representation are closer than in Figure 5.15 but they are still not superimposed. In the above representation it is also possible to see the characteristic line for engine A with a non dimensional mass flow of 3060.

If the two operating lines were merged into only one a cell operating line could have been identified. Consequently every engine-detuner ejector pump established would have had its operating point on that curve. As it happens for engine A the characteristic line crosses the cell operating line at its operating point. This means that it would have been possible to derive the cell entrainment ratio for every engine in the cell just running the ejector analytical model at the Accommodation Region. Indeed, by running the ejector model it is possible to work out all the secondary and primary flow values at the Accommodation Region which allow the calculation of the cell entrainment ratio for the effective operating point.

Anyway at this point it is very important to verify the uniqueness of the cell characteristic line at the Accommodation Region for different engine and cell configurations (keeping the same engine power setting). If for common cell dimensions the ejector characteristic changes with both the engine and the cell configurations, the above procedure can not be validated. However this discussion will be continued in the next chapter where with the help of CFD the same primary jet and the same detuner cross sectional area are modelled in different engine and cell configurations.

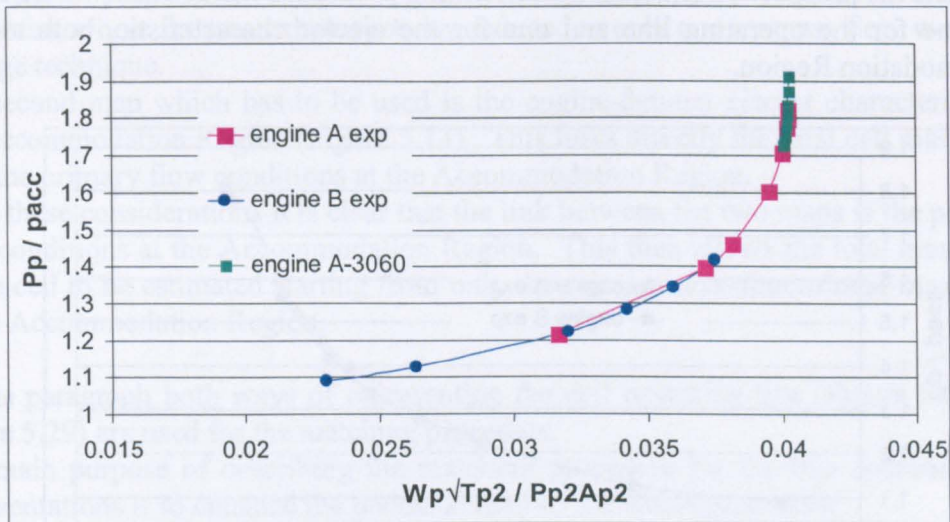


Figure 5.28: Non dimensional Representation of the Cell Operating and Characteristic Lines

The non dimensional case represented in Figure 5.27 has been used to describe the global aim of this non-dimensional analysis even though it does not represent the right set of parameters. It is considered that a global understanding of the whole aim would, using a specific example, be preferable than a theoretical treatment. Anyway, during the further consideration of other cases, the opportunity of having a representation with only one cell operating line is underlined more deeply.

The non dimensional primary flow at the Accommodation Region (Figure 5.28) has been used as a second attempt to merge the two engine-detuner ejector operating lines.

In this case, the two operating lines lay on top of each other as does the characteristic line.

The same colours have been used to facilitate the understanding of this map.

The objective of finding a representation where the two operating lines merge together has, therefore, been achieved.

However, this representation is not able by itself to work out the system operating point when different engines are tested in the same cell.

The main requirement, however, is to have a unique engine-detuner characteristic line. This as has already been said will be shown in the next chapter (paragraph 6.3.4) by the use of CFD. For now and for the rest of this chapter the uniqueness of the characteristic line at the Accommodation Region is assumed.

Following the considerations related to Figure 5.28 and after many other attempts, the opportunity of representing the cell operating line (the two single superimposed) at the Accommodation Region and the ejector characteristic as only one plot has been abandoned.

This opens the prospect of establishing a matching procedure which uses two different plots, one for the operating line and one for the ejector characteristic, both at the Accommodation Region.

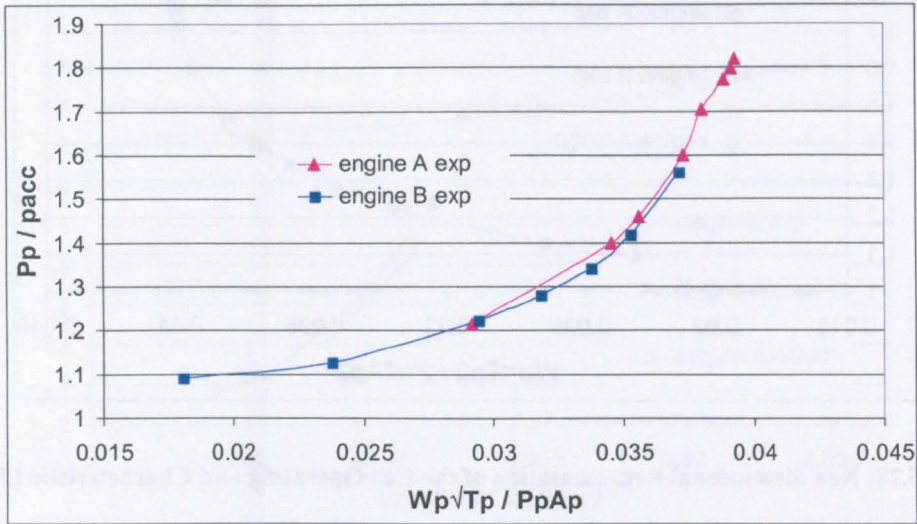


Figure 5.29: Non dimensional Representation of the Cell Operating Line

However, before describing this matching procedure, another useful representation of the parameters worked out at the Accommodation Region will be presented in this paragraph.

It will be very close to that shown in Figure 5.28 with the only difference that the non dimensional primary flow will be calculated at the engine nozzles if the engine is a turbojet and at the Preliminary Region if the engine is a turbofan.

Looking at the matching procedure prospect it is important to be able to enter a map (as that shown above) just using engine parameters. In this case there is no need to use any other analytical model. Figure 5.29 gives an example of this representation which will be better understood in the next paragraph (5.4.2) where the matching procedure is attempted.

#### 5.4.2. Matching Procedure at the Accommodation Region

The idea of predicting the cell entrainment ratio by a matching procedure between two different plots at the Accommodation Region arises because of the impossibility of representing in the same map both the cell operating line and the engine-detuner ejectors characteristic.

Therefore two maps have to be used at the same time.

The first map is that previously referred to as the cell operating line. This characterizes together both engine parameters and flow conditions at the Accommodation Region. In the previous paragraph it has been shown that there are two different ways of representing the cell operating lines, Figure 5.28 and Figure 5.29. In the former the flow properties at the Accommodation Region are linked with the primary flow conditions at the Accommodation Region.

In the second, the flow properties at the Accommodation Region are linked with the primary flow conditions directly at the nozzles. In this case it can be said that the

primary flow properties are taken at the Preliminary Region, if the engine under test is a turbofan, where the two exhaust jets are reduced to only one by mass flow weighted average technique.

The second map which has to be used is the engine-detuner ejector characteristic at the Accommodation Region (Figure 5.13). This links directly the total cell mass flow with the primary flow conditions at the Accommodation Region.

From these considerations it is clear that the link between the two maps is the primary flow conditions at the Accommodation Region. This then allows the total mass flow in the cell to be estimated starting from only the primary non-dimensional mass flow at the Accommodation Region.

In this paragraph both ways of representing the cell operating line (Figure 5.28 and Figure 5.29) are used for the matching procedure.

The main purpose of describing the matching procedure for the two operating line representations is to enhance the understanding of the whole procedure.

Although, since now it is known that one of them will not work.

Figure 5.30 shows the idea of the iterative procedure using the non dimensional primary mass flow at the Accommodation Region.

When a new engine runs in an already in use test cell the matching procedure described above provides an opportunity to know the cell entrainment ratio without measuring it experimentally. Even better the matching procedure can predict the cell entrainment ratio before testing the engine.

Indeed, with knowledge of the engine performance parameters and by guessing different cell entrainment ratios, we can establish the engine-detuner characteristic at the Accommodation Region (Figure 5.30 b)). Ideally this characteristic line crosses the cell operating line (unique for a given cell) at only one point which will be the operating point of the new engine in the test cell. Knowing the position of this point in the cell operating line allows the static pressure in the Accommodation Region for such conditions to be estimated (Figure 5.30 a)). Once this is known it is easy to work out from the engine-detuner characteristic (Figure 5.30 map on the right) the cell entrainment ratio.

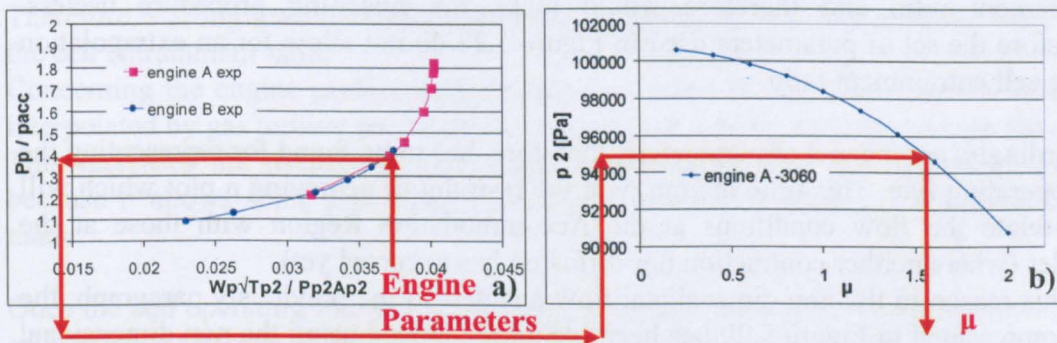


Figure 5.30: Matching Procedure Using the Non-Dimensional Primary Mass Flow at A.R.

A few rows above the word “ideally” it has been used. The right word would probably have been “possibly” because it is already known that in such a representation the engine-detuner ejector characteristic will not cross the cell operating line at one point only. This is clearly shown in Figure 5.28 where the three lines superimpose.

This compromises the usefulness of the matching procedure because it will not be possible to find the real operating point of the system in such representation. Figure 5.31 is no more than a zoom into Figure 5.28 in order to show that the characteristic line lies on top of the operating line.

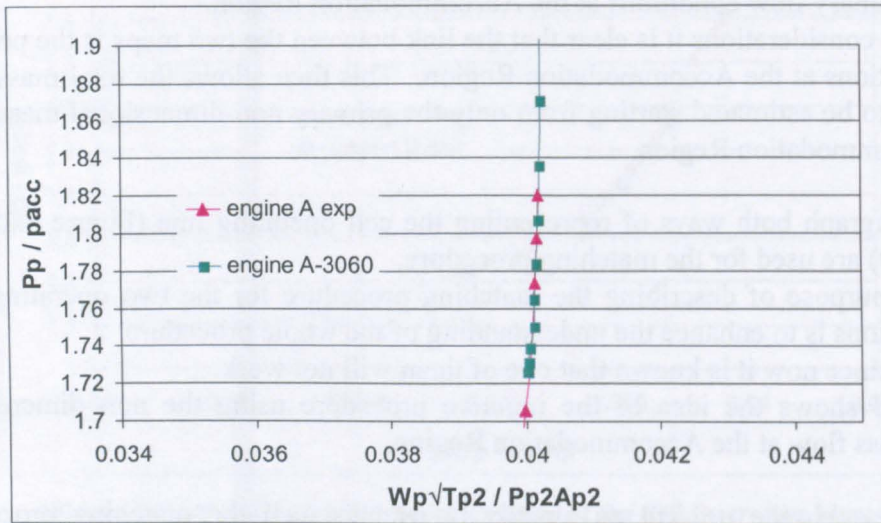


Figure 5.31: Zoom of Figure 5.28

This happens because if the non dimensional primary mass flow at the Accommodation Region is used, the area of the primary jet will play an important role. Indeed the jet coming from the engine will readjust itself by diffusion and contraction processes which will lead to a change in the primary flow area as a function of the secondary mass flow.

Furthermore, the impossibility of achieving a matching procedure using the representation of Figure 5.28 is underlined also by another fact. For entering the cell operating line plot with the effective non-dimensional primary mass flow at the Accommodation Region it is necessary to know the cell operating point in the Accommodation Region Characteristic. This requires the knowledge of the cell entrainment ratio and therefore would make the matching procedure useless. Therefore the set of parameters used in Figure 5.28 do not allow for an extrapolation of the cell entrainment ratio.

Accordingly, another set of parameters, therefore, has to be found for representing the cell operating line. This time though with the restraint of achieving a plot which will inter-relate the flow conditions at the Accommodation Region with those at the nozzles (where neither contraction nor diffusion has occurred yet).

For this reason in the non dimensional flow analysis in the previously paragraph, the case represented in Figure 5.29 has been included. Indeed using the non dimensional primary mass flow at the Preliminary Region (for a turbofan engine) the representation will be free from any Accommodation Region readjustment. Furthermore, using the Preliminary Region results it is not anymore required the knowledge of the operating point on the characteristic at the Accommodation Region a priori.

Therefore, a matching procedure is now finally proposed using the operating line representation of Figure 5.29.

## Matching Procedure

As a first step the engine-detuner ejector characteristic at the Accommodation Region has to be worked out (Figure 5.32b)) by guessing different cell entrainment ratios and following the iterative procedure described above (Figure 5.6).

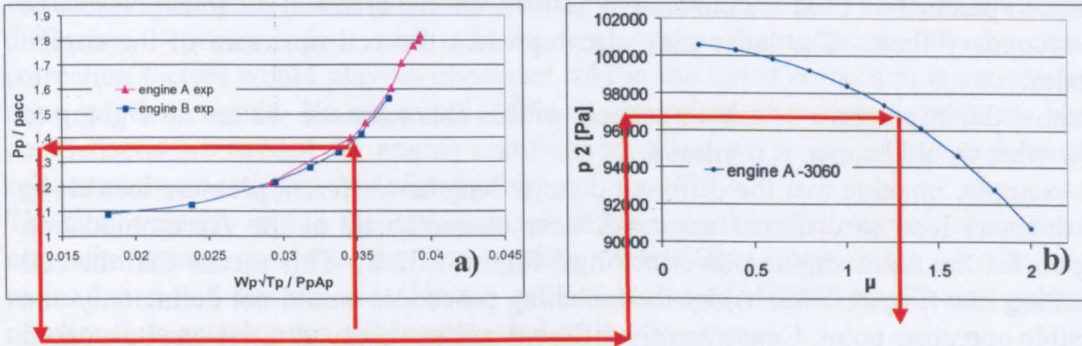


Figure 5.32: Matching Procedure Using the Non-Dimensional Primary Mass Flow at P.R.

After that, knowing the engine jets non dimensional mass flow (calculated at the nozzle or at the Preliminary Region depending on the engine type) it is possible to enter the map on the left of Figure 5.32(a)) from the horizontal axes and find out the operating point in the cell operating line. Once the operating point has been found in the vertical axes of the same map it is possible to read the total to static primary pressure ratio. The total pressure of the engine jet is known directly as a performance parameter in the case of a jet engine and by running the Preliminary Region procedure (paragraph 5.2.3) when the engine is a turbofan.

Consequently the static pressure at the Accommodation Region can also be worked out. This will allow to entry into the map on the right of Figure 5.32 from the vertical axis (static pressure Accommodation Region). Following this the cell entrainment ratio can be worked out once the operating point has been transferred to the characteristic engine-detuner curve.

Therefore, starting from the engine performance parameters, it is possible to work out the cell entrainment ratio.

Concerning the engine performance parameters, it can be said that they can also be interpolated by gas turbine performance codes rather than be measured inside the cell. This increases the usefulness of a matching procedure like that described above because it allows some preliminary considerations before running the engine to be made.

Once the cell operating line in the matching procedure described above is known, the cell entrainment ratio can be worked out for a new engine by running the analytical ejector model at the Accommodation Region.

### 5.4.3. The Uniqueness of the Engine-Detuner Characteristic

Before describing more deeply the usefulness of this matching procedure at the Accommodation Region the importance of the uniqueness of the engine-detuner characteristic in the whole procedure is described. This is for two main reasons, firstly

because whenever (for the same engine power setting) such a characteristic changes, the whole procedure can not be validated. Secondly, to allow the reader to think about possible validation using CFD tools.

In a way, the considerations in this paragraph are an introduction to the CFD work used to validate the above methodology.

In order to derive the engine-detuner characteristic at the Accommodation Region the main cell parameters used are the detuner cross sectional area and the total pressure of the secondary flow. The latter may also represent the cell upstream of the engine nozzles.

To show the importance of the uniqueness of this characteristic we are now going to show what would happen if it misses.

For example, imagine that the different detuner lengths (different pressure loss along the detuner) lead to different engine-detuner characteristic at the Accommodation Region for the same engine power settings, Figure 5.33 a). This means that the cell operating line (Figure 5.33, b)) by the matching procedure would not define only one possible operating point. Consequently different cell entrainment ratios can be worked for the same engine power setting.

Therefore, a survey to verify the uniqueness of the engine-detuner characteristic at the Accommodation Region is needed for validating the matching procedure at such region.

Obviously the definition of a unique characteristic at the Accommodation Region does not imply a unique characteristic at other sections downstream of the detuner where the system pressure loss and the mixing process affect the whole ejector performance (see Figure 5.33).

The above consideration is the main reason which has driven the author to choose the Accommodation Region as representative section for the engine-detuner ejector.

However, it has to be said that the ejector theory by itself specifies that the ejector theory is unique and that the operating point is defined along it by the system pressure losses downstream of the Accommodation Region.

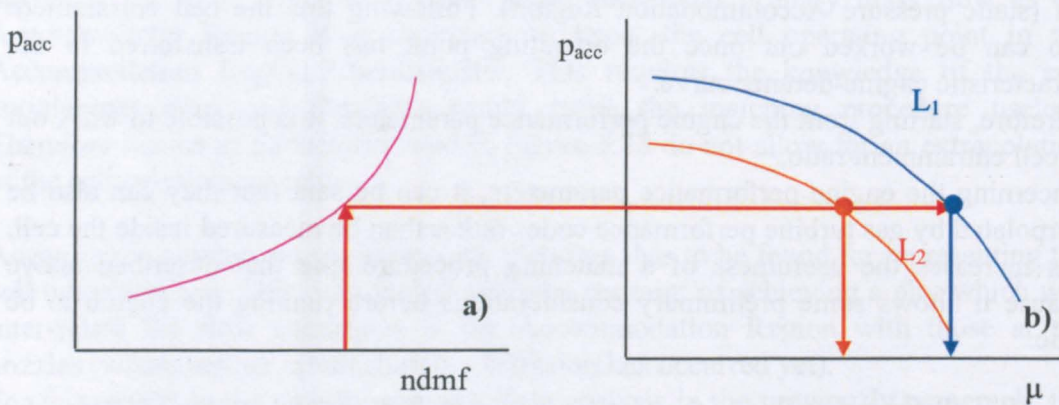


Figure 5.33: Matching Procedure with two Characteristic Lines

## 5.5. The usefulness of the Matching Procedure at the Accommodation Region

At this stage and prior to any further validation the matching procedure could be used for preliminary study regarding gas turbine engines in enclosed test bed facilities.



However, in this panorama, six main contributors can be given from a preliminary estimation of the entrainment ratio for new engines in an in use test cell facility.

The first is related directly with the amount of mass flow going through the cell. Indeed, the mass flow entering has to be kept within defined limits. The reasons for this are mainly related to the flow velocity within the cell. A very high flow velocity would lead to higher thrust correction factors inside the cell and this means a bigger difference between indoor and outdoor test results. Consequently all the thrust correction factors would play an important role in the thrust correction equations and none of them could be neglected. This is very important when back to back comparisons are needed for engine certification purposes. So it is usual to keep the cell entrainment ratio below defined limits.

The flow velocity within the cell does not affect only the total amount of the thrust correction factors but also the flow quality. Indeed flow phenomena as distortion, recirculation and separation inside the cell are seriously affected by the total amount of mass flow entering the cell (paragraph 2.4)

Furthermore, following the consideration made in the literature review the above mentioned flow phenomena demand for conflicting entrainment ratio. Therefore, its knowledge has an even more attractive feature.

The knowledge of the total mass flow entering the cell before running the engine can give valid indications on the use of the cell.

The second advantage of knowing the cell entrainment ratio before running the engine is related to the thrust correction factor. Indeed useful relations for the thrust correction factors have been derived in Chapter 4 which links the magnitude of the correction with the engine and cell dimensions as well as the entrainment ratio. This means that once the entrainment ratio is known it is even possible to estimate the total amount of the thrust correction factors which have to be applied to the load measured.

The third contribution is not directly related to the use of indoor test facilities but with their study. The static pressure at the Accommodation Region could be used as a boundary condition for CFD studies. This would avoid the need to model the whole exhaust stack with all the difficulties that this would involve.

Indeed the exhaust stack contains one of the most difficult parts to model by CFD, the blast basket. A big perforated cylinder located at the end of the detuner which collects all the exhaust gases which are not completely mixed yet. These gases after have being collected start to mix in the cylinder by recirculation and leave it going through the small holes. Plenty of flow phenomena not completely understood yet occur in the blast basket slowing down the modelling and the convergence of the CFD models. Furthermore the whole exhaust stack represents by itself a huge volume to model which would require a massive number of calculation cells alone (see cell dimensions Figure 5.10).

Therefore a bigger number of cells could be concentrated where it is needed dependently on the aim of the simulations.

So the knowledge of the flow properties at a section upstream of the exhaust stack would facilitate the entire CFD modelling. It is also worth saying that at the Accommodation Region the static pressure is constant across the section and so the necessity to work with a velocity profile would be avoided.

However there are several reasons which push to model the entire cell. First of all, the necessity to understand the flow behaviour along the exhaust stacks. Therefore,

depending on what the real aims of the CFD analysis are, it could be interesting to have knowledge of the Accommodation Region as a possible boundary condition. It can be said that when the test chamber is the main part under study, the Accommodation Region as a boundary condition can really be an attractive opportunity.

Another possible use of the matching procedure, the fourth, is the validation of the CFD results. Indeed, comparing the engine-detuner characteristic at the Accommodation Region analytically obtained with that obtained by CFD is useful to understand the reliability of the computational result.

Another point which makes the combination of the analytical ejector tool and the matching procedure very useful, the fifth, is their contribution to the general understanding of the flow phenomena inside the cell. Indeed, together they allow the understanding of how the engine-detuner system works.

Finally the matching procedure can also be used in order to control the entrainment ratio inside the cell. The methodology for this is proposed during the final discussions (paragraph 7.4) of this thesis.

## 6. CFD Modelling for Enclosed Test Cell Facilities

CFD plays an important role in several aspects of this project. Indeed, each analytical study has been followed by a computational analysis. Indeed, in this chapter all the main areas handled are looked at from a CFD point of view.

The CFD application, for studying the thrust correction factors, has been used primarily to derive those components not experimentally measurable, for example, the pre-entry force. Afterwards, the entire set of thrust correction factors have been derived and compared with the one dimensional gas dynamic analysis proposed in Chapter 4. Since the literature does not give references regarding this specific CFD application, the main purpose of this analysis was to understand the capabilities of commercial fluid dynamic software to interact with thrust correction factors.

For the analytical tool developed in Chapter 5, the CFD analysis has supported the matching procedure at the Accommodation Region. Running different engine-cell configurations the uniqueness of the engine-detuner ejector characteristic curve has also been proven.

Furthermore, several models have been generated to understand how the operating point of the system moves along the characteristic curve with the main purpose of controlling the cell entrainment ratio.

The majority of the work listed above has been carried out using only the test cell main chamber. However, several attempts have also been made to model the other test cell components. The aim of this is to reach a better understanding of the flow field inside the cell.

In this chapter the software used for the CFD analysis is not described in detail. Indeed, the Fluent user manual provides by itself a complete description of how the software works and gives also a description of the possible computational choices available.

For each part where CFD has given its contribution the work methodology and the results are discussed during this chapter. However, before starting with the analysis the global approach used during the CFD work is explained.

### 6.1. Author Approach to the CFD

Computational fluid dynamics represents an extremely powerful tool to analyse flow fields. Indeed, the state of the art nowadays has reached a high level of confidence in terms of development and application for fluid dynamic codes.

However, having said that, a distinction has to be made here between those who originate CFD packages as an analysis tool and those who merely use it as a tool for analysis.

Even though the final aim of both categories would be improve the knowledge and the understanding of the fluid dynamics, the approach from the research point of view is quite different. From one side there is he or she who writes his own code for his specific need. These will be very specific codes, useful for a restricted number of problems, but able to give very accurate answers within the assumption made.

Another common approach is that for one who writes his own code, starting from commercial software platforms, and afterwards the “homemade” routines can be integrated. In this way the commercial software will be able to give more specific answers concerned with the particular problem being dealt with.

However, at the same time there is also one who uses the commercial fluid dynamic codes as they are without making any integration but just as a user. In general the commercial codes are able to model a wide range of situations from changes of state to the shock waves from turbomachinery flows to combustions processes, leaving the accuracy of the results varying with the code set up.

All three approaches are interesting at the same level but as is possible to understand they do not suit all the research fields in the same way. For example it would be pointless to spend a lot of time trying to model something that is not completely clear and about which there are not specific indications. In such a case, it is probably better to try to understand the flow phenomenon before and only afterwards concentrate attention on a more accurate modelling process.

By itself, the indoor gas turbine test facility includes plenty of flow phenomena which occur at the same time and among which there are some still not completely identified.

Following the above considerations, in this work, it was decided to adopt for the CFD analysis a “user” approach.

Several models have been generated; each one of them particularly oriented to one specific aspect (thrust correction factors, analytical ejector model, and cell components influence) but always the standard Fluent options have been used.

The main aim of the computational fluid dynamic analysis in this work is that of exploring the flow fields inside the test cell in order to work out useful outcomes for their global understanding.

In a way it can also be said that the CFD analysis proposed here is used for both supporting and validating the findings arising from the one dimensional gas dynamics illustrated in the Chapters 4 and 5.

Concluding this introductory paragraph, the work presented in this Chapter is seen by the author as a starting point from where more interesting and accurate results can be generated including also other CFD techniques.

## **6.2. CFD Modelling for the Cell Thrust Correction Factors**

### ***6.2.1. Aim of Calculating the TCF by CFD***

As described in the literature review and confirmed in paragraph 4.4.1, the ideal environment for checking the real thrust delivered by a gas turbine engine is the free stream condition. Indeed, it has been shown in paragraph 4.4.1 that in such a condition and with no wind, the thrust measured is the real thrust delivered. However, these ideal conditions are very difficult to satisfy due to the increasing ambient restrictions (noise and pollution) and to the unforeseeable weather conditions. These impediments make an outdoor master test very expensive and provide incentives toward indoor test research facilities.

In such a background, CFD can provide valid support to the experimental data carried out during ordinary indoor test. Furthermore it can also give useful information about flow structures which are difficult to understand by either experimental measurements or visualizations.

In this part of the work the computational fluid dynamic has been used as support of the one dimensional thrust correction analysis carried out in Chapter 4.

The thrust correction equations derived is compiled with the data extracted from CFD models and a final comparison is made between CFD and one dimensional gas dynamic.

### **6.2.2. CFD Modelling Approach and Methodology**

Figure 4.43 and Figure 4.44 show the longitudinal and transversal dimensions of an indoor test cell. It's very big volume makes it very difficult to model in CFD. In situations like this, there are several factors to consider before generating the model. First of all the accuracy of the results and the time spent in running the model. The accuracy of the results is dependent on several parameters which at the moment can be usefully split into two main categories, the computational choices and the volume discretization (grid).

The former are made in order to use the right set of equations and the right procedure for representing the flow inside the whole control volume. These include, for example, the choice of the turbulence model or of the solver used by the software to solve the equations system (Fluent incorporated b).

The latter is very important because it defines first the geometry of the model and secondly the dimensions and the number of the volumes where each spatial and time differential equation is to be integrated. The bigger the volume (cell) the bigger the uncertainty related with the discretization.

Concerning the former factor, in general the choice is driven by past experiences or by the modelling it self which has to satisfy some conditions instead of others. So, in the trade off process between accuracy and running time, the computational choice is often constrained by the nature of the problem.

The time needed for each step of the iteration process is controlled by the number of discretization volumes chosen as is the accuracy of the solution. Such dependency is non-linear.

From the above consideration it appears that probably the better trade off involves limitation on the whole control volume. Indeed, if the control volume is kept within certain dimensions a good density of discretization elements can be achieved without working a massive number of elements.

This balance satisfies also another important point which concerns with the capability of the calculation facilities. Indeed it is not only matter of calculation time but the success of a CFD simulation is also strongly affected by computational resource available. If these resources are not enough the calculation process either does not start or stop.

Accordingly, with the above considerations it has been decided from the outset to examine only a part of the test cell using CFD. In particular, the test main chamber

has been chosen from downstream of the cascade elbow to the end of the detuner or upstream of the blast basket.

Figure 6.1 shows enclosed in the red oval the part of the cell where the CFD analysis has been concentrated. This is called the “main test chamber.”

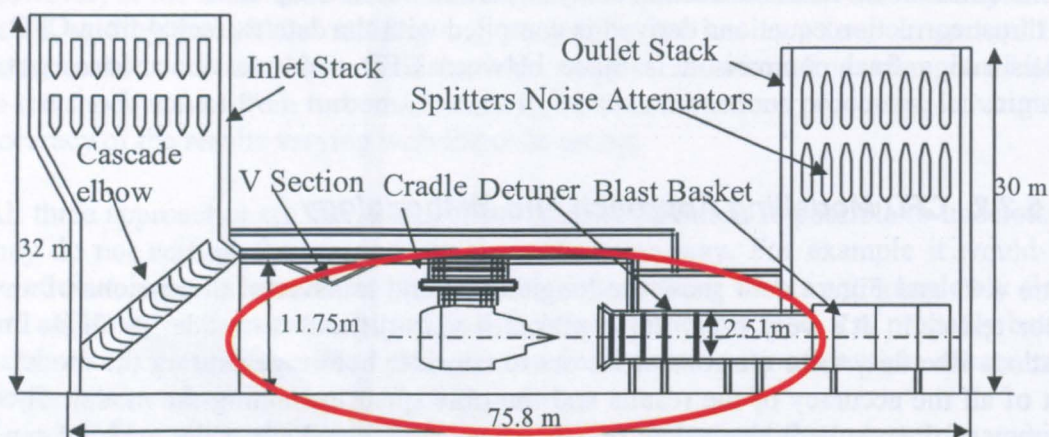


Figure 6.1: Sea-Level Test Cell

Obviously this choice implies some assumptions are included in the model.

The first assumption, using as inlet condition a section downstream the cascade elbow, is that the flow is uniform entering the cell. In reality the flow downstream of the elbow is not completely smooth and uniform since it is still affected by some distortion generated along the cascade. This distortion is dependent on the cell design and on the cell operating conditions (paragraph 2.4.1). Usually for normal operating conditions the flow is quite smooth at that section and the assumption of uniformity is not so far out. However, it is still an assumption whose impact on the results depends also on the aim of the simulation. The author believes that the uniformity of the flow at the cell entrance is not one of the main parameters for an estimation of the thrust correction factors. However, it has to be said that it may become a fundamental parameter if the quality of the flow inside the cell is the driven parameter for the simulation.

This will be shown later on during this chapter when some cell components are analysed separately.

The second main assumption is related to both the exhaust stack and the blast basket. If these components are not included in the simulation any outlet control of the flow is lost. However, if the inlet stack is not included in the cells, its influence can be represented by the use of the total pressure measured in the cell downstream (inlet pressure loss).

The outlet stack situation is a bit more complicated. The primary and secondary flow enter the blast basket still not completely mixed and at that section the flow measurements are difficult to accomplish due to nature of the flow itself. Downstream the blast basket the assumption of complete mixing can be made and flow measurements can be taken.

From the above considerations it can seem that a natural cut to the cell is downstream of the blast basket where the assumption of flow uniformity is not so far away from reality.

However, such a cut would involve the modelling of the blast basket which by its shape and geometry would require a massive number of elements to achieve a good discretization. This will compromise the main trade off between accuracy, time and computational capability.

Going back to what has already been said in Chapter 5, the flow before entering the blast basket has already passed the Accommodation Region and consequently the static pressure along the detuner will grow uniformly. This consideration allows the possibility of using a uniform static pressure as the outlet boundary condition for the main test chamber model.

However, the static pressure at the entrance of the blast basket is an unknown parameter.

The fact that the matching procedure developed in paragraph 5.4.2 is able to predict the cell entrainment ratio (and the static pressure at the Accommodation Region) is very useful. Indeed the static pressure derived in such a way can be used as an outlet boundary condition for the modelling of the main test chamber.

However, the CFD analysis had already started before the analytical matching procedure had been developed. Accordingly, it has not been used to derive the outlet boundary conditions for the computational simulations.

Indeed, another process has been used to match the real cell entrainment ratio by running the test cell main chamber only.

In this case, the parameter used as a handle is always the uniform static pressure profile along the detuner. The secondary flow entering the cell is then driven by the value of the static pressure at the exit of the detuner. Accordingly, cell mass flow matching will occur for only a single value of static pressure.

This concept represents the main idea of the matching process for the CFD analysis.

The main purpose of the matching process then is to match the computational solution with the experimentally measured entrainment ratio.

The total mass flow can be split into two parts; the first is the one going directly into the engine and the second is that driven by the engine-detuner ejector pump.

The mass flow going through the engine is driven by the static conditions at the engine face (assuming that the conditions at the cell inlet are fixed) and the secondary flow is defined by the static pressure at the exit of the detuner.

Therefore, once the engine conditions have been fixed (engine performance data) it is possible to change the total cell mass flow by varying the static pressure along the detuner. This can be repeated until the CFD simulations give the same cell entrainment ratio as that experimentally measured.

It is believed that once the cell entrainment ratio is matched, the majority of the flow similarities between the real case and the simulation can also be captured. In particular, for example, thrust correction factors can be examined.

Indeed, assuming that the computational geometry is close to the actual geometry and the mass flow is the same, the gauge pressure distributions on the surfaces will also be very close. This is of primary importance in any computational study regarding distribution of forces.

Figure 6.2 summarises the model used and the whole procedure adopted for matching the cell entrainment ratio for pure turbo-jet engines. Knowing the engine mass flow, the exhaust mass flow and the total conditions at the cell inlet, the magnitude of the

cell entrainment ratio is computationally forced by changing the static pressure at the detuner outlet.

The case for a turbo-fan engine is shown on Figure 6.3.

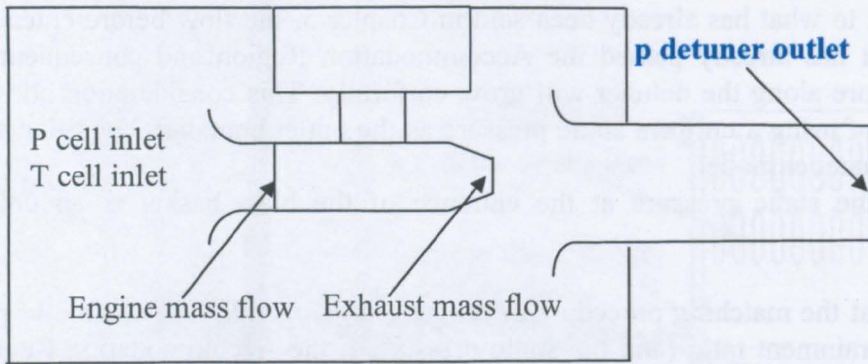


Figure 6.2: CFD Model for Turbojet Engine

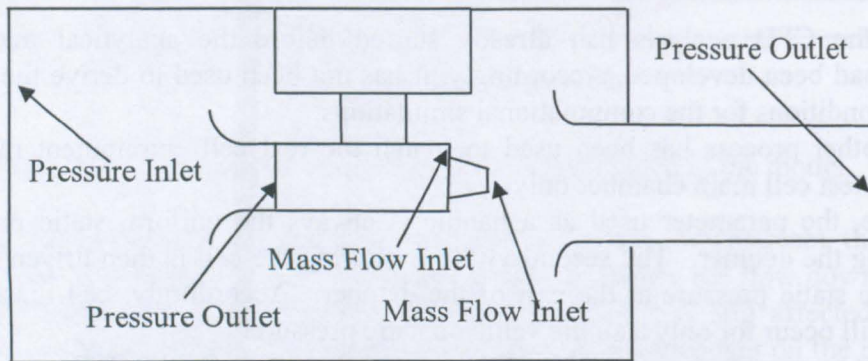


Figure 6.3: Boundary Condition for a Turbofan Engine

The need to achieve second order discretisation (Fluent incorporated b ) makes the process very laborious. This is especially so if the equations are not all changed to second order at the same time. Indeed for each step of the simulation the cell entrainment ratio will vary and useful reference parameters can only be taken when the last step has converged. This means that in order to match the correct entrainment ratio with a second order of accuracy, several models must be run.

This is explained in detail later (paragraph 6.2.6) when a step-by-step approach is illustrated.

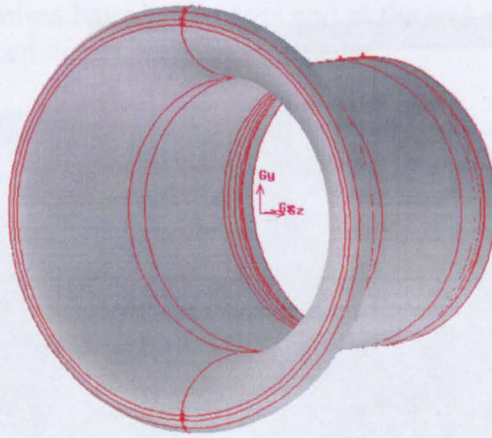
### 6.2.3. Model Geometry and Grid

This part of Chapter 6 is dedicated to the thrust correction factor analysis using CFD tools. In particular, the work done for the Rolls-Royce engine C in the test cell “Y” is described.

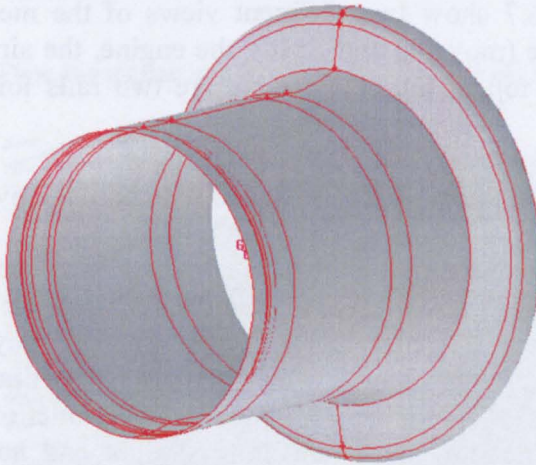
The main cell geometric dimensions have already been described in paragraph 4.5.2. The main details of the model are illustrated by the following pictures which have been taken directly from the CFD model.

Figure 6.4 shows detail of the bellmouth. The internal part is generated by an ellipse and is connected to the external part by a circular joint (Figure 6.5).





**Figure 6.4: Bellmouth Front View**



**Figure 6.5: Bellmouth Rear View**

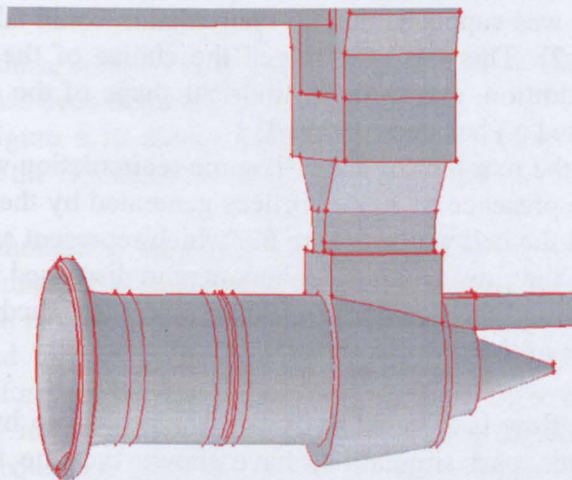


**Figure 6.6: Metric Assembly Side View**

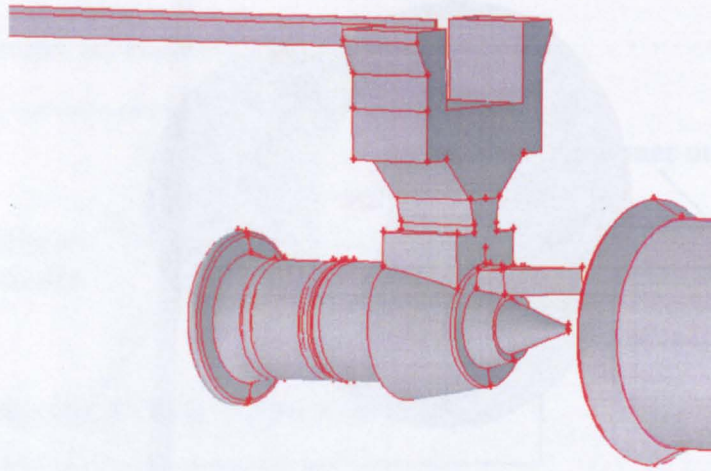


**Figure 6.7: Metric Assembly Rear View**

Figure 6.6 and Figure 6.7 show two different views of the metric assembly. It is possible to see the cradle (movable and fixed), the engine, the airmeter and the entry part of the detuner. On top of the cradle there are two rails for setting the engine inside the cell.

It is interesting to note that the engine is modelled with both the pylon and the plug.

In terms of the grid several attempts to mesh the model have been made. Due to the large dimensions of the cell more than one kind of mesh scheme has been used. For most of the cell hexahedral elements have been used. Indeed they can map (Fluent incorporated a) an entire volume more regularly than tetrahedral cells, requiring in this way a lower number of elements. Furthermore, at the inlet of the main chamber and up to the engine, the flow paths are quite straight and not disturbed by any obstacle inside the cell. In such a situation, hexahedral cells can speed up the simulation compared to the tetrahedral (Fluent incorporated b). The flow paths inside the detuner were not known before running the model. However, due to the amount of mass flow involved in the simulation and to the length of the detuner not being extremely big (24 m) it was supposed that no recirculation could take place along the detuner (paragraph 2.4.2). This has encouraged the choice of the hexahedral mesh along the detuner. In addition, due to the cylindrical shape of the detuner, a Cooper mesh (Fluent incorporated a) has been adopted.

Around the detuner, in the rear part of the cell, some recirculation was expected. Past models have shown the presence of some vortices generated by the interaction of the ejector pump effect and the cell walls. Figure 6.8 which represent another engine in a different cell, underline the flow separation phenomenon discussed in paragraph 2.4.3 and the recirculation around the detuner. For this reason a tetrahedral mesh structure was used in the rear part of the test chamber.

Around the engine, the flow is affected by the deflections given by the engine itself and the cradle. However, past simulations have shown that the flow maintains its paths without recirculation (Figure 6.9, shows the flow around the engine from past simulations). Following this consideration, many attempts have been made to achieve a hexahedral mesh structure. Due to cylindrical shape of the engine, the Cooper scheme has been quite helpful in this part of the model, allowing most of it to be

meshed with hexahedral elements. However, in a large model such as the test bed facility, some compromises have to be made and at the end a few volumes around the engine have been meshed with a tetrahedral scheme.



**Figure 6.8: Flow Separation and Recirculation in the Rear Part of the Cell**

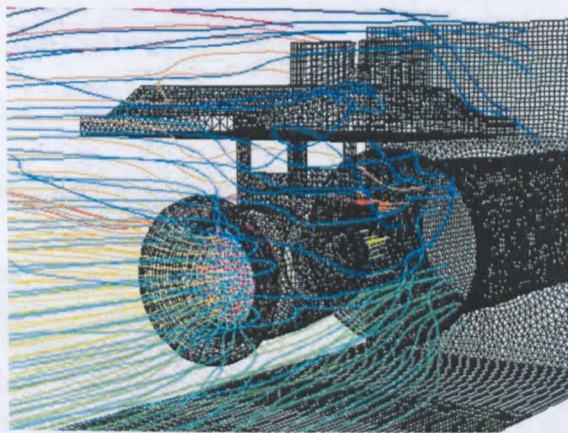


**Figure 6.9: Flow Path around the Engine**

In order to reduce these compromises or concentrate them where it is more convenient the cell volume it has been divided into many volumes.

As an example, Figure 6.10 shows the entire cell and Figure 6.11: Enlargement of Figure 6.10 around the Bellmouth an enlargement around the bellmouth.

The Bellmouth is thought to be a quite sensitive part of the model, indeed following the considerations made in Chapter 4 the force acting on it has to be estimated. So, a quite accurate mesh is needed around the bellmouth. At the same to respect the main compromises stated in paragraph 6.2.2 a very fine mesh scheme can not be used everywhere. Therefore, the density of the cells has to be differentiated. Moreover, not only is the density important but also the shape of the elements is relevant for the calculation. Consequently, several volumes have been generated around the bellmouth. In each of them the grid density is different, decreasing as the elements get further from the body surfaces. The shape of these secondary volumes is important as well. Indeed, if a certain kind of grid needs to be adopted, the shape of the volume is of fundamental importance. This is because, not all the volume shapes can be meshed

with a defined scheme. There are quite a lot of rules to follow in order to apply a defined grid scheme (Fluent incorporated a).

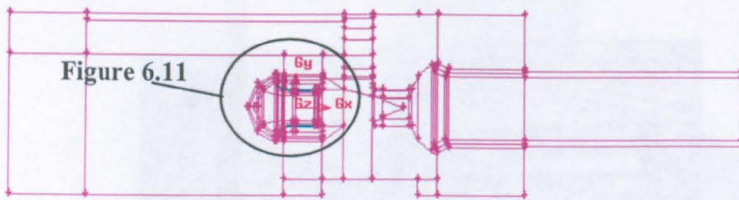


Figure 6.10: Test Chambre Geometry

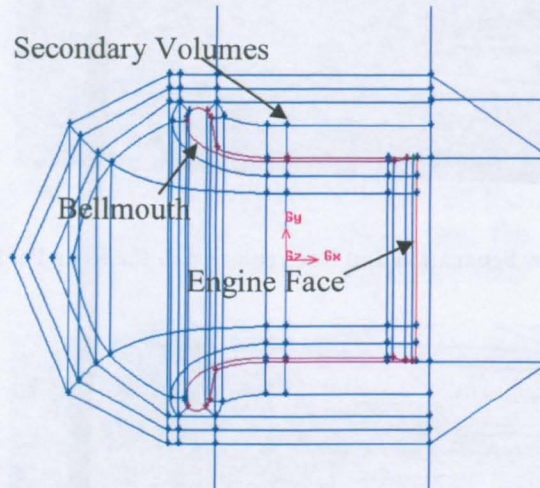


Figure 6.11: Enlargement of Figure 6.10 around the Bellmouth

For the bellmouth, hexahedral elements were used along the surfaces, so the secondary volumes have been drawn keeping in mind all the possible configurations which allow such kinds of elements.

Another consideration can be made concerning the density and the shape of the elements. Indeed in such a big model it is useful to alter the model after convergence is reached. The adaptation process is useful because it allows refinement of the mesh only where it is needed and without making the model too heavy where it is not needed. So, it is suggested to keep in mind since the beginning of the modelling the opportunity of making grid adaptation. Indeed, the shape of the adapted cells it depends on that of the original.

The bellmouth has been taken as an example to illustrate all the compromises involved in a meshing process. At the same time, however, the above consideration can be repeated also for the flow along the detuner where the layer closer to pipe surfaces are more difficult to mesh.

Figure 6.12, shows an overview of the mesh for the entire cell main chamber and Figure 6.13 and Figure 6.14 show two details of the mesh around the bellmouth.

These pictures have been extracted from the last of the model for the engine C in test cell "Y". This model has six million elements.

The geometry and the mesh have been generated using the mesh generator included in the Fluent CFD package, Gambit (Fluent incorporated a).

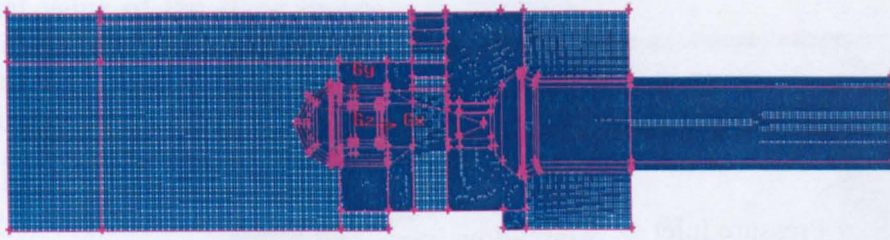


Figure 6.12: Overview of the Mesh for Engine C in Test Cell “Y”

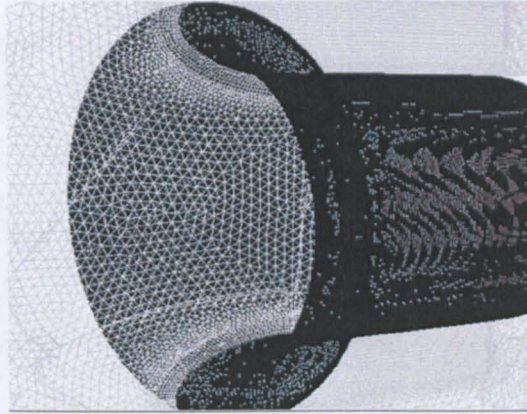


Figure 6.13: Grid around the Bellmouth for Engine C in Test Cell “Y”

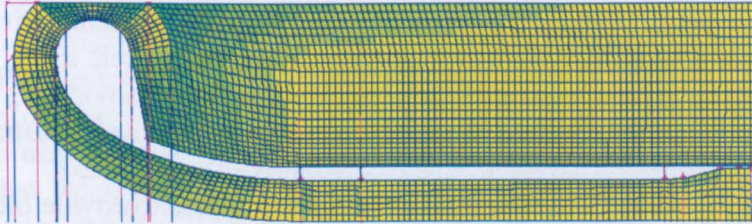


Figure 6.14: Grid around the Bellmouth for Engine C in Test Cell “Y”

#### 6.2.4. Boundary Conditions for Engine C in the Test Cell “Y”

Once the geometry has been drawn and the grid is ready the model can be imported to the solver Fluent.

After checking the scaling processes in Fluent, the model boundary conditions can be set. How the boundary conditions work is well explained in the paragraph dedicated to them in the Fluent Manual (Fluent incorporated b ). Furthermore, in paragraph 6.2.2 has been given an overview about how which boundary conditions are used in this work. Now the boundary conditions are going to be illustrated in relation with the whole test main chamber model. For confidentiality reasons the values used as boundary conditions can not be published.

Figure 6.15 shows the kinds of conditions used.

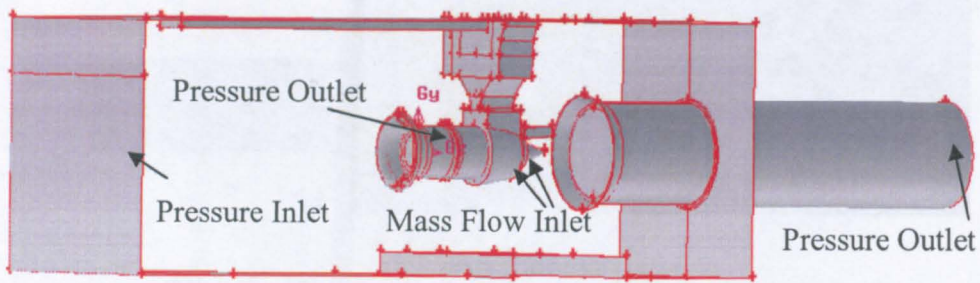


Figure 6.15: Boundary Conditions

At the cell inlet, Pressure Inlet is chosen as inlet conditions. This condition uses the total pressure as main parameter (Fluent incorporated b ) which is experimentally measured inside the cell.

The total mass flow entering the cell needs to be split in two parts, one has to go through the engine and the other has to by-pass the engine and enters the detuner. To achieve this, an outlet flow boundary condition is needed at the engine inlet. Indeed, the flow which is sucked by the engine has to leave the model. At the engine face the static pressure drops due to the increase of flow velocity, and this depression is used as boundary conditions for the computational model. It is worth saying that Fluent does not use any mass flow outlet boundary conditions.

The Pressure Outlet boundary condition uses the static pressure as main parameter for this calculation.

A direct value of the static pressure at the engine face is not provided; consequently it has been derived by an isentropic compressible flow calculation. To do this, the engine mass flow (measured by the airmeter Figure 6.14), the geometric area of the engine face and the total cell temperature (measured at the cell inlet) are needed. Assuming that there are no pressure loss (isentropic flow) it is possible to work out the static pressure by an iterative procedure similar to that one illustrated for the Preliminary Region of the Analytical Ejector model (paragraph 5.2.3).

The static pressure worked out by this methodology does not provide the right mass flow at the engine face as final result of the simulation. Indeed, Fluent works with real flow and therefore takes also into account the pressure losses. Therefore, the value extrapolated from the isentropic flow calculation can be used only as a starting point. Accordingly, at the end of the simulation the static pressure at the engine face has to be readjusted in order to match the real mass flow entering the engine.

So the physical effect of a Pressure Outlet boundary condition at the engine inlet is to generate a depression region, so that a part of the total cell mass flow is allowed to flow through it.

As has already been said, Fluent does not work with mass flow outlet boundary conditions but uses the Mass Flow Inlet. So the same mass flow which has left the model at the engine face has to flow in the model (plus the fuel mass flow) again from the engine nozzles. To simulate this, a Mass Flow Inlet boundary condition has been chosen. By this Condition the mass flow entering the model is fixed and the rest of the parameters can vary in order to match it (Fluent incorporated b ).

The meaning of the last boundary condition at the detuner outlet has been explained in the previous paragraph (6.2.2). This practically represents the handle parameter of a trial procedure whose scope is to match the actual cell entrainment ratio. The

numerical value of the static pressure at the detuner exit is not important for the calculation of the TCF but its influence on the cell mass flow is vital. Due to the strict dependence of the forces acting on the metric assembly on the entrainment ratio, matching the correct proportion of the primary and secondary flow is relevant.

### 6.2.5. *Fluent Settings*

The aim of this chapter is not to show how the Fluent CFD package works and what all the possible options available within it are. So in this paragraph only the main settings chosen for the simulations are listed. In the Fluent Manual (Fluent incorporated b ) more useful information can be found concerning the approaches used for solving the governing equations.

The Segregated solver is used in this set of simulations. Mainly the three solvers used by Fluent (Segregated, Coupled Implicit and Coupled Explicit (Fluent incorporated b ) are valid for a broad range of flows and some advantages can only be seen for highly compressible flows in the use of the Coupled solvers (Fluent incorporated b ). However, at the same time, to solve together all the governing equations for each discrete volume requires more memory than is available. Therefore, due to the model dimensions and with a mesh of six millions elements, the Segregated Solver has been preferred. This implies the use of an implicit linearization of the governing equation. In such a way each “scalar” equation it is solved once a time for all the cells at the same time.

Concerning the Turbulence Model, for memory and time economy the choice has been addressed towards the Reynolds Average Navier-Stokes (RANS) equations. They, compared to the Large Eddies Simulations (LES) equations (the alternative to the RANS), account only for the mean flow quantities including all scales of turbulence. This, especially for steady problems, reduces the computational effort quite a lot. Compared with LES which excludes small scales of turbulence, but computes in a time dependent form the large eddies. This choice has also been driven by the fact that the application of LES to industrial flows has not been extensively used. It has however been used for standard problems.

Inside the RANS configuration the choice of how the Reynolds stresses are represented needs to be made. These so-called Reynolds stresses are additional terms (Fluent incorporated b ) which appear in the governing equations because each single variable of the system has been split into two components, namely the mean and the fluctuating. This approach increases the number of unknown in the system and so requires either new assumptions or new equations to be added.

Two main approaches are offered by Fluent for solving the governing equations with the RANS assumption. The first is the Boussinesq (Fluent incorporated b ) approach and the second is the Reynolds Stress Transport Model. Even though the second is clearly superior and more accurate, it requires a much bigger computational effort (it adds seven more equations to the system). Also the Boussinesq hypothesis (which adds one or two equations to the system) performs very well especially for industrial flows.

Different calculation models use the Boussinesq hypothesis (Fluent incorporated a ). In this chapter, the choice made is justified. The turbulence models which use the Boussinesq assumptions and are available in Fluent are the Spalart-Allmaras, the standard  $k-\epsilon$ , the RNG  $k-\epsilon$ , the realizable  $k-\epsilon$ , the standard  $k-\omega$  and the SST  $k-\omega$ . The main criteria driving such a choice have been the computational effort required and

the reliability of the model. In terms of computational effort, the Spalart-Allmaras model introducing only one equation to the governing equations system is convenient compared to all the others. At the same time, in terms of accuracy by introducing two further equations to the governing system and a higher degree of non-linearity, the other models ( $k-\epsilon$  and  $k-\omega$ ) can provide better results. From the beginning, the choice was oriented towards a two auxiliary equations turbulence model. In terms of CPU the standard  $k-\epsilon$  (as the standard  $k-\omega$ ) model requires 10-15 % time less than the RNG, the Realizable and the SST.

A fundamental parameter which has lead to the choice toward the Realizable  $k-\epsilon$  has been the past application and one of the main purposes of the model. Indeed, the realizable version of the  $k-\epsilon$  model presents substantial improvement in flows with a high degree of stream-line curvature (Fluent incorporated b ). This is thought to be particularly interesting for the determination of the pre-entry force. It is worth remembering that this is the force acting on the pre-entry stream tube. Also such a model is shown to provide more realistic results in the determination of the pressure coefficient along body surfaces. This is also the case for the pre-entry stream tube on the bellmouth. At the end, the larger CPU needed for the  $k-\epsilon$  Realizable has been compromised in favour higher accuracy in the results.

The  $k-\epsilon$  models are primarily for turbulent core flows, ie for the flows somewhat far from the walls. Indeed the turbulence is seriously affected by the presence of the wall in a no-trivial ways. The non-viscous condition impacts in the reduction of the tangential velocity fluctuations and the kinematic blockage impacts in the reduction of the normal velocity fluctuations. As is described in the Fluent Manual (Fluent incorporated b ) this affects the fidelity of the numerical simulations. Practically, in Fluent there are two different ways to face such a problem the Near Wall Treatments and the Wall Functions. Due to the computational effort required by the Near Wall Treatment, which would imply the generation of a specific grid along all the walls, the Wall Function approach has been chosen. The test bed is a very big volume by itself and if the engine is also added it becomes really expensive in terms of the number of elements to generate boundary layer cells everywhere.

This may justify the assumption of using the semi-empirical formulations enclosed in the Wall Functions approach

Fluent offers the choice between two different Wall Function formulations, the standard and the non-equilibrium. The first is more robust and economic in terms of calculation the second is particularly good for situations where the flows depart from the standard equilibrium conditions, such as flow separation. In the test bed case previous model have not shown big separations from the surfaces especially from those of interest in the TCF calculation. This led the choice toward the Standard Wall Functions.

The Wall Functions treatment is very useful but it should not be forgotten that their validity is strictly connected to the  $y^+$  parameter (Fluent incorporated b ). So an estimation of the  $y^+$  has to be made when the simulation has converged. If it is out of the range of validity some grid adaptations has to be made.

### ***6.2.6. Step-by-Step Approach for the Discretization***

By default, in Fluent the discretization process which converts the governing equations into algebraic equations is set at the first order. So the numerical values at the faces of the cells are calculated from those at the centre by linear equations. In



order to improve the accuracy of the solution this calculation can also be done using a second order scheme by a Taylor series expansion (Fluent incorporated b ).

In general, better results are obtained with the second order of discretization when the flow is not aligned with the grid. Therefore, it is especially useful when, tetrahedral cells are used. At the same time the convergence of the model slows down with a second order of discretization. It is also possible that the same model which has already converged using the first order does not converge with the second order. This makes the discretization process quite sensitive.

It is highly recommended to use the second order of discretization for compressible flows.

The main equations which need to be discretized are the momentum and the continuity. However the discretization process also involves the scalar equations as the kinetic turbulence (in this work k), the turbulence dissipation ( $\epsilon$ ) and the energy equation. Furthermore, the pressure and the density interpolation schemes can be included in the discretization process. It is worth saying that the interpolation of the density comes as result of the discretization of the continuity equation. So the continuity equation is not listed in fluent between the discretization parameters.

As has already been said above, a change to the second order discretization may result in convergence difficulties. So to overcome this, a step-by-step approach is used. The first run of the model uses first order for all the terms until it has converged. Once the first solution is obtained, pressure, density and momentum equations are changed to second order and the model is allowed to run until it converges. After that the two turbulence equations are changed to second order and the final model is run until it also converges.

Now that also the step-by step approach has been introduced it is probably clearer all the labour which needs to be done to match the right cell entrainment ratio, as was attempted to be explained in paragraph 6.2.2.

### 6.2.7. Convergence Criteria

For all the CFD run the main convergence criteria used in this work is the default residual at single precision.

This means that a model has converged when continuity, x velocity, y velocity, z velocity, k and  $\epsilon$  residual have reached 0.001 and the energy 0.000001.

After the discretization the generic variable  $\xi$  at a cell q can be written as equation (6.1) (Fluent incorporated b )

$$a_q \xi_q = \sum_{nb} a_{nb} \xi_{nb} + c \quad (6.1)$$

Following the above definition for the Segregated Solver Fluent defines the scaled residual as equation (6.2)

$$R\phi = \frac{\sum_{cells-q} \left| \sum_{nb} a_{nb} \xi_{nb} + c - a_q \xi_q \right|}{\sum_{cells-q} a_q \xi_q} \quad (6.2)$$

Instead, for the continuity equations the scaled residual defined by Fluent is defined as equation (6.3). Where, the denominator is the largest of the continuity residual in the first five iterations.

$$R^c = \frac{\sum_{\text{cells}-q} |\text{rate of mass criteiron in cell } q|_{\text{iteration } N}}{\sum_{\text{cells}-q} |\text{rate of mass criteiron in cell } q|_{\text{iteration } 5}} \quad (6.3)$$

### 6.2.8. Pre-Entry Force Calculation Methodology by Using CFD

The pre-entry force has already been defined in Chapter 4 paragraph 4.3.7. In this paragraph a quantitative estimation of the pre-entry force is made using CFD.

It is worth remembering that the engine simulated is the Rolls-Royce engine C and the cell is the Rolls-Royce test bed Y. The data shown here are extracted from a model which matches the cell entrainment ratio experimentally measured. It also uses as boundary conditions the same engine and cell conditions used for the thrust correction equations comparison proposed in paragraph 4.5.4.

Indeed a comparison between one dimensional gas dynamics and CFD will be made.

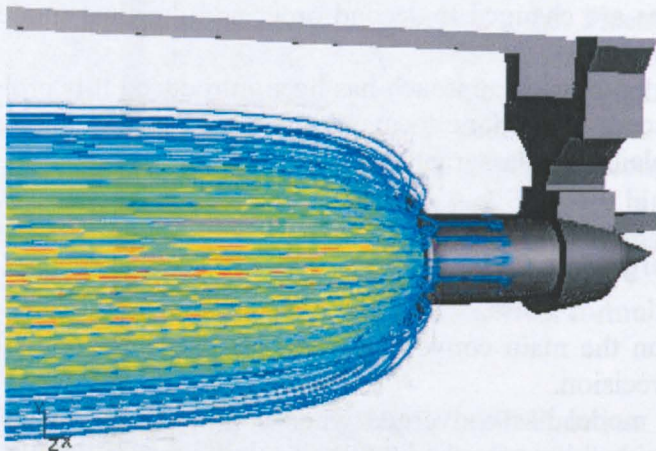


Figure 6.16: Pre-Entry Stream Tube

As far as the author is aware a direct calculation of a force acting on a stream tube is not possible by the standard post-processing Fluent tools. Indeed, the pressure field's integration surfaces are not solid and further more their shape and dimensions are unknown until the simulation has converged. Figure 6.16 shows the shape of the pre-entry stream tube for the model under study.

It is possible to see that due to the flow velocity up-stream of the engine the stream tube shape in suction conditions. The cell conditions such as density and velocity, allow for the engine mass flow a larger cross sectional area than the bellmouth sectional area. This means that the stream tube must have a convergent shape to carry the air through the engine.

Since a direct calculation is not allowed with Fluent, some assumptions have to be made in order to define a way of calculating such a force. The first assumption is that each path line, which defines the stream tube boundary, belongs to a single

longitudinal plane. In order to understand this assumption, it is probably better to start to describe the procedure used for the calculation of the pre-entry force.

The starting point of the calculation is the definition of the stream tube boundary with CFD. Such a stream tube starts from the bellmouth surfaces, where it defines a stagnation region and develops up-stream (it could also be said that it starts up-stream the engine and end up on the bellmouth surfaces with a stagnation region). A generic stagnation region is characterized by a reduction of the velocity until it becomes zero at the walls. This corresponds to an increase of the static pressure which on the wall will match the value of the total pressure (stagnation pressure). The starting point to define the pre-entry stream tube is to spot the stagnation region around the bellmouth.

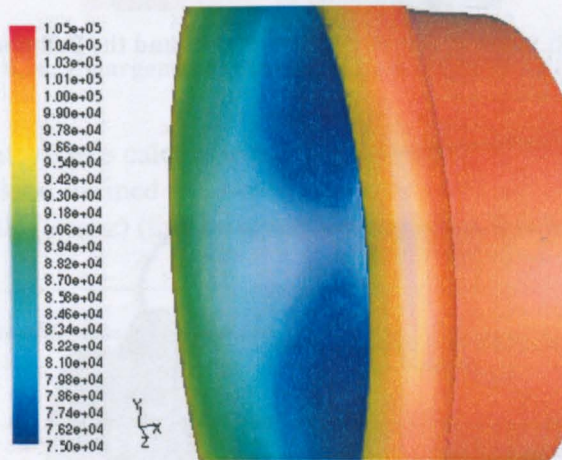


Figure 6.17: Static Pressure Contour around the Bellmouth

Figure 6.17 shows the static pressure contour for the bellmouth. Entering the bellmouth the engine mass flow starts to accelerate due to the reduction in cross sectional area available. This implies a significant drop in static pressure as is shown in the figure. At the same time the secondary flow due to the shape of the bellmouth diffuses around it. Between these two regions there is on the bellmouth, another region where the static pressure has reached the stagnation value and the flow is stationary.

Figure 6.18 shows the static pressure contour around the bellmouth lip. Now, the pressure field is clearer and it is also possible to see the increase of static pressure, which goes from the green field to the gold.

Figure 6.18 also shows the grid used to simplify the identification of the static pressure peak.

The static pressure field is the plot used to identify the stagnation pressure region.

Once the stagnation region has been identified it is possible to visualise the pre-entry stream tube.

Indeed, using Fluent, the flow path lines (Fluent incorporated b) can be released in reverse mode (opposite to the main direction of the flow). This is also shown in Figure 6.16.

However, it is not permissible to release the path lines from one single point. Accordingly, a rake traversing the stagnation point has been drawn and the path lines have been released from there. This is shown in Figure 6.19 and Figure 6.20.



**Figure 6.18: Static Pressure Distribution around the Bellmouth Lip**

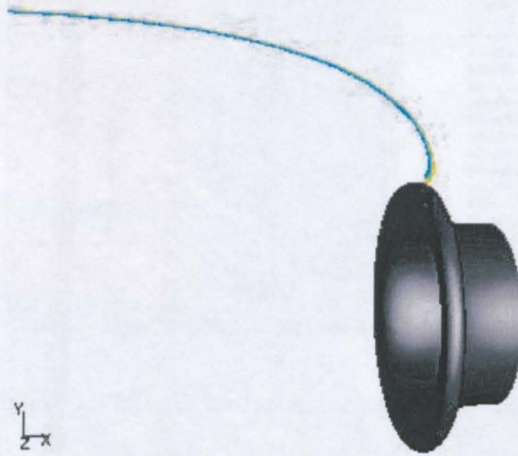


**Figure 6.19: Flow Path Lines Released from the Rake**

From each path line released from the rake it is possible to extract by Fluent all the geometric and flow parameters for each grid node crossed by it. For example, it is possible to extract the coordinates of such nodes, the static and total pressures, etc.

All the information extracted is in the form of text files which can easily be read by common software.

Once the rake's path lines are plotted in numerical maps, it is easy to understand which defines the pre-entry stream tube boundary.

As is possible to imagine, these path lines do not belong to a single longitudinal plane. Indeed, there could be a small distortion due to the interaction between the flow and the walls of the cell.

The first assumption made at the beginning of this paragraph is related to this flow behaviour.



Figure 6.20: Enlargement of the Flow Path Lines From the Rake

Indeed for the pre-entry force calculation the stagnation path line has been assumed to belong to a single plane defined by the engine axis (axis x) and the vertical axis (y axis) or the transversal (axis z) (these are the axes defined in Figure 6.16).

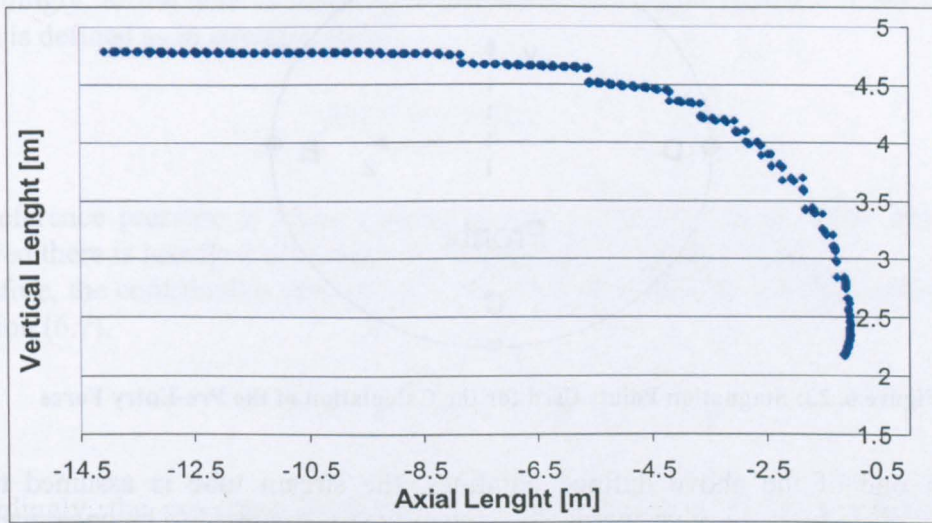


Figure 6.21: Coordinate of the Stream Line which Defines the Pre-Entry Stream Tube

Figure 6.21 shows the plots of the co-ordinate values extracted from Fluent in the longitudinal symmetric cell plane (x and y).

Following the above indications it is possible to plot in a way similar to Figure 6.21 also the other flow parameters such as the gauge static pressure (different plotting will be shown later on).

In terms of TCF only the axial component of the force acting on the pre-entry stream tube is needed.

To find out this value a numerical method it has been developed.

Each single path line is discretized using the same discretization used by Fluent for the calculations. Indeed the grid nodes have been used to divide the path line in several segments (Figure 6.22).

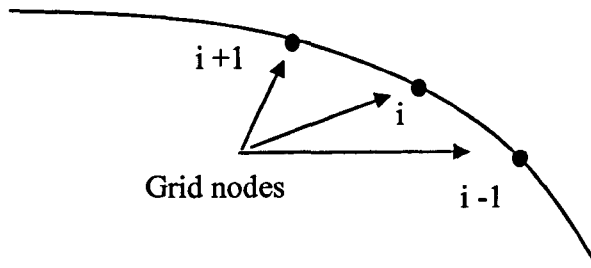


Figure 6.22: Discretization of the Stream Line

Before describing the numerical integration it is worth stating the second main assumption used for the calculation of the pre-entry force.

The exact calculation of such a force would require the integration of static gauge pressure field all along the boundary surface of the stream tube.

At the moment this integration is made using the static pressure field extracted by four stagnation path lines. These path lines are released from four different stagnation points (A, B, C and D) symmetrically disposed with respect to the engine axis (Figure 6. 23)

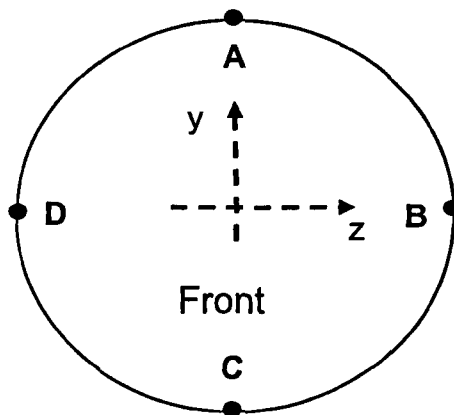


Figure 6. 23: Stagnation Points Used for the Calculation of the Pre-Entry Force

For each one of the above defined pathlines, the stream tube is assumed to be uniformly made by it. In other words, the stream tube is assumed to be once made by all path lines like A (released from A), once by all path lines like B (released from B), once by all path lines like (released from C), and once by all path lines like D (released from D).

For each one of these cases a pre-entry force is calculated by the procedure defined below.

Finally, the average of the four forces is taken as the estimation of the pre-entry force. By definition the gauge pre-entry force is defined as the integral of the gauge static pressure along the axially projected area of the stream tube (equation (6.4)).

$$\phi_{Gpre} = \int_{stream-tube} (p - p_0) dA \quad (6.4)$$

The first step of the numerical integration is to associate at each node of the discretization a projected area.

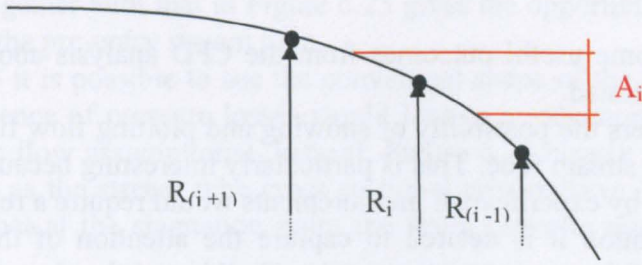


Figure 5.24: Area Associated at each Discretization Point

Figure 6.22 and Figure 5.24 show three different nodes with their respective radii. The area associated with each of them is defined by the following equation (6.5)

$$A_i = \left\{ \left[ \left( \frac{R_{i+1} - R_i}{2} \right) + R_i \right]^2 - \left[ \left( \frac{R_i - R_{i-1}}{2} \right) + R_{i-1} \right]^2 \right\} \pi \quad (6.5)$$

In such a way is defined an under discretization which reduces the area associated to each node of the discretization.

Accordingly, to the area element  $A_i$  is associated the gauge pressure of the node (i) which is defined as in equation (6.6).

$$p_{Gi} = (p_i - p_0) \quad (6.6)$$

The reference pressure is taken 15m up-stream of the stagnation point, where it is believed there is less flow distortion due to the presence of the engine.

Therefore, the contribution given by the node (i) to the pre-entry force is estimated in equation (6.7).

$$\phi_{Gpre-i} = (p_i - p_0) A_i \quad (6.7)$$

Accordingly, the pre-entry force associated with the path line which the node (i) belongs to is represented by equation (6.8) (which refers to the stagnation path line of kind A)

$$\phi_{Gpre-A} = \sum_{i=1}^n \phi_{Gpre-i} = \sum_{i=1}^n (p_i - p_0) A_i \quad (6.8)$$

The above procedure is repeated for the four path lines used for this estimation and finally the value of the pre-entry force is given by the equation (6.9).

$$\phi_{Gpre} = \frac{\sum_{j=A}^D \phi_{Gpre-j}}{4} \quad (6.9)$$

### 6.2.9. Pre-Entry Stream Tube CFD Considerations

In this paragraph some useful outcomes from the CFD analysis about the pre-entry stream tube are illustrated.

Indeed the CFD offers the possibility of showing and plotting flow fields around and across the pre-entry stream tube. This is particularly interesting because the provision of such information by experimental measurements would require a really huge effort. As a first consideration it is desired to capture the attention of the reader to the effective structure of the pre-entry stream tube. To this end the above analysis for the calculation of the pre-entry force is used.

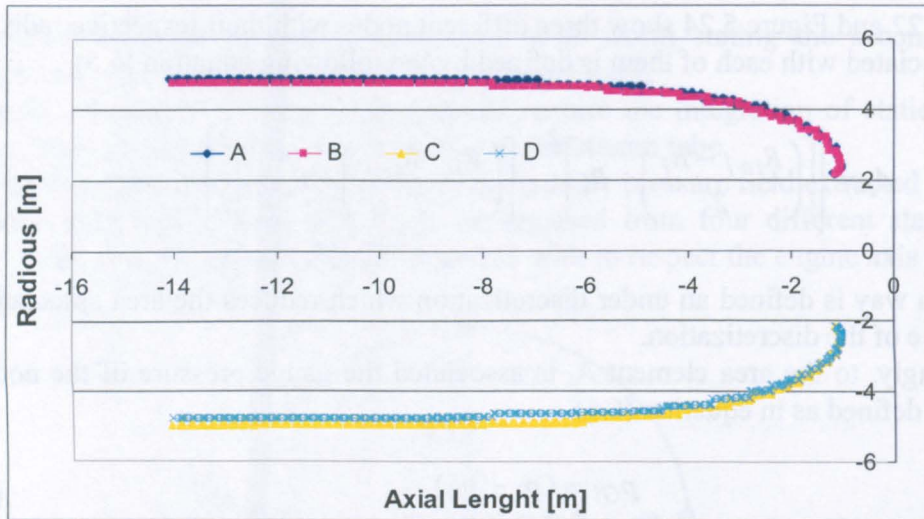


Figure 6.25: Pre-Entry Stream Tube Dimensions

Figure 6.25 shows the radial dimensions of the pre-entry stream tube by the four stagnation path line defined in the previous paragraph. This plot does not offer a lot of to say, but it is important to visualize the pre-entry stream tube and to understand better the following plots.

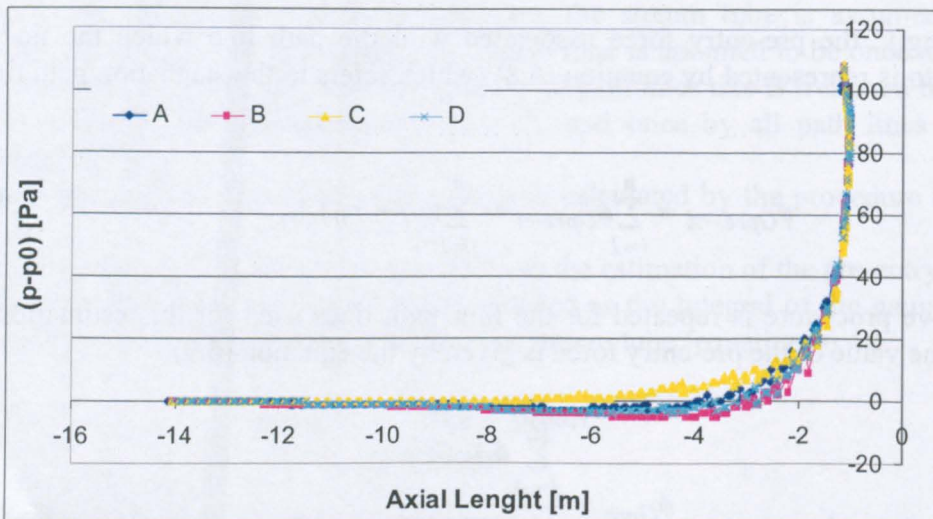


Figure 6.26: Gauge Static Pressure along the Stagnation Stream Lines



Figure 6.26 shows the trends of the gauge static pressure for the four stagnation path lines. This plot together with that in Figure 6.25 gives the opportunity to visualize the flow structure of the pre-entry stream tube.

From Figure 6.25 it is possible to see the convergent shape of the stream tube which assuming the absence of pressure losses would lead to a reduction of static pressure (by the isentropic flow assumptions). Instead, Figure 6.26 clearly shows an increase of static pressure as the stream tube cross sectional area reduces. This is essentially due to the fact that at the stagnation point the static pressure must match the total pressure.

Such a trend makes the pre-entry stream tube a difficult region to understand and consequently the pre-entry force difficult to calculate.

It is also interesting to visualise the flow field across the stream tube. Indeed, the boundary walls of the pre-entry stream tube also represent the equilibrium region between the primary and secondary flows.

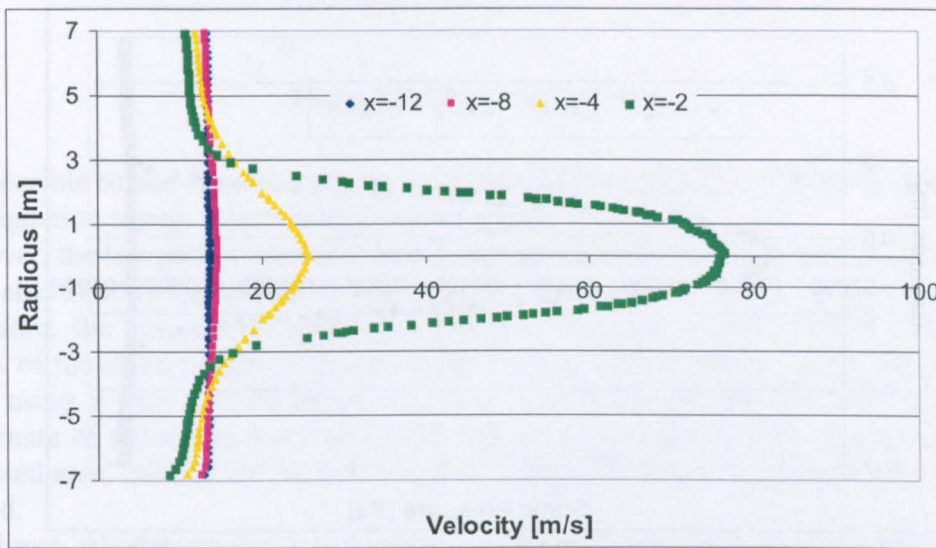


Figure 6.27: Velocity Plots across the Pre-Entry Stream Tube

To analyse the flow field across the stream tube it has been necessary to draw some vertical lines (Fluent incorporated b) through the stream tube and plot along them the flow parameters. Figure 6.27 shows the velocity field across the stream tube for different lines at different distances from the engine (the distance from the engine can be clearer understood by combining Figure 6.27 with Figure 6.25). Moving towards the engine the velocity of the flow inside the stream tube increases, as already stated above. However, it is interesting to note that from the cell walls the velocity gradient of the primary and secondary flows grow uniformly. This can be better seen if the two figures are superimposed. Figure 6.28 is an experimental superimposition of Figure 6.27 and Figure 6.25. Such a representation can be misleading but shows clearly that the velocity gradient grows uniformly from the cell walls. In a way, this could also be seen as flow uniformity across the stream tube.

The same outcomes can also be drawn when looking at the plot of the static pressure across the stream tube (Figure 6.29). The pressure gradient across the stream tube is uniform.

This means that in these engine and cell conditions, the pre-entry flow is not affected by the interaction with the cell which could destabilise the equilibrium of primary and secondary flows along the stream tube.

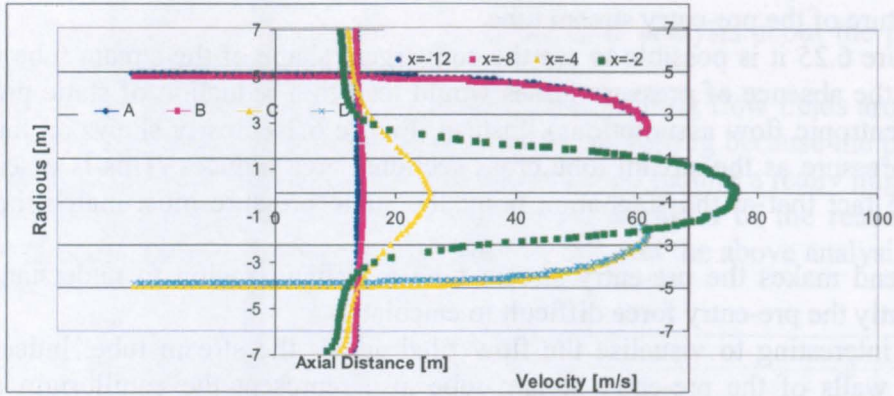


Figure 6.28: Superimpose of Figure 6.25 and Figure 6.28

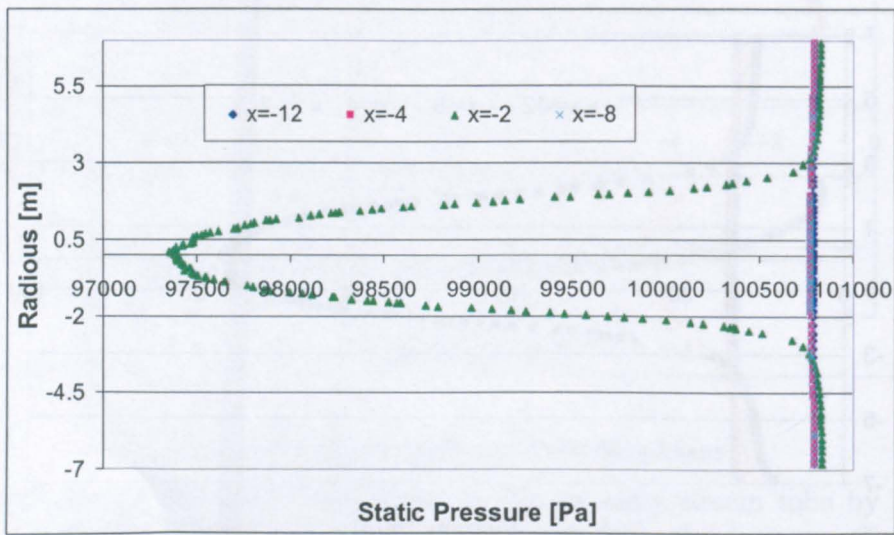


Figure 6.29: Static Pressure Plots across the Pre-Entry Stream Tube

### 6.2.10. Bellmouth Force Calculation Methodology by CFD

In order to compile the TCF equations defined in Chapter 4 two different bellmouth gauge forces have to be defined. Indeed, in equation (4.87) only the external bellmouth force is needed whilst in equation (4.126) the whole bellmouth force must be accounted for.

In paragraph 4.3.7 it has been underlined that in order to calculate the external bellmouth force it is necessary to spot the stagnation region on the bellmouth lip.

How such a region is identified has been said in paragraph 6.2.8.

However, it is worth remembering that the stagnation region can not be defined a priori before the simulation has converged.

This does not allow the division of the bellmouth in opportune surfaces which would suit a direct calculation of the external bellmouth force using Fluent (Fluent incorporated b).

Therefore, some assumptions have also to be made for the bellmouth external force.

Such a problem was known before starting the modelling. Therefore, the bellmouth model has been divided into several surfaces. In this way for the larger part of the bellmouth, the force acting on it can be calculated directly by Fluent integrating the

gauge pressure on the defined surfaces. Figure 6.30 shows the surfaces into which the bellmouth is separated externally.



Figure 6.30: Bellmouth Surfaces

It is possible to see several surfaces have been generated on the bellmouth lip where the stagnation region was expected to be located.

However, the last part of the bellmouth force, around the stagnation region, can not be calculated directly by the Fluent integration tools.

Therefore, the assumption made was that of extracting manually from Fluent the values of the static pressure. These values are extracted from the grid nodes (Figure 6.18) using a very narrow range of limits. Together with the pressure values the coordinate of the nodes were also extracted in order to allow the calculation of the projected area. Indeed, for the bellmouth also, only the axial component of the force is needed.

The direct calculation of the gauge forces by Fluent includes the integration of the gauge static pressure on the entire three-dimensional surfaces (Fluent incorporated b). Instead, manually the gauge static pressure values have been extracted only from one side of the bellmouth and afterwards averaged (arithmetically).

$$\phi_{G_{bell-lip}} = \frac{\sum_{i=1}^n (p_i - p_0)}{n} A_{lip} \quad (6.10)$$

Equation (6.10) summarises the above calculation  $A_{lip}$  represents the axially projected area of the bellmouth lip, from the know surface up to the stagnation point and  $n$  is the number of the node in such a space.

At the same time the gauge force acting on the entire bellmouth is calculated directly using the Fluent integration tools.

From the previous plot of Figure 6.17 it is expected to find the force acting on the internal part of the bellmouth directed in the up-stream direction (due to the depression represented on that figure). In addition there is another force acting on the external part of the bellmouth and directed in the up-stream direction (due to the flow diffusion described above).

### 6.2.11. Base Force Calculation Methodology by Using CFD

The ejector pump effect generated by the interaction between the engine exhausts and the detuner (described in Chapter 5) gives rise to a low pressure region around the engine afterbody. Such a depression sucks the engine backward and affects the thrust measured by the load cells.

One-dimensional gas dynamics can be easily used to estimate the base force. This is because the pressure field around the engine afterbody can not be computed.

Accordingly, the comparison with the CFD result and the one-dimensional result is made using the experimental results.

Indeed, by the First Principle Anemometer (paragraph 2.3.2), the static pressure around the engine afterbody is directly measured by a piezo-ring and the twelve static probes fitted on the outside of the fan duct (paragraph 2.3.2).

Accordingly, experimentally the axial base force is measured by the product of these static pressure measurements and the axial projected area of the fan duct (equation (6.11) where  $n$  is the number of static pressure measurements and  $A_{base}$  is the projected area of the fan duct).

$$\phi_{Gbase} = \frac{\sum_{i=1}^n (p_i - p_0)}{n} A_{base} \quad (6.11)$$

The engine inside the cell is tested without the nacelle and this makes the definition of the exact engine shape quite difficult especially for the fan duct which starts from the engine face and ends at the cold nozzle.

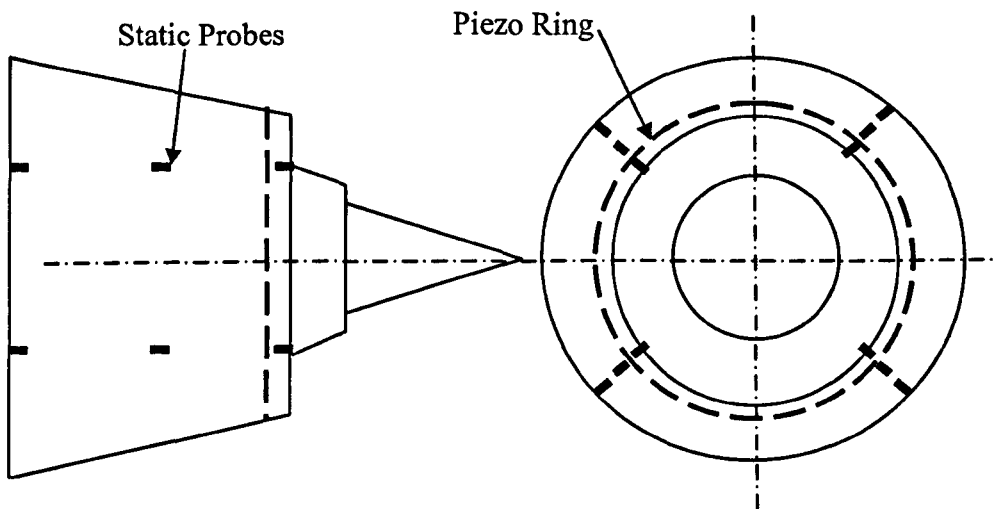


Figure 6.31: Location of the Static Pressure Probes during the Experimental Tests

The CFD model has been drawn using a singular regular surface for the engine body, with respect to the engine face and the nozzle dimensions.

This does not allow the comparison of the experimentally measured force directly with that integrated by Fluent tools. Indeed, the axial projected area used by Fluent

can be different from that used for the experimental calculation (only the fan nozzle projected area).

For this reason in this work a comparison between the experimental and the computed static pressure field is made.

However, this comparison can estimate the CFD capability of representing the suction force on the engine afterbody during an indoor test and it opens the door to further geometric refinement.

Figure 6.31 shows the location of the static pressure probes during engine tests.

Figure 6.32 shows the static pressure field around the fan duct from the computational model. Also illustrated is the location of the piezo-ring in the CFD model.

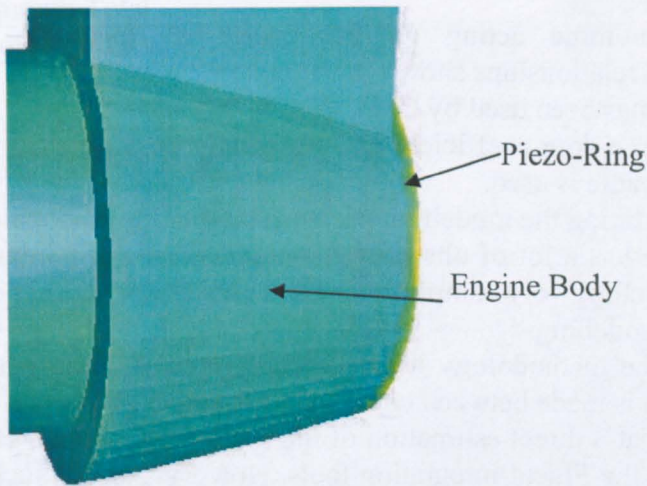


Figure 6.32: Static Pressure Contour along the Fan Duct

### 6.2.12. IMD Calculation Methodology by Using CFD

In the thrust correction one-dimensional analysis the intake momentum drag has been evaluated assuming a known entrainment ratio.

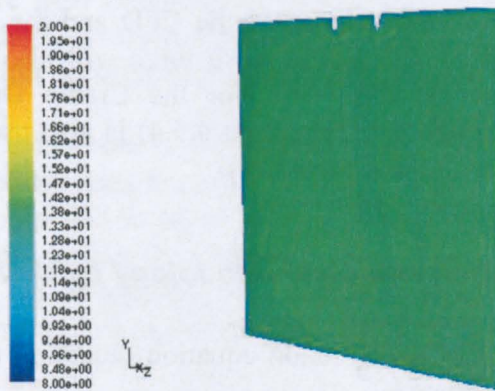


Figure 6.33: Velocity Profile 15m Up-Stream the Engine

Accordingly, with the definition of  $\mu$ , it is possible to derive the total mass flow entering the cell and therefore the flow velocity in a plane up-stream of the engine. Accordingly, the flow velocity up-stream of the engine has been calculated by a mass weighted average integration (Fluent incorporated b). In particular, such a velocity has been calculated at the same plane as the static reference pressure has been evaluated.

Figure 6.33 shows the pressure profile at such a plane. It is possible to see that the flow is quite uniform; this is a consequence of using only the main test chamber for the simulation.

### **6.2.13. Cradle Drag Calculation Methodology by Using CFD**

Experimentally the force acting on the cradle is calculated using velocity measurement by the relationships shown in paragraph 2.3.2.

The same approach has been used by CFD.

Accordingly, the same drag coefficient experimentally used for the evaluation of the drag acting on the cradle is used.

Particular attention during the modelling has been paid to the cradle blockage area.

In reality the cradle has a lot of obstructions mounted around its main frame which make its actual modelling very complicated. Such obstructions have been neglected in the computational modelling.

Accordingly with the methodology followed for the cradle drag evaluation, a flow velocity comparison is made between computational and experimental values.

It is worth saying that a direct estimation of the force acting on the cradle could also have been made by the Fluent integration tools. However, to use such a method it is necessary to have a very fine mesh which respects all the constraints due for the flow calculation around the walls (Fluent incorporated b ). In a model as big as the test facility such constraints would lead to a huge number of cells which would throw off-balance the main compromise made at the beginning of this chapter.

For this reason a direct calculation of the force on all the model's walls has been avoided.

However, particular attention has been paid to the bellmouth force. In particular, a very fine mesh has been generated around it which could lead to the evaluation of the force by a direct integration.

The same approach for assessing the validity of the CFD and the one dimensional thrust correction factors analysis used for the base force will also be used for the cradle drag. Therefore, the same value used for the Cradle Drag in the one-dimensional thrust correction equations (paragraph 4.5.4) is also used for compiling the thrust correction equations with the CFD results.

### **6.2.14. Throat Force Calculation Methodology by Using CFD**

In order to compile the throat thrust correction equation (equation (4.126)) also the gauge stream force has to be evaluated.

This has been done by extracting from Fluent the values of the static pressure and the velocity.

With these two parameters a direct estimation of the gauge throat stream force can be made.

### 6.2.15. CFD Thrust Correction Factors Results

The different methodologies used for extracting the thrust correction factors from the computational model have been illustrated above.

In this paragraph the thrust correction factors calculated by CFD will be tabulated and used for compiling the thrust correction equations derived in Chapter 4.

Parameter	Value
$v_0$	13.383 m/s
IMD	17170 N
$v_{th}$	173.49 m/s
$F_{GTH}$	103851 N
Bellmouth Total	90876 N
Bellmouth External	836,97 N
Pre-Entry Force (A)	1452 N
Pre-Entry Force (B)	1274 N
Pre-Entry Force (C)	1502 N
Pre-Entry Force (D)	1400 N
Pre-Entry Force Average	1407 N
p base nacelle	100700 Pa
p piezo-ring	100543 Pa
Base Force (p nacelle)	342 N
Base Force (p ring)	969 N
$v_{cradle\ CFD}$	8 m/s
$\Delta p_{cradle\ CFD}$ (equation (2.10))	38.95 Pa
$D_{cradle\ CFD}$	845 N

Table 6.1: CFD Thrust Correction Factors

The same assumptions used for compiling the thrust correction equations with the thrust correction factor calculated from the one-dimensional analysis are also used with the CFD results (paragraph 4.5.3).

The same buoyancy terms calculated in Table 4.4 are also used with the CFD data.

As already said in the above paragraphs the experimentally derived Cradle Drag and the Base Force are used also with CFD results for compiling the thrust correction equations (it was the same also for the comparison in paragraph 4.5.4).

The thrust correction equations compiled using the CFD results are equations (4.79) (4.87) and (4.126).

In order to have a better view of these equations, those used in paragraph 4.5.4 for the one-dimensional comparison are reproduced here.

The first to be completed is equation (4.79). Following the above assumptions the term  $D_{metric}$  will only include the Cradle Drag.

From equation (4.79) the term  $F_{G9}$ , which is the real unknown of any thrust correction equation can be written in a explicit form as in equation (4.169) (here renamed (6.12))

$$F_{G9} = L + F_{G0} + D_{metric} - (F_{G9'} - F_{G0})_{ext\ pot} + \phi_{Gbase} \quad (6.12)$$

Expressing the thrust correction factors in terms of percentage of the load measured by the load cell it is possible to obtain equation (4.170) (here renamed as equation (6.13)).

$$\frac{F_{G9}}{L} = 1 + \frac{F_{G0}}{L} + \frac{D_{metric}}{L} - \frac{(F_{G9'} - F_{G0})_{ext\ pot}}{L} + \frac{\phi_{Gbase}}{L} \quad (6.13)$$

Substituting the corresponding values from Table 6.1 into equation (6.13) and using  $A_9 = A_9$  for computing the potential buoyancy term it is possible to obtain

$$\frac{F_{G9}}{L} = 1.041962 \quad (6.14)$$

Using  $A_9 = A_f$  for computing the potential buoyancy term the thrust correction equation (6.13) gives as result

$$\frac{F_{G9}}{L} = 1.042771 \quad (6.15)$$

It is worth to underline, also in this paragraph, that in the above thrust correction equation the contribute of the external part of the bellmouth to the  $D_{metric}$  has been neglected (paragraph 4.5.3)

The next equation to be completed is equation (4.87) which can be expressed by using the base force and, neglecting the carcass drag, as equation (4.173) (here renamed as equation (6.16))

$$L = F_N + \phi_{pre} - \phi_{bell\ ext} - \phi_{base} - D_{cradle} + (F_{G9'} - F_{Gf})_{ext\ pot} \quad (6.16)$$

Expressing equation (6.16) in the same form as equation (6.13) it is possible to obtain equation (6.17)

$$\frac{F_{G9}}{L} = 1 - \frac{\phi_{pre}}{L} + \frac{\phi_{bell\ ext}}{L} + \frac{D_{cradle}}{L} + \frac{\phi_{base}}{L} - \frac{(F_{G9} - F_{Gf})_{ext\ pot}}{L} \quad (6.17)$$

Substituting the values of Table 6.1 into equation (6.17) and using the assumption of  $A_9 = A_9$  for computing the potential buoyancy term it is possible to obtain

$$\frac{F_{G9}}{L} = 1.043192 \quad (6.18)$$

Using  $A_9 = A_f$  for computing the potential buoyancy term the thrust correction equation (6.17)(6.13) gives as result

$$\frac{F_{G9}}{L} = 1.043145 \quad (6.19)$$

The next equation to be completed is equation (4.126). This equation similarly to equation (4.87) can be written by using the base force and neglecting the carcass drag as equation (4.177) (here renamed (6.20))



$$L = F_{G9} - F_{Gth} - \phi_{bell} - \phi_{base} - D_{cradle} + (F_{G9'} - F_{Gf})_{ext\ pot} \quad (6.20)$$

Expressing equation (6.20) as equations (6.13) and (6.17) it can be obtained

$$L \frac{F_{G9}}{L} = 1 + \frac{F_{Gth}}{L} + \frac{\phi_{bell}}{L} + \frac{\phi_{base}}{L} + \frac{D_{cradle}}{L} - \frac{(F_{G9'} - F_{Gf})_{ext\ pot}}{L} \quad (6.21)$$

Completing equation (6.21) with the values of Table 6.1 and using the potential buoyancy from station (f) to station (9<sub>ext</sub>) with A<sub>9<sub>ext</sub></sub>'=A<sub>9<sub>ext</sub></sub> it has been obtained

$$\frac{F_{G9}}{L} = 1.038128 \quad (6.22)$$

At the same time using for the potential buoyancy factor A<sub>9<sub>ext</sub></sub>'=A<sub>f</sub> it can be obtained

$$\frac{F_{G9}}{L} = 1.03808 \quad (6.23)$$

### 6.3. CFD Study of the Engine-Detuner Ejector Pump

The main purpose of using the CFD to study the ejector pump effect in indoor test bed facilities is to understand how the flow in the Accommodation Region is affected by the cell configuration.

The uniqueness of the engine-detuner characteristic curve at the Accommodation Region is a fundamental requirement for the analytical matching procedure described in Chapter 5. Therefore, the CFD has been chosen to represent different engine cell configurations and to analyse for each the flow in the Accommodation Region.

Below, the different cell configurations studied are presented and the engine-detuner ejector characteristic derived for all of them.

#### 6.3.1. CFD Approach and Methodology to Study the Accommodation Region

The main idea is to study how the engine-detuner characteristic in the Accommodation Region is affected by the cell configurations. To achieve this, different cells are modelled, always using the same engine power setting.

One of the main parameters used for the analytical procedure in the Accommodation Region is the detuner diameter. This is the key cell parameter. Indeed, the entire definition of the engine-detuner characteristic depends on the detuner diameter.

Therefore, this parameter is considered fixed during this study.

Furthermore, the detuner diameter even in reality can not be changed unless the whole detuner is replaced. So the detuner diameter is not included within the definition of different cell configurations in this chapter.

At the same time there are other ways to alter the cell configuration. In this work two of them are taken into account. They are the cradle dimensions and the detuner length.

With the former, it is necessary to show the effects on the engine-detuner characteristic at the Accommodation Region of the cell configuration up-stream of both the engine after-body and the detuner.

With the second, it is necessary to show the effects on the engine detuner characteristic of the flow down-stream of the detuner. In particular with different detuner lengths, it can be shown how the level of mixing along the detuner affects the engine-detuner characteristic.

In other way, the detuner length could also represent different exhaust configurations. Therefore, with the help of CFD, different cradle configurations and different detuner lengths are simulated in the indoor test facility. After the simulations have converged,, the Accommodation Region is analysed and the ejector performance parameters at such a region are plotted.

The CFD calculations are also used to derive the engine-detuner characteristic in the Accommodation Region for the original engine and cell configuration.

To achieve this result by Fluent the same approach has been used as shown in the previous paragraph. The static pressure at the outlet of the detuner is varied in order to allow different secondary mass flows to enter the cell. Consequently, the ejector pump operating point will move along its characteristic which will be thereby defined.

Accordingly, the ejector performance derived for different cell configurations (cradle and detuner lengths) is plotted in the same map with the defined computational engine-detuner characteristic in the Accommodation Region. In this way it is shown that such a characteristic curve is still valid for different cell configurations.

At the same time, this characteristic is compared with the one analytically derived in Chapter 5.

It is worth saying again that for this analysis the engine power setting is always kept constant. The engine and the cell used for the simulations are the Rolls-Royce engine A and the test bed cell "X".

### 6.3.2. CFD Models for the Accommodation Region Analysis

In order to study how different cell configuration affect the flow field in the Accommodation Region several models have been created.

As already said in the paragraph above, the first scope of this analysis was to reproduce by CFD the engine-detuner characteristic in the Accommodation Region.

Therefore, a model representing the main test chamber of the engine A in test bed "X" was created (Figure 6.34).

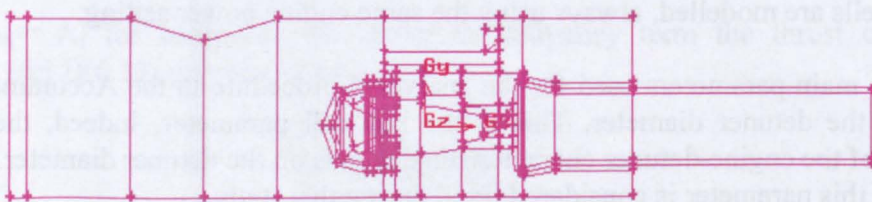


Figure 6.34: Model of Test Cell "X" Main chamber

It is interesting to note the V section up-stream of the engine (Figure 6.35). This section is used to improve the accuracy in the flow measurement within the cell.

Also the cradle is different from that of test bed Y but the criterion adopted for representing it is the same, i.e. matching real blockage area.

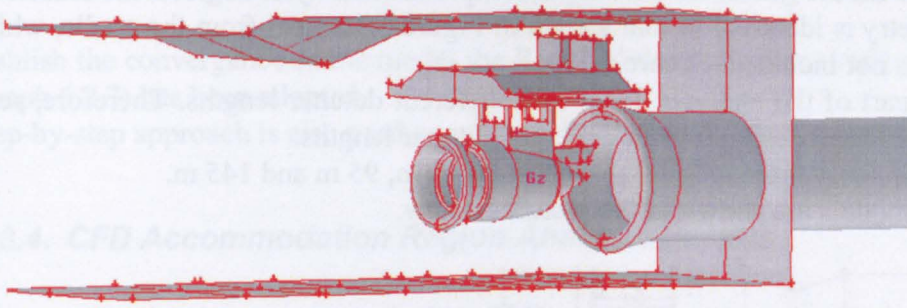


Figure 6.35: Model of Test Cell "X" Main Chamber

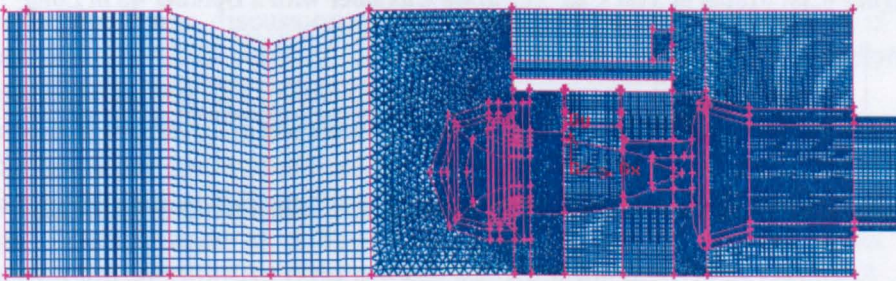


Figure 6.36: View of the Grid for the Accommodation Region Analysis

The grid used for this model is not so fine as that for the engine C in test cell 57 used for the estimation of the thrust correction factors. This happens because the aim of the two studies is different. For the thrust correction study a quantitative estimation of the flow parameters was carried out when for the Accommodation Region only a qualitative study has to be achieved.

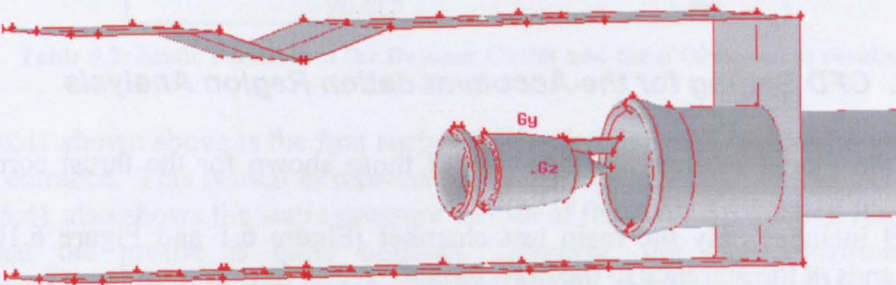


Figure 6.37: Model of Test Cell "X" Main Chamber without the Cradle

However, the criteria followed for the generation of the grid were the same as those used for the model related to the thrust correction factors study. Indeed, past modelling has drawn the generation of the grid (Figure 6.36).

The total number of elements is around one million. However a direct comparison with the previous model cannot be made because of the different cell dimensions (Figure 4.43 and Figure 5.10).

The second model generated for such a comparative analysis neglects the cradle.

The geometry is identical to that shown in Figure 6.35 apart from the cradle, which in this case, is not included (Figure 6.37).

The third part of the analysis deals with different detuner lengths. Therefore, several models have been designed with different detuner lengths.

In this work, only three lengths are reported: 45 m, 95 m and 145 m.

The three models are shown in the pictures below.

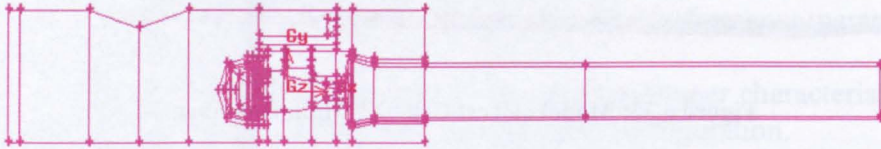


Figure 6.38: Model of Test Cell "X" Main Chamber with a Detuner 45 m Long

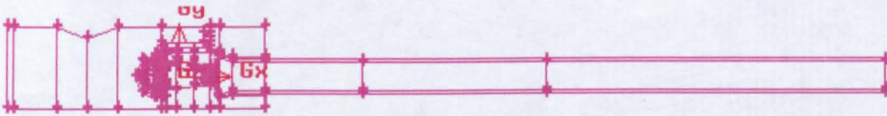


Figure 6.39: Model of Test Cell "X" Main Chamber with a Detuner 95 m Long

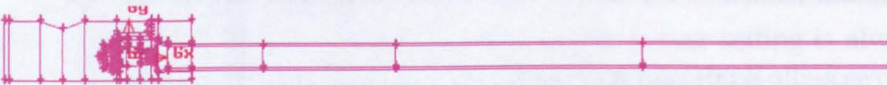


Figure 6.40: Model of Test Cell "X" Main Chamber with a Detuner 145 m Long

It is interesting to underline the fact the grid scheme used for all the model along the detuner is the same. In this way the choice of the grid along the detuner, probably the most important region, in the Accommodation Region study, will not affect the comparisons.

The total cell number for the 145 m detuner length model is 2 million.

### 6.3.3. CFD Setting for the Accommodation Region Analysis

Basically the Fluent settings are the same of those shown for the thrust correction analysis.

The model includes only the main test chamber (Figure 6.1 and Figure 6.10) and therefore, ends at the entrance to the blast basket.

This is considered sufficient for the study of how the Accommodation Region changes with different cell configurations. Indeed, such a study is the starting point of a comparative study rather than a quantitative study. Therefore, the exact representation of the flow field inside the cell is not strictly necessary. By changing the cell configurations, the flow fields are far from being realistic. However, this will facilitate the final comparison proposed in the previous paragraph.

The boundary conditions used are the same as those shown in Figure 6.15.

In addition, as already mentioned, the detuner outlet static pressure is used to alter the performance of the engine-detuner ejector pump.

Also the computational settings are the same as those used in paragraph 6.2 with the difference that the turbulence model used is the standard k-ε rather than the Realizable k-ε.

To establish the convergence of the model the Residual definition for single precision (paragraph 6.2.7) has been adopted.

The step-by-step approach is also used to achieve the second order of accuracy.

### 6.3.4. CFD Accommodation Region Analysis Results

In this paragraph the results of the CFD analysis are presented for the Accommodation Region. In particular, the derivation of the engine-detuner characteristic is given together with the influence of the cradle and of the detuner length on such a characteristic.

A comparison with the one-dimensional analytical model is made in the next chapter which is dedicated to a discussion of the results. Indeed, this comparison is not only of interest from the CFD point of view but also for the entire work. Therefore, it will be described along with the results discussion.

The first result proposed is the determination of the engine-detuner characteristic by CFD. The boundary conditions used for these simulations are those referred to engine A with a non-dimensional mass flow of 3060 (paragraph 5.3.4) (Rolls-Royce ).

The static pressure used as a boundary condition for the detuner outlet is listed together with the entrainment ratio worked out from the models in Table 6.2

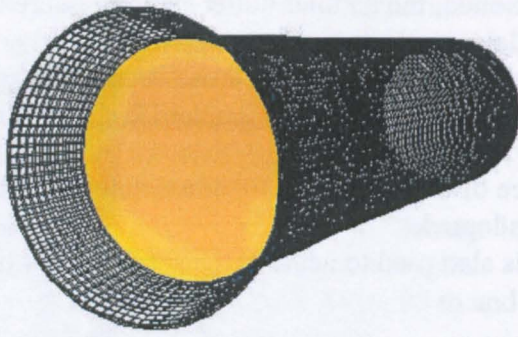
Static Pressure Detuner Outlet [Pa]	$\mu$
103500	0.78
103000	0.84
102000	0.96
101000	1.13
99215	1.33
98215	1.42
96215	1.64

Table 6.2: Static Pressure at the Detuner Outlet and the  $\mu$  Obtained as results

Figure 6.41 shown above is the first section of the detuner with constant area after the conical entrance. This is used as representating the Accommodation Region.

Figure 6.41 also shows the static pressure profile of the Accommodation Region. It is seen that the profile is quite uniform. However, the exact position of the Accommodation Section can not be known before the simulation has been run. Moreover, due to the cell configuration, it is quite complicated to draw a circular plane in the detuner after the convergence is achieved. For this reason the section defined in Figure 6.41 above has been chosen as a compromise.

Figure 6.42 shows a plot of the static pressure in the Accommodation Region as a function of the cell entrainment ratio. This has been extrapolated from the CFD results.



**Figure 6.41: Visualization of the Accommodation Region in the Computational Model**

The values of the static pressure in the Accommodation Section have been extrapolated by a mass weighted integration (Fluent incorporated b).

The shape of the curve is similar to that of Figure 5.12 which represents the ideal target. However, the comparison is made in the chapter dedicated to the discussion of the results.

The engine-detuner ejector characteristic has been calculated also for the model without the cradle. The boundary conditions are the same as those used before. That are those relevant to an engine non-dimensional mass flow of 3060 (Rolls-Royce ).

The static pressure used as boundary condition for the detuner outlet is listed together with the entrainment ratio worked out from the models in Table 6.3.

Static Pressure Detuner Outlet [Pa]	$\mu$
102000	0.97
101000	1.09
100000	1.21
99215	1.31
98215	1.43
97215	1.52

**Table 6.3: Static Pressure at the Detuner Outlet and the  $\mu$  Obtained as results (no-cradle model)**

The results are plotted in Figure 6.43.

Again the shape of the engine-detuner ejector characteristic in the Accommodation Regions looks plausible.

In order to make further validations, APPENDIX C shows the results obtained for different engine power settings.

The influence of the cradle blockage area is also shown in the section of this report dedicated to the experimental work (APPENDIX B). Also shown in this Appendix, the main conclusion is that the blockage area of the cradle does not affect the cell entrainment ratio

The effect of different detuner lengths is the third section which this paragraph deals with.

The lengths of the detuner modelled together with the static pressure used at the detuner outlet (as boundary conditions) and the entrainment ratios evaluated from CFD simulations are listed in Table 6.4.

The results extrapolated in the Accommodation Region are plotted in Figure 6.44.

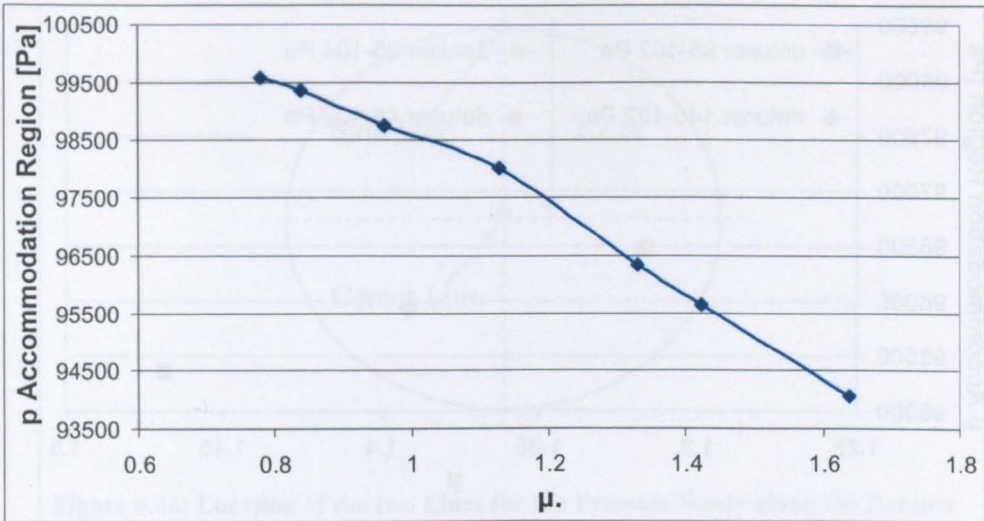


Figure 6.42: Static Pressure at the Accommodation Region, Computational Results

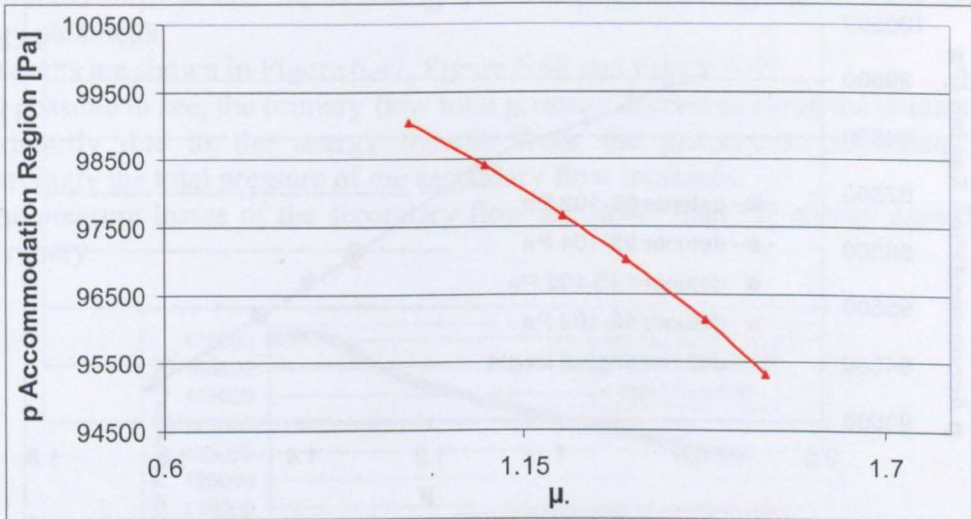


Figure 6.43: Static Pressure at the Accommodation Region, Computational Results (no-Cradle)

Detuner Length [m]	Static Pressure Detuner Outlet [Pa]	$\mu$
45	102000	1.32
95	102000	1.46
95	104000	1.318
145	102000	1.39

Table 6.4: Different Detuner Length, Static Pressure Outlet and  $\mu$  Obtained

Figure 6.44 alone is not of much interest but if the same values are plotted in Figure 6.42 the results make more sense as shown in Figure 6.45.

It is seen that the operating points evaluated using CFD results for different detuner lengths super-impose on the engine-detuner ejector pump characteristic at the Accommodation Region.

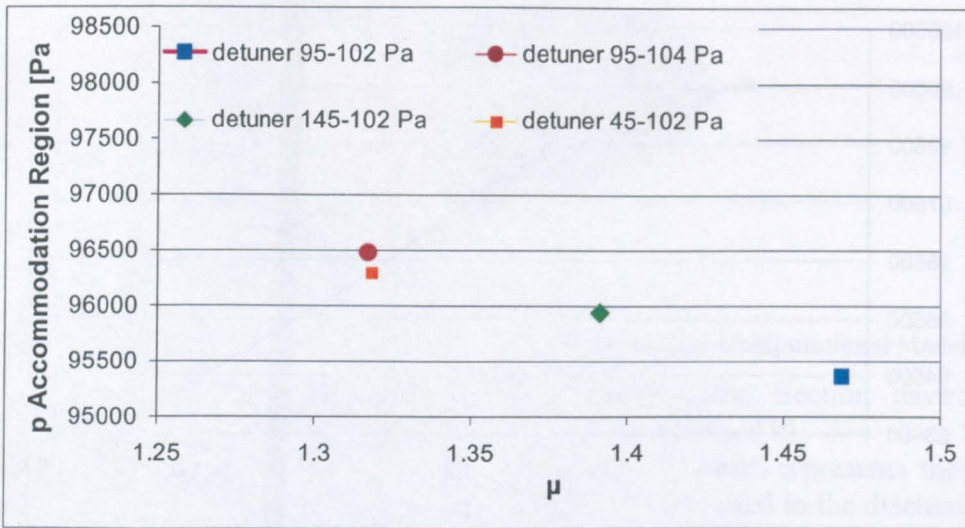


Figure 6.44: Static Pressure at the Accommodation Region for Different Detuner Length

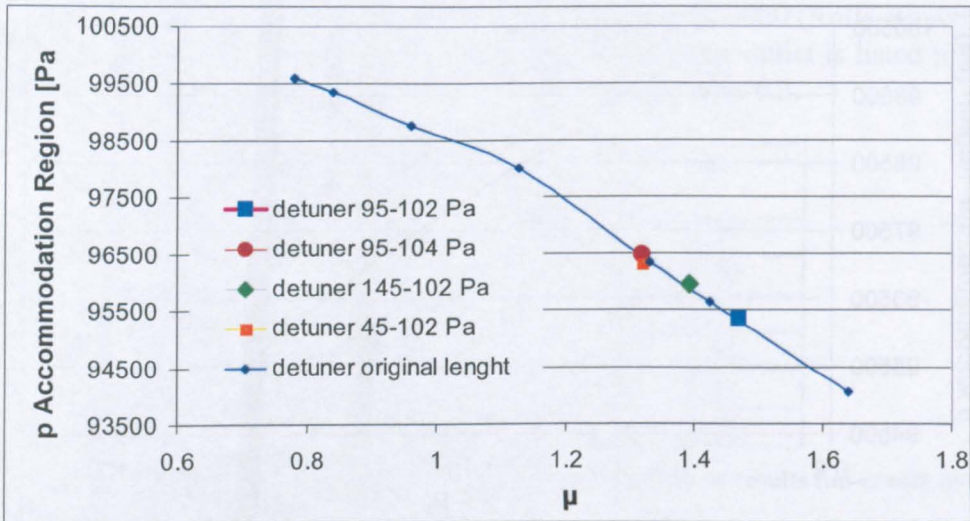


Figure 6.45: Operating Point for Different Detuner Length and the A.R. Ejector Characteristic

The variation of static and total pressure along the detuner when its length is changed is shown in the following pictures.

In order to visualise the primary and secondary flow along the detuner, two different lines have been drawn inside the pipe. One of them is running along the detuner axis and the second close to the detuner wall. The characteristics of the primary flow (with the former line) and the secondary flow (with the second line) can be established. Indeed it is believed and confirmed by previous simulations that until the two flows are completely mixed, the engine exhaust jet occupies the central part of the detuner flow and the secondary the outer part.

Accordingly, Figure 6.46 shows the location of the two lines in the detuner cross sectional area



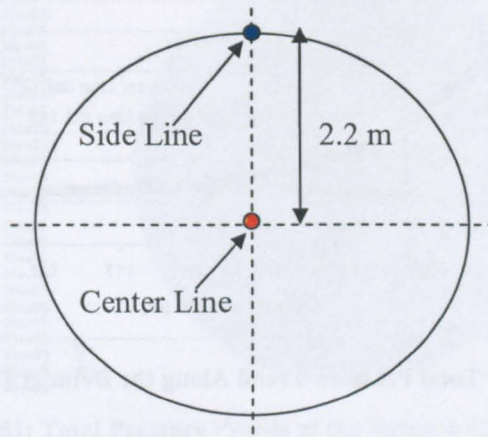


Figure 6.46: Location of the two Lines for the Pressure Study along the Detuner

The main aim of plotting the total pressure along these two lines is that of understanding the state of the mixing along the detuner. Indeed, the total pressure can be assumed as parameter for assessing the mixing level, being also at some stage an energy parameter.

The results are shown in Figure 6.47, Figure 6.48 and Figure 6.49.

As is possible to see, the primary flow total pressure decreases along the detuner. This is primarily due to the energy transfer from the primary to secondary flow. Accordingly the total pressure of the secondary flow increases.

So the pressure losses of the secondary flow are lower than the energy gained from the primary.

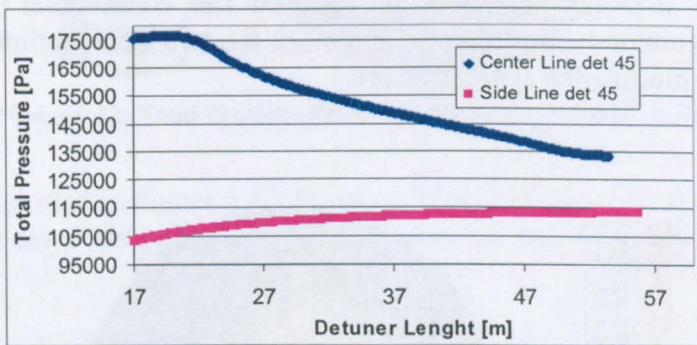


Figure 6.47: Total Pressure Trend Along the Detuner (45 m)

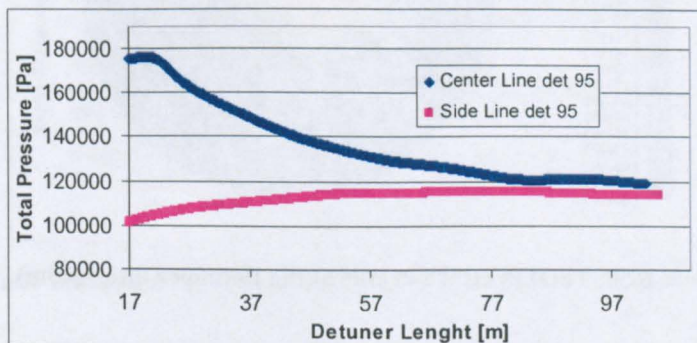


Figure 6.48: Total Pressure Trend Along the Detuner (95 m)

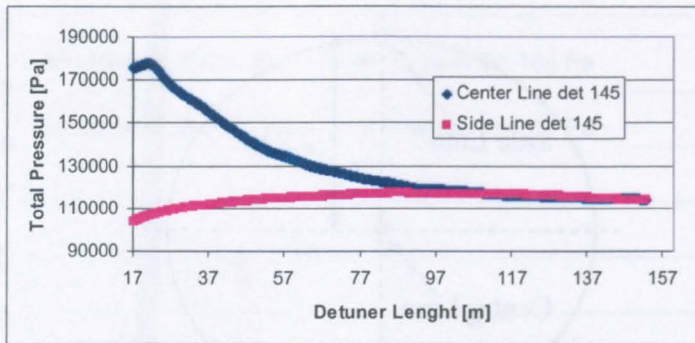


Figure 6.49: Total Pressure Trend Along the Detuner (145 m)

It is clear that for the detuner lengths of 45m and 95m the two flows are not completely mixed yet. Indeed there is still a gap between the two lines.

At the same time for the detuner length of 145m the two lines merge and then start to drop. This is due to the fact that after the mixing is achieved the pressure losses let the total pressure decrease along the detuner.

The trend of the total pressure for different detuner lengths could also be useful for the understanding of the ejector pump performance. Indeed, it can be useful to relate the amount of secondary flow entering the cell with the level of mixing achieved along the detuner.

To confirm the above trends it is possible to extract and compare from Fluent the total pressure profiles at the detuner exit for the three different models. The results are shown in Figure 6.50, Figure 6.51 and Figure 6.52 and it is possible to see that by increasing the detuner length the flow profile is more uniform.

At the same time, it is also interesting to see how this commercial CFD software represents the Accommodation Region. Therefore the two lines defined above have also been used for plotting the static pressure.

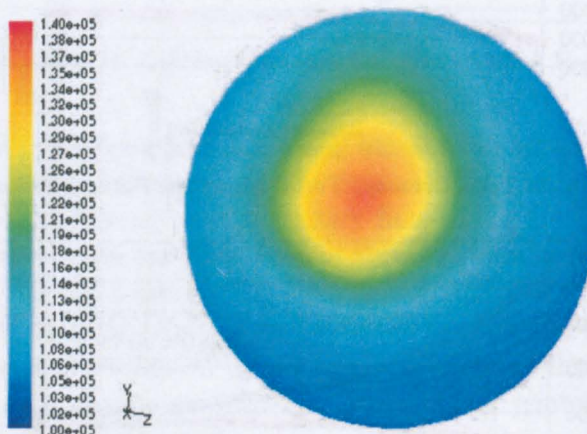


Figure 6.50: Total Pressure Profile at the Detuner Outlet (45m)

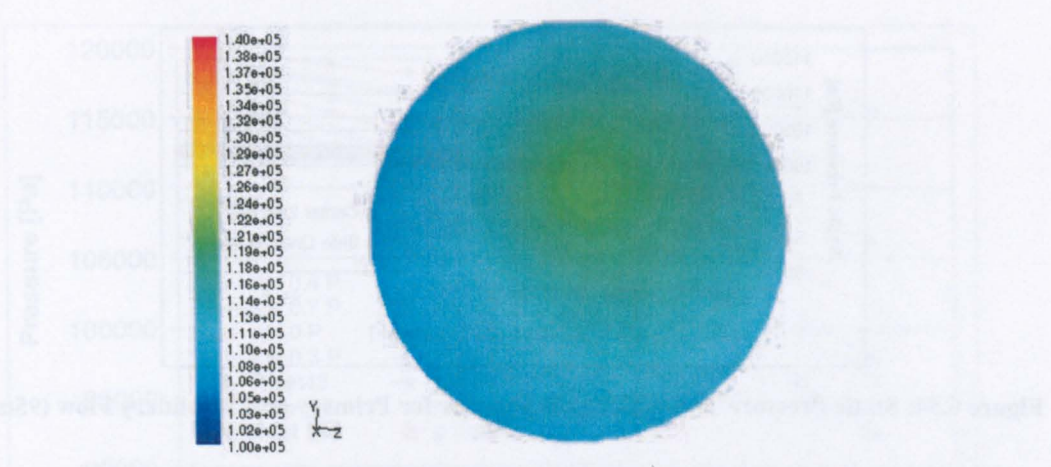


Figure 6.51: Total Pressure Profile at the Detuner Outlet (95m)

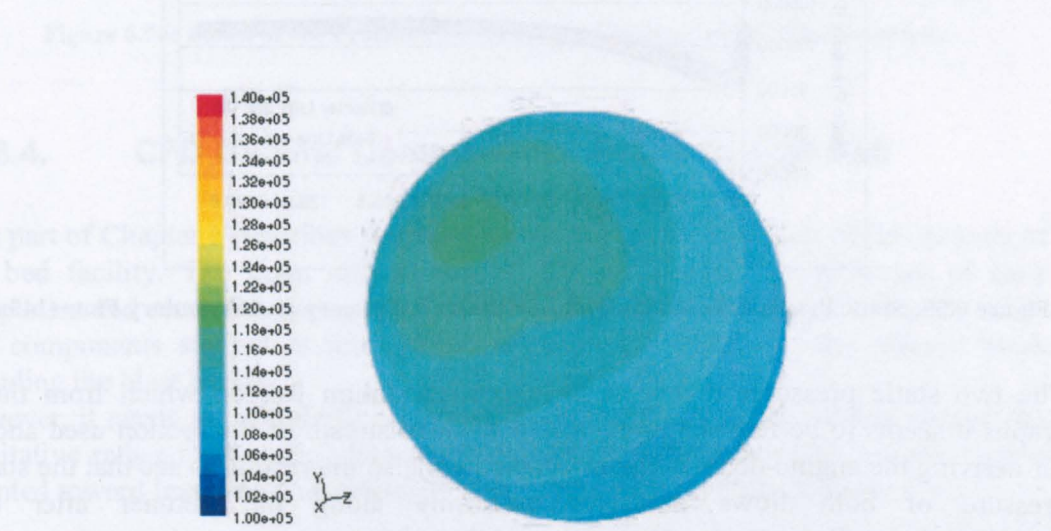


Figure 6.52: Total Pressure Profile at the Detuner Outlet (145m)

The results are plotted in Figure 6.53, Figure 6.54 and Figure 6.55. It is possible to see that the static pressure drops for both the flows before entering the detuner

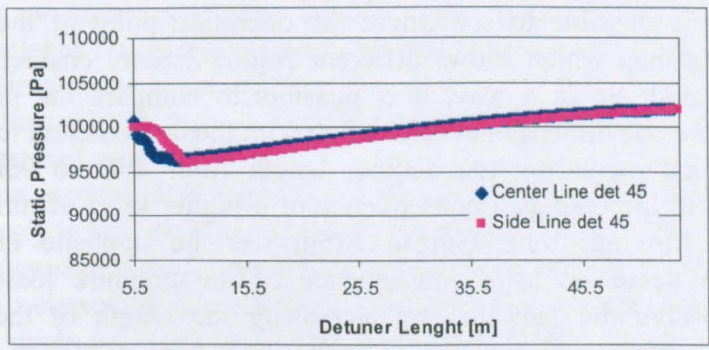


Figure 6.53: Static Pressure Trend along the Detuner for Primary and Secondary Flow (45m)

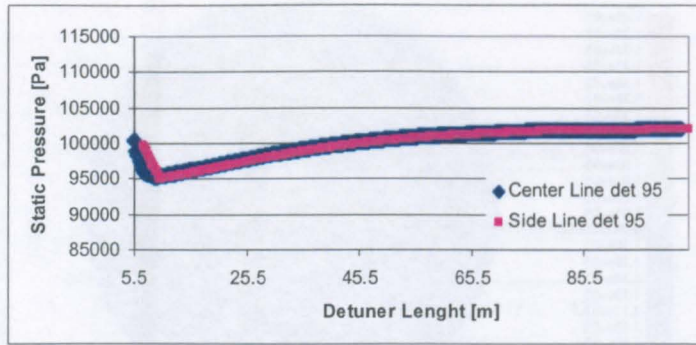


Figure 6.54: Static Pressure Trend along the Detuner for Primary and Secondary Flow (95m)

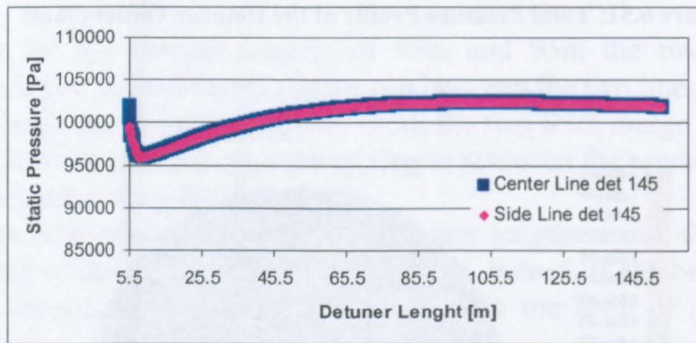


Figure 6.55: Static Pressure Trend along the Detuner for Primary and Secondary Flow (145m)

The two static pressures match at the Accommodation Region which from these graphs it seems to be few centimetres (20cm) downstream of the section used above for deriving the engine-detuner characteristic. It is also interesting to see that the static pressure of both flows increases uniformly along the detuner after the Accommodation Region as a consequence of the mixing process.

Chapter 5 also takes into consideration the effects of the pressure losses along the detuner and how they affect the performance characteristics.

It is interesting to plot together the results of the analytical model and those extrapolated by CFD.

Indeed, this can help the understanding of how Fluent treats the pressure losses.

The results are shown in Figure 6.56.

In this picture it is possible to see where the operating point of the pseudo-cells modelled lay on a map which shows different engine-detuner characteristics at the After-Mixing Region. So in a way, it is possible to compare the pressure losses accounted for in the one dimensional calculation with those accounted for in Fluent.

It can be seen that increasing the detuner length from 45m to 95m allows the entrainment ratio to increase as a consequence of a higher level of mixing achieved (paragraph 2.2). Moving from 95m to 145m has the opposite effect and the entrainment ratio decreases as a consequence of the pressure losses. It is also interesting to observe the fact that by increasing the length of the detuner the operating point moves toward a characteristic line with a higher pressure loss coefficient.

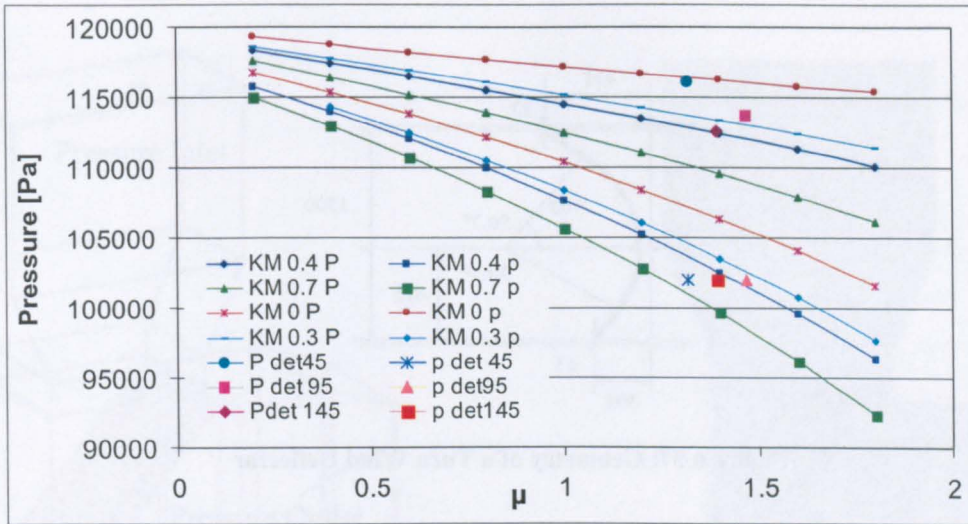


Figure 6.56: Effect of the Pressure Losses on the Engine-Detuner Characteristic

## 6.4. CFD General Components Modelling Test Cell

This part of Chapter 6 describes several attempts to model separately different parts of test bed facility. The main aim of this is first to analyse the influence of each component and second to gather together such components and model the entire cell. The components studied in this section are the inlet stack and the exhaust stack including the blast basket.

However, it needs to be underlined that the attempts made are in order to extrapolate qualitative rather than quantitative results. Therefore, the main CFD compromise is oriented toward less time consuming models rather than accurate models.

### 6.4.1. Test Cell Inlet Stack Modelling

The main objective of an inlet system for indoor test cell facilities is to provide a smooth flow. Within the cell there are several sources for flow distortions (paragraph 2.4.1) which can easily affect the whole performance of the engine. Moreover, such flow instability can also compromise the life of the engine. At the moment there are no methods available for predicting the flow distortion downstream of the inlet stack apart from the simple rule given in paragraph 2.4.1.

In this section the cell and the engine used for the CFD simulations are Rolls-Royce engine A and test bed cell 56.

Such a cell has a vertical inlet stack as is shown in Figure 5.10. Therefore, a cascade elbow is necessary to turn the flow into the engine axial direction.

Figure 6.57 above shows the cross section of one element of this cascade. The shape is quite simple, a circumferential arc with a straight tangential element on both sides.

The cascade is made up of 20 deflectors. However, it has to be noted that deflectors are not equally-distant. Actually their concentration is higher in the top part of the cascade than in the bottom. This is to ease the straightening of the flow in the top corner beneath the test chamber ceiling where the bend is very tight.

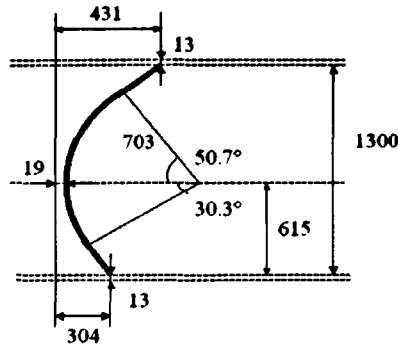


Figure 6.57: Geometry of a Turn Wind Deflector

To take this particularity into account, an exponent grading scheme (Fluent incorporated a ) has been applied on inter-distances. This grading scheme implies that the ratio of any two succeeding interval lengths is constant:

$$\frac{l_{i+1}}{l_i} = R = e^{\left(\frac{L}{n}\right)\left(x - \frac{1}{2}\right)} \quad (6.24)$$

L is the length of the cascade, n the number of intervals (n=21) and x a user-specified input parameter, in this case x=0.46.

As a result, the distance between the bottom corner and the first deflector is 911mm whereas the one between the top corner and the last deflector is only 623mm.

The inclination of the cascade air deflectors is 47.5° with respect to the cell axis.

Figure 6.58 shows the geometry of the entire inlet stack, including the cascade.

In order to mesh such a geometry, several sub-volumes have been generated.

Different volumes have been generated along the cascade , one for each deflector. In such a way, 21 hexahedral volumes are generated and each of them can be meshed with hexahedral mappable grids. This allows the grid elements to be orientated in the flow direction. This reduces the calculation time (Fluent incorporated b ).

In addition, the rest of the inlet stack has been meshed with hexahedral elements (Figure 6.58). Following such a scheme two different grids have been generated, one with 200,000 elements (Grid I) and another with 400,000 elements (Grid II).

Inlet pressure for the atmospheric side of the inlet stack and outlet Pressure for the internal side have are chosen as boundary conditions for these two models (Figure 6.58). The values have been worked out from the experimental data provided in order to give a total mass flow entering the cell close to the actual value.

Fluent settings are the same as those used for the engine-detuner ejector pump study and a step-by-step approach has also been applied.

Since the main objective of having two different grids for the same model is that of studying the influence of the grid (Rubini ) on the results as convergence criteria also the mass flow convergence history has been used.

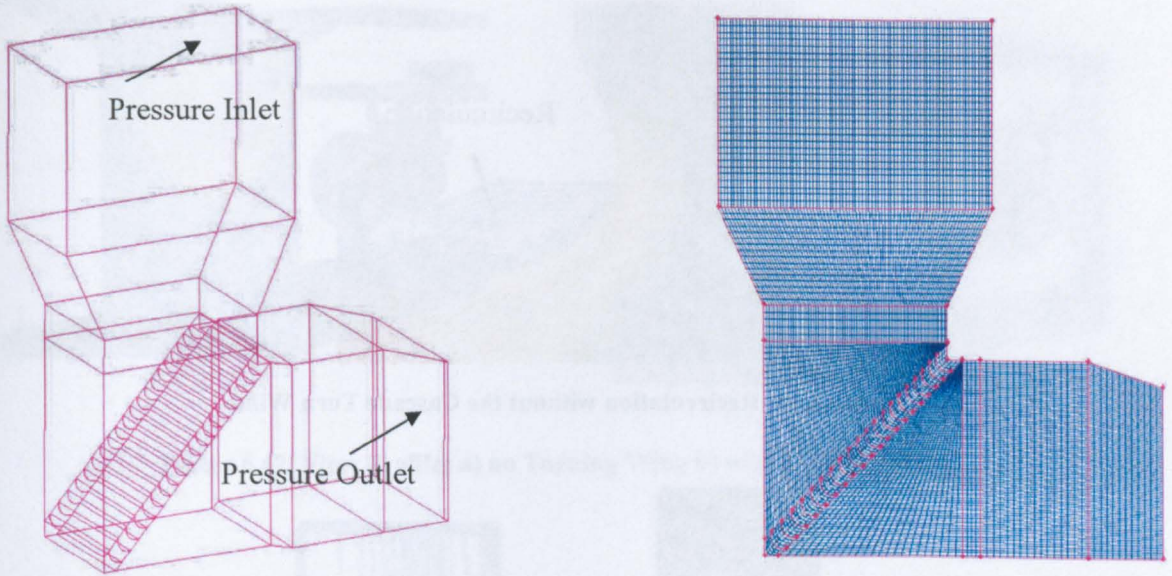


Figure 6.58: Geometry and Grid of the Inlet Stack

#### 6.4.2. CFD Test Cell Inlet Stack Results

The first result is that related with the grid independence study. The two grids have given the same result in terms of mass flow going through the cell; of course, the calculation time using Grid II was longer. The mass flow history is shown in Figure 6.59.

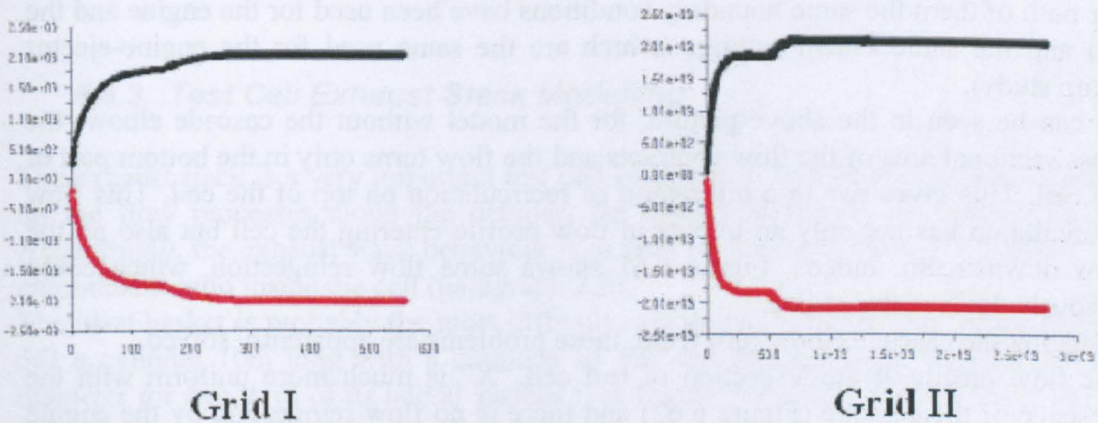


Figure 6.59: Mass Flow History for the two Simulations with Different Grid

The comparison between the two models has also been made in terms of static pressure, velocity and flow recirculation. For all these parameters the models have proved to be very similar (APPENDIX D). For this reason further study is carried out with Grid I.

Now, in order to understand the effects of the cascade, the model described above is added to the main test chamber of test cell 56 and a new model generated.

Such a model includes Rolls-Royce engine A and the boundary conditions used are those related to the engine non-dimensional mass flow of 3060 (Rolls-Royce)

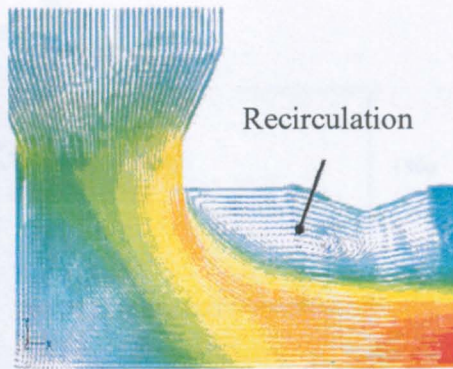


Figure 6.60: Recirculation without the Cascade Turn Wind

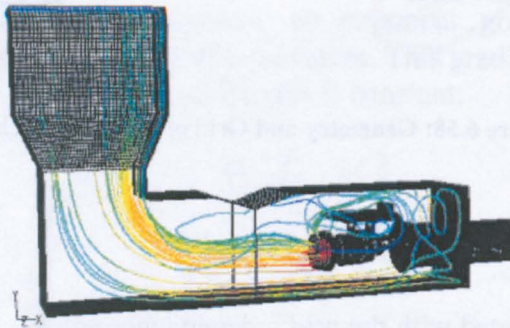


Figure 6.61: Flow Recirculation and Re-Ingestion

The results of this new model are compared with those obtained from a past model (Gullia 2003) which includes the inlet stack but not the wind deflectors (Figure 6.60). For both of them the same boundary conditions have been used for the engine and the cell and the same Fluent settings (which are the same used for the engine-ejector pump study).

As can be seen in the above picture, for the model without the cascade elbow, the cross sectional area of the flow contracts and the flow turns only in the bottom part of the cell. This gives rise to a big region of recirculation on top of the cell. This flow recirculation has not only an impact in flow profile entering the cell but also on the flow downstream. Indeed, Figure 6.61 shows some flow reingestion, which could seriously damage the engine.

Including the cascade elbow turn wind, these problems are apparently solved.

The flow profile at the V section of test cell "X" is much more uniform with the presence of the cascade (Figure 6.62) and there is no flow reingestion by the engine (Figure 6.63).

Looking at the flow profile (turbulence intensity) at the V section of the model including the cascade, (Figure 6.62), another interesting factor can be seen. Indeed, such a uniformity of the flow can partially justify the assumption made in all the previous analyses about running only the main test chamber. Using this assumption at the inlet of the cell, the flow profile was considered uniform. However, this does not exclude the effect of the V section which (see Figure 6.62) is responsible for most of the distortion at that section.



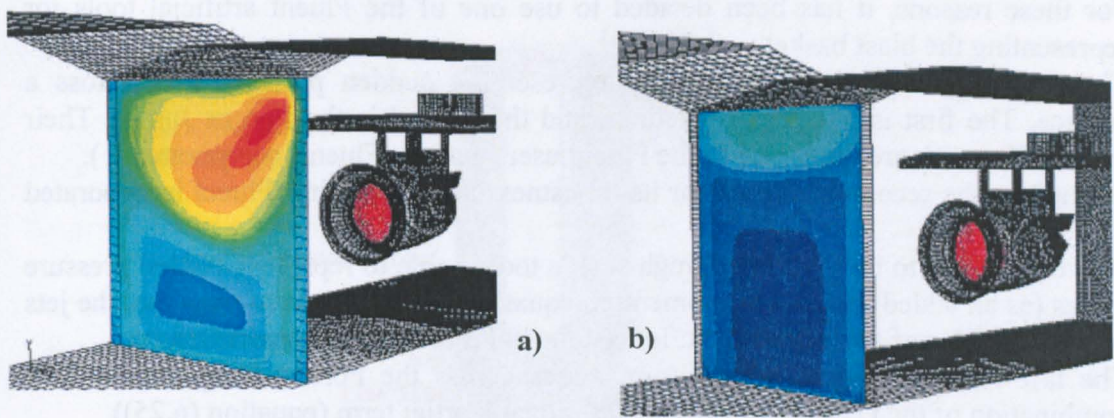


Figure 6.62: Flow Profiles a) no Turning Wing b) with Turning Wing

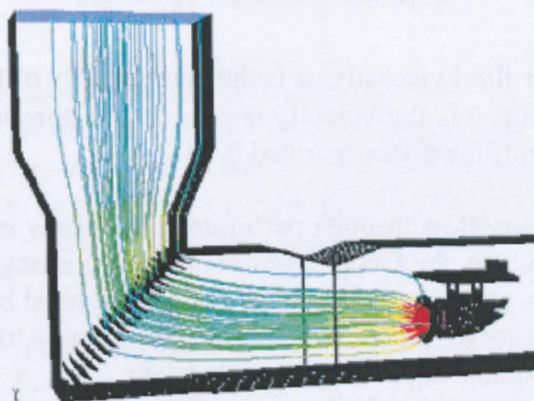


Figure 6.63: Flow Paths With Turning Wind

### 6.4.3. Test Cell Exhaust Stack Modelling

The exhaust stack is a very important test cell component. Indeed the mixing depends on the flow processes along the detuner, the blast basket and the exhaust stack. Accordingly, the exhaust stack behaviour is very important because it controls the entrainment ratio inside the cell (paragraph 2.2).

The blast basket is probably the most difficult component to model. It is (for test bed 56) a cylinder 10m long with a diameter of 5m and perforated by holes of 35mm diameter for two third of its lateral surface (see Figure 2.22). The total porosity ( $\psi$ ) is 20%.

There are two possible ways to model such a component. The first is to represent the exact geometry of the perforated cylinder. The second is to use an artificial Fluent tool to simulate the sudden total pressure loss across the blast basket boundary.

The former of the two methods is probably the more accurate but at the same time would require the generation of a very specific grid. In a cylinder 10m long to mesh thousands of 35mm holes it would require a big gradient in the grid dimensions and consequently a massive number of elements. Furthermore, if such a model of the exhaust system needs to be connected to the test cell main chamber and the inlet stack the entire model would be both extremely big and difficult to run.

For these reasons, it has been decided to use one of the Fluent artificial tools for representing the blast basket.

There are two different methods for representing sudden pressure loss across a surface. The first is the Porous Medium and the second is the Porous Jump. Their main differences are described in the Fluent user Manual (Fluent incorporated b ).

Of the two the second is chosen for its robustness and simplicity (Fluent incorporated b).

However, it has to be said that though such a tool is able to represent sudden pressure losses (as an added sink in the momentum equation) it is not able to represent the jets across the holes of the blast basket. Indeed the holes are not even modelled.

The law for representing the pressure losses across the Porous Jump surface is a combination of the Darcy Law plus an additional inertial term (equation (6.25))

$$\Delta P = - \left( \frac{\mu_v}{\alpha} v + C_2 \frac{1}{2} \rho v^2 \right) \Delta m \quad (6.25)$$

Where  $\mu_v$  is the laminar fluid viscosity,  $\alpha$  is the permeability of the medium,  $C_2$  is the pressure-jump coefficient,  $v$  is the velocity normal to the porous face, and  $\Delta m$  is the thickness of the medium (Fluent incorporated b ).

However, for high velocity flow through perforated plates only inertial pressure losses are accounted for. Therefore, the Darcy's law contribution is neglected in the pressure loss definition by the porous jump method (Fluent incorporated b).

However, the total pressure drop across the porous jump needs to be quantified.

To do this the Adkins method is used (paragraph 2.1.8).

The first step is to work out the discharge coefficient from Figure 2.23. However, Adkins derived this map considering a blast basket perforated in its external surface. In reality the blast basket in test cell 56 has only two third of its external surface perforated (Figure 2.22)

Therefore, to overcome such a difference, two discharge coefficients have been determined. The first using the real porosity and an equivalent diameter for the blast basket (Table 6.5 b))and the second using the real diameter (Table 6.5 a) ) and an equivalent porosity.

The equivalent diameter found is 3.3m instead of 5m and the equivalent porosity is 13% of the entire area. Using a cell mass flow of about 2500 Kg/s the total pressure losses calculated by the Adkins formula (paragraph 2.1.8) are listed in the following tables. The surface thickness used for the calculation is 20mm.

Parameter	Value
L	10 m
D	5 m
W	2500 Kg/s
$\psi$	20%
$c_d$	0.41
$\Delta P$	50 K Pa
$C_2$	290 m <sup>-1</sup>

a)

Parameter	Value
L	10 m
D	3.3 m
W	2500 Kg/s
$\psi$	13%
$c_d$	0.5741
$\Delta P$	20 K Pa
$C_2$	135 m <sup>-1</sup>

b)

Table 6.5: a) B.B. Real Diameter b) B.B. Equivalent Diameter

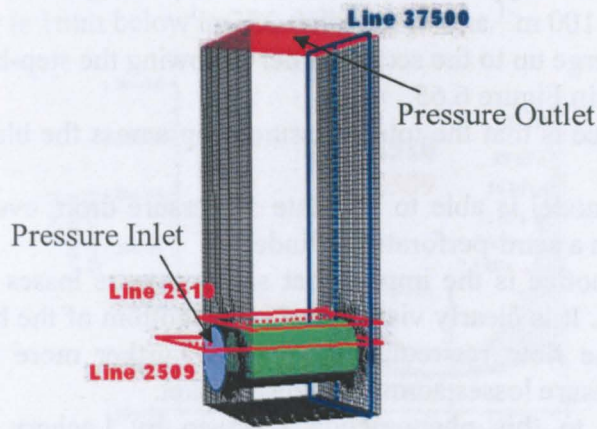


Figure6.64: Exhaust Stack Model

Figure6.64 shows the model for the exhaust stack.

It is seen that a part of the detuner is included in the model (1 m).

The grid used for meshing the blast basket is made by hexahedral elements using the Cooper scheme (Fluent incorporated a). And that for the exhaust stack is made by hexahedral elements as well by a map scheme (Fluent incorporated a).

The fluent setting are the same as those used for the inlet stack, apart from the introduction of the porous jump as a boundary condition for the blast basket top boundary, as shown in the picture (Figure6.64).

#### 6.4.4. Test Cell Exhaust Stack Results

Different models have been run for the exhaust stack in order to improve the understanding of the flow fields along it.

The first uses a uniform profile for the total pressure inlet boundary condition.

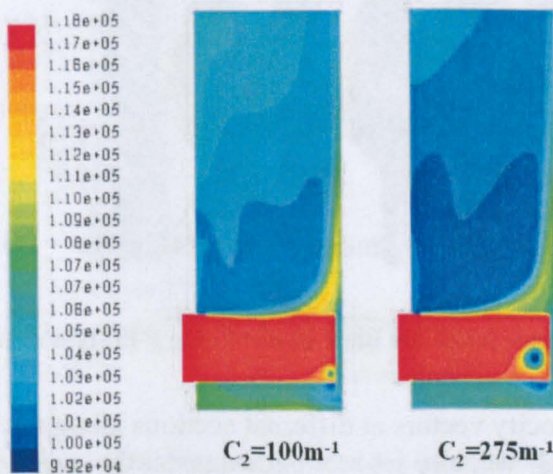


Figure 6.65: Static Pressure Profiles for Different  $C_2$

To see how the pressure drop affects the flow fields, two models with different  $C_2$  were run. In one  $C_2$  is  $100\text{ m}^{-1}$  and in the other  $275\text{ m}^{-1}$ .

The simulations converge up to the second order following the step-by-step approach. The results are shown in Figure 6.65.

The first thing to notice is that the total pressure drop across the blast basket is from 110 K Pa to 118 K Pa.

This means that the model is able to simulate a pressure drop, even in the extreme case of parallel flow in a semi-perforated cylinder.

The second thing to notice is the impact that such pressure losses have in the flow inside the blast basket. It is clearly visible that at the bottom of the blast basket, close to its final part, some flow recirculation appears. Further more this recirculation increases with the pressure losses across the blast basket.

A first interpretation to this phenomenon is given by Lachery (Lachery ) who attributes such a recirculation to the inbalance of total pressure due to the sudden pressure loss. To trade off this inbalance, the internal flow loses some energy starting the recirculation. Another aspect worth noticing is the difference in mass flow between the two models. That with higher pressure losses carry less mass flow inside the exhaust stack compared with that involving lower pressure loss (respectively 3596 Kg/s and 3565 Kg/s). This can be justified by the fact that the two different pressure losses imply two different static pressure drops along the stack which affects the flow velocity and consequently the mass flow.

The second model, adopting the porous jump, includes as inlet boundary conditions, profiles of total pressure and temperature referred to un-mixed conditions extracted from previous simulations of the main test chamber at the Accommodation Region.

These simulations converge only up to the first order of discretisation. However, it is valid to extrapolate qualitative considerations beyond that. Also in this case, two different pressure jump coefficients were run ( $C_2 = 100$  and  $C_2 = 300$ ).

By this model, it is possible to distinguish the behaviours of the primary and the secondary flow along the blast basket.

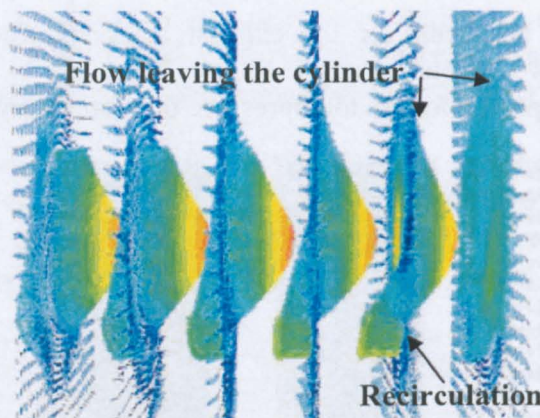


Figure 6.66: Velocity Vector inside the Blast Basket Using P Profiles as Inlet Boundary

Figure 6.66 shows the velocity vectors at different sections along the blast basket.

It can be seen that the high velocity jet rebounds against the wall of the blast basket and then divides in two. One part goes up and leaves the “perforated cylinder and the other goes down forming a recirculation region.

To carry on with the analysis of pressure losses, the pressure difference between the flow inside the blast basket and the flow outside can be plotted by Fluent.

Two lines are shown in Figure 6.64, one is 1mm above the pressure jump surface (line 2510) and the other is 1mm below it (line 2509).

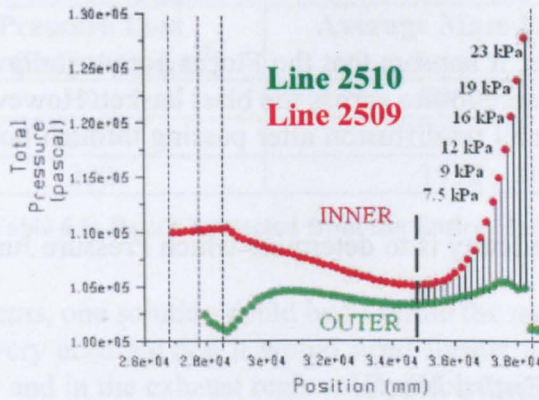


Figure 6.67: Pressure Drop across the Blast Basket

Figure 6.67 show the evolution of the total pressure gap between the two lines. The dashed line represents the limit at the right hand side of which the flow leaves the cylinder and at its left hand side the flow does not cross the blast basket. This plot allows the visualization of the total pressure drop imposed on the flow. It is also interesting to notice that such a drop seems to follow a second order law. Another interesting consideration can be made by plotting the total pressure along the line 37500 represented in Figure 6.64.

This is shown in Figure 6.68.

It can be seen that there are two peaks of total pressure inside the blast basket. One is a maximum and is picked up at the centre of the cylinder where the primary flow is. The second peak is a minimum and is located at the bottom of the cylinder where the recirculation has been noticed. As already said, two different  $C_2$  coefficients have been used for these simulations. The model with high pressure losses shows higher values of total pressure before the pressure jump (approximately in correspondence with line 2509) and values of the two peaks lower than those calculated with the small pressure losses.

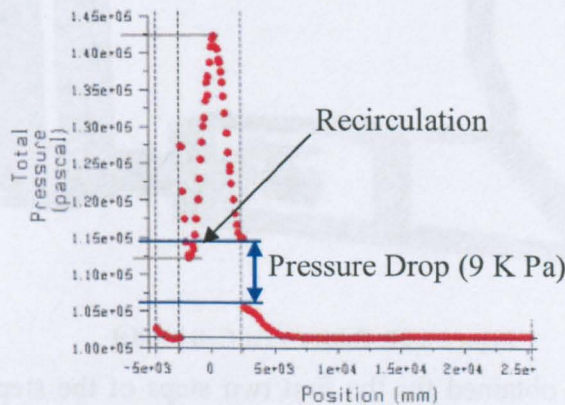


Figure 6.68: Pressure Trend along the Vertical Stack

A first explanation of this phenomenon is that with the higher pressure drop the flow finds more difficulty in passing through the porous jump. Accordingly, more mixing is achieved inside the blast basket and the flow becomes more uniform.

To summarise these tests, it appears that the Fluent porous jump model is robust and able to simulate the pressure losses across the blast basket. However, it can not model the mixing due to the small jet diffusion after passing through holes since it does not take porosity into account.

Using this model, the difficulty is to determine which Pressure Jump Coefficient ( $C_2$ ), matches the real case.

#### 6.4.5. Test Cell Entire Model

Adding to the test main chamber model (defined in the previous paragraph) the inlet and exhaust cell models it is possible to define the entire test bed (in this case the Rolls-Royce test bed 56).

The total model is shown in Figure 6.69.

This allows the study of the flow along the all cell and also how the cell configuration would affect the flow behaviour inside the cell. Indeed, changing the pressure jump coefficient ( $C_2$ ) at the blast basket would allow the study of how the engine-detuner ejector pump operating point would move itself along the ejector characteristic (Figure 6.56).

At the moment there are no experimental data which would help quantify the pressure losses across the actual blast basket. Therefore, the main idea is to derive the engine-detuner ejector characteristic by keeping the engine power setting fixed and changing only the pressure jump coefficient at the exhaust. This is the case until the experimentally measured entrainment ratio is matched.

Unfortunately many convergence problems arose so that the entire cell model did not converge.

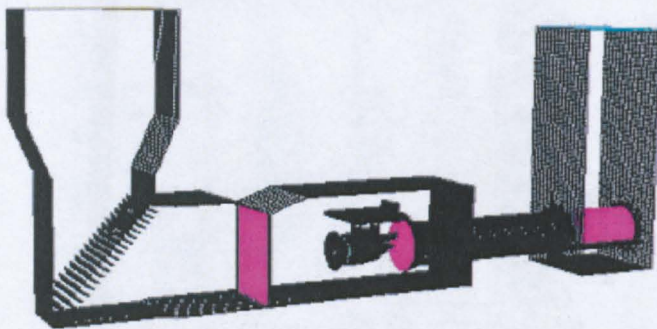


Figure 6.69: Entire Test Cell Model

Convergence was only obtained for the first two steps of the step-by-step approach when the porous jump boundary condition was not activated.

The results are promising and are shown in the Table 6.6

Indeed, for different pressure jump coefficients different mass flows have also been calculated respecting the trend found in previous simulations. Increasing the pressure losses decreases the mass flow entering the cell.

The convergence was not achieved for the first step when the porous jump was activated.

<b>Pressure Loss Coefficient <math>C_2</math> [m<sup>-1</sup>]</b>	<b>Average Mass Flow (kg.s<sup>-1</sup>)</b>
0	2050
100	2020
200	1950

**Table 6.6: Result Extracted from the Entire Model**

To tackle these problems, one solution could be to refine the mesh. The mesh used for these models is not very accurate and it would need further adaptation especially in the engine after-body and in the exhaust regions. Probably this would lead to needing a model with more than 10 millions cells. In addition special facilities would be required.

Another interesting study could be involving the turbulence models. In this work the standard k-ε is used. It is believed that this is responsible for the high pressure losses especially during the mixing process. Indeed, also without any pressure jump loss the mass flow entering the cell is much lower than the real case.

To illustrate this point the results obtained for the exhaust model alone can also be taken into account. Both the models with uniform entry profiles and with special profiles have the same average total pressure as the inlet conditions (the outlet condition is the same, atmosphere). But the mass flows obtained as a result are quite different. For the model with uniform profiles the entering mass flow is 3500 Kg/s and for the other 2100 Kg/s. This huge difference in mass flow between the two models could lead to the fact that the standard k-ε turbulence model under these conditions does not work very well. In addition, too much pressure loss during the mixing procedure is accounted for. For this reason, a study of turbulence models could be greatly beneficial.

## **7. Discussion**

### **7.1. Introduction**

In this chapter the project objectives, fixed in Chapter 3, are discussed after the findings achieved in the three main areas of work: Thrust Correction Factors, Ejector Analytical Model and CFD.

The discussions of the findings are structured into three levels.

The first includes the analysis of the findings of each single area of work.

The second includes the comparison between the results obtained from different area of work.

The third represents the combination of the experiences reached in the three different areas of work

### **7.2. First level of Discussion**

#### **7.2.1. Thrust Correction**

The research undertaken in recent years about the determination of thrust and drag for gas turbine propulsion systems in in-flight conditions (MIDAP Study Group 1979; MIDAP 1980; SAE Committee E-33 1985) is applied in Chapter 4 to indoor sea-level test beds.

The aim of this knowledge transfer from the in-flight condition to the enclosed sea-level cell is the determination of a number of equations capable of evaluating the real gross thrust delivered by the engine during the tests.

In reality this is not only a simple knowledge transfer. Indeed, because of the completely different conditions, the general equations for in-flight condition has to be significantly re-arranged to satisfy the cell environment. However, it must be said that the approach followed in the main reference regarding the thrust and the drag determination for in-flight thrust conditions has been really useful.

This approach has involved the study of the forces and drags acting on what has been called the metric-assembly from different points of view. In addition, different system interfaces (Figure 4.13) have been studied from the point of view of different accounting system (force, drag and hybrid).

In order to move from in-flight to the test cell conditions a step-by-step approach has been used. This was thought to improve the understanding of the difference between the two kinds of environment. Accordingly, a pseudo-infinite cell has been defined and used as a first step for representing the forces acting on the metric assembly (paragraph 4.3.3). With the results obtained from the pseudo-infinite cell analysis it has been possible to move to a finite cell (paragraph 4.3.4) with the consequent inclusion of the static pressure gradient inside the cell.



From the analysis of the finite cell three different thrust correction equations have been evaluated.

These equation are :

$$L = F_N - D_{carcasse} - D_{cradle} - D_{bell-ext} + (F_{G9} - F_{G0})_{ext\ pot} \quad (7.1)$$

$$L = F_N + \phi_{Gpre} - \phi_{Gbell\ ext} - D_{carcasse} - D_{cradle} + (F_{G9} - F_{Gf})_{ext\ pot} \quad (7.2)$$

$$L = F_{G9} - F_{Gth} - \phi_{bell} - D_{carcasse} - D_{cradle} + (F_{G9} - F_{Gf})_{ext\ pot} \quad (7.3)$$

Using the considerations made in paragraph 4.3.4 about the possibility of measuring experimentally the base force, it is also possible to write the above thrust correction equations in a different form.

$$L = F_N - D'_{carcasse} - D_{cradle} - D_{bell-ext} + (F_{G9} - F_{G0})_{ext\ pot} - \phi_{Gbase} \quad (7.4)$$

$$L = F_N + \phi_{Gpre} - \phi_{Gbell\ ext} - D'_{carcasse} - D_{cradle} + (F_{G9} - F_{Gf})_{ext\ pot} - \phi_{Gbase} \quad (7.5)$$

$$L = F_{G9} - F_{Gth} - \phi_{Gbell} - D'_{carcasse} - D_{cradle} + (F_{G9} - F_{Gf})_{ext\ pot} - \phi_{Gbase} \quad (7.6)$$

Where the term  $D'_{carcasse}$  means that the drag of the engine carcasse has to be taken into account up to station (9) (Figure 4.21).

Using equations (7.4), (7.5) and (7.6) the first objective of those proposed in 3.2.1 has been achieved. Indeed, by the application of different system interfaces and accounting systems the forces and the drag acting on the metric assembly have been identified and related in different thrust correction factors.

This also represents the first novelty of this work indeed, in the open literature there is no thrust correction equations approach as complete as this. Furthermore, this approach is able to name all the forces and drags acting in the metric-assembly that are taken into account.

However, the incompleteness of the above equations when turbofan with unmixed exhaust and engine with the pylon are tested has to be defined. Indeed, the interactions of the flow with part of engine after-body (hot nozzle duct and plug) and the pylon have not been taken into account. Therefore, this defines a first limit of these thrust correction equations about their ability of estimating the real gross thrust delivered by the engine.

Once the thrust correction equations have been defined a potential one-dimensional gas-dynamic approach has been used in an attempt to correlate each thrust correction factor with the engine-cell dimensions and performance.

The aim of this is to derive useful relations which allow the calculation of the thrust correction factors either by ordinary flow measurement in the test cell or by calculation once the engine and cell dimensions and performance are known.

This has been achieved by using the basic principles of Newton's second and third laws, the continuity equation, isentropic compressible flow theory and the equation of the energy conservation.

The results of this study are summarised in the following equations which represent the above attempt to quantify the thrust correction factors.

$$\frac{\phi_{Gbell\ ext}}{q_0 A_{cell}} = \left\{ \left[ \frac{\mu}{(1+\mu)} \right] \left\{ \frac{\lambda}{\left[ \left( \lambda - 1 - \frac{(A_1 - A_{th})}{A_{th}} \right) \right]} + 1 \right\} \frac{\left[ (\lambda - 1) - \frac{(A_1 - A_{th})}{A_{th}} \right]}{\lambda} + \right. \\ \left. - \left( 1 - \frac{1}{\lambda} \right) \left\{ \left[ \left( \frac{\mu}{\mu+1} \right) \left( \frac{\lambda}{\lambda-1} \right) \right]^2 + 1 \right\} \right\} \quad (7.7)$$

$$\frac{\phi_{Gpre}}{q_0 A_{cell}} = \left\{ \left[ \frac{\mu}{(1+\mu)} \right] \left\{ \frac{\lambda}{\left[ \left( \lambda - 1 - \frac{(A_1 - A_{th})}{A_{th}} \right) \right]} + 1 \right\} + \right. \\ \left. \times \frac{\left[ (\lambda - 1) - \frac{(A_1 - A_{th})}{A_{th}} \right]}{\lambda} - 2 \frac{\mu}{\mu+1} \right\} \quad (7.8)$$

$$\Delta F_{09\ ext\ pot} = -\left\{ \mu^2 \left[ (b-c)^2 + 1 - 2b - 2c \right] + 2\mu \left[ (b-c)^2 - b + c \right] + \right. \\ \left. + (b-c)^2 \right\} \times \frac{W_p}{2\rho A_{cell0}} \quad (7.9)$$

$$\Delta F_{f9\ ext\ pot} = \left[ \frac{(1-f)}{(1-d)} + (1-f)^2 \left( \frac{(1-f)}{(1-d)} - 1 \right) - \frac{(1-f)^2}{(1-d)^2} \right] \frac{\mu^2 W_p^2 (1-d)}{\rho (1-f)^2 A_{cell0}} \quad (7.10)$$

$$\frac{\phi_{Gbell} + F_{Gth}}{q_{th} A_{th} \frac{\rho_{th}}{\rho_0}} = \left[ \left( \frac{1+\mu}{\lambda} \right)^2 (\lambda - 1) - \left( \frac{\mu^2}{\lambda - 1} \right) \right] \quad (7.11)$$

All the parameters included in the equations are explained well in Chapter 4.

As can be seen, the terms enclosed in the above equations are only cell-engine dimensions and performance parameters like the entrainment ratio, the engine mass flow and other flow parameters at sections (0) and (th). All these terms are commonly measured inside the cell by energy balances (paragraph 2.2.5) or by engine cell instrumentation as engine air meters or anemometers at station (0) (paragraph 2.3.2).

However, once the cell entrainment ratio is known all the other performance parameters ( $\rho_0$  and  $\rho_{th}$ ) can be derived (in first approximation) using basic aerodynamics principles. It is worth remembering that in such calculations the hypothesis

of an incompressible flow has to be well assessed. In addition, whenever it is appropriate compressibility effects have also to be taken into account. This is the approach used for compiling equations (7.7), (7.8), (7.9), (7.10), (7.10). The results of these calculations are reported in Table 4.4 (here renamed Table 7.1).

TERM	FROM	VALUE
Load Measured	RR First Principle Measurements	385161 N
IMD ( $F_{G0}$ )	Equation (4.64)	17263 N
( $F_{GTHROAT} + \Phi_{Bellmouth}$ )	Equation (4.138)	14462 N
$\Phi_{BASE}$	RR First Principle Measurements	969 N
$\Phi_{pre}$	Equation (4.103)	2307 N
$\Phi_{Bellmouth\ ext}$	Equation (4.99)	-504 N
$D_{Cradle}$	RR First Principle Measurements	723N
( $F_{G9'} - F_{G0}$ ) <sub>ext pot</sub> [ $A_{9'ext} = A_f$ ]	Equation (4.114)	2388 N
( $F_{G9'} - F_{Gf}$ ) <sub>ext pot</sub> [ $A_{9'ext} = A_f$ ]	Equation (4.119)	0 N

**Table 7.1: Thrust Correction Factors**

The above equations are not only useful for filling the thrust correction equations derived above, but also to allow parametric analysis to be accomplished. These kinds of studies help the understanding of how the engine-cell dimensions and performance affect the cell flow structure and accordingly the thrust measured by the load cell. Analytically derived maps are reported in paragraphs 4.3.10, 4.3.12 and 4.4.3 showing how some of the thrust correction factors change with the engine-cell dimensions and performance. In particular the thrust correction factors analysed are the potential buoyancy term, the ( $F_{GTH} + \Phi_{bell}$ ) and the pre-entry force.

One important result has been obtained analysing the term ( $F_{GTH} + \Phi_{bell}$ ) of equation (7.6). The two terms, inside the brackets, are singularly the largest thrust correction factors of that equation. Therefore, it can be assumed that the trend of the entire equation depends on the magnitude of their relative contributions. Figure 7.1 shows the parametric analysis of the term ( $F_{GTH} + \Phi_{bell}$ ) as a function of the cell entrainment ratio and  $\lambda$  ( $\lambda = A_{cell} / A_{th}$ ). It is seen that the magnitude of the thrust correction factors increases in a very non-linear fashion when  $\lambda$  is reduced and the cell entrainment ratio increases. This means that the thrust correction factor decreases either by increasing the cell dimensions or by reducing the engine dimension. It is possible to see that they tends asymptotically to zero as  $\lambda$  continues to increase. At the same time, however, the amount of secondary flow entering the cell also affects the thrust correction factors. In fact, the curves of Figure 7.1 are shifted upwards to increasing thrust correction factor as entrainment ratio increases.

From equations (7.7), (7.8), (7.9), (7.10) and (7.11) and the map shown in Figure 7.1 the second objective proposed in paragraph 3.2.1 is achieved. Indeed, the equations show the possibility of representing the thrust correction factor by ordinary engine-cell dimension and performance parameters. This allows the calculation of the corrections either by cell measurements or by basic first principle aerodynamics. Furthermore, parametric analyses as shown in Figure 7.1 enhance the understanding of the enclosure effects on thrust correction factors.

These are also novelties of this work. In fact,, in the open literature, the effects of the test cell enclosure are only qualitatively mentioned. To the author's knowledge the latter effects have not before been derived analytically.

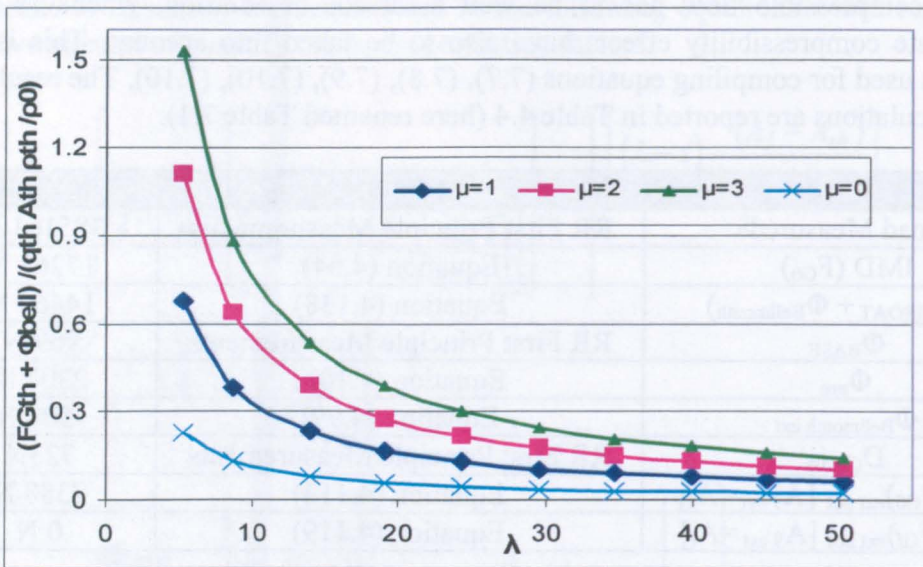


Figure 7.1: Parametric Analysis of the Term  $(F_{Gth} + \Phi_{bell})$  Function of  $\lambda$  and  $\mu$

However, not all the thrust correction factors, named in the thrust correction equations, have been analytically derived. The base force, the cradle drag and the carcass friction drag are left apart. However, the most important thrust correction for which analytical derivation has not been achieved is the external bellmouth drag. This does not, in fact, allow a complete comparison between the above thrust correction factors. In equation (7.1) (or (7.4)) an estimation of such a drag is required to fully compile it. Therefore, despite the fact that the above thrust correction equation is included in the comparison it has to be underlined that it is not complete. Further study should concentrate on the analytical representation of the above missing factors.

In order to validate both the thrust correction equations derived above (equations (7.4), (7.5) and (7.6)) and the thrust correction relationships ((7.7), (7.8), (7.9), (7.10) and (7.11)) Rolls-Royce genuine data (engine C in test cell "X") have been used to make a comparison. The assumptions for this comparison are listed in paragraph 4.5.4.

The comparison is shown in paragraph 4.5.4 by using for each thrust correction equation two approaches for the potential buoyancy effect. Here the results of the comparison are tabled for only one approach for the potential buoyancy term used. This is in order to avoid complication on the understanding of the value.

The comparison, as shown in Table 7.2, is made in terms of the percentage of the load measured. In this way an estimation of the amount of the thrust correction factors in relation to the total load measured is also given.

The results obtained for the different equations show a very good agreement since the maximum difference between them is the 0.115% of the total load measured.

This to some extent validates the derivation of the thrust correction equations and the thrust correction factor relationships.

Therefore, the results in Table 7.2 represent further confirmation that the first two objectives stated in paragraph 3.2.1, within the assumption made, have been achieved.

Thrust Correction Equation	$F_{G9}/L$
$L = F_N - D_{cradle} - D_{bell-ext} + (F_{G9} - F_{G0})_{ext\ pot} - \phi_{Gbase}$ $(A_{9'ext} = A_f)$	1.043014
$L = F_N + \phi_{Gpre} - \phi_{Gbell\ ext} - D_{cradle} + (F_{G9} - F_{Gf})_{ext\ pot} - \phi_{Gbase}$ $(A_{9'ext} = A_f)$	1.041913
$L = F_{G9} - F_{Gth} - \phi_{bell} - D_{cradle} + (F_{G9} - F_{Gf})_{ext\ pot} - \phi_{Gbase}$ $(A_{9'ext} = A_f)$	1.041943

Table 7.2: Thrust Correction Equation Comparison

Following the discussions of Chapter 4 it could be thought that equation (7.6) is the most suitable for a direct calculation of the thrust correction factors by flow measurement inside the cell.

Indeed, due to the quality of the flow at the engine throat (usually it is well defined) the distortion problems can be avoided. Flow distortion up-stream of the engine can affect the flow measurement and consequently the determination of the force acting on the metric-assembly. It has to be underlined that between the engine face and the bellmouth there is usually an airmeter for measuring the engine performance. Therefore, the same airmeter can be used for measuring the flow conditions at the engine throat.

Concerning the force acting on the bellmouth, a static pressure field can be obtained by mapping the bellmouth with pressure taps. Such measurements are not something completely new. Indeed, in some of the Rolls-Royce facilities there are already sets of static pressure tappings along the engine bellmouth.

Furthermore, the contribution of the potential buoyancy term to the total thrust correction factor is much lower if it has to be calculated between station (f) and (9) than between station (0) and (9). Therefore, this is another advantage of equation (7.6) (compared to equation (7.4)) which in such a way allows a more accurate estimation of the thrust correction by flow measurements in the cell.

However, it has also to be said that the thrust correction equation which involves the use of the stream gauge force at the engine throat also requires the measurement of the force acting on the entire bellmouth. The magnitude of these two terms is quite large and therefore even a small error in the measurement can bring a sizeable alteration to the results. This fact plays a role against the use of this thrust correction equation and would address the correction of the thrust measured by the means of another thrust correction equation. From this point of view the thrust correction equation which involves  $\Phi_{pre}$  and  $\Phi_{bell-ext}$  would suit the above considerations better. The use of this equation involves an additional term to measure ( $\Phi_{pre}$ ) if compared with that which uses the engine throat as interface, but the magnitude of each single term is smaller. However, the main concern with the use of this thrust correction equation is the pre-entry force. Indeed, this term can not be directly measured during the test and therefore its estimation requires the use of either CFD software (paragraph 6.2.8) or the analytical approaches proposed in equation (7.8).

The thrust correction equation which uses the potential buoyancy term calculated from station (0) to station (9) appears to be the most direct to use. However, this equation is the one which has least confirmation with the experimental data. Indeed, the most of the thrust correction factors are enclosed in the potential buoyancy term which is not measured but is analytically computed (equation (7.9)). Furthermore, in this equation the external bellmouth drag also appears. This would be extremely

expensive and time consuming to determine. Indeed, experimental test which must reproduce the same test cell environment would be required to make such an estimation.

Underlining the advantages and the disadvantages of each thrust correction equation, the above considerations partially answer the third objective in paragraph 3.2.1. Indeed, the reliability and the accuracy of the thrust correction equation depends on the confidence in the measurement systems and computational tools available. Therefore, depending on the cell set up and on the method used, each thrust correction equation developed could be the more appropriate for the calculation of the thrust delivered by the engine.

Following the same approach used for studying the indoor sea-level test facilities, the outdoor stands have also to be taken into account. The aim of this was to understand the main differences between the flow structures in the two situations.

Using the engine model represented in paragraph 4.4.1 it has been found that in free air conditions with a head wind in the engine axial direction, the force acting on the bellmouth is equal to the difference between the gauge throat stream force and the intake momentum drag (equation (7.12))

$$-\phi_{G_{bell-freeair}} = F_{G_{th}} - F_{G_0} \quad (7.12)$$

The above equation has been derived by assuming that the wind velocity was sufficiently high to allow the stagnation point to be around the engine bellmouth lip. Assuming now that the wind velocity drops to zero equation (7.12) can be rewritten as:

$$-\phi_{G_{bell-freeair}} = F_{G_{th}} \quad (7.13)$$

Equation (7.13) shows that in free air condition the gauge force acting on the bellmouth compensates the stream gauge force acting on the engine throat. Substituting equation (7.13) into equation (7.6) (re-arranged for free air conditions with no-air flows around the engine if the wind velocity is zero) it is possible to obtain equation (7.14).

$$L = F_{G_9} \quad (7.14)$$

Equation (7.14) shows that for outdoor tests, in zero-wind conditions, the gross thrust delivered by the engine is equal to the load measured by the load cells.

In paragraph 4.4.1 it has also been proven that equation (7.13) is also valid when the wind velocity is not so high and the stagnation point lays on the engine carcass.

Substituting equation (7.13) into equation (7.11) it is possible to compare the force acting on the bellmouth in free air conditions with that acting on it in the indoor conditions

$$L_{bell-freeair} > L_{bell-freeair} \quad (7.15)$$

Equation (7.15) shows that the force acting on the bellmouth in free air conditions is larger than the force acting on it in indoor conditions.

This result confirms the trends of Figure 7.1. There it is shown that for an indoor test the term  $(F_{GTH} + \Phi_{bell})$  is always bigger than zero and it tends to zero only for infinite cells dimensions (free air condition).

Therefore, the above considerations underline the fact that the main difference between the outdoor and the indoor is the recovery of the throat gauge force by the gauge force acting on the bellmouth. In fact in free air conditions this force recovery achieved is 100% whilst for indoor conditions it is only partially achieved.

The above findings answer to the fourth objective proposed in paragraph 3.2.1. Indeed, it has been shown in equation (7.14) that in free air conditions the load measured is the real gross thrust delivered by the engine. Furthermore, it has also been identified that the bellmouth force is the main difference between the outdoor and indoor condition.

However, it has to be said that further studies are needed to improve the understanding of the flow around the engine. In particular, the effects of the engine jets on the hot nozzle duct, on the plug and on the pylon have to be taken into account for a complete balance of the forces acting on the system.

## **7.2.2. Analytical Prediction Tool**

In Chapter 5 a one dimensional ejector pump analysis has been applied to the indoor sea-level test facilities to analytically study the influence of the interaction between the engine and the exhaust collector on the flow inside the cell.

The ejector analysis is based on basic aero-dynamics principles including the continuity equation, momentum and energy conservation, the ideal gas relationship and assumes compressible flow in every part of the model.

The main assumption of this model is the theoretical division of the detuner into three regions, the Accommodation Region, the Mixing Region and the After-Mixing Region. Furthermore, to make such an analysis applicable also to turbofan engines a fourth region is used, the Preliminary Region. All the characteristics of the above regions are explained in paragraphs 5.2.3, 5.2.4, 5.2.5 and 5.2.6.

The decision to use this approach is driven by the fact that for the usual cell dimensions the flow along the detuner does not achieve fully mixed conditions. Therefore, another reference section (before the mixing section) is needed to study the engine-detuner ejector performance.

Due to the difficulties of defining a pressure loss coefficient for unmixed flows the analytical model does not take into account pressure losses until the flow is fully mixed.

The application and the assumptions of this analytical study are explained in paragraphs 5.2.3, 5.2.4, 5.2.5 and 5.2.6.

The Analytical Model derived is able to define the engine-detuner characteristics for the three detuner regions (Accommodation, Mixing and After-Mixing). This is shown in paragraphs 5.3.4, 5.3.5 and 5.3.6 by using Rolls-Royce engine-cell dimensions and performance data

The first result of this analysis is the enhancement of the understanding of the flow phenomena taking place inside the facility and in particular along the detuner. Figure 5.13 shows how the static pressure changes at the Accommodation Region and

therefore characterises the engine-detuner ejector effect. Figure 5.16 illustrates the static pressure recovery along the detuner when complete mixing is achieved.

shows how pressure losses affect the engine-detuner characteristic. The understanding of these phenomena is very important to increase the confidence with engine-cell performance. Indeed, for example, the knowledge of the pressure trends along the detuner can be useful for setting up CFD (or experimental study) or to propose modifications achieved through performance enhancements.

Using the experimentally measured cell entrainment ratio the Analytical Model is also able to define the operating lines of the engine-detuner system as is shown in Figure 5.15 for the Accommodation Region.

This allows a complete study of the three regions defined along the detuner. Indeed, by derivation of the characteristic lines it is possible to know where the system operating point can move and using the operating line, it is possible to locate it.

This approach assumes more relevance if related to the Accommodation Region. Indeed, such a region is the only one (of the three defined) which really takes place along the detuner (for common cell dimensions) and therefore can be used as a link with the actual engine-detuner system.

The importance of this approach is also supported by the fact that the analytical results at the Accommodation Region agree pretty well with the experimental ones (Hickman, Gilbert, and Carey 1970).

The above considerations underline the possibility of deriving a tool able to predict the cell entrainment ratio once the cell operating line is known. The attempt to derive such a tool is described in paragraph 5.4.

The first requirement to satisfy is to find a representation which allows the definition of a unique cell operating line which is independent of the engine type. Indeed, Figure 5.15 shows that not all the parameters provide a representation of a unique cell operating line.

To achieve this goal, a non-dimensional analysis is been carried out.

Several attempts at this analysis are shown in paragraph 5.4.1.

The results show that it is possible to find a set of parameters which allow the representation of only one operating line for the system. However, such a choice is not able to represent the system by the means of only one map. Indeed, the operating line and the characteristic line lay one on top of each other.

This is shown in Figure 7.2.

These results open the prospect of establishing a matching procedure able to predict the cell entrainment ratio between two separated plots (one for the operating line and the other for the characteristic line).

Accordingly, by using two different plots the necessity of representing both the lines at the Accommodation Region is no longer a constraint (the horizontal parameter of Figure 7.2 is the non-dimensional primary flow at the Accommodation Region (paragraph 5.4.1)). Therefore, another set of parameters able to represent a unique cell operating line is found (Figure 7.3)



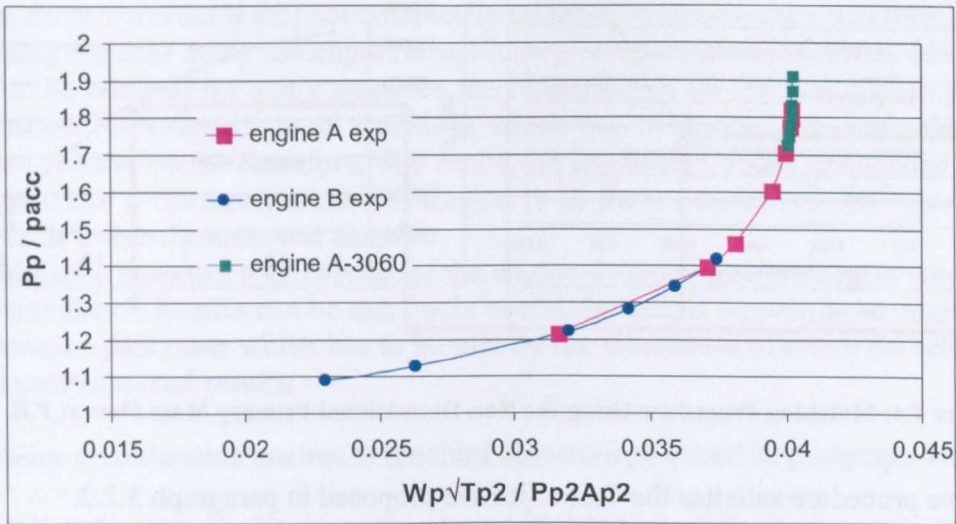


Figure 7.2: Non-Dimensional Representation of the Cell Operating and Characteristic Line

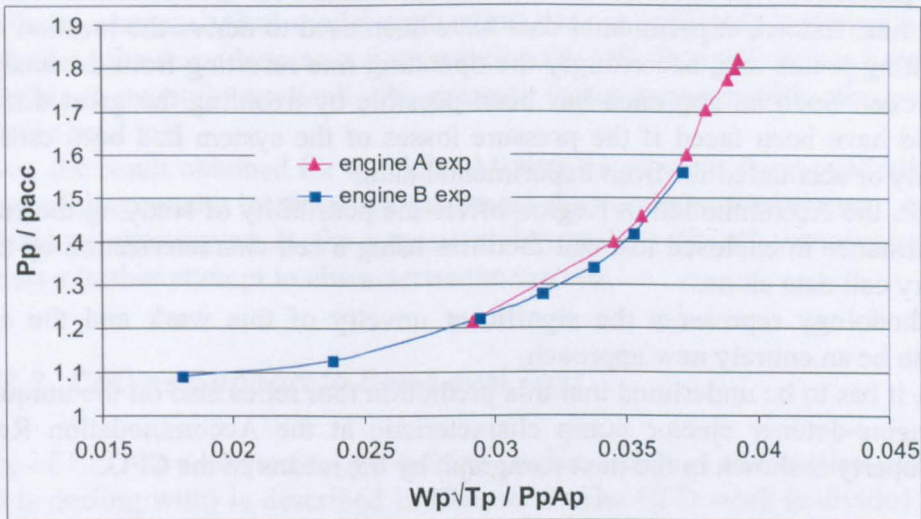


Figure 7.3: Non-Dimensional Representation of the Cell Operating and Characteristic Lines

This time the horizontal axis of Figure 7.3 represents the non-dimensional primary mass flow at the Preliminary Region.

It is now possible to establish a matching procedure between the cell operating line and the cell characteristic line (Figure 7.4).

Knowing the non-dimensional primary flow at the Preliminary Region (from the engine performance parameters) it is possible to enter the map on the left hand side of Figure 7.4 (from the horizontal axis) and find out the static pressure at the Accommodation Region (vertical axis). Once the static pressure at the Accommodation Region has been found it is possible to enter the map on the right hand side of Figure 7.4 to find the entrainment ratio (on the horizontal axis).

Therefore, starting from the engine performance parameters, it is possible to work out the cell entrainment ratio.

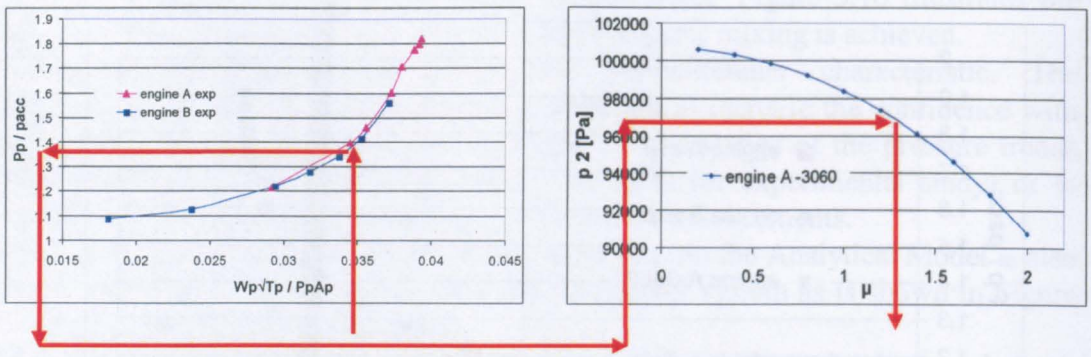


Figure 7.4: Matching Procedure Using the Non-Dimensional Primary Mass Flow at P.R.

The above procedure satisfies the first objective proposed in paragraph 3.2.2. Indeed, a new tool able to predict the cell entrainment ratio has been developed. Such a tool requires only engine-cell dimensions and performance parameters which are usually measured during standards tests. This new prediction tool relies on the cell characterisation for the definition of the cell operating line. Indeed, experimental data have been used to derive the location of the cell operating points and, accordingly the operating line resulting from the analytical ejector model. Such an approach has been possible by avoiding the great difficulty that would have been faced if the pressure losses of the system had been estimated analytically or accounted for from experimental data. As a result, the Accommodation Region offers the possibility of studying the engine-cell performance in enclosed test cell facilities using a cell characterization by means of ordinary cell data alone. This methodology represents the significant novelty of this work and the author claims it to be an entirely new approach. However, it has to be underlined that this prediction tool relies also on the uniqueness of the engine-detuner ejector pump characteristic at the Accommodation Region. Such a property is shown in the next paragraph by the means of the CFD.

The benefits of knowing the cell entrainment ratio before running the engine in the cell are manifold. First of all the cell can be protected from the negative flow phenomena which affect the engine and cell performance. Indeed, if the entrainment ratio predicted does not satisfy the requirements for a clean cell flow field the cell can be modified in order to accomplish these requirements. Secondly, by knowing the entrainment ratio, the thrust correction factors can also be estimated by the one dimensional gas-dynamic analysis described in paragraph 7.2.1.

The combination of the analytical ejector model and the prediction tool is also very useful for CFD analysis. In particular, two distinct advantages can be obtained, one for modelling purposes and the other for validation purposes.

During the modelling process, the knowledge of static pressure at the Accommodation Region can be used as an outlet condition for the cell. This saves the modelling of the exhaust stack and therefore would allow for a larger grid concentration in the test bay in respect of the main compromise that CFD modelling requires (paragraph 6.2). The modelling of the exhaust stack also represents one of the most difficult parts of the

model. This is mainly due to the mixing process along the detuner and into the blast basket. Such a process is still not completely understood theoretically and therefore its modelling requires many assumptions and heavy computational resources. However, it has to be said that for many purposes, the modelling of the exhaust system can not be avoided. For example, in all situations which deal with the flow fields along the exhaust vertical stack. Therefore, this limits the usefulness of the knowledge of the static pressure at the Accommodation Region to all those simulations dealing with the flow fields inside the main test chamber.

For validation purposes a knowledge of the engine-detuner ejector characteristic at the Accommodation Region can be extremely useful. Indeed, it represents an engine-cell performance parameter which has to be met by the simulation to prove the reliability of the computational results.

The above consideration answer to the third objective proposed in paragraph 3.2.2.

Concerning the second objective of paragraph 3.2.2 this will be discussed in the third level of the final discussion of this work. At that time a methodology will be proposed which may prove useful for characterising the entire engine-cell system and, therefore, in controlling the cell entrainment ratio. Indeed, the results worked out during the ejector analytical model application are not sufficient to derive a method for controlling the secondary mass flow entering the cell. Basically this is because it is not possible to quantify practically the pressure losses represented by the proportion of dynamic head lost.

However, the result obtained for the After-Mixing Region can show qualitatively the influence of the pressure losses on the total mass flow entering the system.

is a further improvement in the general understanding of cell aero-dynamics and represents a further attempt to characterise the system.

### ***7.2.3. CFD as Support to Sea-Level Test***

The use of CFD as a support to gas turbine engine sea-level test studies (which this project is dealing with) is described in Chapter 6. The CFD work is divided in three main areas: i) the estimation of the thrust correction factors (paragraph 6.2), ii) the engine-cell characterisation (paragraph 6.3) and iii) general modelling of the cell components (paragraph 6.4). In this chapter each one of these areas is discussed separately.

#### *Quantitative estimation of the thrust correction factor*

The first area to be discussed is the quantitative analysis of the thrust correction factors.

The compromise between final accuracy of results, computational resources available and simulation running time does not allow the modelling of the entire test cell (paragraph 6.2.2). Another approach has therefore been adopted. The inlet and the exhaust systems are not included. The engine mass flow was defined by imposing the static pressure at the engine face (experimental parameter). The total mass flow entering the cell has been matched to the experimentally measured cell entrainment ratio by changing the static pressure at the detuner exit section (Figure 6.2).

Therefore, it is required that the simulation of several model are undertaken until cell entrainment ratio is matched. The application of the step-by step approach to increase the accuracy of the discretization of the governing equation makes the above procedure for matching the cell entrainment ratio even more complicated. Indeed, for each step, the cell entrainment ratio changes and therefore before varying the static pressure at the detuner exit has to be waited that the last step of the discretization approach has converged.

However, it is believed that once the cell entrainment ratio was matched the majority of the flow similarities between the real case and the simulation could also be captured. Therefore, the thrust correction factors could be examined. Indeed, assuming that the computational geometry is close to the actual geometry and since the mass flow and the total inlet pressure are the same. Similarly, the gauge pressure distributions on the surfaces will also be very close. This is of primary importance in any computational study regarding distribution of forces. Accordingly, the total inlet pressure is fixed at the model inlet as a pressure inlet boundary condition and is taken directly by experimental measurements. The summary of the boundary conditions used is reported in Figure 6.15.

All the details about the geometry, the grid and the Fluent settings have been given in paragraphs 6.2.3, 6.2.4, 6.2.5, 6.2.6 and 6.2.7.

The first thrust correction factor to be calculated is the force acting on the pre-entry stream tube defined as the pre-entry force.

The method used for the calculation of this force is based on three steps: the identification of the stagnation region on the bellmouth, the identification of the stream tube and the integration of the pressure along the tube.

The identification of the stagnation points has been achieved by the analysis of the static pressure field around the bellmouth lip. In particular, four stagnation points diametrically opposite around the bellmouth lip have been identified (Figure 6. 23). From each stagnation point a path line in reverse mode has been released using the Fluent path lines tool. Once the four stagnation path lines have been identified a stream tube has been associated to each one of them (identification of the stream tube). This is the main assumption of the pre-entry force calculation. Indeed, in order to account for possible three dimensional effects, which would not allow for a uniform stream tube, four different stream tubes have been taken into account. Each one of the stream tube was assumed to be uniformly made by the path line released from only one of the defined stagnation points. Once the dimensions of the four stream tubes have been found (by extracting the coordinates from the path lines released) it is possible to use a numerical method to associate at each node of the path line a correspondent area (equation (6.5)). Using the Fluent path line tool it is also possible to extract from each node of the path lines the flow properties. Therefore, knowing the gauge static pressure and the element of axial projected area for each node it is possible to compute four different axi-symmetric pre-entry stream forces (equation (6.8)) (pressure integration along the stream tube). The final value of the pre-entry force is computed by averaging the four values defined above (equation (6.9)).

The value of the pre-entry force computed is reported in Table 7.5.

The derivation of the pre-entry force has also led to a more deep study of the pre-entry stream tube. One interesting property of the pre-entry stream tube that the CFD is able to represent is related to the static pressure distribution along the path line. Despite the

convergent shape of the stream tube the static pressure increases moving toward the bellmouth lip. This apparently does not agree with the convergent duct in subsonic flow theory, which would lead to a velocity increase and a static pressure reduction. However, the static pressure along the stagnation stream line has to increase moving toward the bellmouth in order to match the total pressure at the stagnation point. Therefore this justifies the static pressure trend described above but has to be underlined that, such a trend is valid only for the stagnation path line. This is confirmed by the plotting in Figure 6.27 and Figure 6.29 which show a drastic velocity increase and pressure reduction of the stream tube core while moving towards the bellmouth.

Another interesting fact that the CFD plottings are able to show, is that there are not pressure or velocity gradients across the stream tube.

The second thrust correction factor calculated by CFD is the gauge force acting on the entire bellmouth and on the external bellmouth.

The calculation of the gauge force acting on the entire bellmouth does not show any complication and it can be made by a direct integration using the Fluent integration tools. It is however worth to remember that for direct force calculations the accuracy of the grid along the surfaces is of vital importance. Therefore, since the beginning the grid has to be generated taking into account possible grid adaptation (Fluent incorporated b) in order to meet the final standards for the integration accuracy.

About the gauge force acting on the external part of the bellmouth, the first step is that to identify the external part of the bellmouth. Therefore, it is necessary to identify the stagnation region on the bellmouth lip. The methodology used is the same described above. In order to help the integration of the gauge pressure, since the beginning of the modelling the bellmouth surface was divided in several different surfaces. Indeed, the stagnation region can not be understood unless the simulation has converged. Therefore, the division of the bellmouth surface in several components allows for a more complete direct integration by the Fluent tools and it leaves then a smaller part to be integrated manually (equation (6.10)).

The results of the integration are reported in Table 7.5.

The next thrust correction factor calculated by CFD is the base force.

No relation for computing the base force has been defined by the one dimensional aero-dynamics analysis. Therefore, for filling the thrust correction equations reported in paragraph 7.2.1 the experimental measured base force has been used.

In order to compare the thrust correction equations and analyse the validity of the one dimensional analysis also in the thrust correction factor equations filled with CFD results the base force is accounted as that experimentally measured.

However, a comparison between the CFD value of the static pressure at the engine after-body and that experimentally measured is shown.

Two different ways of extracting the static pressure at the engine after-body have been used. The first defines a ring similar to that used in the R-R First Principle Anemometer Method. The second averages the static pressure along the engine cold nozzle duct (engine body).

The results of this are in table Table 7.3.

It is possible to see from the values in Table 7.3 the static pressure calculated by CFD at the cold ring matches the value experimentally measured. This can confirm the capacity of Fluent of representing the depression region experienced by the engine after-body inside the test cell.

CFD		Experimental
p average nacelle [Pa]	p average cold ring [Pa]	Piezoring [Pa]
100700	100543	100543

**Table 7.3: Static Pressure Comparison for the Base Force Calculation**

The next thrust correction factor to be computed by CFD is the cradle drag. In the thrust correction equations reported in paragraph 7.2.1 the experimental measured cradle drag has been used. Therefore, in order to make the comparison between the CFD and the one dimensional results the value experimentally measured is also used in the thrust correction equation compiled with the CFD result. However in Table 7.4 a comparison between the velocity measured around the cradle by the anemometers (paragraph 2.3.2) and the value computed by CFD is presented. By CFD it is possible to compute the velocity around the cradle in several ways. Here two of them are reported. The first calculation is done by drawing a set of vertical planes across the cradle which cut the entire cell and extract the average velocity along them. The second way is a manual velocity measurement by picking up the velocity around the cradle close to where the anemometers are positioned.

CFD		Experimental
Planes Average [m/s]	Manual [m/s]	Anemometers [m/s]
10.5	8.1	7.3

**Table 7.4: Velocity around the Cradle**

Still the CFD results show a good agreement with the experimental values, this is true, especially when the manual approach is used. The main differences are probably due to the blockage area of the cradle. Indeed, the CFD model uses the same structural blockage area of the real cradle but it does not take into account the area of all the instrumentations and tools positioned around the cradle. Furthermore, it has to be underlined the fact that the velocity measurements are also influenced by the distance from the cradle. The manually picked values are taken at a distance from the cradle where the velocity profiles were completely developed. This can justify the slightly higher value. About the values derived by averaging the velocity along cross sectional planes it has to be said that such velocities are computed accounting for the entire cross sectional area of the cell. Therefore, they include also regions located not very close to the cradle.

The next thrust correction factor to be calculated by CFD is the gauge stream force at the throat.

This has been done by extracting from Fluent the values of the static pressure and the velocity.

With these two parameters a direct estimation of the gauge throat stream force can be made.

The last thrust correction factor calculated by CFD is the intake momentum drag.

Accordingly with the definition of the intake momentum drag, the flow velocity has been computed directly by Fluent integration tool 15 m up-streams the engine. At such a distance the flow profile is almost uniform as it is shown in Figure 6.33. After that this velocity has been multiplied by the engine mass flow directly measured by

the Fluent integration tool. The value of the intake momentum drag computed is reported in Table 7.5.

Using the values reported in table Table 7.5 it is possible to compile the thrust correction equation reported in paragraph 7.2.1 in the same form of those expressed in Table 7.2.

Parameter	Value
$v_0$	13.383 m/s
IMD	17170 N
$v_{th}$	173.49 m/s
$F_{GTH}$	103851 N
Bellmouth Total	-90876 N
Bellmouth External	-836,97 N
Pre-Entry Force (A)	1452 N
Pre-Entry Force (B)	1274 N
Pre-Entry Force (C)	1502 N
Pre-Entry Force (D)	1400 N
Pre-Entry Force Average	1407 N
p base nacelle	100700 Pa
p piezo-ring	100543 Pa
Base Force (p nacelle)	342 N
Base Force (p ring)	969 N
$v_{cradle\ CFD}$	8.1 m/s
$\Delta p_{cradle\ CFD}$ (equation (2.10))	38.95 Pa
$D_{cradle\ CFD}$	845 N

Table 7.5: TCF Computed Using CFD Results

Thrust Correction Equation	$F_{G9}/L$
$L = F_N - D_{cradle} - D_{bell-ext} + (F_{G9} - F_{G0})_{ext\ pot} - \phi_{Gbase}$ ( $A_{9'ext}=A_f$ )	1.042771
$L = F_N + \phi_{Gpre} - \phi_{Gbell\ ext} - D_{cradle} + (F_{G9} - F_{Gf})_{ext\ pot} - \phi_{Gbase}$ ( $A_{9'ext}=A_f$ )	1.043145
$L = F_{G9} - F_{Gth} - \phi_{bell} - D_{cradle} + (F_{G9} - F_{Gf})_{ext\ pot} - \phi_{Gbase}$ ( $A_{9'ext}=A_f$ )	1.03808

Table 7.6: Thrust Correction Equation Comparison

Regarding the calculation of the potential buoyancy term the same values reported in table Table 7.1 are used also with the CFD results.

Again it has to be underlined that for the first equation in the table the thrust corrections estimation does not include the value of the external bellmouth drag.

The above two tables fulfil the fifth objective presented in paragraph 3.2.3.

Indeed a quantitative estimation of the thrust correction factors has been made using CFD.

Comparing the result obtained by compiling the thrust correction equations it is possible to obtain a first validation of the findings. Indeed all the equation of Table

7.6 should give the same result (apart for the neglecting of the external bellmouth drag for equation (7.1)).

The bigger difference between the three thrust corrections equations compared is about 0.5% of the load measured. It is worth to notice that regardless the method used to compute the thrust correction factors (i.e back-to-back test, experimental measurements, computational analysis etc.) errors will be always present. The error reported here is within the acceptable margin defined by Rolls-Royce.

Considering that the above thrust correction equations involve quite different terms and the fact also that each term has been computed by some assumption this difference does not appear to be very big. The equation which seems to have more problems is that one which involves the gauge stream throat force. The high flow velocity experienced by the internal part of the bellmouth could be a possible reason to explain the difference. Indeed, the modelling of such high velocity profile could require a more accurate approach than the “standard wall function” (Fluent incorporated b) used in this work. However, at the same time it has to be said that more accurate modelling would require a greater number of cells around the bellmouth. This would increase the computational resources required to allow the simulation to run. Therefore, the main compromise between accuracy, computational resources and simulation time defined at the beginning of Chapter 6 would come back again to play its role.

However, the results shown in Table 7.6 are a very good starting point to enhance the CFD confidence for modelling the flow inside a sea-level test facility and attempting quantitative extrapolations. Furthermore, it has to be underlined the fact that the methodology delivered for achieving this quantitative extrapolation of the thrust correction factors does not involved the study of any improvement of the results. Changing the Fluent settings and compare the different CFD approaches is a valid point for future work.

It has to be underlined that the results provided in Table 7.5 and Table 7.6 represent a novel approach for the calculation of the thrust correction factors in indoor sea-level test cell.

### *CFD study of the engine-detuner ejector pump effect*

The second area, of CFD application in this project, to be discussed is the computational study of the engine-detuner ejector pump effect.

The main purpose of the application of the CFD for studying the ejector effect taking place in indoor test facilities is to understand how the Accommodation Region is affected by different engine-cell configuration.

In order to study the effects of the engine-cell configuration two parameters have been studied: the cradle blockage area and the detuner length. The former represents the influences of the cell configuration up-stream to the detuner on the engine-detuner characteristic at the Accommodation Region. The latter represents the influence of different exhaust system configurations on such a characteristic.

Furthermore, the CFD calculations are also used to derive the engine-detuner characteristic at the Accommodation Region for the original engine and cell configuration.

The computational geometries and settings are described in paragraphs 6.3.2 6.3.3.



Table 6.2 and Table 6.3 show the results obtained for the derivation of the engine-detuner characteristic at the Accommodation Region after the second order of discretization is achieved (the former is related to the model with the cradle and the second to the model without the cradle).

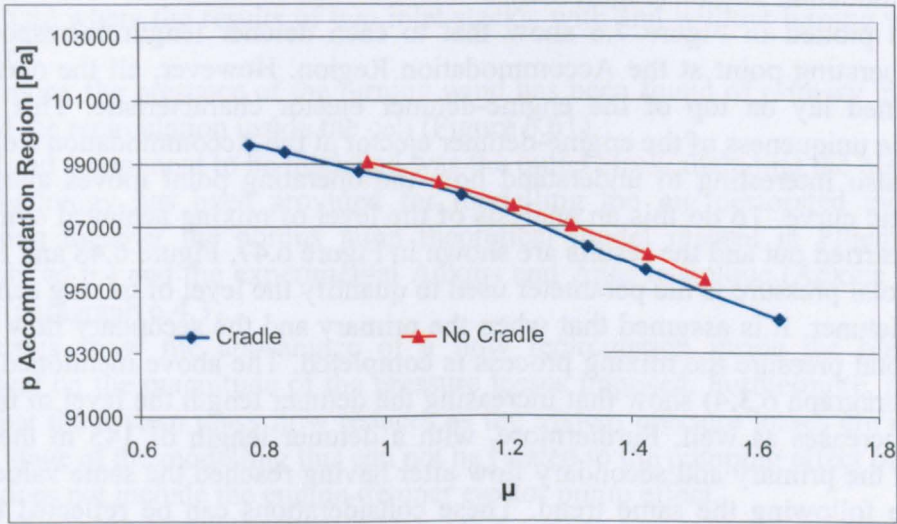


Figure 7.5: Characteristic at the Accommodation Region for Models with and without the Cradle

Figure 7.5 shows the representation of the ejector characteristic at the Accommodation Region for the two models, with and without the cradle.

As it is possible to see in both cases the CFD is able to represent the right shape of such a characteristic. Furthermore, the results of the two set of simulations show that the two characteristics are almost identical. From this consideration it is possible to understand that the ejector characteristic at the Accommodation Region does not depend on the cell configuration up-stream to the detuner.

However, it is possible to see that for equal static pressure, used as outlet boundary conditions for the models, the operating points are not the same. This means that the engine-cell system operating point moves on the characteristic as a function of the cell configuration.

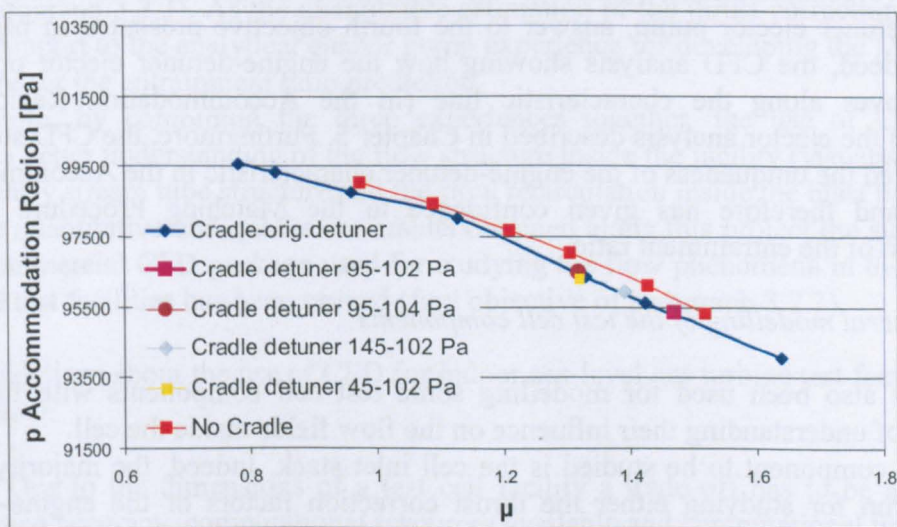


Figure 7.6: Effects of Detuner Lengths on the Operating Point at the Accommodation Region

Table 6.4 lists the results obtained from the models with different detuner lengths (these models include the Cradle).

These results can be plotted in the same map represented in Figure 7.5 in order to show the effect of changing the detuner length on the engine-detuner characteristic at the Accommodation Region (Figure 7.6).

The results plotted in Figure 7.6 show that to each detuner length corresponds a different operating point at the Accommodation Region. However, all the operating points defined lay on top of the engine-detuner ejector characteristic. This result confirms the uniqueness of the engine-detuner ejector at the Accommodation Region. It can be also interesting to understand how the operating point moves along the characteristic curve. To do this an analysis of the level of mixing achieved along the detuner is carried out and the results are shown in Figure 6.47, Figure 6.48 and Figure 6.49. The total pressure is the parameter used to quantify the level of mixing achieved along the detuner. It is assumed that when the primary and the secondary flow reach the same total pressure the mixing process is completed. The above mentioned three pictures (paragraph 6.3.4) show that increasing the detuner length the level of mixing achieved increases as well. Furthermore, with a detuner length of 145 m the total pressure of the primary and secondary flow after having reached the same value start to decrease following the same trend. These considerations can be reflected to the trend of the plot of Figure 7.6 and to relate the level of mixing with the amount of air entering the cell. Indeed, in such a picture it is possible to see that the entrainment ratio increases while moving from a detuner of 45m to one of 95m but it decreases for a 145m detuner length. Therefore, this means that until the fully mix conditions are achieved, an increase of the detuner length brings more flow into the cell. Instead, when the flow is fully mixed an increase of the detuner length brings a reduction to the flow entering the cell. This behaviour is basically due to the pressure losses effects. Indeed, until mixing is not fully achieved, the total pressure of the secondary flow increases despite the system pressure losses. When the energy transfer between the primary and the secondary flows ends, the system pressure losses act to reduce the total pressure of the mixed flow. Therefore, once the mixing is fully achieved the system pressure losses act to reduce the pumping effect and the secondary mass flow entering the cell reduces.

The above considerations, related to the application of the CFD for studying the engine-detuner ejector pump, answer to the fourth objective presented in paragraph 3.2.3. Indeed, the CFD analysis showing how the engine-detuner ejector operating point moves along the characteristic line (in the Accommodation Region) has improved the ejector analysis described in Chapter 5. Furthermore, the CFD study has also proved the uniqueness of the engine-detuner characteristic in the Accommodation Region and therefore has given confidence to the Matching Procedure for the prediction of the entrainment ratio.

#### *CFD general modelling of the test cell components*

CFD has also been used for modelling some test cell components with the main purpose of understanding their influence on the flow fields inside the cell.

The first component to be studied is the cell inlet stack. Indeed, the majority of the models run for studying either the thrust correction factors or the engine-detuner ejector pump did not include the inlet stack but uniform conditions at the main test chamber inlet.

The results show that an inlet stack which also includes the cascade turn winds is able to provide a very uniform flow inside the cell and up-stream to the engine. This is shown by the plots of

Figure 6.62 where the results of two inlet stacks, with and without turning winds, are compared.

Furthermore, the presence of the turning wind has been found of primary importance to avoid the recirculation inside the cell (Figure 6.61).

The second component to be modelled was the outlet stack, including the blast basket. A methodology has been provided for modelling the big perforated cylinder by combining together the porous jump theoretical model present in Fluent ((Fluent incorporated b ) and the experimental Adkins and Anas technique (Adkins and Anas 1996)) (paragraph 6.4.3).

The results show the appearance of a flow recirculation inside the blast basket dependent on the magnitude of the pressure losses imposed. Furthermore, the results show that the system mass flow reduces as the system pressure losses are increased. At this stage of the modelling this can not be related to the pumping effect because the model does not include the engine-detuner ejector pump effect.

Another interesting consideration which can be made by analysing the total pressure trend along the entire exhaust stack is that, by increasing the pressure drop the mixing level inside the blast basket increases (Figure 6.68).

To summarise the tests made by using the Fluent porous jump, it appears that this is a robust model able to simulate the pressure losses across the blast basket. However, there are limitations to take into account. The first limitation is the impossibility of studying the mixing process between the small holes of the blast basket. The second limitation is uncertainty on the determination of the pressure losses. Indeed, the combination of the Adkins and Anas experimental analysis ((Adkins and Anas 1996)) with the Fluent porous jump has to be trimmed in order to provide the same results.

In this paragraph the use of CFD for modelling the flow field inside a gas turbine sea-level test cell has been discussed from several points of view. They can now be summarised in three main points: i) thrust correction factors estimation, ii) engine-detuner ejector analysis and iii) test cell components modelling. The analysis of each point has allowed the achievement of some of the objectives fixed for this part of the work (paragraph 3.2.3). As the quantitative estimation of the thrust correction factors and the support to the analytical ejector pump experience for developing the Matching Procedure for the entrainment ratio prediction.

Furthermore, by combining the three experiences together, the use of CFD has allowed a better understanding of the flow structure inside the facility (visualisation of the pre-entry stream tube structure and the flow recirculation inside the blast basket).

With the quantitative and qualitative results obtained along this project the suitability of the commercial CFD package used for studying the flow phenomena in the indoor sea-level test facilities has been proved (first objective of paragraph 3.2.3).

Some guidelines about the use of CFD for indoor sea-level gas turbine test facilities as listed below.

- Due to the dimensions of a test cell facility a trade off has to be achieved between accuracy, computational resources available and computational time

- To support the above point, a model including only the main test chamber can be used, once the real cell entrainment ratio has been matched, to study the flow inside the cell. Two different approaches have been developed to match the entrainment ratio. The first is to use the analytical ejector model and find out the static pressure at the Accommodation Region corresponding to the actual  $\mu$ . Such a pressure can be used as outlet boundary condition for the model (which ends at the Accommodation Region) and when combined with the actual total pressure at the inlet of the model gives the right mass flow entering the cell (paragraph 5.5). The second method is an iterative procedure by which the static pressure at the exit of the detuner is changed until the actual cell mass flow is matched (paragraph 6.2.2). However, it has to be said that this two processes always need some final adjustments of the boundary conditions in order to match the engine and the cell mass flows.

- Split the cell volume in many detailed volumes in order to achieve the type of mesh required. Such an approach is important because it avoids the use of inappropriate grid typologies with the consequence of keeping always under control the number of the grid elements.

- In such a big model as the test cell facility it is advised to use the grid adaptation tools once the convergence is achieved. This approach avoids running extremely long simulations which would not converge because of some setting problems.

- If the calculation of the force acting either on the external or in the internal part of the bellmouth is one of the targets of the simulation it is advised to split the bellmouth geometry in several surfaces. With the bellmouth split in several parts, first the identification of the stagnation region is easier. In addition for a larger part of the bellmouth surface the calculation can be done automatically using integration tools present in the software package.

- If the calculation of the base force is one of the targets of the simulation it is advised to represent the exact geometry of the fan duct (for a turbofan engine with unmixed nozzle).

- It has been proved that the cradle does not affect the engine-cell performance inside the cell. Therefore it is advised to exclude from the model all the instrumentations and the cell equipment fixed on the cradle and use only the main frame for the simulation.

- If the pre-entry force has to be calculated it is advised to generate a very fine mesh around the bellmouth lip to facilitate the identification of the stagnation stream line. Second it is also advised to have a fine grid also in front of the engine in order to allow an easier data extraction from the path line.

- If a cell characterisation in the Accommodation Region has to be done it is advised to cut the detuner (close to its entrance) with several cross sectional surfaces since the beginning of the modelling. This would facilitate the location of the Accommodation Region.

### 7.3. Second Level

In this second level of discussion the findings reported in the different chapters (Chapters 4, 5 and 6 (and summarised in paragraphs 7.2)) of this work are compared.

#### *One-Dimensional vs CFD Thrust Correction Comparison*

The first comparison is between the calculations of the thrust correction factors using the one-dimensional relationships developed in Chapter 4 and those extrapolated by CFD in Chapter 6.

Table 7.7 gathers together the results previously shown in Table 7.2 and Table 7.6, and Table 7.8 encloses the results previously shown in Table 7.1 and Table 7.5.

As it is possible to see the results obtained by compiling the thrust correction equations either with the CFD data or with the one-dimensional data, are in good agreement.

The maximum difference between them is around 0.39% of the thrust measured by the load cell. This is below the limit which is usually set at 0.5% (private conversation with R-R Staff) for the uncertainty on the determination of the gross thrust delivered by an engine.

The larger differences on the estimation of the thrust correction factors refer to the determination of the pre-entry force and the term  $(F_{GTHROAT} + \Phi_{Gbellmouth})$ .

The estimation of the pre-entry force using the CFD results has been made by a numerical integration of the gauge static pressure along the pre-entry stream tube. Such a procedure contains by itself some uncertainties in both the definition of the pre-entry stream tube and on the integration process as described in Paragraphs 6.2.8 and 7.2.3. Accordingly these uncertainties can affect the value computed. In order to improve the calculation of the pre-entry force it is advised to refine the mesh not only around the bellmouth but also up-stream to the engine where the pre-entry stream tube is located. In such a way more nodes are available for the numerical integration proposed as a method for estimating the the pre-entry force. A better mesh up-stream the engine can also provide a more definite pressure field which can allow a more accurate calculation.

Thrust Correction Equation	$F_{G9}/L$		$\Delta\%$
	CFD	1-D	
$L = F_N - D_{cradle} - D_{bell-ext} + (F_{G9} - F_{G0})_{ext\ pot} - \phi_{Gbase}$ ( $A_{9'ext} = A_f$ )	1.04277	1.04301	0.0242
$L = F_N + \phi_{Gpre} - \phi_{Gbell\ ext} - D_{cradle} + (F_{G9} - F_{Gf})_{ext\ pot} - \phi_{Gbase}$ ( $A_{9'ext} = A_f$ )	1.04314	1.04191	0.123
$L = F_{G9} - F_{Gth} - \phi_{bell} - D_{cradle} + (F_{G9} - F_{Gf})_{ext\ pot} - \phi_{Gbase}$ ( $A_{9'ext} = A_f$ )	1.03808	1.04194	0.386

Table 7.7: Thrust Correction Equation Comparison CFD-1-D

TERM	CFD	1-D	$\Delta$
IMD ( $F_{G0}$ )	17170 N	17263 N	93 N
$(F_{GTHROAT} + \Phi_{Gbellmouth})$	12975 N	14462 N	1487 N
$\Phi_{pre}$	1407 N	2307 N	900 N
$\Phi_{Bellmouth\ ext}$	-836 N	-504 N	332 N

Table 7.8: Thrust Correction Factor Comparison CFD-1-D

Also for the term  $(F_{GTHROAT} + \Phi_{Gbellmouth})$  it is believed that a mesh refinement can improve the results. Indeed, as already said in paragraph 7.2.3, the determination of the throat gauge force and the bellmouth gauge force involve the solution of a high velocity field. Therefore, the “standard wall function” approach used by Fluent (and chosen for these simulations) may not be appropriate. The “enhance wall treatment” is the best alternative offered by Fluent to study the flow in the proximity of bounding walls. However, this approach (also if used only around the bellmouth) would lead to a massive increase of computational elements for modelling the cell which would compromise the computational resource available and the computational time. Therefore its use has to be well evaluated.

A comparison like the one proposed in Table 7.7 and Table 7.8 represent another novelty of this project.

It would be really interesting to have the opportunity of comparing the above presented data with the actual experimental results from back-to back. This would definitely confirm the validity of both CFD and one-dimensional numerical results.

Unfortunately, outdoor test results for computing the real thrust delivered by the engine have not been provided.

### *Ejector Pump Analytical Model vs CFD*

The second comparison is between the CFD result about the engine-detuner ejector pump characterisation in the Accommodation Region and those obtained by the analytical procedure. The aim of this comparison is to have an auto-validation of both the approaches. Indeed, if the two ways of representing the engine-detuner characteristic lead to the same result, the Matching Procedure for the prediction of the cell entrainment ratio is better supported.

Figure 7.7 shows the engine-detuner characteristic curves in the Accommodation Region developed with both CFD and the analytical procedure. In particular Figure 7.7 plots the characteristics derived with CFD using the model with cradle (blue curve) and the model without cradle (red curve) plus the operating points of the different systems associated with different detuner lengths.

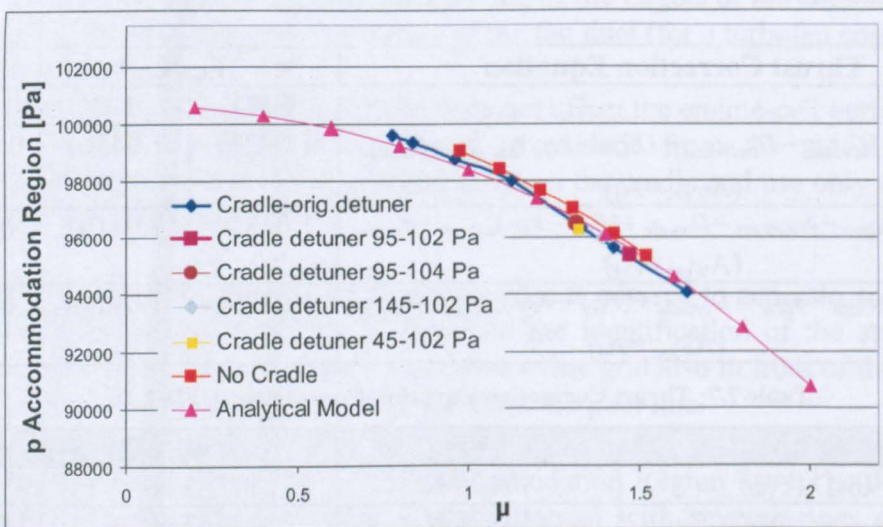


Figure 7.7: Comparison between Analytical and CFD Results in the A.R.

As it is possible to see, all the characteristics are very close to each other. This means that the engine-detuner characteristic in the Accommodation Region predicted using CFD is almost identical to that derived by using the analytical ejector model. This provides a confirmation about the validity of the Matching Procedure and furthermore confirms the validity of the CFD as useful tool for studying the flow in indoor sea-level test facilities.

The above considerations answer to the sixth objective presented in paragraph 3.2.3 which includes the comparison between the thrust correction factors calculated using CFD and those computed by the one-dimensional relationships. Furthermore, by showing that the characteristic at the Accommodation Region calculated using CFD modelling is almost identical to the one computed by the ejector analytical model, also the third and the fourth objectives of paragraph 3.2.3 are fulfilled. Indeed, it has been shown that CFD can improve the analytical approach for modelling the engine-detuner ejector pump but also that the analytical ejector model approach can be used to improve the CFD modelling of the indoor sea-level test facilities.

Dimension	Performance
$A_{cell-(0)}$	$\mu$
$A_{cell-(1)}$	$v_0$
$A_{cell-(9)}$	$v_{th}$
$A_{nozzle}$	$\rho_0$
$A_{eng-(f)}$	$\rho_{th}$

**Table 7.9: Parameters for the Thrust Correction Factors Relationship**

On this second level of discussion it is also interesting to pay attention to the possible interaction between the work presented in Chapter 4 and Chapter 5.

In Chapter 4 the relationships for calculating some of the most important thrust correction factors (equations (7.7), (7.8), (7.9), (7.10) and (7.11)) have been developed as function of common engine-cell dimension and performance parameters (Table 7.8).

As it is possible to see in Table 7.9, where the required parameters are listed, the only parameter unknown before running the engine in the test cell is the entrainment ratio. Indeed, once this parameter is known it is possible to extract the cell velocity at station (0) by knowing the engine mass flow and the cell dimensions. About the throat density, it can be computed either using the isentropic compressible flow relationship (in first approximation) or by knowing the characteristic curve of the engine inlet system.

Therefore, the entrainment ratio is the main unknown for using the above listed equations and calculating the thrust correction factors. In the above listed equations, the intake momentum drag is not mentioned because it is assumed to be known when the flow velocity at station (0) is known (equation (4.50)).

At the same time, the main output of Chapter 5 is the development of a prediction tool able to predict the cell entrainment ratio.

Therefore combining together the one-dimensional relationships for the calculation of the thrust correction factors and the Analytical Prediction tool it is also possible to estimate the thrust correction factors before running the engine inside the cell.

This represents another benefit from knowing the cell entrainment ratio before running the engine. It is worth to say that the above result is supported also by the findings from the CFD studies and their comparison with the engine-detuner analytical ejector model and the thrust correction factors results.

The combination of the thrust correction factors and ejector pump theories developed in this work represents a novel approach for improving the capacity of the test cell.

## 7.4. Third Level

In the third level of discussion, the attention is concentrated on the development of a methodology for predicting and controlling the cell entrainment ratio in sea-level test facilities. Such a methodology is based on the experience and the results obtained from each area of work.

A Matching Procedure for predicting the cell entrainment ratio has been presented in the first level of the discussion (paragraph 7.2.2). Such a procedure, is based on the use of two maps (the operating and the characteristic curves) developed in the Accommodation Region using an ejector pump analytical model. The CFD analyses have improved the understanding of this method (First Level of discussion) and supported its validity (Second Level of discussion).

In the First Level of discussion the possibility of controlling the cell entrainment ratio, predicted using different pressure losses for characterising the system, has been introduced.

An analytical approach for modelling the influence of the pressure losses would require the study of flows not fully mixed (primary and secondary flows in the detuner) whose behaviour is not completely understood. Furthermore, an analytical approach would leave unsolved the problem of transferring its application to the actual cells. Indeed, the practical quantification of the pressure losses analytically applied would require several sets of time consuming and expensive experimental tests.

Therefore, another approach is suggested here.

The method, proposed in this third level of discussion, is based on a cell characterization method using real test data.

In Chapter 5 (paragraph 5.3.4), the derivation of the cell operating line by the application of an analytical ejector model was shown. Such an operating line has been derived by using as input the entrainment ratio experimentally measured for the different engine power settings tested. Such a derivation is based on the actual engine-cell configuration and has been proved to be independent of the engine parameters. In Figure 7.3 a unique operating line has been identified for different engines and power settings. Therefore the operating line depends only on the cell configuration.

By changing the cell configuration the system's operating points, for different engine power settings, will alter their position along their characteristic curve in the Accommodation Region. Accordingly, they would define another operating line, similar to that obtained for the original cell configuration but this time shifted to a different position on the map.

The fact that the system operating point moves along the engine-detuner characteristic in the Accommodation Region has been shown in Figure 7.6 by using different detuner lengths.

Figure 7.8 shows a comparison between the cell operating line worked out for the actual cell configuration and two system operating points for two different cell configurations. As can be seen, altering the cell configuration the system operating



points do not lay on the existing cell operating line. Therefore, different engine-cell operating lines must pass through the new operating points.

Bearing in mind, the findings described above and by (paragraphs 7.2.2 and 7.2.3) running the same set of engine power settings in different cell configurations provides a map similar to that drawn in Figure 7.9. In this map several cell operating lines are plotted as a function of the cell configuration which is represented by the pressure losses of the system,  $\Delta P \%$ .

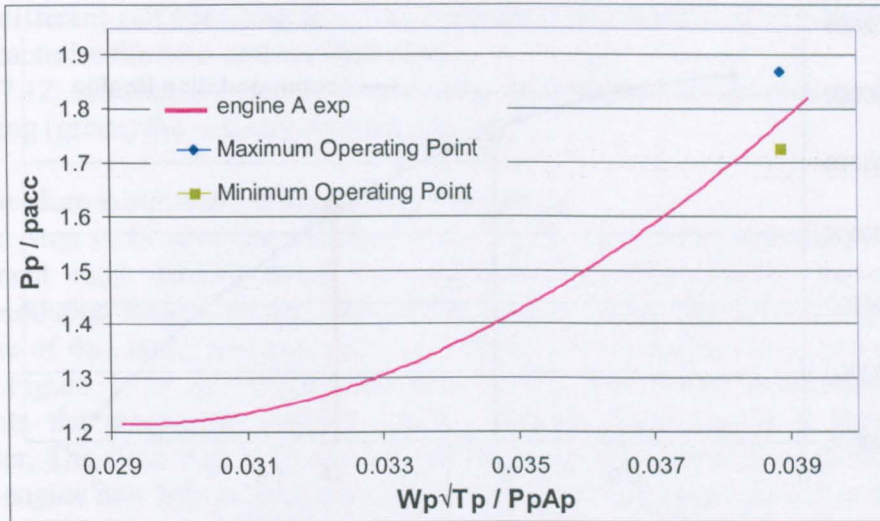


Figure 7.8: Comparison between the Engine-Cell Operating Line Worked Out by the Analytical Ejector Pump Model for the Actual Cell Configuration and Two Different Operating Points Representing the Extreme Working Conditions for the Ejector Pump Characteristic Curve.

Once this map is derived, it is possible to establish another matching procedure which can help control the cell entrainment ratio. Such a procedure would define a complete method for predicting and controlling the cell entrainment ratio.

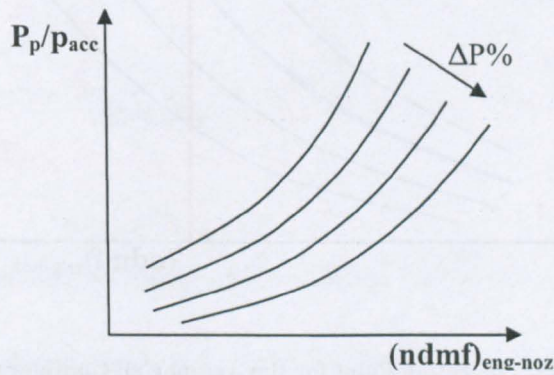


Figure 7.9: Different System Operating Lines for Different  $\Delta P\%$  of the System

The matching procedure for predicting the cell entrainment ratio has already been discussed in paragraph 7.2.2. Attention is now paid to produce a matching procedure for controlling the cell entrainment ratio.

There are two maps used for predicting and controlling the cell entrainment ratio.

The engine-detuner characteristic in the Accommodation Region and the map which includes the different cell operating lines (Figure 7.9). As a starting point it is

assumed that the entrainment ratio that the engine would experience in the test cell has been already predicted and its value is named  $\mu^*$  (Figure 7.10).

This point,  $\mu^*$ , corresponds to a point  $o^*$  on the engine-cell operating line. This is clearly shown in Figure 7.11 where the blue line represents the cell operating line for the original cell configuration and  $o^*$  the operating point of the system for this system configuration. These are the results provided by the application of the prediction tool.

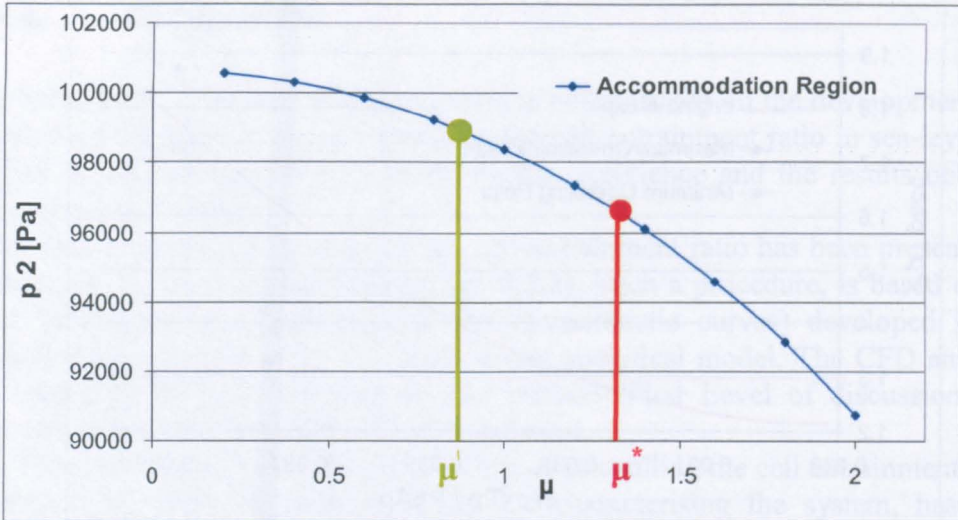


Figure 7.10: Predicted (Red) and Desired (Green) Cell Entrainment Ratio

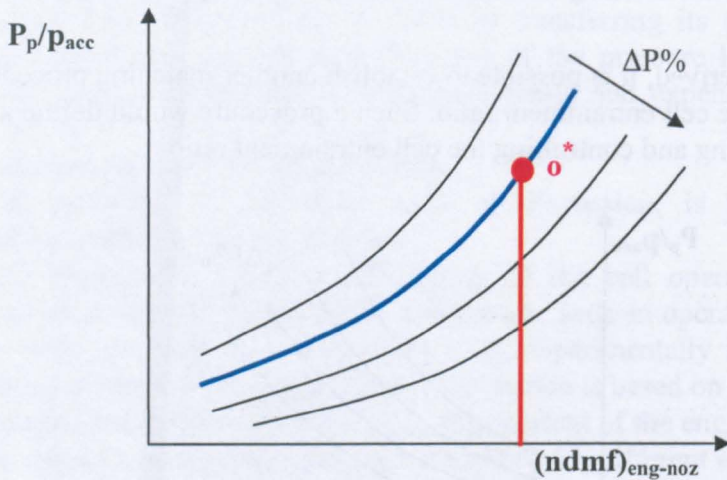


Figure 7.11: Operating Point for the Actual Cell Configuration

In Figure 7.10 is also shown the ideal cell entrainment ratio ( $\mu'$ ) which for the current engine and cell configuration avoids the presence of adverse flow phenomena in the cell (recirculation, separation, distortion). As shown in Figure 7.8 the operating point related with  $\mu'$  does not lay on the existing operating line (in the case of Figure 7.11 this means in the blue line) Indeed, for the existing cell configuration and engine power setting, (engine non dimensional mass flow at the nozzle) the operating point is  $o^*$ . However, the selected entrainment ratio would correspond to an operating point

which lays on another cell operating line, defined for different system pressure losses. Combining together the two maps shown in Figure 7.10 and Figure 7.11 it is possible to provide the system pressure losses which would allow the matching of the entrainment ratio  $\mu'$ , to be defined as target.

Indeed, from Figure 7.10 it is possible to extract the static pressure at the Accommodation Region corresponding to  $\mu'$ . This value can then be used as an input to the vertical axis of the map represented in Figure 7.11. Since the engine power setting remains the same it is therefore possible to find another system operating point along a different cell operating line. The pressure losses associated with this operating line characterise the new cell configuration.

Figure 7.12 summarises the two matching procedures for predicting (red) and controlling (green) the cell entrainment ratio.

This procedure is summarised in the following steps.

The first step is to spot the value of the static pressure corresponding to the cell entrainment ratio desired along the engine-detuner characteristic curve (in the Accommodation Region (right hand side of Figure 7.12)). The second step is to use the value of this static pressure and use it in the cell operating lines map (left hand side of Figure 7.12) by defining the ratio  $P_p/p_{acc}$ . The reader is reminded that  $P_p$  represents the stagnation pressure of the primary flow and is a known engine parameter. The third step consists of using the ratio  $P_p/p_{acc}$  derived in the second step and the engine non dimensional mass flow to find the operating line where the system operating point has moved to. The identification of the new cell operating line allows the estimation of the system pressure losses required to achieve the desired entrainment ratio.

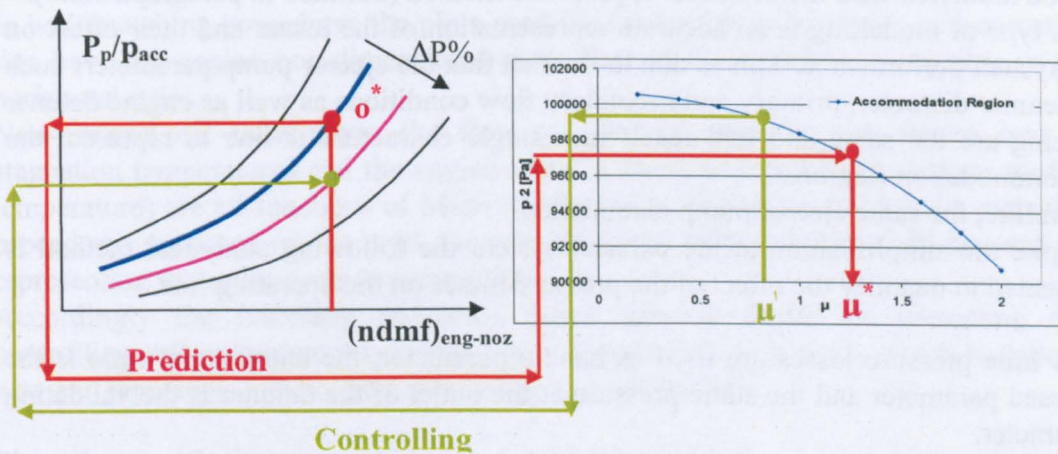


Figure 7.12: Prediction and Controlling Matching Procedures

The main concern related with the application of the controlling matching procedure is the definition of a map which includes the engine-cell operating lines as a function of the pressure losses. As already said during this chapter the flow along the detuner is highly unmixed and therefore an attempt of quantifying its pressure losses would require expensive and time consuming experiments. For this reason at the beginning of this paragraph it has been stated that the controlling matching procedure is based on a cell characterisation using real test data. By this it is intended that the different system operating lines are not derived by direct pressure losses estimations but by characterising the test results derived by altering the configuration of the cell.

The following example is given.

It is suggested that the percentage of the open air of the blast basket is used as a handle. Indeed, it is possible to use plates to cover a percentage of the holes present on the surface of the cylinder.

By covering part of the holes, the engine-cell performance is altered and therefore different cell entrainment ratios can be obtained. Accordingly, testing different engine power settings with the changed blast basket configuration provides a new set of cell entrainment ratios. This new set can be processed with the use of the analytical ejector model (discussed in paragraph 7.2.2) and a new engine-cell operating line will be derived. It is suggested that the new engine-cell operating line is referred to the percentage of the free area of the blast basket and not to the analytically derived pressure losses.

This procedure can be repeated for different blast basket configurations and accordingly different engine-cell operating lines are derived. Such a process eliminates the need to evaluate analytically the pressure losses of the system.

The map shown in Figure 7.9 is qualitative picture of typical pressure loss characteristics.

The validity of the method has been illustrated and a procedure to characterise the cell, using a series of tests, has been presented.

The method suggested eliminates the need to quantify the pressure losses experienced in the blast basket. However, in theory the effect of the pressure losses experienced in the exhaust system can be idealised through the use of an infinite length, constant area detuner which expands the flow to atmospheric conditions.

In such a case, mixing will be achieved in the detuner and therefore pressure losses can be modelled with the use of an appropriate method (outlined in paragraph 5.2.6).

This type of modelling is an accurate representation of the losses and their effect on the system performance. This is due to the fact that the ejector pump parameters such as detuner diameter, primary and secondary flow conditions as well as engine detuner spacing are the same and will result in a single characteristic line to represent the Accommodation Region.

Therefore, the same ejector pump is modelled.

Despite the simplification at the exhaust system the following analytical method is presented to quantify the effect of the pressure losses on the operating line.

This time pressure losses are used as handle parameter, the entrainment ratio is the guessed parameter and the static pressure at the outlet of the detuner is the validating parameter.

An initial guess of the entrainment ratio at the Accommodation Region is required. For this value of entrainment ratio the iterative procedure developed for the Accommodation Region and presented in paragraph 5.2.4 is used to define the flow parameters in that a region.

Once the flow conditions in the Accommodation Region are known the iterative procedure defined for the Mixing Region (outlined in paragraph 5.2.5) is applied.

In this case for the entrainment ratio initially guessed the iterative procedure at the Mixing Region is initialised using the atmospheric pressure.

If the static pressure value computed is equal to the atmospheric then the entrainment ratio guessed equals the entrainment ratio at zero pressure losses.

If the static pressure computed is different than the atmospheric a new value for the entrainment ratio at the Accommodation Region is guessed and the process is repeated until the static pressure is computed as equals to the atmospheric.

For any value of pressure losses other than zero the process is initialised by guessing a value for the entrainment ratio and following the iterative procedure developed for the Accommodation Region.

Once the flow parameters at the Accommodation Region are computed the iterative procedure at the Mixing Region can be applied by guessing a value of the static pressure for initialising it.

This time the static pressure is allowed to vary with the only constraint being that for the given entrainment ratio the static pressure computed must be equal to the static pressure guessed (check condition).

Once the conditions in the Mixing Region are known the After-Mixing iterative procedure (outlined in paragraph 5.2.6) is initialised by guessing the value of the static temperature and using the pressure losses as an independent parameter.

The convergence criterion is that the static pressure computed for the initially guessed entrainment ratio and defined pressure losses must be equal to the atmospheric.

Therefore, if the atmospheric static pressure is not matched another value of entrainment ratio must be guessed and the entire process repeated.

The matching procedure derived here for controlling the cell entrainment ratio also offers the opportunity of controlling the thrust correction factors. Indeed, the cell entrainment ratio can also be varied in order to match a previously fixed value for the thrust correction factors. This is on the basis that one-dimensional relationships have been derived and expressed in terms of generic engine-cell dimensions and performance parameters (paragraph 7.3).

Another important input for improving both the matching procedures for predicting and controlling the cell entrainment ratio comes by non-dimensional analysis considerations.

In both matching procedures the plots used for representing the engine-cell operating line have the engine non-dimensional mass flow at the nozzle as a variable in the horizontal axis.

Non-dimensional mass flow, the flow velocity (divided by the square root of stagnation temperature) and the engine specific thrust (divided by the square root of temperature) are all functions of Mach number only. Therefore, in both the matching procedures proposed in this work the specific thrust of the engine could be used for representing the engine-cell operating line.

Accordingly the matching procedure using specific thrust for predicting and controlling cell entrainment ratio has been originated by this work, which is entirely new and represents a major step forward in test cell analysis.

Since the specific thrust is an engine designed parameter this method of characterising cell performance is extremely useful for the test cell operator.

A complete validation, against real cell data, has not been fully accomplished in this work. However, for the validation of the prediction tool, the performance data of different engines, tested in a defined cell, can be used to produce the engine-detuner characteristic line in the Accommodation Region. Following this, such characteristics can be used in association with the engine-cell operating line to compute the cell entrainment ratio.

The values computed could then be compared with those experimentally measured. Basically the data needed to accomplish this validation process are the dimensions and performance of the engine previously tested in a cell whose engine-cell operating

line has been derived already (in the case of this thesis test cell Y). These data are sufficient for producing the engine-detuner characteristic in the Accommodation Region and therefore, also for using the entrainment ratio prediction tool. Accordingly the entrainment ratios predicted can be compared with those measured in the cell. For the validation of the one-dimensional thrust correction factors, back-to back test (indoor and outdoor) data are necessary.

Further validation is also required for the characteristic curve in the Accommodation Region for both the analytical method and CFD analysis. Indeed, the accuracy and the limitation of both approaches should be studied.

The main limitation for the ejector pump analytical method is that of assuming isentropic flow for the calculations in the Accommodation Region. Such an assumption can be true only under very specific operating conditions (i.e the engine nozzle is positioned in the Accommodation Region plane).

The analytical model does not take into account the effect of the distance between the engine and the detuner which can affect the engine-detuner ejector performance, as has been shown in paragraph 2.2.2.

At the same time the method does not take into account any flow phenomena such as flow recirculation, separation and fluctuation along the detuner which if present, alters the engine-detuner ejector performance.

Another limitation of the engine-detuner ejector analytical model is that in every section the flow parameters are computed as bulk properties (one-dimensionally) and therefore, three-dimensional effects are not taken into account.

The fact that the engine jets (for turbofan engines) are averaged at the Preliminary Region represents another limitation of the engine-ejector model.

The influences of the above limitations on the characteristic line in the Accommodation Region need to be further studied and understood.

In this part of the validation process some experimental tests could be undertaken using the small scale test facility of Cranfield University (described in APPENDIX B). Indeed, the possibility of having experimental data for different cell configurations will be of great importance for this validation process.

From the point of view of the CFD analysis an increase in the modelling accuracy is required. First of all a grid independency analysis is necessary. Indeed, up to now different grids have been tested with the aim of comparing the characteristic curve in the Accommodation Region for different cell configurations. However, a rigorously correct grid analysis for comparing the influence of the mesh in each engine-cell operating point has not been undertaken.

Furthermore, a CFD study related to the quantification of the pressure losses is necessary for understanding those software settings which better represent the flow inside the cell. That is, how the operating points move along their characteristic.

The above considerations satisfy the final outcome proposed in paragraph 3.3 about the development of an analytical tool able to predict and control the cell entrainment ratio and the thrust correction for indoor sea-level test facilities.

Figure 7.13 represents the entire procedure presented in this research for predicting and controlling the cell entrainment ratio and the thrust correction factors for sea-level indoor gas turbine engine test facilities.

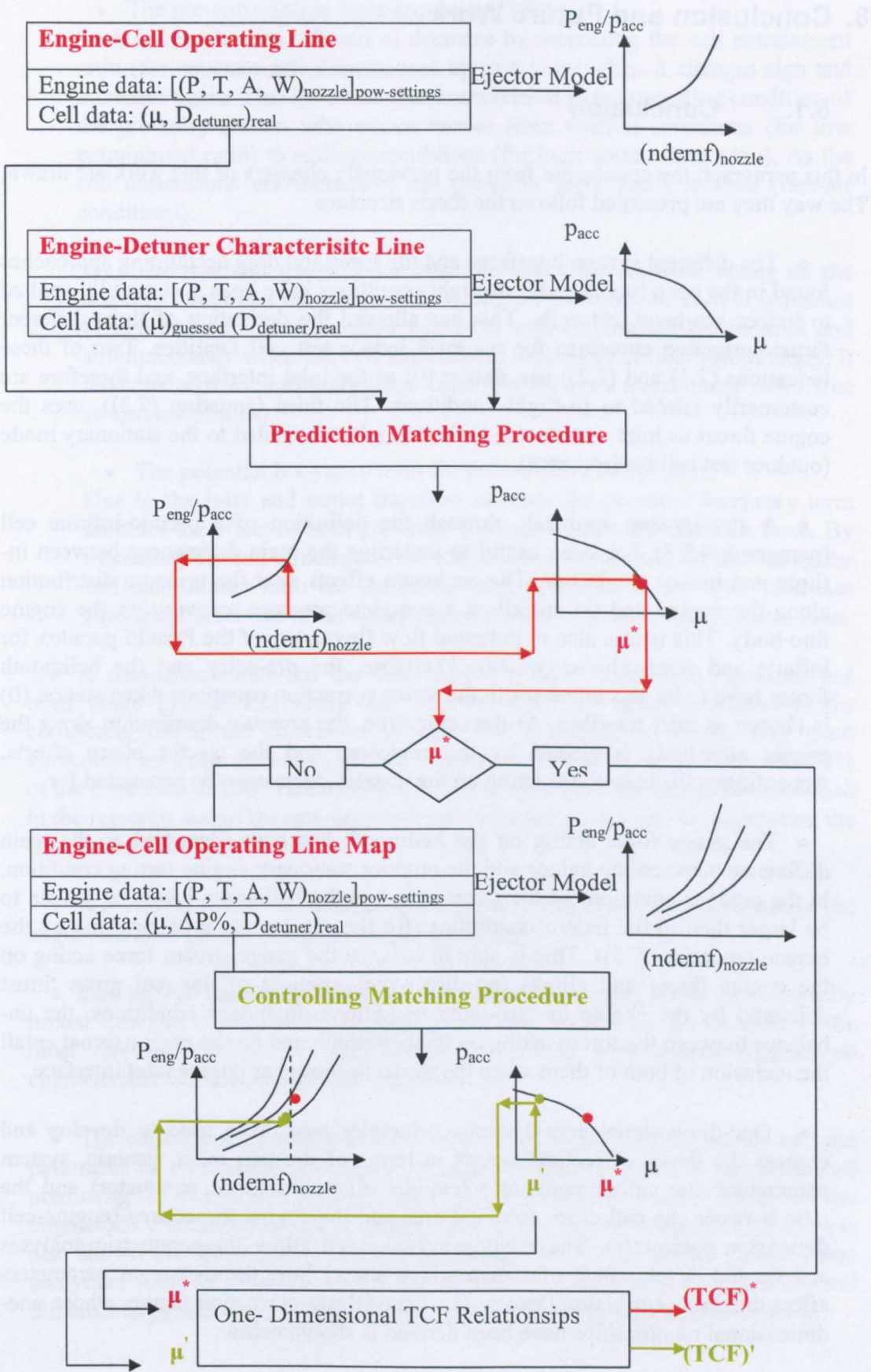


Figure 7.13: Block Scheme

## 8. Conclusion and Future Work

### 8.1. Conclusion

In this paragraph the conclusion from the previously chapters of this work are drawn. The way they are presented follows the thesis structure

- The different system interfaces and the force and drag accounting approaches found in the open literature for in-flight conditions have been successfully applied to indoor sea-level test cells. This has allowed the derivation of three different thrust correction equations for sea-level indoor test cell facilities. Two of these (equations (7.1) and (7.2)) use station (0) as the inlet interface, and therefore are customarily related to in-flight conditions. The third (equation (7.3)), uses the engine throat as inlet section and is therefore better related to the stationary mode (outdoor test cell environment).

- A step-by-step approach, through the definition of a pseudo-infinite cell (paragraph 4.3.3), has been useful to underline the main differences between in-flight and indoor conditions. The enclosure effects alter the pressure distribution along the engine and do not allow a complete pressure recovery on the engine fore-body. This is true also in potential flow (invalidity of the Prandtl paradox for infinite and semi-infinite bodies). Therefore, the pre-entry and the bellmouth forces have to be accounted for in the thrust correction equations when station (0) is chosen as inlet interface. At the same time, the pressure distribution along the engine after-body is altered by the enclosure and the ejector pump effects. Accordingly, the base force acting on the nozzles ducts must be accounted for.

- The gauge force acting on the bellmouth has been identified as the main difference between the indoor and the outdoor stationary engine testing condition. In the outdoor environment the force acting on the bellmouth has been proven to be larger than in the indoor conditions (for the same amount of air draw by the engine (equation (7.5)). This is able to balance the gauge stream force acting on the engine throat and allows the direct measurement of the real gross thrust delivered by the engine in zero-wind conditions. In indoor conditions, the unbalance between the forces acting on the bellmouth and on the engine throat entail the inclusion of both of them when the throat is chosen as engine inlet interface..

- One-dimensional aero-dynamic principles have been used to develop and express the thrust correction factors in terms of the two main, generic, system parameters: the entrainment ratio (engine-cell performance parameter) and the ratio between the cell cross sectional area and the engine throat area (engine-cell dimension parameter). The relationships derived allow for parametric analyses and for the development of a map which shows how the two main parameters affect the thrust correction factors. The list of thrust correction factors whose one-dimensional relationships have been derived is shown below:

- The gauge force acting on the external part of the bellmouth (equation (7.7)).



- The pre-entry gauge force (equation (7.8)).

Such a force has been found to decrease by increasing the cell entrainment ratio (for constant cell dimensions) up to a point when it changes sign and increases again. This behaviour has been related to the operating condition of the pre-entry stream tube which moves from suction conditions (for low entrainment ratio) to spillage conditions (for high entrainment ratio). As the cell dimensions are increased, the pre-entry force tends to zero (free-air conditions).

- The resultant gauge force from the gauge stream force acting on the engine throat and the gauge force acting on the entire bellmouth (equation (7.11)). Such a force increases when the cell dimensions are reduced and simultaneously when the cell entrainment ratio is increased. Accordingly, it tends to zero for infinitely large cells and for zero entrainment ratio (free stream conditions).

- The potential buoyancy term (equations (7.9) and (7.10)).

Due to the inlet and outlet interface sections the potential buoyancy term includes the effect of both pre-entry force and external bellmouth force. By increasing the cell dimensions the buoyancy term reduces. By increasing the cell entrainment ratio the buoyancy term first reduces and then increases (this trend is related to the operating conditions of the pre-entry stream tube).

- A comparison between the three different thrust correction equations has been made (Table 7.2) using the derived one-dimensional relationships for computing the thrust correction factors. The results have shown very good agreement between the equations (the maximum difference is less than the 0.2% of the measured thrust). This supports the validity of both the equations developed in the research and of the one-dimensional relationships derived for computing the thrust correction factors.

- It is shown that a one-dimensional model is able to accurately represent the engine-detuner ejector pump in indoor test cells.

- Due to well known difficulties in representing pressure losses in a non-fully mixed flow, an Accommodation Region has been identified and selected as the most relevant section for representing the ejector performance (engine-cell characteristic line and engine-cell operating line).

- The engine non dimensional mass flow (at the engine nozzle) is used as input parameter in a developed matching procedure which is shown to be capable of predicting the engine-cell performance. Such a procedure involves the use of the engine-cell characteristic and operating lines in the Accommodation Region. It is also shown that these two curves can be derived by the use of the ejector-pump analytical method proposed by knowing only the engine-cell performance and dimensions parameters (such as:  $P_{noz}$ ,  $T_{noz}$ ,  $A_{noz}$ ,  $W_{eng}$ , Detuner diameter and  $\mu$ ).

- This research has led to the significant conclusion that the flow conditions in the Accommodation Region computed using the analytical ejector-pump model

can be used as boundary conditions for the CFD modelling. A great benefit of this approach has been that it also avoids the need to independently model the complex cell exhaust system (blast-basket and exhaust stack). Very importantly and as a result, more attention can then be given to the modelling of the main test chamber.

- It is also concluded from the CFD analysis that the static pressure at the exit of the detuner can be used as handle in an iterative procedure for matching the actual cell entrainment ratio when only the main test chamber is being modelled.

- It is further concluded that CFD can be used to quantitatively estimate the thrust correction factors and that their values can be directly used for compiling the thrust correction equations.

- A comparison has been made between the different thrust correction equations compiled using CFD values. The outcome is a close agreement between them. In fact the difference is as low as 0.5% of the load measured by the load cells. This therefore supports the declared validity of CFD as a useful tool for predicting thrust correction factors.

- A very significant outcome of this research is the conclusion that properly applied CFD is able to represent the engine-detuner ejector characteristics. Similarly, CFD is able to demonstrate how the system operating point moves along the characteristics as a function of the system pressure losses both up-stream and down-stream of the detuner. Furthermore the work has shown that these results are in good agreement with those computed from the one-dimensional ejector pump model developed in the work. Indeed, one of the strongest outcomes of this work has been the conclusion that both the engine-cell characteristic lines computed with the one-dimensional model and those computed with CFD for different cell configurations are almost identical.

- A further important outcome of the research is that the engine-cell characteristic line in the Accommodation Region is unique. This supports the validity of the matching procedure derived for predicting the cell entrainment ratio.

- The CFD results presented here have shown that the cascade elbow in the first bend of the inlet stack allows a very smooth flow at the cell reference section (Rolls-Royce test cell X with the engine A). This partially justifies the assumption of using a constant flow profile at the inlet of the test main chamber.

- The experience gained during this research has allowed the derivation of useful guidelines for modelling indoor sea-level test cell with CFD tools (paragraph 7.2.3).

- The pressure losses along the detuner, through the use of the analytical ejector model, can be used as handle parameter for characterising the engine-cell system. Accordingly, a methodology for controlling the cell entrainment ratio has been developed. Such a methodology is based on the use of the engine-cell operating lines map and of the engine-cell characteristic map.

- To overcome the usual difficulties in experimentally measuring pressure losses along a detuner, a novel approach to cell characterisation using ordinary test cell data (e.g., entrainment ratio) is proposed. The parameter used to alter the cell configuration is the percentage of free holes in the blast basket. The cell entrainment ratio measured for each different blast basket configuration can be processed through the ejector pump analytical model. Accordingly, different cell operating lines can be derived. The matching procedure developed for controlling the cell entrainment ratio can then be applied and the cell configuration which best suits the desired engine-cell performance can be selected. These parameters include desired entrainment ratio for avoiding negative flow phenomena inside the cell and desired thrust correction factors to best suit the flow measurements.

- A further important outcome of this research is the matching procedure using specific thrust for predicting and controlling cell entrainment ratio, which is entirely new and represents a major step forward in test cell analysis.

## 8.2. Future Work

- To validate the possibility of producing the operating lines map for different system pressure losses by applying to the already existing engine-detuner ejector model another iterative procedure. Such an additional iterative procedure would allow moving from the After-Mixing Region back to the Accommodation Region and accordingly to evaluate the difference in entrainment ratio as function of the pressure losses. This procedure has been outlined a first validation to achieve before planning any other cell characterization by experimental testing.

- To improve the validation of the matching procedure for predicting the cell entrainment ratio using the performance data of different engines and comparing their experimental entrainment ratios with those predicted by the method.

- To include in the thrust correction equations already developed the effect of the interaction between the engine afterbody components (such as pylon, hot duct and plug) and the engine and cell flows.

- To develop one-dimensional relationships for calculating the gauge forces acting on the engine after-body components (such as pylon, hot duct and plug) using engine-cell ordinary dimensions and performance parameter.

- To improve the CFD modelling in order to extract more accurate value for the determination of the thrust correction factors. In particular, it is recommended that the grid density and shape are improved to understand how the pre-entry force and the term ( $F_{GTHROAT} + \Phi_{Gbellmouth}$ ) are affected.

- To investigate the opportunity of having a representation of the cell operating lines which includes the engine specific thrust as a parameter for characterizing the engine performance.

• *To compare the thrust correction factor derived using the one-dimensional relationships and CFD with the result of experimental back-to-back tests (which also include outdoor tests)*

• To improve the CFD Modelling of the entire cell by adding the different cell components already modelled and using the experience gained.

• To understand the possibility of using an ejector pump model which would allow the control of the flow all along the detuner rather than in three different sections. Furthermore, another step forward would be to include the pressure losses in each part of the detuner rather than only after the flow is fully mixed.

## Reference

### Reference List

1. Adkins, C and A. Anas. 1996. The Blast Basket a New Component Used in Testing Large, High By-Pass Ratio, Fan Engines. International Gas Turbine and Aeroengine Congress and Exhibition.
2. Aeronautical Research Council. 1955. Report of the Definitions Panel on Definitions of the Thrust of a Jet Engine and of the Internal DRag of Ducted Body. Her Majesty's Stationary Office.
3. A.R.C. 1958. Report of the Definitions Panel on Definitions to be used in the Description and Analysis on Drag A.R.C. C.P. No.369. Her Majesty's Stationary Office.
4. Airflow TA45 Thermal Anemometer Operating Instructions.
5. AMT Netherland Manual Olympus. AMT Netherland Revision 2.09.
6. Anderson, E.R. and P.A.Graham. 1968. Improvement of Ejector Diffuser Performance by Reduction of Backflow. Journal of aircraft vol 6 NO. 1 pp73-74.
7. J. D.Anderson, 2001. Fundamental of Aerodynamics Mc Graw Hill.
8. Ashwood, P.F. 1972. An Altitude Test Facility For Large Turbofan Engines. AIAA/SAE 8th Joint Propulsion Specialist Conference.
9. Operation and Performance Measurement on Engine in Sea Level Test Facilities. Operation and Performance Measurement on Engines in Sea Level Test Facilities: 1984. AGARD Lecture Series No. 132 .
10. Barton, J.M. 1984. The Role of Computational Fluid Dynamics in Aeropropulsion Ground Testing. Journal of Aircraft Volume 21 number 10.
11. Beale, D.K. 2002. Development of Improved Methods for Simulating Aircraft Inlet Distortion in Turbine Engine Ground Level Test. AIAA 22nd Aerodynamics Measurements Technology and Ground Testing Conference.
12. Beanland, M.H. 1984. Development Testing - Use of Sea Level Test Beds and Rigs. Operation and Performance Measurement on Engines in Sea Level Test Facilities : AGARD Lecture Series No. 132 .
13. Brix, S., G. Neuwerth, and D. Jacob. 2000. Jet Engine Operating Near the Ground. AIAA 2000-3998.
14. Cell Aerospace Test Equipment , [www.cel-aerospace.ca](http://www.cel-aerospace.ca).

15. Chapman, R.D. 1979. Computational Aero-Dynamics Development and Outlook. AIAA Journal vol 17 pp1293-1313: AIAA 79-0129R.
16. Choi, Y.H. and W.Y. Soh. 1990. Computational Analysis of the Flow Field of a Two Dimensional Ejector Nozzle. AIAA 90-1901 26th Joint Propulsion Conference .
17. Cronin, C.E. 1984. Instrumentation Techniques in Sea Level Test Facilities. Operation and Performance Measurement on Engines in Sea Level Test Facilities: AGARD Lecture Series No. 132 .
18. Cross, M. A. 1997. Application of Computational Fluid Dynamics to Analysis of Exhaust Gas-Diffuser Interactions in a Turbine Engine Altitude Test Cell. AIAA 87-2412 23th Joint Propulsion Conference.
19. J.Deen 2004. Turbine Test Cell Phenomena: The Inlet Vortex a Computational and Empirical Analysis, . Cranfield University.
20. Dejean, R.R. 2003. CFD Prediction of test Cell Thrust Correction on High By-Pass Ratio Turbofan (Trent 800). Cranfield University.
21. J. F. Douglas, J. M. Gasiorek, and J. A. Swaffield, Fluid Mechanics 1995.Longman.
22. Elysee, D. 2005. Thrust Equations Applied to a Model Enclosed Test Cell. Cranfield University.
23. Fluent incorporated a) Gambit 2.2 Tutorial and User Guides. Fluent 6.2 Documentation.
24. Fluent incorporated b) User's Guide HTML format. Fluent 6.2 Documentation.
25. Franco, S. 2000. Gas Turbine Test Cell Simulation. Cranfield University.
26. Freuler, R.J. 1982. Current Techniques for Jet Engine Test Cell Modelling. AIAA 82-1272 Joint Propulsion Conference.
27. Freuler, R.J. 1993. Recent Successes in Modifying Several Existing Jet Engine Test Cells to Accomodate Large, High- By-Pass Turbofan Engines. AIAA 93-2542 29th Joint Propulsion Conference and Exhibit.
28. Freuler, R.J. and K.A. Montgomery. 1995. Reducing Large Pressure Fluctuation in REDucing Large Pressure Fluctuation in an Engine Test Cell by Modifying the Exhaust Blast Basket End Configuration. Joint Aeroacoustic Conference 1st.
29. Glenny, D.E. 1968. Ingestion of Debris into Intakes by Vortex Action. N.G.T.E. Pystock Current Paper No. 1114, Ministry of technology.
30. Gonzalez Galinez, S. E. 2003. Thrust Correction Factors for Small Gas Turbine Indoor Test Bed. Cranfield University.

31. Graves, J.R . 1982. Computational Fluid Dynamics the Revolution. *Astronautics & Aeronautics Journal*.
32. Gullia, A. 2003. Computational and Experimental Analysis of Gas Turbine Engines in the Ground Level Test Bed Cell. Cranfield University .
33. Gullia, A. and others. 2005. A Preliminary Investigation of Thrust Measurement Correction in an Enclosed Engine Test Cell Facility. AIAA 43rd Aerospace Sciences Meeting and Exhibit.
34. Hagues, A. 2005. Gas Turbine Performance in Test Bed: 3D CFD Exhaust System Modelling . Cranfield University.
35. Hastings, R.R. 1983. Simulation of a Jet Engine Test CELL. National Research Council Canada LTR-ENG-110.
36. Henderson, K. 2000. Ascertaining the Flow Coefficient of the PT75 Airmeter. Rolls-Royce plc. Test 005.
37. Hickman, E.K., J.B. Gilbert, and J.H. Carey. 1970. Analytical and Exprimental Investigation of High Entrainment Jet Pumps. NASA Contractor Report CR-1602.
38. 1958. Fluid-Dynamic Drag, S.F. Hoerner, Published by the Author.
39. Holmes, M. 1984. Data Aquisition and processing in Sea Level Test Beds. Operation and Performance Measurement on Engines in Sea Level Test Facilities\_: AGARD Lecture Series No. 132 .
40. Houghton E.L. and P.W. Carpenter 1993 *Aerodynamics for Engineering Students*, Edward Arnold.
41. Huddleston, D.H., G.H. Cooper, and W.J. Phares. 1986. A Computational Fluid Dynamic Evaluation of Test Cell Recirculation Effects on High-By-Pass Turbofan Engine Surface Pressure Distributions. AIAA 86-1384 Joint Propulsion Conference.
42. Jaques, R. 1984. Aero-Thermodynamic and Acoustic Considerations in the Design of test-beds for Turbojets and Turbofans. Operation and Performance Measurement on Engines in Sea Level Test Facilities : AGARD Lecture Series No. 132 .
43. Karamanlis, A.I., W. Holmer, and D. C. Bellomy. 1985. A Universal Turbohaft Engine Test Cell DEsign Consideration and Model Test Result. AIAA 23rd Aerospace Sciences Meeting.
44. Karamanlis, A. I and others. 1986. Theoretical and Experimental Investigation of Test Cell Aerodynamics for Turbofan Application. AIAA 86-1732.
45. Kleemann, J 2004. Gas Turbine Test Bed Performance-CFDand Experimental Investigation. Cranfield University.
46. Kline, H. 1957. An Aerodynamic Screen For Jet Engines. Douglas Aircraft

Company Report, No. SM-22625.

47. Kodres, C.A. and G.L. Murphy. 1998. Jet-Engine Test Cell Augmentor Performance. *Journal of Propulsion and Power* vol. 14 NO 2 pp 129-134.
48. Krengel, J.H. 1981. Air-Breathing Engine Test Facilities Register. AGARDograph No. 269.
49. Kromer-Oehler, S.L. and D. A. Dietrich. 1984. Computational Analysis of the Flow Field in an Engine Test Cell. AIAA 84-0285.
50. Kromer, S. L. and D. A. Dietrich. 1985. Flow Field Analysis of Low By-Pass Ratio Test Cell. *Journal of Aircraft* vol. 22 No 2 pp 99-100.
51. Lachery, G. 3D CFD modelling of an enclosed sea level test cell for large bypass ratio turbofan engine . Cranfield University: August 2004.
52. Laidlaw, W. R. 1950. Ejector and its Application to Induction Type Wind Tunnel. National Research Council of Canada Report No. Ma-232.
53. Lathi, D.J. and A. Hamed. 1993. Verification of the Theoretical Discharge Coefficient of a Subcritical Airflow Meter. *Journal of Propulsion and Power* Vol. 9, No. 4.
54. Le Fay, A. 2002. Flow Path Analysis within a Model Engine Test Bed. Cranfield University.
55. McLoughlin. 2005. Entrainment Ratio Prediction in Gas Turbine Test Beds. Cranfield University.
56. MIDAP. 1980. Guide to Drag Estimation of Aircraft and Weapons (U). Defense Research Information Centre.
57. MIDAP Study Group. 1979. Guide to In-Flight Thrust Measurement of Turbojets and Fan Engines. AGARDograph No.237.
58. Motycka, D. L. 1975. Ground Vortex - Limit to Engine / Reverse Operation. ASME PAPER 75 GT 3 .
59. Nakayama, A. and J. R. Jones. 1996. Vortex Formation in Inlet Flow Near a Wall. AIAA 96-0803 34th Aerospace Sciences Meeting and Exhibit.
60. Osborn, A.R. 1990a. The Basis for Facility Comparison. Comparitive Engine Performance Measurement: AGARD Lecture Series No. 169.
61. Osborn, A.R. 1990b. Experience in Developing and Improving Altitude Test Capability. Comparitive Engine Performance Measurement: AGARD Lecture Series No. 169.
62. Parfitt, R.N. 2001. Performance Engineering Technical Guide to the Compability, Commissioning and Calibration/Correlation of a Gas Turbine Engine Test Facility. Rolls-Royce DNS 81496.



63. Parfitt, R.N. 2002a. Concept Demonstration and Initial Derivation of Aerodynamics Thrust Correction for Trent 500 on RR Derby 56 Test Bed Using the Indoor "First Principle" Anemometer Method. Rolls-Royce DNS86648.
64. Parfitt, R.N. 2002b. Derivation and Prediction of Aerodynamic Thrust Correction for Trent 800 on RR Derby 56 Test Bed, Using The Indoor "First Principle" Anemometer Method (2nd Enigne Example). Rolls-Royce DNS89450.
65. Power, D. and B.D. Heikkenen. 1993. CFD Applications in Aeropropulsion Test Environment. AIAA 93-1924 "9th Joint Proulsion Conference and Exhibit.
66. Propulsion and Energetics Pannel Working Group 15. 1990. The Uniform Engine Test Programme: AGARD Advisory Group Report No. 248.
67. Prufert, M.B., M.D. McClure, and G. D. Power. 1994. Computational Support to Engine Test. SAE Aerotech -942141.
68. Prufert, M.B., M.D. Mclure, and G.D. Power. 1994. Computational Support to Engine Test. SAE 942141.
69. Prufert, M.B. and J.W. Williamson. 2000. Computational Analysis of Turbine Engine Test Cell Flow Phenomena. AIAA 2000-2210 Aerodynamic Measurement and Ground Testing Conference.
70. Quinn, B.Ejector Performance at High Temperature and Pressure. Journal of Aircraft Volume 13, number 12.
71. Rios, R. M. and others. 1998. Thrust Correction on Jet Engine in Sea Level Test Facility. AIAA 98-3109 34th AIAA/ASME/SAE/ASEE Joint Propulsion Conference and Exhibit.
72. Rolls-Royce Confidential Test Data 01/November/2002 Document No. DKC135688.
73. Rolls-Royce Confidential Test Data 04/April/2005 Book No. 558 Specific Test 251619.
74. Rolls-Royce plc., [www.Rolls-Royce.com](http://www.Rolls-Royce.com).
75. Rolls-Royce plc 2003. Thrust Measurement Rig for a Micro Gas Turbine. Assembly Operation and Maintenance Manual. Rolls-Royce plc. Document Ref. 16180.
76. Rowlands, J. 1984. Unistalled Aero Engine Testing in Operation in the Royal Air Force. Operation and Performance Measurement on Engines in Sea Level Test Facilities : AGARD Lecture Series No. 132 .
77. Rubini, P.An introduction to Numerical Method for Low Speed Flows. Cranfield University School of Engineering.

78. Rudnitski, D.M. 1984. Performance Derivation of Turbojet and Turbofans from Tests in Sea-Level Test cells. Operation and Performance Measurement on Engines in Sea Level Test Facilities: AGARD-LS-132.
79. Rudnitski, D.M. 1990. Experience in Developing and Improving Ground-Level Test Capability. Comparative Engine Performance Measurement: AGARD Lecture Series No. 169.
80. SAE aerospace. 2002. Turbofan and Turbojet Gas Turbine Engine Test Cell Correlation. SAE ARP741.
81. SAE Committee E-33. 1985. In-flight Thrust Determination. SAE AIR 1703.
82. SAE international. 1999. Modeling Techniques for Jet Engine Test Cell Aerodynamics. SAE AIR 4827.
83. Sapp, C. N. and D. W. Netzer. 1978. Experimental Investigation of Turbojet Test Cell Augmentors. Monterey, California: Naval Post Graduate School 67-78-009.
84. H. I. H. Saravanamuttoo, G. F. C. Rogers, and H. Cohen, 1996. Gas Turbine Theory, Prentice Hall.
85. School of Engineering Cranfield University. 1999. The Turbomatch Scheme. Cranfield University.
86. Seddon, J. and E.L. Goldsmith, 1985. Intake Aerodynamics, Collins Professional and Technical Books.
87. A H Shapiro, Dynamic and Thermodynamic of Compressible Flow 1953. Ronald.
88. Shin, H.W. and others. 1986. Circulation Measurement and Vortical Structure in an Inlet-Vortex Flow Field. Journal of Fluid Mechanics, vol 162, pp463-487.
89. Torella, G., G. Liotti, and G. Bruno. 1988. Endurance Ground Testing of the AR318 Turboprop Engine. AIAA/ASME/SAE/ASEE 24th Joint Propulsion Conference 88-3018.
90. Vyas, B. D. and S. Kar. 1975. Study of the Entrainment and Mixing Process for an Air to Air jet Ejector. 2ND Symposium on Jet Pumps and Ejectors and Gas Lift Techniques, From C2-15 to C2-25.
91. P. P Walsh and P Fletcher, 1998. Gas Turbine Performance , Blackwell Science.
92. Williams, D.D. and A.Gullia a) Internal Report 01/03/2005. Cranfield University.
93. Williams, D.D. and A.Gullia b) Internal Report 05/06/2005. Cranfield University.

94. Williams, D.D. and A.Gullia c) Internal Report 08/01/2005. Cranfield University .
95. Williams, D.D. and A.Gullia d) Internal Report 28/07/2005. Cranfield University.
96. Wilson, G. J. 1999. RB211-Trent 800, 51188/1 56 Bed Cross Calibration Test Bed Configuration Control Status . Rolls-Royce TFR 095040.
97. Wunder, M.D. 1984. Testing of Turboshaft Engines. Operation and Performance Measurement on Engines in Sea Level Test Facilities : AGARD Lecture Series No. 132 .

## APPENDIX A. Analytical Model

### A1. Preliminary Region

The Preliminary Region is used when the engine is a turbofan and by a mass weighted average technique the two engine jets are reduced to only one jet.

The starting parameters are shown in the next table.

Cold Nozzle	Hot Nozzle
$P_{pc}$	$P_{ph}$
$T_{pc}$	$T_{ph}$
$A_{pc}$	$A_{ph}$
$W_{pc}$	$W_{ph}$
	FAR

Table A. 1: Preliminary Region Starting Parameters

By the fuel to air ratio (FAR) it is possible to calculate the Universal Gas Constant for the hot jet by the equation (a.1) which is valid for combustion products of kerosene.

$$R = 287.05 - 0.0990FAR + 1E - 07FAR^2 \quad (a.1)$$

At the same time for the cold nozzle can be used R valid for dry air (287.05).

Below it is possible to find the equation used for the iterative procedure at the Preliminary Region referred to the cold jet (with the suffix pc). The same equations and the same procedure are used for the hot jet.

$$p_{pc} = P_{pc} \left( 1 + \frac{\gamma - 1}{2} M_{pc}^2 \right)^{\frac{\gamma}{\gamma - 1}} \quad (a.2)$$

$$t_{pc} = T_{pc} \left( 1 + \frac{\gamma - 1}{2} M_{pc}^2 \right) \quad (a.3)$$

$$W_{pc} = \frac{P_{pc}}{R_{pc} t_{pc}} M_{pc} \sqrt{\gamma_{pc} R_{pc} t_{pc}} A_{pc} \quad (a.4)$$

However, before starting the procedure has to be said that a value of  $\gamma$  has to be guessed for both the flows. Without knowing the static temperature it is not possible to work out the right specific heat at constant pressure value (cp) and so even  $\gamma$  is unknown. A value of  $\gamma$  has been assumed following the experience of Saravanamuttoo et al. (Saravanamuttoo, Rogers, and Cohen 1996), for the cold jet 1.4 and for the hot jet 1.33.

The Mach number is the handle parameter of the iterative procedure and has to be guessed for any iteration until the convergence is achieved.

Compiling equations (a.2) (a.3) with the guessed Mach number it is possible to find out the static pressure and the static pressure which used in equation (a.4) give the mass flow rate of the primary cold jet. As convergence criteria the calculated primary

cold mass flow can be compared with real primary cold mass flow and if the difference is less than 0.001 the results are accepted.

The same procedure is followed for the hot primary jet.

Once the static values are known for both jets it is possible to calculate their respective specific heat at constant pressure,  $c_p$ .

Equation it has been used for the cold jet.

$$\begin{aligned}
 c_{p_{pc}} = & 0.992313 + \frac{0.236688t_{pc}}{1000000} - \frac{1.852148t_{pc}^2}{1000000} + \frac{6.08352t_{pc}^3}{1000000} + \\
 & - \frac{8.893933t_{pc}^4}{1000000} + \frac{7.097112t_{pc}^5}{1000000} - \frac{3.234725t_{pc}^6}{1000000} + \frac{0.794571t_{pc}^7}{1000000} + \\
 & - \frac{0.081873t_{pc}^8}{1000000}
 \end{aligned} \tag{a.5}$$

And Equation (a.6) it has been used for the hot jet (ph).

$$\begin{aligned}
 c_{p_{ph}} = & 0.992313 + \frac{0.236688t_{ph}}{1000} - \frac{1.852148t_{ph}^2}{1000} + \frac{6.08352t_{ph}^3}{1000} + \\
 & - \frac{8.893933t_{ph}^4}{1000} + \frac{7.097112t_{ph}^5}{1000} - \frac{3.234725t_{ph}^6}{1000} + \frac{0.794571t_{ph}^7}{1000} + \\
 & - \frac{0.081873t_{ph}^8}{1000} + \frac{0.081873t_{ph}}{1000} + \frac{FAR}{1+FAR} (-0.718874 + \frac{8.747481t_{ph}}{1000} + \\
 & - \frac{15.863157t_{ph}^2}{1000} + \frac{17.254096t_{ph}^3}{1000} - \frac{10.233795t_{ph}^4}{1000} + \frac{3.081778t_{ph}^5}{1000} + \\
 & - \frac{0.361112t_{ph}^6}{1000} - \frac{0.003919t_{ph}^7}{1000} )
 \end{aligned} \tag{a.6}$$

Knowing the two  $c_p$  it is possible to calculate the two  $\gamma$  by the following formulas.

$$\gamma_{pc} = \frac{c_{p_{pc}}}{(c_{p_{pc}} - R_{pc})} \tag{a.7}$$

$$\gamma_{ph} = \frac{c_{p_{ph}}}{(c_{p_{ph}} - R_{ph})} \tag{a.8}$$

Once the  $\gamma$  of the two jets are known it is possible to find the whole primary flow  $\gamma_p$  by a mass weighted average.

$$\gamma_{ph} = \frac{W_{pc}\gamma_{pc} + W_{ph}\gamma_{ph}}{W_{pc} + W_{ph}} \tag{a.9}$$

For the secondary flow it has been assumed a  $\gamma_s$  of 1.4 since the beginning.

## A2. Accommodation Region

As it has been said in Chapter 5 the main condition at the Accommodation Region is that a uniform static pressure profile is reached where the primary and secondary flow are the same.

The iterative procedure it has been explained in Chapter 5, in this appendix are going to be proved the two checking equations used to work out the Mach number of the secondary flow (handle parameter in the procedure).

The secondary mass flow per unit of area at the Accommodation Region can be written as in equation (a.10).

$$\frac{W_s}{A_{s2}} = \rho_{s2} v_{s2} \quad (\text{a.10})$$

Using the equation for ideal gas the density of the secondary flow at the Accommodation Region can be written as in equation (a.11).

$$\rho_{s2} = \frac{P_{s2}}{R_s t_{s2}} \quad (\text{a.11})$$

And by definition the Mach number of the secondary flow at the Accommodation Region is represented by equation (a.12).

$$M_{s2} = \frac{v_{s2}}{\sqrt{\gamma_{s2} R_s t_{s2}}} \quad (\text{a.12})$$

Using equations (a.11) and (a.12) in equation (a.10) it is possible to derive equation (a.13)

$$\frac{W_s}{A_{s2}} = \frac{P_{s2}}{R_s t_{s2}} M_{s2} \sqrt{\gamma_{s2} R_s t_{s2}} \quad (\text{a.13})$$

The static pressure of the secondary at the Accommodation Region is represented in equation

$$P_{s2} = \frac{P_{s2}}{\left(1 + \frac{\gamma_s - 1}{2} M_{s2}^2\right)^{\frac{\gamma_{s2}}{\gamma_s - 1}}} \quad (\text{a.14})$$

The static temperature of the secondary flow at the Accommodation Region can be expressed as

$$t_{s2} = \frac{T_{s2}}{\left(1 + \frac{\gamma_s - 1}{2} M_{s2}^2\right)} \quad (\text{a.15})$$

Equation (a.14) and (a.15) can be substituted in equation (a.13)

$$\frac{W_s}{A_{s2}} = \frac{P_{s2}}{\left(1 + \frac{\gamma_s - 1}{2} M_{s2}^2\right)^{\frac{\gamma_{s2} - 1}{\gamma_{s2}}}} \frac{1}{R_s} \frac{\left(1 + \frac{\gamma_s - 1}{2} M_{s2}^2\right)}{T_{s2}} M_{s2} \sqrt{\gamma_{s2} R_s t_{s2}} \quad (\text{a.16})$$

The secondary flow area at the Accommodation Region is given by the total detuner cross sectional area minus the area of the primary flow (equation (a.17)).

$$A_{s2} = (A_m - A_{p2}) \quad (\text{a.17})$$

Equation (a.16) can be rewritten as (a.18) by using equations (a.17) which is the same of equation (5.4) used for the first check of the iterative procedure at the Accommodation Region

$$\frac{W_s \sqrt{T_{s2}}}{(A_m - A_{p2}) P_{s2} \frac{\sqrt{\gamma_{s2}}}{R_s}} = \frac{M_{s2}}{\left(1 + \frac{\gamma_{s2} - 1}{2} M_{s2}^2\right)^{\frac{\gamma_{s2} + 1}{2(\gamma_{s2} - 1)}}} \quad (\text{a.18})$$

If the area of the primary flow used in equation (a.18) is the area of the nozzle (or the sum of the nozzles area in case of turbofan) neither diffusion nor contraction can be taken into account.

Therefore a second check equation is needed in order to account for the primary flow readjustment at the Accommodation Region.

Such checking equation is directly derived by equation (a.17) using the isentropic relations for compressible flow.

The primary flow area at section (2) can be found by equation (a.19).

$$A_{p2} = \frac{W_{p2}}{v_{p2} \rho_{p2}} \quad (\text{a.19})$$

Which using equations (a.11), (a.12), (a.14) and (a.15) (referred to the primary flow) can be written as equation (a.20).

At the same time the secondary area at the Accommodation Region can be written as equation (a.21) by using the same consideration already used for the primary cross sectional area. Equations (a.20) and (a.21) can be included in equation (a.17) as it is shown in equation (a.22).

$$A_{p2} = \frac{W_p \sqrt{T_{p2}} \sqrt{R_p} \left( 1 + \frac{\gamma_{p2} - 1}{2} M_{p2}^2 \right)^{\frac{\gamma_{p2} + 1}{2(\gamma_{p2} - 1)}}}{M_{p2} P_{p2} \sqrt{\gamma_{p2}}} \quad (\text{a.20})$$

$$A_{s2} = \frac{\mu W_p \sqrt{T_{s2}} \sqrt{R_s} \left( 1 + \frac{\gamma_{s2} - 1}{2} M_{s2}^2 \right)^{\frac{\gamma_{s2} + 1}{2(\gamma_{s2} - 1)}}}{M_{s2} P_{s2} \sqrt{\gamma_{s2}}} \quad (\text{a.21})$$

$$A_m = \frac{W_p \sqrt{T_{p2}} \sqrt{R_p} \left( 1 + \frac{\gamma_{p2} - 1}{2} M_{p2}^2 \right)^{\frac{\gamma_{p2} + 1}{2(\gamma_{p2} - 1)}}}{M_{p2} P_{p2} \sqrt{\gamma_{p2}}} + \frac{\mu W_p \sqrt{T_{s2}} \sqrt{R_s} \left( 1 + \frac{\gamma_{s2} - 1}{2} M_{s2}^2 \right)^{\frac{\gamma_{s2} + 1}{2(\gamma_{s2} - 1)}}}{M_{s2} P_{s2} \sqrt{\gamma_{s2}}} \quad (\text{a.22})$$

$$A_m = \frac{\left( \frac{\sqrt{T_{p2}} \sqrt{R_p} \left( 1 + \frac{\gamma_{p2} - 1}{2} M_{p2}^2 \right)^{\frac{\gamma_{p2} + 1}{2(\gamma_{p2} - 1)}}}{M_{p2} P_{p2} \sqrt{\gamma_{p2}}} + \left\{ 1 + \frac{\gamma_{s2} - 1}{2} \left[ \left( \frac{P_s}{P_p} \right)^{\frac{\gamma_{s2} - 1}{\gamma_{s2}}} \left( 1 + \frac{\gamma_{p2} - 1}{2} M_{p2}^2 \right)^{\frac{\gamma_{p2}(\gamma_{s2} - 1)}{\gamma_{s2}(\gamma_{p2} - 1)}} - 1 \right] \frac{2}{\gamma_{s2} - 1} \right\}^{\frac{\gamma_{s2} + 1}{2(\gamma_{s2} - 1)}} \mu \sqrt{T_{s2}} \sqrt{R_s} \right)}{\sqrt{\gamma_{s2}} P_s \left\{ \left[ \left( \frac{P_s}{P_p} \right)^{\frac{\gamma_{s2} - 1}{\gamma_{s2}}} \left( 1 + \frac{\gamma_{p2} - 1}{2} M_{p2}^2 \right)^{\frac{\gamma_{p2}(\gamma_{s2} - 1)}{\gamma_{s2}(\gamma_{p2} - 1)}} - 1 \right] \frac{2}{\gamma_{s2} - 1} \right\}^{0.5}} \quad (\text{a.23})$$

Equation (a.22) can also be expressed also in term of primary flow Mach number living as secondary flow parameters only its total pressure and temperature. To do this the Accommodation Region main conditions represented by equation (a.18) can be



used to extrapolate the secondary flow Mach number as function of the primary flow Mach number (equation (a.23))

Once the secondary flow Mach number satisfies the two check equations (a.18) and (a.23) within an error of 0.0005 the procedure is completed and this Mach number is used to working out all the conditions of primary and secondary flow at the Accommodation Region.

In this procedure specific heats of both the flows are not up-dated at each step but calculated at the end once the static temperatures are known by using again (a.5) and (a.6).

### A3. *Mixing Region*

The Mixing Region iterative process starts by guessing a value of the static pressure at section (m),  $p_m$ .

From the Momentum equation (equation (5.19)) it is possible to work out the explicit value of  $v_m$  by writing such equation in the form of equation (a.24)

$$v_m = \frac{W_p}{W_m} \left( \frac{A_{s2} P_{s2}}{W_p} - \frac{A_m P_m}{W_p} + v_{p2} - \frac{W_s v_{s2}}{W_p} \right) \quad (a.24)$$

The universal gas constant at section (m) it is worked out by a mass flow weighted average between the primary and the secondary flow (equation (a.25))

$$R_m = \frac{R_p W_p + R_s W_s}{W_p + W_s} \quad (a.25)$$

Once the velocity at section (m) is known from the continuity, mass flow rate and idea gas equation it is possible to work out the static temperature at section (m).

$$t_m = \frac{P_m A_m v_m}{R_m W_m} \quad (a.26)$$

Once the static temperature at station (m) is known, the specific heat  $cp_m$  can be worked out as mass flow weighted average of the two singles  $cp$  (keeping in mind that the two flows have different composition) as it is shown in equation (a.27).

Knowing the  $cp_m$  the energy equation (5.20) can be used a checking equation for the static pressure at section (m). Equation (a.28) shows how the static pressure at section (m) can be worked out from the energy equation. When the difference between the static pressures calculated by two different iterations is less than 0.1% the procedure is converged and the values  $p_m$ ,  $t_m$  and  $v_m$  are assumed to be true. Using the above parameters it is possible to calculate with the isentropic flow equations the total pressure and temperature at section (m) by equations (a.14) and (a.15), this time referred to section (m). However to do this it is necessary to calculate  $\gamma_m$  with the same relation used for the Preliminary Region but this time using the  $cp_m$ .

$$\begin{aligned}
& W_s \left[ 0.992313 + \frac{0.236688t_{ph}}{1000} - \frac{1.852148t_{ph}^2}{1000} + \frac{6.08352t_{ph}^3}{1000} + \right. \\
& - \frac{8.893933t_{ph}^4}{1000} + \frac{7.097112t_{ph}^5}{1000} - \frac{3.234725t_{ph}^6}{1000} + \frac{0.794571t_{ph}^7}{1000} + \\
& - \frac{0.081873t_{ph}^8}{1000} + \frac{0.081873t_{ph}}{1000} + \frac{FAR}{1+FAR} (-0.718874 + \\
& \frac{8.747481t_{ph}}{1000} - \frac{15.863157t_{ph}^2}{1000} + \frac{17.254096t_{ph}^3}{1000} + \\
& \left. - \frac{10.233795t_{ph}^4}{1000} + \frac{3.081778t_{ph}^5}{1000} - \frac{0.361112t_{ph}^6}{1000} - \frac{0.003919t_{ph}^7}{1000} \right] + \\
& + W_p \left( 0.992313 + \frac{0.236688t_{ph}}{1000} - \frac{1.852148t_{ph}^2}{1000} + \frac{6.08352t_{ph}^3}{1000} + \right. \\
& - \frac{8.893933t_{ph}^4}{1000} + \frac{7.097112t_{ph}^5}{1000} - \frac{3.234725t_{ph}^6}{1000} + \frac{0.794571t_{ph}^7}{1000} + \\
& \left. - \frac{0.081873t_{ph}^8}{1000} + \frac{0.081873t_{ph}}{1000} \right) \\
cp_m = & \frac{\hspace{15em}}{W_p + W_s} \tag{a.27}
\end{aligned}$$

$$p_m = \frac{W_p R_m}{v_m A_m cp_m} \left[ (cp_{p2} t_{p2} + \frac{v_{p2}^2}{2}) + (cp_{s2} t_{s2} + \frac{v_{s2}^2}{2}) \right] - \frac{W_p R_m (1 + \mu) v_m}{2 A_m cp_m} \tag{a.28}$$

#### A4. After-Mixing Region

The first step of the iterative process at the After-Mixing Region is to define a value for the pressure loss coefficient  $K_{MT}$ . The whole procedure assumes  $K_{MT}$  fixed at the starting point.

The handle parameter is the static temperature  $t_m$ .

The first step is work out the specific heat  $cp_m$  following the equation (a.27) shown in the appendix dedicated to the Mixing Region. Knowing  $t_m$ , it is possible to work out the flow velocity at section (m) by using the energy equation (5.27) here represented in the form of equation (a.29).

$$v_{m'} = \sqrt{2 \left[ cp_m t_m + \frac{v_m^2}{2} - cp_m t_m + \frac{v_m^2}{2} \right]} \tag{a.29}$$

From the Mach number equation (5.29)  $M_{m'}$  can be calculated and used in the pressure loss equation in order to find out the static pressure at section (m') by equation (a.30).

$$P_{m'} = \left[ P_m \left( 1 + \frac{\gamma_m - 1}{2} M_m^2 \right)^{\frac{\gamma_m}{\gamma_m - 1}} - K_{MT} \frac{\rho_m v_m^2}{2} \right] \frac{1}{\left( 1 + \frac{\gamma_{m'} - 1}{2} M_{m'}^2 \right)^{\frac{\gamma_{m'}}{\gamma_{m'} - 1}}} \quad (\text{a.30})$$

The continuity and the ideal gas equations used together allow finding a checking equation to for the static temperature initially guessed at station ( $m'$ ) as it is written in equation (a.31).

$$t_{m'} = \frac{P_{m'} v_{m'}}{R_{m'} \rho_m v_m} \quad (\text{a.31})$$

The universal constant of gas at station ( $m'$ ) is the same that at station ( $m$ ) because the gas composition is not changed.

When the difference between the guessed value of  $t_{m'}$  and that one calculated is less than 0.001% the procedure it is assumed converged and the values calculated to be true.

## ***APPENDIX B. Experimental Work in Cranfield University***

In this appendix the experimental work related to the indoor test bed facilities and carried out in Cranfield University.

The work described below is part of a parallel project going on at the university and especially undertaken by post graduated students (MSc students).

The author of this thesis has worked very closely with these students and to some extent has led and followed them through their single projects and beyond.

A paper has been published by the author in this topic to an international conference (AIAA 43<sup>rd</sup> Aerospace Science Meeting and Exhibit) as a result of further investigations carried out afterward the master students.

However, the work done has been already partially published in the Master student's theses. For this reason the originality of such a work can not be claimed in this PhD thesis. At this time, however, it is interesting to summarize such work and underline its findings.

It has to be said from the beginning that the accuracy of the results is not as good as it should be for two reasons. The first is because the students who worked in these projects did not have all the time they would have wished to complete their research. Indeed, to set up experimental sessions requires several months. The second reason is related to the CFD aspect of the experimental work. Indeed most of the experimental cases studied were also represented by Fluent. At this stage, the main purpose was to asses the capability of this commercial software to represent the flow in the test bed. Therefore, rather than to match quantitative values, the CFD has been used to indicate the trend of these parametric studies.

### ***B1. Test Bed Facility in Cranfield University***

In model test cell there are two areas which are of official importance to the success or the failure of the experimental investigation to produce meaningful results. The first of these is the modelling of the test cell geometry in sufficient detail so as to ensure the correct aerodynamics of the system. The second is the simulation of the engine of the engine configuration in relative size, placement and flow characteristics (SAE international 1999).

The test bed facility used in Cranfield University is small scale which allows testing of micro gas turbines only. Such a cell does not represent the scale model of any real test bed cell. Therefore a main scale factor can not be defined (SAE international 1999). Comparing the main chamber with Rolls-Royce test bed X a scale factor can be found around 1:12. Such a value is among those suggested in the SAE AIR 4827 (SAE international 1999) where plenty of useful information related to scale test can be found.

The main particularity of the Cranfield test cell is its flexibility in accomplishing parametric studies.

Indeed, such a cell can change configuration quite easily just by unscrewing a few bolts.

In particular the parameters that can be changed are the engine-detuner distance, the cradle blockage area, the cell cross sectional area and the distance from the engine inlet to the floor.

The on use engine will be described later on, in this paragraph special attention will be made about the cell inlet and cradle.

Figure B.1 shows the Cranfield University test facility.

The cell, which is of axial type allows fairly uniform flow. Indeed, the flow does not need cascade vanes for turning the flow in the engine axial direction. It also does not need an exhaust stack to allow the flow to exit the cell because detuner discharges directly into the atmosphere without the need for a blast basket.



Figure B.1: Cranfield Small Scale Test Facility

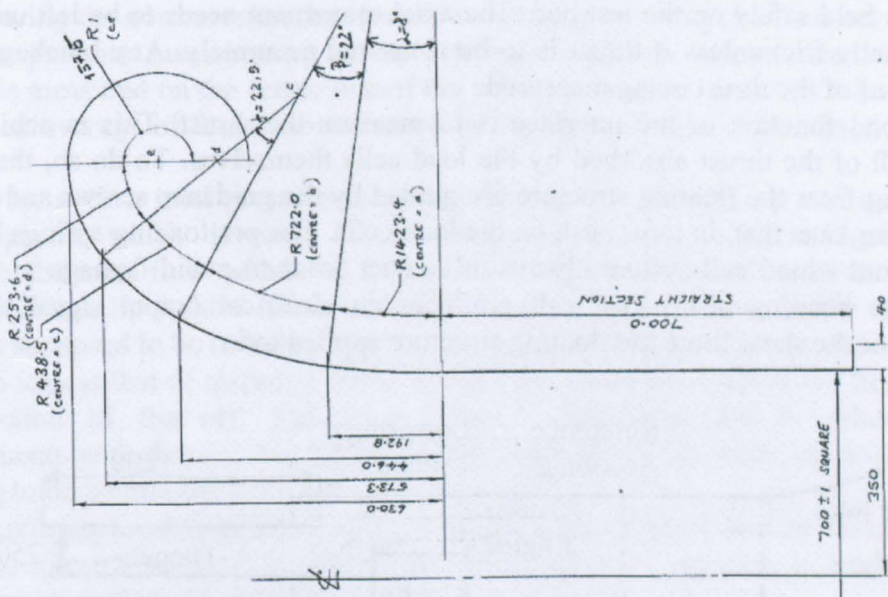


Figure B.2: Cell Inlet Bellmouth

Horizontal cells are generally less expensive than those equipped with vertical stacks. At the same time, however, they need more noise absorption material to meet required noise attenuation criteria (Jaques 1984). However, this is not strictly necessary for the Cranfield model facility whose engine has a much lower pressure ratio (the biggest responsible for the noise production) compared with real turbojets and turbofans tested in real test beds.

The cell is enclosed inside a test house in order to minimise cross wind disturbances. However, there is a lot of room to allow the flow to turn without recirculation (flow visualization shows the flow is quite stable around the cell especially if the doors of the test house are closed (Kleemann 2004)).

Very important for the smoothness of the flow is the cell inlet.

This component it has been recently substituted after that flow visualization shown a relevant separation from the previous circular inlet. Now the cell inlet has an elliptical shape (Figure B.2) converging asymptotically to the square cell cross sectional area (side of 700 mm). Since the beginning this new intake has not shown any separation. This is very important because in front of the engine flow measurements have to be done and they could be seriously affected by the separation (mass flow measurements). However, a calibration for the intake has been made and it will be described in the next paragraph.

Figure B. 3 shows the layout of the Cranfield test facility.

The thrust measurement device (TMD); has been designed by Rolls-Royce and can be used for both indoor and outdoor tests (Figure B.4).

The TMD is firmly attached to the test bed and contains a floating structure held within to which the engine is attached. There are two load cells aligned with the engine centreline, which are themselves aligned with shafts along which the floating cradle axis can move. There obviously exists an interface between the fixed and floating structures to facilitate these two functions (Rolls-Royce plc. 2003).

The first is accomplished by shaft brackets. Shafts and linear bearings impede all relative movement between the fixed and floating structures except along the axial translation where thrust is applied. By blocking 5 of the 6 degrees of freedom, the engine is held safely on the test bed. The axial movement needs to be left unblocked and virtually frictionless if thrust is to be measured accurately. Any blockage would absorb part of the thrust being measured.

The second function of the interface is to measure the thrust. This is achieved by having all of the thrust absorbed by the load cells themselves. To do so, the fingers protruding from the floating structure are guided by the guidance screws and push on the pushing nuts that, in turn, push on the load cells. The pre-loading springs keep the finger - nut - load cell system always in contact so as to avoid damage to the load cells. The bending beam load cell produces an electrical output signal that is a function of the shear force the floating structure applied to it.

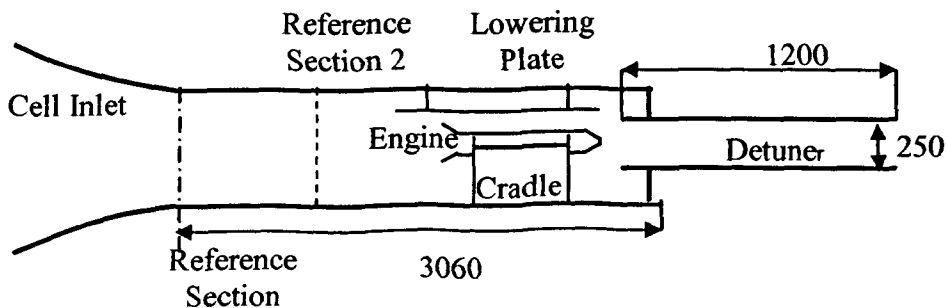


Figure B. 3: Cranfield Test Cell Layout

It is highly recommended to calibrate the load cells every time the engine is unplugged from the cradle.

How the load cells are calibrated will be described in the next paragraphs.

Another useful fact related to the thrust measuring device, is that its drag coefficient has been estimated at 1.79 and the frontal area at 0.005856 (Gonzalez Galinez 2003).

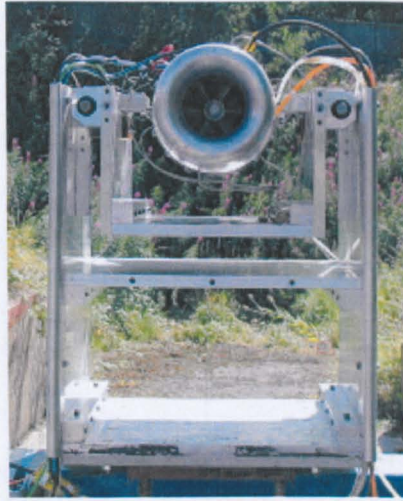


Figure B.4: Cranfield Outdoor Stand

### B.1.1 Test Cell Inlet Calibration

A cell inlet calibration is needed in order to relate the real mass flow entering the cell to that measured each time by the instrumentation set in the cell.

Indeed, during the normal tests, the mass flow entering the cell is worked out by total and static pressure measurement at the reference sections. In particular, the total pressure is measured on the centre line of the reference section by a Pitot tube and the static as an average of four probes located in the sides of that section ( $p_{ref}$ ) (Figure B.5).

In this way, such a total pressure measurement may be affected by a non-uniform velocity profile which develops in the cross-section along a pipe (Figure B.6). Therefore, the mass flow calculated with just the reference measurements is not very accurate. With a lip welded all around the inlet, the boundary layer at the reference section is supposed to be turbulent and therefore, the velocity profile more uniform.

The main idea is that of mapping the total and static pressure fields at the first useful cross section of the cell (reference section). And afterward to relate those measurements with those of the reference Pitot tube and of the static tappings which are going to be permanently set in the cell ( $P_{ref}$  and  $p_{ref}$ ).

Indeed, knowing the difference between total and static pressure and by assuming the flow to be incompressible (low velocity inside the cell) it is possible to work out the velocity and therefore, the mass flow.

In order to map the total pressure field at the reference section, special probes have been made and located in rakes which are shown in Figure B.5 by the blue lines. Each rake has six total probes. Furthermore, the total pressure is measured by traversing a Pitot tube across the reference section at different locations (green lines in Figure B.5).

The static pressure is measured by seven probes in each side of the cell (green circles Figure B.5). It is worth remembering that absolute values of total and static pressure are not needed. Instead, for each point where the total pressure is measured, the difference between total and static pressure is needed. Indeed, for incompressible flow the velocity can be worked out by the relationship (b.1) shown below.

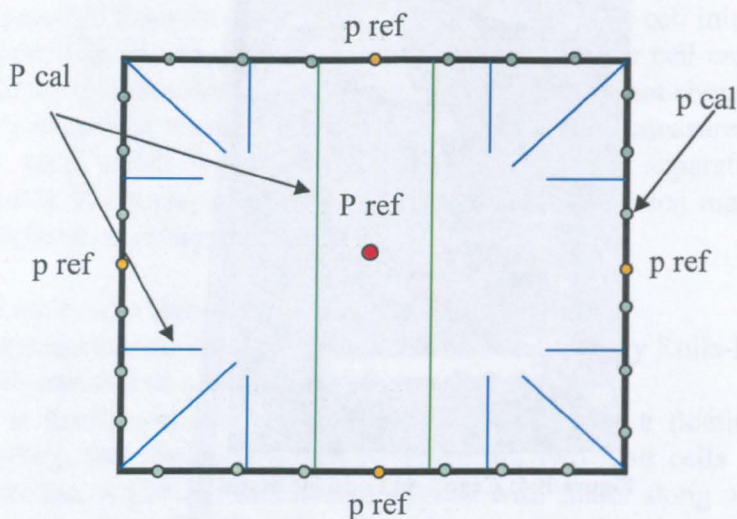


Figure B.5: Pressure Rakes for Mapping the Cell Inlet

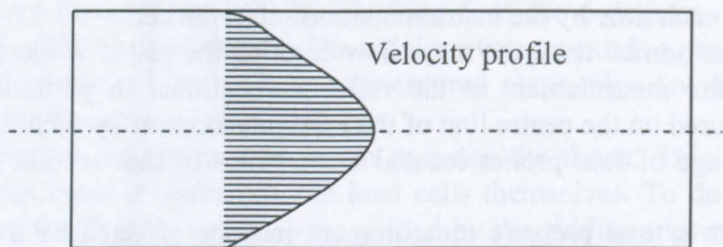


Figure B.6: Velocity Profile

$$P - p = \frac{1}{2} \rho v^2 \quad (\text{b.1})$$

Therefore, at each total pressure probe is associated a static pressure. In particular it is associated with the closest between those located in cell sides.

Once the velocity is known, an area value has to be associated with each total pressure probe. Therefore, the reference section is divided in different small areas, 121 areas. Furthermore, a value of the density has to be associated with each area. This could seem a contradiction with the fact that the flow is assumed incompressible but it is necessary because not all the measurements for the inlet calibration have been taken the same day. Indeed, several days of tests have elapsed to map the whole reference section. Therefore, atmospheric temperature and the pressure were variables.

Accordingly for each area an average density has been defined and an average value of the velocity calculated. It is emphasised that the averages mentioned above could also be necessary because in the same area more than one total pressure probe could be enclosed.

$$\rho_l = \frac{\sum_{j=1}^n \frac{P_{cellj}}{Rt_j}}{n} \quad (\text{b.2})$$



The cell static pressure at the reference section is computed by the measurements shown in (b.3) (this will be better discussed in B.1.6).

$$P_{ref} = P_{atm} + (P_{TH} - P_{atm}) + (p_{ref} - P_{TH}) \quad (b.3)$$

Where the  $P_{atm}$  is the atmospheric pressure, the  $P_{TH}$  is the total pressure inside the test house and  $p_{ref}$  is the average static pressure of the four orange probes in Figure B.5. The cell temperature is measured by thermocouples located on top of the cell. Using relation (b.1) the velocity related to each total pressure probe is calculated by (b.4)

$$v_j = \sqrt{\frac{2(P_j - p_j)}{\rho_j}} \quad (b.4)$$

And the velocity related to each area (in the case that in the same area there are more than one total probe) by (b.5) where  $r$  is the number of the probes enclosed the same area.

$$v_l = \frac{\sum_{j=1}^r v_j}{r} \quad (b.5)$$

Therefore, following the above relationships it is possible to come out with the total mass flow entering the cell (equation (b.6)).

$$W_{cell} = \sum_{l=1}^m v_l A_l \rho_l \quad (b.6)$$

Where,  $m$  is the number which the cell reference is divided into.

At the same time it is possible to use the same methodology and compute the cell mass flow using the reference values.

The values at the reference section have been measured constantly during each day of calibration measurement. Therefore the reference values are calculated as an average of the all measurements made.

$$W_{ref} = \sum_{k=1}^n \frac{\left( \sum_{i=1}^q \sqrt{\frac{2(P-p)_{ref\ i}}{\rho_{cell\ i}}} A \frac{\rho_{cell\ i}}{Rt_i} \right)_k}{n} \quad (b.7)$$

The velocity can be found by averaging the average of all the  $(P-p)_{ref}$  measurements made during a single day for the number of days test. At each time the  $(P-p)_{ref}$  are measured also the  $p_{ref}$  and the  $t_{cell}$  in order to compute directly the density at the same time.

Equation (b.7) represents the mass flow computed by the reference values, where  $q$  is the number of the measurement made during the day and  $n$  the days of test.

Now, knowing the mass flow derived by using the total pressure profile (actual mass flow) and that by using only the reference values it is possible to derive a coefficient to relate both (equation (b.8)).

$$k_{inl} = \frac{\text{actual mass flow}}{\text{reference mass flow}} \quad (\text{b.8})$$

All the flow measurements are reported in Deen thesis (Deen 2004).

The cell inlet coefficient is computed to be 0.97829.

So, each time the reference values are used to computing the cell mass flow the found value has to be multiplied by 0.97829, in order to reduce the distortions due the velocity profile inside the cell (boundary layer effects).

### B.1.2 Load Cells Calibration

It is highly recommended to calibrate the load cell every time the engine is moved from the cradle or whenever the cradle is moved from the cell.

The calibration device incorporates the use of a dead weight system due to the high degree of accuracy and simplistic design at low cost. It works by recording the electrical output produced by the load cells when a known force is applied, simulating the engine thrust (this methodology is also suggested in Sae arp 741 (SAE aerospace 2002)).

The thrust can then be found from the load cells output signal.

A pulley is positioned on the calibration device with a line attached from either side of the TMD to the engine interface. This runs horizontally along the centre line of the engine (i.e., in the direction of the thrust). The two lines converge to a single line, which runs over the pulley and is connected to dead weights which hang vertically (Figure B.7).

If the friction is low enough the line will pull on the TMD floating structure with a force equivalent to the force applied by the dead weights (Rolls-Royce plc. 2003)

The calibration procedure involves an initial reading of load cell outputs at zero loads followed by readings at progressively larger loads. The weights have to be added carefully to avoid any overshoot thus avoiding hysteresis. After the loads are added the system is allowed to stabilise and then individually the nominal output from the left and right load cells should be recorded. From these values it is possible to infer the thrust at a later stage. The electrical output from the load cells is recorded either when the dead weights are loaded on and also when are loaded off. The results obtained for one load cell calibration are shown in Figure B.8.

It is seen that one of the two cells does not give an output of zero when is un-loaded. However, this is not a problem if it is noticed and recorded during the calibration. Indeed, independently from the cell condition at zero load by Figure B.8, it is possible to translate the electrical output for every load condition and for both the cells. The total thrust delivered by the engine is the sum of the load recorded by the two cells.



Figure B.7: Outdoor Load Cell Calibration

More accurate methodologies for the thrust calibration in sea-level test facilities can be found on the lecture given by Cronin in AGARD LS-132 (Cronin 1984).

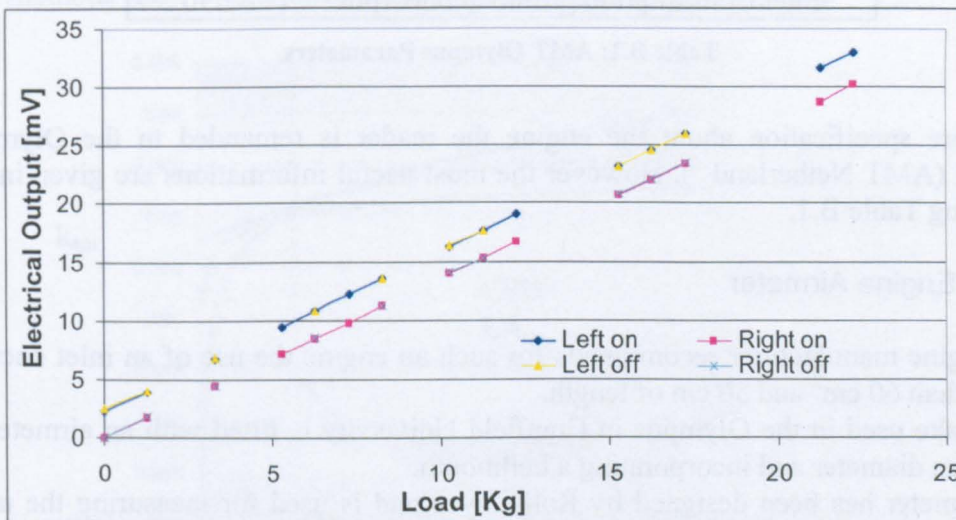


Figure B.8: Load Cells Calibration Output

### B.1.3 AMT OLYMPUS MICRO TURBINE ENGINE

Usually for model test cell there are two kinds of engine simulators the TPS (turbine powered simulator) and the EPS (ejector powered simulator ((SAE international 1999)).

In the Cranfield test facility a micro gas turbine engine (TPS), the Olympus model by AMT Netherlands is used which has been derived from the previous Mk-2 version.

This engine constructed is a single stage radial compressor, an axial turbine and an annular combustion chamber. The engine is protected by an Engine Control Unit ECU which regulates the performance of the turbine such as rotational speed and exhaust temperature. The ECU acts directly on the fuel pump (AMT Netherland ).

Until last year the engine was controlled by a radio-control system which led to a lot of problems (Le Fay 2002). At present, the control system is a desk-control and many problems of engine stability have been solved.

The engine uses propane as a starting gas for pre-heating. After the start-up the engine is switched from the propane to kerosene. For lubrication the Olympus uses oil which has to be premixed with fuel in a percentage of 4.5.

PARAMETER	VALUE
Diameter [mm]	130
Length [mm]	270
Weight [gr]	2400
Thrust @max rpm [N]	190
Thrust @min rpm [N]	7
Pressure Ratio @max rpm	4:1
Mass Flow @max rpm [gr /sec]	400
Maximum RPM	110,000
Exhaust Temperature °C	650
Max Exhaust Temperature °C	700
Fuel Consumption gr/min @max rpm	550

**Table B.1: AMT Olympus Parameters**

For more specification about the engine the reader is remanded to the Olympus Manual (AMT Netherland ). However the most useful informations are given in the following Table B.1.

#### B.1.4 Engine Airmeter

The engine manufacturer recommends for such an engine the use of an inlet duct no bigger than 60 cm<sup>2</sup> and 50 cm of length.

The intake used in the Olympus in Cranfield University is fitted with an airmeter of 61.41mm diameter and incorporating a bellmouth.

The airmeter has been designed by Roll-Royce and is used for measuring the mass flow entering the engine (Henderson 2000).

Indeed, by six static pressure probes mounted around the airmeter it is possible to measure the depression at the engine throat. Such a depression is measured as the difference between the static pressure at the engine throat and in the test house (more specification on the instrumentation systems are given in the next paragraph).

Assuming that the total pressure is constant from the reference section to the engine throat it is possible to work out the Mach number (the velocity at the throat is quite high and therefore the flow as to be treated as compressible). The total temperature is measured on top of the cell and assuming to be the same that at the throat it is possible to work out the static temperature (by the compressible flow relationships).

Once the static temperature is calculated by the ideal gas equation the density can be worked out and from the Mach number, the velocity can also be estimated.

Accordingly, the mass flow passing through the airmeter cross section can be calculated.

However, due to the flow distortion a Flow coefficient ( $k_{am}$  in equation (b.9)) has to be defined (as it happens for the cell intake). Usually this flow coefficient is plotted as a function of the Mach number.

$$k_{am} = \frac{\text{Actual Mass Flow}}{\text{Ideal mass flow}} \quad (\text{b.9})$$

Therefore the airmeter needs to be calibrated.

To ascertain the flow coefficient three different methods have been used two of them are theoretical and one uses CFD.

The two theoretical methods are: the one used by Rolls-Royce for the calibration they made for this airmeter and mentioned by Henderson (Henderson 2000) and the second is that proposed by D.J. Lathy and A Hamed (Lathi and Hamed 1993).

A two dimensional CFD model has been run for nine different boundary conditions and the result plotted. The complete study of the flow coefficient for the Olympus airmeter is proposed in Gozalez thesis (Gonzalez Galinez 2003). Here the final map is shown in Figure B.9. The dashed line in this picture represents the pressure at the operating point as described by the engine manufacturer. Around such a value the differences between the three methods are very small (around 0.02% to 0.08%). The three methods show bigger difference for lower Mach number (around

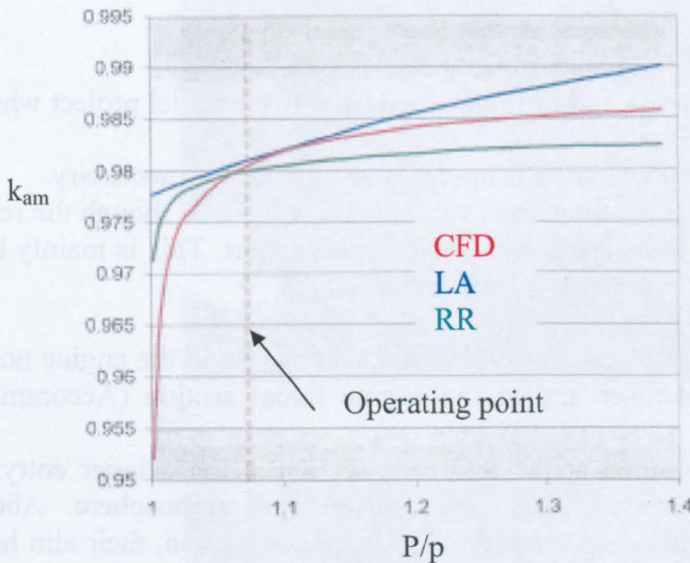


Figure B.9: Flow Coefficient for the Engine Inlet

0.2) especially comparing the CFD results with those obtained by applying Lathy-Hamed method

The Rolls-Royce method has been chosen finally,, because of its smaller discrepancy compared with the other. Therefore, each engine mass flow is computed using the compressible flow tables multiplied by the airmeter coefficient.

### B.1.5 Fuel Flow Calibration

The Fuel Flow calibration is done only at the beginning of the experimental period and does not need to be repeated more than once. It does not include any electronic instrumentation, only a weight scale and a chronometer.

The flow is set at certain level on the scale and then the liquid is allowed to run for a certain time in the balance. The mass flow is obtained dividing the number of grams by the elapsed time. The values of a classic fuel flow calibration are reported in Deen Thesis (Deen 2004). Figure B.10 below shows the results.

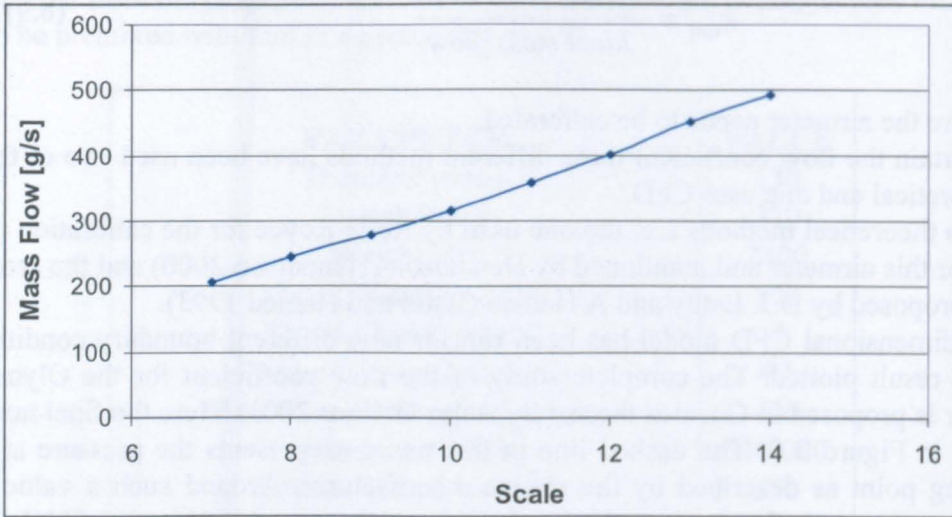


Figure B.10: Fuel Flow Calibration

### B.1.6 Instrumentation

As has already been said, this part of the thesis deal with a parallel project which was on-going at Cranfield University.

Accordingly, the cell instrumentation is up-dated year by year as necessary.

The last up-date of the instrumentation is valid in this work even though the results of the last experimental sessions are not included in this report. This is mainly because the results need to be better understood and better judged.

The static pressure is measured at the reference section, around the engine nozzle, in the first region of the detuner and at the engine throat section (Accommodation Region).

The total pressure is measured at the reference section at the detuner entry, at the engine nozzle, inside the test house and in the open atmosphere. About the measurements in the engine airmeter and at the reference section, their aim has been defined.

As far as measurements around the engine nozzle are concerned, four static probes have been set along the converging shape of the nozzle (Figure B.11). Such measurements are part of the latest up-date and from them the depression generated around the engine after-body can be estimated. The high temperature at the nozzle exit plane does not allow the probes to be set there. Therefore, they have been located at 8 mm, 18 mm, 28 mm and 38 mm downstream of the the nozzle exit plane.

Tapping downstream location from detuner entry [mm]	Number of tapings
3	4
7	4
12	4
18	4

25	2
33	2
42	2
52	2
67	2
97	4

**Table B.2: Static Probes Position along the Detuner**

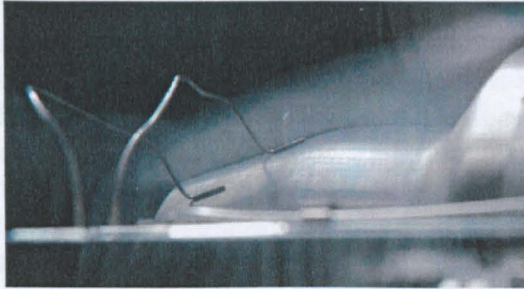


**Figure B.11: Static Probes around the Engine Nozzle**

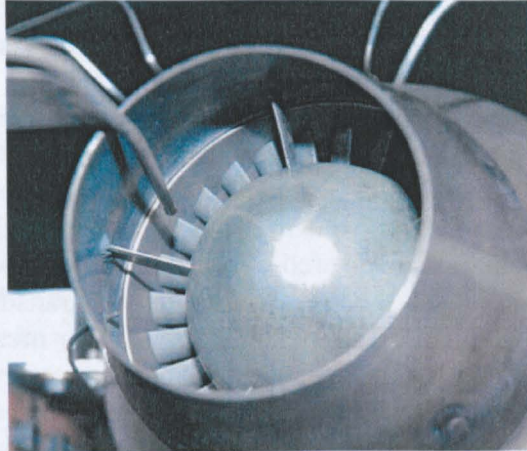


**Figure B.12: Total Pressure Probe Inside the Nozzle**

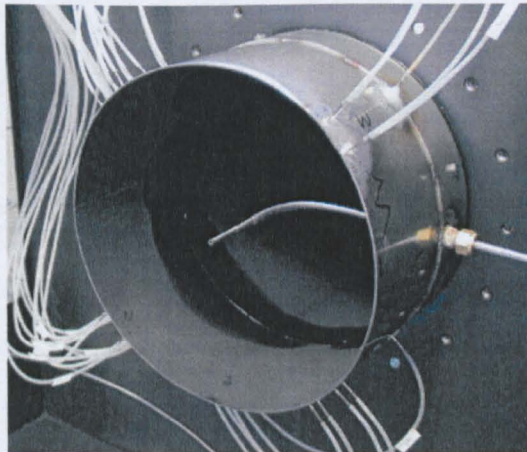


**Figure B.13: Static Pressure Taps and Total Pressure Probe along the Detuner Entrance**

A total pressure probe has been set inside the engine nozzle and is shown in Figure B.12

In addition, the thirty static probes located downstream of the detuner entry plane are part shown in Figure B.13. They are located at different positions along the detuner in coplanar groups (see Table B.2). These measurements are needed to estimate the depression in the Accommodation Region. Together with these static probes, a total pressure probe is been set at the entrance of the detuner (see Figure B.13).

The total pressure inside the test house is measured by a water differential manometer. This measures the difference between the total pressure inside and outside the test house. This manometer is located behind the cell where the flow is almost stationary. Accordingly, the total pressure here is assumed to also be the static.

The atmospheric pressure measured by a barometer is the only absolute value.

Apart from the atmospheric pressure, the test house pressure, the pressures at the Accommodation Region and all other pressures are measured by pressure transducers. Such an instrument is able to measure pressure differences between the pressures recorded from its two channels. Therefore, all the pressures read by the pressure transducer are relative and not absolute values.

Accordingly the transducers need to be scaled and as already said the reference parameter will be the atmospheric pressure,. Usually the second channel of the transducer is connected to a region of steady flow inside the test house. It therefore measures the total pressure of the test house.

For example, let us suppose we need to calculate the static pressure at the reference section. The pressure transducer gives directly the pressure difference between the four static probes and the total pressure in the test house. Accordingly, following equation (b.3) it is possible to work out the static pressure at the reference section. The first term of that equation is measured by the atmospheric barometer, the second by the differential manometer and the third by the pressure transducer.

Figure B.14 shows the two differential manometers used for measuring the static and total pressure at the Accommodation Region and the total pressure of the test house.

The temperature measurements recorded are: the engine nozzle temperature, the fuel temperature, the load cell temperature, the cell temperature and the temperature on top of the bellmouth.

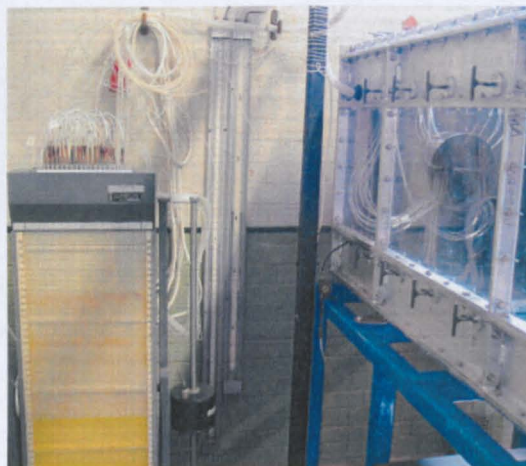


Figure B.14: Differential Manometers



The temperature at the engine nozzle is recorded so as to monitor the performance of the Olympus and is read directly in the ECU.

The fuel temperature is recorded for fuel flow calculation (SAE aerospace 2002).

The load cell temperature is necessary because the signals are temperature dependent. The cell temperature is important for the mass flow calculation (as already described above).

The temperature on top of the bellmouth is monitored to track the flow recirculation inside the cell which would lead the engine to re-ingest hot gasses.

The probes used are the Type K thermocouples which are Nickel /Aluminium or Nickel / Chromium. These thermocouples have a wide range of use and for this reasons are the most used (Cronin 1984). The accuracy is different from different ranges. From  $-44\text{ }^{\circ}\text{C}$  to  $333\text{ }^{\circ}\text{C}$  is  $\pm 2.5\text{ }^{\circ}\text{C}$  and from  $333\text{ }^{\circ}\text{C}$  to  $1275\text{ }^{\circ}\text{C}$  is  $0.0075(t\text{ }^{\circ}\text{C})$ .

The rotational speed of the engine is measured by a magnetic probe located at the compressor wheel and is displayed directly in the ECU. Furthermore, the engine rotational speed is also used as a handle for engine power setting.

The engine thrust is measured by load cells which have been described above.

Inside the cell the velocity is measured by a thermal anemometer (Airflow ). Its accuracy is within  $1\text{ m/s}$  if positioned within an angle of  $\pm 15^{\circ}$  from the flow direction.

Such an anemometer is particularly useful for laminar flow when the flow direction is well defined.

Seven velocity measurements are taken inside the cell in front of the engine (SAE international 1999), on the centre line of what has been called reference section 2 in Figure B. 3. Furthermore, nine velocity measurements are taken in front of the cradle (Figure B.15)

The aim of the former measurements is to understand the velocity profile at that section and to compute the IMD. The second measurements allow the calculation of the cradle drag (Figure B.15)

Table B.3 summarizes the instrumentation available for the Cranfield test bed.

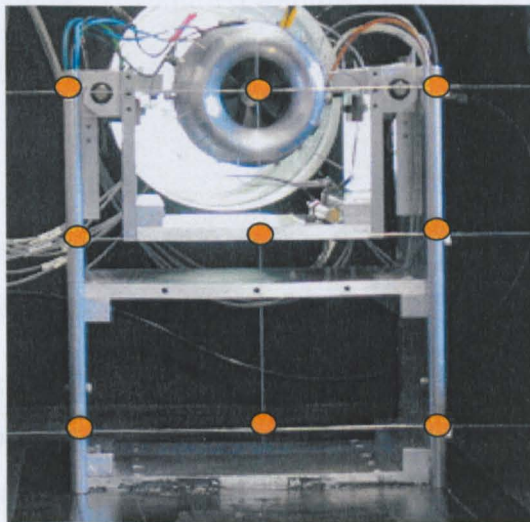


**Figure B.15: Velocity Measurements in front of the Cradle**

Value	Instrument	Section
$P_{atm}$	Barometer	Test house
$T_{amb}$	Thermometer	Test house
$P_{atm} - P_{TH}$	Water Manometer	Test house
$(P-p)_{ref}$	Pitot tube-four static probes-Pressure Transducer	Reference
$(P_{TH}-P_{ref})$	four static probes – Pressure Transducer	Reference
$(P_{TH}-P_{eng})$	Engine airmeter- Pressure Transducer	Engine throat
Thrust	Load cells left and right	TMD
$T_{cell}$	Thermocouple	Cell roof
$v_{ref}$	Thermal anemometer	Reference 2
$v_{cradle}$	Thermal anemometer	Cradle
RPM	Engine control unit	ECU
Fuel flow	Engine control unit	Scale-meter
$p_{nozzle}$	Static probes- Pressure Transducer	Nozzle ext
$P_{nozzle}$	Pitot tube- Hg Manometer	Nozzle surf
$P_{detuner}$	Water Manometer	Accom. Reg.
$P_{detuener}$	Hg Manometer	Accom. Reg
$T_{nozzle}$	Thermocouple	Nozzle
$T_{fuel}$	Thermocouple	Fuel tank
Fuel flow	Scale	
RPM	ECU	
Humidity	Hydrometer	

**Table B.3: summary of the MEaurements**

Within the instrumentation smoke generation has also to be included. This has been used to visualise the flow inside and outside the cell and also around the engine.

A very accurate and extensive treatment of the possible measurements within an enclosed test facility can be found in Holmes (Holmes 1984). In that report not only what the measurement are or how they are taken are described but also the signals transmission, the data acquisition and the calibrations are treated. In this case, everything is especially relevant to sea level test beds.

## **B2. Test Plan**

In the test plan section of this report, all tests undertaken by the author are described.

### **B.2.1 Test Plan year 2004**

Four different engine-detuner distances at three different power setting and three different blockage area of the cradle at 65% of power are described.

Distance	Power Setting
0d	50%-65%-80%
1d	50%-65%-80%

2d	50%-65%-80%
4d	50%-65%-80%

**Table B.4: Different Engine Detuner Tested**

Number of Plates	Cradle Blockage Area [m <sup>2</sup> ]	Blockage Ratio
0	0.026088	0.053
1	0.048288	0.098
2	0.068688	0.14
3	0.089832	0.18

**Table B.5: Different Cradle Blockage Areas Tested**

In Table B.4 the distance between the engine and the detuner is referred to an engine nozzle diameters (d) which is 63 mm.

In the cell description the effect of changing the blockage area of the cradle is also important. To do this some plates can be added to the front of the original cradle in order to increase its blockage area. Table B.5 shows how the blockage area of the cradle changes by adding the plates. The blockage ratio is defined as the blockage area of the cradle divided by the cross sectional area of the cell.

In addition, an outdoor test session was carried out in 2004 to measure the real thrust delivered by the engine.

### B.2.2 Test Plan 2005

In 2005 the cell instrumentation was up-dated with the static pressure probes around the engine nozzle in order to estimate the base force acting on the engine after-body. The up-dating includes also the total pressure probe inside the nozzle and the static and total pressure probes at the Accommodation Region.

The main purposes for the 2005 tests are: to estimate the thrust correction factors (for different engine configuration) and validate the analytical engine-detuner ejector model described in Chapter 5.

Two different engine-detuner distances are used: two nozzle diameter (2d) and four nozzle diameter (4d).

For the two configurations the complete set of measurements available are taken, as described in Table B.3.

All the measurement process is well described in Elysee (Elysee 2005) and McLoughlin (McLoughlin 2005) theses.

### B3. *CFD Modelling for the Cranfield Test Bed Facility*

Before describing the results of the experiments it is thought useful to introduce also the CFD modelling which has been undertaken in Cranfield as part of this parallel project.

In this way the experimental results will be plotted together with those coming from the simulations, and comparisons will then be possible.

The CFD analysis for the project related with the Cranfield test bed facility is aimed at establishing how effectively commercial CFD software can be used to indicate the real flow phenomena inside an experimental engine test cell.

The study is preliminary.

For this reason model accuracy has been seen as of secondary importance compared with the computational time and power required (Chapter 6).

The computational code used in this research comprises the solver Fluent, the pre-processor for geometrical modelling Gambit and an additional mesh generator T-Grid. Basically all the CFD settings are the same than those used for the modelling the large Rolls-Royce cells and described in Chapter 6. Therefore the reader can refer to those comments for better understanding the choices made.

Also the step-by-step approach to achieve the second order of accuracy has been used. The boundary conditions used are the following: Pressure inlet for the cell entry plane, Pressure Outlet for the engine face, Mass Flow Inlet for the nozzle and pressure outlet for the detuner exit section.

At the beginning of the project some boundary conditions were derived by Turbomatch (School of Engineering Cranfield University 1999) due to lack of accuracy in the measurements. Especially for the nozzle conditions (Kleemann 2004). Indeed, until 2005 it was not possible to take any measurements at the nozzle.

In the model presented in this appendix the nozzle conditions are derived partially by experiments such as the mass flow which is the mass flow entering the engine plus fuel mass flow and partially by the results of the performance simulation code Turbomatch.

The results shown in this appendix come from a model with 500000 elements.

The criteria for grid generation follow the results obtained for the big cells, and therefore the reader can refer to Chapter 6.

Figure B.16, Figure B.17 and Figure B.18 show three views of the computational model.

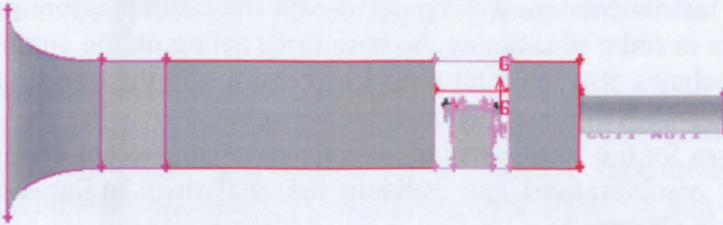


Figure B.16: CFD Model of the Cranfield Test Facility

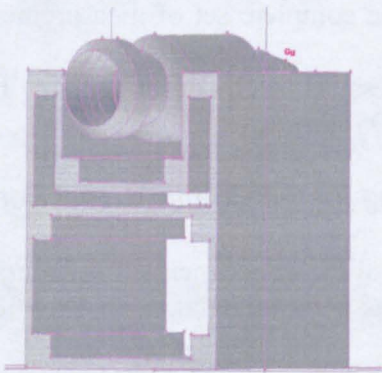


Figure B.17: CFD Model of the Engine and of the Thrust Stand

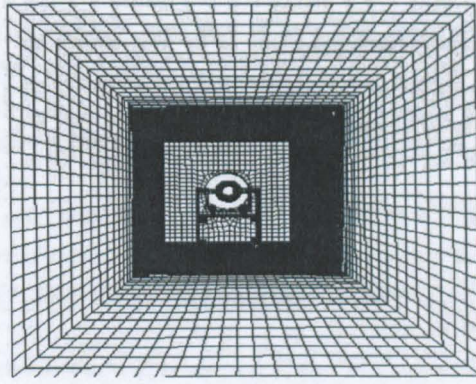


Figure B.18: CFD Grid of the Cranfield Test Facility

It is worth saying that several models have been made since the results obtained in 2004 (McLoughlin 2005). In particular, during the 2005 a lot of improvement has been made and the latest model runs with 1,500,000 elements. The results are promising (McLoughlin 2005) (Elysee 2005))but still are not ready to be published.

#### B4. Experimental and CFD Results

##### B.4.1 Data Normalization

Of course, the experimental work can not be completed in one day.

Accordingly the atmospheric conditions were not always the same for all the tests. This of course can affect the comparison of the results and therefore a normalization of the data is required before any comparison ((SAE aerospace 2002)).

The standard conditions used for the normalization are 15 °C (288 K) and an atmospheric pressure of 101325 Pa.

The relationships used for the normalization are listed below (equation (b.10), (b.11) and (b.12)).

$$W_n = \frac{W 101325 \sqrt{T_{amb}}}{P_{amb} \sqrt{288}} \quad (b.10)$$

$$Thrust_n = \frac{Thrust 101325}{P_{amb}} \quad (b.11)$$

$$RPM_n = \frac{RPM \sqrt{288}}{\sqrt{T_{amb}}} \quad (b.12)$$

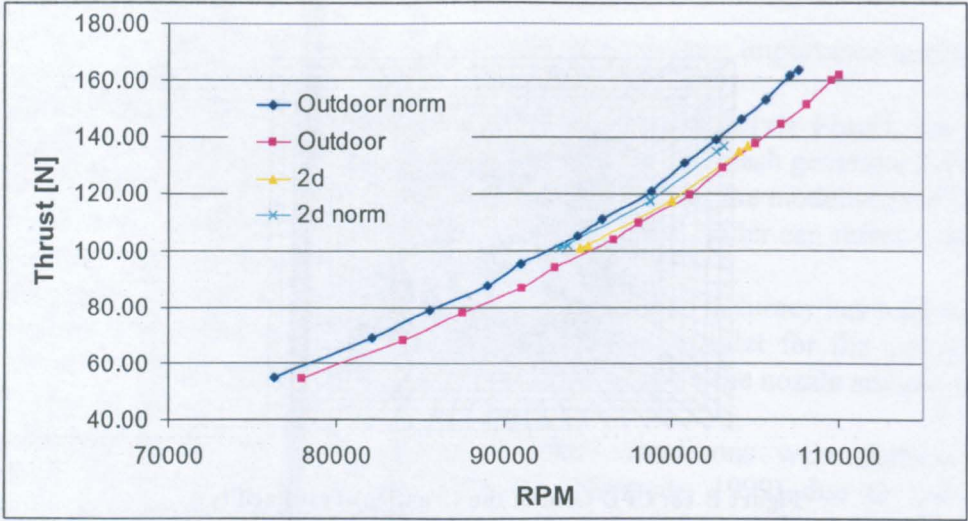


Figure B.19: Data Normalization Effects

A clear impact of the normalization is noticeable in Figure B.19.

It is clear that without normalization in the outdoor test the engine delivers less thrust than in indoor conditions. Clearly this is not correct and is due to the fact the outdoor test was carried out in the summer time when the ambient temperature was 28 °C and the ambient pressure 100126 Pa.

The same thing happens when the indoor measurement are compared by themselves. Therefore, all the results plotted in the following maps are all normalized.

#### B.4.2 Experimental and CFD Comparison

The first result to be shown is concerned with the influence of the engine-detuner distance on the flow fields inside the cell. Such a parameter can affect the cell entrainment ratio and therefore the thrust correction factors. Accordingly an interesting result is to plot how  $\mu$  changes with the engine-detuner gap (Figure B.20). Both computational and experimental results show that the cell entrainment ratio increases as the engine-detuner distance increases. This trend is confirmed by Jacques in (Jacques 1984).

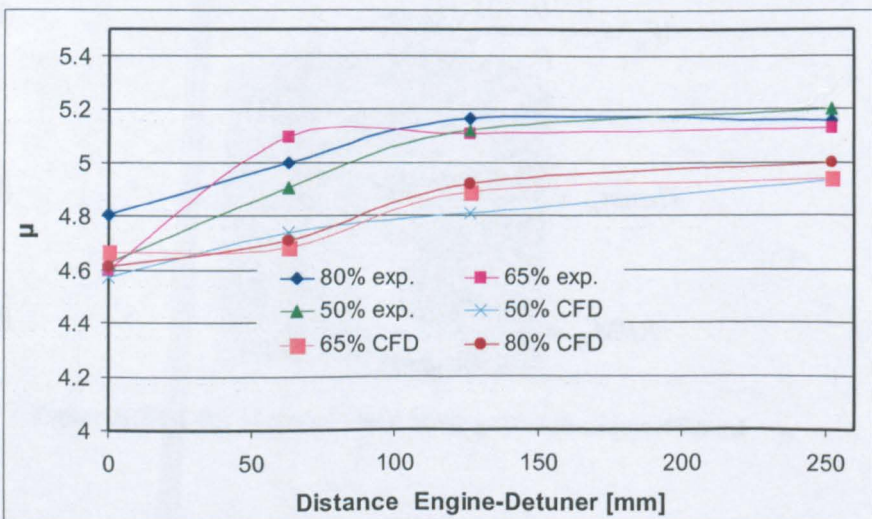


Figure B.20: Entrainment Ratio as Function of the Engine-Detuner Gap

Although the absolute values predicted by CFD are not directly comparable with the experimental results yet, the trends are the same.

Since the beginning it was known that the CFD model could not match the experimental values due to the actual accuracy of the models. However the fact that the trends are matched justifies further study in both experimental and computational directions. Indeed, the experimental apparatus used in 2004 shows some lack of accuracy (Kleemann 2004).

Before going ahead and attempting to discuss the above trends it is worth saying that the main difference between the computational and experimental results are due to the fact that the CFD does not match the experimentally measured engine mass flow.

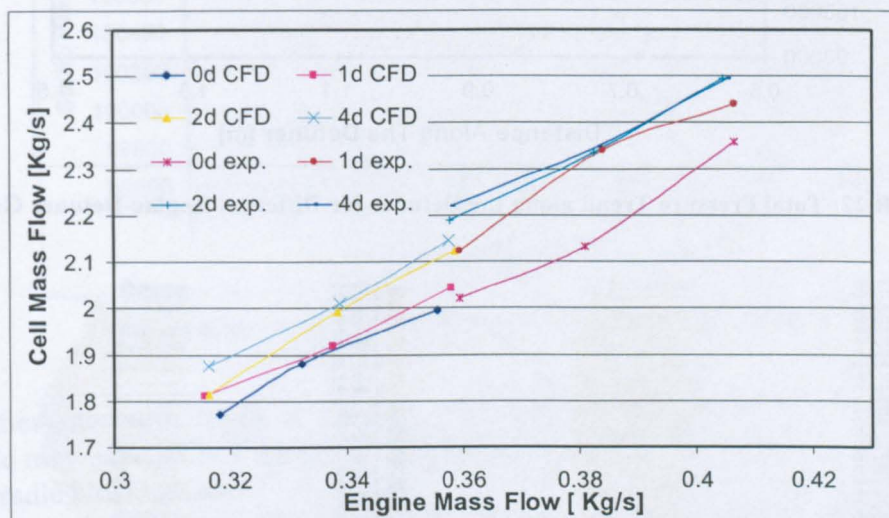


Figure B.21: Difference in Engine Mass Flow Between Experimental and CFD

Figure B.21 shows the results from both CFD and experiments. The reasons for this are probably due to the accuracy of the measurements with the engine airmeter and the inaccuracy of the computational grid at the engine face.

However, another important thing that needs to be said is that for the different engine power settings, the differences in engine mass flow is relatively small in absolute terms. This is primarily because the engine mass flow by it self is relatively small. Accordingly, every inaccuracy either in the measurements or in the computational settings can make a big difference in the results.

At the same time, however, the comparison between CFD and experiments can be useful for defining the trend lines and understand if the computational tools are able to predict them.

In Chapter 6 it was found that the level of secondary mass flow entering the cell is proportional to the level of mixing achieved along the detuner (Figure 6.56).

Following that conclusion the same plots used in Chapter 6 are used in this appendix. Accordingly, two lines are defined along the detuner: the first along the centre line and the second close to the detuner top boundary.

Figure B.22 shows a plot of the total pressure along the detuner for both the primary and the secondary flow (from the computational model) and for 1d and 4d engine-detuner distances.

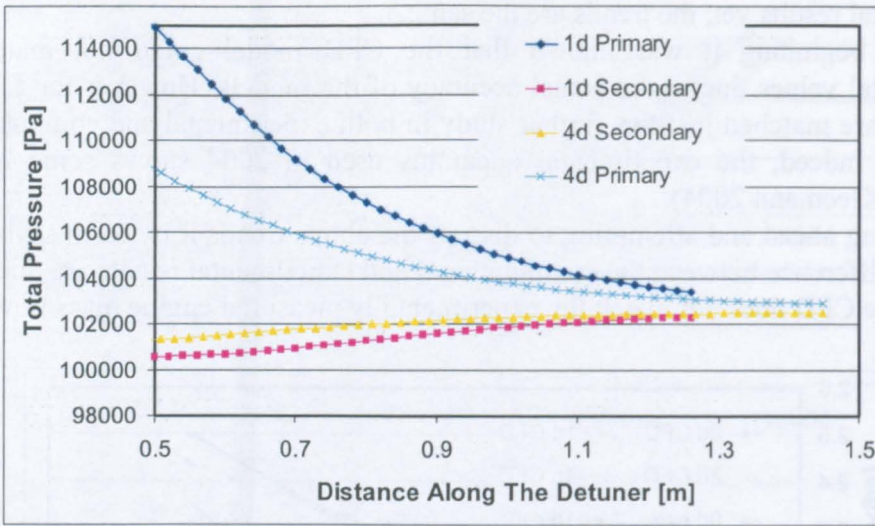


Figure B.22: Total Pressure Trend along the Detuner for Different Engine-Detuner Gap

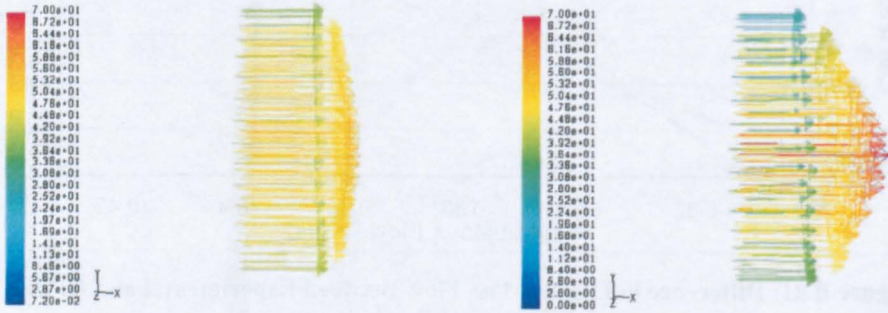


Figure B.23: Velocity profiles at the Exit of the Detuner for 4d on the left and 1d on the right

It is clearly shown that for four engine nozzle diameters distance the flow achieves a higher level of mixing along the detuner. This confirms the findings related to the large scale test facility which have been described in Chapter 6.

Another plot which can help to identify the level of mixing achieved along the detuner for different engine-detuner distances is the velocity vectors.

Figure B.23 shows a velocity vector plot at the exit of the detuner for the CFD models 4d (left) and 1d (right). The model with a larger distance between the engine end the detuner shows more uniform velocity at the exit of the detuner. Accordingly the primary and the secondary flows have achieved more uniform conditions.

Following these results it is also interesting to see how the CFD models predict the flow at the Accommodation Region.

It is also clear from Figure B.20 that the entrainment ratio increases with the engine power setting. Therefore the plot at the Accommodation Region is referred to two models having the same engine-detuner distance but different power settings (50% and 80%).

Figure B.24 shows the static pressure drop at the Accommodation Region for the two different engine power settings.

Similar trends were also found by Sapp and Netzer (Sapp and Netzer 1978) and Laidlaw (Laidlaw 1950).

It is also seen that the higher mass flow going through the detuner for the 80 % (according with cell entrainment ratio) allows for a higher static pressure drop.



Consequently at this level of accuracy, the CFD code is able to represent the flow at the Accommodation Region. Also the plot of Mach number at the Accommodation Region for the two power settings confirms the trends described above (Gullia et al. 2005).

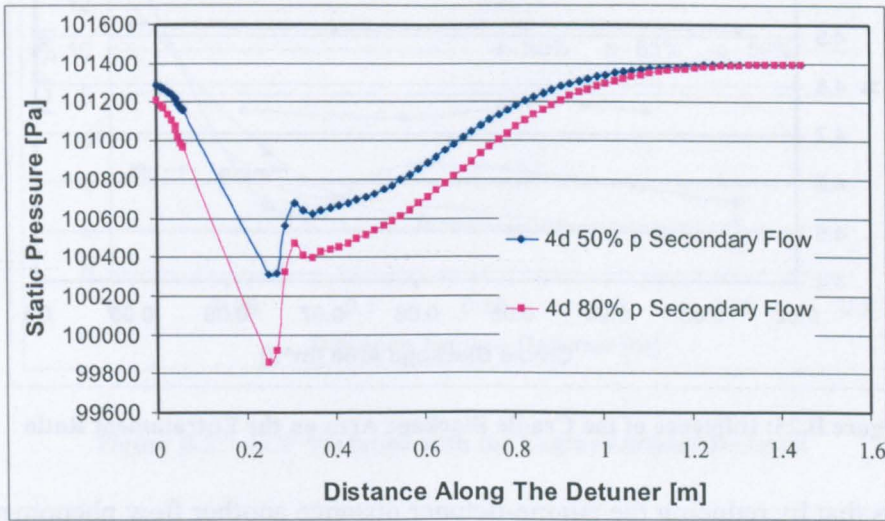


Figure B.24: Static Pressure Drop at the Accommodation Region

Another interesting result in terms of cell entrainment ratio is the influence that the cradle may have on it. Figure B.25 shows that the entrainment ratio is not affected by the cradle blockage area.

This is probably due to the low velocity inside the small scale test bed facility and therefore such a result can not be straightforwardly extended to all the engine-cell configurations. However, in Chapter 6 (paragraph 6.3.4) the influence of the cradle for the large cells has been discussed. From those results it is possible to see that the cradle does not significantly affect the cell entrainment ratio for those different configurations.

These conclusions could be extremely useful to CFD users.

Indeed, they allow one to neglect all those particulars concerning the cradle frame which would otherwise make the model too complicated.

Figure B.26 shows the comparison between the load measured by the load cells outdoor and at different engine-cell configurations. The difference between the outdoor line and the other single lines represents the amount of the thrust correction factors needed for the different configurations.

Such trends show that the difference between the outdoor and indoor load measured increases as engine detuner distance reduces. This could seem a bit misleading. Indeed, up to now, most of the thrust correction factors have been found to be proportional to the cell entrainment ratio. But at the same time from both experiments and CFD results, the entrainment ratio came out to be inversely proportional to the engine-detuner distance (Figure B.27).

This appears to agree with the experimental analysis conducted by K A Campbell in the Glen test house and summarize by (Ashwood 1984).

Even at that time the thrust correction factors increased as engine-detuner gap reduced. Furthermore, Ashwood analysis (Ashwood 1984) also shows a TCF peak for a very short gap similar to that represented in Figure B.27.

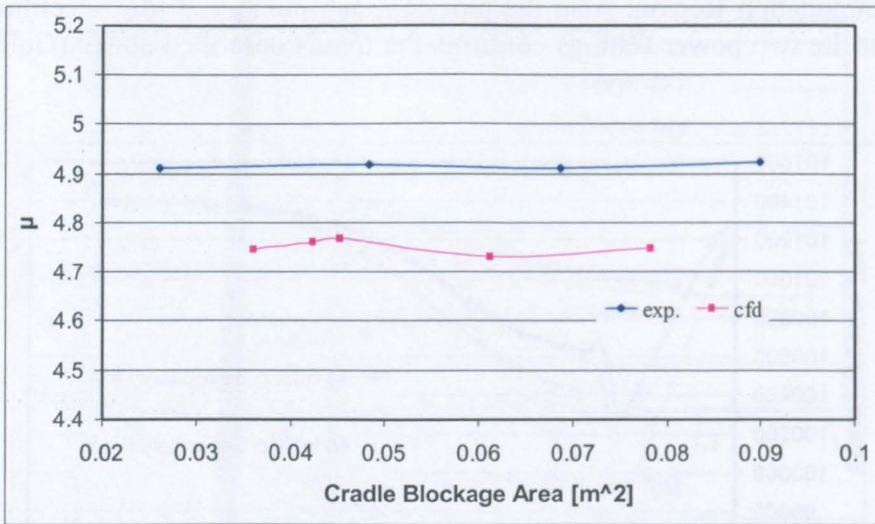


Figure B.25: Influence of the Cradle Blockage Area on the Entrainment Ratio

This means that by reducing the engine-detuner distance another flow phenomena, not related with the secondary flow, comes to play a fundamental role.

Usually the greatest thrust correction factor is the intake momentum drag (paragraph 4.5.4). It is possible with the measurements available (all the analysis is referred to 2004) it is possible to compute this as a function of the engine-detuner distance.

The corresponding plot is shown in Figure B.28.

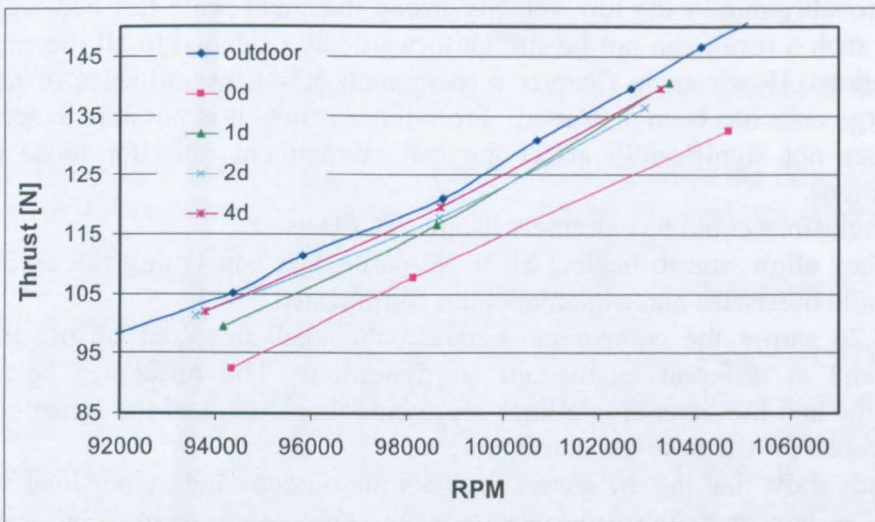


Figure B.26: Load Measured By the load Cells Indoor and Outdoor

This plot confirms that both CFD and experiments predict an increase in IMD by increasing the engine-detuner distance, which also means increasing the entrainment ratio. This is also the expected trend for the effect of intake momentum drag.

The cradle drag is computed by nine velocity measurements (Figure B.15) and by knowing its drag coefficient and its blockage area (equation (b.13)).

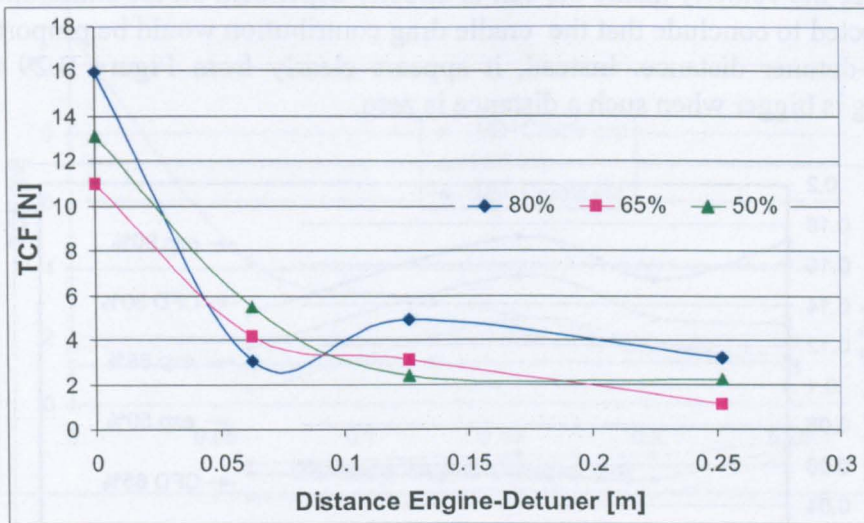


Figure B.27: TCF Variation with the Engine-Detuner Distance

$$D_{Cradle} = cd \frac{1}{2} \rho v^2 A_{ref} \quad (b.13)$$

The same method has been used for computing the cradle drag using CFD. This is mainly because a direct calculation of the force acting on the movable part of the cradle cannot be made at this stage due to the inaccuracy of the grid around it.

The trends related to the cradle drag as a function of the engine-detuner distance are shown in Figure B.29 which includes both experimental and CFD results.

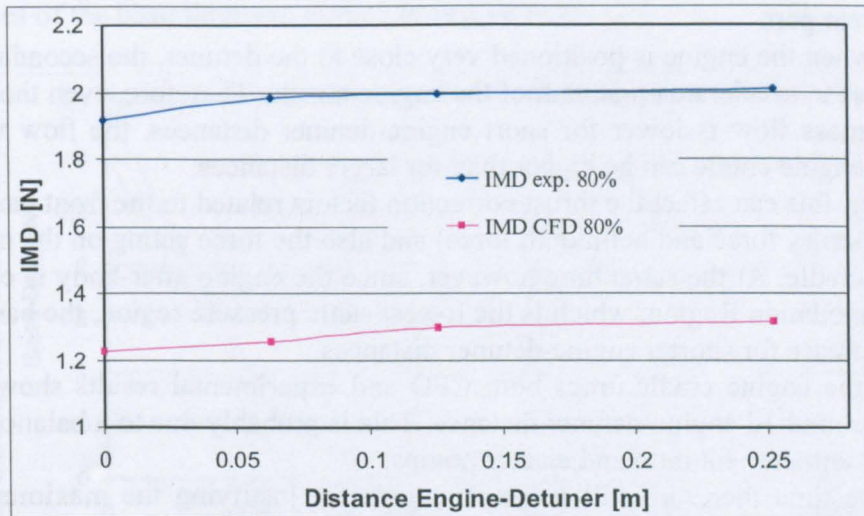


Figure B.28: Intake Momentum Drag Variation with the Engine-Detuner Distance

The computational results still give almost the same trend when compared with the experimental.

These trends show a characteristic which was not expected before.

Indeed, since the velocity inside the cell is directly dependent on the entrainment ratio it was expected to conclude that the cradle drag contribution would be proportional to the engine-detuner distance. Instead, it appears clearly from Figure B.29 that the cradles drag is bigger when such a distance is zero.

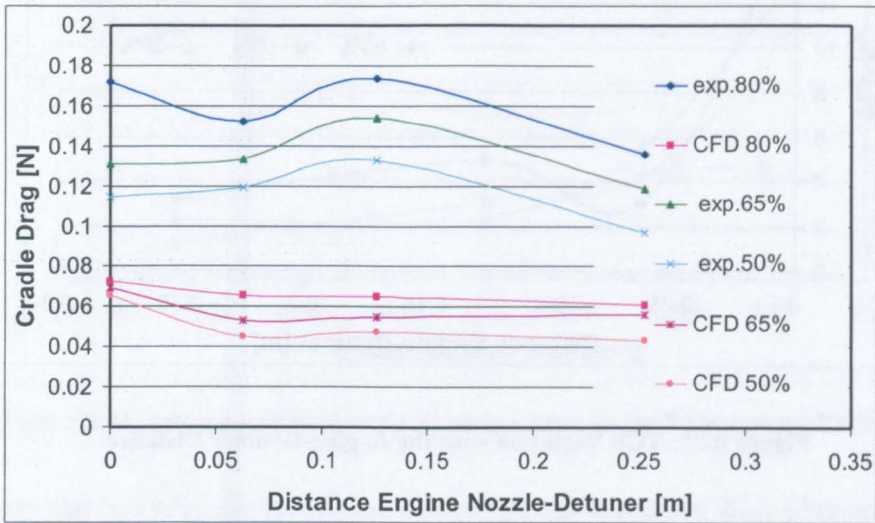


Figure B.29: Cradle Drag Comparison Between Experimental and Computational Results

An explanation for the cradle trends and for the trend of the thrust correction factors, which both increase by reducing the engine detuner distance, can be found if the engine-detuner ejector pump effect is taken into account (Ashwood 1984).

As described in the literature review (paragraph 2.2) around the engine after-body the secondary flow starts to accelerate as consequence of the low pressure region at the Accommodation Region.

For the usual engine-detuner distances such an acceleration is felt by the engine only around its rear part.

However, when the engine is positioned very close to the detuner, the secondary flow can also start to accelerate up-stream of the engine nozzle. Therefore, even though the secondary mass flow is lower for short engine-detuner distances, the flow velocity around the engine cradle can be higher than for larger distances.

Accordingly, this can affect the thrust correction factors related to the front part of the engine (pre-entry force and bellmouth force) and also the force acting on the movable part of the cradle. At the same time however, since the engine after-body is closer to the Accommodation Region, which is the lowest static pressure region, the base force will also increase for shorter engine-detuner distances.

Regarding the engine cradle drags both CFD and experimental results show also a minimum around 1d engine-detuner distance. This is probably due to a balance of the two effects, entrainment ratio and ejector pumps.

At the same time there are still no explanations for justifying the maximum peak around the 2d engine-detuner distance.

However, by itself the cradle drag is not able to explain the high TCF needed at 0d. Indeed, if the intake momentum drag and the cradle drag are added together, there still is a quite large correction to be identified at such a distance.

Figure B.30 shows this difference.

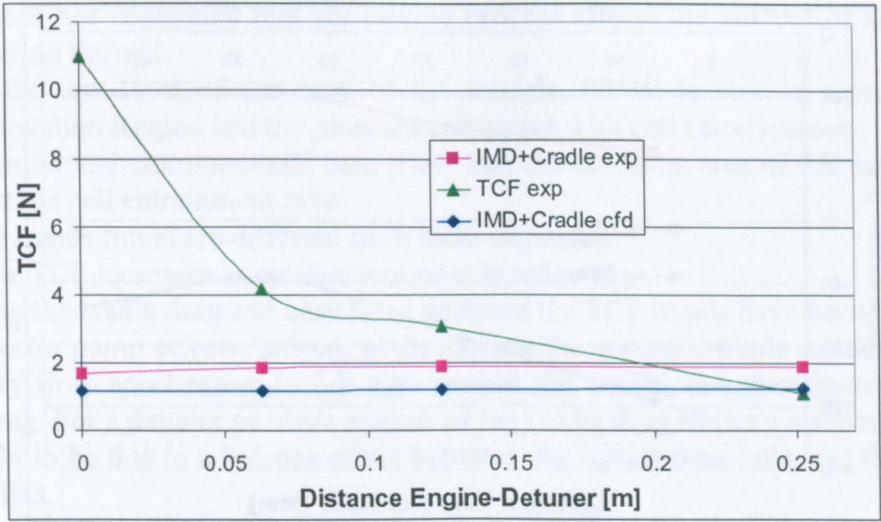


Figure B.30: Unmeasured TCF

Unfortunately, in 2004 it was not possible to measure experimentally more parameters and therefore to calculate further thrust correction factors.

However since the beginning attention was oriented to the suction force acting on the engine after-body as a possible explanation for the trends of the thrust correction factors.

Indeed, more likely, the engine gets closer to the detuner the larger the suction force acting on it.

Therefore at that time a CFD analysis for the base force was attempted though the model accuracy was not so good. The aim was to show the trends of the base force with the engine-detuner distance and understand the difference in magnitude.

Several pressure values have been extracted from the engine nozzle surface and the base force has been computed by equation (6.11)).

The values of the base force are plotted in Figure B.31.

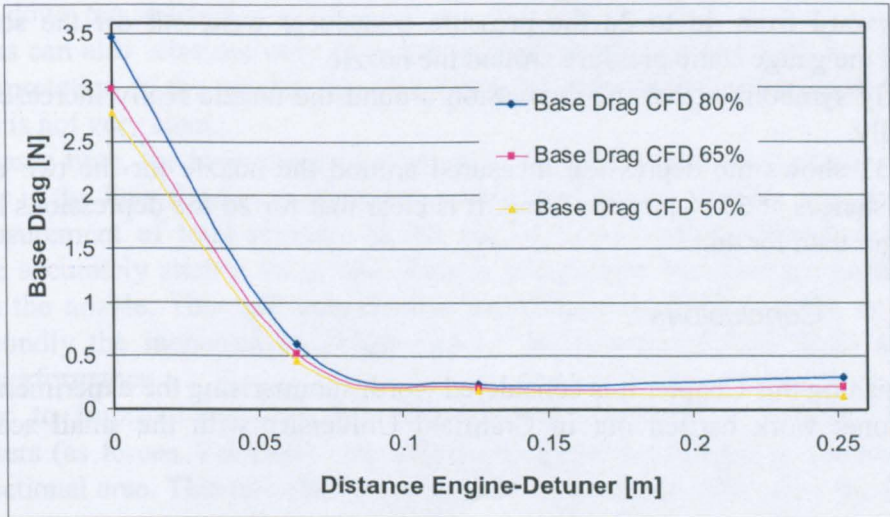


Figure B.31: CFD Analysis of the Base Force

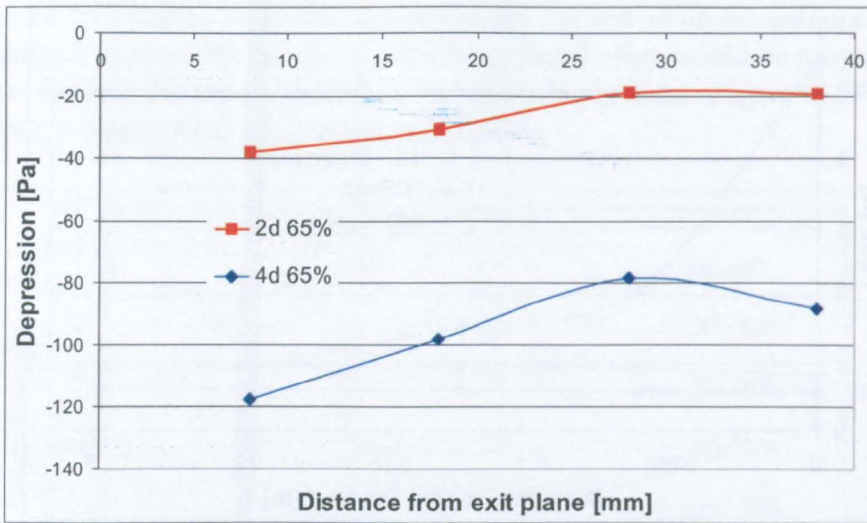


Figure B.32: Depression Measured around the Nozzle

The base force trends are almost the same as those representing the total thrust correction factors, having the maximum at 0d and decreasing with increasing distance. Such trends fit the difference between the total thrust correction factors very well and match those already measured. Furthermore, it is possible to estimate the sudden increase of base force close to 0d to be around one order of magnitude bigger than that for the other distances

Therefore, by reducing the engine-detuner distance, the force acting around the engine afterbody increases and becomes the larger of the thrust correction factors.

In order to investigate such a phenomenon in 2005, four static pressure probes were set around the nozzle (Figure B.11).

The first results publicized in Elysee thesis (Elysee 2005) confirm the large increase in base force as the engine-detuner distance is reduced.

At the moment only two distances have been checked (2d and 4d).

However, the results are promising. During the measurement when the detuner was moved forward from 4d to 2d the pressure transducer went out off the scale for measuring the gauge static pressure around the nozzle.

This clearly symbolizes that the depression around the nozzle really increases quite dramatically.

Figure B.32 shows the depression measured around the nozzle for the two engine-detuner distances at 65 % power setting. It is clear that for 2d the depressions is three times bigger than for 4d.

## B5. Conclusions

Before finishing this Chapter it is considered worth summarising the experimental and computational work carried out in Cranfield University with the small scale test facility.

Computational and experimental data confirm that the entrainment ratio increases proportionally with the engine-detuner distance.

This flow behaviour can be related to the level of mixing achieved along the detuner between primary and secondary flows (as is shown in Chapter 6). Indeed, it has been seen that by increasing the engine-detuner gap the level of mixing increases as well.

Therefore it has confirmed that the mixing process affects the amount of secondary flow entering the cell.

Despite the low level of accuracy of the models, Fluent is able to represent the Accommodation Region and the plots are consistent with cell aerodynamics.

Experimental and computational data show that the blockage area of the cradle does not affect the cell entrainment ratio.

The TCF trends found are different from those expected.

In fact the TCF increases as entrainment ratio is reduced.

Following the cradle drag and base force analyses the TCF trends have been attributed to the ejector pump effects. Indeed, when moving the engine towards the detuner, the secondary flow acceleration is felt also around the cradle, therefore increasing the cradle drag. For a detuner position around 1d the cradle drag shows a minimum which is thought to be due to a balance effect between the entrainment ratio and the ejector pump effect.

Furthermore, if the engine is positioned closer to the detuner, the suction force is much stronger as therefore is the base force. Actually, from the CFD analysis the base force at 0d seems to have a much bigger impact on the thrust correction factors than the rest of the TCF's (1 order of magnitude greater).

Following the above conclusions, the commercial CFD software used is able to predict the experimental trends. Therefore, the computational model can now be improved further so to achieve a higher level of accuracy.

The possibility of working with a small scale test bed facility may give the opportunity to analyse several flow phenomena arising inside the cell. This is especially the case if the test cell allows parametric study like the Cranfield model test cell.

However an important point has to be stated.

Due to cell and engine characteristics, the flow parameters are very small until the analysis is taken to the limit (engine nozzle plane and detuner entry plane coplanar, for example). This makes flow measurement very difficult. Indeed, very accurate instrumentation is needed to pick up all the flow characteristics.

Therefore, quite often doubts can arise about the quality of such measurements, slowing down the analysis.

Problems can also arise not only from the measurements point of view but also from the interpretation of the results. In some cases the differences are so small that their analysis is not very clear.

At the same time, the instrumentation has to satisfy the requirement of not being too intrusive in the flow field as to invalidate engine performance results. One example is the measurement of total pressure at the engine nozzle plane. Indeed, in order to measure accurately such a value and identify the profile, the pressure probe should traverse the nozzle. This will compromise the structural stability of the nozzle first and secondly the increased blockage area of the instrumentation could affect the engine performance.

In order to improve partially this situation and therefore to increase the flow parameters (as forces, velocities, pressures) a suggestion could be to reduce the cell cross sectional area. This possibility is within the opportunity offered by the Cranfield facility.

However, in doing this, secondary flow phenomenon (as vortex ingestion and recirculation) can arise inside the cell and compromise the whole measurements.

The situation is tricky and therefore, each parameter has to be taken into account quite carefully.

### APPENDIX C. Accommodation Region Analysis for Different Engine Power Setting

Following, the results obtained from the CFD analysis at the Accommodation Region for different engine power settings are compared with the the results obtained from the analytical model (paragraph 5.2.4)

These results together with those already shown in paragraph 6.3.4 help the validation of the Analytical Method procedure described in Chapter 5.

In the following plots, the blue line represents the Analytical Model results while the red line represents the CFD results (Hagues 2005)

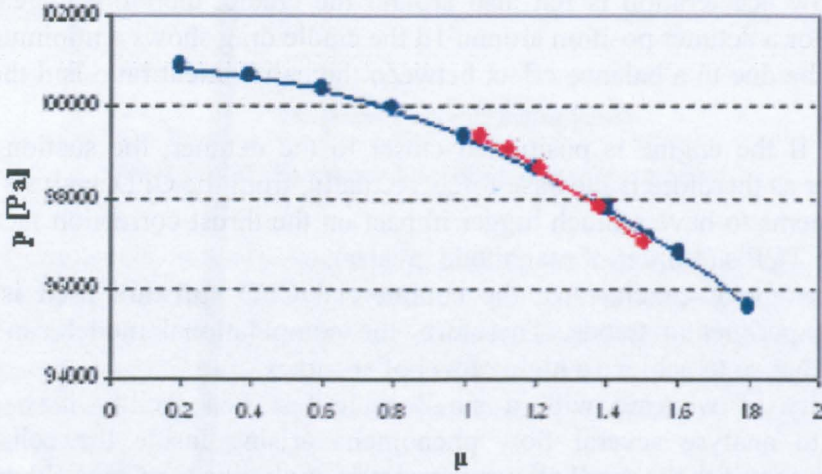


Figure C. 1: Accommodation Region Characteristic (Engine ndmf = 2596.34)  
(Hagues 2005)

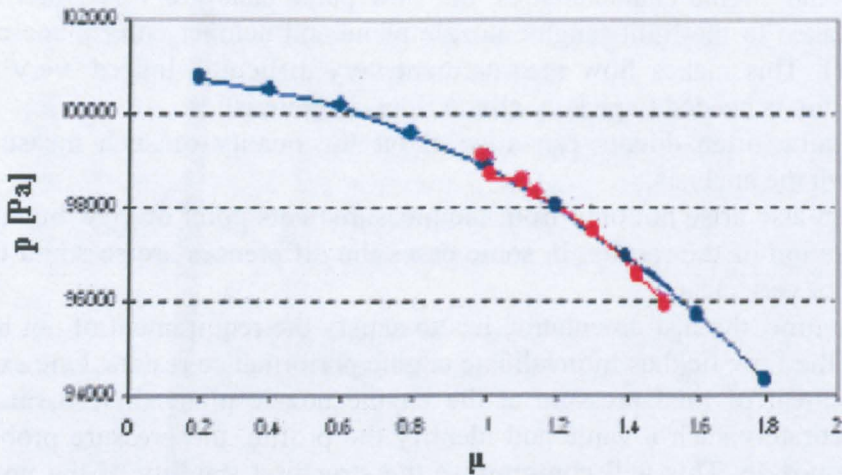


Figure C. 2: Accommodation Region Characteristic (Engine ndmf = 2844.88)  
(Hagues 2005)



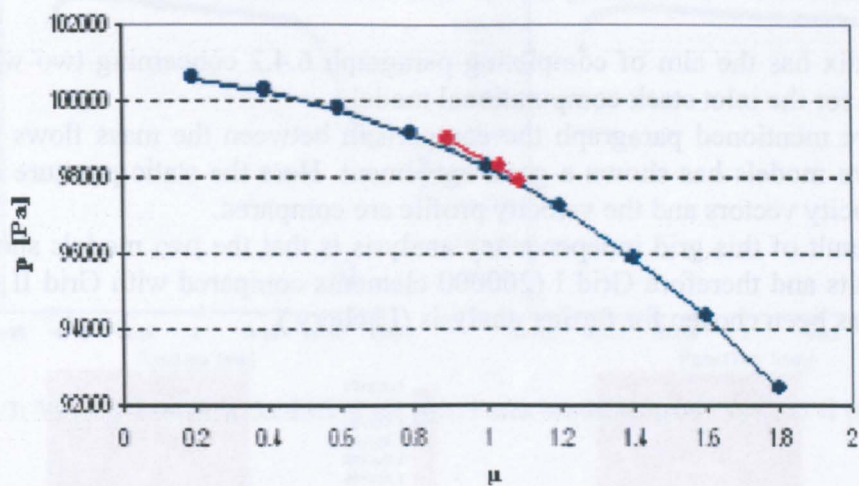


Figure C. 3: Accommodation Region Characteristic (Engine ndmf = 3006.58)  
(Hague 2005)

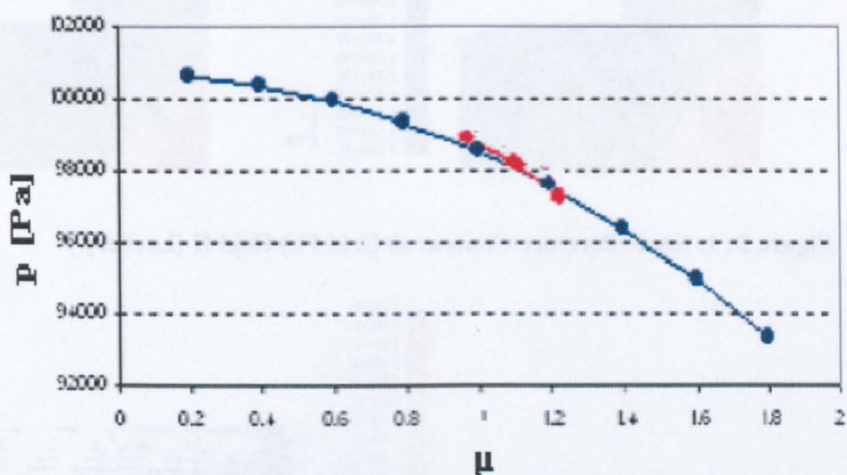


Figure C. 4: Accommodation Region Characteristic (Engine ndmf = 3126.94)  
(Hague 2005)

## APPENDIX D. Grid Analysis for the Inlet Stack

This appendix has the aim of completing paragraph 6.4.2 concerning two with grid comparison for the inlet stack computational model.

In the above mentioned paragraph the comparison between the mass flows pointed from the two models has shown a good agreement. Here the static pressure contour and the velocity vectors and the velocity profile are compared.

The final result of this grid independency analysis is that the two models show very similar results and therefore Grid I (200000 elements compared with Grid II 400000 elements) has been chosen for further analysis (Lachery )

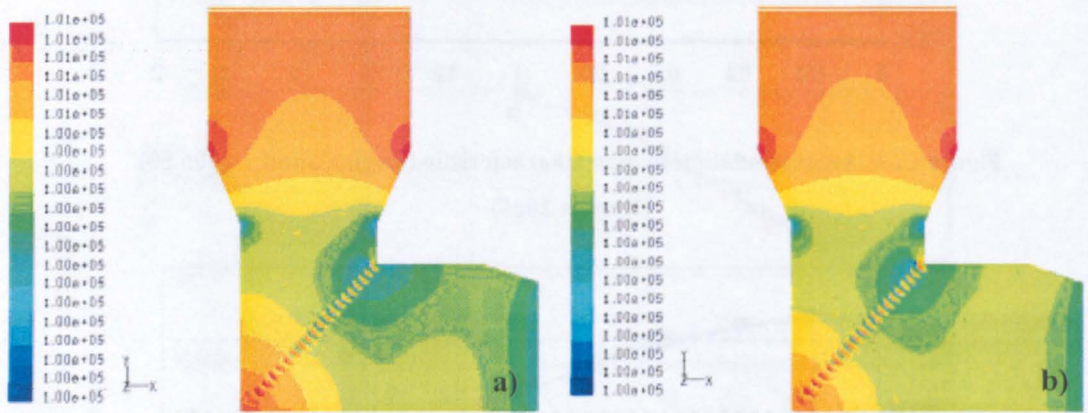


Figure D. 1: Static Pressure Contour a) Grid I b) Grid II (Lachery )

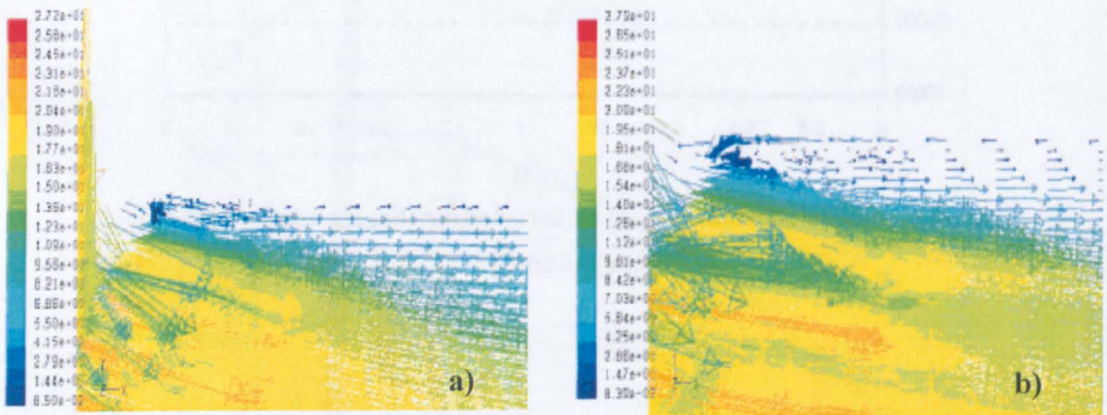


Figure D. 2: Velocity Vector a) Grid I b) Grid II (Lachery )

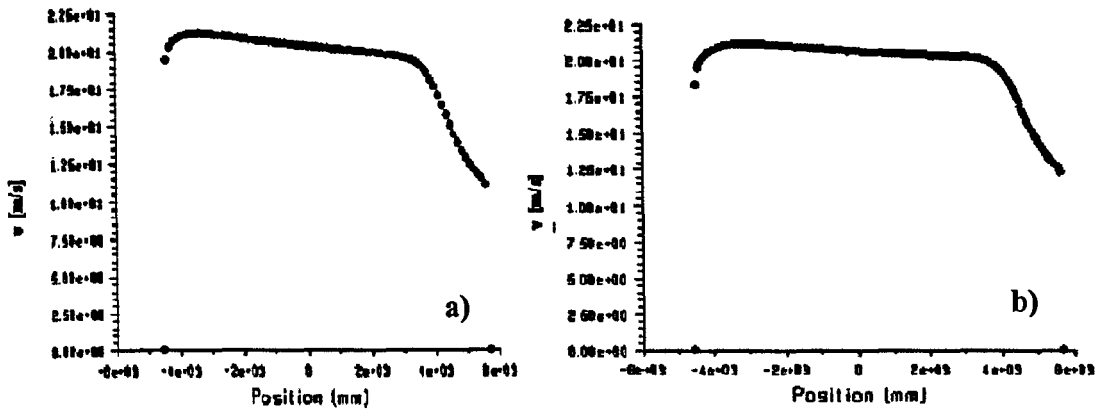


Figure D. 3: Velocity Profile at the Exit of the Inlet Stack Model a) Grid I b) Grid II ((Lachery ))